Development of a Sample Preparation Platform for Bacterial and Viral Pathogens

by

AARON D. J. A. EVANS

This thesis was submitted to the

College of Engineering Design and Physical Sciences, Brunel University London

upon the completion of research for the degree of Doctor of Philosophy

March 2022

Supervisors:

Dr. Ruth Mackay

Prof. Wamadeva Balachandran

I. Abstract

Molecular diagnostics plays a crucial role in reducing the impact of infectious diseases on a population. A key stage during the process is sample preparation, viewed as a bottleneck in the field of diagnostics. There are currently no standalone sample preparation systems able to process a range of sample types in a streamlined and reliable manner away from specialised infrastructure. The contribution to knowledge, described in this thesis, demonstrates a proof-of-concept sample preparation platform that was designed for deployment in the developed and developing world. The focus was placed on processing cloacal swab samples collected from chickens, and respiratory swab samples collected from humans, for the amplification and detection of poultry related infections and SARS-CoV-2, respectively, in a separate platform.

A lysis protocol (the boiling method) was tested on cloacal samples before conducting both PCR amplification and colorimetric LAMP. 100 mg of a cloacal sample was suspended within 200 µL of a buffer, which was then incubated at 92 °C for 15 minutes. Performing the boiling method in a PBS buffer was found to offer the highest DNA yield (182 ng/µL), while the highest A280/260 ratio was found with the TE/PK buffer (1.06). Both the PCR and LAMP methods showed successful amplification of *E. Coli* following a 1:10 dilution step.

A sample preparation platform was developed to accept cloacal and respiratory (NP and OP) samples on a swab, lyse the cells using thermal lysis, and dispense 1 – 3 µL droplets into PCR tubes. As it was not possible to produce droplets within this range using standard dripping configurations, an EHD module was employed to overcome the effects of surface tension at a metallic capillary. The platform was designed using Solidworks 2020, and optimised using COMSOL simulations. The platform was then fabricated using 3D printing techniques and tested.

The platform demonstrated capabilities of performing cell lysis in a single thermal heating step at 92 °C. Droplets with a volume of 1.3 µL were dispensed on-demand, 86% smaller than possible with standard dripping configurations. The multidisciplinary work presented in this thesis reduced the complexity of sample preparation into a ready-to-assemble platform. Although universal sample preparation has yet to be fully achieved, the research conducted in this thesis may offer the first step towards the realisation of this goal.

II. Acknowledgements

I am thankful to the Engineering and Physical Sciences Research Council, UK (EPSRC, UK) for funding the research project and supporting multidisciplinary research.

I would like to express my gratitude, first and foremost, to my primary supervisor Dr. Ruth Mackay for her support and guidance throughout my research. Her wisdom, guidance and scientific expertise have been immensely valuable. For that, I am truly thankful. I would also like to thank my secondary supervisor, Professor Wamadeva Balachandran. His knowledge and insight have motivated me during my academic research.

I would like to offer my special thanks to Mr. John Wenn and Mr. Kevin Robinson from the Mechanical and Aerospace Department, and Mr. Paul Josse and Mr. Doug Rosario from the Design & Manufacturing Department. Your insight was instrumental in defining the path of my research. For this, I am extremely thankful.

Assistance provided by the Electronic & Computer Engineering Systems was greatly appreciated. I wish to acknowledge the help provided by Mr. Gopal Jeyasundra, Mr. William Schkzamian, Mr. Michael Lateo and Mr. Emile Thomas. You provided me with the right tools I needed to choose the right direction to successfully complete my thesis.

I would like to thank various people from the Biosciences Department; Dr. Ashley Houlden, for his valuable and constructive suggestions during the development of the sample preparation protocol; and Dr. Darren McCabe and Dr. Freya Crawford, for their assistance throughout my study.

The successful completion of this thesis would not have been possible without Dr. Manoharanehru Branavan and Dr. Angel Naveenathayalan. I am thankful for your insightful advice and unparalleled support.

III. Declaration

I, Aaron Evans, hereby declare that the work presented in this thesis entitled, “Development of a Sample Preparation Platform for Bacterial and Viral Pathogens” was carried out by myself at Brunel University London, College of Engineering Design and Physical Sciences, and that all the sources I have used or quoted have been indicated or acknowledged by means of completed references

_____

March 2022.

Aaron Damani Jovelle Anthony Evans

IV. Contents

V. List of Figures

VI. List of Tables

VII. Abbreviations

Term	Description
µTAS	Micro Total Analysis Systems
AIV	Avian Influenza Virus
AN	Anterior nares
APEC	Avian pathogenic *Escherichia coli*
BAL	Bronchoalveolar lavage
BME	Beta-mercaptoethanol
CDC	Centers for Disease Control and Prevention
cDNA	Complimentary Deoxyribonucleic Acid
CFD	Computational Fluid Dynamics
CPA	Cross Priming Amplification
CsCl	Caesium chloride
ddPCR	Digital droplet Polymerase Chain Reaction
DH_2O	DNase/RNase-Free Distilled Water
DI H_2O	Deionized Water
DNA	Deoxyribonucleic Acid
dNTP	Deoxynucleotide triphosphate
DOD	Drop-on demand
dsDNA	Double-stranded Deoxyribonucleic Acid
EDTA	Ethylenediaminetetraacetic acid
EPSRC	Engineering and Physical Sciences Research Council
EtBr	Ethidium Bromide
ExPEC	Extra-intestinal pathogenic *E. coli*
FDM	Fusion deposition modelling
FEA	Finite Element Analysis
FINA	Filtration of nucleic acids
FoS	Factor of Safety
FTA	Flinders Technology Associates
GITC	Guanidinium Thiocyanate
HCL	Hydrochloride
HDA	Helicase Dependant Amplification
HIV	Human immunodeficiency virus
HPV	Human papilloma virus
IBD	Infectious bursal disease virus
IBV	Infectious bronchitis virus
LAMP	Loop-Mediated Isothermal Amplification
LFD	Lateral Flow Device
LLE	Liquid-liquid extraction
LOD	Limit of Detection
LSE	Liquid-solid extraction
MG	*Mycoplasma gallisepticum*
MgCl	Magnesium chloride
mRNA	Messenger RNA
MRSA	*Methicillin-resistant S. aureus*
MTN	Mid-turbinate nasal
NA	Nucleic Acids

NAAT	Nucleic acid amplification testing
NPA	Nasopharyngeal aspirates
NASBA	Nucleic Acid Sequence-Based Amplification
NDV	Newcastle disease virus
NMP	No moving parts
NP	Nasopharyngeal
OP	Oropharyngeal
PBS	Phosphate-buffered saline
PC	Polycarbonate
PCI	Phenol–chloroform–isoamyl
PCR	Polymerase Chain Reaction
PDMS	Polydimethylsiloxane
PEG	Polyethylene glycol
PETG	Polyethylene terephthalate glycol
PMMA	Poly(methyl methacrylate)
POCT	Point-of Care-Testing
PPE	Personal protective equipment
PSR	Polymerase Spiral Reaction
qPCR	quantitative Polymerase Chain Reaction
qRT-PCR	Quantitative reverse transcription Polymerase Chain Reaction
RCA	Rolling Circle Amplification
RNA	Ribonucleic Acid
RPA	Recombinase Polymerase Amplification
rRNA	Ribosomal Ribonucleic Acid
RT-LAMP	Reverse Transcription Loop-Mediated Isothermal Amplification
RT-PCR	Reverse Transcription Polymerase Chain Reaction
SARS-CoV-2	Severe acute respiratory syndrome coronavirus 2
SBSE	Stir-bar sorptive extraction
SCD	Sample collection device
SDA	Strand Displacement Amplification
SDS	Sodium dodecyl sulphate
SLA	Stereolithography
SPD	Sample preparation device
SPE	Solid-Phase Extraction
SPME	Solid-phase microextraction
ssRNA	Single-stranded Ribonucleic Acid
STI	Sexually transmitted infections
TAT	Turn-around time
TB	Tuberculosis
TE	Tris-EDTA buffer solution
TE/PK	Tris-EDTA and proteinase K solution
TMA	Transcription Mediated Amplification
TPU	Thermoplastic polyurethane
tRNA	Transfer RNA
UK	United Kingdom
USA	United States of America
VoF	Volume of Fluid
VTM	Viral transport medium
WHO	World Health Organisation

VIII. Symbols, Subscripts and Subscripts

Prefixes for Powers of 10 used with Metric Units						
Prefix	**nano-**	**micro-**	**milli-**	**centi-**	**kilo-**	**mega-**
Abbreviation	n	μ	m	c	k	M
Power	10^{-9}	10^{-6}	10^{-3}	10^{-2}	10^{3}	10^{6}

Standard Symbols		
Symbol	**Description**	**Unit**
A	Area in square metres	m^2
D	Diameter	m
Di	Diodicity	(-)
E	Voltage	V
F	Force	N
F_f	View factor between the two surfaces	(-)
I	Current	A (*Amps*)
L	Length	m
$\dot{M}$	Momentum flow rate	kg·m/s
P	Power	W
$\dot{Q}$	Volumetric Flow rate	m^3/s or L/s
R	Resistance	Ω (*ohms*)
Re	Reynolds Number	(-)
T	Temperature	°C or K
U	Velocity	m/s
V	Volume in cubic meters	m^3 or L
W	Droplet Diameter at the neck	m
Z	Distance between needle and grounded Electrode	m
a	Acceleration	m/s^2
c_p	Specific heat capacity at constant pressure	J/kg K
g	Gravitational constant (≈9.81)	m/s^2
h_c	Convective heat transfer coefficient	W/m^2K
k	Stiffness	N/m
m	Mass in kilograms	kg
$\dot{m}$	Mass flow rate	kg/s
p	Pressure	Pa
r	Radius	m
s	Stroke length of the syringe pump	m
t	Time or time step in seconds	s
y	Displacement	m

Subscripts		
Symbol	**Description**	**Unit**
F_e	Force (electrostatic)	N
F_g	Force (gravity)	N
F_{st}	Force (surface tension)	N
T_{AVG}	Average temperature across the heating system	°C
T_s	Temperature (surface)	°C
T_f	Temperature (fluid)	°C
T_0	Initial Temperature	°C
T_t	Final Temperature	°C
T_a	Temperature of surface A	K
T_b	Temperature of surface B	K
p_f	Pressure change within a Tesla valve (forward flow)	Pa
p_r	Pressure change within a Tesla valve (reverse flow)	Pa
p_i	Pressure within a droplet	Pa
p_0	Ambient pressure	Pa

Greek Symbols		
Symbol	**Description**	**Unit**
E_0	Electric Field Strength	V/m
Φ_{net}	Net heat generated	J
$\dot{\Phi}_{cond}$	Rate of heat energy transfer (conduction)	W
$\dot{\Phi}_{conv}$	Rate of heat energy transfer (convection)	W
$\dot{\Phi}_{rad}$	Rate of heat energy transfer (radiation)	W
α	Temperature coefficient of resistivity	$°C^{-1}$
γ	Surface Tension	N/m
δ	Deflection	m
ε	Emissivity	(-)
θ	Contact angle	°
κ	Thermal conductivity	W/mK
μ	Dynamic Viscosity	Pa·s
ν	Poisson's Ratio	(-)
π	Pi (≈3.14159)	(-)
ρ	Density	kg/m^3
ρ_R	Resistivity	Ω·m
ρ_{R0}	Resistivity at T_0	Ω·m
ρ_{Rt}	Resistivity at T_t	Ω·m
σ_{SB}	Stefan-Boltzmann constant	W/m^2K^4
σ_S	Stress	Pa
σ_{ys}	Yield stress	Pa
σ_{vM}	von Mises stress	Pa
$\dot{\phi}_{cond}$	Heat Flux (conduction)	W/m^2
$\dot{\phi}_{conv}$	Heat Flux (Convection)	W/m^2
τ	Shear Rate	s^{-1}
τ_S	Tangential (shear) stress	Pa

1. Introduction

1.1. An Introduction to Molecular Diagnostics

Infectious diseases exert a heavy impact on economic, veterinary and human health. Viral pathogens can be viewed as a major threat, due to the high rate of mutation and the ability to adapt to new hosts. While less potent, a large number of pathogens are bacterial in nature, possessing the ability to adapt and increase in drug resistance if treated inaccurately [1].

An accurate diagnosis of a disease is the first and most crucial step towards reducing the effect of a disease on a population. Traditional diagnostic procedures involve a study of an individual's medical history or a physical examination, typically followed by a differential diagnosis where potential causes are evaluated until the most likely cause remains. This process can take a long time, greatly delaying treatment [2]. As an alternative, pattern recognition may be utilised to identify a disease through the recognition of common clinical symptoms. In this instance, the chance of a misdiagnosis is increased should the symptoms be non-specific, or should the infected individual be asymptomatic [3]. For both of these cases, trained healthcare workers are required to recognise symptoms and interpret results.

Molecular diagnostics plays a key role in the detection, characterisation and quantification of infectious diseases, as well as the monitoring of treatment [4]. Many treatments are specific and require a fast and accurate diagnosis to be effective. The approach can offer a reliable alternative or addition to the aforementioned techniques, yielding definitive results before treatment is offered. Molecular diagnostics usually involves the testing of a sample collected from the individual, which is then subjected to methods such as microbiological culturing, blood chemistry testing, immunoassays and flow cytometry, among others [5]. While routine in laboratory-based environments, these methods are not suitable in low-resource settings lacking in trained personnel, reliable or sufficient power supplies, or refrigeration [6]. While several diagnostic tests are available, they are either costly or inaccessible, particularly for patients in the developing world [7].

On-site molecular diagnostics has been suggested as a method to apply diagnostics on a larger scale, omitting the prerequisite of large laboratory-based analysers, skilled technicians, storage facilities, and a high quantity of reagents and consumables [8]. Recent innovations in technology have led to the conception of point-of-care-testing (POCT), where diagnostic tests are performed by the patient, which has played an important role in the detection and tracking of diseases at an early stage [9]. POCT can be performed either in small benchtop analysers or handheld devices, each of which can automate or omit some of the more demanding manual processes involved with preparing a sample

for analysis, decreasing the user interactivity while increasing the portability [10]. This is particularly beneficial as it allows for self-testing to be conducted, which can alleviate pressure on healthcare professionals, while allowing for testing to be conducted on patients who are unable to travel to specialised facilities. In recent years, POCT has become a widely accepted alternative to traditional laboratory-based diagnostics [9]. Overall, the successful implementation of POCT can greatly improve clinical and economic outcomes.

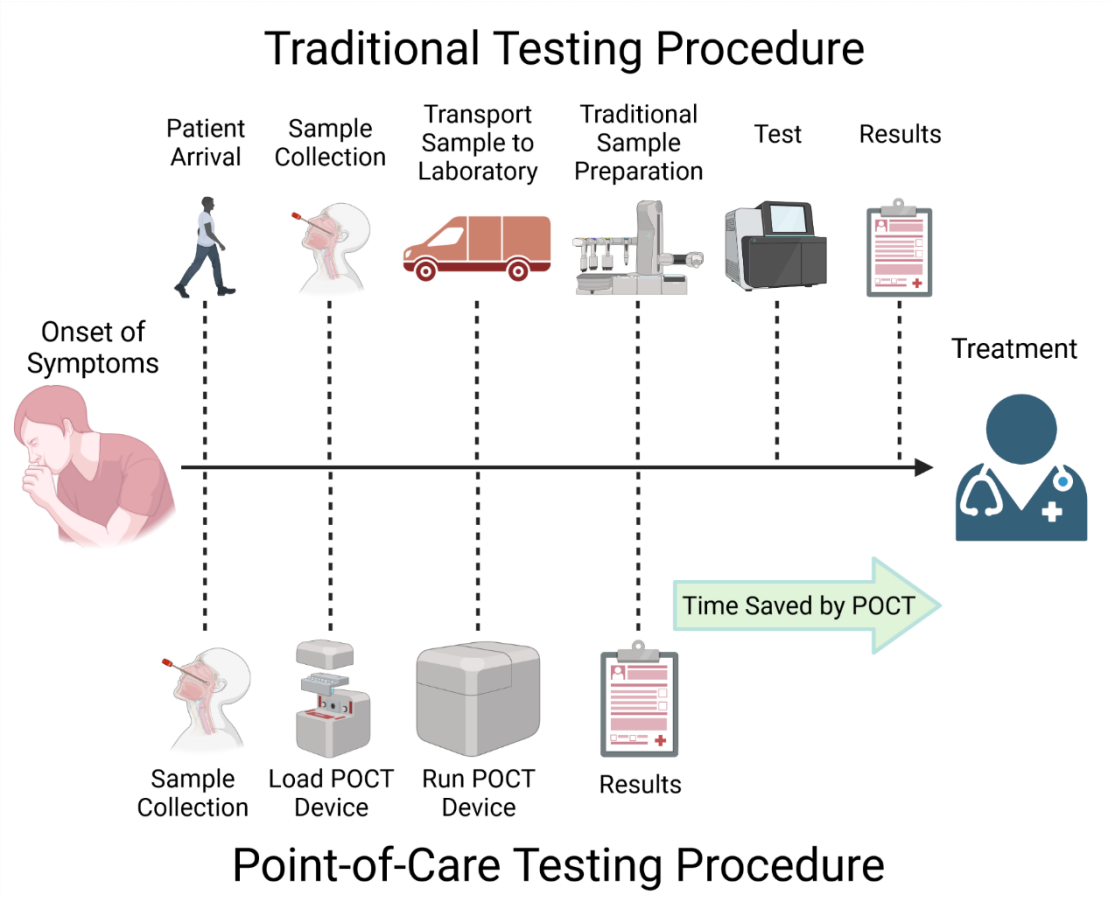

Figure 1.1 – A diagram comparing the traditional testing procedure with point-of-care-testing [11] (Created with BioRender.com)

1.2. An Introduction to Sample Preparation

Between collection and analysis, a raw sample commonly undergoes a preliminary treatment process, or series of processes, to convert it into usable material and improve the accuracy of the results. This is known as sample preparation. Sample preparation is necessary when a sample either cannot be or gives low quality or unreliable results when analysed directly [12]. While specific sample preparation processes may differ between specific samples types, the procedure typically involves the removal of inorganic contaminants and inhibitors and the isolation and concentration of the target analyte. In some cases, the rheology of the sample may also be adjusted, to transform the sample into a less viscous form [13].

Sample preparation plays a crucial role in molecular diagnostics, and has been a long-time bottleneck of the analytical process, with many in the field seeking more convenient and cost-effective methods [14,15]. Conventional sample preparation techniques are labour intensive and time consuming, typically taking 70 – 80% of the total analysis time [16-18]. While the development of automated and high-throughput platforms has somewhat addressed the problem that is sample preparation, these solutions are expensive and restricted to centralised laboratories, and as a result, a reliable and standardised approach compatible with POCT remains lacking [13]. An ideal approach would prepare a sample for analysis in as few steps as possible, to reduce the processing time as well as the number of potential sources of sample contamination or degradation. While recent trends have trended towards the simplification and miniaturisation of sample preparation, an approach that meets the demands of POCT remains elusive [15].

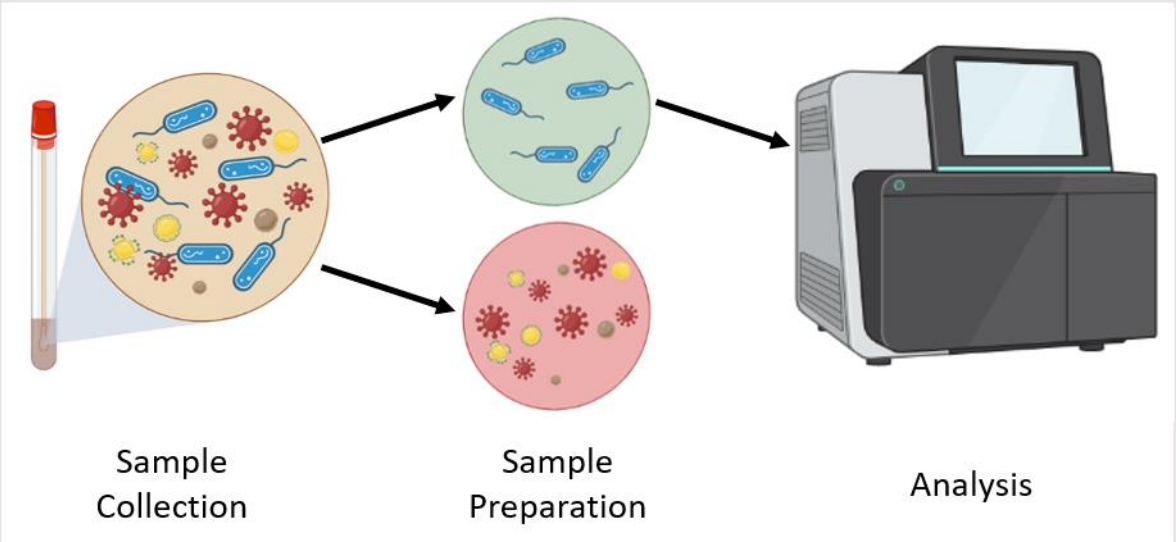

Figure 1.2 – A Simplified Sampling Procedure
(Created with BioRender.com)

1.3. ASSURED and REASSURED Criteria

In 2003, the World Health Organisation (WHO) published a set of criteria applicable to all levels of diagnostics across the developing world. This set of criteria became known by the acronym ASSURED, which became the benchmark of POCT [7,19]. ASSURED is a summation of seven factors: **A**ffordable, **S**ensitive, **S**pecific, **U**ser-friendly, **R**apid and **R**obust, **E**quipment-free and **D**eliverable to end-users.

Affordability is considered to be one of the major considerations when evaluating the development and approval of new technology. Typically, a more affordable technology will increase the number of potential users [20]. Important factors affecting the affordability are the costs of implementation, the costs to employ staff and the material costs. While there is no standard for what is considered affordable, less than $1.00 USD is accepted for a lateral flow device (LFD), while less than $10.00 USD is accepted for molecular assays [21].

Sensitivity is the minimisation and avoidance of false negatives, offering results comparable to the gold standard. When considering diagnostics, increased sensitivity is achieved through two-stage testing, either performed in parallel or in series. The primary test should identify the individuals at risk using a high-sensitivity, low-specificity test, while the secondary test should confirm the infection using a test with a higher specificity. In cases of uncertainty or discrepancies between the results, a third test may be used for confirmation [20]. Specificity is the minimisation and avoidance of false positives, offering results comparable to the gold standard. While a high specificity is desirable, a lower specificity may be accepted in cases where the treatment offered in cases of false positives offers a lower risk in comparison with the further proliferation of the disease in cases of false negatives [20].

User friendliness is the easiness of the testing procedure to be conducted without prior knowledge or training. Typically, POCT is considered “user friendly” when performed in less than 3 steps [20]. Rapidness addresses the turnaround time (TAT) of the testing procedure. Rapid testing is beneficial, as it allows for the patient to be diagnosed and offered treatment during the same visit. Following sample collection, results should be available in 15 to 30 minutes for the procedure to be considered rapid. The robustness of the test is the ability of the platform to resist environmental variables, mainly, temperature and humidity during use or transportation, without the necessity for refrigeration or specialised storage conditions [20].

Equipment-free covers the ability of the POCT device to perform without external equipment or power sources. Ideally, the device should contain either an internal battery supply, or should be able to function using solar power. In addition, the platform should be able to contain all steps of sample

processing [20]. Deliverability to end-users refers to the ability to ship, store and distribute POCT devices to users in remote locations. This factor is more important in resource limited settings, where diagnostic alternatives are not easily accessible [20].

To address future trends in diagnostics, the acronym has evolved from ASSURED to REASSURED, including **R**eal-time connectivity and **E**ase of specimen collection. The criteria equipment-free has also been expanded to include **E**nvironmental friendliness. Real-time connectivity refers to the transmission of the results to the relevant patients and healthcare workers in a short TAT following the making decision to test. Results should be provided as soon as possible to ensure that action is taken without delay. It should be noted that should the results be provided either directly to patients or lowly trained healthcare workers, then the results must be easily interpretable to prevent a misdiagnosis. Furthermore, the POCT device should also record and report environmental conditions in real-time, allowing for testing and storage conditions to be monitored. Ease of specimen collection refers to the ability to collect a sample without the need for complex and invasive collection methods. This criterion also considers the ability to perform sample preparation steps directly within the POCT device. Lastly, environmental friendliness ensures that the materials used for the fabrication of the POCT devices are either recyclable, or do not produce toxic fumes when incinerated. This criterion also considers the prevention of potentially harmful chemicals contained within the POCT device cartridges escaping into the environment [20].

1.4. Aims and Objectives

The project began due to poultry related outbreaks in the developing world as part of an Engineering and Physical Sciences Research Council (EPSRC) project. The initial aim of the project was to develop a platform capable of delivering small, precise aliquots of a collected sample in its preferred form, for the detection of 6 bacterial and viral pathogens. Based on initial research into existing literature, it was decided that cloacal and faecal samples collected on a swab would offer the largest opportunity to detect the aforementioned pathogens in the least invasive manner. The platform would be cartridge-based, and would contain all of the necessary reagents to purify and prepare the nucleic acids, which would be dispensed into PCR reaction tubes. During the project, changes were made to the initial volume of the sample to be collected, as well as the final volume to be dispensed. Ultimately, these changes caused several delays, which resulted in a proof-of-concept device being developed to accept varying starting volumes, and dispense droplets of a set size, which could be adjusted depending on specific user needs. Throughout the progression of the project, the focus changed to address the Covid-19 pandemic. Consequently, the project aims evolved to encompass the detection of SARS-CoV-2 from respiratory swab samples. The ultimate aim of the project consequently evolved as a result, with the goal to process virtually any sample type, while allowing for simultaneous DNA and RNA delivery.

1.4.1. Research Questions

The goal of the project was to understand the design problem thoroughly, and produce a quality product that complies with current regulations and standards in the biomedical industry. The main research questions which would be answered throughout the project are:

1. Can a universal sample preparation device be designed for manufacture and assembly in a low-income country?
2. Can a manually actuated device be designed, with the ability to accurately dispense multiple aliquots on demand?

Finally, with the evolution of the project to address the Covid-19 pandemic, the following research questions would also be raised:

1. Is it possible to streamline sample preparation into a portable device?
2. What are the wider applications of the project beyond sample preparation?

1.4.2. Engineering Impact

There is a delicate balance concerning healthcare when considering treatment methods. Non-specific treatment can cause an increase in microbial resistance, resulting in future infections being more difficult to treat and increase the risk of subsequent outbreaks. Alternatively, extensive laboratory-based screening for pathogens can greatly increase the TAT, resulting in further proliferation of the disease. The SARS-CoV-2 pandemic has further highlighted the lack of reliable solutions to prevent the spread of infections [22]. Thus, a compromise between selective screening and targeted treatment, allowing for the detection and treatment of diseases at an early stage, is vital.

Such a compromise can be found through the use of POCT. The purpose of POCT is to conduct laboratory tests outside of a laboratory setting to obtain information about a biological material within a short TAT. The ability to reliably diagnose diseases can allow for infections to be detected and tracked at an early stage, lowering the time needed to achieve a diagnosis and enact a solution, greatly lowering the impact on veterinary, economic and human health [22].

While centralised laboratories offer a wider range of tests, POCT offers tailored testing of a specific disease within a much shorter TAT. In comparison to standard laboratory tests which require a range of several hours to days to yield results, POCT can yield results within an hour. As demonstrated by the comparison of diagnostic approaches shown in Figure 1.1, POCT allows for healthcare decisions to be made sooner, saving crucial time [23].

The platform developed throughout the progression of this project assisted with the monitoring of infectious diseases in veterinary applications across the developing world, and later, to monitor SARS-CoV-2 infections. In both cases, the platform would offer the ability to detect infections away from a laboratory, mitigating the necessity for specialised storage, refrigeration and transportation. In the case of veterinary applications, testing may be conducted within the farm; while in the case of SARS-CoV-2, testing may be conducted within a doctor's surgery, or more crucially, in a patient's home. Such solutions are key when confronting infectious diseases, where the TAT can significantly affect the impact of the disease. Localised testing in remote locations increases the frequency to which testing may be performed, reducing the number of follow-up appointments required within centralised facilities, reducing the burden on the healthcare industry and improving medical care [23].

1.5. Thesis Arrangement

The aim of the project was to develop a sample preparation device capable of processing swab samples for the detection of infectious pathogens from poultry samples; and SARS-CoV-2 from human respiratory samples. The following chapters of this thesis are structured in the following manner: Chapter 2 introduces sample preparation in its entirety. As a goal of the project was to develop a universal sample preparation device, the chapter commences with an introduction to nucleic acids and sample types, a preface to the sample preparation steps required to convert the samples into purified nucleic acids. Additionally, the current state-of-the-art for diagnostic and POCT platforms were reviewed, evaluating their benefits and limitations, with considerations towards future trends.

Chapter 3 presents the preliminary experiments conducted in order to determine a tangible starting point for the platform. These include an evaluation of commercially available swabs to determine which would be optimal for use with the platform and an evaluation of dispenser needles to determine the achievable unassisted droplet volume. Finally, a simple sample preparation protocol for cloacal samples collected from layer chickens is presented.

Chapter 4 introduces the specifications which were considered during the development of the platform and introduces the key designs which were conceptualised during the progression of the project. An evaluation of each of the designs was conducted, before the final design idea is presented.

Chapter 5 encompasses the development of selected designs introduced in Chapter 4. Computational simulations were utilised in order to approximate the fluidic, structural and heat transfer performances within models representative of the designs. Based on the results of the computational simulations, the design ideas were optimised where possible to improve performance in the aforementioned areas, while implausible designs were omitted from further study.

Chapter 6 demonstrates the fabrication of the sample collection and preparation devices and concludes with testing being conducted on the heating and EHD modules within the final device. This is contextualised through comparisons to the computational designs presented in Chapter 5.

Chapter 7 discusses the results obtained from the previous chapters, and where relevant, compares the results with the computational simulations presented in Chapter 5. The fabricated sample preparation device is evaluated against the current state-of-the-art presented in Chapter 2, as well as the REASSURED criteria presented in this chapter. Finally, a conclusion is provided to the thesis, with considerations offered towards potential future works required to develop the current platform into a true POCT platform for use in remote and resource-limited settings.

2. Literature Review

A key stage of molecular diagnostics between “sample-in” and “answer-out” is sample preparation. As stated in section 1.4, the initial aim of the project was to develop a standalone sample preparation device for deployment in low-resource settings. While the intention was to develop a device capable of handling all types of biological samples, this task would be impossible to achieve during the span of a single research project. Thus, the focus of the project became extracting and purifying DNA and RNA from poultry samples to detect infectious viral and bacterial pathogens related to outbreaks across the developing world. As the project progressed, the aims of the project evolved to include the detection of SARS-CoV-2 from respiratory samples.

For this project, isothermal amplification followed by end-point colorimetric detection, would be applied in each case to detect the pathogens. The amplification and detection processes would not be conducted within the sample preparation platform developed in this project. However, a consideration of these downstream processes would be required in order to fully understand the sample preparation processes suitable for the task.

This chapter will consist of a literature review of sample preparation in its entirety, as well as a review of the current state-of-the-art which contains integrated sample preparation steps. A review of nucleic acids and the relevant bacterial and viral pathogens provided insight into the sample types required for analysis. Sample collection procedures and the related sample types provided a tangible starting point for the conception of the sample preparation platform developed during this project. A review of sample preparation, followed by a brief review of PCR and iNAAT techniques, would serve as a guideline for the required processes to be conducted within the platform. Finally, a review of the state-of-the-art for molecular diagnostics and POCT provided crucial information on the steps other manufacturers had taken to incorporate sample preparation into their respective platforms, while highlighting some of the benefits and limitations of each.

2.1. Nucleic acid Diagnostics

2.1.1. The Cell and Nucleic Acids

Discovered by Friedrich Miescher in 1869, nucleic acids (NA) are small biopolymers that can be found within all living organisms [24]. NAs can be separated into two main categories: deoxyribonucleic acid (DNA) and ribonucleic acid (RNA). DNA (Figure 2.1) is a double stranded structure arranged in a double helix, found within the nucleus of a cell. DNA is comprised of 4 types of nucleotides, which are molecules containing a phosphate group, a sugar group and a nitrogenous base. These nucleotides are adenine (A), cytosine (C), thymine (T), and guanine (G). These nucleotides are covalently linked by hydrogen bonds, with adenine being paired with thymine, and guanine being paired with cytosine, forming a nucleobase [25].

Contrary to DNA, RNA (Figure 2.2) is a single stranded structure, found within the cytoplasm of the cell. While all cells within an organism contain the same DNA profile, the expression of RNA varies. RNA is also comprised of 4 nucleotides, with uracil (U) replacing thymine. While RNA typically is single stranded, it can also form a double stranded hybrid when bonded to complimentary (cDNA) or foreign DNA [25].

A sequence of at least 4 nucleobases forms a gene. In human cells, genes range from a few hundred to hundreds of thousands of nucleobases. The human body holds over 40,000 genes; however, many are inactive in human cells [26]. Segments of DNA may be converted into RNA through a process known as transcription. During this process, all instances of thymine are replaced with uracil. In contrast, RNA can be converted into DNA through a process known as reverse transcription.

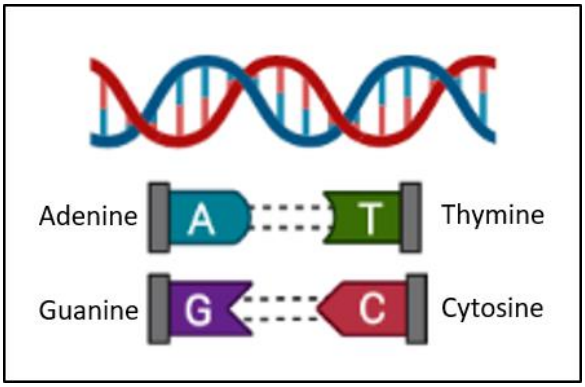

Figure 2.1 – Schematic of DNA
(Created with BioRender.com)

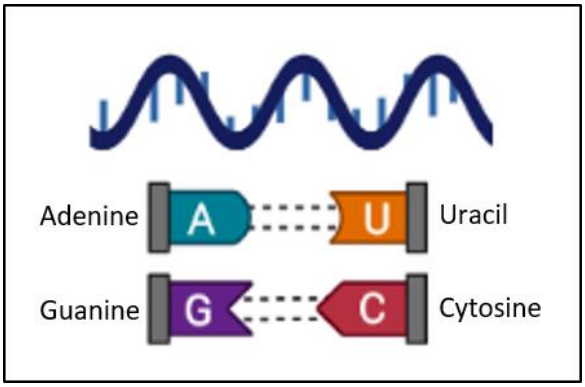

Figure 2.2 – Schematic of RNA
(Created with BioRender.com)

There are 3 major classes of RNA which can be found within the cell, which can be seen in Table 2.1. The sequence of DNA can be transcribed into ribosomal RNA (rRNA) or transfer RNA (tRNA), or translated into proteins using a messenger RNA (mRNA). These different classifications of RNA feature different levels of stability, with more stable RNA having a longer half-life. In comparison to DNA, RNA is more susceptible to degradation and is more easily altered. Therefore, the isolation of intact, unaltered RNA is important for successful analysis. RNA is particularly vulnerable to RNases, which can break down the RNA. Such RNases can be found in abundance within contaminated equipment found within a laboratory. Many commonly used samples, such as hair and skin tissues, contain RNases. In light of these issues, it is more difficult to obtain high quality RNA from a sample, than DNA [26].

Table 2.1 – 3 Major Classes of RNA [26]

RNA Type	Abbreviation	Percentage	Size	Stability
Ribosomal RNA	rRNA	80 – 85%	Varies	Stable
Transfer RNA	tRNA	15 – 20%	Small	Stable
Messenger RNA	mRNA	1 – 5%	Varies	Unstable

There are two main types of cells: eukaryotic and prokaryotic cells. Eukaryotic cells (known as eukaryotes) can be found in multicellular organisms such as animals or plants, while in contrast, prokaryotic cells (known as prokaryotes) are typically found within single celled organisms, such as bacteria. All cells share four common components: a plasma membrane, cytoplasm, NAs, and ribosomes; however, the main differences lie in their structure and organisation.

Viruses are sub-microscopic non-living particles, ranging from 20 to 250 nm in diameter, consisting of a plasma membrane, a cell wall and a protein capsid containing either a single or double stranded NA core. Viruses typically bind to a host cell in order to achieve replication. Viruses may also be classified into four main categories: Filamentous, isometric (or icosahedral), enveloped and head and tail.

With the exception of bacteriophages which possess single-stranded DNA (ssDNA), bacteria and higher organisms contain double-stranded DNA (dsDNA). Viruses contain both DNA and RNA, but require host cells to replicate. The length and content of the DNA varies from species to species. With simple bacteria such as *E. coli*, their DNA is roughly 1 mm in length and contains approximately 4 million nucleobases. In contrast, human cells have a DNA length of 174 cm and vary between 50 to 263 million nucleobases. As a result, solutions containing DNA can become very viscous and non-Newtonian in nature. Furthermore, DNA within the solution may be damaged or fragmented by mechanical shearing forces which can be generated by standard laboratory procedures such as pipetting [26].

2.1.1.1. Poultry Related Infections – An Overview

The Philippines currently has a population of 109.58 million (see Table 2.2), ranking the country 13th on the global scale [27]. With the population forecast to increase by 14.12 million by the year 2030, the provision of food is set to become a major concern. Poultry farming in the Philippines offers a major contribution to the agricultural industry, generating 17% of the country's agricultural output [28]. In these farms, birds are typically raised in the hundreds of thousands and stored in confined, enclosed conditions to increase biosecurity [29]. However, this can result in the proliferation of harmful pathogens, creating a large impact on the surrounding inhabitants.

In 2004, a report was issued by the WHO, which issued a warning for a potential influenza pandemic, which if unconstrained would result in the deaths of up to 7 million people, with additional tens of millions requiring medical attention [30]. In 2005, an outbreak of Avian Influenza Virus (AIV) occurred, spread by wild birds during migration. Particular strains of the disease were highly pathogenic, and while initially assumed to be limited to poultry, the disease was transmitted to humans through proximity or consumption, causing 54 deaths among the 108 reported cases [31]. In 2017, an outbreak of AIV re-emerged, with 17 human cases reported in China [32].

Treatment of the entire flock was attempted when symptoms of the disease were observed; however, as many birds were asymptomatic, treatment was delayed [31]. This blanket treatment approach was also expensive, and consequently increased drug resistance [29]. As an alternative approach, targeted treatment was offered after analysing samples collected from each bird using conventional molecular detection techniques. This involved cell culturing followed by microscopy, allowing antigenic or pathogenic information to be identified and quantified [33]. While this reduced the quantity of medication used, the requirements for equipment needed for the storage, transportation, processing and analysis of samples were greatly increased. This process also had a TAT of several days, allowing for the further proliferation of the disease [29]. Thus, it was considered highly impractical to attempt to inspect each bird individually.

Table 2.2 – Current and Forecast Demographics of the Philippines [27]

	2020 (Current)	2030 (Predicted)	2050 (Predicted)
Total Population (million)	109.58	123.7	144.49
Population Growth Rate (%)	1.35	1.15	0.57
Population Density (people/Km^2)	368	415	485
Rural Population (million)	57.57	59.553	51.023

It has been suggested by the WHO to perform an examination from of a representative sample of the birds, to determine the condition of the entire flock [34]. These are typically performed on at least 10 birds per house containing both healthy and sick birds and are performed post-mortem following humane culling [29]. For such sampling techniques, the examinations must be performed on carcases no older than 24 hours to prevent sample degradation through decomposition [29,34]. With an increase in poultry consumption worldwide, the outbreak of AIV highlighted a major problem. In addition to causing major economic losses, similar pathogenic infections could be transmitted to humans, which are difficult to implement effective control measures for due to increased global trade. Thus, the proposed project would address major infections found in poultry, of which, 6 will be discussed.

Salmonella enterica

Salmonella enterica (*S. enterica*) is a respiratory disease which is transmitted to humans through contaminated eggs or meat [35]. *S. enterica* can be divided into 2 groups: *S. enterica* serovars Typhimurium and Enteritidis, responsible for paratyphoid and gastrointestinal diseases; and a smaller number of serovars, responsible for systemic typhoid-like diseases in specific host species [36]. *S. enterica* infections occur through the faecal-oral route, following the consumption of contaminated food products [37]. Young birds are more susceptible to infection of the gastrointestinal tract within a few days of life following either vertical transmission by egg, or horizontal transmission during feeding or handling [35]. Following infection, the pathogen colonises the intestinal, alimentary and reproductive tract, where it can proliferate asymptomatically [36,38].

Infectious Bursal Disease Virus

Infectious bursal disease virus (IBD) is an immunosuppressive virus in poultry. While typically affecting chickens, other species such as turkeys, ducks and ostriches can also be susceptible, albeit resistant, to the virus [39,40]. Most chicks are exposed to IBD early in life, typically between 3 – 6 weeks of age. The most common mode of infection is through the faecal-oral route or through inhalation [41]. The virus replicates in the gut, before spreading to other organs, including the liver, the kidney, but mainly, the bursa of Fabricius through the blood stream [42]. After an incubation period of two to three days, clinical symptoms become apparent, which include signs of distress or depression [41], prostration, ruffled feathers, anorexia and diarrhoea [43]. Following the spread of the virus to the bursa of

Fabricius, lesions appear on the bursa of Fabricius, tonsils, thymus and spleen. What follows is the haemorrhaging and eventual atrophy of the bursa of Fabricius, as well as the thigh and breast muscles [41]. Typically, mortality rates among affected flocks range between 10 – 50%; however, more virulent strains can result in between 50 – 100% mortality rates, due to the infected birds being more susceptible to secondary infections caused by other viruses, bacteria and parasites [41].

Infectious Bronchitis Virus

Infectious bronchitis virus (IBV) is a highly infectious avian-borne gammacoronavirus that causes respiratory diseases primarily in chickens, but also can be found in pheasants and fowls [44,45]. The pathogen typically infects the upper respiratory tract, gut, kidney, and reproductive systems following the ingestion of contaminated feed or water [45]. Following infection, the virus colonises the nose and trachea, reaching saturation within three days, where it can remain at saturation for up to five days [46,47]. Following infection, the pathogen is then transmitted between chickens through aerosols, following respiratory or faecal discharge [44]. Clinical signs of IBV include coughing, sneezing and tracheal rales for up to 2 weeks. For chicks, feed consumption and weight gain are also reduced. For hens, egg production can reduce by up to 70% and often appear misshapen, of poor quality, and contain a watery content. Following infection, concurrent bacterial infections are common [48]. In cases of a secondary bacterial infection to the sinuses, common symptoms include conjunctivitis and facial swelling [44]. For outbreaks across flocks, mortality is on average 5%; however, mortality rates can increase to up to 60% in cases of a concurrent bacterial infection [44].

Mycoplasma gallisepticum

The avian borne pathogen *Mycoplasma gallisepticum* (MG) is a respiratory and systemic disease, commonly inducing severe chronic respiratory diseases in chickens and infectious sinusitis in turkeys, induced mainly by stress [49,50]. MG typically colonises the mucosal surface of the respiratory tract, and while many infections can be asymptomatic, it can progress to a systemic infection, resulting in arthritis, salpingitis, conjunctivitis, and fatal encephalopathy [51,52]. Infected birds can become life-long carriers, either transmitting horizontally *via* aerosol droplets or vertically through eggs [51,52].

Newcastle disease Virus

Newcastle disease virus (NDV) is considered to be one of two major diseases in poultry, alongside AIV [53]. It is a member of the *Paramyxoviridae* family infecting the respiratory tract following inhalation or ingestion [54]. Over 250 species of birds are susceptible to NDV, leading the disease to be considered as highly infectious [53,55]. There are 3 major strains of NDV: velogenic, which are highly virulent; mesogenic, which are moderately virulent; and lentogenic, which are of low virulence [55]. Infections can lead to a broad range of symptoms. Lentogenic strains can either be asymptomatic, or cause a mild infection to the respiratory tract. Mesogenic strains can cause a greater effect on the respiratory and nervous systems, with a low potential for mortality. Velogenic strains can result in more extreme symptoms, including haemorrhagic lesions in the intestinal tract and a high potential for mortality [53]. In extreme cases, an infection can cause up to 100% mortality across a flock [56].

Avian Pathogenic E. coli (APEC)

Avian pathogenic *Escherichia coli* (APEC) is an extra-intestinal pathogenic *E. coli* (ExPEC), causing systemic infections in chickens and other poultry [57]. Birds can become infected by contaminated feed or water sources, with further transmission occurring through faecal-oral, aerosols, or vertical transmission through eggs [57,58]. APEC colonises the gastrointestinal and respiratory tracts, and the extra-intestinal sites should the pathogen migrate [58]. APEC can surface as a primary infection, or secondary to a viral infection, commonly AIV, MG, NDV, IBV, and IBD [57]. Chickens suffering from APEC can experience a multitude of symptoms commonly referred to as colibacillosis, with symptoms including a 2% decrease in live weight, a 20% decrease in egg production and a decreased hatching rate for hens [58]. APEC is also responsible for the mortality of 53.5% of young chickens [59].

2.1.1.2. Covid-19 – An Overview

In December 2019, a strain of severe acute respiratory syndrome coronavirus 2 (SARS-CoV-2) was reported in Wuhan City, Hubei Province, China [60]. The virus spread rapidly following the initial outbreak, resulting in millions of global cases across over 200 countries, being declared as a pandemic by the WHO on 11 March 2020 [61]. As of 1 March 2022, (see Figure 2.3), there have been over 439,000,000 total cases and over 5,900,000 reported deaths [62].

Common symptoms of the disease include fever, fatigue and a dry cough; however, uncommon cases may include symptoms such as coughing up sputum, loss of smell, diarrhoea, shortness of breath, joint and muscle pain, among many others [63]. Due to the assortment of symptoms which may result from the disease, as well as many cases being asymptomatic, early detection and isolation of case positive patients prior to or without the onset of symptoms is crucial to prevent the transmission of the virus, while avoiding the quarantining of negative individuals [64].

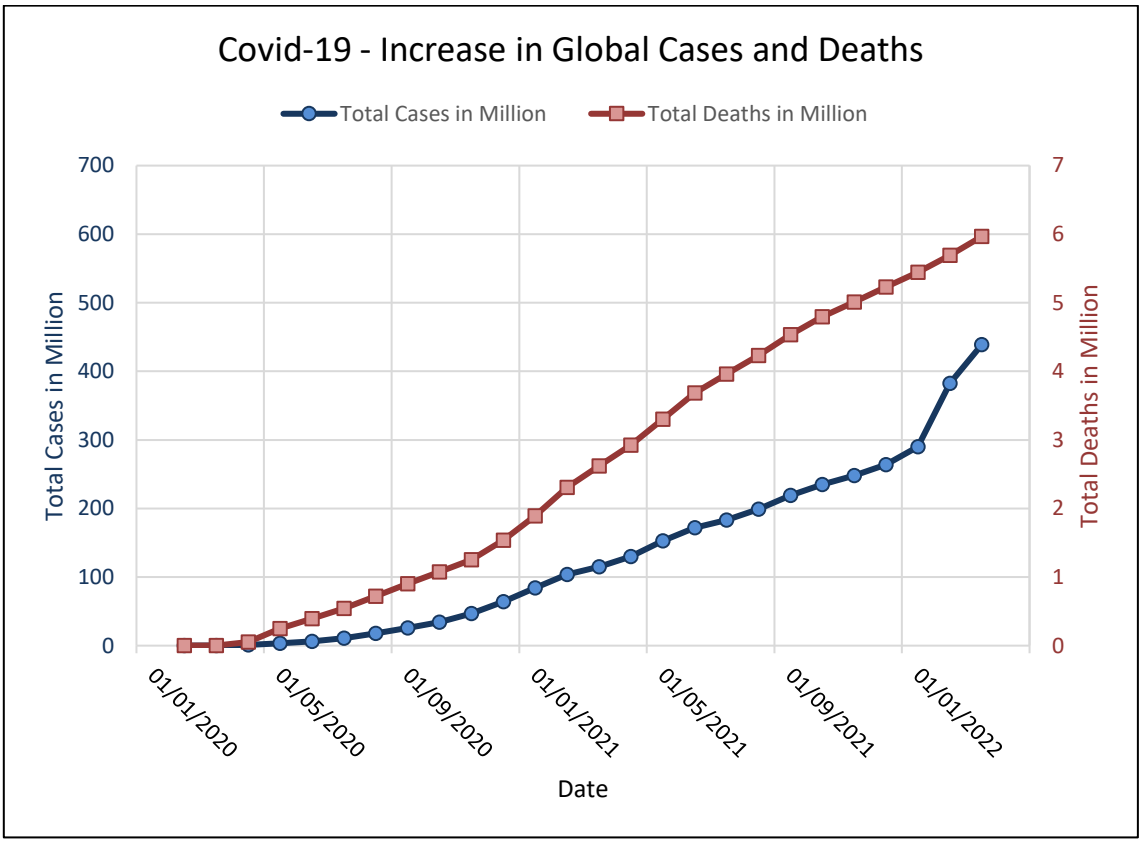

Figure 2.3 – Covid-19 – Global Increase in Total Cases and Deaths [62]

2.1.2. Sample Collection

2.1.2.1. Sample Collection for Diagnostics

In order to perform a diagnostic test *in vitro*, a sample representative of the original infected body must be analysed. In cases where the biological composition between individual aliquots varies, the analysis of multiple samples may be necessary [26]. Non-invasive sample collection procedures may be performed on site. Conversely, for invasive cases such as blood or tissue collection, procedures are performed within specific facilities. Diagnostic tests may be performed on a variety of samples (see Table 2.3), each with different chemical compositions. Typically, cleaner samples (such as urine) will behave differently from thick fluids (such as blood) and solid material (such as stool or sputum). Solid samples are more difficult to handle, as they can not only restrict and block flow through components, but are difficult to mix with liquid solutions, which are easier to manipulate.

There are several risks of environmental contamination during the sample collection process, resulting from mishandling the sample, or non-sterile collection or storage conditions. There is also a risk of sample contamination, should unnecessary processes be performed, leading to unreliable results. Some of the sample which has been collected may be lost due to its evaporation, adsorption or absorption. Thus, it is important to maximise the amount of usable sample which is collected. Swab sampling is typically used to detect organic or inorganic substances, typically on the surface level. The process begins with the selection of the chosen area to swab, dependant on the sample type to be assessed. A swab is removed from sterile packaging and is wet with an appropriate solvent, to encourage adhesion to the swab. The swab is then passed across the entirety of the selected area, or inserted into the selected orifice. Alternatively, the use of boot swabs allows for pooled samples to be collected from the flock, reducing the time taken to collect samples and the attributed costs [29].

Table 2.3 – Summary of Collection and Testing Methods for Various Sample Types

Sample	Collection Method	Tests Performed	REF
Cloacal	Swab	Molecular testing, bacterial culture	[34,65,66]
Faecal	Stool, Swab, scoop	Molecular testing, microscopy, bacterial culture	[34,66]
Pus	Syringe, surgical drain, swab	Molecular testing, bacterial culture, microscopy	[65,67]
Saliva	Swab, sponge, vial	Genetic testing, molecular testing	[65,67-69]
Sputum	Sputum container	Bacterial culture	[65,67]

2.1.2.2. Sample Collection for SARS-CoV-2

SARS-CoV-2 can be detected in various respiratory samples, commonly nasal, nasopharyngeal (NP) and oropharyngeal (OP) samples; as well as faecal samples [64,70]. These are usually collected using NP mini-tip or OP swabs; mid-turbinate nasal (MTN) flocked tapered swabs; anterior nares (AN) flocked or spun polyester swabs; or from saliva, collected either by a trained healthcare personnel or by supervised self-collection. Alternatively, nasal aspirates and NP aspirates (NPA) may be collected by trained healthcare personnel. The following protocols are currently suggested by the Centres for Disease Control and Prevention (CDC) following the decision to test. In cases where personnel are to collect samples, personal protective equipment (PPE) should be worn [71].

The procedure varies depending on the sample type and the condition of the patient. Samples are taken from the upper respiratory tract (NP and OP) in general cases; and the lower respiratory tract (saliva or sputum) in extenuating circumstances. For NP samples, a mini-tip swab is inserted into the nostril and moved parallel to the palate until either resistance is encountered or the swab reaches a depth equal to the distance from the nostrils to the outer opening of the ear. The swab is then rotated in the nostril to absorb nasal secretions. Samples should be taken from both nostrils; however, the swab does not need to be saturated following the first collection. For OP samples, the swab is inserted into the mouth and rubbed along the tonsillar pillars and posterior oropharynx areas without touching the tongue, teeth or gums. NP swabs are preferred to OP swabs, due to a higher viral load in the nasal area in comparison to the throat [72]. However; it is suggested by the CDC to collect and pool both NP and OP swabs from a patient into a single tube to maximise sensitivity [71].

For MTN samples, the head is tilted backwards by 70 degrees and the swab is gently inserted 2 cm into the nostril, or until resistance is met at the turbinates. The swab is then gently rotated several times against the nasal wall and removed. The process is then repeated in the other nostril using the same swab. For AN samples, the swab is inserted 1 cm into the nostril and rotated for 10 to 15 seconds. The swab is then removed and the process is repeated in the other nostril with the same swab [71].

For nasal aspirates and NPA samples, the patient's head tilted backwards and 1 to 3 mL of non-bacteriostatic saline (pH 7.0) is added to one nostril. A catheter attached to a suction apparatus is then inserted into the nostril parallel to the palate reaching a distance equal to the distance from nostrils to the outer opening of the ear. Gentle suction is then applied and the catheter is removed while being rotated gently. The collected sample is stored in a sterile tube [73]. For saliva samples, 1 to 5 mL of saliva is collected in a sterile, screw cap container. For sputum samples, the patient rinses their mouth with water, before expectorating sputum directly into a sterile, screw cap container [71].

Following collection, samples are placed in a sterile transport tube containing 2 to 3 ml of the viral transport medium (VTM), Amies transport medium, or sterile saline. The preservative used depends on the sample type. In specific cases where the samples are analysed directly, the preservative can be omitted completely. For saliva and sputum samples, preservatives are not typically required. Samples may then be stored at 2 to 8 °C for up to 72 hours following collection, or at -70°C for prolonged storage [71]. Prior to testing, samples are often heated to 95 °C in an initial processing step to inactivate the virus to prevent infection [74].

2.1.2.3. Sample Preservation

Following collection, an additional preservation step may be employed to prevent the degradation of the sample through physical, chemical or biological processes prior to analysis [75]. This prevents the sample from being exposed to contaminants or inhibitors, resulting in inaccurate results [26]. Effective sample preservation must preserve the sample in the same concentration and constitution as the time of collection, unless a preconcentration step is applied during the collection step. The method must be simple to implement and operate and must be able to be utilised across a range of sample types without a large variation in the setup or process [75]. Common sample preservation techniques involve filtering the sample to remove contaminants and concentrate the pathogen of interest before immediate freezing in liquid nitrogen [76]. However, this approach requires cold storage equipment with both a large footprint and a large power requirement. Thus, alternative preservation methods must be assessed.

A collected sample may be stored within a sealed container, or suspended within a medium. These containers must be air and water tight, to prevent cross contamination during transportation, as well as sample degradation, adsorption, oxidation or reduction. In specific cases, light exposure can also cause sample degradation [77].

For bacterial samples, a charcoal base medium may be used to neutralise fatty acids or toxic substances which can be found on the skin, isolating the bacteria. In the cases of viral sample collection, the sample will need to be stored in a medium prior to storage or transportation, due to particular viruses being unable to survive outside of the host. In both cases, the temperature at which the sample is stored and transported is important [65]. While it is a common practice to store collected samples within a chemical preservative, knowledge of which processes will be utilised downstream to treat and prepare the sample is needed [77]. Typical chemicals used to preserve samples such as formaldehyde can deactivate RNA and DNA within samples, preventing downstream analysis [78].

Saito *et al.* tested the performance of 5 different preservatives against a control immediately frozen following collection, using marine *Synechococcus* WH8102 culture grown in SN media. While the immediate freezing of the sample yielded the highest total protein recovery overall, the sample stored in sodium dodecyl sulphate (SDS) yielded the highest recovery between the preservative techniques and RNAlater® demonstrated the highest effectiveness for preserving DNA, RNA and proteins within a sample in conditions similar to expected field deployment [76].

The material of which the container is comprised of also contributes to the stability of the contained sample. Particular plastics may release particulates over time, which may cause interferences during the analysis stage, while others may adsorb the important components from the sample resulting in cross contamination between samples from previous uses, leading to either an over detection of the pathogen of interest, or non-specific detection [77,79]. Alternatively, glass containers are not ideal due to their relatively high costs [80]. It should be noted that there is no single material that will not create some change in the sample constitution over time, and thus, sampling should ideally be conducted within a day of collection to avoid the destabilisation of the sample. However, this may not always be possible due to logistical issues [77].

2.1.3. Sample Types

Biological samples are complex in nature, containing varying quantities of cells, proteins, salts, metals and other biomolecules which can interfere with the detection of pathogens [81]. It is important to understand the sample type to be analysed in order to determine the ability to extract high quality NAs from said sample. One of the research questions posed in section 1.4.1 considered the possibility of developing a universal sample preparation device capable of processing a wide array of sample types. Thus, the following section will elaborate on the different sample types which are commonly analysed in diagnostic tests, comparing their composition and some of the common challenges associated with each.

2.1.3.1. Bacteria

Bacterial cells can be divided into two categories, gram-positive and gram negative. Gram-positive bacteria contain a thicker cell wall, and are harder to lyse using conventional techniques than gram negative. Bacteria cells can be isolated from sample volumes taken from culture and grown to saturation. For typical DNA extraction procedures, the bacterial culture is centrifuged to create a pellet, which is then vortexed in a 10 mM tris(hydroxymethyl)amino-methane-chloride (tris-Cl) buffer and 1 mM ethylenediaminetetraacetic acid (EDTA) buffer at pH 8. The cells are then treated with proteinase K and SDS in order to disrupt the cellular membrane and digest the proteins contained within the cell. Following cell lysis, phenol-chloroform, guanidinium salts and detergents are used, followed by treatment in ethanol, to extract and precipitate the DNA [26].

2.1.3.2. Buccal and Saliva

Following the cleaning of the mouth with water or mouthwash, buccal samples may be collected by rotating a buccal brush inside of the mouth of the patient. The collected brush is then placed into a tube containing 50 mM sodium hydroxide (NaOH), which is then vortexed and incubated at 95 °C for 5 minutes to lyse the cells. The brush is then removed and 1 M Tris-Cl (pH 6.5) is added. Following centrifugation, the supernatant containing the DNA can be used for downstream analysis [26].

Saliva is a mixture consisting of 98% water and 2% electrolytes, minerals, hormones, enzymes and other biomolecules [81]. Saliva samples are favoured in molecular analysis due to its non-invasive nature, able to be collected using swab sampling, pads, or sponges. The saliva sample may be frozen in order to prevent degradation; however, if freezing is unavailable, Oragene® may be used to preserve the DNA at room temperature [82].

2.1.3.3. Faecal and Cloacal

Faeces is the solid or semi-solid remains of food that is passed through the large and small intestine without being digested [83]. It is comprised of water, proteins, undigested fats and bacterial biomass, with its composition varying based on dietary intake [84]. Furthermore, it has a pH range of 5.3 to 7.5, with an average pH of 6.6 [85]. Stool samples can be collected directly into sterile and dry screw-cap containers following excretion in order to prevent any further proliferation of the bacteria and to

ensure accurate analysis [86]. For animals, samples can be collected by placing a plaster over the posterior opening, and collecting the sample following defecation [87].

Stool samples are abundant, collectable through non-invasive methods and contain a large quantity of genetic material. In light of the aforementioned, such samples can be favourable when assessing for a multitude of pathogenic infections. However, there are several common contaminants which have been reported to inhibit NA-based detection methods [88-90]. For human stool samples, these include, but are not limited to, bilirubin and bile salts [91-93], cholic and deoxycholic acid [94], haemoglobin and heparin [95-97], polysaccharides [98-100] and urea [95,101]. Stool samples collected from poultry also contain inhibitors, mainly bacterial and fungal in nature, which may either be acid resistant or spore forming [102]. These samples are also lower in moisture in comparison to other animals [103]. As a result, difficulties can arise when homogenising the samples in buffers [104].

The cloaca is a single posterior opening for the digestive, reproductive and urinary tracts for many animals, including amphibian, reptiles, some mammals and birds. These animals excrete both faeces and urine through this opening, allowing for several intestinal infections to be detected using relatively straight-forward collection procedures. Typically, cloacal samples are collected using sterile cotton swabs, which are moistened in phosphate-buffered saline (PBS) and then inserted and rotated in the cloaca of the birds. This approach is advantageous over stool samples, which may be unreliable if obtained following defecation due to sample degradation or contamination. Furthermore, cloacal samples can be collected more frequently than stool samples, reducing the time between tests should follow-up testing prove necessary [87].

2.1.3.4. Respiratory

Respiratory samples can be divided into those found in the upper respiratory tract, such as AN, NP and OP samples; and those found in the lower respiratory tract, such as sputum and bronchoalveolar lavage (BAL) fluid. Typically, samples collected from the respiratory tracts should be refrigerated between 2 – 8 °C for less than 5 days between sample collection and analysis and should be stored on dry ice at –90 °C for above 5 days [105].

Bronchoalveolar Lavage Fluid

Bronchoalveolar lavage (BAL) is a sampling method used to detect various infections found in the lower respiratory system, typically performed when a patient is unable to produce sputum, is affected by a persistent cough, is experiencing breathing problems, or is coughing up blood [106,107]. BAL samples may be used to detect infections which are bacterial in nature, such as tuberculosis (TB) and bacterial pneumonia; viral, such as influenza and SARS-CoV-2; fungal; as well as pulmonary fibrosis and lung cancer [107]. A bronchoscope is passed through the mouth or nose and into the lungs. A fluid, typically saline, is then introduced and aspirated into a sterile container using suction [81]. The aspirated BAL fluid may then be used for further analysis.

Nasal and Nasopharyngeal

Nasal samples are collected from secretions along the nostrils, leading to the nasopharynx. Depending on the depth into the nostril, the type of sample collected will vary. AN samples are collected from the external portion of the nose, just inside the nostril. This area of the nose is commonly sampled when bacterial *staphylococcus aureus* [108] and viral SARS-CoV-2 [109] infections are suspected. To collect an AN sample, a swab is placed 1.5 cm into the nostril in an upwards direction, which is then rotated inside the nostril to collect nasal discharge [110]. Alternatively, MTN samples may be collected, which are located slightly further behind the nostrils, along the palette [111]. MTN samples may be used to detect several respiratory infections, including, but not limited to, influenza [112,113] and SARS-CoV-2 [114]. To collect an MTN sample, a swab is placed 2 cm into the nostril in a direction parallel to the palette, which is then rotated inside the nasal passage to collect secretions [114]. Swab sampling in both the AN and MTN regions is less invasive when compared to the recovery of NP and OP specimens. Furthermore, due to the ease of the sample collection, both may be self-collected by adult patients, rendering this method of sampling well suited for POCT [111].

Nasopharyngeal (NP) specimens can be collected from secretions in the back of the nose and throat area and are used to detect for viral and bacterial infections, such as MERS [115], SARS-CoV-2 [73] and *Streptococcus pneumoniae* [116]. NP samples are preferred over nasal samples, due to having a higher sensitivity [117,118]. Currently, NP swabs are the reference sampling method for SARS-CoV-2 [72].

Oropharyngeal and Sputum

Oropharyngeal (OP) samples are collected from the centre of the throat (pharynx) at the back of the mouth, to detect both viral infections, including SARS-CoV-2, influenza, Rhinovirus and respiratory syncytial virus (RSV) [72,119,120]; as well as bacterial infections, including *Streptococcus pneumoniae* (pneumococcus), *Haemophilus influenzae* and *Moraxella catarrhalis* [121,122]. OP samples are collected by passing a swab through the mouth and rubbing the swab across the tonsils and oropharynx [72]. While it is possible to collect OP swabs by self-swabbing, it is recommended by the Food and Drug Administration (FDA) for samples to be collected by a healthcare professional [123].

Sputum is produced in the lower respiratory system and is collected from a patient after being coughed up. The highest quality samples should contain as little saliva as possible, to prevent contamination with oral bacteria [124]. If sputum cannot be produced naturally through a deep cough, then it may be induced either by encouraging the patient to inhale a saline aerosol, or using a laryngeal swab [125]. Collected sputum samples are mixed with a guanidinium thiocyanate (GITC) buffer and zirconia beads, before being lysed in a bead beater for 3 minutes and boiled. After centrifugation, the DNA pellet is then collected, and precipitated using isopropanol [126].

2.1.3.5. Discussion of Sample Types

A summary of the infectious diseases can be seen in Table 2.4. As demonstrated, each of the 6 diseases may be detected through the analysis of cloacal samples, demonstrating the effectiveness of this sample type for molecular testing. As a single sample may contain several of the pathogens of interest, the possibility for multiplexing assays becomes apparent, which can greatly reduce the cost of diagnostics, as well as the TAT. When compared to collecting blood or tracheal samples, cloacal samples are relatively non-invasive, and are less likely to cause lasting stress to the birds.

Consideration must also be given to the reliability of the sampling method. Cloacal samples will contain faecal matter, which will also contain inhibitors which can affect the amplification and detection steps of molecular diagnostics. While it is possible to remove these contaminants through several common purification methods, this may prove challenging when applied in POCT arrangements. The inclusion of additional sample preparation steps will increase the overall TAT and can introduce manual handling steps, which in nature, contrast with the general concept of POCT, which is to provide rapid results with limited user interaction.

Table 2.4 – Infectious Diseases Common to Poultry in the Philippines
Cloacal sample types have been highlighted to demonstrate its prevalence among the 6 pathogens of interest
dsDNA, double-stranded Deoxyribonucleic Acid; ssRNA, single-stranded Ribonucleic Acid; OP, oropharyngeal

Diseases	Pathogen (Target)	Location	Sample Type(s)	Targeted Gene
Avian Pathogenic *E. coli*	GN Bacteria (dsDNA)	Extra-intestinal tract	• **Cloacal** • Faecal	ipaH/blaCTX-M for enteroinvasive E. coli
Mycoplasma gallisepticum	GN Bacteria (dsDNA)	Respiratory tract	• **Cloacal** • Faecal	pdhA/mgc2
Salmonella enterica	GN Bacteria (dsDNA)	Gastrointestinal tract	• **Cloacal** • Tracheal	invA for Salmonella ssp.
Newcastle Disease Virus	Virus (ssRNA)	Bursa of Fabricius	• **Cloacal** • OP • Blood	M/F
Infectious Bronchitis Virus	Virus (ssRNA)	Respiratory tract	• **Cloacal** • OP • Blood	N/5'UTR/S1
Infectious Bursal Disease Virus	Virus (dsDNA)	Respiratory tract	• **Cloacal** • Blood	VP1/VP4/VP2

As the analysis of individual samples can prove to be time consuming and expensive, the pooling of samples may act as a means to reduce the consumables used. This approach was first proposed by Robert Dorfman in 1943, who theorised that the target pathogen from an individual sample will be detectable within a pooled sample, and thus, results for multiple subjects may be confirmed simultaneously, with further individual testing available to be conducted on any remaining sample if necessary [127]. For pooled sampling to be economically viable, it must be more efficient to observe a group within a single test than to observe individuals separately. The pooling of samples should also only be used in cases where the expectation of positive results is low [128].

Primary factors which may influence the effectiveness of pooled sampling is if the amount of impurities within a pooled sample exceeds the average within individual samples, or if the amount of the valuable pathogenic material is diluted. Both factors mean additional reagents or processing steps may be required to prevent a decrease in sensitivity [128]. The integrity of individual samples may be further affected depending on the collection procedures. A study conducted by the University of Nebraska Medical Centre concluded that a pooled sample size of 5 samples per test is the most efficient for reducing the cost of the reagents while increasing the testing capability by 69% [129].

2.1.4. Sample Preparation

Sample preparation is a pivotal step for pathogenic detection in molecular diagnostics, converting a raw sample into a simpler form by removing the interferents and inhibitors that might affect downstream analysis [130]. Conventional NA sample preparation involves the disturbance of the cell membrane, followed by the separation of the unwanted cellular debris from the NA using enzymatic digestion and centrifugation in concentrated salt solutions. Phenol-chloroform is then used to isolate the NA, allowing for its washing and precipitation using ethanol and salts and subsequent elution using a buffer. Alternatively, guanidinium salts and detergents may be used for similar results [26]. A comparison between the traditional sample preparation steps for different sample types can be seen in Table 2.5..Traditional sample preparation is simple and yields large quantities of high purity NA. However, the approach is not without its drawbacks, requiring phenol and chloroform, as well as the transfer of the sample between multiple tubes, increasing the opportunity for contamination [130].

Despite the developments in the process over the years, many consider sample preparation to be a bottleneck in the field, particularly concerning POCT in low-resource settings. All processes within sample preparation will affect the following analysis steps. Therefore, it is crucial for effective sample preparation outside of a laboratory-based setting that the process is able to isolate detectable NAs from a raw sample and remove contaminants that can interfere with the detection, without the need for expensive equipment. Furthermore, it is a goal to automate as much of the sample preparation process as possible, reducing manual operation [131]. The following section will discuss each stage of sample preparation in greater detail, highlighting the different ways that the cells may be treated, along with some of the benefits and challenges associated with each method.

Table 2.5 – Summary of traditional sample preparation techniques for different sample types
EDTA, ethylenediaminetetraacetic acid; SDS, sodium dodecyl sulphate; RBC, Red Blood Cell; RT, Room Temperature; GITC, Guanidinium Thiocyanate; PBS, phosphate-buffered saline; CTAB, cetyltrimethylammonium bromide;

Specimen	Cell Lysis	NA Extraction	Long Term Storage Temperature	REF
Bacteria	• Vortexing in 10 mM Tris-EDTA + 1mM EDTA, followed by incubation in proteinase K + SDS • Bead beating in a GITC lysis buffer	• phenol-chloroform extraction and ethanol precipitation	-80 °C	[26,132]
Buccal and Saliva	• Vortexing in 50 mM NaOH, followed by incubation at 95 °C	• Centrifugation in 1 M Tris-EDTA	-80 °C RT (Oragene)	[26,82]
Faecal	• Homogenisation in a PBS buffer at 4 °C, followed by incubation at 95 °C • Incubation in guanidium isothiocyanate in 50 mM Tris buffer	• Centrifugation in 1 M Tris-EDTA and isopropanol precipitation	-80 °C	[133,134]
Cloacal	• Bead beating in a lysis buffer, followed by incubation at 95 °C	• phenol-chloroform extraction and ethanol precipitation	-80 °C	[133,134]
Bronchoalveolar lavage	• Incubation in a proteinase K solution at 60 °C, followed by boiling • Incubation in 10mM Tris-EDTA + SDS + proteinase K at 60°C, followed by incubation in 5M NaCl + CTAB at 65°C	• phenol-chloroform extraction and isopropanol precipitation	-80 °C	[135,136]
Nasal and Nasopharyngeal	• Incubation in Tris buffer + Proteinase K at 60 °C, followed by heat inactivation at 97°C	• phenol-chloroform extraction and ethanol precipitation	2 – 8 °C (<5 days) –90 °C (>5 days)	[105,137]
Oropharyngeal	• Chemical lysis in a DNA extraction buffer and proteinase K, followed by incubation at 55 °C	• phenol-chloroform extraction and ethanol precipitation	2 – 8 °C (<5 days) –90 °C (>5 days)	[105]
Sputum	• Bead beating in a GITC lysis buffer, followed by boiling	• Centrifugation and isopropanol precipitation	2 – 8 °C (<5 days) –90 °C (>5 days)	[105,126]

2.1.4.1. Cell Lysis

In order to extract NAs from a sample, a cell wall must first be disrupted to release its cellular components, through a process known as lysis. The majority of modern diagnostic techniques employ a two-step process employing cellular lysis followed by DNA/RNA fragmentation to tune the base pair sizes within the lysed sample, known as a lysate. There is no generic method of cell lysis which works with cells from all biological origins, with each specific method dependent on the individual cell characteristics and types, as well as the final application of the purified NA. Traditional methods of lysis were expensive, due to the requirement of expensive equipment such as centrifuges or bead beaters [26]. The traditional cell lysis could also take several hours to complete due to the number of necessary steps, however; the ability to perform sample preparation on a microfluidic scale greatly reduced the time taken, as well as the costs due to the reduced volume of reagents.

There are several features of the sample which must be considered when attempting cell lysis. Cells will differ in wall thicknesses, or resistance towards a particular chemical. Older cells are easier to lyse than younger ones and larger cells are much easier to lyse than smaller cells [26]. With each process the sample is subjected to, a component is removed irreversibly. Consequently, it is important to ensure that the necessary material is maintained during each process. Cell lysis can be classified under mechanical and non-mechanical techniques. When considering an appropriate technique, the main concern is the ability of the selected method to rupture the cell membrane, without damaging the target NAs. The following section will describe and evaluate several lysing methods for obtaining high quality NAs.

Pressure Shearing

Pressure shearing is a widely used mechanical method for conducting cell lysis. The sample is suspended within a medium and compressed using hydraulic forces, creating high shear forces within the solution as it is passed through an orifice. These high shear forces rupture the cell membranes, releasing the lysate. This method is effective for lysing gram-negative bacteria and some gram-positive bacterium with a thicker cell wall [26]. The inclusion of nano-scaled barbs may also increase the efficiency of this lysing method; however, this approach is susceptible to the clogging of the channels, should debris become stuck to the barbed walls [138-140]. In addition, as DNA is sensitive to mechanical shear forces, it may be fragmented or damaged during this procedure [26].

Chemical and Enzymatic Lysis

Chemical lysis (Figure 2.4) is a non-mechanical process which uses chemical or enzymatic compounds, known as a lysis buffer, to dissolve the cell membrane with minimal mechanical damage [141,142]. The lysate may then be treated with enzymes, which can remove NA or protein contaminants from the sample [26]. Early methods of cell lysis involved the use of alkaline chemicals such as sodium hydroxide to lyse and separate proteins from the NA [143]. Typically, for DNA extraction, a sample is lysed with a detergent and treated with DNase-free proteinase and RNase enzymes to digest the protein and RNA molecules, respectively. In order to denature the proteins within the sample, the detergent SDS was used [144]. It was later discovered that SDS could deactivate bacterial and viral material and it was replaced with the detergent Triton X-100 [145], with protease enzymes used to digest proteins within the sample, such as serine protease, proteinase K [146] and Proteinase EA1 [147]. These are commonly used today in sample preparation protocols.

Chemical lysis is a gentler and faster method of lysing cells and poses a lower risk of damaging the target DNA or RNA when compared with mechanical alternatives [26]. As the cells are suspended within the lysing reagent, a higher percentage are lysed when compared to mechanical methods, resulting in a higher yield of the target NA. This increases the reproducibility of the results. Due to the abundance of possible lysis buffers, the technique may be implemented for various sample types [148]. Chemical compounds may be combined to allow for multiple applications, both disrupting the cell membrane and deactivating contaminants. Several commercially available kits employ this approach to extract and purify DNA, RNA or proteins. Notable kits which are currently used in limited resource settings are the ChargeSwitch® kits by Invitrogen, the DNA IQ™ and MagaZorb® kits by Promega, and the QuickPick kits by Bio-Nobile [149]. These kits require minimal equipment, and are available for a large array of sample types. However, many commercial kits can fail to completely remove inhibitors and organic from the collected samples [150].

A drawback to the use of chemical lysis is the expensiveness due to the large volume of reagents which may be required. However, the use of microfluidic techniques may serve to offset these costs. As stated prior, a wide array of chemical reagents are available for cell lysis. If the selected chemicals are incompatible with the cells to be lysed, then the lysing method will either be unsuccessful, or the cellular contents may be damaged irreversibly. Particular chemicals may also pose health risks to the user, meaning that the techniques require trained personnel to perform safely and may need to be performed underneath a laminar flow hood to prevent inhalation. This in turn restricts the possible portability of the process. It is also to be noted that complex pathogens such as bacterial spores can be challenging to lyse and may require more “aggressive” approaches [149].

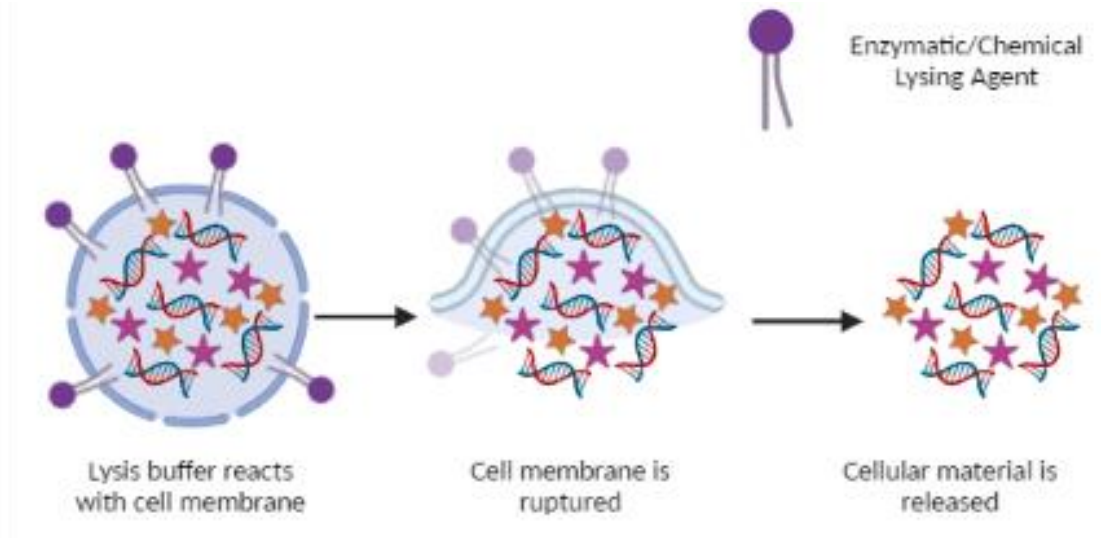

Figure 2.4 – Chemical lysis using a lysis buffer [151]
(Created with BioRender.com)

Manual Grinding

This mechanical method of cell lysis is commonly used for the lysing of plant tissue cells. The tissues are frozen in liquid nitrogen at -90 °C and broken down manually using a mortar and pestle. While these methods do not generate much heat in comparison to other mechanical methods, it is time consuming and somewhat primitive, with no reliable method of quantification. The use of an electronically powered mortar grinder may increase the speed of cell lysis; however, the throughput remains low, making the approach unsuitable for large volume operation [152].

Ultrasonic disintegration

This mechanical method of lysis is achieved by invoking the rapid vibration of the sample using an ultrasonic probe tip, causing cavitation. This creates microscopic gas bubbles, which generate high shear forces which rupture the cell membrane. Ultrasonic disintegration is not particularly useful for initial lysis; however, this technique can be used to separate the inner and outer membranes of gram-negative bacteria. Ultrasonic disintegration is not instantaneous, requiring several minutes to lyse a large percentage of the sample. The ultrasonic disintegrators also generate a high amount of heat and should be kept as cold as possible in order to prevent the evaporation of the sample [26].

Bead-mill homogenizers

Bead-mill homogenizers is a common mechanical method used to achieve cell lysis. The technique (also known as “beadbeating”) is achieved by agitating a sample within a bead mill filled with glass, steel or ceramic beads, which collide with the cells to cause cell disruption [149,151]. While this method can be achieved using manual means, vortex mixing can alleviate any manual requirements. The size of the beads, as well as the material of the beads, may be adjusted based on the sample type to be lysed [26]. The technique is considered to be highly efficient. However, due to the complete disintegration of the cells, it can be difficult to remove cellular debris from the NA in subsequent processing steps. In addition, the process can result in the production of heat which can lead to the degradation of RNA [151].

Thermal Lysis

Thermal lysis employs high temperatures to denature the cell membrane. A contained sample may be subjected to a water bath at 100 °C for 40 minutes, which would lyse the cells without causing irreversible damage to the contents. This method may also be used in conjunction with chemical lysis, where the sample may be mixed with a lysis buffer and then heated [26]. This process requires constant monitoring of the temperature, to prevent the loss of sample volume. Due to the high energy consumption, employing thermal lysis can be expensive, however, this cost is lessened when processing smaller volumes, which do not require much energy to lyse [138,140].

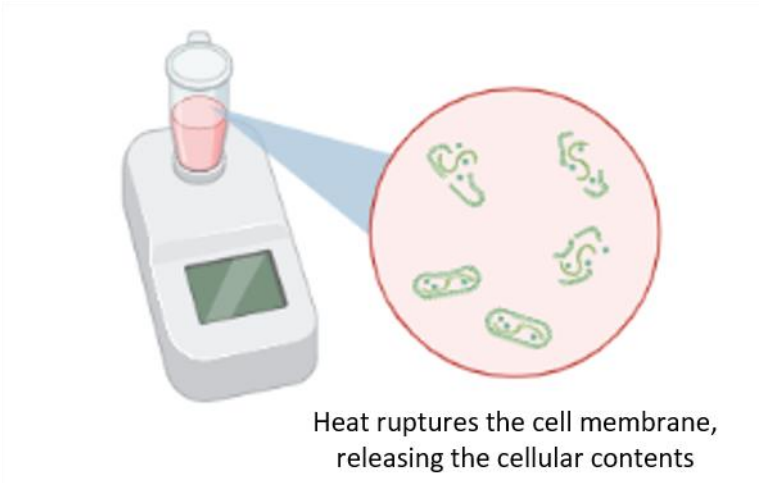

Figure 2.5 – Thermal lysis using a heater block
(Created with BioRender.com)

Freeze Thawing

Particular cell walls may be weakened by freezing and thawing them in a cyclic process, creating swelling and contracting within the cell. This has been particularly effective for gram-negative cells, which can render them more receptive to detergent based lysis, allowing for a larger scale isolation of NAs [26]. Johnson *et al.* used freeze thawing to extract proteins from *E. coli* cells, demonstrating the ability of this method to lyse up to 90% of the cells without using supplementary techniques [153].

Microwave Lysis

Microwave lysis may be used as a non-mechanical method to lyse cells. The sample may be placed into deionized water, before being subjected to microwave irradiation, which causes the water to expand, degrading the cell membrane. The lysate may then be collected and prepared for analysis.

Lyse-It LLC introduced the trademarked Lyse-It™, which claimed to "lyse virtually any cell within 30 seconds". The device is comprised of a silicon container and a glass microscopic slide, containing a gold bow tie structure which focuses the microwaves through the sample. Typically, the sample is placed into a 900 W microwave and irradiated at 30 % power for 30 seconds. The power may be tailored to allow for the fragmentation of NAs, removing subsequent purification steps. However, this change to the process may result in losses of the sample volume [154]. The single use Lyse-it slides may be purchased in packs of 10, 25, 50 and 100, with the lattermost costing $875. The silicon sample chambers range in volumes from 500 µL to 5 mL and may also be purchased in packs of 100 for $275. The resulting cost is $11 per sample. As the slides are disposable, there are no maintenance costs; however, costs will accrue due to the replenishment of consumed products [154].

Melendez *et al.* employed a two-step approach to lyse bacterial cells, bacteriophages and spores. It was noted that sample volumes of 1, 3 and 5 mL could be lysed at times of 30, 60 and 90 seconds respectively, with minimal losses of the sample. They also used the Lyse-It slides to lyse frozen vaginal swab samples; however, centrifugation was required to remove the cellular debris [154]. Santaus *et al.* also utilised the Lyse-it slides for the lysing of *Listeria monocytogenes*. When testing the reusability and durability of the slides, it was concluded that more than 120 seconds of irradiation would cause the gold coating on the Lyse-it slides to crack, hindering the ability for the slides to be reused [155].

Osmotic Lysis

Osmotic lysis occurs when a cell bursts due to osmotic imbalances. A solute concentration is used, which enters the cell membrane through membrane channels, known as aquaporins, which exerts a high internal pressure. As fluid continues to enter the cell, the volume increases to a critical point where the cell bursts [26]. Many microorganisms cannot be lysed through this approach, due to the cells adapting in ways which prevent osmotic lysis. These include the presence of vacuoles within paramecium cells, which remove excess fluid from the cell, as well as the growth of cell walls and thicker cell membranes, which are less permeable to fluids. This method is therefore more suitable for animal or protozoa cells, which do not have cell walls [156]. It is possible to utilise this method with cells with a weakened cell membrane, following preliminary lysing processes [26].

Electroporation

Electroporation is a non-mechanical process in which an electrical field is passed through a conductive solution, creating micropores in the cell membrane. If the electrical field is high enough, the cell membrane will rupture [26,157]. This approach can employ an electrical discharge of between 0.2 – 1.5 V to rupture the cell membrane within a timespan of between 5 milliseconds and 20 minutes [141,158]. While initially designed for lysing mammalian cells, it may be set-up for use with several cell types [157]. The electrical field must not exceed a threshold determined by the cellular shape, size, and structure. Typically, an electrical field strength of 0.2 MV/m is used [138], and electrodes are placed 10 µm away from the cells to prevent cellular damage by joule heating [141,157].

Discussion of Cell Lysis Techniques

While some methods may offer a faster processing time or a higher processing volume, the conditions required to lyse the cells using the method may only be achievable in laboratory settings or using complex equipment. Zheng *et al.* compared several lysing techniques, which can be seen in Figure 2.6 [159]. It is preferable for samples to be processed in the shortest time possible, and thus, manual grinding and microwave lysis can be seen as favourable approaches. In contrast, enzymatic lysis can be viewed as offering a less favourable performance in terms of processing time. When considering the volume per operation, a larger volume is ideal. In this instance, manual grinding and enzymatic lysis can be concluded to be the preferred approaches. However, among both comparisons, manual grinding outperformed the other analysed methods [159].

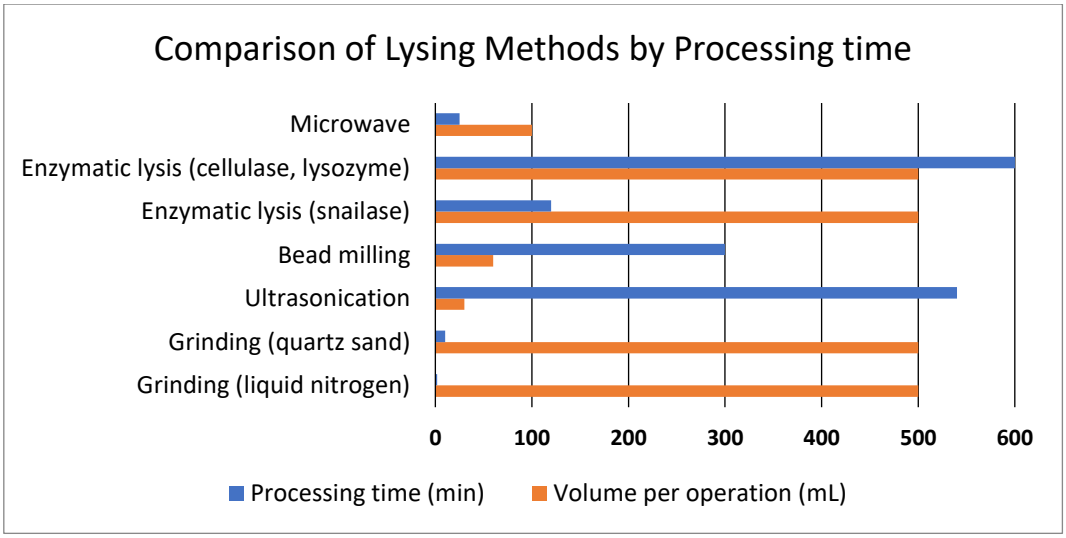

Figure 2.6 – Comparison of Lysing Methods by Processing Time and Volume [159]

Table 2.6 demonstrates a comparison between various lysing techniques. The lysis method can influence the subsequent processes needed to prepare the sample. It is important to consider the viability and the ease of the application of the approach. Particular techniques may be incompatible, or too complicated to implement into compact devices for the lysis of smaller volumes [26]. A major concern was the functionality of the lysis method without refrigeration or freezing. Techniques such as manual grinding and freeze thawing require refrigeration or freezing in liquid nitrogen. As these cannot be reliably provided in low-resource settings, these approaches were not considered further.

Mechanical methods are more robust than their non-mechanical counterparts. Furthermore, they do not introduce chemicals which require future deactivation [149]. However, mechanical methods may be harsh on particular cell types, fragmenting NAs. In addition, the number of cells lysed can vary greatly between operations, resulting in issues regarding reproducibility. Pressure shearing requires the generation of forces between 15 – 150 MPa, leading to the use of both expensive and complex instruments incompatible with POCT [160,161]. Bead beating is less vigorous in comparison; however, the heat generated during the process can also cause DNA fragmentation. In many cases, the inclusion of cooling methods can be vital for preventing the degradation of the sample. However, this greatly restricts its ability to be deployed in low-resource settings [162].

Alternatively, non-mechanical methods provide a gentler approach to cell lysis and tend to lyse a higher percentage of cells in comparison, increasing the reproducibility of results. Non-mechanical methods are also more abundant and can be used for a larger range of sample types. Nevertheless, techniques such as electroporation, ultrasonic and microwave lysis require complicated instruments

which can increase engineering complexities; and techniques such as osmotic lysis also must be conducted following preliminary lysis steps. As the goal of the project was to achieve sample preparation without the use of complex equipment, these approaches were not considered further.

Thus, among the techniques discussed, the thermal and chemical lysis approaches were selected as considerable options to integrate into a POCT platform. These techniques are not without their challenges, however. Should a lysis buffer require the introduction at a specific stage of the sample preparation process, then suitable fluid control is required, which can increase engineering complexities. Furthermore, chemicals which are introduced to the sample must be deactivated to prevent the inhibition of downstream analysis.

Table 2.6 – Comparison of Cell Lysing Techniques

Lysis Method	Cell Types	Mode of Lysis	Required Apparatus	Ref
Pressure Shearing	GN Bacteria GP Bacteria	Harsh	French press vessel Nano scale barbed channels	[141]
Manual Grinding	Plant	Harsh	Liquid nitrogen Mortar & pestle/Electric grinder	[152]
Ultrasonic	GN Bacteria Spores Tissue	Moderate	Ultrasonic probe tip Ice bath or Refrigerator	[26]
Bead Beating	*Various*	Harsh	Glass/Silica/ beads Vortex mixer	[26,149]
Thermal	GN Bacteria GP Bacteria	Gentle	Water bath Temperature sensor	[26,138,140]
Chemical/Enzymatic	*Various*	Gentle	Commercial kits Detergents/Enzymes	[141]
Osmotic	Animal Protozoa	Gentle	Solute concentration *Preliminary lysing techniques*	[26,156]
Freeze Thawing	Mammalian GN Bacteria	Gentle	Ice bath or liquid nitrogen Detergents	[26,153]
Microwave	*Various*	Moderate	900 W Microwave Lyse-It® Slides, Silicon containers	[154]
Optical	Cancerous Mammalian	Gentle	Suspension medium Laser generator	[141]
Electroporation	*Various*	Moderate	Electroporation system Conductive medium	[141]

2.1.4.2. Nucleic Acid Extraction

For the majority of the pathogens of interest, DNA is found within the nucleus of the cell while RNA will be found in the cytoplasm. Contrary to this notion, both DNA and RNA may be found within the cytoplasm of bacterial cells, due to the lack of a nucleus [26]. DNA and RNA are naturally acidic, and exert a negative charge. By manipulating the pH, the temperature, chemical exposure, or other conditions, the DNA and RNA can be manipulated, in the form of strand separation or denaturation. Through this knowledge, it is possible to utilise techniques to extract DNA or RNA from a sample following sufficient lysis, allowing for more accurate analysis.

Following cell lysis and nuclease inactivation, solid cellular debris should be removed from the lysate, allowing for the purified NAs to be isolated, purified and concentrated. Examples of common molecules found in samples include proteins, polysaccharides, metals, salts and other organic compounds [149]. The following section will discuss the processes used to extract NAs from a sample.

Liquid-Liquid Extraction

Liquid-liquid extraction (LLE) is an extraction process involving the interface between two immiscible liquid phases, one typically being an aqueous phase containing the lysate and the other an organic extracting solvent. The target analyte is drawn into the organic solvent due to its favourable solubility within the solvent, and due to the different molecular weights between the two phases, the phase containing the NA will sit on top of the denser phase containing the proteins and other contaminants, allowing for its removal using a membrane or vacuum pressure [26]. Traditional LLE extraction methods employ the centrifugation of the lysate within a caesium chloride and ethidium Bromide (CsCl-EtBr) gradient, separating the DNA by molecular weight. While this method yields NA of a high purity at a low cost, the process requires many time consuming and technical steps, which can take between one and two days [163]. EtBr is also a mutagen, posing potential health risks to the user.

As an alternative, phenol chloroform may be used. Following cell lysis, the lysate is passed through the phenol-chloroform, which denatures the proteins within the sample while leaving the NA suspended within the aqueous phase. The sample is then treated with DNase-free RNase enzymes to remove the RNA, before ethanol or isopropanol is used to precipitate the DNA. Despite many successful implementations of this method in sample purification, phenol-chloroform is avoided in present day due to its toxicity and corrosiveness, as well as the risk of the transitioning of the DNA into the phenol phase [164]. Modern replacements for phenol-chloroform include organic solvents,

alcohols, detergents and chaotropic agents, with GITC–based methods becoming popular for isolating high quality RNA from various cells and tissues [26].

A common drawback of the LLE techniques is that a small volume of the two phases will be miscible, meaning a small percentage of the target analyte may be lost during the process [26]. In traditional approaches, there is a requirement for glassware, which greatly increases costs; however, recent developments in microfluidics and automation have been beneficial in overcoming this issue.

Liquid-Solid Extraction

Liquid-solid extraction (LSE) was developed as a robust method to exhaustively extract a target pathogen from a lysate, while overcoming the drawbacks of LLE techniques. Instead of the interfacing of two liquid phases, an aqueous phase is passed through a solid phase, allowing the pathogen of interest to become trapped within the solid phase. The solid phase may then be separated from the liquid phase and the extracted pathogen eluted during a succeeding process. As particular inhibitors may become bound to the solid phase, it is vital to first employ filtration, using materials which do not contain organic binders which can adsorb any of the organic material [165].

Solid-Phase Extraction

Solid-Phase Extraction (SPE) is a form of LSE, introduced as a low-cost alternative to LLE. Similar to LSE, a sorbent phase is used to absorb target NAs within the lysate. The sorbent is then washed with alcohols to remove trace contaminants before the NAs are eluted from the phase using a saline buffer. This technique requires little biochemical knowledge and can extract genetic material in less than an hour with a low risk of contamination [132]. SPE offers a higher concentration of analytes when compared with LLE, allowing for a much better isolation of the target pathogen [26].

Traditional SPE techniques used GITC which can react with acids, meaning an alkaline waste storage component is necessary [132,166]. This, along with the use of phenol-chloroform, increased the overall health risks. In 1989, McCormick used a silica-based substitute to bind proteins to the solid phase, while the DNA remained suspended in solution. By eliminating the phenol, the toxicity was removed [167]. This approach is currently one of the preferred approaches to NA extraction in laboratory settings, with commercially available kits incorporating silica membranes into spin columns (Figure 2.7). As the lysate passes through the spin column, the NA is adsorbed into a silica membrane

while other molecules pass through the column and into a waste container. The DNA is then washed using salts and alcohols such as ethanol or isopropanol to remove waste particles, prior to the elution of the DNA allowing for the NA to be recovered using a weakly alkaline buffer, commonly a Tris-EDTA buffer or ultra-pure water. The result is purified DNA in an aqueous solution [168]. Despite the popularity of this approach, the method typically requires several washing steps which require external instruments to facilitate, such as a centrifuge or a vacuum.

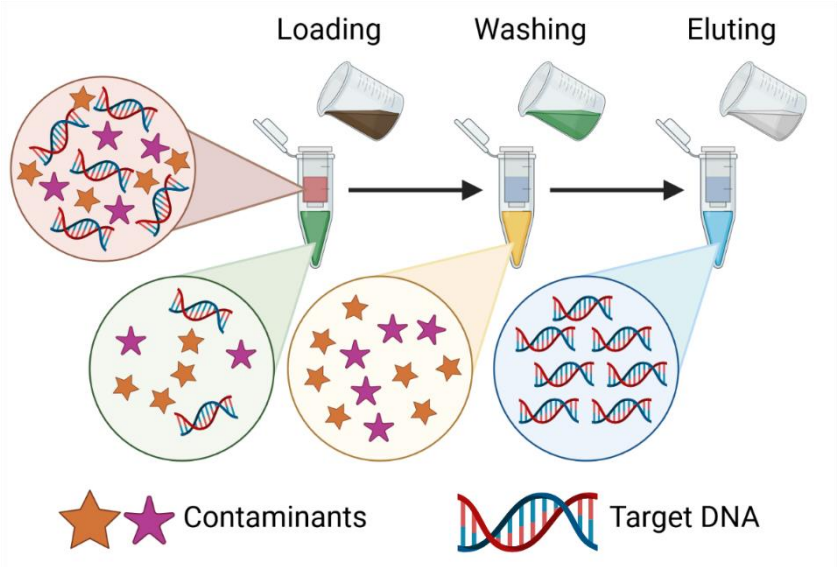

Figure 2.7 – General process for Solid-Phase Extraction
(Created with BioRender.com)

In the 1990s, Boom *et al.* used magnetic particles to purify NAs in a process referred to as the Boom method [132]. Current commercially available kits also use silica or glass-based beads, to prevent DNA from permanently binding to the solid phase. A variation to this process applies carboxylate coated magnetic beads, which binds to the NAs in the presence of alcohols [169] or chaotropic salts [170]. Magnets are then used to secure the beads while the lysis buffer is removed. By introducing an alkaline buffer, the NA may then be eluted. This technique is useful for eliminating both centrifugation and solvent extraction and precipitation steps, allowing for the fast isolation of NAs with a high rate of reproducibility [26]. The processes of lysis and extraction may also be combined by using the beads to both lyse the cells and extract the NAs, reducing the costs of reagents, as well as the complexity of the resulting platform. Many microfluidic devices utilise magnetic beads for NA isolation [171-173].

The process of SPE may be adapted into solid-phase microextraction (SPME), where a sorbent coated surface or channel is used to extract NAs. As the amount of the analyte extracted is independent of the initial sample volume, this approach may be directly applied to in field sampling. However, this

extraction technique is non-exhaustive, meaning that a percentage of the target pathogen will remain in the original sample following sample collection. The process may also be configured into a stir bar configuration, known as stir bar sorptive extraction (SBSE). Similar to SPME, a stir bar, coated in the sorbent, is immersed in a sample and is used to extract the target analyte from the solution. This technique is performed in less than 1 hour and has a greater capacity for extraction than SPME [26].

Chelex DNA Extraction

The Chelex sample preparation method was developed by Bio-Rad Laboratories (USA), for the extraction of DNA from forensic samples. The Chelex-100 chelating resin functions through ion exchange, allowing for metallic ions within the DNA to bind to the Chelex [174]. Typically, the cells are lysed using suitable methods, prior to the addition of the Chelex resin. Once the DNA is bound to the Chelex, it is protected from DNases, preventing degradation [175]. Following the removal of the supernatant, the Chelex-DNA compound is also considered purified and stable and can be stored for 4 months if refrigerated at 4°C [176]. It is possible to elute the DNA using salt-based buffers [149]. This method is simple, fast and inexpensive, with a higher efficiency than phenol-chloroform [177]. This process also does not introduce organic solvents into the protocol, which may contain materials which can require deactivation prior to downstream analysis [174]. Thus, it is favoured in resource limited settings. However, as the Chelex beads must be distributed evenly throughout the solution during the extraction process, a method of continuously mixing the solution during the process is required.

Membrane Based Filtration and Extraction

Membrane filtration is a process using a porous membrane to capture and remove cellular debris from the lysate following cell lysis, without shearing the NAs. The pore size is typically less than a micron in width, allowing for small particles within the sample – the filtrate – to pass through [26]. Membrane filtration bypasses the need for centrifugation, a laborious step in conventional sample preparation. As the filter does not bind to the NA, minimal amounts are lost during this step. Due to the low cost of the membrane, along with the high throughput and robustness of the approach, membrane filtration can be seen as an ideal initial step for general sample purification [26,178].

A drawback to filtration is that large particles may form an obstructive layer across the surface of the membrane, preventing the filtrate from passing through. The retention of cellular components is

sensitive to the flow rate at which the lysate is passed through the membrane [26]. Mueller *et al.* evaluated the variables concerning the extraction of NAs from plankton within seawater, using nanoporous aluminium oxide membrane filters. It was concluded that a flow rate between 12 – 16 mL/min was acceptable [178]. It was also advised to avoid guanidinium-based salts in conjunction with this method, due to causing a permanent binding between DNA and the membrane [179,180].

A filter-extraction protocol was later devised, where an extraction buffer is flushed through the membrane in reverse rather than in the same direction as the sample, preventing the trapping of NAs with a high molecular weight [178]. Many modern filtration kits are commercially available, combining the filtration and SPE processes, without the need for further purification steps. This allows for NA extraction without the use of detergents or alcohols, which increases the risk to the user [26].

The filtration of nucleic acids (FINA) approach was recently used for NA extraction from whole blood samples in less than two minutes. Following lysis with a detergent, the lysate is applied by pipette to the FINA membrane. The lysate wicks across the membrane, allowing the NA to be isolated on the surface. The membrane is then washed to remove inhibitors and placed into a reaction chamber for analysis. This method is a simple three-step process requiring little laboratory equipment, making it easy to implement in several conditions. However, this method is not exhaustive, with the ability for the membrane to isolate NAs proportional to its diameter, which in turn is limited by the size of the reaction tubes used. Should the membrane diameter exceed a threshold, the overlapping will result in a reduction of the surface area exposed to the reaction mix. A larger membrane will also require a large volume of the reaction mixture to function effectively, increasing costs. Should the membrane be too small, it may become saturated by the initial sample, preventing effective washing. For a 200 µL reaction tube, 9 mm is advised as the maximum limit for the FINA membrane [181].

Discussion of Nucleic Acid Extraction Techniques

Similar to cell lysis, there is no optimal method of NA extraction suitable for every application. Instead, a suitable method must be selected based on its applicability. Specific procedures may yield a higher quality NA, but may prove more complex to implement. The extraction efficiency will also vary depending on the sample type. In some cases, if the sample is “clean”, then NA extraction may be omitted. In other cases, the extraction process will also act as a means of concentrating the NAs, reducing the number of steps required [149]. However, in resource limited settings, many methods may be unavailable due to cost limitations. Ultimately, trade-offs are necessary.

A comparison between the previously discussed NA extraction techniques can be seen in Table 2.7. The optimal approach to NA extraction is to minimise the required apparatus and processing time, while maximising the amount of said NA extracted from the sample. For POCT specifically, the desire is to reduce the number of chemicals involved in the process as much as possible. In addition, the process needs to be as exhaustive as possible to ensure the highest quantity of NA is collected for analysis [162]. LLE techniques were not considered further due to requiring hazardous chemicals and glassware in the cases of phenol-chloroform and CsCl-EtBr based extraction protocols [182]. The Chelex extraction method also was not considered further due to the low purity of NAs yielded from the process [183]. As a result, only LSE and similar techniques were considered.

Table 2.7 – Comparison of Nucleic Acid Extraction Techniques
LLE, Liquid-Liquid Extraction; LSE, Liquid-Solid Extraction; SPE, Solid-Phase Extraction; SPME, Solid-phase microextraction; SBSE, stir bar sorptive extraction

Extraction Method	Processing Time	Exhaustive?	Removal of Contaminants?	Required Apparatus	REF
LLE	High	Yes	Yes	Glassware, organic solvents	[26,163,164]
LSE	Low	Yes	No	Solid phase, filtration system	[26]
SPE	Low	Yes	Yes	Sorbent phase	[26,132]
SPME	Low	No	No	Sorbent coated surface(s)	[26]
SBSE	Low	Yes	No	Sorbent coated stir bar	[26]
Chelex	Low	Yes	Yes	Stir bar	[174]
Membrane	Low	No	Yes	Porous membrane, commercial kits	[26,181]

2.1.5. Nucleic Acid Amplification and Detection

Following sample preparation, purified NAs may undergo an amplification process to increase the concentration of the NA within the sample, allowing for easier detection of the target analyte [184]. Such processes are referred to as nucleic acid amplification testing (NAAT). As NAAT techniques increase the amount of NAs contained within the sample exponentially, the required sample volume can be greatly reduced, thus lowering the risk of contamination, along with the cost of reagents [185]. The performance of NAAT is typically quantifiable and may be performed in real-time in specific configurations, allowing for the earlier detection of target pathogens. The focus of the research presented in this thesis was based on the sample preparation steps which would be conducted prior to NAAT. However, the understanding of the downstream processes was important to determine which sample preparation steps would be ideal. This section of the report will discuss some of the prevalent NAAT techniques which have been utilised.

2.1.5.1. Polymerase Chain Reaction

Defined as the "gold standard" of molecular biology, Polymerase Chain Reaction (PCR) was invented by Kary Mullis in 1983 for use in NAAT [186]. Similar to the *in vivo* process of DNA replication, PCR is an *in vitro* technique which amplifies target DNA, producing up to 10^6 or 10^9 copies of a specific sequence. The first step of PCR is denaturation at 90 – 95°C, causing partnered DNA strands to separate. Primers are designed to direct DNA polymerase to flank the extremities of the DNA segment of interest to amplify. An annealing step follows at 55 – 60 °C, allowing primers to anneal to the complimentary strands. At 72°C, DNA polymerase catalyses the addition of deoxynucleotide triphosphate (dNTPs) to match the parent strand and create new dsDNA. The cycle is repeated up to 40 times, exponentially increasing the number of DNA copies with each cycle.

However, there are limitations to the process. Should the annealing temperature be too low, or if the concentration of dNTPs is incorrect, the wrong sequence could be amplified. If the annealing temperature is too high, or should the incorrect primer sequence be used, then no DNA sequences would be amplified. The quality of the amplified sequence may also be affected if too few cycles of PCR are performed [186]. Furthermore, PCR requires precise and rapid temperature control in a process known as thermocycling, which consumes a high amount of power [184]. PCR methods are also known to be severely affected by the presence of inhibitive substances, substances which can interfere with cell lysis, bind to or degrade the target NA, or inactivate the DNA polymerase [100,187].

Reverse Transcription PCR

Reverse Transcription PCR (RT-PCR) allows for PCR to be performed on an RNA template by including a reverse transcription process as outlined in section 2.1.1. First, an mRNA sequence is synthesised with a DNA template. Using an RNase enzyme, a portion of the DNA is digested, producing a ssDNA sequence. Finally, a dsDNA template is created using polymerase activity, known as complimentary DNA (cDNA), which is then amplified [188]. RT-PCR is simple, specific and sensitive, able to detect trace amounts of mRNA within small sample volumes [189]. However, due to the exponential growth of the cDNA during the PCR cycles, it can be difficult to quantify the results using end point detection [190]. With the fluctuations in amplification efficiencies, the errors in the quantified mRNA are further increased [189]. Furthermore, due to the high sensitivity, slight DNA contamination can lead to either false positives or an over estimation of the yield [189].

Real-Time PCR

Real-Time or quantitative PCR (qPCR) measures the absolute amount of DNA within the sample during the PCR process, overcoming one of the major drawbacks of standard PCR, that being its difficulty in determining the initial value of the target template. This is achieved by co-amplifying the template DNA with an internal standard. These bind to similar sites as the primers, but are distinguishable from the primers due to a difference in sequence or size. During amplification, both the standard and the target DNA amplify at a comparable rate. By monitoring the growth curve of the standard through fluorescent response after each cycle, the growth curve of the template DNA can be determined [189]. It is also possible to detect RNA using quantitative reverse transcription PCR (qRT-PCR). In this configuration, it is vital to include DNase to digest any contaminating DNA, which can compete with the internal standard during amplification, resulting in the incorrect quantification of the mRNA [191].

2.1.5.2. Isothermal Nucleic Acid Amplification Testing

Recent approaches to NA amplification have attempted to exploit the advantages offered by PCR while overcoming its dependency on thermocycling. Isothermal NAAT (iNAAT) is a term attributed to a series of techniques which amplify NA sequences at a constant temperature. Compared to PCR, iNAAT is designed to be simple, low-cost and robust, allowing easier integration into POCT [184]. These techniques are designed to provide results comparable to PCR, despite varying external factors such as foreign contaminants or inhibitors, which commonly compromise PCR amplification.

For many iNAAT techniques, the minimum of a lysis step is required. For RNA analysis, the removal of RNases is also required to prevent degradation. If there is too high a concentration of the target NA in the sample, then the process can result in errors. A dilution step may be included to reduce both the concentration of the template NA and the number of contaminants in the sample. In some instances, a denaturation step is vital to initiate the reaction and ensure that primers anneal at the specific target sites. This may be conducted chemically or thermally; the latter of which prevents the process from technically being isothermal. In addition, certain polymerases can be inactivated by heat and must be introduced following denaturation, increasing engineering complexities [192].

There are several variants of iNAAT, including but not limited to, Cross Priming Amplification (CPA), Helicase Dependant Amplification (HDA), Nucleic Acid Sequence-Based Amplification (NASBA), Polymerase Spiral Reaction (PSR), Rolling Circle Amplification (RCA), Recombinase Polymerase Amplification (RPA), Strand Displacement Amplification (SDA), and Loop-Mediated Isothermal Amplification (LAMP). A review of these techniques was conducted, available in section 8.1. A summary of these methods can be seen in Table 2.8 and Table 2.9.

For POCT, speed is crucial to prevent the delay of action. In this regard, methods such as SDA and RPA may seem favourable. Contrastingly, methods such as RPA and RCA may seem preferable due to their lower operational temperatures. However, other factors play a crucial role in each process. Some methods struggle with multiplexed amplification due to the lack of synchronicity between the temperature steps and the processes [193,194]. Others may require complex primers which are difficult to design and may lead to non-specific amplification. Finally, the option to conduct readings in real-time should be possible, eliminating the need to conduct time-consuming end-point detection processes. However, many of the available real-time detection methods require tailored instruments, which can greatly increase costs [195,196]. Due to a lack of standardisation, it is difficult to accurately compare the performance of the various iNAAT methods [185].

Prior to the start of this project, it was foreknown that LAMP and Reverse-Transcription LAMP (RT-LAMP) would be used. RT-LAMP is conducted at 60 – 65 °C. In contrast to the 2 primers used for PCR techniques, LAMP uses 4 to 6 sets of primers to target specific gene regions, increasing the robustness and sensitivity of the process [64,197]. LAMP based assays also bypass the need for RNA isolation and purification steps, allowing for the detection process to be streamlined, reducing costs and time. Through this approach, it is possible to integrate the process into a single use tube or cartridge, which may be used in place of larger equipment [197]. Following amplification, the presence of the target can be confirmed by visual inspection following a turbidimetric or colorimetric change. While several RT-LAMP based assays are currently in development [198-203]; few have had commercial success.

Table 2.8 – Comparison of Nucleic Acid Amplification Techniques [185,204]

PCR, Polymerase Chain Reaction; CPA, Cross Priming Amplification; HDA, Helicase-Dependent Amplification; NASBA, Nucleic Acid Sequence Based Amplification; RCA, Rolling Circle Amplification; PSR, Polymerase Spiral Reaction; RPA, Recombinase Polymerase Amplification; SDA: Strand Displacement Amplification; LAMP: Loop-Mediated Isothermal Amplification; dsDNA, double-stranded Deoxyribonucleic Acid; ssDNA, single-stranded Deoxyribonucleic Acid; RNA, Ribonucleic Acid; (1), Denaturation; (2), Annealing; (3), DNA synthesis

	Amplicon	Enzymes	Primers	Time (min)	Amplification Limit	Temp (°C)	Detection Method	Tolerance to crude samples?	REF
PCR	dsDNA	1	2 (Simple)	60 – 180	10^9	90 – 95$^{(1)}$ 55 – 60$^{(2)}$ 72$^{(3)}$	• Gel electrophoresis	Low	[186]
CPA	dsDNA	1	5 (Complex)	60 – 90	10^4	63	• Fluorescence • Gel electrophoresis • Turbimetric • Lateral flow devices	Low	[205]
HDA	dsDNA	2	2 (Simple)	30 – 120	10^{10}	64	• Intercalating DNA dye • Fluorescence • Electrochemical analysis • Gel electrophoresis	High	[206]
NASBA	ssRNA	3	2 – 3 (Simple)	60 – 180	10^9	37 – 42	• Fluorescence	Medium	[207]
PSR	dsDNA	1	2 (Simple)	45 – 60	10^9	61 – 65	• Fluorescence • Gel electrophoresis • Turbimetric	Low	[208]
RCA	ssDNA	2	1 (Simple)	60 – 120	10^9	30 – 65	• Fluorescence • Electrophoresis	Low	[209]
RPA	dsDNA	2	1 (Simple)	20 – 40	10^9 – 10^{11}	25 – 42	• Fluorescence	Low	[210]
SDA	ssDNA	2	2 – 4 (Simple)	20 – 120	10^9	37 – 49	• Fluorescence • Lateral flow devices	Low	[211]
LAMP	ssDNA	1	4 – 6 (Complex)	60	10^9	60 – 65	• Intercalating DNA dye • Fluorescence • Turbimetric	High	[212]

Table 2.9 – Comparison of Nucleic Acid Amplification Techniques (continued) [185,204]

CPA, Cross Priming Amplification; HDA, Helicase-Dependent Amplification; NASBA, Nucleic Acid Sequence Based Amplification; RCA, Rolling Circle Amplification; PSR, Polymerase Spiral Reaction; RPA, Recombinase Polymerase Amplification; SDA, Strand Displacement Amplification; LAMP, Loop-Mediated Isothermal Amplification; DNA, Deoxyribonucleic Acid; RNA, Ribonucleic Acid

	Advantages	Challenges
CPA	• Does not require an initial denaturation step	• Low tolerance to crude samples • Complex primer design
HDA	• Rapid amplification (less than 60 min) • Can be performed on DNA and RNA • Higher tolerance to crude samples	• Requires heat treating at 65 °C and 95 °C to increase sensitivity • Susceptible to contamination and non-specific amplification • Difficult to multiplex
NASBA	• Low operating temperature • Lower susceptibility towards contamination	• Requires denaturation at 95 °C • Limited to RNA templates (requires RNase-free conditions) • Susceptible to non-specific amplification and false positives
PSR	• Rapid amplification (less than 60 min) • Simple primer design • Does not require complex instruments	• Low tolerance to crude samples
RCA	• Low operating temperature • Lower susceptibility towards contamination • Compatible with commercial PCR primers • May be performed within a solid phase or in solution	• Requires heat denaturation step • Low tolerance to crude samples • General primers can lead to primer dimers and false positives • Difficult to amplify short DNA templates
RPA	• Low operating temperature • May be performed within a solid phase or in solution • Rapid amplification (less than 60 min) • Compatible with PCR primers	• Inhibited by high concentrations of DNA and proteins • RPA kits are only sold by a single company
SDA	• Rapid amplification (less than 60 min) • Low operating temperature	• Low tolerance to crude samples • Requires denaturation at 95 °C • Unable to amplify long target sequences • Susceptible to non-specific amplification
LAMP	• Higher tolerance to crude samples • Highly specific • Does not require complex instruments	• Complex primer design • Susceptible to non-specific amplification • Difficult to multiplex

2.2. State-Of-The-Art for Sample Preparation for Molecular Diagnostics

In contrast to POCT which seeks to return results to a smaller number of patients in the shortest TAT possible, laboratory-based diagnostics seeks to return results to a larger number of patients, at the cost of an increased TAT. As a result, laboratory-based diagnostic platforms aim to maximise the overall throughput in order to most effectively utilise the time taken to yield results. Many of the platforms require refrigerated or frozen reagents, laborious protocols, complex instrumentation, reliable electrical power, trained personnel, and appropriate infrastructure and consumables. As a result, these platforms are restricted to use in laboratories. It is important to consider the capabilities of these platforms, as the desired output is similar in terms of the quality of the NA extracted from the raw samples. These considerations of the current state-of-the-art for laboratory-based platforms which employ sample preparation techniques will serve as a guideline on what can be considered to be the gold standard.

2.2.1. QIAGEN Platforms

The QIAGEN® Company (Germany) introduced several platforms and kits, which use various lysing and extraction techniques to offer a comprehensive and robust method for performing NA extraction [177,213]. The extraction techniques may be performed manually by a technician, or automatically using the corresponding QIAGEN platform. The automated platforms allow for protocols to be performed at a higher throughput and an increased accuracy, with the trade-off of an increased cost.

2.2.1.1. QIAcube

The current gold standard from QIAGEN is the QIAcube Connect. Developed from the standard QIAcube, the platform is capable of processing “virtually any sample type” to yield purified DNA or RNA, with a relatively high throughput. The QIAcube platform utilises a selection of chemical and bead beating techniques for cell lysis, followed by filtration using a vacuum driven system. The lysate is then subjected to a series of binding and washing steps performed on disposable troughs, containing the necessary buffers and reagents. The purified NAs are finally eluted, allowing for its analysis [214].

The QIAcube platform is capable of processing between 24 and 96 samples in parallel, in increments of 8 samples. This is achieved by the use of an 8-channel pipetting head, which transfers the sample between the troughs [214]. The platform also uses two compartments during sample preparation to

prevent cross contamination. The QIAcube Connect offers the ability to automate and track protocols remotely using a tablet. The platform also contains centrifuges, heated shakers and a robotic gripper, allowing for tailored protocols to be performed while eliminating manual processing steps [215].

Several kits compatible with the QIAcube platform are available; with kits compatible with the samples of interest shown in Table 2.10. A particular kit of interest was the QIAamp 96 DNA Swab BioRobot Kit. Following collection, the swab is air dried and placed into the platform and the cells are lysed in the presence of proteinase K. The lysate is then treated with ethanol, to assist the binding of the DNA to a silica membrane. The bound DNA is then subjected to two washing steps, prior to its elution in either a buffer or water. It is possible to process up to 192 swab samples in parallel, with each swab sample yielding between 1 – 2 µg of purified DNA [216].

Despite many favourable attributes, it was found by Van der Zee *et al.* that the QIAGEN kits were susceptible to producing false positives during testing species of *legionella*. While it was possible to treat the QIAamp columns with DNAse and gamma irradiation, it was noted that all tests contained some contamination, ranging between 10 – 70% [213]. Evans *et al*. reported similar cases of contamination during an attempt to characterise the contaminating DNA, recording positive signals in the negative control columns. Further investigation reported that the contamination occurred during a water flushing process during production. For this reason, it was determined that the QIAGEN kits are unsuitable for diagnostics concerning water-based environmental organisms [217].

Table 2.10 – List of compatible QIAGEN Hybrid Kits

QIAamp Kits						
Name	**Sample Type**	**Processing**	**Nucleic Acid**	**Yield (µg/mL)**	**Time (min)**	**REF**
96 DNA Swab BioRobot Kit	Swabs	Automated	DNA	1 – 2 (per swab)	< 120	[216]
DNA Stool Kit	Faecal	Manual Automated	DNA	10–30	25 – 50	[218]

2.2.1.2. QIAsymphony

The QIAsymphony is a modular device with a similar functionality to the QIAcube, able to process a wide range of samples to allow for the extraction of purified DNA or RNA. The QIAsymphony is available in two formats: the SP (Sample Preparation) and AS (Assay Setup). The QIAsymphony SP allows for 1 – 96 samples to be processed in parallel, in batches of 24. The platform employs silica-

based purification in conjunction with magnetic particles to isolate NAs. In comparison to the QIAcube, less kits are available; however, the optimised protocols which can be performed on the platform allow for a wide array of samples to be processed [219]. The utility of the QIAsymphony is increased using the AS format, which includes an additional module to automate the setup of PCR and RT-PCR assays, following sample preparation. As the sample is purified and prepared for analysis by transferring the sample between the SP and AS modules, the reproducibility of the results is increased and the risk of contamination is decreased [219]. Despite the potential for this system, there are currently no kits compatible with the sample types addressed in this thesis.

2.2.2. AutoGen Platforms and Kits

2.2.2.1. XTRACT 16+

The AutoGen Company (USA) have developed several platforms which contain integrated sample preparation for specific samples through the use of corresponding kits. The current state-of-the-art is the XTRACT 16+, with claims to be able to process "virtually all molecular diagnostic, biological, clinical, and forensic sample types" in a TAT between 30 and 90 minutes [220]. Similar to the QIAGEN platforms, the XTRACT 16+ utilises magnetic beads to bind NAs following cell lysis. The kits of particular interest can be seen in Table 2.11. The XTRACT 16+ can process up to 16 samples in parallel and is compatible with the largest range of kits tailored towards a wide array of sample types, supporting the claim of being able to process virtually all samples. Similar to the QIACube Connect, the XTRACT 16+ allows for the user of the device to remotely monitor the process in real-time through a phone or tablet using an app, with the user being notified of any errors which occur during the process. Thus, this platform can be considered among the current state-of-the-art for sample preparation devices.

Table 2.11 – List of compatible AutoGen XTRACT16+ Kits

XTRACT 16+ Kits						
Name	**Sample Type**	**Processing**	**Nucleic Acid**	**Yield (µg/ml)**	**Time (min)**	**Ref**
Genomic DNA Bacterial Kit	Bacterial Culture, Mucosal Specimen	Automated	DNA	*Varies*	39	[221]
Cultured Cells DNA Kit	Cultures Cells, Amniotic Fluid	Automated	DNA	*Varies*	39	[222]

2.2.2.2. QuickGene Platforms

The AutoGen Company also introduced the QuickGene-810, which uses chemical lysis and membrane-based NA extraction to isolate DNA or RNA from up to 8 samples in parallel within 6 – 20 minutes. The collected sample is manually loaded into a cartridge, which is then loaded into the device. The platform will then prepare the sample automatically with a pre-programmed protocol, dependent on the sample type [223]. This platform was later developed into the QuickGene-Auto12S, which features a fully automated operation and is able to process up to 12 samples in parallel [224].

A key platform for consideration is the QuickGene-Mini80, an economically viable alternative to the QuickGene-810 for resource limited settings. This device is capable of processing up to 8 samples in 10 – 30 minutes using specific kits and offers a performance comparable to the QuickGene-810 [225]. The device is lightweight and features a relatively small footprint, features which would be beneficial for POCT. Additionally, the platform is capable of performing sample preparation without the use of centrifugation during the process. Despite these advantages, however, the device requires a mains electricity power supply, limiting its portability. The kits compatible for the QuickGene platforms can be seen in Table 2.12. In contrast to the XTRACT16+, the number of kits compatible with the Quickgene platforms is limited, reducing the number of protocols able to be performed on the platform.

Table 2.12 – List of compatible AutoGen QuickGene Kits

AutoGen QuickGene Kits						
Name	**Sample Type**	**Processing**	**Nucleic Acid**	**Yield (µg/ml)**	**Time (min)**	**Ref**
RNA Cultured Cells Kit (810/Mini80)	Cultured cells	Automated Manual	RNA	*Undefined*	15 – 20	[226]
RNA Cultured Cells Kit (Auto12S)	Cultured cells	Automated	RNA	*Undefined*	50	[227]

2.2.2.3. FlexSTAR Platforms

The FlexSTAR is a semi-automated platform, able to extract and isolate DNA from up to 30 samples in parallel. Similar to the QuickGene platforms, the FlexSTAR uses a series of kits which employ chemical lysis and NA precipitation to extract DNA [228]. The FlexSTAR+ functions similarly to the standard FlexSTAR platform, but offers improved fully automated protocols [229]. This platform is marketed as being easy to use, requiring little manual involvement. However, the size, footprint and power requirements for the platform make it unsuitable for diagnostics in resource stressed environments.

The kits compatible with the FlexSTAR platforms can be seen in Table 2.13. Similar to the Quickgene platforms, the number of compatible kits is limited, reducing the number of protocols able to be performed on the platform.

Table 2.13 – List of compatible AutoGen FlexSTAR Kits

FlexSTAR Kits						
Name	**Sample Type**	**Processing**	**Nucleic Acid**	**Yield (µg/ml)**	**Time (min)**	**Ref**
Blood DNA Finishing Kit	Cultured Cells, Whole Blood, Buffy Coat, Bone Marrow	Automated	DNA	10 – 40	120 - 180	[230]
DNA Whole Blood Kits	Cultured Cells, Whole Blood, Buffy Coat, Bone Marrow	Automated	DNA	10 – 40	120 - 180	[231]
Oragene Saliva Kit	Saliva	Automated	DNA	10 – 50	60 – 120	[232]

2.3. State-of-the-art for POCT Platforms

In absence of laboratory standard reagents and infrastructure, there is a requirement for simpler diagnostic techniques. Many NAAT-based POCT devices are designed for use in small or mobile laboratories and in remote locations [233]. These platforms offer patient-oriented convenience, promoting speed, simplicity and user-friendliness. Compared to laboratory-based platforms, the prime advantage of POCT platforms is their shorter TAT, typically between 5 – 30 minutes. The concession however is a lower throughput. Currently, POCT is considered to be a developing concept, with limited commercially available options [234]. This section of the thesis will address some of the developing NAAT-based POCT platforms and evaluate their performance.

2.3.1. Table top Instruments

Table top instruments should weigh less than 25 kg and should be robust and immune to vibrations and shocks. They should also function remotely, ideally offering wireless connectivity. Furthermore, they should offer battery powered alternatives should mains electricity be unavailable [235].

2.3.1.1. Alere Inc. Alere-q

The Alere™ q (Alere Inc., Waltham, MA, USA) is a tabletop instrument which employs multiplex PCR to detect HIV 1 and 2, Ebola virus, TB and Hepatitis C (HCV) from blood and plasma samples in a TAT of less than 1 hour. A sample, collected using a standard finger prick or venous blood draw, is loaded directly into the cartridge, where it is subjected to cell lysis using chaotropic salts, followed by RNA isolation using Streptavidin-Sepharose particles. Following washing steps to remove contaminants, the remaining RNA molecules are amplified using RT-PCR [236]. Despite being reported to have a 100% sensitivity, the Alere-q has demonstrated over-quantification, resulting in a 19% specificity [237].

2.3.1.2. Quidel Corporation AmpliVue

The AmpliVue® (Quidel Corporation, San Diego, CA, USA) is a handheld cassette which is used to detect *Bordetella, Clostridium difficile, Trichomonas,* Group A and B Streptococcus; as well as Herpes simplex virus (HSV) 1 and 2 from stool, NP, vaginal and rectal samples within a TAT of 60 – 90 minutes. Following heat treatment using a heater block, an aliquot of the lysate is transferred into the cassette, which contains the reagents and primers required to conduct HDA. Following HDA, detection is achieved using an LFD, providing simple qualitative results [238].

2.3.1.3. QIAGEN QIAstat-Dx

The QIAstat-Dx™ (formerly DiagCORE) Analyser (QIAGEN, Hilden, Germany) is a portable system, able to detect bacterial pathogens, including *Mycoplasma pneumoniae*, *Legionella pneumophila* and *Bordetella pertussis*; and viral strains, including, but not limited to, influenza A and B, coronavirus and RSV A/B. Following the insertion of a swab sample or a sample in liquid transport medium (LTM) into a QIAstat-Dx (DiagCORE) cartridge, the cartridge is loaded into the analyser, where the sample is lysed using mechanical and chemical means and purified using membrane-based NA extraction. Contactless pneumatic pressure actuators are used to transfer the sample and reagents to their intended destination. Furthermore, air filters for both incoming and outgoing air are used to safeguard the environment during use. After use, the cartridge remains sealed, allowing for its safe disposal [239].

2.3.1.4. Epistem Ltd Genedrive

The Genedrive® (Epistem Ltd, Manchester, England, UK) is a low-cost platform capable of detecting Mycobacterium tuberculosis complex (MTBC), HCV and SARS-CoV-2 from buccal swabs, nasal swabs and plasma. The system functions using a disposable cartridge for automated sample preparation, along with a 3-microtube disposable device for qPCR [240]. A study of the Genedrive was conducted by Castan *et al*., assessing the performance of the platform to detect MTBC from spiked sputum samples, reporting an overall sensitivity and specificity was 90.8% and 100%, respectively [241].

2.3.2. Handheld Portable Instruments

Handheld portable instruments should offer similar features to tabletop instruments, with the main differences being a significant decrease in weight (less than 1 kg) and that the platform should be fully battery operated [235].

2.3.2.1. QuantuMDx Q-POC

The Q-POC™ (QuantuMDx, Newcastle upon Tyne, England, UK) is a handheld and battery operated platform, able to provide multiplex qPCR testing to detect malaria, multidrug-resistant TB and sexually transmitted infections (STIs) in less than 30 minutes. The platform contains a disposable test cassette which can purify the collected sample. While the current iteration of the platform is able to process blood, tissue, sputum, and urine samples for the detection of the aforementioned diseases, a SARS-CoV-2 assay is being developed using MTN swab samples [242].

2.3.2.2. PositiveID Corporation Firefly Dx

The Firefly Dx (PositiveID Corporation™, Delray Beach, FL, USA) is a two-part device, consisting of a single use cartridge and a portable handheld instrument. The cartridge contains the reagents and elements to lyse and purify accepted samples, as well as the reagents required to conduct qPCR. The instrument is battery powered and features a wireless Bluetooth connection to allow for results to be obtained and processed using either a smartphone or a laptop. The platform is capable of accepting and processing a variety of samples, including whole blood, buccal, NP swabs and urine, for the detection of bacterial infections, including *Methicillin-resistant S. aureus* (MRSA), *Bacillus anthracis, Yersinia pestis*, and *Francisella tularensis*; as well as viral infections, including Human papilloma virus (HPV), influenza, Ebola virus, Dengue fever virus, Chikungunya virus, Nipah virus and Zika virus [243].

2.3.2.3. ChipCare Corporation Polyvalent Analyzer

The Polyvalent Analyzer (PAx) platform (ChipCare Corporation, Toronto, ON, Canada) is a portable analyser which can detect human immunodeficiency virus (HIV) and syphilis in multiplexed PCR or immunoassays, as well as Hepatitis C from whole blood, in a TAT of 15 minutes. The platform contains a low-cost disposable microfluidic cartridge which, once loaded into the platform, allows for automated sample preparation to be conducted. These cartridges contain preloaded reagents which are shelf-stable and able to be stored without refrigeration. Furthermore, the platform is battery operated, able to provide up to 8 hours of operation [244].

2.3.2.4. GenePOC Inc. GenePOC Platform

The GenePOC Diagnostics Platform (Québec City, QC, Canada) is a microfluidic platform designed for qPCR and qRT-PCR based detection for microbial pathogens from nasal, rectal, stool, throat, urine and vaginal samples within an hour. The disposable cartridge is compact and contains preloaded stable reagents required to perform up to 12 tests. The GenePOC platform is capable of processing up to 8 cartridges in parallel. The device utilises centipetal forces and passive valves to actuate fluids through the cartridge. Following the insertion of the sample conditioned in a GenePOC buffer, the sample undergoes a universal sample preparation process involving mechanical NA extraction using glass beads and a following dilution step [245,246].

2.3.3. Discussion of State-of-the-art for POCT Platforms

A comparison between the state-of-the-art for POCT can be seen in Table 2.14. Instruments which were handheld and fully portable were preferred over their tabletop counterparts, particularly in consideration of the device developed throughout this thesis. Thus, instruments such as the Firefly Dx, the Q-POC, the GenePOC and the Polyvalent Analyzer were preferred. The number of sample types which could be processed through a platform was a key consideration, as this would support the possibility and feasibility of developing a universal sample preparation device, as outlined in section 1.4.1. The GenePOC platform is capable of processing the largest number of sample types among the platforms considered. These included nasal, stool and rectal samples, which were of particular interest due to the nature of the project. The Q-POC platform followed in terms of the number of acceptable sample types. Among the listed sample types, MTN swab samples were listed for the purpose of detecting SARS-CoV-2. Thus, this platform was of particular interest.

Another major criterion used to evaluate the platforms was the TAT. Strategies to manage the window between infection and detection are crucial for preventing the spread of a disease, a common problem surrounding centralised testing. Thus, POCT can be seen as a vital strategy for patient management serving to reduce the distance between the site and where the analysis is performed, reducing the TAT. The Polyvalent Pax, the Firefly Dx and the Q-POC platforms offered the shortest TATs among the platforms evaluated, and consequently, were preferred based on this criterion.

Finally, simple sample preparation was seen as another important weighting criterion for evaluating the platforms. Ideally, the procedure should feature as few technical steps as possible in order to be considered effective for POCT. A common method utilised for molecular diagnostic devices is to conduct the entire sample preparation procedure within a disposable cartridge, which can be replaced following use. This was observed for each of the POCT platforms, which employed a form of cartridge-based technology, with integrated sample preparation steps. Thus, the sample-to-answer capabilities of each platform was measured. The Firefly Dx, Q-POC, Polyvalent PAx, QIAstat-Dx and Alere™-q platforms were among those which featured fully sample-to-answer protocols, requiring minimal to no addition or transfer of reagents through manual means.

Overall, the Firefly Dx and the Q-POC platforms offered the most favourable attributes among the platforms considered.

Table 2.14 – State-of-the-art for Point-of-Care-Testing Platforms

HDA, Helicase Dependant Amplification; LTM, Liquid Transport Medium; MTN, Mid-turbinate Nasal, NA, Nucleic Acid; NPS, nasopharyngeal swab; PCR, polymerase chain reaction; qPCR, qualitative polymerase chain reaction; RT-PCR, reverse transcription polymerase chain reaction; TAT, Turnaround time;

Instrument	Manufacturer	Platform Type	Sample Source	Sample Preparation	Sample-to-answer?	Amplification	Wireless connectivity?	TAT	Ref
Firefly Dx	PositiveID Corporation™	Handheld (portable)	• NPS • Whole Blood • Buccal • Urine	• NA purification using a cartridge	Y	qPCR	Yes	20 min	[243]
Polyvalent PAx	ChipCare Corporation	Handheld (portable)	• Whole Blood	• NA purification using a cartridge	Y	PCR	Yes	15 min	[244]
Q-POC	QuantuMDx	Handheld (portable)	• Blood • Tissue • Sputum • Urine • MTN swab	• NA purification using a cartridge	Y	qPCR	Yes	30 min	[242]
GenePOC	GenePOC Inc.	Handheld (portable)	• Nasal • Rectal/Stool • Vaginal • Throat swabs • Urine	• Glass bead-based mechanical lysis • Dilution	Y	qPCR	Yes	< 1 h	[245]
Alere™ q	Alere Inc.	Table top	• Whole Blood • Plasma	• Chaotropic salts cell lysis • Sepharose particle RNA isolation	Y	RT-PCR	Yes	< 1 h	[236]
AmpliVue®	Quidel Corporation	Table top	• Rectal/Stool • NPS • Vaginal	• Thermal lysis	N	HDA	No	60 – 90 min	[238]
GeneDrive	Epistem Ltd	Table Top	• buccal swabs • nasal swabs • plasma	• NA purification using a cartridge	Y	qPCR	No	45 – 75 min	[241]
QIAstat-Dx	QIAGEN	Table top	• Swab • LTM samples	• Mechanical/chemical cell lysis • Membrane-based NA extraction	Y	qPCR	Yes	< 1 h	[239]

2.4. State-of-the-art for SARS-CoV-2 Assays

The SARS-CoV-2 pandemic highlighted the need for rapid testing. An increase in demand has led to shortages in viral-purification kits, PCR kits and PCR products, as well as other consumables [192]. As a result, the focus of this project shifted towards the detection of SARS-CoV-2 using minimally invasive respiratory samples. There are currently 2 major categories to test for SARS-CoV-2: molecular assays, used to detect early stages of infection; and serological assays, used to detect antibodies produced within individuals as a result of previous exposure to the virus [64]. A review of prominent serological assays can be found in section 8.2. This section of the thesis will present molecular assays tailored towards the detection of SARS-CoV-2 and the corresponding platforms in which the assays are conducted.

2.4.1. Polymerase Chain Reaction based Assays

The current gold standard approach for SARS-CoV-2 detection is through qRT-PCR amplification to detect specific regions of the virus. These include the ORF1b or ORF8 regions and the nucleocapsid (N), spike protein (S), RNA-dependent RNA polymerase (RdRP), or envelope (E) genes [64]. RT-PCR may be performed as a one-step or two-step procedure. While the two-step procedure offers a higher flexibility and sensitivity in comparison, the one-step procedure is typically used as the gold standard approach, as it reduces handling time and decreases the likelihood of errors resulting from pipetting or cross contamination between reaction tubes.

The CDC recommend the CDC 2019-nCoV Real-Time RT-PCR Diagnostic Panel as the gold standard for SARS-CoV-2 detection, designed for use in temporary testing sites, such as pharmacies, physicians' offices, care facilities, school health clinics, among others. The recommended protocol utilises RNA extraction methods from commercially available kits to extract and purify RNA from upper and lower respiratory samples. These extraction protocols are performed using commercially available instruments. Finally, amplification and fluorescent detection using an Applied Biosystems 7500 Fast Dx Real-Time PCR instrument is used to obtain results within minutes [247].

Despite being highly specific, however, the sensitivity of the assay can vary depending on the viral load, viral replication, the RNA isolation method used and the time of swab collection in relation to the stage of the disease [248]. These variations can be further stressed by attempts to perform pooled

sampling, which can increase the likelihood of false negatives due to the dilution of the individual genetic material. In addition, the assay requires stationary laboratory-based instruments, which are both expensive and require trained personnel to operate, limiting their applicability in low-resource settings [197,247]. Furthermore, as samples must be transported to a centralised testing site, as well as the additional complexities involved with RNA isolation, the overall TAT can take up to several days [249]. These drawbacks reduce the viability of the CDC assay, particularly where remote testing is preferred and highlights a gap in the market between current needs and the gold standard [64,197]

2.4.1.1. Abbott RealTime SARS-CoV-2 Assay

Abbott Laboratories (Chicago, Illinois, USA) developed the Abbott RealTime SARS-CoV-2 Assay, intended for the qualitative detection of SARS-CoV-2 from nasal, NP and OP swabs, in addition to BAL fluid. The assay utilises a magnetic microparticle based protocol to capture the NAs, which are then purified and eluted into 96 well plates for PCR based amplification and fluorescent detection [250]. This assay may be performed on the Realtime m2000 system, a platform capable of performing automated sample purification, amplification and detection for NAs. The platform contains integrated liquid handlers and robotic arms, removing user interaction and allowing for a sample-to-answer process for up to 470 samples within 24 hours. Despite these benefits, however, the large size (34 x 49 x 45 cm) and weight (34.1 kg), as well as the required mains power makes the device unsuitable for portable diagnostic applications [251].

2.4.1.2. Cepheid Xpert Xpress SARS-CoV-2 test

Cepheid (Sunnyvale, California, USA) introduced the Xpert Xpress SARS-CoV-2/Flu/RSV test assay, able to process NP swabs and nasal wash specimens in universal transport medium (UTM) or VTM to detect SARS-CoV-2, Influenzas A and B, and RSV [252]. Each test is performed using an automated GeneXpert® system within a cartridge, requiring less than 1 minute of hands-on time and can yield positive and negative results in 30 and 46 minutes, respectively [253,254]. It has also been reported that positive results may be obtained within 25 minutes [252]. Following the insertion of the sample into a cartridge, sonication and glass beads are used to mechanically lyse the cells. The lysate is then passed through a membrane for RNA extraction, where wash steps are conducted to remove inhibitors. Finally, the RNA is combined with the PCR reagents [255].

A comparison between three sample-to-answer platforms reported that the Xpert Xpress had the lowest limit of detection (LOD) of 100 copies/mL, in comparison to the ePlex at 1000 copies/mL, and the ID NOW at 20,000 copies/mL [254]. Clinical agreement tests conducted within the platform for SARS-Cov-2 exhibit a 97.9% positive percent agreement and a 100% negative percent agreement [256]; however, a positive percent agreement of 98.3% has been reported [254]. While each cartridge is relatively low cost, priced at $19.80, an appropriate GeneXpert system is required, with costs ranging between $11,530 and $64,300 [257].

2.4.1.3. CovidNudge

DNANudge (London, UK) developed the portable POCT platform, the CovidNudge, to detect SARS-CoV-2 gene targets from NP and OP swabs, without the need for laboratory handling or pre-processing. The platform consists of two components: the DNAcartridge and the NudgeBox, the dimensions of which can be seen in Table 2.15. The DNAcartridge is a disposable, lab-on-a-chip based system, containing a sample preparation and an amplification unit. Following collection, a swab is inserted directly into the DNAcartridge and broken, remaining in the chamber during operation. Controlled by the Nudgebox using pneumatic techniques, the virus is then deactivated and lysed chemically and subjected to RNA extraction on a silica filter. Following elution, the sample is moved from the sample preparation unit to the amplification unit, where a qRT-PCR reaction is employed. Imaging is then used to confirm the presence or absence of the targeted gene. The DNAcartridge can be removed and disposed of following use. The TAT ranges between 60 and 90 minutes [258].

A key feature of the CovidNudge platform is the ability to detect the *RNaseP* human gene, serving as a control to verify that the sample has been captured on the swab, thus lowering the occurrence of false negatives [259]. A comparison between the CovidNudge platform and traditional laboratory RT-PCR techniques reported a sensitivity and specificity of 94% and 100%, respectively, proving its accuracy [258]. However, the drawback to this platform is its low throughput, only capable of assessing a single sample at a time [258,259].

Table 2.15 – Dimensions and weight of the CovidNudge components [36]

	Dimensions (mm)	Weight (kg)
DnaCartridge	25 × 78 × 85	0.04
CovidNudge	280 × 155 × 135	5

2.4.1.4. Roche cobas SARS-CoV-2 Test

Roche Molecular Diagnostics (Basel, Switzerland) developed the cobas® SARS-CoV-2 test, a qualitative assay, to detect SARS-CoV-2 from NP and OP swab specimens. The assay is performed within an enclosed system requiring 3 manual interactions (loading of reagents and consumables, loading of samples and emptying of waste), allowing for a walk-away time of up to 8 hours [260]. The 2 instruments used to conduct the assay are the cobas® 6800 and 8800 systems. Both instruments offer a throughput of 96 samples within 3.5 hours, with an additional 96 results produced every 90 and 30 minutes, respectively. The drawback is the size and weight of both platforms (shown in Table 2.16), as well as their reliance on mains electricity, preventing them from being a viable option for POCT [261].

An alternative is the Cobas Liat sample-to-answer PCR instrument, used to detect Influenza A and B, RSV, Group A Streptococcus and *Clostridium difficile* from stool and respiratory samples. The instrument has a TAT between 15 to 20 minutes and can store up to 20,000 results which can be exported [233]. The device has been evaluated by several groups, collectively reporting a sensitivity and specificity above 85% and 93% on various sample types using both in house and commercially available protocols, respectively [262-280]. The device is small (19 x 11.4 x 24.1 cm) and lightweight (3.76 kg); however, its lack of a portable battery option limits its effectiveness for POCT [233].

Table 2.16 – Dimensions and weight of the cobas® 6800/8800 systems [261]
**Refers to the weight including the instrument gateway server*

		Dimensions (W x H x D) (m)	Weight (kg)
cobas® 6800	**Fixed**	2.9 x 2.2 x 1.3	1573/1624*
	Movable	2.9 x 2.2 x 1.3	1701/1752*
cobas® 8800		4.3 x 2.2 x 1.3	2354/2405*

2.4.1.5. ePlex SARS-CoV-2 test

GenMark Diagnostics (Carlsbad, California, USA) developed the ePlex SARS-CoV-2 assay, capable of detecting SARS-CoV-2 in NP swabs. Unlike many PCR-based and NAAT-based protocols, the ePlex includes a “true sample-to-answer” protocol within a cartridge, including all steps from the collection of the sample, to RNA extraction, to PCR amplification, to the detection of the pathogen. The platform is modular, allowing for up to 288 tests to be performed within 24 hours [197]. The platform has been subjected to clinical tests, in which a positive and negative percent agreement of 91.4% and 100% was reported, respectively [254]. However, a major drawback to the ePlex platform is its large size and weight, making it an unviable option for portable diagnostics.

2.4.1.6. BioFire RP2.1-EZ Panel Assay

BioFire Diagnostics (Salt Lake City, Utah, USA) developed the BioFire RP2.1-EZ Panel Assay for the detection of SARS-CoV-2 in NP and OP swabs. The assay requires 2 minutes of hands-on-time and is designed to run automatically on the BioFire® FilmArray® 2.0 EZ Configuration System to yield results in 45 minutes [281]. It is also possible to tailor the assay for a higher throughput by using the BIOFIRE® FilmArray® Torch system, a multiplex PCR system able to provide results for up to 12 tests in parallel within an hour. Each test is performed within a self-contained, single use disposable packet, which comes pre-packaged with the necessary reagents and components to mechanically lyse the target cells, extract RNA and perform PCR. Each packet also contains an additional control, to ensure that the extraction process is operating properly [282]. The performance of the BioFire assay had been reported by various groups [283-286], as shown in Table 2.17.

Table 2.17 – Clinical Performance of the BioFire Covid-19 Test
PPA, Positive Percent Agreement; NPA, Negative Percent Agreement; PPV, Positive Predictive Value; NPV, Negative Predictive Value

	Sensitivity	Specificity	PPV	NPV	PPA	NPA	REF
Liotti *et al.*	93%	100%	100%	85%			[283]
Creager *et al.*					98%	100%	[284]
Eckbo *et al.*	100%				100%	100%	[285]
Smith *et al.*					98.7%	100%	[286]

2.4.1.7. TaqPath COVID-19 Multiplex Diagnostic Solution Kit

ThermoFisher Scientific (Waltham, Massachusetts, USA) developed the TaqPath Covid-19 Combo Kit, a multiplex qRT-PCR diagnostic kit able to detect SARS-CoV-2 from samples, including nasal, NP, OP and MTN swab specimens. The sample purification process may be performed manually using magnetic bead-based RNA extraction, or automatically using a KingFisher™ Flex Purification System. Following RNA extraction, RT-PCR is performed using an Applied biosystem 7500 Real-Time PCR system, allowing for up to 382 samples to be processed in under 2 hours [287,288].

The assay was reported to have a positive and negative percent agreement of 96.1% and 100%, respectively, when performed using the Applied biosystem 7500 Real-Time PCR system. While intended for single samples, an evaluation of the kit using pooled samples was conducted, which yielded a 100% sensitivity, specificity and accuracy. Furthermore, a LOD of 2 copies/µL was reported [289]. However, a similar comparative study reported a lower sensitivity of 85.3% [290].

2.4.1.8. Simplexa COVID-19 Direct Kit

DiaSorin Molecular (Cypress, California, USA) developed the Simplexa® COVID-19 Direct Kit to detect SARS-CoV-2 from nasal swabs and aspirates, NP swabs and BAL fluid [291]. The test is performed on a Direct Amplification Disc, within a LIAISON® MDX instrument. The Direct Amplification Disc is available in either an 8-well or 96-well configuration, allowing for up to 8 or 96 samples to be process in parallel, respectively. The platform accepts direct samples for analysis, omitted RNA extraction techniques to enable a faster TAT of approximately 1 hour [291,292]. The LIAISON® MDX instrument is small (31 x 21 x 31 cm) and light weight (8 kg), making it suitable for POCT. Despite this however, the platform is mains powered, limiting its portability [292].

A clinical evaluation conducted by Bordi *et al.* compared the performance of the Simplexa assay with traditional laboratory methods. The results were a 100% clinical sensitivity and specificity, in addition to a 100% overall percentage agreement [292]. A similar study conducted by Zhen *et al.* yielded similar results, reporting a positive and negative percent agreement of 100%. Furthermore, the LOD (39 copies/mL) was reported to be the lowest in comparison to similar PCR based methods. [293].

2.4.1.9. TrueNAT testing for SARS-CoV-2

Molbio Diagnostics (Verna, Goa, India) developed the TrueNAT system, a qRT-PCR test for the detection of SARS-CoV-2 from OP and NP swab samples stored in VTM. Tests performed on the platform are conducted in two stages: A screening procedure using the TrueNAT Beta CoV E-gene screening assay used to screen for “true negatives” and a succeeding confirmation procedure on positive tests using the TrueNAT SARS-CoV-2 RdRp gene-confirmatory assay for “true positives”. Recent developments have resulted in the TrueNAT Covid-19 Multiplex assay, allowing for both screening and confirmatory processes to be conducted within a single test, with positives being treated as “true positives” and negatives being treated as “true negatives” [294]. The complete workstation contains a sample preparation and RNA extraction unit (the TruePrep Auto) and a RT-PCR machine (the Truelab UnoDx) and disposable kit components, all of which can be stored in a suitcase. The RT-PCR machine is also available in a 2-slot (the Truelab Duo) and 4-slot (the Truelab Quatro) configuration, allowing for 2 or 4 tests to be conducted in parallel, respectively [295]. Each system is lightweight and battery operated, designed for deployment in remote locations. Furthermore, as the processes are conducted at low temperatures, the risk of aerosol production is lessened, reducing the risk of contamination.

However, as sample preparation and RT-PCR are conducted in separate systems, manual transfer is required, which can introduce contamination. However, a comparison between the TrueNAT and reference standard assays demonstrated a 100% sensitivity, specificity, negative and positive predictive value [296]. However, a LOD of 486 copies/mL was reported, higher than that of comparable technology, the Xpert® Xpress SARS-CoV-2, which had a LOD of 250 copies/mL [297].

2.4.1.10. VitaPCR SARS-CoV-2 assay

Menarini Diagnostics Ltd (Winnersh, UK) developed the VitaPCR™ SARS-CoV-2 assay, a qRT-PCR system able to provide semiquantitative detection of SARS-CoV-2 RNA from NP and OP swabs. The VitaPCR™ platform features rapid processing, resulting in a 20-minute TAT. In addition, the low weight (1.2 kg) and small footprint (15.5 x 16.5 x 20.5 cm) increases the field of deployment. However, the requirement for mains electricity greatly limits portability. Clinical agreement tests conducted within the platform demonstrate a 100% positive and negative percent agreement, as well as a LOD of 2.73 copies/µL [298]. However, other clinical tests have reported a positive and negative percent agreement, a specificity and sensitivity of 88.6 %, 99.7%, 94.7% and 99.3%, respectively [299].

2.4.2. Non-PCR based Molecular Assays

2.4.2.1. Abbott ID NOW COVID-19 test platform

Abbott Laboratories introduced the ID Now™ (formerly Alere™ i) Covid-19 test platform, a sample-to-answer device which utilises nicking enzyme amplification reaction (NEAR) to detect viral pathogens from clinical samples [254]. The ID Now is capable of processing raw samples and samples within a VTM solution, yielding positive and negative results within 5 and 13 minutes, respectively [300]; however, it has been reported that the actual lowest time to achieve results per specimen is 17 minutes [254]. Samples may be collected on a swab and loaded directly into a solution contained within the ID now sample receiver, or a swab may be collected and stored within a VTM solution, which may then be transferred into the sample receiver using a pipette [301]. The ID Now Covid-19 test platform has a small footprint (20.7 x 14.5 x 19.4 cm) and weight (3 kg), allowing the platform to be portable. Each kit also contains all components necessary for performing up to 24 tests [302]; however, each test must be performed individually [64].

The sensitivity of the ID Now Covid-19 test has been scrutinised, as performance tests conducted by Basu *et al.* reported that 33% and 45% of positive samples were determined to be false negatives by the ID Now using NP swabs in VTM and dry nasal swabs, respectively [303]. Further tests have been conducted on the ID Now, using commercially available and customised assays [275,277,304-319].

2.4.2.2. Aptima SARS-CoV-2 TMA assay/ Panther Fusion SARS-CoV-2 RT-PCR

The Aptima® SARS-CoV-2 assay was developed by Hologic (Marlborough, Massachusetts, USA) to diagnose SARS-CoV-2 from nasal, NP, MTN and OP swabs, and nasal and NP aspirates [320,321]. The assays may be automated using the Panther® and Panther Fusion® instruments, allowing for up to 500 samples to be processed in 8 hours. Furthermore, by using a reagent cartridge, manual preparation steps are removed, reducing errors [322]. Furthermore, both the TMA and PCR assays may be run in parallel on the Panther® and Panther Fusion® instruments [320].

Following the insertion of the sample into the Panther platform, a 360 µL of aliquot is taken from the lysate, which is subjected to magnetic-bead based RNA extraction and washing steps to remove impurities. Finally, 50 µL of purified RNA is eluted for analysis. Following Transcription-Mediated Amplification (TMA), fluorescent detection is used to detect the presence of SARS-CoV-2 [293]. Alternatively, the Panther Fusion® SARS-CoV-2 assay may be utilised on similar sample types as the Aptima assay, in addition to lower respiratory tract specimens [320]. The RNA extraction process is similar to the Aptima assay; however, qRT-PCR amplification is conducted instead of TMA.

Several studies have assessed the performance of the Aptima and Panther Fusion SARS-CoV-2 assays, the results of which may be seen in Table 2.18. Despite the numerous benefits the platform offers, the TAT using the platform is approximately 2 hours to obtain the first set of results. Furthermore, the setup of the instruments involves the manual loading of all necessary primers, probes and other consumables, as well as the manual transfer of clinical samples into the lysis buffer tubes using manual pipetting. These manual processes will further increase the overall TAT, adding an additional 2 hours of hands-on time to the process per run [293]. Thus, such a system is considered to be more suitable for clinical or public health testing instead of POCT, which typically is performed in environments where rapid results for a low-to-moderate volume of samples is required.

Table 2.18 – Comparative study of the Aptima® against the Panther Fusion® SARS-CoV-2 assay
LOD, Limit of detection; PPA, Positive Percent Agreement; NPA, Negative Percent Agreement; OPA, Overall Percent Agreement

	LOD (copies/mL)	Sensitivity (%)	Specificity (%)	PPA (%)	NPA (%)	OPA (%)	REF
Aptima vs. RT-PCR	5.5×10^2	98 – 98.1	100	98.1	100	99.1	[323]
Panther Fusion vs. 3 Assays	83			100	97		[293]
Aptima vs. Panther Fusion				97.3	100	99	[324]
Aptima vs. Panther Fusion				100	98.7	99.3	[321]
Aptima vs. consensus	62.5			94.7	100	97.3	[286]
Panther Fusion vs. consensus	125			98.7	100	96.64	[286]

2.4.2.3. Color SARS-CoV-2 RT-LAMP Diagnostic Assay

Color Genomics (Burlingame, California, USA) developed the SARS-CoV-2 LAMP Diagnostic Assay, able to qualitatively detect Sars-CoV-2 within 55 minutes. The assay may be performed using a myriad of sample types including nasal, NP, OP and AN swabs; MTN, NP and nasal aspirates; and BAL specimens. Each test may also be performed using self-collected dry nasal swabs, allowing for samples to be collected by the patient in a home setting. The platform is designed for a high throughput and low cost, able to automate bead-based RNA extraction and RT-LAMP reaction setup through the use of the Chemagic 360 Hamilton STAR/STARlet instruments, respectively [325]. The clinical performance of the assay shows a LOD of 0.75 copies of viral RNA per µL and a 100% positive and negative percent agreement, indicating a high level of specificity and sensitivity. Despite this, the bead-based sample preparation process is expensive in terms of time and costs [326].

2.4.2.4. Specific High Sensitivity Enzymatic Reporter Unlocking

Sherlock Biosciences (Cambridge, Massachusetts, USA) developed a LAMP-based assay, integrating RT-LAMP with specific high sensitivity enzymatic reporter unlocking (SHERLOCK) clustered regularly interspaced short palindromic repeats (CRISPR) detection, allowing for quantitative detection of predefined sequences in SARS-CoV-2 RNA. These are the E gene sequence, used to detect SARS-CoV-2 exclusively, the N gene sequence, found within SARS-CoV-2, SARS-CoV and bat-SL-CoVZC45 strains, and the *RNaseP* gene, used as a control. While assays are currently conducted within a laboratory-based setting, an Internal Splint-Pairing Expression Cassette Translation Reaction (INSPECTR™) platform is currently in development, allowing for the assay to be used in a similar approach to a home pregnancy test, for use in any setting [327]. The two-step assay consists of LAMP amplification in a

single tube where SARS-CoV-2 genomic RNA within unprocessed saliva or NP samples in UTM is reverse transcribed into DNA, followed by the transcription of the amplified DNA to activate the cleavage activity of a CRISPR complex to target the RNA sequence. Results for the assay are then presented using an LFD for visual confirmation [327].

The integration of SHERLOCK was adapted by Joung *et al.* to allow for the process to be conducted in a single tube, a process known as SHERLOCK testing one pot for COVID-19 (STOPCovid). By using fluorescent detection, results were able to be obtained in 40 minutes, with a sensitivity comparable to qRT-PCR-based SARS-CoV-2 tests [328]. The process was also combined with CRISPR-Cas12 to yield a method for detecting SARS-CoV-2 called DNA Endonuclease-Targeted CRISPR Trans Reporter (DETECTR). While an LFD was used to provide a visual confirmation; fluorescence readings were also taken, reducing the time to result from five minutes with the LFD to less than one minute. Again, a high specificity was reported, along with a 95% positive predictive agreement and a 100% negative predictive agreement with the CDC qRT-PCR assay [329].

The assay is relatively low-cost and is able to be applied in a variety of settings without additional instrumentation, making it well suited towards POCT applications. The use of CRISPR processing also reduces the reaction time to 1 hour, making the process faster than PCR. Moreover, the an EUA clinical evaluation revealed an LOD of 6.75 copies/µL, as well as a 100% sensitivity and specificity, indicating a high level of accuracy [327].

2.4.3. Discussion of State-of-the-art for SARS-CoV-2 Assays

The summary of PCR-based and non-PCR-based assays can be seen in Table 2.19 and Table 2.20, respectively. As stated earlier in this section, the detection of SARS-CoV-2 is achievable by analysing samples collected from the upper (AN, MTN, NP, nasal aspirates) and lower (OP and BAL) respiratory tracts. As shown in Figure 2.8, these samples have different degrees of invasiveness. For the purposes of this discussion, AN and nasal samples will be considered as equivalent to each other. Ideally, samples should be as minimally invasive as possible, without sacrificing the sensitivity and specificity of the assay. Thus, samples such as ANS and MTN are favourable, while samples such as nasal aspirates and BAL should be avoided. The TaqPath COVID-19 combo kit, the Panther Fusion and Aptima SARS-CoV-2 assays can be seen as preferable among those assessed, offering both the largest array of sample types, as well as providing the largest number of minimally invasive sample types. Recent efforts have been made to use saliva in place of respiratory samples for the detection of SARS-CoV-2 [330]. Thus, the Taqpath COVID-19 combo kit and the SHERLOCK kits can be deemed as favourable.

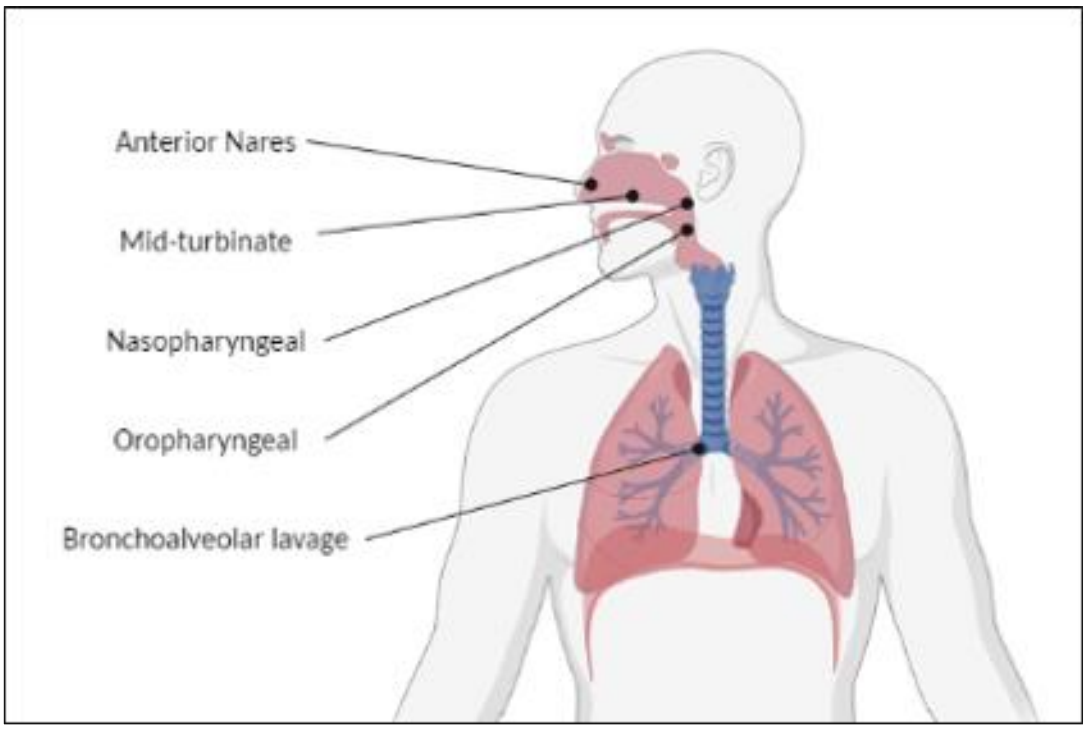

Figure 2.8 – Sample collection from the upper and lower respiratory tracts (Created with BioRender.com)

For the purpose of assessing viable options for POCT strategies, assays offering a high throughput have not been considered. The Abbott ID NOW test offers the shortest TAT compared to the other diagnostic tests, followed by the TrueNAT and VitaPCR assays. The hands-on-time of each assay also plays a vital part in the overall TAT. While the majority of the assays claim to have a TAT of less than 2 minutes, assays aimed towards a higher throughput require reagents and consumables to be loaded into a platform, which can greatly increase the overall TAT. As a result, the only assays with a truly hands-on-time of less than 2 minutes are the Abbott ID NOW, the TrueNAT, the VitaPCR, the Xpert Xpress, the SHERLOCK and the CovidNudge assays. Finally, the Abbott ID NOW, the TrueNAT and the CovidNudge were the assays compatible with portable platforms, making them preferable in POCT, and consequently, low-resource settings.

Table 2.19 – State-of-the-Art diagnostic assays for SARS-CoV-2 (PCR based) [64]

ANS, Anterior nares swabs; BL, Bronchoalveolar lavage; MTNS, mid-turbinate nasal swab; NS, nasal swab; NPS, nasopharyngeal swab; OPS, oropharyngeal swab

Assay Name	Manufacturer	Sample Source	Compatible Instrument(s)	TAT	Hands-on time	Portable?	REF
CDC 2019- Novel Coronavirus Real-Time RT-PCR Diagnostic Panel		• NPS, OPS • BL fluid • Tracheal aspirates • Sputum	• Applied Biosystems 7500 Fast Dx Real-Time PCR Instrument	36 min (Fast) <2 h (Standard)	n/a	N	[247]
Abbott RealTime SARS-CoV-2 Assay	Abbott	• NS, NPS, OPS • BAL fluid	• Realtime m2000 system	470 tests in 24 h	< 2 min	N	[250,251]
Xpert Xpress Sars-CoV-2	Cepheid	• NS, NPS • Nasal aspirates	• GeneXpert Dx • GeneXpert Infinity	36 min 25 min (Sars-Cov-2)	< 1 min	N	[252,254]
CovidNudge	DNANudge	• NPS • OPS	• NudgeBox	60 – 90 min	< 1 min	Y	[258,259]
ePlex SARS-CoV-2 test	GenMark	• NPS	• ePlex systems	288 tests in 24 h	< 2 min	N	[197,254]
cobas SARS-CoV-2 Test	Roche	• NPS, OPS	• cobas® 6800/8800	96 tests in 3.5 h	< 2 min	N	[260,261]
BioFire RP2.1-EZ Panel Assay	BioFire Diagnostics	• NPS, OPS	• BioFire® FilmArray® 2.0 EZ Configuration System • BIOFIRE® FILMARRAY® Torch system	45 min	< 2 min	N	[281,282]
Simplexa COVID-19 Direct	DiaSorin Molecular	• NS, NPS • Nasal aspirates • BAL fluid	• LIAISON® MDX	~1 h	< 2 min	N	[291,292]
TaqPath COVID-19 combo kit	ThermoFisher	• ANS, NS, NPS, OPS, MTNS • Saliva • BAL Fluid	• KingFisher™ Flex Purification System • Applied biosystem 7500 Real-Time PCR system	<2 h (382 samples)	< 2 min	N	[287,288]
TrueNAT Covid-19 Multiplex assay	Molbio Diagnostics	• NPS, OPS	• TruePrep Auto (sample preparation) • Truelab UnoDx/Duo/Quatro (RT-PCR)	20 min	< 2 min	Y	[294]
VitaPCR SARS-CoV-2 assay	Menarini Diagnostics	• NPS, OPS	• VitaPCR™	20 min	~1 min	N	[298]

Table 2.20 – State-of-the-Art diagnostic assays for SARS-CoV-2 (non-PCR based) [64]

ANS, Anterior nares swabs; BAL, Bronchoalveolar lavage; MTNS, mid-turbinate nasal swab; NS, nasal swab; NPS, nasopharyngeal swab; OPS, oropharyngeal swab

Assay Name	Manufacturer	Technology	Sample Source	Compatible Instrument(s)	TAT	Hands-on time	Portable?	Ref
CDC 2019- Novel Coronavirus Real-Time RT-PCR Diagnostic Panel		real-time RT-PCR	• NPS or OPS • BAL fluid • Tracheal aspirates • Sputum	• Applied Biosystems 7500 Fast Dx Real-Time PCR Instrument	36 min (Fast) <2 h (Standard)	n/a	N	[247]
Abbott ID NOW COVID-19 test	Abbott	NEAR	• NS, NPS • Throat swabs	• Abbott ID NOW	~5 min (Positive) 13 min (Negative)	~2 min	Y	[254,300]
Color SARS-CoV-2 LAMP Diagnostic Assay	Color Genomics	RT-LAMP	• MTNS, NPS, OPS • Nasal aspirates • BAL fluid	• Chemagic 360 (RNA extraction) • STAR/STARlet system (RT-LAMP)	< 55 min	~ 4 min	N	[325,326]
Aptima SARS-CoV-2 assay	Hologic	RT-TMA	• MTS, NS, NPS, OPS • Nasal aspirates	• Panther Fusion	2 – 3.5 h (800 tests in 8 h)	~2 h	N	[320,321]
Panther Fusion SARS-CoV-2 assay	Hologic	RT-PCR	• MTS, NS, NPS, OPS • Nasal aspirates	• Panther Fusion	2 – 3.5 h (800 tests in 8 h)	~2 h	N	[320,321]
Specific High Sensitivity Enzymatic Reporter Unlocking	Sherlock Biosciences	RT-LAMP + CRISPR	• Saliva • NPS	• (INSPECTR™) platform	~40 min	~2 min	Y	[327]

2.5. Challenges and Future Trends

Populations both in the developed and developing worlds can greatly benefit from rapid molecular POCT devices. Table 2.21 highlights the strengths and challenges of each POCT method compared the ASSURED standard. Despite the high probability of PCR-based assays detecting an active infection within a single sample, their accuracy hinges on the quality of the primers, the gene targets and the sample type [331]. In their current format, PCR-based assays are not suitable for integration into POCT devices that meet the ASSURED criteria.

A great number of POCT across the developed and developing world are serological in nature, mainly, LFDs [11,245]. Serological tests are typically more rapid and less expensive when compared with NAAT counterparts, providing easily interpretable results. However, NAAT platforms are more sensitive and specific. Antigen tests typically require a concentration of analytes above 10^4 – 10^5 to yield a positive result and are susceptible to cross reactivity between closely related bacterial and viral pathogens. Thus, it can be difficult to achieve accurate diagnoses without pre-processing steps, increasing costs and introducing external equipment [20].

Antibodies are produced within the patient long after the pathogen has fallen below detectable levels [331]. As a result, the concentration of the antibodies within the infected patient will exceed that of the infectious pathogen, allowing antibody-based tests to outperform both NAAT and antigen-based alternatives. However, as the production of detectable antibodies can take over a week, the effectiveness of such tests to confirm current infections is severely limited [332]. Furthermore, some patients may fail to raise a detectable antibody response, which can lead to a misdiagnosis [331]. Ultimately, iNAAT tests can be seen as a compromise between serological and PCR-based assays that meets the ASSURED criteria.

Table 2.21 – Strengths and weaknesses of different test formats using the ASSURED criteria [20]
+, less favourable; ++ moderately favourable; +++, more favourable

	Serological Assays		Nucleic Acid Amplification Testing	
	Antigen	Antibody	PCR	iNAAT
Affordable	++	+++	+	++
Sensitive	+	+++	++	+++
Specific	++	+	+++	+++
User-Friendly	+++	+++	+	++
Rapid and robust	++	+++	+	++
Equipment Free	++	+++	+	++
Deliverable to end-users	++	+++	+	++

Future trends in NAAT diagnostics is to offer rapid, sensitive and specific assays within a compact and contained environment to provide sample-to-answer analysis at virtually any site [245,333]. Many existing and developing platforms function through the use of onboard reagents, reducing the need for refrigeration. In some instances, the reagents may be either dried or freeze dried to improve shelf life. In such cases, the aqueous and homogenised sample may be introduced to rehydrate these reagents. However, there are cases where the sample is insufficient; and thus, water or a rehydration buffer is required. This is less convenient, as it introduces engineering challenges, such as valving and the requirement for an environmentally-stable rehydration buffer [245].

Despite being considered to be the gold standard, several iNAAT methods have been reported to outperform PCR and similar methods, while being less time or energy consuming; and robust isothermal methods are quickly becoming more commercially available [11]. However, despite not requiring thermocycling like PCR, many iNAAT methods require heating in order to conduct the assay. Particular iNAAT methods are difficult to multiplex. RT-LAMP in particular with end-point colorimetric detection cannot be multiplexed. A limitation of iNAAT techniques, particularly concerning POCT devices is the common restriction to processing a single sample at a time, which can limit the utility of the platform, and ultimately, lead to a backlog should an increase in sampling become necessary [334].

In resource stressed settings, the environment can affect the chemical and biochemical analysis of samples. Temperatures in excess of 40 °C and humidity levels in excess of 70%, can compromise the efficiency of electrical components, as well as the integrity of heat-stable reagents [245,335]. Furthermore, changes in temperature and humidity in these environments can fluctuate, and thus, be unpredictable [6].

While several POCT platforms integrating NA extraction through sample preparation have been highlighted in this literature review, there are, to date, no standalone sample preparation systems able to address a wide range of sample types in a simple and reliable system away from specialised infrastructure. Such a platform is of high demand in both the developed world as well as in resource-limited settings.

3. Preliminary Experiments

3.1. Introduction

A review of sample preparation techniques and state-of-the-art POCT devices presented in Chapter 2 provided a solid theoretical foundation from which to construct the platform. The work presented in this section offered a tangible basis from which to progress. It was decided based on a review of literature that swab sampling was the most suitable method of sample collection. Thus, the most logical progression was to assess commercially available swabs to define a starting volume for the fluidic input. Each of the assessed poultry related diseases required an output of DNA or RNA in solution, in the range of several microlitres. As the goal of the project was to develop a low-cost and low-power platform, an experiment comparing the droplet volumes produced by different sized needles would determine whether the platform would be able to yield droplets in the desired range absent of external instrumentation. Initially, a sample preparation protocol was to be designed by collaborators of the EPSRC project; however, no protocol was provided. Consequently, a simple sample preparation protocol was developed using a minimal number of steps to simplify the engineering and reduce the number of times a user would need to interact with the device.

3.2. Swab Absorption Experiment

3.2.1. Introduction

As discussed in Chapter 2, swabs are often used for sample collection. There are many commercially available swabs which are used for diagnostics, varying in tip materials (cotton, nylon, rayon, polyester and polyurethane), microstructure (flocked fibre, tightly wound, knitted), head size and length [336]. Depending on the source or the sample to be collected, swabs with variations in the aforementioned features may be used, with diagnostic accuracy depending on the characteristics of the swab [337]. When placed into a liquid solution, swabs absorb a percentage of the solution, resulting in a loss of usable sample for analysis. Thus, absorption properties of the different materials used for swab sampling must be known in order to determine which swab type would be preferable for use in a POCT device, where the sample and buffer volumes are minimal.

3.2.2. Aims and Objectives

The aim of the experiment was to determine the absorption rate of different commercially available swabs used for sample collection, in order to determine what volume of the solution would be lost during the suspension of the sample into a buffer. Based on initial research, polymer materials were expected to absorb the least amount of liquid, while the cotton and Dacron swabs were expected to absorb the highest amount of fluid. Furthermore, swabs with a larger bud size were expected to absorb more liquid than swabs with a smaller bud size due to the larger surface area. A comparison between swabs with a similar bud size and different materials would be used to determine which materials absorb the highest volume of fluid. In addition, a comparison between swabs with a different bud size and the same materials would be used to determine the influence of the swab size on the absorption of the fluid.

3.2.3. Experimental Setup

3.2.3.1. Materials

A total of 12 commercially available swabs were tested, shown in Figure 3.1. These swabs are described in further detail in Table 3.1. Polypropylene centrifuge tubes (15 ml; Cole Palmer, UK) were used to hold the liquid that would be used for the experiment. The geometry of the tube allowed for each swab to be fully submerged in 1 ml of deionized water (DI H_2O). A Mettler AC 100 Analytical Balance was used to weigh each of the tubes.

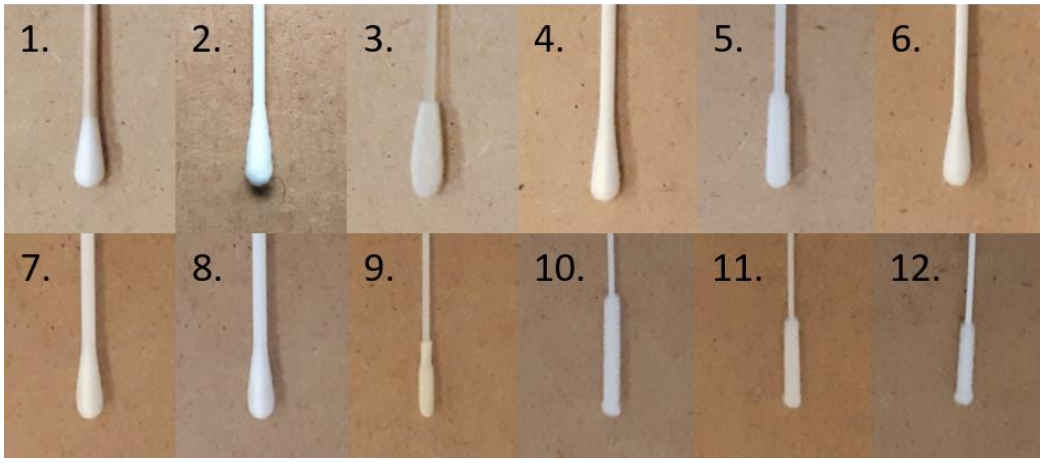

Figure 3.1 – A comparison between the 12 commercially available swabs tested in this study
***1**, Cotton (Standard Tip); **2**, Dacron (Standard Tip); **3**, FLOQSwab® (Standard Tip); **4**, Nylon, Flock (Standard Tip); **5**, Polyester (Standard Tip); **6**, Viscose (Standard Tip); **7**, Rayon (Standard Tip); **8**, Polyurethane (ENT Tip); **9**, Cotton (Mini-Tip); **10**, Nylon Flock 1 (Mini-Tip); **11**, Nylon Flock 2 (Mini-Tip); **12**, Nylon Flock 3 (Mini-Tip)*

Table 3.1 – List of Swabs used for the Swab Absorption Experiment

Swab	Material (Bud)	Bud Size	Material (Shaft)	Company	REF
1	Cotton	Standard	Wood	Technical Service Consultants (UK)	[338]
2	Dacron	Standard	Plasticised Paper	MWE Medical Wire (UK)	[339]
3	FLOQSwab®	Standard	Polymer	Copan (Italy)	[340]
4	Nylon, Flock	Standard	Polymer	MWE Medical Wire (UK)	[341]
5	Polyester	Standard	Polymer	MWE Medical Wire (UK)	[339]
6	Viscose	Standard	Polymer	Technical Service Consultants (UK)	[342]
7	Rayon	Standard	Polymer	MWE Medical Wire (UK)	[339]
8	Polyurethane	ENT	Polymer	MWE Medical Wire (UK)	[343]
9	Cotton	Mini-Tip	Plasticised Paper	Technical Service Consultants (UK)	[344]
10	Nylon, Flock	Mini-Tip	Polymer	Goodwood Medical Care LTD (China)	[345]
11	Nylon, Flock	Mini-Tip	Polymer	Jiangsu HanHeng Medical Technology (China)	[346]
12	Nylon, Flock	Mini-Tip	Plasticised Paper	MWE Medical Wire (UK)	[341]

3.2.3.2. Methodology

Before conducting the experiment, the ambient temperature and the temperature of the liquid were measured using a Brannan Immersion Glass Thermometer (RS Components, Corby, England), recorded as 24 and 22 °C, respectively. Each of the centrifuge tubes were labelled and weighed using the analytical balance to determine the initial empty mass of the tubes (m_0). 1 ml of DI H_2O was added to each container, sealed with its lid and weighed to determine the initial mass (m_1). Each swab was then placed into each tube, agitated within the liquid using a circular motion for ten seconds and then left to sit in the liquid for an additional 10 seconds. The swab was then removed, discarded and the tubes were sealed and weighed to determine the final mass (m_2). The difference in mass (Δm) between the final and initial weights were calculated using Equation 3.1.

$$Mass\ Difference\ =\ Final\ Mass - Initial\ Mass \qquad [\text{kg}] \qquad \textit{Equation 3.1}$$

$$\Delta m = (m_2 - m_0) - (m_1 - m_0)$$

Finally, the volume absorbed by the swab (ΔV) was calculated using Equation 3.2, where the density of the DI H_2O was assumed to be 997.77 kg/m^3.

$$Volume\ absorbed\ by\ the\ swab\ =\ \frac{Mass\ Difference}{Density\ (water)} \qquad [\text{m}^3] \qquad \textit{Equation 3.2}$$

$$\Delta V = \frac{\Delta m}{\rho}$$

Care was taken during the experiment to prevent the swabs from touching the sides of the tubes which could release an indeterminable amount of liquid from the swab, causing discrepancies between results. It was important that all of the tubes remained sealed outside of the addition of the DI H_2O and the insertion and removal of the swab. This would ensure the mass did not change due to additional particulates or liquid loss by evaporation. It was observed during the experiment that minute fluctuations (±0.5 mg) would occur on the recordings displayed on the analytical balance. To account for the fluctuations, an average between 3 readings were taken for each measurement, with 5 measurements taken for each swab type.

3.2.4. Results and Discussion

3.2.4.1. Results

A comparison between the initial and final volumes for each swab is shown in Figure 3.2, tabulated in Table 3.2. The swab with absorbed the least volume of fluid was swab 8 which had an average absorption of 27.5 µL.

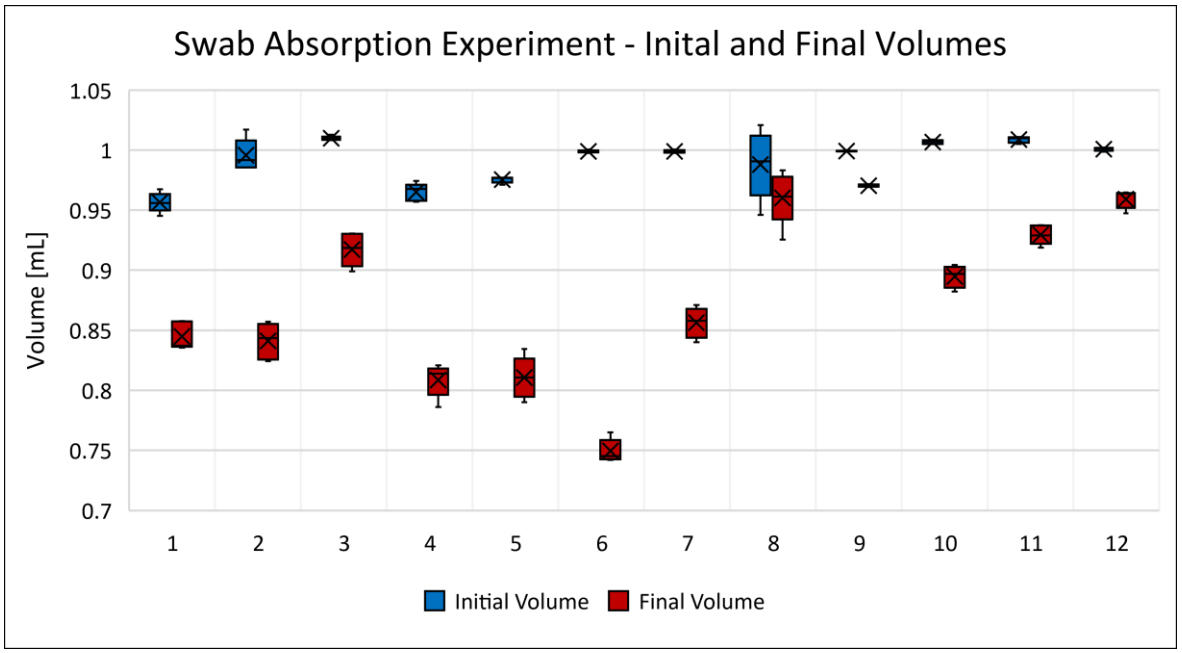

Figure 3.2 – Box plot comparing the initial and final volumes for each swab
***1**, Cotton (Standard Tip); **2**, Dacron (Standard Tip); **3**, FLOQSwab® (Standard Tip); **4**, Nylon, Flock (Standard Tip); **5**, Polyester (Standard Tip); **6**, Viscose (Standard Tip); **7**, Rayon (Standard Tip); **8**, Polyurethane (ENT Tip); **9**, Cotton (Mini-Tip); **10**, Nylon Flock 1 (Mini-Tip); **11**, Nylon Flock 2 (Mini-Tip); **12**, Nylon Flock 3 (Mini-Tip)*

Table 3.2 – Volume of water absorbed by various types of swabs (µL)
Results for the range and mean are given to 1DP. The standard deviation is given to 2DP.

Swab		Mean ± SD	Range
1	Cotton, Standard Tip	111.6 ± 7.28	16.8
2	Dacron, Standard Tip	154.7 ± 7.33	15.9
3	FLOQSwab®, Standard Tip	92.5 ± 15.10	35.7
4	Nylon Flock, Standard Tip	156.5 ± 13.43	36.4
5	Polyester, Standard Tip	164.6 ± 18.64	46.4
6	Viscose, Standard Tip	249.3 ± 10.33	24.6
7	Rayon, Standard Tip	142.6 ± 12.44	31.4
8	Polyurethane, ENT Tip	27.5 ± 12.75	30.6
9	Cotton, Mini-Tip	28.7 ± 0.82	2.2
10	Nylon Flock, Mini-Tip (1)	112.1 ± 8.81	21.7
11	Nylon Flock, Mini-Tip (2)	79.2 ± 6.58	13.7
12	Nylon Flock, Mini-Tip (3)	41.6 ± 6.62	16.0

3.2.4.2. Discussion

There were no recorded results determined to be outliers within 2 standard deviations, based on the results shown in Table 3.2. it was found that the ENT-tip polyurethane had the best lowest absorption rate among the swab types tested, closely followed by the mini-tip cotton swab. Those with the highest absorption rate were the standard-tip viscose and standard-tip polyester swabs. Among the five nylon flock swabs tested, three (swabs 3, 11 and 12) offered a favourable performance, absorbing less than 100 µL of fluid. However, the remaining two nylon flock swabs (swabs 4 and 10) were among the most absorbent among their respective tip types, that being standard-tip and mini-tip. Thus, it is important to source the correct type of nylon flock swab, due to the discrepancy between the results.

A comparison of the volume of fluid lost between the standard- and mini-tip swabs can be seen in Figure 3.3 and Figure 3.4, respectively. The range of the standard tip swabs was 92.5 – 249.3 µL, while the range of the mini-tip swabs was 27.5 – 112.1 µL, demonstrating that mini-tip swabs are preferable in terms of volume loss. However, the smaller surface area of the mini-tip swabs may collect a lower volume of secretions than standard-tip swabs, lowering the chance of collecting the target pathogen.

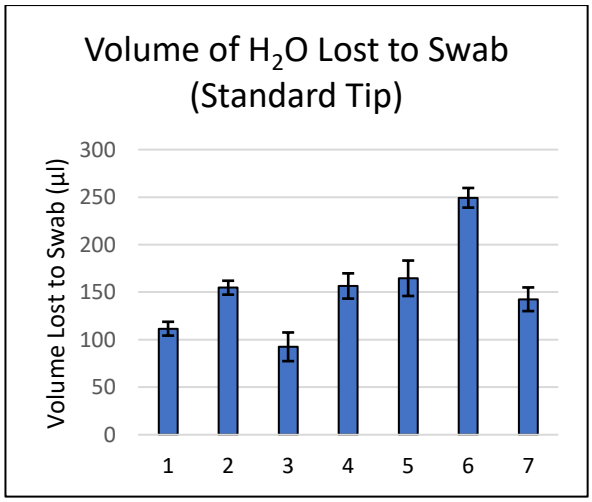

Figure 3.3 – Comparison between Volume of Fluid Lost between Standard-Tip swabs

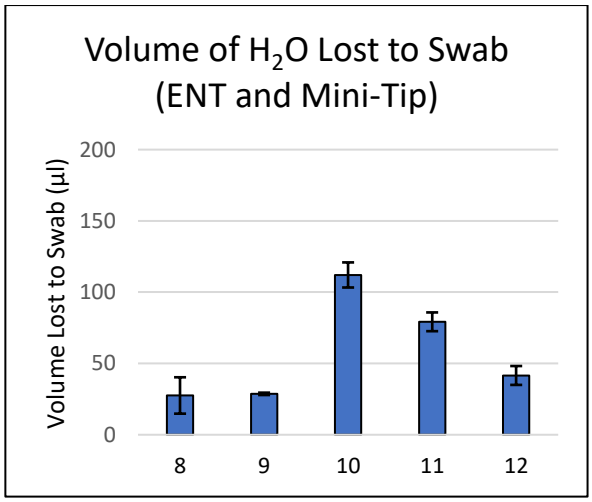

Figure 3.4 – Comparison between Volume of Fluid Lost between ENT and Mini-Tip swabs

***1**, Cotton (Standard Tip); **2**, Dacron (Standard Tip); **3**, FLOQSwab® (Standard Tip); **4**, Nylon, Flock (Standard Tip); **5**, Polyester (Standard Tip); **6**, Viscose (Standard Tip); **7**, Rayon (Standard Tip); **8**, Polyurethane (ENT Tip); **9**, Cotton (Mini-Tip); **10**, Nylon Flock 1 (Mini-Tip); **11**, Nylon Flock 2 (Mini-Tip); **12**, Nylon Flock 3 (Mini-Tip)*

As stated in section 2.1.3.5, samples are pooled to save the time and costs involved with sample preparation. When considering the pooling of swabs in a single medium, it is vital that a usable volume remains in order to be actuated through the device. Based on the assumption that 5 swab samples would be pooled into a single medium, then a starting volume of at least 2.25 ml would be required to allow for each swab tested in this experiment to be utilised with this device.

A study by Zasada *et al.* compared the volume of water absorbed by various swabs with the results shown in Figure 3.5 [336]. A comparison between the study in this report and the study conducted by Zasada *et al.* both concluded that the polyurethane swabs had a much lower absorption rate of water compared to the swabs in each of the studies. The performance of the Dacron and rayon tip swabs also offered results which agreed with each other, with the performance of the Dacron band rayon being comparable; however, with the rayon tip having a slightly lower absorption rate when compared to the Dacron tip. The results for the nylon flock swabs however disagreed with each other. The FLOQSwabs® tested in this study offered a lower absorption rate than both the dacron and rayon tip swabs; however, the FLOQSwabs® tested in the study by Zasada *et al.* reported a higher absorption rate than the two. However, when comparing the performance of the standard-tip nylon flock from MWE Medical Wire testing in this study, the performance agrees with those reported by Zasada *et al.* The study by Zasada *et al.* was extended to conduct research into the DNA recovery from the tested swabs, shown in Figure 3.6 [336]. The nylon flock swabs demonstrated the highest DNA recovery, followed by the polyurethane swabs. Consequently, nylon swabs may be considered as a preferable option in this regard.

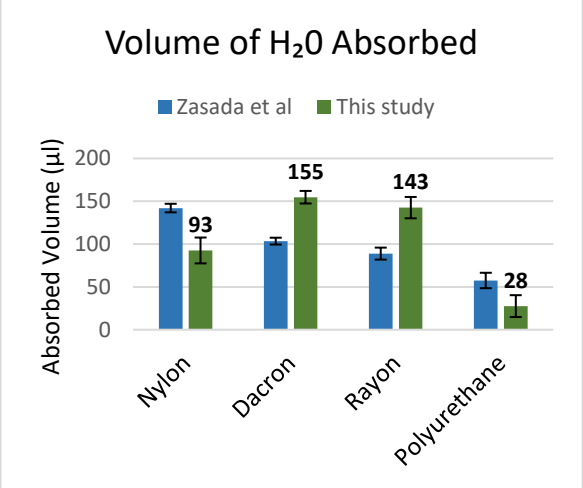

Figure 3.5 – The volume of water absorbed by investigated types of swabs [336]

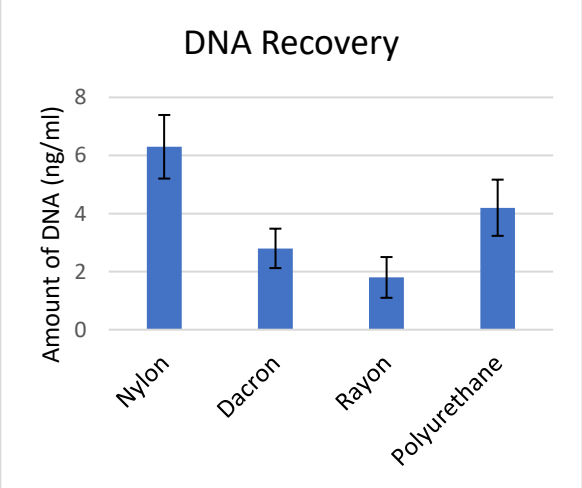

Figure 3.6 – Amount of DNA recovered from investigated types of swabs [336]

The swabs tested by Zasada et al. were compared to swabs tested in this study as follows: Nylon – Swab 3; Dacron – Swab 2; Rayon – Swab 7; and Polyurethane – Swab 8.

A study conducted by Kahamba *et al.* compared the performance of 3 mini-tip nylon flock swabs in PBS solution [337]. The performance of the mini-tip nylon flock swabs tested in this study agreed with the performance of the swabs reported by Kahamba *et al.* (see Figure 3.7).

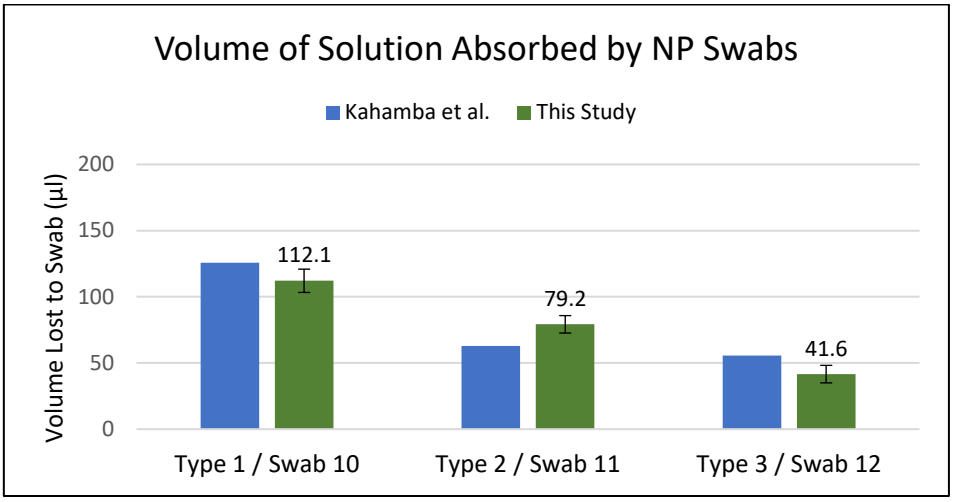

Figure 3.7 – Volume of spiked PBS absorbed and released by the nasopharyngeal swabs [337]
The swabs tested by Kahamba et al. were compared to those in this study as follows: Type 1 – Swab 10; Type 2 – Swab 11; Type 3 – Swab 12

Panpradist *et al.* showed similar results to Zasada *et al.* and this study when comparing six swab types (Figure 3.8) [347]. The polyurethane swab showed the lowest absorption rate. However, the results for the remaining swab types gave conflicting results. For the results presented in this thesis, the volume absorbed by the polyester swab was higher than the nylon, rayon and cotton swabs tested. A comparison between both nylon swabs sourced from Copan diagnostics (Italy) and both cotton swabs yielded comparable results.

However, in the study conducted by Panpradist *et al.,* it was reported that the absorption rate of the polyester swabs was much lower than the nylon, rayon and cotton alternatives. Panpradist *et al.* used a mini-tip polyester swab whilst a standard-tip was used in this study. A similar discrepancy was noted between the results for the rayon tip swabs, with the rayon tip used by Panpradist *et al.* reporting an average volume loss of 63 µL, while the rayon test in this study reported over twice the volume loss, at 143 µL.

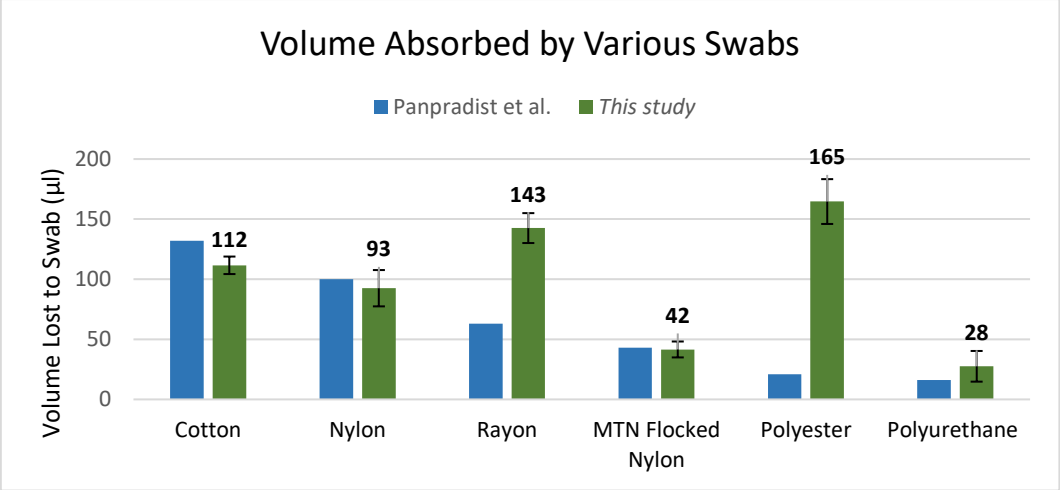

Figure 3.8 – Comparison of the Volume Recovery from each swab [347]
The swabs tested by Panpradist et al. were compared to those in this study as follows: Cotton – Swab 1; Nylon – Swab 3; Rayon – Swab 7; MTN Flocked Nylon – Swab 12; Polyester – Swab 5; and Polyurethane – Swab 8

Based on the results, the hypothesis that polymer-based materials being less absorbent than the alternative materials was both proven by the favourable performance of the polyurethane and nylon swabs and disproven by the performance of the polyester swabs. The performance of the cotton swabs also disproved the hypothesis, with the mini-tip cotton swab being among those with the lowest absorption rate. The premise of the larger swabs being more absorbent than the smaller swabs was also supported by this experiment; however, the performance of the FLOQSwab® highlighted the significance of material choice. Among three of the five nylon swab types tested, a disparity in performance was noted, independent of swab size. While this could suggest that the material choice has a greater influence on the absorption than the swab size, a performance comparison between the nylon swabs (4, 10, 11 and 12), as well as the two cotton swabs (1 and 9) suggests that the head size is as influential as the swab material. Some of the challenges with this experiment was the inability to standardise the swabs, particularly regarding the shaft material. As the difference in absorption between the plasticised paper, wood and polymers shafts was not tested, the variance as a result remains a variable. Further testing may be useful to determine this variation.

In light of this experiment, it was decided that the polyurethane swabs would be preferable for use in further experiments, due to having the lowest volume of absorption. This decision was supported by the research conducted by Zasada *et al.*, which also suggested that the DNA recovery would be sufficient without absorbing a large percentage of the solution the swab would be inserted into.

3.3. Droplet Size Experiment

3.3.1. Introduction

There is an increasing demand to supply small liquid volumes for the miniaturisation of diagnostic assays, or to fabricate microscale components. To produce droplets ≤1 µL, microdroplet dispensing technologies are required. In such cases, knowing the exact volume of the droplet is vital. Microdroplet dispensing may be divided into continuous and drop on-demand (DOD) techniques [348]. As the name suggests, continuous droplet dispensing is a process in which a continuous stream of droplets is ejected from the dispenser; in contrast, DOD generates a single droplet when needed, offering an improvement in control [348]. These two categories may further be classified by the dispensing mechanism they employ, contact and non-contact. Contact dispensing typically requires a larger driving force and simpler control methods in comparison to non-contact dispensing [349]. Furthermore, the interaction between the dispensing nozzle and the target may lead to contamination [350,351]. Thus, non-contact dispensing is seen as preferable for biological sampling.

There are several non-contact systems that have been developed, including, but not limited to piezoelectric, pneumatic, thermal and electrostatic. Thermal dispensers typically utilise a heat of over 100 °C, creating bubbles within a nozzle. This results in an increase in pressure, displacing the fluid and ejecting a small volume from the nozzle. While the method is highly flexible and is able to be integrated into a system in numerous ways, the high temperatures may damage biological samples [352]. Pneumatic systems involve the use of a pneumatic actuation unit and a “dispensing well plate”, which consists of a reservoir, a nozzle and a connection channel. The nozzle is primed using capillary forces from the reservoir and through the connection channel. Following the application of a pressure pulse to the dispensing well plate, the liquid is driven out of the nozzle. Whilst this method allows for the production of droplets in the nanolitre range, there is a need to manually transfer the sample into the reservoir prior to use, which introduces potential contamination associated with manual handling [353]. In a similar approach, piezoelectric dispensing is achieved by applying an electrical pulse across a piezoelectric material. When adjoined to a rigid material, the piezoelectric material will deform, either generating an impulse or creating a pressure increase sufficient to cause the fluid to be ejected from the nozzle. A drawback to this approach is the need to overpressure the reservoir to prevent backflow into the microchannels that supply the fluid [354]. Finally, electrostatic dispensing utilises a pair of electrodes at a different potential to generate an electrical field, causing fluid to elongate and eventually detach from the nozzle [355,356].

3.3.2. Aims and Objectives

The device developed throughout this project required a method to dispense small droplets with a precise volume into PCR tubes following adequate sample preparation steps. This method would need to prime the dispenser nozzle and operate without contacting the target or operator without producing unwanted (satellite) droplets. An output of 3 µL was required for the analysis of poultry related samples. Following the shift in focus to SARS-CoV-2, a protocol was developed which required an output of 1 µL.

This section studied the effects of the nozzle diameter on the droplets produced, assessing dispenser needles with different gauges. This experiment determined the range and limits of droplet volumes that could be achieved through natural dripping, prior to deciding if the aforementioned non-contact dispensing methods would be required for droplet attachment. Needles with an increasing gauge had a smaller inner and outer diameter, resulting in a smaller surface area at the tip of the needle. Thus, it was expected that the increase in gauge would result in a decrease in the droplet volume, due to the reduction in weight that would be required to overcome the surface tension.

3.3.3. Experimental Setup

3.3.3.1. Materials

A total of 5 commercially available blunt tip dispenser needles of 6 differing gauges were tested, the dimensions of which can be seen in Table 3.3. Extraction buffer tubes sourced from Flowflex™ SARS-CoV-2 Antigen Rapid Test kits (Flowflex Components LTD, Buxton, England, UK) were also analysed in this experiment. A Fusion 200 Two-channel syringe pump (Chemyx, Stafford, Texas, USA) was used to supply a steady rate of droplets from the dispenser needle while ensuring that the process would not be subject to sudden impulses which could cause non-uniform droplet detachment. A 10 mL BD syringe was used, which was filled with DI H_2O. 15 mL Polypropylene centrifuge tubes were used to contain the liquid that was ejected from the dispenser tip. A 3D printed jig was used to hold the dispenser needle perpendicular to the ground to reduce any variations caused by differing angles. Finally, a Mettler AC 100 Analytical Balance was used to weigh each of the tubes.

Table 3.3 – List of Needles used for the Droplet Size Experiment [357]

Needle Gauge	Inner Diameter (mm)	Inner Area (mm^2)	Outer Diameter (mm)	Outer Area (mm^2)	Needle Length (mm)
14	0.84	0.5554	1.27	1.2668	12.7
18	0.51	0.204	0.81	0.5153	25.4
20	0.41	0.132	0.71	0.3959	12.7
21	0.33	0.0855	0.64	0.3217	12.7
25	0.25	0.0491	0.51	0.2043	12.7
30	0.15	0.0177	0.3	0.07069	12.7

3.3.3.2. Methodology

Before conducting the experiment, the ambient temperature and the temperature of the liquid were measured using a Brannan Immersion Glass Thermometer, recorded as 23 and 22 °C, respectively. Each of the centrifuge tubes were assigned to a specific dispensing needle or extraction tube and labelled accordingly. The initial weight of each of the tubes were weighed using the analytical balance to determine the initial mass of the tubes (m_1).

3.3.3.3. Droplet Size Experiment using the Flowflex Extraction Buffer Tubes

Each of the Flowflex extraction buffer tubes were filled with 1 mL of DI H_2O, which were then closed and labelled. A total of 10 drops were then released from extraction buffer tubes into the assigned centrifuge tubes, which were immediately sealed with a lid and weighed to obtain the final mass (m_2).

3.3.3.4. Droplet Size Experiment using the Dispenser Needles

The syringe was filled with 10mL of DI H_2O and inserted into the syringe pump. The syringe was then connected by silicon tubing to a barb-to-male Luer-lock connector, which was secured into a 3D printed jig by interference fit. The jig was then secured to a laboratory stand, allowing the needle to be held in place in a vertical position (Figure 3.9).

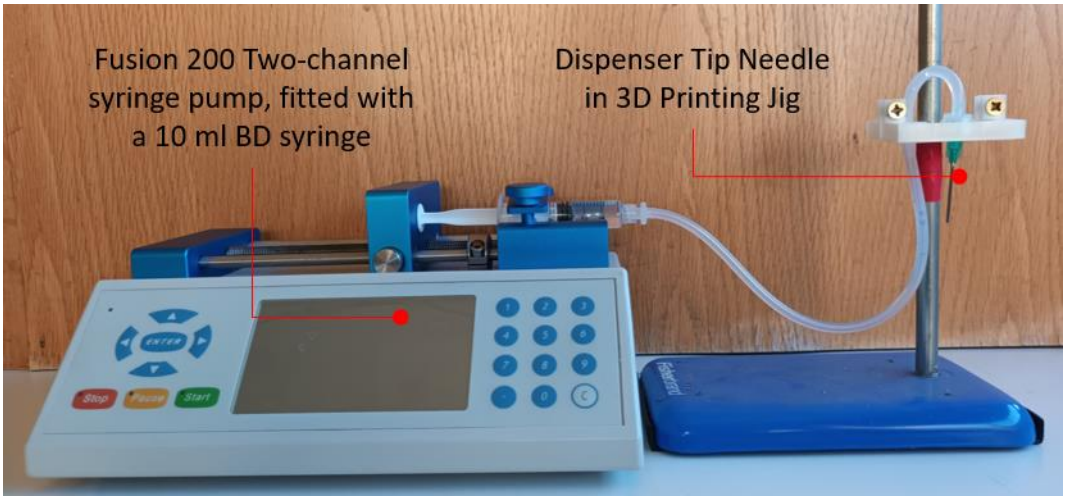

Figure 3.9 – Setup for the droplet experiment

The first needle was secured to the Luer-lock connector and its assigned tube was placed in a rack placed directly underneath the dispenser needle. To ensure standardised results were obtained and to reduce potential errors, the syringe pump was set to a flow rate of 1 mm^3/s (3.6 mL/hr on the syringe pump) and used to eject 10 droplets from the dispenser needle and into the tube. The tube was then removed from the rack, sealed with its lid and then weighed to obtain the final mass (m_2). The process was then repeated for each dispenser needle.

The difference in mass (Δm) between the final and initial weights were calculated using Equation 3.3. The mass difference was divided by 10 to obtain an estimate for the weight of a single droplet. Finally, the volume (ΔV) was calculated using Equation 3.2, where density was assumed to be 997.77 kg/m^3.

$$Mass\ Difference = \frac{Final\ Mass - Initial\ Mass}{10} \quad [\text{kg}] \qquad \textit{Equation 3.3}$$

$$\Delta m = \frac{m_2 - m_1}{10}$$

Tubes remained sealed to avoid contamination or evaporation. To account for the minor fluctuations on the balance, an average between 3 readings were taken for each measurement, with 5 measurements taken for each dispenser needle and extraction tube.

3.3.4. Results and Discussion

3.3.4.1. Results

A visual and graphical comparison between the dispensing methods can be seen in Figure 3.10 and Figure 3.11, respectively. Droplets produced during the experiment ranged between 6.10 and 43.05 µL. The 30-gauge dispenser needle yielded the smallest average volume per droplet at 6.24 µL. The 25, 21, 20, 18, and 14-gauge needles had an increasing droplet volume of 9.28, 13.97, 15.75, 20.82 µL and 35.23 µL, respectively. Finally, the Flowflex extraction tubes yielded the largest droplets among the dispensing methods, with an average droplet volume of 40.08 µL.

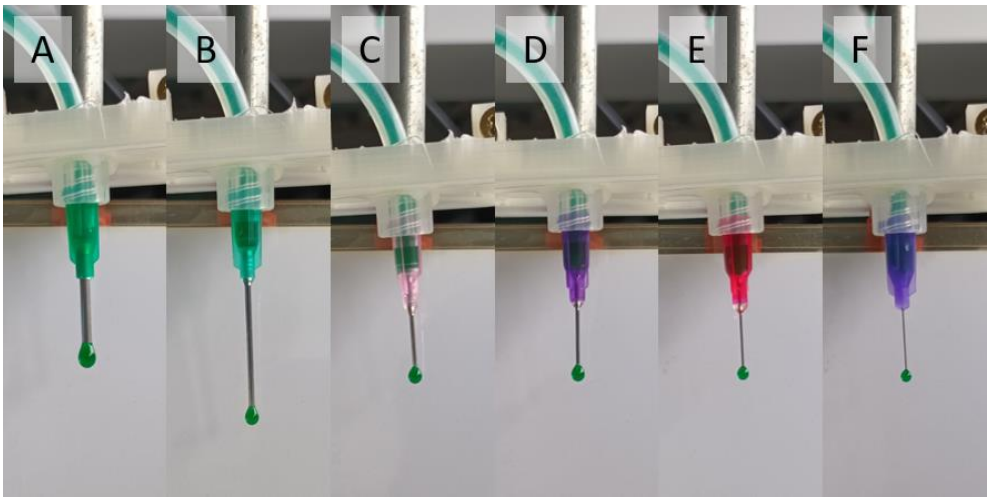

Figure 3.10 – Comparison between droplet volumes for needles used in the experiment
***A** – 14-gauge; **B** – 18-gauge; **C** – 20-gauge; **D** – 21-gauge; **E** – 25-gauge; **F** – 30-gauge*

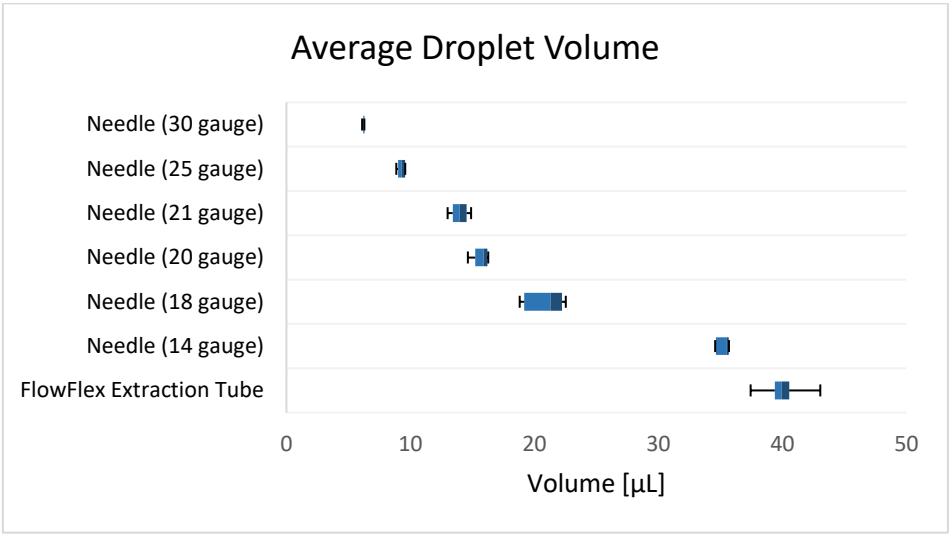

Figure 3.11 – Box plot of average droplet volumes from dispenser needles

3.3.4.2. Discussion

The results demonstrated that an increase in the needle gauge resulted in a decrease in the droplet volume. This supported the hypothesis. Five outliers were discovered among the Flowflex extraction buffer tubes within 2 standard deviations. There were no outliers among the dispenser needles of any gauge size. The variation between the results among the 18-gauge needles was significantly larger than the other dispenser needles tested during this experiment, at 3.72 µL. In comparison, the variation between the other of dispenser needles ranged from 0.18 – 1.89 µL. These results can be seen in Table 3.4. A possible reason for this larger variation between the ranges can be attributed to variations in the manufacturing process as a result of the needles being sourced from different companies.

Table 3.4 – Average Volume of Droplets Dispensed from Dispenser Needles, given to 2DP.
Gauge 14 (n = 5); Gauge 18 (n = 5); Gauge 20 (n = 5); Gauge 21 (n = 5); Gauge 25 (n = 5); Gauge 30 (n = 5); Flowflex (n = 20)

Needle Gauge	Mean ± SD (µL)	Range (µL)
Flowflex	40.07 ± 0.97	5.62
14	35.23 ± 0.49	1.11
18	20.83 ± 1.41	3.72
20	15.75 ± 0.58	1.64
21	13.97 ± 0.61	1.89
25	9.28 ± 0.27	0.72
30	6.24 ± 0.07	0.18

Plastic droppers are cheaper and easier to manufacture than dispenser needles. However, they yield a significantly larger mean and range between the droplet volumes [358]. While manual actuation plays a large role in the variation between results, it is accepted that decreasing the tip diameter will decrease the average droplet size. Thus, a similar expectation can be expected for dispenser needles.

Works by Tripp *et al.* also studied the effects of needle gauge sizes ranging between 22G and 30G. This experiment also considered the needle type and orientation of the droplet volume dispensed employing a similar methodology. It was reported that blunt tip needles yielded a larger droplet volume when compared with sharp bevel tip needles; however, these differences were not considered to be statistically relevant. It was also reported that needles in a vertical configuration produce droplets two and three times larger than droplets produced from the same needles in a horizontal configuration [359]. As droplets typically adhere to the surface area of the tip due to surface tension, a change in orientation away from the vertical orientation reduces the cross-sectional area of which the droplet is attached to; and thus, the weight required to overcome the surface tension and detach the droplet is reduced [358]. It should be noted that a comparison between the results of the

experiment conducted by Tripp *et al.* reported droplet sizes of 10.1 µL for a 30G needle in a vertical orientation. In contrast, the results from this experiment yielded droplets 6.24 µL in volume. A reason for this discrepancy was attributed to the larger flow rate (30 mL/hr) used in comparison to this experiment (3.6 mL/hr).

The experiment conducted in this thesis was repeated using the 14- and 30-gauge needles to study the effects of the needle orientation on the droplet size. The results from this experiment yielded conflicting results. The average droplet volume for the 14-gauge needles in the horizontal orientation decreased to 30.84 µL, a 12.4% decrease when compared to the droplets yielded by the vertical orientation (Figure 3.12). In contrast, the average droplet volume for the 30-gauge needles in the horizontal orientation increased to 10.75 µL, a 72.3% increase when compared to the droplets yielded by the vertical orientation (Figure 3.13). It was observed during the experiment that the droplets expelled from the 30-gauge needles would adhere to the outside of the shaft before detaching from the tip, and thus, the surface area in the horizontal orientation served to increase the surface area. This meant that a greater droplet weight was required to overcome the surface tension. It was also observed that the range between the droplet sizes in the horizontal orientation increased by an order of magnitude in comparison to the vertical orientation, with the 14- and 30- gauge needles yielding ranges of 10.4 (from 1.11 µL) and 2.4 µL (from 0.18 µL), respectively. Thus, the accuracy of the droplet production in the horizontal orientation was less reliable in comparison to the vertical orientation.

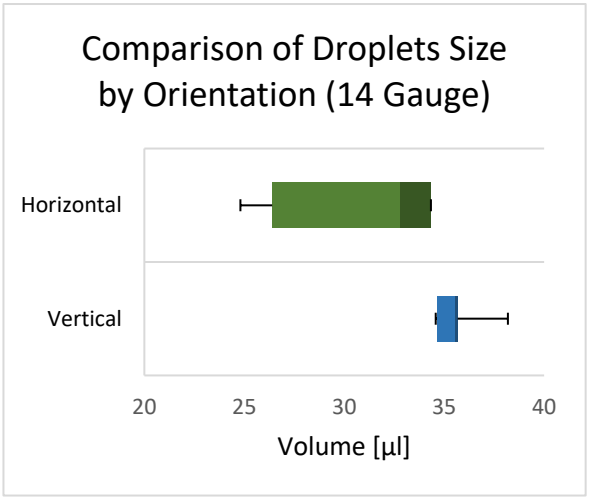

Figure 3.12 – Box plot comparison between orientations (14-gauge needles)

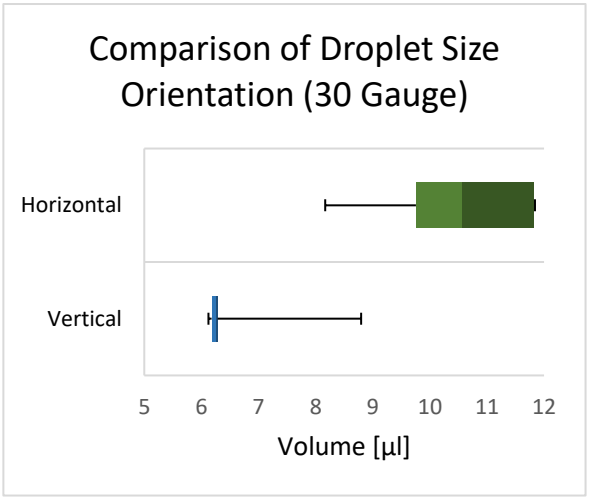

Figure 3.13 – Box plot comparison between orientations (30-gauge needles)

There are several ways to dispense DOD within the microlitre range within a high level of precision and accuracy. A platform developed by Haber *et al.* featured an 8-way manifold which employed a small jet from a pressurised reservoir, controlled by solenoid valves [360]. This system was able to handle fluids with viscosities in the range of 1 – 3 mPa·s, producing droplets within the range of 25 – 250 nL within an accuracy of 6.72%. In a similar approach, Liu *et al.* developed a non-contact dispensing system, utilising a similar 8-way manifold controlled by solenoid valves. This system contained an integrated control sensor, allowing for the opening time of the solenoid valves to be adjusted in real-time to dispense volumes over a range of viscosities, while also detecting the presence of clogs and air bubbles. The platform was able to produce droplets as small as 0.1 µL for liquids ranging from deionised water (≈1 mPa·s) to a 1:1 mixture of deionised water and glycerol (≈8.37 mPa·s). A platform developed by Bammesberger *et al.* used a piezoelectric plunger to create a mechanical impulse within a PipeJet dispensing pipe (length 18 mm, diameter 500 µm; BioFluidix, Freiburg, Germany), providing enough momentum to the droplet to cause it to detach [361]. The platform was reported to handle fluids with a wide range of rheological properties (surface tension: 30.49 – 70.83 mN/m, viscosity: 1.03–16.98 mPa·s), demonstrating the ability of the platform to handle a wide range of biological samples.

Castrejón-Pita *et al.* developed an acoustic actuator to produce droplets either on-demand or as a continuous jet [362]. The device utilised a flexible membrane fixed to a Plexiglass cartridge. A loudspeaker was used to supply a pressure pulse to the membrane, which deformed to eject the liquid from the nozzle. The device operated at a low voltage (< 30 V) and was reported to deliver droplets with a radius of 1.05 mm (≈4.85 µL) for liquids ranging in viscosity and surface tension from 2.4518 – 8.3650 mPa·s and 63 – 72 mN/m, respectively. Kim and Park modified a commercial piezoelectric printer to dispense DOD for microarrays [363]. A minimum droplet diameter of 70.17 µm (≈1.481 nL) was reported; however, the rheological properties of the liquids were not provided.

3.4. Development of a Sample Preparation Protocol for Poultry Samples

3.4.1. Introduction

Rapid and accurate detection of pathogenic diseases is crucial for their control and prevention of outbreaks. As presented in Chapter 2, cloacal samples contain a large quantity of genetic material and offers a wide array of options to analyse intestinal infections through simple and non-invasive methods. However, these samples are complex in nature, containing several compounds which can inhibit PCR and iNAAT methods, resulting in false negatives. Traditional sample preparation can prove labour intensive, particularly for a large number of samples [187]. Furthermore, materials commonly used for sample preparation such as salts, detergents and alcohols, can also act as inhibitors. As stated in section 1.4., the initial aim of the project was to develop a platform capable of preparing cloacal or faecal samples for the purpose of detecting poultry related pathogens in the developing world. Due to the environment the platform would be deployed in, the resources available were of paramount concern due to their expected scarcity. This section will present a fast and robust sample preparation method (the boiling method) that was used to detect *E. coli* within cloacal samples. A faecal sample was collected, taken from the bottom of the hen house during cleaning, from a local family in the UK that keeps layer hens for fresh eggs. This allowed for a proof-of-concept assay to be tested on real samples. The performance of the boiling method was compared to a commercial kit to assess the yield and purity of the DNA.

3.4.2. Materials and Methods

3.4.2.1. Preparation of the Crude Lysates

Following collection, 100 mg from the collected cloacal sample was aliquoted into individual 1.5 mL microcentrifuge tubes, which were then homogenised in 200 µL of each medium by vortexing. These mediums were: DNase/RNase-Free Distilled Water (DH_2O); Tris-EDTA buffer solution (1M Tris/HCL pH 8.0; TE); PBS buffer solution (PBS); and Tris-EDTA and proteinase K solution (TE/PK). Each homogenised sample was then incubated in a Peqlab HX-2 Digital Block Heater (VWR, Erlangen, Germany) at 95 °C for 15 minutes. The samples were then centrifuged at maximum speed for 3 minutes and the supernatants were then transferred into new 1.5 mL tubes. These lysates were then labelled and frozen at –20 °C to prevent degradation.

3.4.2.2. Preparation of the Lysates using the Genomic DNA Kit

The protocol for preparing the gram-negative bacterial cell lysate was used [364], using a PureLink™ Genomic DNA Mini Kit [365]. 100 mg of the collected cloacal sample was aliquoted into 1.5 mL microcentrifuge tubes, which were then homogenised in 180 µL of PureLink™ Genomic Digestion Buffer and 40 µL Proteinase K (20 mg/mL) by vortexing, followed by brief centrifugation at 2,000 g to remove bubbles. The tubes were then incubated at 55 °C for 30 minutes, vortexed at 10-minute intervals. Following incubation, 20 µL of RNase-A (20 mg/ml) was mixed with each sample by vortexing and incubated at room temperature for 2 minutes. 200 µL PureLink™ Genomic Lysis/Binding Buffer and 200 µL of 96% ethanol was added to each of the tubes, which were then vortexed briefly.

The tubes were centrifuged at maximum speed for 3 minutes and 640 µL from each tube was then transferred into a PureLink® Spin Column with Collection Tubes. The spin column was centrifuged at 10,000g for 1 minute at room temperature and the spin column was transferred into a clean PureLink® Collection Tube. 500 µL of PureLink™ Genomic Wash Buffer 1 mixed with 96% ethanol was added to the spin column, which was then centrifuged at 10,000 g for 1 minute at room temperature. 500 µL of PureLink™ Genomic Wash Buffer 2 mixed with 96% ethanol was added to the spin column, which was then centrifuged at maximum speed for 3 minutes at room temperature. The spin column was then transferred into sterile 1.5 mL microcentrifuge tubes beside a lit Bunsen burner and 200 µL of PureLink™ Genomic Elution Buffer was added to the spin column. Following incubation at room temperature for 1 minute, the spin column was centrifuged at maximum speed for 1 minute at room temperature. The eluates (Purelink) were then frozen at –20 °C to prevent degradation.

3.4.2.3. Preparation of the 1:10 Dilution Samples

Following the preparation of the crude lysates and the lysates prepared using the PureLink™ Genomic DNA Mini Kit, a 1:10 dilution was performed. Each of the samples were thawed at room temperature and placed on ice to prevent degradation. 20 µL of each of the thawed lysates were transferred into sterile 1.5 mL microcentrifuge tubes, which were then mixed with 180 µL of DH_2O by vortexing. These diluted lysates were then labelled and refrozen at –20 °C to prevent degradation.

3.4.2.4. Nanodrop Quantification

The quantity and purity of the lysates were analysed using a NanoPhotometer® N60 (Nanodrop). All lysates were thawed at room temperature and placed on ice to prevent degradation during the process. The Nanodrop was switched on and "Nucleic Acid" was selected from the main menu. The sensor pedestal was wiped with a Kimwipe and 2 µL of DH_2O was pipetted onto the sensor pedestal to initialise the equipment. The Nanodrop was then blanked against the corresponding medium (DH_2O for the crude lysates in DH_2O; TE for the crude lysates in TE; PBS for the crude lysates in PBS; and TE/PK for the crude lysates in TE/PK), before 2 µL of each sample was measured on the Nanodrop, selecting DNA-50 from the sample type menu. The quantification process was repeated for each of the 1:10 dilution lysates; with each sample set as blank against DH_2O.

3.4.2.5. Qubit Quantification

The Qubit™ 1X dsDNA HS (High Sensitivity) Assay Kit was used to quantify the DNA content in each lysate [366]. A Qubit™ working solution was prepared by vortexing the components for 5 seconds. The composition of the master mix can be seen in Table 3.5. 10 µL from each of the pure lysates were transferred into labelled Qubit™ Assay Tubes and 190 µL of Qubit™ working solution was added to each tube. The solutions were vortexed for 5 seconds and all tubes were incubated at room temperature for 2 minutes. The readings were taken on a Qubit 2.0 Fluorometer, using the 1X dsDNA High Sensitivity (HS) assay setting. Following the reading of standards 1 and 2, each of the assay tubes were loaded into the sample chamber and the tubes were read.

Table 3.5 – Volumes of Mastermix for Qubit™ working solution
10 µL of template DNA from each of the tested lysates were combined with 190 µL of Qubit™ working solution to create a total volume of 200 µL in each tube.An excess of 2 additional reactions was prepared to account for pipetting errors.

	Volume (µL)
Component A – Qubit™ 1X dsDNA HS Working Solution	2890
Component B – Qubit™ 1X dsDNA HS Standard #1	170
Component C – Qubit™ 1X dsDNA HS Standard #2	170

3.4.2.6. PCR Amplification and Gel Electrophoresis on Prepared Lysates

A PCR master mix was prepared in a 1.5 mL microcentrifuge tube. Each master mix consisted of 12.5 µL of DreamTaq Green PCR Master Mix (2X) (ThermoFisher Scientific, Waltham, Massachusetts, USA), 1 µL each of 1 µM forward and reverse primers (Table 3.6) and 9.5 µL of DH_2O. All pure lysates were thawed at room temperature and centrifuged before being placed on ice to prevent degradation. 1 µl of template DNA from each sample was combined with 24 µl of the prepared master mix in 200 µl PCR tubes. For the positive and negative controls, 1 µl of *Gardnerella Vaginalis* and 1 µl of DH_2O was combined with 24 µl of the master mix, respectively.

The lysates were loaded into a GeneAmp 9700 PCR System (Applied Biosystems, Waltham, Massachusetts, USA) and PCR was conducted under the program shown in Table 3.7. The process was repeated with the diluted lysates using the same methodology. The amplified products were then analysed by gel electrophoresis in a 1% agarose gel solution (Sigma-Aldrich, St. Louis, Missouri, USA) using 1x TAE buffer (Sigma-Aldrich, St. Louis, Missouri, USA) at 80 V for 45 minutes. To visualise the DNA bands, the DNA was stained using a SYBR® Safe DNA Gel Stain dye (ThermoFisher Scientific, Waltham, Massachusetts, USA) and visualised under UV light with a Biorad Universal Hood II Imaging System (Bio-Rad Laboratories, Hercules, California, USA).

Table 3.6 – PCR Primers used in this study [367]

	Sequence
F3_PCR_ECOLI	CKGTAGAAACCCCAACCCG
B3_PCR_ECOLI	AWACGCAGCACGATACGC

Table 3.7 – Recommended Thermocycling Conditions

		Temp (°C)	Time (hh:mm:ss)	Number of cycles
1	Initial Denaturation	95	00:05:00	1
2	Denaturation	95	00:01:00	30
3	Annealing	55	00:00:30	
4	Extension	72	00:01:00	
5	Final Extension	72	00:10:00	1

3.4.2.7. LAMP Amplification

The primers used for this LAMP assay were designed by Farhan *et al.* [367]. The primers were resuspended in DH_2O (the primers and corresponding volumes can be seen in Table 3.8). A 10X LAMP Primer Mix was prepared in a 1.5 mL centrifuge tube, consisting of 16 µL each of the 100 µM forward and backward inner primers, 2 µL each of the 100 µM forward and backward outer primers, 4 µL each of the 100 µM loop forward and loop backward primers and 56 µL of DH_2O. 1 µL of template DNA was combined with 12.5 µL of WarmStart Colorimetric LAMP 2X Master Mix (New England Biolabs, Ipswich, Massachusetts, USA), 2.5 µL of the prepared master mix and 9 µL of DH_2O in 200 µL PCR tubes by vortexing, followed by brief centrifugation. For the positive and negative controls, 1 µL of *E. coli* DH5α and 1 µL of DH_2O was combined with 24 µL of the master mix, respectively. Prior to amplification, each tube was checked for a bright pink colour, ensuring a suitable pH for a successful LAMP amplification. The lysates were loaded into a GeneAmp 9700 PCR System and LAMP was conducted under the program shown in Table 3.9.

Table 3.8 – LAMP Primers used in this study [367]
Each oligonucleotide concentration was prepared at 100 µM through suspension in DH_2O using the provided volumes

Primer	Sequence	Volume of DH_2O
FIP	TAACGCGCTTTCCCACCAACGGCCTGTGGGCATTCAGTC	280 µL
BIP	TAACGATCAGTTCGCCGATGCACTGCCCAACCTTTCGGTAT	288 µL
F3	CKGTAGAAACCCCAACCCG	238 µL
B3	AWACGCAGCACGATACGC	290 µL
LoopF	TCCACAGTTTTCGCGATCCA	250 µL
LoopB	ACGTCTGGTATCAGCGCGAAGT	227 µL

Table 3.9 – Setup used for the LAMP reaction.
The Lid temperature was maintained at 100 °C for the duration of the heating process to prevent evaporation. A final heating step at 95 °C for 5 min was used to stop the LAMP reaction

		Temp (°C)	Time (hh:mm:ss)	Number of cycles
1	**Heating Step**	65	00:30:00	1
2	**Termination Step**	95	00:05:00	1

3.4.3. Results

The purpose of this project was to develop a simple protocol which can be employed in low-resource settings. The ensuing section will report the results of the boiling method used on the cloacal samples, in comparison to the commercial sample preparation method.

3.4.3.1. Sample Comparison

To determine if inhibitors present in crude lysates would prevent PCR and LAMP amplification, faecal samples were suspended in 200 µL of various mediums and boiled for 15 minutes. The samples were then centrifuged to remove sediment from the samples, allowing the supernatant to be collected. These were treated as crude lysates, which were amplified using PCR and LAMP. Figure 3.14 compares the crude lysates produced using the boiling method against purified DNA produced using the PureLink™ Genomic DNA Mini Kit before and after dilution. The pure lysates (Figure 3.14a) obtained using the boiling method exhibited a brown colouring, which indicated the presence of contaminants in the sample. This brown colouring was greatly reduced following the 1:10 dilution (Figure 3.14b), indicating a reduction in contaminants. This brown colouring was not observed for either of the eluates produced using the PureLink™ Genomic DNA Mini Kit.

pH testing was conducted on both the pure lysates prior to further analysis. The pH of each of the lysates in DH_2O and PBS were 6. The pH of the lysates in solely TE ranged from 6 to 8, while the pH of the lysates in TE/PK ranged between 7 and 8. The pH of the lysate produced using the PureLink™ Genomic DNA Mini Kit was 8. Following dilution, pH testing was repeated on the diluted samples. The pH of the diluted lysates in DH_2O ranged between 6 and 7. The pH of the lysates in PBS buffer and the TE/PK was 7. The pH of the lysates in solely TE ranged between 7 and 8. The pH of the lysate produced using the PureLink™ Genomic DNA Mini Kit ranged between 7 and 8.

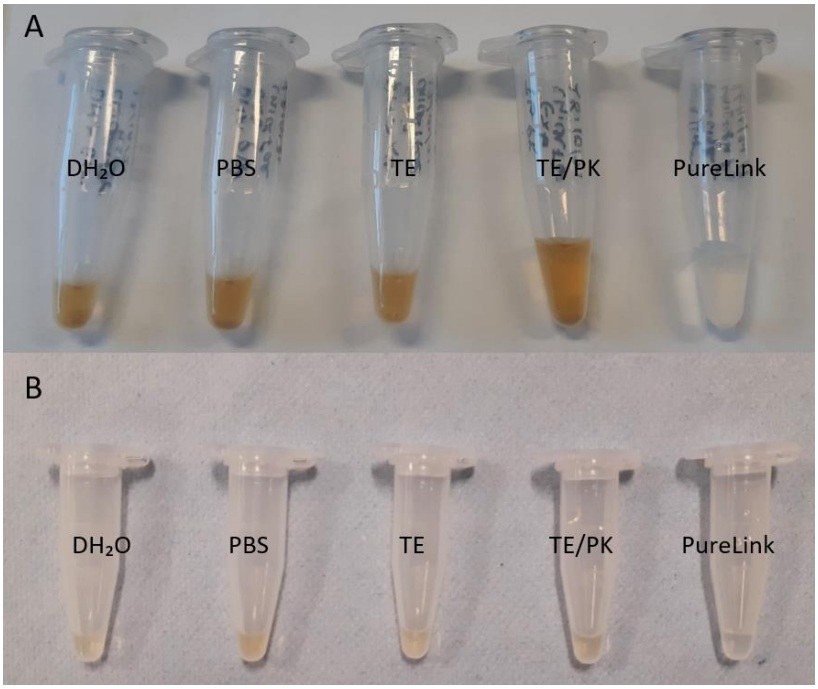

Figure 3.14 – Comparison between crude lysates from boiling and spin column methods
***A.** Pure lysates* ***B.** 1:10 dilution lysates*

3.4.3.2. DNA Yield and Purity from the Qubit and Nanodrop

Qubit readings were taken to quantify the DNA yield of each of the 4 crude lysates and the Purelink eluate. The results can be seen in Figure 3.15. The Purelink Genomic DNA Extraction Kit produced the highest DNA yield (354 ng/µL). For the crude lysates produced by boiling the sample in a buffer, the PBS produced the highest yield (182 ng/µL), followed by the TE (141 ng/µL), followed by the DH_2O (114 ng/µL). The crude lysate boiled in TE/PK yielded the lowest amount of DNA (113 ng/µL).

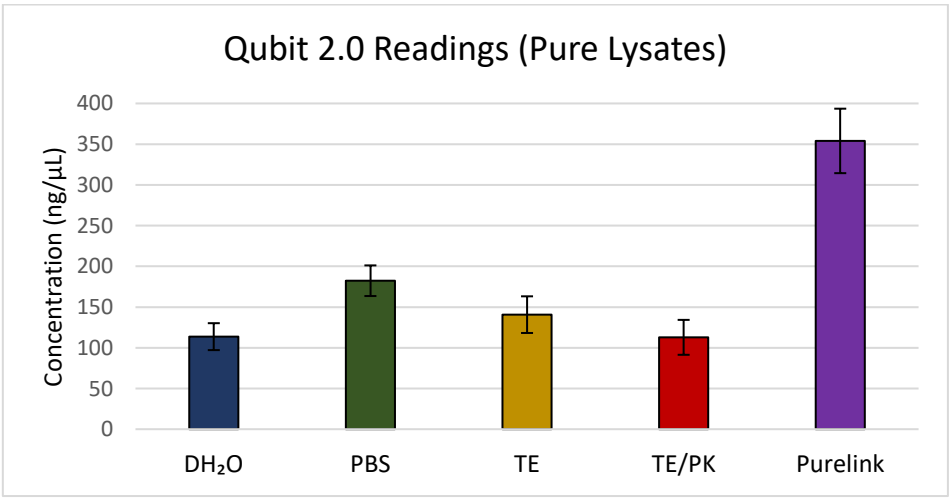

Figure 3.15 – DNA Quantification on Pure Lysates using the Qubit 2.0 Fluorometer

Nanodrop readings were taken to quantify the DNA yield and to assess the purity of the obtained DNA from the 4 crude lysates and the Purelink eluate. The results can be seen in Figure 3.16. The TE/PK produced the highest yield of DNA (634 ng/µL), followed by the TE (598 ng/µL), followed by the PBS (394 ng/µL), followed by the DH_2O (340 ng/µL). The Purelink Genomic DNA Extraction Kit produced the lowest DNA yield (124 ng/µL). The results for the diluted lysates were also quantified using a Nanodrop, as shown in Figure 3.17. In this instance, the TE buffer gave the highest average yield of DNA (226 ng/µL), followed by the PBS (195 ng/µL), followed by the DH_2O (187 ng/µL), followed by the TE/PK (125 ng/µL). Akin to the pure lysates, the Purelink Genomic DNA Extraction Kit produced the lowest DNA yield (17.4 ng/µL).

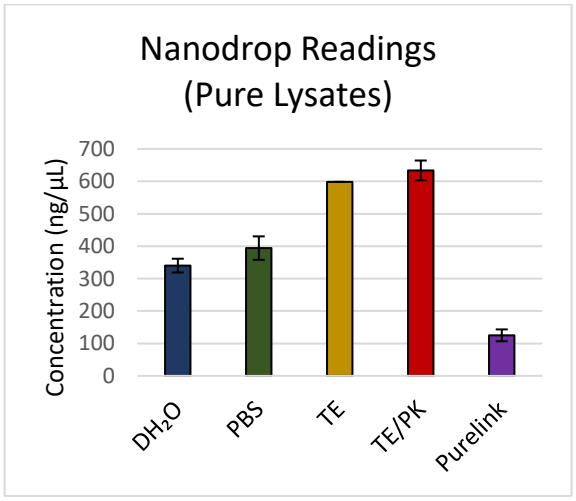

Figure 3.16 – DNA Quantification on Pure Lysates using the Nanodrop

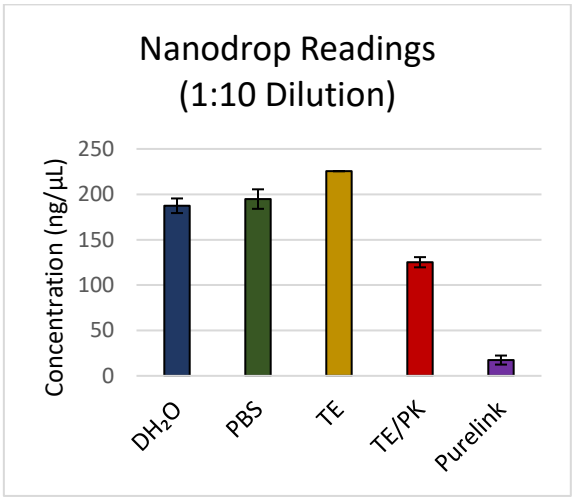

Figure 3.17 – DNA Quantification on Diluted Lysates using the Nanodrop

The results for the DNA purity of the pure lysates were also recorded, which can be seen in Figure 3.18. The A260/280 ratio values are as follows: DH_2O, 1.04; PBS, 1.04; TE, 1.10; TE/PK, 1.06; Purelink, 2.15. The A260/230 ratio values are as follows: DH_2O, 0.326; PBS, 0.313; TE, 0.410; TE/PK, 0.437; Purelink, 1.68.

Following dilution, the DNA purify was reanalysed, which can be seen in Figure 3.19. The A260/280 ratio values are as follows: DH_2O, 1.11; PBS, 1.09; TE, 0.895; TE/PK, 1.02; Purelink, 2.04. The A260/230 ratio values are as follows: DH_2O, 0.368; PBS, 0.324; TE, 0.356; TE/PK, 0.340; Purelink, 1.50.

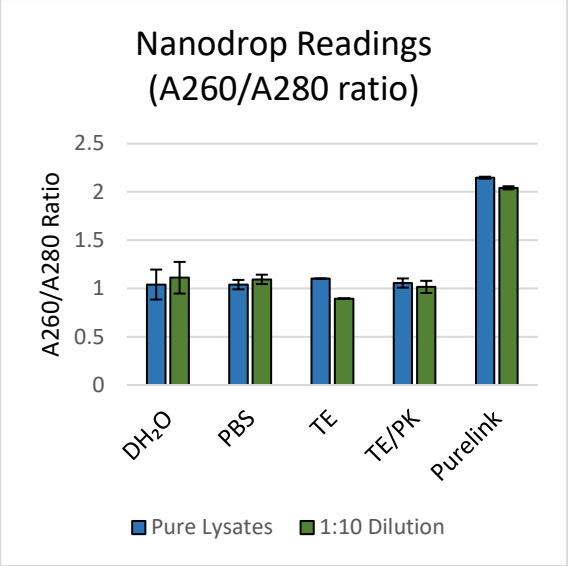

Figure 3.18 – DNA Purity reading on Pure Lysates using the Nanodrop

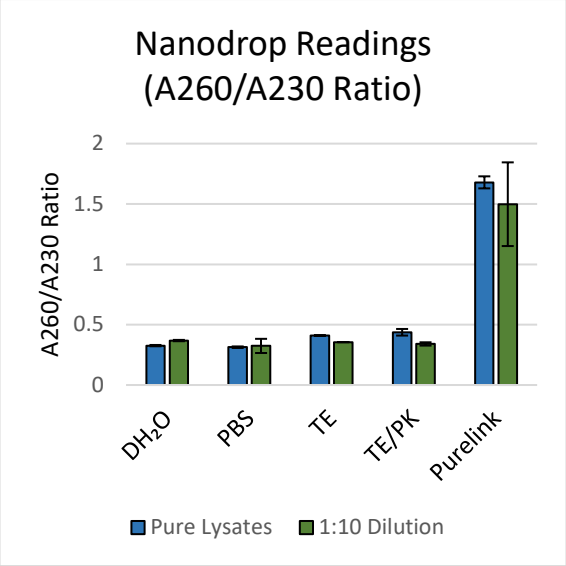

Figure 3.19 – DNA Purity reading on Pure Lysates using the Nanodrop

3.4.3.3. PCR Amplification and Gel Electrophoresis Results

The pure lysates were analysed by a 1% agarose gel electrophoresis study, shown in Figure 3.20. Non-distinct banding was observed in lanes 1 – 12, indicating the presence of DNA in each lane. However, there was also a large amount of smearing observed, indicating potential protein contamination in the lanes. A clearer banding was observed in lanes 13 – 15, indicating less contamination for the samples prepared using the PureLink™ Genomic DNA Mini Kit in comparison with the pure lysates.

The products of conventional PCR amplification on the pure lysates was also subjected to a 1% agarose gel electrophoresis study, which can be seen in Figure 3.21. In this instance, the presence of a clear DNA band was only observed in lanes 10 and 11, corresponding to the crude lysate in TE/PK. The products of conventional PCR amplification on the diluted lysates was also subjected to a 1% agarose gel electrophoretic study, which can be seen in Figure 3.22. In this instance, the presence of a clear DNA band was observed in lanes 1 – 7 and 10 – 15, demonstrating the presence of DNA in each sample. DNA bands were not observed in lanes 8 and 9, indicating a lack of DNA in the tested samples.

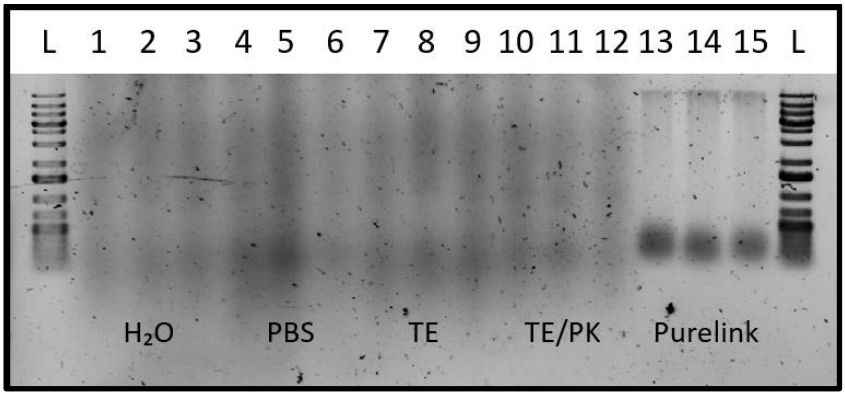

Figure 3.20 – Gel Electrophoresis on pure cloacal samples prepared by the boiling method
Lanes 1 – 3, DH_2O; Lanes 4 – 6, PBS; Lanes 7 – 9, TE; Lanes 10 – 12, TE/PK; Lanes 13 – 15, PureLink™

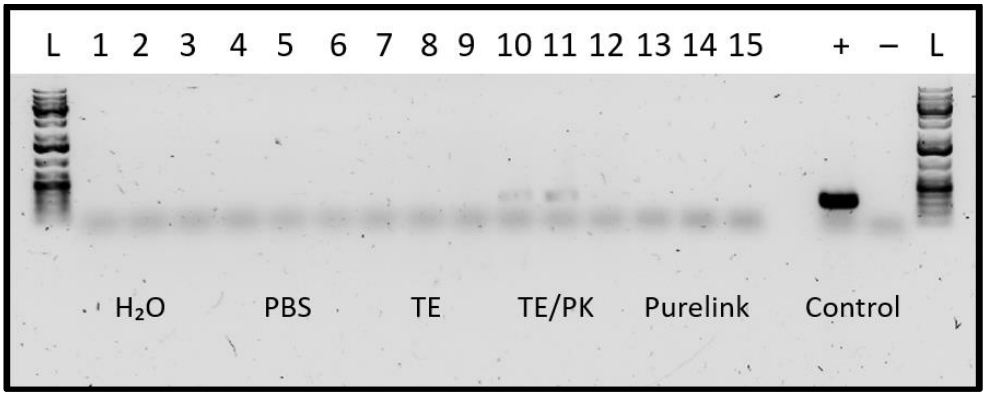

Figure 3.21 – Gel Electrophoresis on pure lysates of cloacal samples after PCR amplification
Lanes 1 – 3, DH_2O; 4 – 6, PBS; 7 – 9, TE; 10 – 12, TE/PK; 13 – 15, PureLink™; + and – signify the positive (Gardnerella Vaginalis) and negative (DH_2O) controls, respectively; L signifies the DNA ladder used for this electrophoretic study

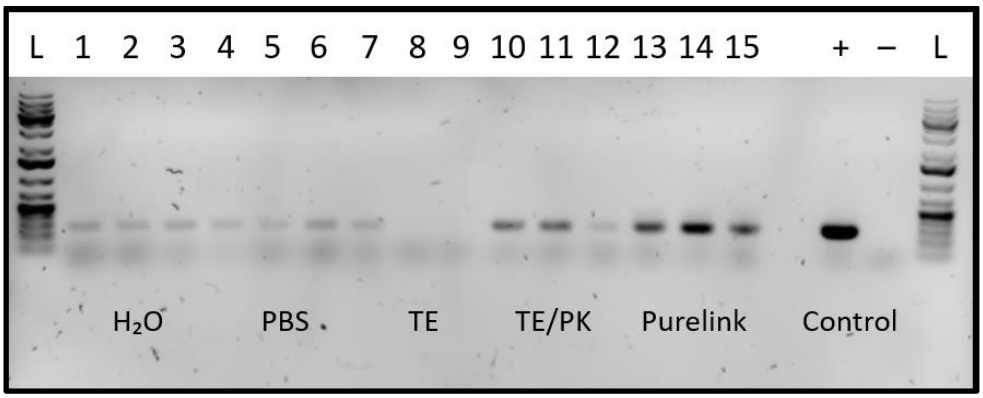

Figure 3.22 – Gel Electrophoresis on 1:10 diluted lysates after PCR amplification
Lanes 1 – 3, DH_2O; 4 – 6, PBS; 7 – 9, TE; 10 – 12, TE/PK; 13 – 15, PureLink™; + and – signify the positive (Gardnerella Vaginalis) and negative (DH_2O) controls, respectively; L signifies the DNA ladder used for this electrophoretic study

3.4.3.4. LAMP Amplification

The LAMP products of the pure lysates can be seen in Figure 3.23. A visual colour change was observed in each tube with the exception of tubes 8 and 9. The colour change from pink to yellow indicates the presence of *E. coli*. The products of the diluted samples can be seen in Figure 3.24. A visual colour change was observed in each tube indicating the presence of *E. coli* in each of the samples, with the exception of tube 8. By comparing the products of each experiment, a stronger visual colour change was observed among the diluted lysates when compared to the crude lysates, indicating an improvement in performance following dilution.

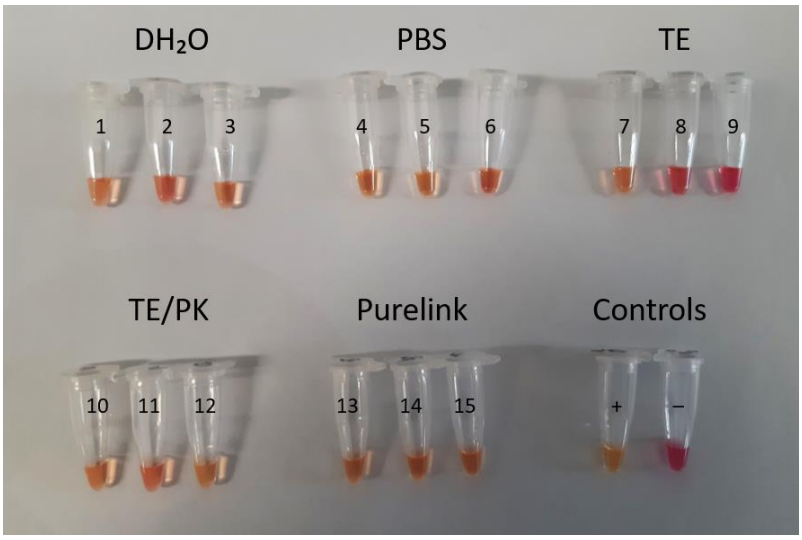

Figure 3.23 – LAMP products of pure cloacal lysates prepared by the boiling method
1 – 3, DH_2O; 4 – 6, PBS; 7 – 9, TE; 10 – 12, TE/PK; 13 – 15, PureLink™;
*+ and – signify the positive (*E. coli DH5α*) and negative (DH_2O) controls, respectively*

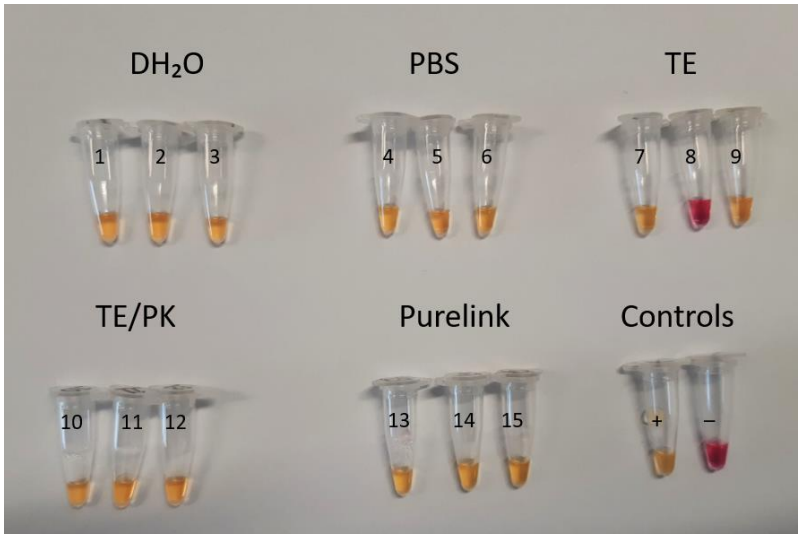

Figure 3.24 – LAMP products of 1:10 diluted cloacal lysates prepared by the boiling method
1 – 3, DH_2O; 4 – 6, PBS; 7 – 9, TE; 10 – 12, TE/PK; 13 – 15, PureLink™;
*+ and – signify the positive (*E. coli DH5α*) and negative (DH_2O) controls, respectively*

As LAMP was performed using pH sensitive dyes, it was hypothesised that the weakly acidic (pH ≈6) samples could cause a colour change, resulting in false positives. The LAMP reaction was repeated with the lysates in DH_2O, without including the LAMP primers. The result (Figure 3.25) demonstrated no colour change, indicating that the pH of the samples was not the cause of the colour change.

Figure 3.25 – LAMP products of DH_2O cloacal lysates without LAMP primers

3.4.4. Discussion

A major limiting factor was the centrifugation step to precipitate the solid particulates within the lysate prior to the aliquoting of samples. It was hypothesised that, following cell lysis, filtration using a membrane with an appropriate pore size would be sufficient for removing particulates and cellular debris. An aim in section 1.4 was to deliver DNA and RNA; however bacterial cells, viral particles, as well as their contained NAs, are heterogenous in topologies [368]. As a result, DNA and RNA protocols are typically performed separately. Kim and Gale have reported that small micropores provide a better extraction efficiency for pure DNA samples; however, mid-sized nanopores (100 nm) are better when used with realistic samples [369]. A centrifugation-free extraction system was reported by Lee *et al.*, using vacuum pressure within the range of 0.7 – 3.3 kPa to draw a fluid through a silica membrane adapted from a QIAamp circulating nucleic acid kit (QIAGEN, Hilden, Germany) [370]. A DNA yield of 90% that of centrifugation at 12,000 g was reported, independent of the initial volume, demonstrating the effectiveness of this method. However, the inclusion of mineral oil as an immiscible phase atop the elution buffer plays a crucial role in the process, that is, to block pores upon contact to prevent irregular openings. It was also reported that this approach was limited to a 70% volume recovery without the inclusion of the mineral oil, with the volume recovery was as low as 16% in extreme cases.

It has been reported that commonly used materials within NA extraction, such as cellulose and nitrocellulose, can inhibit PCR [371]. Alternatively, materials such as polytetrafluoroethylene (PTFE) and polycarbonate (PC) are recommended, as they have been reported not to present inhibitory effects. It has also been reported that silica membranes can absorb between 40 – 50 µL of liquid [370]. Thus, further research to determine a membrane material compatible with LAMP is needed, particularly, to study potential inhibitory effects. The results seem to indicate that a dilution step could be used to circumvent the need for additional sample preparation, simplifying the process and improving suitability for resource-stressed settings; however, further research is needed to support this claim. Furthermore, faecal samples were collected from a hen house for analysis. These samples were expected to be abundant in *E. coli* and would serve to verify the functionality of the protocol. However, determining a LOD using spiked samples would offer quantitative values to which the target analyte could be detected with a level of stated probability.

3.4.4.1. LAMP vs. PCR

A comparison between the PCR and LAMP products showed that LAMP outperformed PCR amplification for both pure and diluted lysates. A comparison between the amplification techniques performed on crude lysates revealed that LAMP successfully detected *E. coli* in each of the samples, with the exception of samples 8 and 9 (Figure 3.23). Contrastingly, PCR produced weak bands in samples 10 and 11 (Figure 3.21). Following the dilution step, both the LAMP and PCR techniques demonstrated an improvement in performance. PCR detected *E. coli* in each of the samples, with the exception of samples 8 and 9 (Figure 3.22). LAMP detected *E. coli* in each of the samples, with the exception of sample 9 (Figure 3.24). This improvement in performance for both the PCR and LAMP techniques signify the importance of the dilution step; however, LAMP was better suited towards the higher quantity of DNA and contaminants when compared to PCR.

Both amplification techniques were unsuccessful in detecting the presence of *E. coli* in sample 8. The corresponding readings from the Nanodrop reported unreliable results prior to and after dilution (3005 and 3.5 ng/µL, respectively). These were determined to be outliers within 2 standard deviations and were thus excluded from the presented results. These discrepancies would allude to the lack of *E. coli* being present in sample 8, indicating the sample was of low quality.

The introduction of real-world samples into microfluidic cartridges remains a challenge. Stool sampling in particular is considered to be a major challenge, requiring several laborious pre-treatment steps including chemical treatment and centrifugation prior to insertion into a cartridge [372,373].

However, examples of direct sample insertion into a device have been shown. Mosley *et al.* demonstrated an immiscible filtration assisted by the surface tension (IFAST) system to process clinical stool samples within a single cartridge in 7 minutes [374], developing upon previous IFAST applications for NA extraction [375-379]. This method offers a solution to the issue commonly encountered in regards to magnetic bead-based approaches to sample preparation, that being the requirement for complex cartridge designs to conduct multistep washing and purification steps [380,381]. Despite the sophistication of this approach; however, careful calculation and adjustment of the interfacial energies is required. Furthermore, following PCR amplification, weak and no PCR products were observed in the 3-chamber design, despite reporting A260/A280 ratios in the range of 1.1 – 1.3 [374].

One might expect that such crude lysates would significantly inhibit the performance of the PCR and LAMP amplification techniques. The data in this experiment revealed similar signs of amplification inhibition for the PCR process for crude lysates (Figure 3.21), showing weak PCR products across 2 of the 12 crude lysates. The LAMP products in comparison (Figure 3.23) revealed signs of amplification inhibition across 2 of the 12 crude lysates, demonstrating the difference in efficacy between the two processes. Furthermore, the 1:10 dilution step was seemingly sufficient to circumvent the effects of the inhibitors, improving the efficacy of both the PCR (Figure 3.22) and LAMP (Figure 3.24) processes.

3.4.4.2. Qubit vs. Nanodrop Detection

A comparison between the Qubit and Nanodrop results (Figure 3.26) offered conflicting results. The Nanodrop detected a much higher concentration of DNA in each sample when compared to the Qubit. Pure nucleic acid ratios (A260/280) should have a range of 1.8 – 2.1, with 1.8 being accepted as pure for DNA and 2.0 being accepted as pure for RNA [382]. When considering the DNA quality ratios produced by the Nanodrop, each of the crude lysates produced by the boiling method in various mediums has a relatively low value (0.825 – 1.184), indicating a high level of impurities within the samples. In comparison, the DNA extracted using the Purelink Genomic DNA Extraction kit demonstrated an A260/280 ratio ranging between 2.132 and 2.155, indicating a high level of purity. From the pH test, it was observed that many of the samples were slightly acidic, at pH 6. It has been reported that acidic solutions can cause the A260/280 ratio to be under-represented by 0.2 – 0.3 [383]. Furthermore, many spectrophotometers have a wavelength accuracy of ±1 nm, which can result in a variance of ±0.4 in the A260/280 ratio.

For nucleic acid ratios (A260/230), values for “pure” nucleic acids are typically higher than the A260/280 ratios, in the range of 2.0 and 2.2. Ratios lower than 1.8 indicate the presence of

contaminants [382]. Due to a low level of sample preparation steps performed on the crude lysates, the presence of contaminants was expected, resulting in a significantly lower A260/230 ratio than the standard. However, it was demonstrated by the LAMP products that these contaminants would not prevent the detection of the *E. coli* present in the sample; however, the presence of these contaminants may have had an effect on the PCR amplification.

The quantification of NAs through the Nanodrop employs spectrophotometry to measure ultraviolet (UV) light absorbance at 260 nm. However, as the spectrophotometer is unable to distinguish between DNA, RNA and proteins, results can be unreliable [384-387]. Cloacal samples contain varying amounts of proteins and bacterial biomasses [84]. As the crude lysates did not undergo NA extraction or purification, it is likely that the DNA yield was overrepresented. The Qubit™ 2.0 Fluorometer uses a fluorescent dye which specifically binds to the DNA. As a result, DNA quantification may be provided with an improved specificity [388-390]. The results for the DNA yield provided by the Qubit were deemed to be more reliable. Nevertheless, the results for the Nanodrop were useful for determining the DNA purity, which the Qubit could not. As expected, the purity of the crude lysates was significantly lower than the eluates produced by the PureLink™ Genomic DNA Mini Kit. Despite the low purity values however; both PCR and LAMP products were able to detect the presence of *E. coli* following the 1:10 dilution step. This was an interesting result compared to work by Mosley *et al.*, where PCR inhibition was reported despite higher A260/280 values [374].

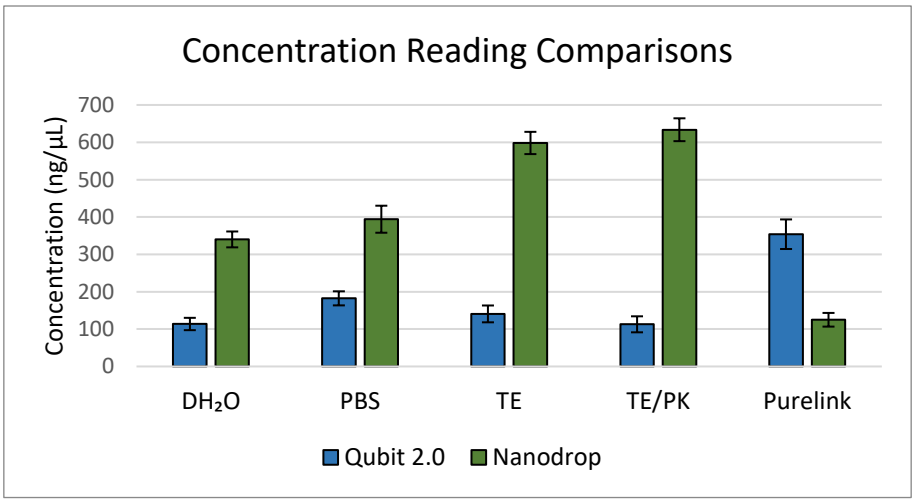

Figure 3.26 – Comparison of readings taken from the Qubit 2.0 and the Nanodrop

3.5. Chapter Summary

There were many crucial lessons learned from each of the experiments presented in this chapter. The absorption across the commercially available swabs ranged between 27.5 – 249.3 µL. From a fluidic perspective, nylon flock, cotton or polyurethane mini-tip swabs are favourable. Furthermore, this experiment provided concrete values of absorption rates for both single and pooled sampling, providing insight into the geometry of a swab interface that was required to facilitate either case, mitigating the requirement for further redesigns.

The volume of the droplets yielded by the dispenser tip needles were smaller than those by the Flowflex extraction tubes. With a decrease in needle size from 14 to 30-gauge, a significant decrease in the droplet volume was observed, from 35.23 to 6.24 µL. While the 25- and 30-gauge needles were capable of producing droplets within the single microliter range, assistance would be required to reach the desired goal of 1 – 3 µL. Thus, assistance to release a hanging droplet was required, in conjunction with a 30-gauge needle.

Finally, the sample preparation protocol demonstrated the significant different in the quality of the DNA produced by crude extraction methods in comparison to the gold standard. Despite this vast difference; however, LAMP was able to achieve detection at a higher sensitivity compared to the gold standard, PCR, demonstrating the potential of iNAAT techniques. Based on the results of this experiment, using a PBS buffer offered the highest yield of DNA among the crude lysates, while each offered similar levels of purity. Therefore, a PBS buffer was recommended for subsequent protocols. Moreover, this experiment demonstrated that a simple dilution step in DH_2O greatly improved the performance of both the PCR and LAMP methods. Ultimately, a simple protocol with the potential for use in a low-resource setting was created, which could easily be integrated into a sample preparation platform.

4. Design of a Sample Preparation Platform

4.1. Introduction

Based on the literature review presented in Chapter 2 and the preliminary experiments presented in Chapter 3, initial design specifications were drafted. Throughout the project, the design specifications were frequently adjusted to suit new user needs. As a result, the designs underwent several changes to accommodate each updated set of design specifications. The design specifications presented in this chapter show the user needs for the sample preparation platform following the change in focus from poultry related infections to SARS-CoV-2. The final design specifications were tabulated and used to develop a final design idea that was fabricated and tested. A discussion is given highlighting some of the major challenges faced during the design stage.

4.2. Design Specifications

Guidelines for a sample preparation device were developed based on a set of criteria using the MUMSFACES method: **M**aterial, **U**ser, **M**anufacture, **S**ize, **F**unction, **A**esthetics, **C**ost, **E**rgonomics and **S**afety. As the aesthetics and ergonomics of the platform were less important due to the research nature of the project, these criteria were therefore discounted.

4.2.1. Function

The platform was designed to accept raw macro-sized swab samples, perform sample preparation and dispense purified NAs in an aqueous solution in "micro-sized" volumes. A sample was collected using traditional swab sampling and inserted directly into a chemical buffer. Heat treating was then used to deactivate and thermally lyse the pathogenic cells, yielding a crude lysate containing the target NAs. Following lysis, an aliquot of the sample was dispensed from the total volume into 200 µL 8-strip PCR Tubes with attached caps (STARLAB, Milton Keynes, UK). The PCR tube was then transferred to a portable POCT platform, where the sample underwent a LAMP reaction, followed by end-point colorimetric detection. This allowed for sample-to-answer POCT to be achieved at virtually any site.

As discussed in 2.3.3. many POCT devices employ single-use cartridges to conduct sample preparation. The proposed platform developed during this project utilised similar technology, a single-use collection device containing necessary components to achieve sample preparation. The difference between the state-of-the-art and the platform developed during this project is that downstream amplification and detection was conducted within a separate device. This allowed for the sample preparation process itself to be tailored towards multiple applications. Finally, the collection device was disposable, to prevent cross-contamination through repeated use.

A fluid control system was used to move the aqueous sample through the collection device and to dispense the aliquots into the PCR tubes. Furthermore, as lysis was achieved through a combination of chemical and thermal means, a heating system was included. This would be powered using a USB power bank instead of using a mains power supply, increasing the portability of the device. In order to prevent both overheating and unnecessary power consumption, a system was developed to monitor and control the temperature during operation.

4.2.2. User

The initial users of the device were veterinarians in the Philippines. During the progression of the Covid-19 outbreak, the user evolved to include adults with limited biological knowledge. Consequently, the device was redesigned to collect and prepare NAs from virtually any biological cell. Currently, there are no commercially available platforms applicable to all sample types. As discussed in Chapter 2, swab sampling is a convenient method for collecting several sample types with minimal invasiveness, reducing the risk of contamination and preventing trauma during collection. For human sampling, swab samples can be self-collected, reducing the costs involved with hiring trained personnel to obtain the samples. The proposed platform was designed to accept swab samples.

The device was intended to be lightweight and portable, to allow for easy transportation and convenient use. As is the nature of POCT, the device would be subjected to testing in sub-optimal environments, meaning robust techniques were required to allow functionality in such conditions. In addition, the platform was designed to require minimal user interaction following the insertion of the swab sample into the device. This would reduce the amount of training necessary for the operation and ensure more reliable results were achieved. Furthermore, access to the sections of the device would be restricted in order to prevent user interaction with the internal components. This would prevent sample contamination and protect the user and the device from damage.

4.2.3. Size

The focus of the project was to develop a portable sample preparation device. A device is considered portable if the weight is less than 10 kg, and thus, this was considered as the maximum weight [235]. A maximum footprint of 20 x 30 x 20 cm (L x W x H) was chosen to make the device manageable by one person. A power bank (20,000 mAh capacity, 18 W output) was selected in place of mains electricity, the specifications of which were chosen based on common commercially available options.

It has been reported that the viral transfer efficiency is low for swabs eluted into volumes of VTM less than 100 µL and close to 100% for volumes above 500 µL [197]. This meant that the initial starting volume must be above 500 µL. Furthermore, as demonstrated in section 3.2, the absorption rate of commercial swabs ranged between 27.5 and 249.3 µL. To factor in allowances for the volume of fluid lost for both singular and pooled samples, a starting volume of 2.25 mL was selected. The swab inlet was designed to allow for a volume in excess of 3 mL, to account for any displacement caused by the insertion and agitation of the swab, as well as volume losses caused by absorption.

4.2.4. Manufacture

The platform was developed in the UK for fabrication in the Philippines following a technology transfer. It was important to utilise simple and low-cost manufacturing steps. As discussed in section 2.3, many platforms conduct sample preparation inside a microfluidic cartridge. These are designed in individual layers by hot embossing and injection moulding plastic materials [391,392], or using soft lithography techniques [393,394]. In both cases, layers are constructed using suitable moulds for each component, requiring fabrication in specialised facilities (i.e. a cleanroom). Following fabrication, they must carefully be aligned and bonded together [395,396]. This significantly increases the fabrication time, making developers apprehensive to attempt such techniques for novel devices.

As many of the components would be designed from thermoplastic polymers, injection moulding was considered for end-point fabrication, due to the ability to create high strength components with a complex geometry. In conjunction with automation, it was possible to manufacture components at a high production rate. A major advantage of this method was the ability to include inserts and create internal channels within the device, without post-machining. Despite its advantages, however, the high initial tooling costs made this option unviable during the development of the device. As a result, 3D printing became the main method considered to manufacture and test prototype components. 3D printing can reduce the time required for developing components. In contrast to hot embossing or injection moulding, 3D printed components can be manufactured in one step, omitting the need for layer-by-layer fabrication and bonding. 3D printing does not need to be conducted in a cleanroom, allowing for components to be manufactured in non-specialised locations. Ultimately, this allows for trial-and-error fabrication to be utilised while being less costly in terms of time and resources [396].

Stereolithography (SLA) is a viable option for creating components with complex internal features. Such devices are printed layer-by-layer from photosensitive resins, which are cured using a light source. Following the printing process, uncured resin is drained to create internal channels; omitting the need for bonding and alignment [397]. Despite the high resolution of SLA printing, the technique is limited to commercially available resins, which may be incompatible with biological materials [396]. A low-cost alternative is fusion deposition modelling (FDM), where a thermoplastic material is extruded through a nozzle head onto a build plate. The material hardens as it cools post extrusion, meaning a light source is not needed to cure the material. A disadvantage to this approach is the low interlayer structural strength, increasing the potential for leaks to occur [398]. Furthermore, support material can be required between layers, which can be difficult to remove, particularly for internal features [399].

4.2.5. Material

Many microfluidic devices are prototyped using polydimethylsiloxane (PDMS), which are favourable due to the low cost of the raw materials and safe fabrication steps [400]. Moreover, it is transparent, allowing for optical elements to be incorporated; flexible, allowing for elastically deformable components to be incorporated; and biocompatible, allowing for use in medical applications [397]. However, PDMS requires fabrication in a cleanroom using predesigned moulds, both of which require specific facilities and increase costs. PDMS and related polymers are also subject to the adsorption of NAs and other biological components [401,402]. In diagnostics, this can lead to a misdiagnosis or an incorrect quantification due to an underrepresentation of a pathogen of interest within a sample.

The materials used for the sample preparation device were established based on the user needs. The platform needed to be lightweight, robust and impact resistant, to enable portability and to prevent damage during transportation or mishandling. As electrical components were used within the device, ensuring the platform was electrically insulated would reduce shock hazards. In addition, as heating elements would reach temperatures up to 100 °C, thermal resistance was required.

Thermoplastic polymers were considered for end-point fabrication, due to their mechanical and chemical properties. Typical thermoplastics used for the production of such components are polystyrene, poly(methyl methacrylate) (PMMA) and polyurethane [398]. However, many of the materials that were compatible with the available manufacturing methods featured glass transition temperatures around or below 100 °C. Thus, the components directly in contact with heating elements were fabricated from a heat resistant resin.

4.2.6. Cost

It was important that the final platform was low-cost, both in terms of the raw materials required and the manufacturing processes used. While many of the sections, such as the outer casing, external fluid control components and heating elements, were reusable, others, such as the disposable component and internal fluid control components were single-use, resulting in increased costs. During the progression of this project, off-the-shelf components were integrated into the platform to replace costly components, reducing the cost per prototype. Many of the components were also designed to be fabricated using low-cost 3D printing methods, meaning parts could be produced cheaply. Due to the aim of this project being to develop the platform, concerns regarding the cost were considered to be of greater importance once the device has reached the commercialisation stage.

4.2.7. Safety

There were three primary safety concerns. The heating elements presented a risk of burns. This was addressed by placing the high temperature heating elements within insulative components to prevent direct contact. The high voltage module contained wiring that presented a shocking hazard. The platform was designed to place these components within insulative materials and beyond reach. The major concern was the risk of potentially infectious samples coming into contact with the user should the components in contact with the sample rupture. Consequently, the platform was designed to be self-contained, to ensure that ruptures within the platform would result in the system leaking into itself in place of into the surroundings where it could come into contact with the user.

POCT is typically required in low-resource settings. Such environments can have a low level of biosecurity and contamination is a high possibility. The sample within the device must be separated from external airborne particulates, such as dust, dirt and aerosols. Many of the theorised designs were developed to prevent contaminants from entering into the device, while also preventing any reagents and chemicals within the device from escaping into the environment. As mentioned in section 4.2.5, the optimal materials to use were thermoplastic polymers, which are thermally and electrically insulative and resistant to both environmental and chemical pollutants.

4.2.8. Summary of Design Specifications

The product specifications were drafted with reference to the specifications presented in this section, shown in Table 4.1. These served as guidelines during the development of the device. The device would be designed to accept swab samples which were inserted into 3 mL of fluid. Following sample preparation, 3 µL of the purified NA in solution was expelled from the device directly into PCR tubes for the analysis of poultry related infections, while 1 µL was expelled for the analysis of SARS-CoV-2.

It was decided that the proposed platform should produce uniform droplets with a fixed 1 µL volume on-demand, allowing for the desired volume to be released in increments. This was considered to be a simpler solution in comparison to metering specifically sized droplets. This also circumvented another major issue encountered during the project, which was the frequent alterations to the desired accepted and dispensed volumes as per new user needs. The control and release of a 1 µL droplet posed a major challenge, as a precise level of accuracy was required within an extremely limited budget, which greatly limited the fluid control methods available.

The footprint and mass requirements were chosen to ensure the device would be operable and manoeuvrable by a single person. As a result of ensuring portability, the device was to be powered by a power bank, which set the power requirements. In order to ensure functionality using a standard 20,000 mAh power bank, the start-up and total processing time were minimised. The operating conditions were selected based on the conditions of both the UK and the Philippines. In the UK, the temperature and humidity ranges are 1 – 21 °C and 40 – 60%, respectively [403]. In the Philippines, the temperature and humidity ranges are 6 – 42 °C and 71 – 85%, respectively [404]. Thus, the extremes of each environment were chosen.

Table 4.1 – A summary of the specifications for the sample collection and preparation device

Sample Type	Cloacal swab (*Poultry related infections*) NP and OP swab (SARS-CoV-2)
Volume of Fluid In	≤ 3 mL
Volume of Fluid Out	3 µL (*Poultry related infections*) 1 µL (SARS-CoV-2)
Maximum Footprint	20 x 30 x 20 cm
Maximum Mass	< 10 kg
Start Up Time	2 – 5 min
Processing Time	30 – 60 min
Power Requirements	10 – 18 W (capacity of power bank ≈20,000 mAh)
Operating Environment	Temperature range: 1 – 42 °C Humidity range: 40 – 85%
Operating Skills Required	*Minimal*
ISO/Medical Standards	• Device should be corrosion and chemical resistant (BS6105:1981) • ISO 9001:2015 standards must be adhered to, to maintain level of quality • ISO 13485:2016 standards of quality management for the design and manufacture of medical devices must be adhered to • Electrical components must be disposed of in the Waste Electrical and Electronic Equipment Direction (WEEE 2012/19/EU) • Spare parts must be available for product 3 years should the product is replaced with a newer model (ISO 14040:2006)

4.3. Design Ideas

The platform was discretised into two major components: The sample collection device (SCD) and the sample preparation device (SPD). The designs presented in this section of the thesis were not indicative of the final design specifications presented in section 4.2.8; however, these designs serve as crucial building blocks from which the final specifications were constructed.

4.3.1. Initial Design Ideas

Initial Design Idea 1 (Figure 4.1) was designed as a handheld SPD. A collected swab sample would be placed within a disposable SCD containing the lysis buffer, which would then be inserted into the SPD along with a disposable cartridge. A small volume (0.5 – 1 mL) from the lysis buffer would be drawn into the disposable cartridge using a non-contact internal pumping system and a heater would then be used to heat and lyse the cells. Following lysis, the pumping system would then expel the lysate from the cartridge and through the dispenser needle. Valving would be used to prevent backflow into the SCD. Following use, the SCD, the disposable cartridge and the dispenser needle components would be removed and discarded, while the SPD would be stored for future use. Internal sensors will be used to monitor the process and report errors on a screen.

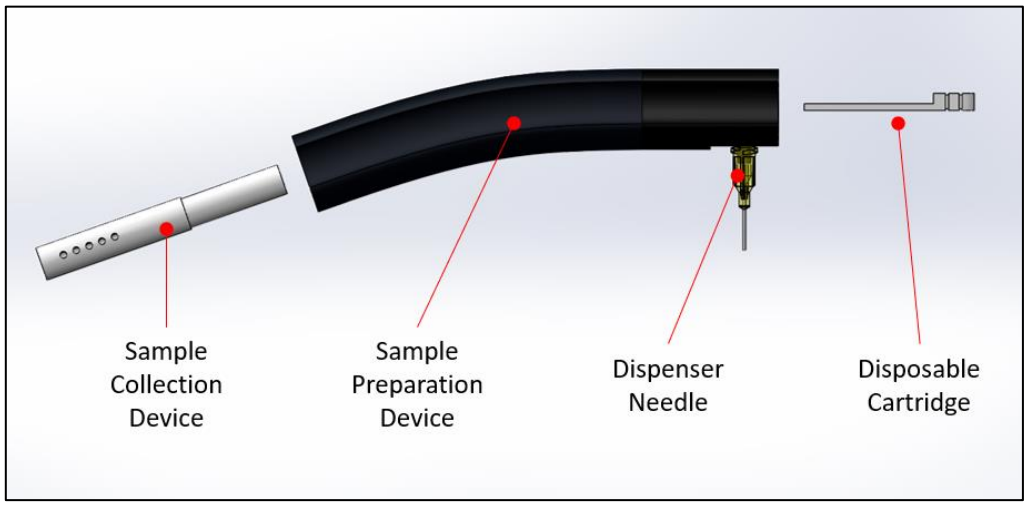

Figure 4.1 – Initial Design Idea 1 (Side View, Annotated)

The first iteration of the SCD (Figure 4.2) was based on a Hygiena™ UltraSnap Surface ATP Test (Camarillo, California, USA) [405]. Following the collection of the sample, the swab would be inserted into the swab container and the VTM holder would be squeezed to release either a UTM or VTM into the swab container, allowing the cells to be suspended within the solution. The lysis buffer container would also be squeezed to release the chemical lysis buffer. Both valves would restrict backflow from the swab container into the respective holders. A schematic demonstrating the function of the SCD can be seen in Figure 4.3. Finally, the VTM holder would be removed and the SCD would be inserted into the SPD (see Figure 4.4).

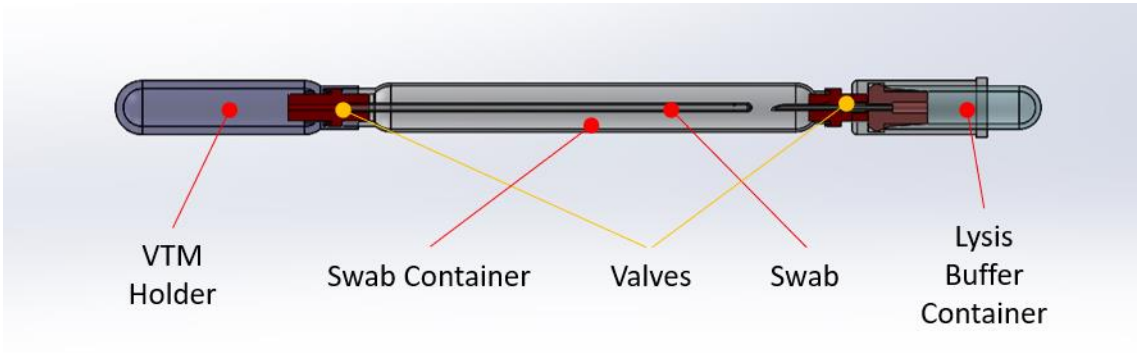

Figure 4.2 – Initial Design Idea, Sample Collection Device 1 (Side View, Annotated)

This SCD was designed for simplicity, allowing for use with little training. Each SCD would contain a specific volume of UTM and lysis buffer to suspend and lyse each sample. This would ensure that should sample pooling be necessary, then the rheological properties of the sample would remain consistent, ensuring that downstream detection methods were not affected. Furthermore, should the use of VTM be omitted as discussed in section 2.1.2.2, the sample may be directly suspended into the lysis buffer. In this case, the function of the VTM holder may be repurposed as a lysis buffer holder and the lysis buffer container may be repurposed as a SCD – SPD interface. This would reduce the number of components and steps involved in the process.

A major concern with this design was the openings on either end of the swab container, which increased the risk of contamination should the device leak. Furthermore, the swabs proposed with this design required the fabrication of customised shafts to introduce the reagent into the sample, making it incompatible with off-the-shelf swabs.

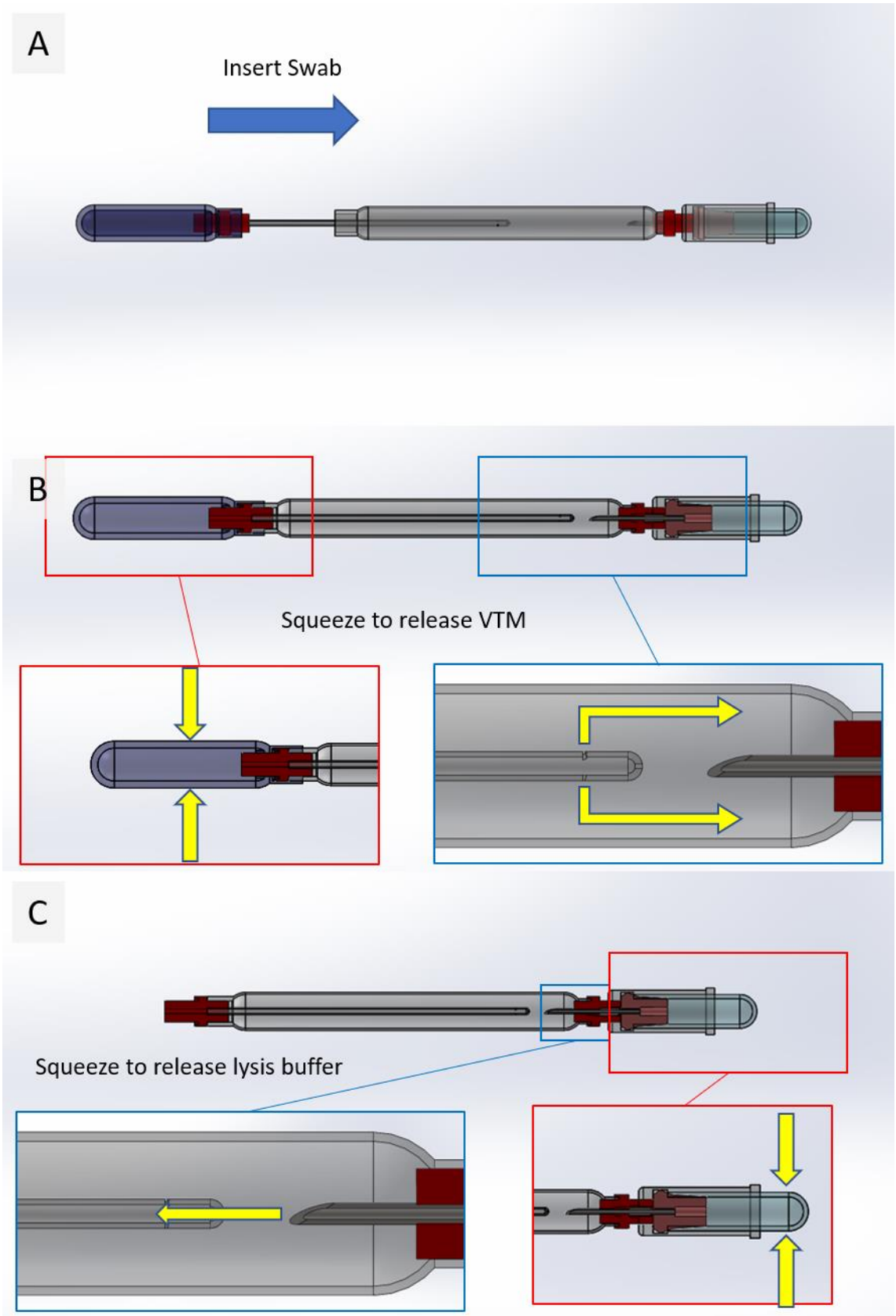

Figure 4.3 – Function of Sample Collection Device 1

A. *Insertion of swabs into the sample collection device* ***B.*** *Release of the VTM into the sample collection device*
C. *Release of the lysis buffer into the sample collection device*

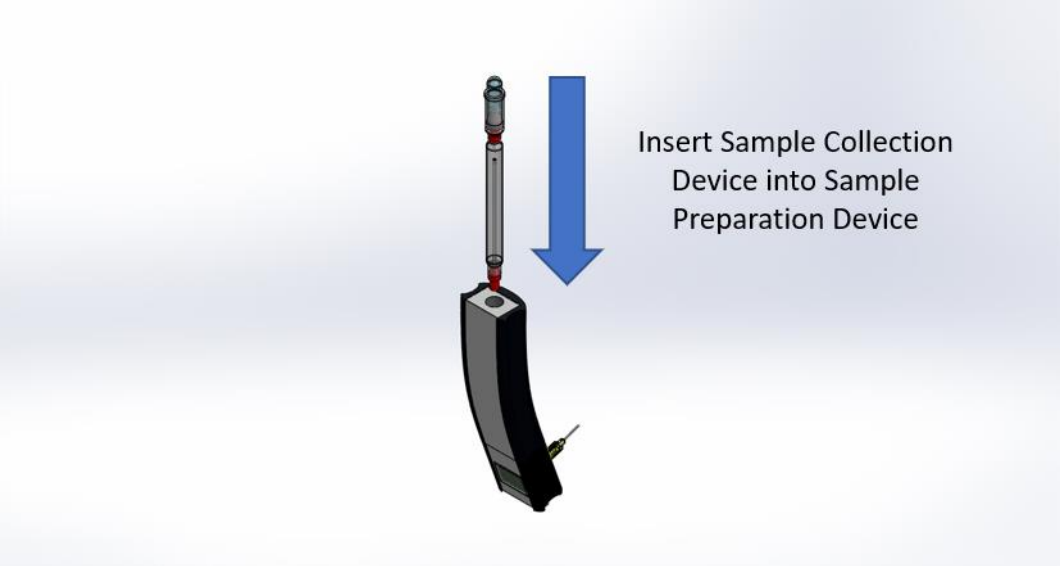

Figure 4.4 – Insertion of the Sample Collection Device 1 into the Sample Preparation Device

The second iteration of the SCD (Figure 4.5) was designed to integrate pumping directly into the SCD, which would reduce the complexity of the SPD. This iteration would use a graduated pumping configuration, (Figure 4.6) employing a series of fluidic diodes and a membrane pump to guide the fluid from the swab container, through a metering well and into the SPD through the interface. The pumping concept was based on a design reported by Xu, Begley and Landers [406]. The graduated pumping system was designed to produce repeatable pumping with simple finger activation, reducing power consumption. The pump could also be automated using an actuator, increasing the repeatability of the process.

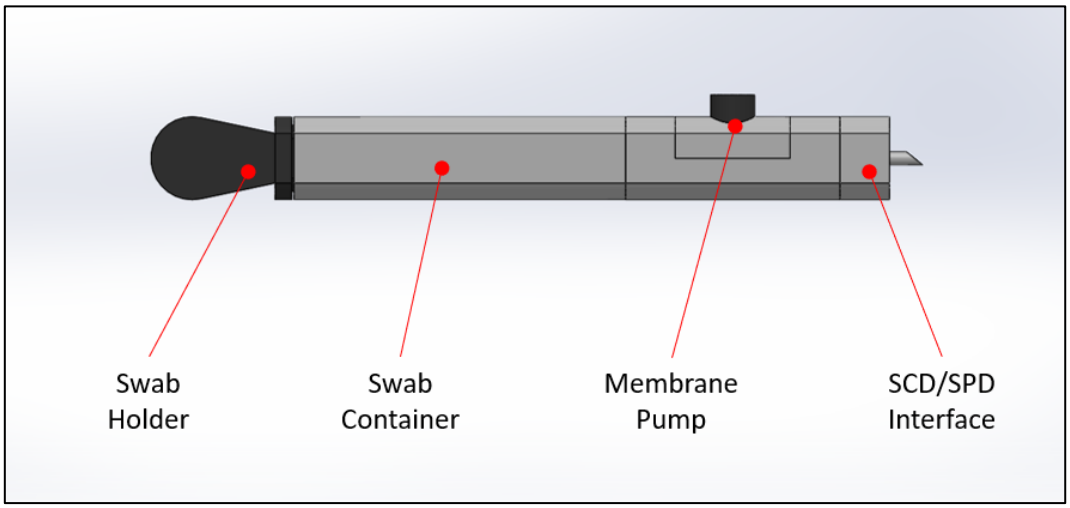

Figure 4.5 – Initial Design Idea, Sample Collection Device 2 (Side View, Annotated)

For this design iteration, a collected swab sample would perforate a foil seal within the SCD, allowing the swab to interact with the lysis buffer. The swab holder would seal the SCD following the insertion of the sample and the SCD would be inserted into the SPD in a similar approach shown in Figure 4.4. When the pump is pressed, the air is expelled through the outlet, creating a negative pressure within the SCD. When the pump is released, the sample is drawn in through the inlet at the desired volume, with the excess fluid being stored within the pump. When the pump is pressed again, the fluid would be expelled from the well and through the outlet. Fluidic diodes would be included to restrict backflow to ensure that fluid will flow as desired throughout the device.

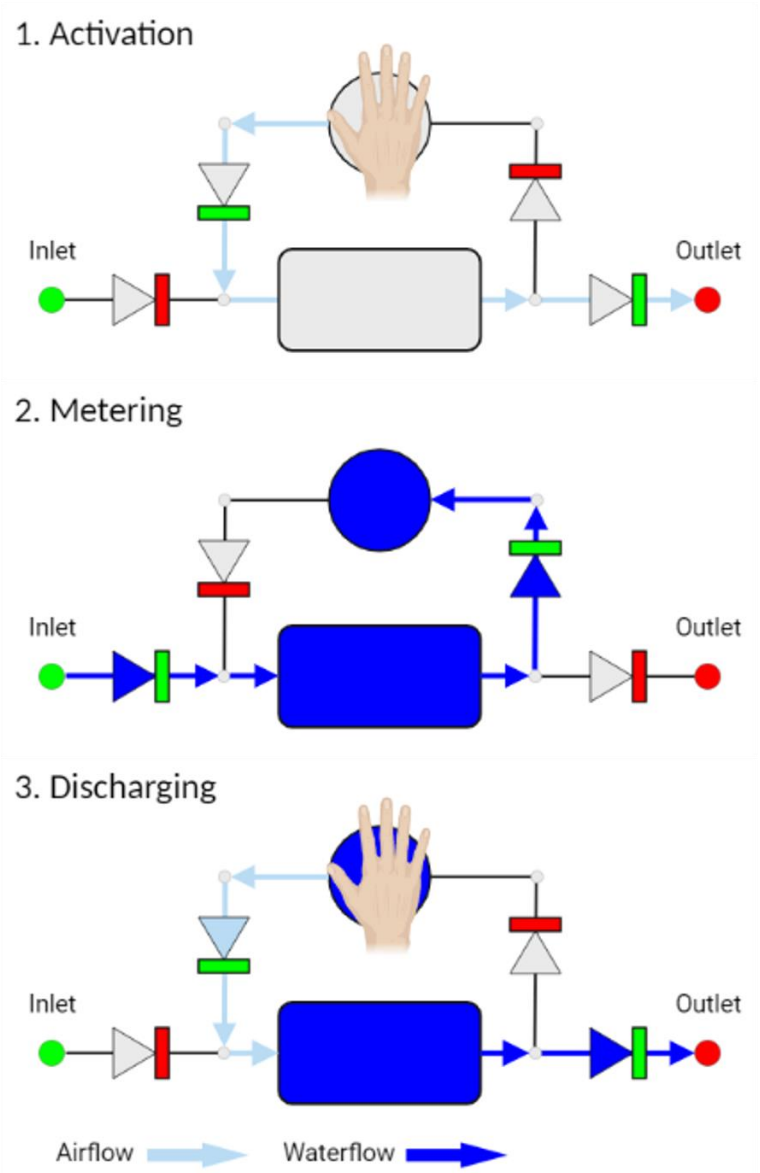

Figure 4.6 – Function of Membrane Pump within Sample Collection Device 2 [406]
Instances of permitted and restricted flow have been highlighted green and red, respectively.

4.3.2. Design Idea 1

The SCD (Figure 4.7 and Figure 4.8) was developed based on works by Krawzak *et al*. [407]. The SCD consisted of a reservoir and dispenser chamber, connected by a one-way check valve. Following the insertion of the swab into the reservoir chamber, a moving piston would be inserted and the chamber would be sealed using a cap. A lysis buffer would be introduced to the sample through the plug to fill the reservoir and the moving piston would displace upwards during the filling process.

The spring-loaded plunger would then be pressed, expelling air from the dispenser chamber. As the plunger returned to its original position, the negative pressure would cause the ball check valve between the nozzle and dispenser chamber to seal. This would force the one-way valve between the reservoir and dispenser chambers to open, drawing liquid into the dispenser chamber. A subsequent press of the plunger would expel liquid contained in the dispenser chamber through the ball check valve, where it would be dispensed through the needle. The ball check valve would contain grooves to ensure the sample could flow around the ball and to the nozzle. Fluid flow from the dispenser chamber back into the reservoir would be prevented due to the one-way valve between the chambers. As the volume within the reservoir chamber decreased, the moving piston would move in contact with the liquid, meaning little air would be present within the reservoir chamber during priming or use.

The SCD would be mounted in a vertical orientation to reduce the risk of leaks during operation. This device was also designed to ensure that no metallic parts came into contact with the liquid during operation. The spring which operated the plunger was mounted outside of the plunger system and both the ball and one-way valves would be fabricated from polymer materials.

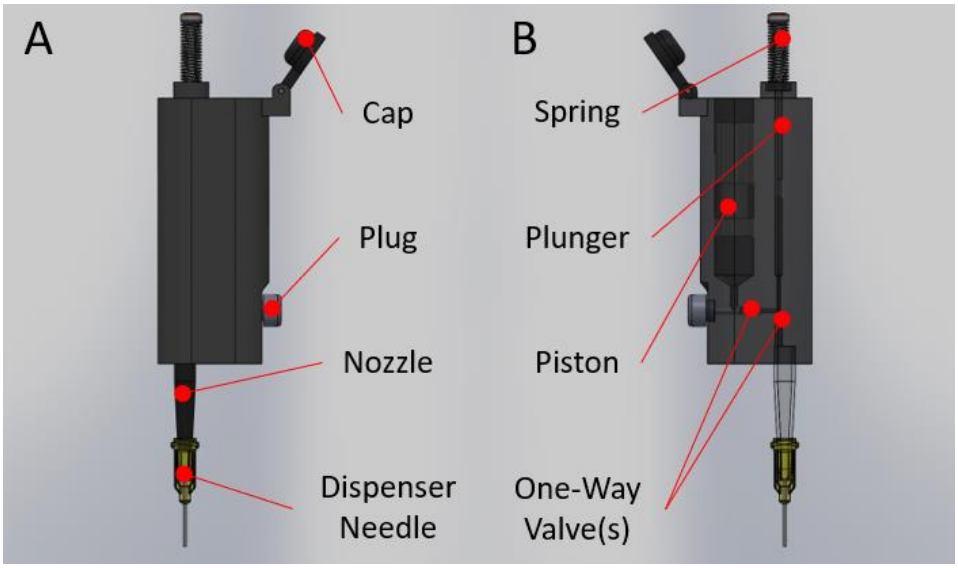

Figure 4.7 – Design Idea 1, Sample Collection Device 1 (Side View, Annotated)
A. *Side View of Sample Collection Device 1* ***B.*** *Transparent Side View of Sample Collection Device 1*

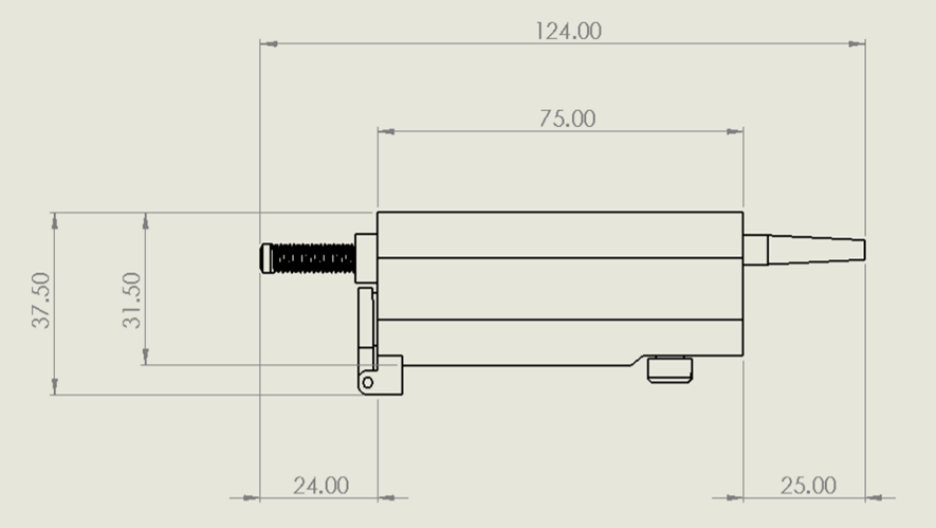

Figure 4.8 – Design Idea 1, First Iteration 1 (Side View, Dimensions)

This SCD underwent several design iterations. The first iteration (Figure 4.8) had a main body length of 75 mm, which was too small to be comfortably operable in a human hand. Thus, the second design iteration (Figure 4.9) adjusted the dimensions of the SCD to resemble those of a handheld pipette. The main body length was increased to 175 mm and the profile of the device was changed to give the device an oval shape. In addition, the spring-loaded system was changed to a sliding switch-based system, to prevent the SCD from automatically re-priming and making the overall dispensing process more controllable. A transparent pipette tip was also included in place of the opaque dispensing needle to allow for the function of the device to be observed visually.

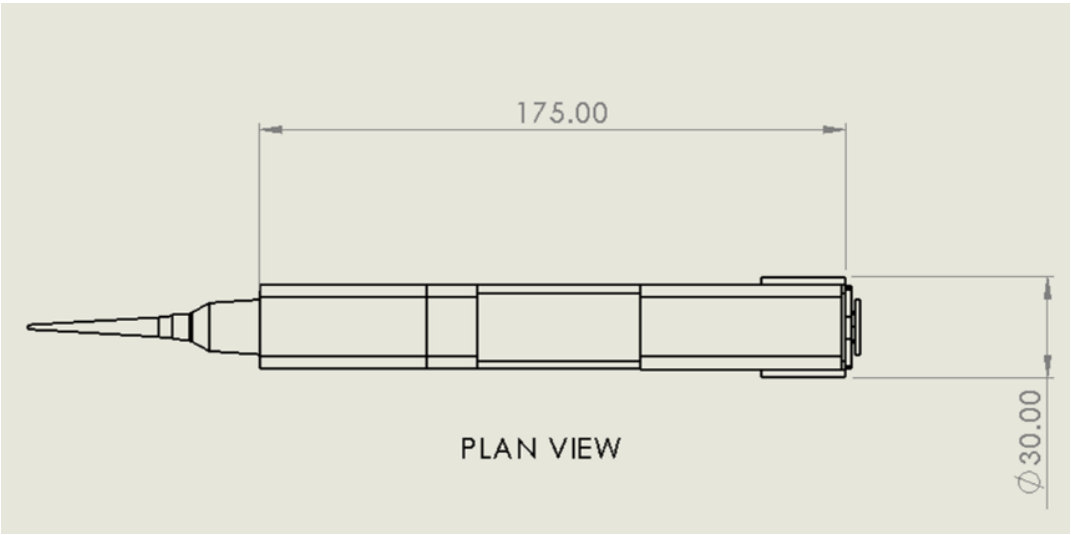

Figure 4.9 – Design Idea 1, Second Iteration (Plan View, Dimensions)

The third design iteration (Figure 4.10) removed many of the flat edges which were present in the second design iteration. Furthermore, due to the larger dead volume within the pipette tip, the design returned to the use of a dispenser needle. The major change between the second and third design iterations was the reduction in the size of the plunger actuator head and the redesign of the spring-loaded system which would function in a similar means to a retractable pen. This allowed for the advantage of automatic priming offered by the spring-loaded system shown in Figure 4.7, as well as the controllability of the sliding switch-based system shown in Figure 4.8.

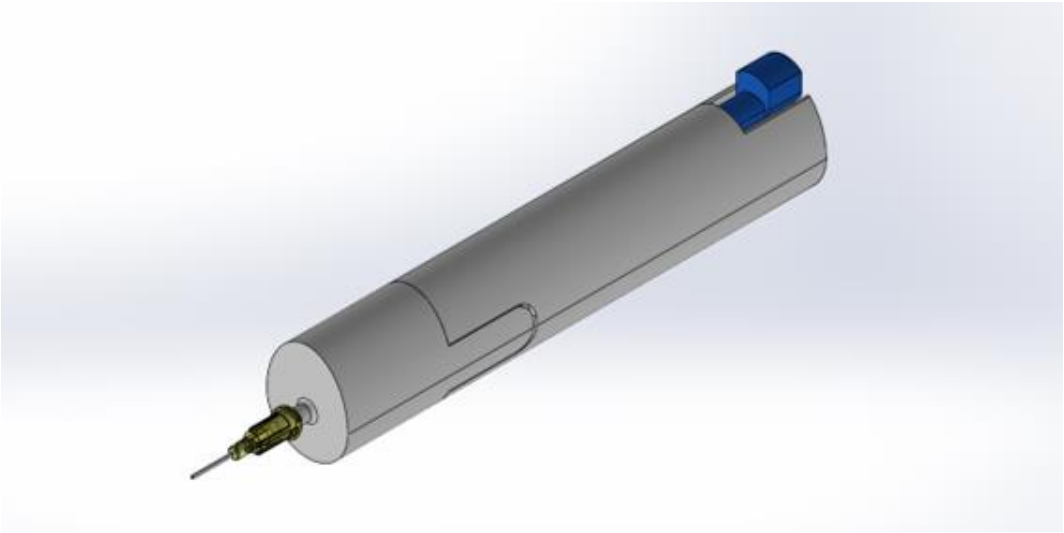

Figure 4.10 – Design Idea 1, Third Iteration (Isometric View)

The fourth design iteration (Figure 4.11) underwent further iterations, based on the open source micropipette developed by Baden *et al.* [408]. This iteration allowed for each of the components to be fabricated using low-cost FDM 3D printing techniques, reducing costs during prototyping. In contrast to the preceding designs, the plunger shaft would utilise a biro pen filling and spring to actuate the fluid through the device. A laboratory glove would be used to create an airtight seal between the T-junction and the main body, allowing the deforming glove material to act as an elastic membrane pump. This would remove the need to utilise soft lithography fabrication techniques to develop PDMS membrane pumps. This design also included 3D printable components to house commercially available valves. This redesign was necessary due to the difficulty in installing the valves into the previous designs without increasing the risk of leaks.

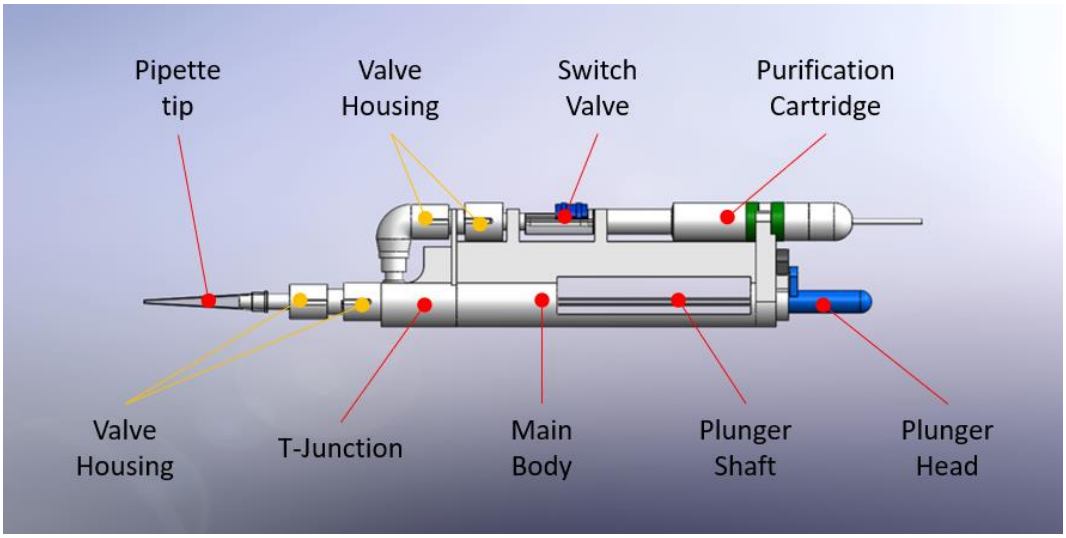

Figure 4.11 – Design Idea 1, Fourth Iteration (Side View, Annotated)

The final design iteration (Figure 4.12) created a suitable casing for the small components. This redesign also included Luer connectors between the switch valve and the valve housing, as well as between the T-junction and the main body. This allowed for the purification cartridge and the dispenser chamber designs to be prototyped using commercially available syringes. In addition, the valve housing and T-junction components (Figure 4.11) were combined into a single component, both reducing the material and time required for fabrication.

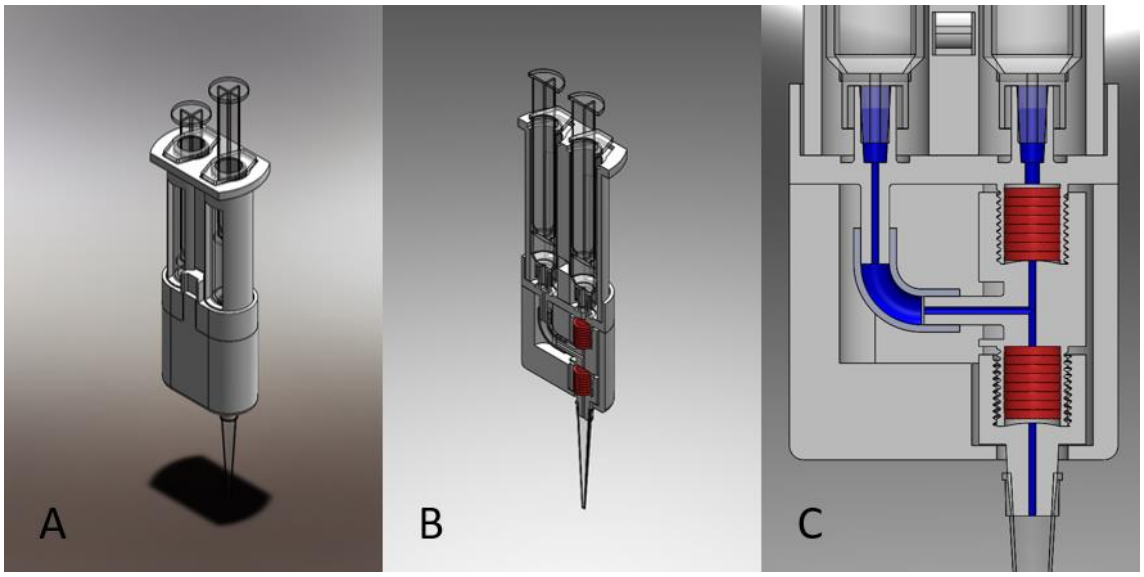

Figure 4.12 – Design Idea 1, Final
***A.** Isometric View **B.** Section View (Isometric) **C.** Section View (Side)*
The fluid pathway has been highlighted blue, and the one-way valves has been highlighted in red.

4.3.3. Design Idea 2

Due to the uncertainties involved in fluid handling for the designs shown in section 4.3.2, the SPD was designed utilising a SPME configuration in place of a through-flow configuration. The ensuing section will discuss the design iterations of the SCD component of this design idea. The SCD would act as a cartridge substitute to be inserted into and controlled by a larger SPD. Due to time constraints, the corresponding SPD was not designed.

Swab samples would be loaded into an opening within the SPD where a lysis buffer was contained; however, instead of the sample being actuated through a purification cartridge, a sorbent coated swab would be used to adsorb NAs directly from the lysate. While isolated on the coated swab, the NAs would be purified by subsequent washing steps, prior to elution within individual capsules. The purified NAs would then be transferred from the final capsule into the PCR tubes when required.

By using a sorbent coated swab, uncertainties with fluid handling could be avoided, as fluid handling would be restricted to the interaction between the coated swab and the specific reagent. This meant that a complex purification cartridge with integrated valving could be omitted, reducing the engineering complexity. Furthermore, the process could be easily tailored to match a large array of sample types by tailoring the arrangement of the capsules, without the need to redesign a purification cartridge compatible with individual sample types. Finally, the number of disposable parts would be greatly reduced, as only the individual capsules would require disposal following use.

This design consisted of a sorbent coated swab holder (Figure 4.13) and a reagent capsule holder (Figure 4.14). The swab holder (Figure 4.13) would be spring loaded for manual configurations, or controlled by an actuator mounted within the SPD for automated configurations. Similar to work by Park *et al.* [8], a nylon swab was used as a template. However, with this approach, the nylon swab would be dip coated in chitosan, which would act as the sorbent material and adsorb NAs in acidic conditions (≈pH 5) and desorb DNA in alkaline conditions (≈pH 9), as reported in works by Cao *et al.* [409]. This approach was deemed to be compatible with the downstream process, LAMP, which would utilise a pH change to confirm the presence of the pathogen of interest and typically requires the lysate to be slightly alkaline to function correctly. Furthermore, due to the dip coating process being simple, low-cost and reproducible, the fabrication of the polymer coated swabs could be achieved in low-resource settings.

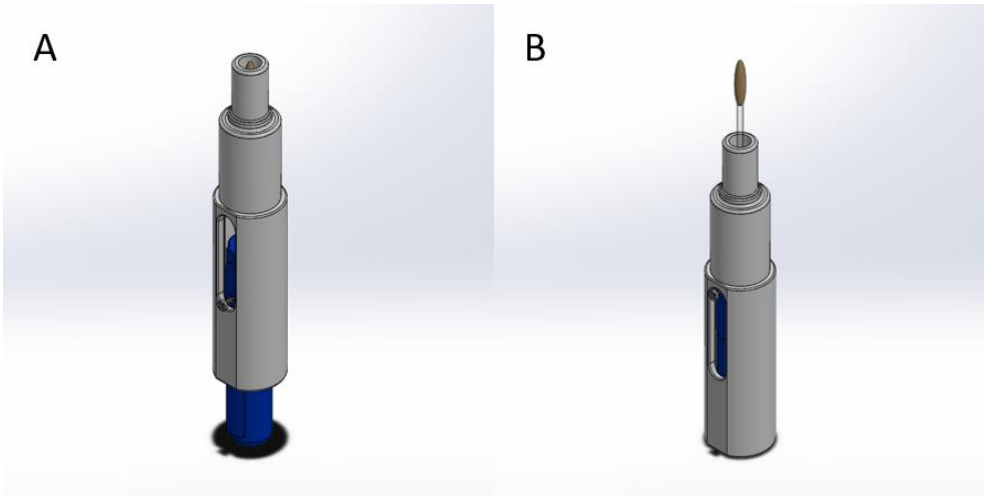

Figure 4.13 – Design Idea 2, Sorbent Coated Swab Holder (Isometric View)
***A.** Swab Covered **B.** Swab Exposed*

The reagent capsule holder (Figure 4.14) contained capsules which would conduct individual sample preparation steps. The sorbent coated swab would be introduced to each capsule in series until the NA is eluted into the final capsule. Following use, each of the capsules would be removed and discarded, while the holder would remain uncontaminated. Two configurations of the reagent capsule holder were designed. The cylindrical configuration (Figure 4.14a) reduced the footprint of the device, while the linear configuration (Figure 4.14b) allowed for the simpler alignment of the coated swab with the reagent capsules, reducing engineering complexity.

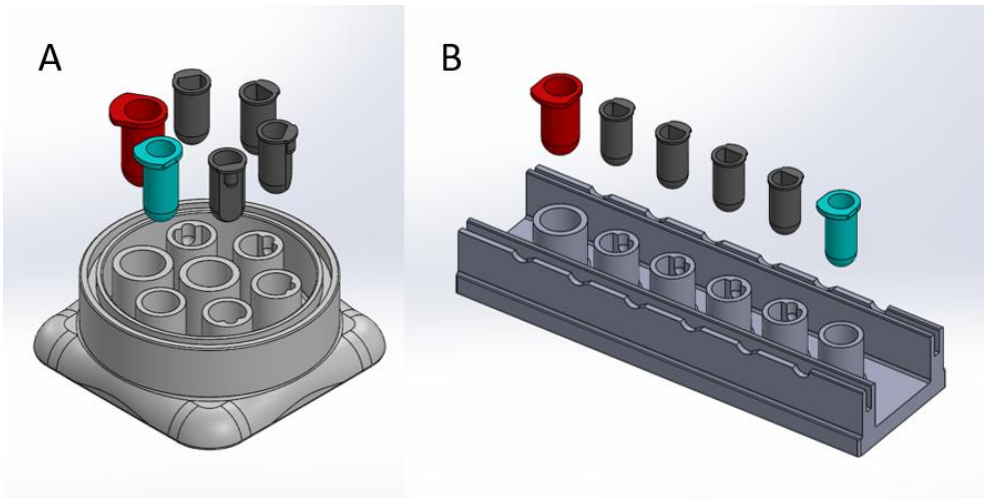

Figure 4.14 – Design Idea 2, Reagent Capsule Holder (Isometric View)
***A.** Cylindrical Configuration **B.** Linear Configuration*

The two components would function in unison as depicted in Figure 4.15. The swab holder would be stationary, while the reagent capsule holder would move relative to the swab holder to align the swab

with the reagent capsule, controlled by the SPD. For the cylindrical configuration, a barrel contained within the reagent capsule holder would rotate to align the swab with the correct tube, while the entire reagent capsule holder would move the capsules linearly for the linear configuration. Following use, the SCD would be removed from the SPD and the contaminated components would be discarded.

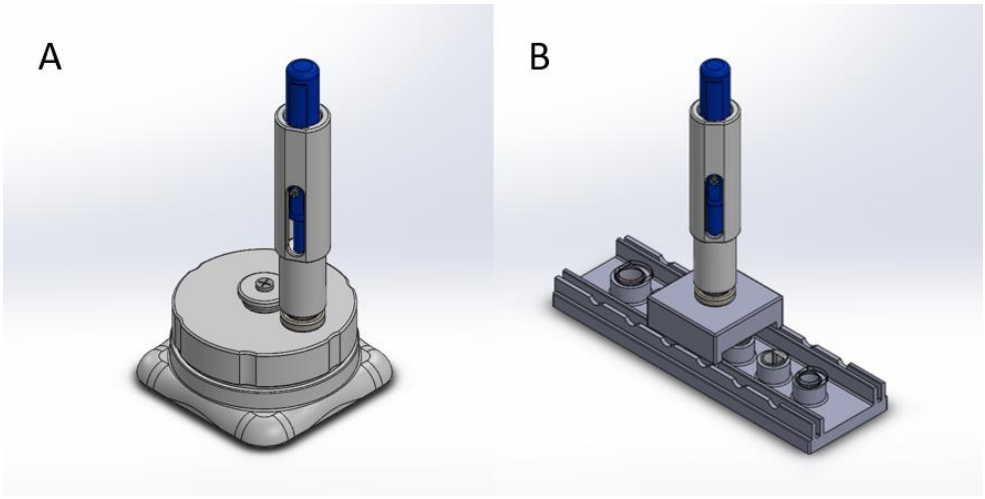

Figure 4.15 – Design Idea 2, First Design Iteration (Isometric View)
***A.** Cylindrical Configuration* ***B.** Linear Configuration*

Due to the larger footprint of the linear configuration, the cylindrical design was retained for the subsequent design iterations (see Figure 4.16). The operation of this design remained consistent with the iteration; however, the rotating barrel design was improved to incorporate resistive heating elements, allowing heating to be conducted within the device, if necessary. The heating elements developed for this design idea will be discussed in further detail in Chapters 5 and 6.

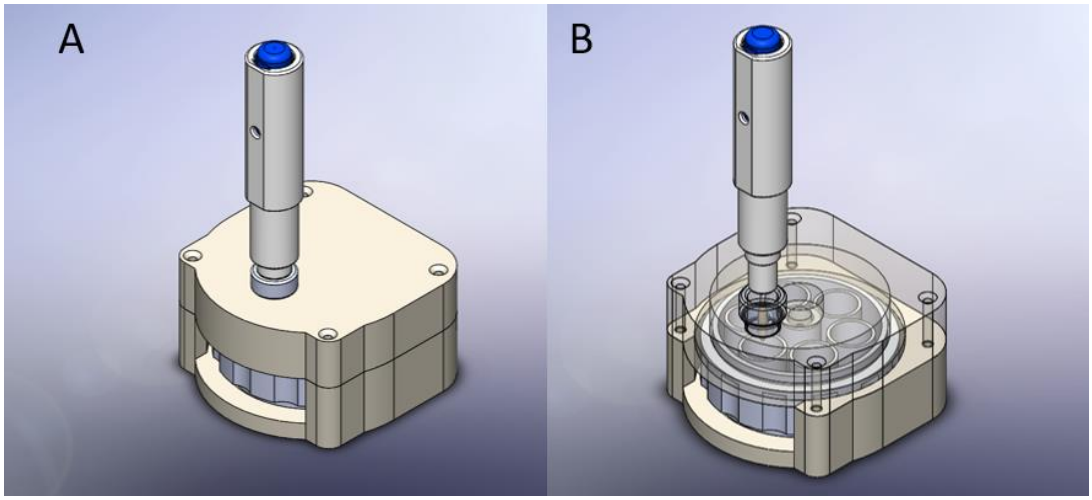

Figure 4.16 – Design Idea 2, Final Design Iteration
***A.** Isometric View* ***B.** Isometric View (transparent lid)*

4.3.4. Design Idea 3

During the progression of the project, research into Tesla valves (demonstrated in section 5.2.4) led to the design idea proposed in this section. This design marked the shift in focus from the preparation of cloacal samples for the detection of poultry related infections to respiratory samples for the detection of SARS-CoV-2. As a result, the less labour-intensive sample preparation steps allowed for the simplification of the device designs. Due to time constraints, only the SCD was designed.

The SCD consisted of a swab receiver (Figure 4.17) and a main body (Figure 4.18a), which fit together as shown in Figure 4.18b. The swab receiver was separated in 3 sections by foil seals. Following the insertion of the swab into the swab receiver, the swab would perforate the first foil seal, introducing the sample to the VTM. The perforation of the second and third foil seals allowed the sample to react with the lysis buffer. The final foil seal would then create room for the sample and lysis buffer to be mixed. The sample would then be heated by the SPD. Following lysis, the lysate would be drawn from the swab receiver into a 1 mL BD Plastipak Luer Slip Syringes (BD, New Jersey, USA) which would act as a metering chamber. The Tesla valve geometry would restrict airflow from the outlet into the metering chamber. When expelled from the metering chamber, the lysate would travel through the Tesla valves to the outlet, while backflow into the swab receiver would be restricted. By using Tesla valves, the single directional flow was achievable without the need for valves requiring moving parts. Furthermore, by using a syringe to actuate fluid through the device, the external mechanism within the corresponding SPD could be designed with simple internal components to facilitate actuation.

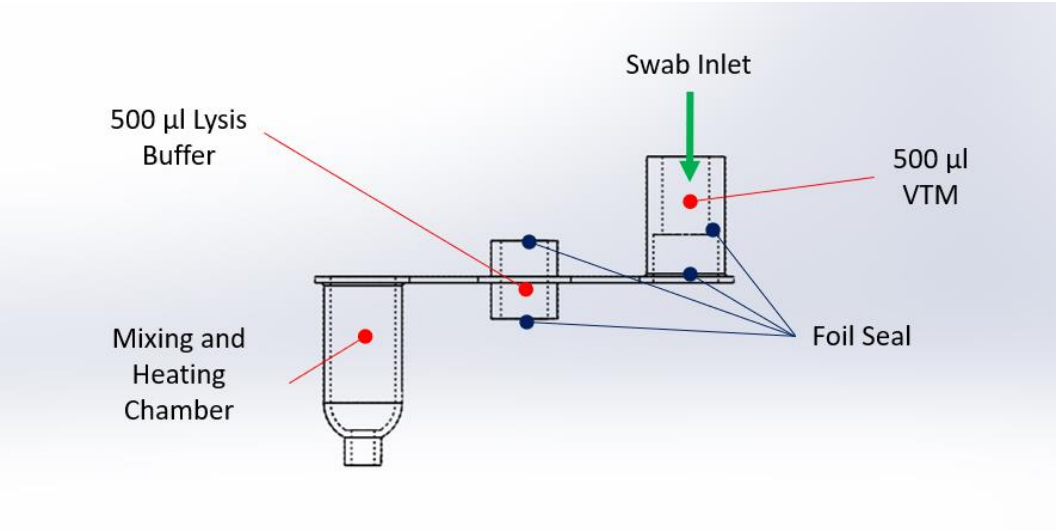

Figure 4.17 – Design Idea 3, Swab Receiver
The three sections of the swab receiver were designed to insert into each other, resulting in a system in which swab could interact with each reagent in series by pushing the swab through the foil seal.

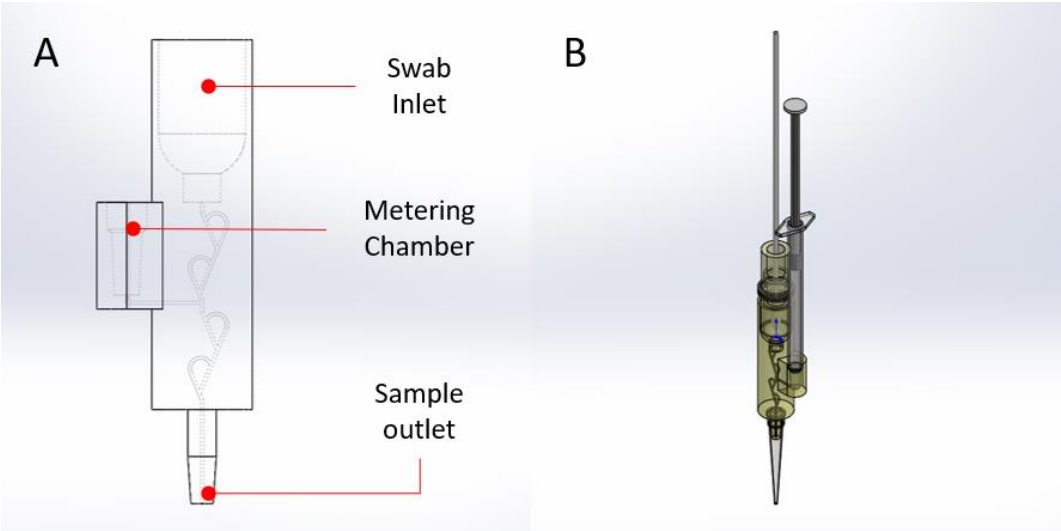

Figure 4.18 – Design Idea 3, First Design Iteration
***A.** Fully Assembled Device (Isometric View)* ***B.** Side View of the Main Body (Internal Lines Visible, Annotated)*

The design underwent subsequent design iterations, resulting in the SCD shown in Figure 4.19. The length of the main body was extended to fully encase the swab receiver, while the internal Tesla valve design was retained for fluid control through the SCD. While a second iteration was created to process a single sample (Figure 4.19a), a third iteration (Figure 4.19b) was created to allow for up to 8 samples to be processed in parallel.

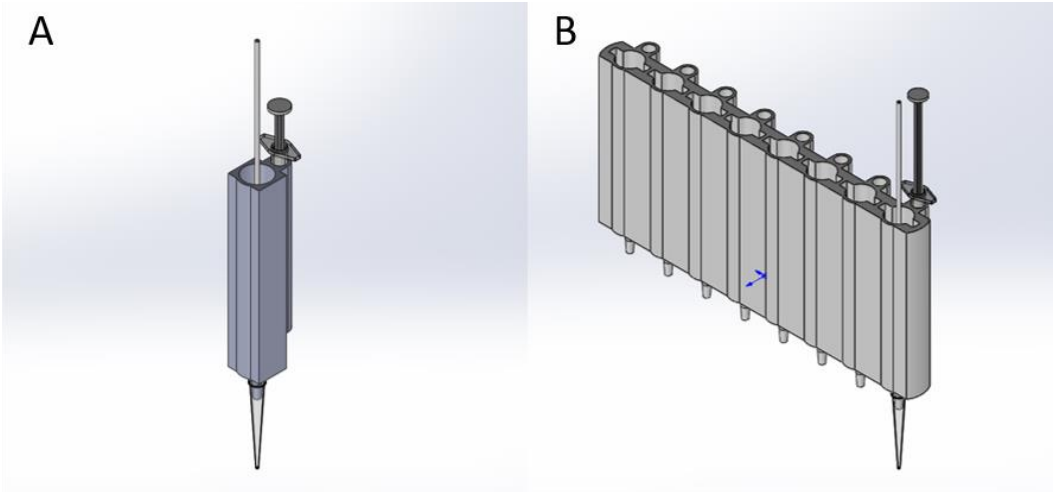

Figure 4.19 – Design Idea 3, Second Iteration (Isometric View)
***A.** Single Device* ***B.** 8-way manifold*

A final design iteration was created, shown in Figure 4.20. The 8-way manifold design was retained from the second design iteration (Figure 4.19); however, the central distance between the SCDs was

reduced to 9 mm (Figure 4.20a). The resulting manifold can be seen in (Figure 4.20b). Following the redesign, each individual SCD was in alignment with each PCR tube, as shown in Figure 4.20c.

As shown in Figure 4.20a, the 1 mL BD Plastipak Luer Slip Syringe had a radius of 5.1 mm, meaning each syringe would obstruct the adjacent syringe and affect the function of the device. Therefore, despite the potential for the 8-way manifold, it was questionable whether this design would be a viable option. During a computational analysis shown in Chapter 5, it was determined that Tesla valves would be an unfeasible option due to being ineffective at the predicted flow rates. Thus, this design idea was discarded for future consideration.

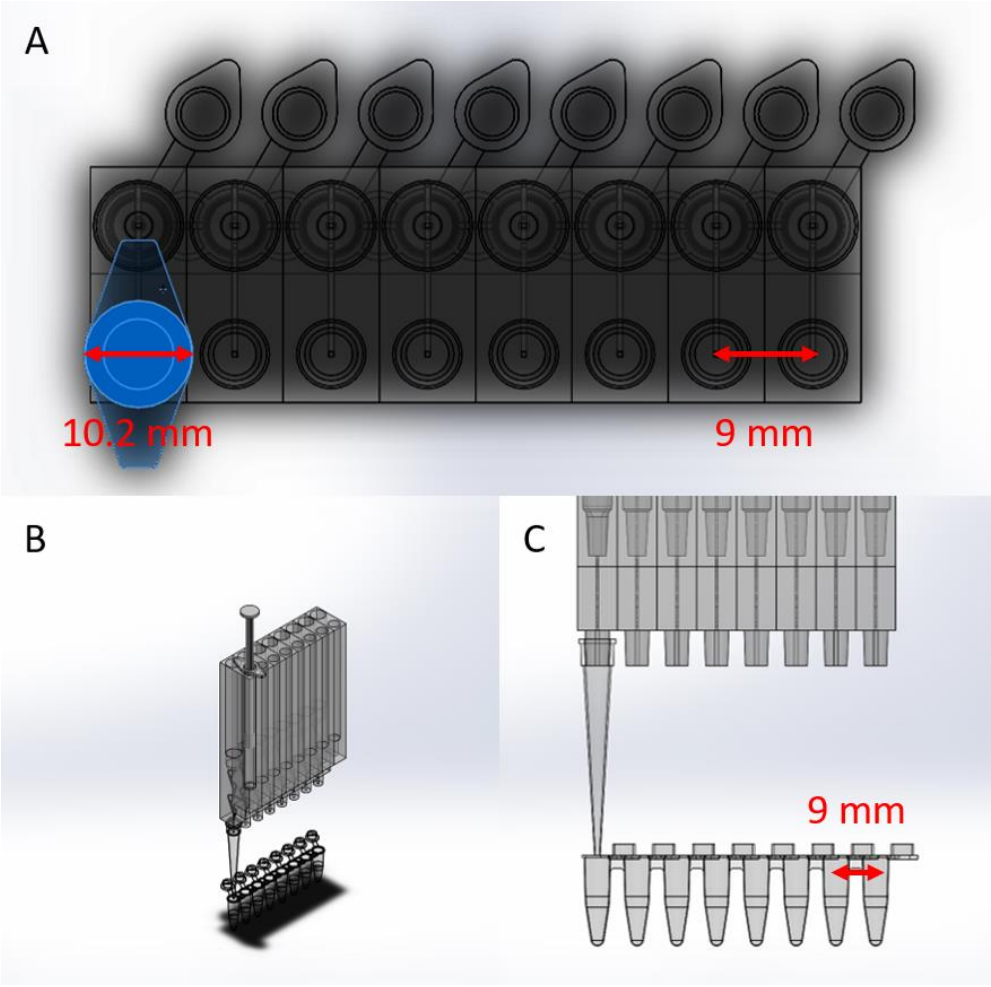

Figure 4.20 – Design Idea 3, Final Design Iteration
***A.** Top View – The diameter of the 1 ml BD syringe (highlighted blue) exceeds the distance between the individual SCDs, and thus, would interfere with each other during use. **B.** Isometric View – Depiction of the relationship between the SCDs and the PCR tubes. **C.** Front View – The distance between the PCR tubes and the alignment between each tube with the corresponding SCD can be seen.*

4.3.5. Design Idea 4

This design idea (Figure 4.21) was developed from Design Idea 3, replacing the unviable Tesla valve system with membrane valves. The design features a swab inlet, two membrane valves, a 1 mL heating chamber and an inflow and outflow pump port, as shown in Figure 4.21b. Each membrane valve would be controlled by air-filled chambers adjacent to each valve, which would deform following an increase in pressure within the chamber, restricting fluid flow through the valve. These control channels can be seen in Figure 4.21c. Each port was designed to interface with 1.5 mm ID barbed connectors, allowing each section of the SCD to connect to syringe pumps; which would be used to control both the fluid flow and the membrane valves.

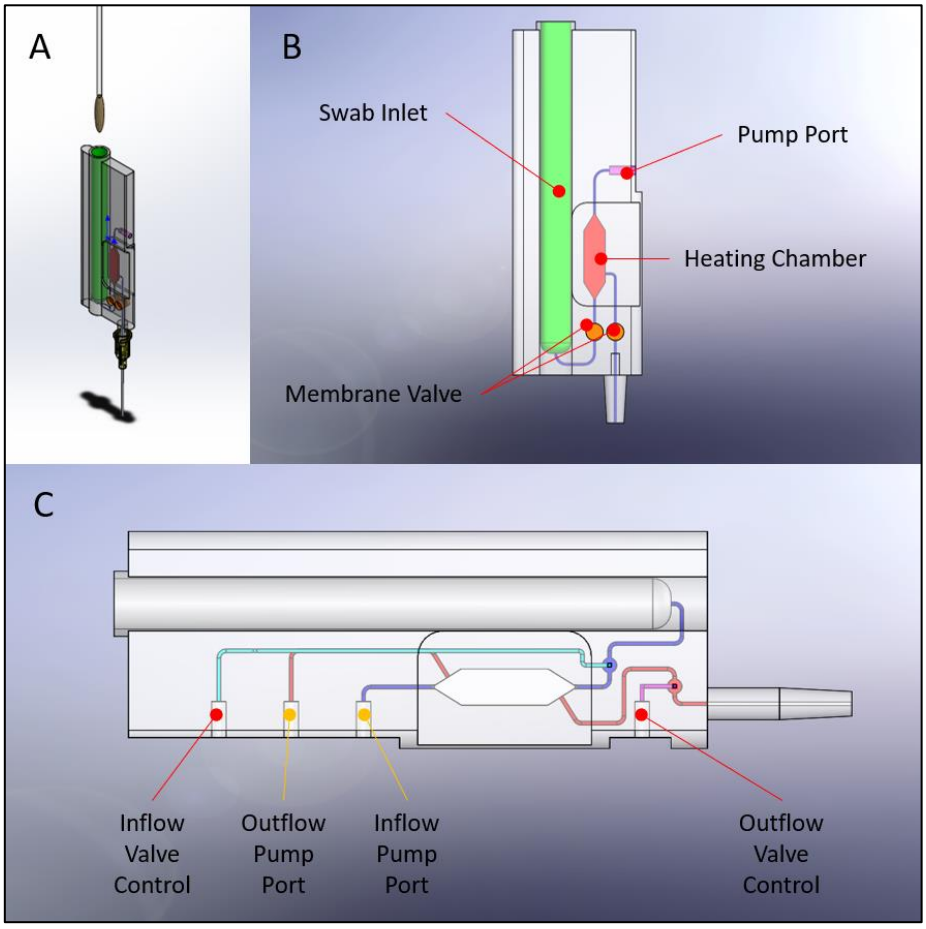

Figure 4.21 – Design Idea 4, Sample Collection Device 1

***A.** Isometric View **B.** The internal channels for the valve controls have been removed, allowing for the visualisation of the fluidic channels (dark blue) used to connect the swab inlet (green), the heating chamber (red), the membrane valves (orange) and the pump port (magenta) **C.** The internal channels for the valve controls have been included to depict their location in relation to the membrane valves. The control channel for the inflow valve is coloured light blue, while the channel for the outflow valve port is coloured magenta. The inflow and outflow channels are blue and red, respectively.*

The swab would be loaded into the swab inlet, in which a volume of lysis buffer would be contained. Following the insertion of the swab into the swab inlet, the SCD would be sealed and inserted into the SPD (Figure 4.22 and Figure 4.23). The outflow valve control would then be activated, closing the outflow membrane valve. The inflow membrane valve would remain open. A syringe pump would then be used to draw the sample from the swab inlet, through the first membrane valve and into the heating chamber, with the excess sample being drawn into the channel connecting the heating chamber to the inflow pump port. The heater block would then supply heat to the sample, thermally lysing the cells. Following lysis, the inflow membrane valve would close and the outflow membrane valve would open. The syringe pump connected to the outflow pump port would then be used to drive the lysate from the heating chamber, through the second membrane valve and out of the dispenser needle. Following use, the SCD would be disconnected from the SPD and discarded.

For this design, the intended goal was to 3D print the SCDs from the flexible filament thermoplastic polyurethane (TPU). This would allow for the SCDs to be printed in a single step, removing all assembly steps while incorporating valving into a compact design. A trade-off compared with Design Idea 3, however, was the necessity for more fluidic control components, increasing the power requirements and the engineering complexity. A concern for the fluidic control was the formation of air bubbles within the heating chamber. Thus, a computational simulation (Two-Phase Flow Modelling) was used to analyse the performance of the design, which can be found in section 5.2.5. Another concern was the ability to produce functional membrane valves using FDM printing, due to the rigidness of the material compared PDMS alternatives. An analysis of the mechanical performance of various 3D printing materials was performed (Membrane Valve Designs), which can be found in section 5.3.3.

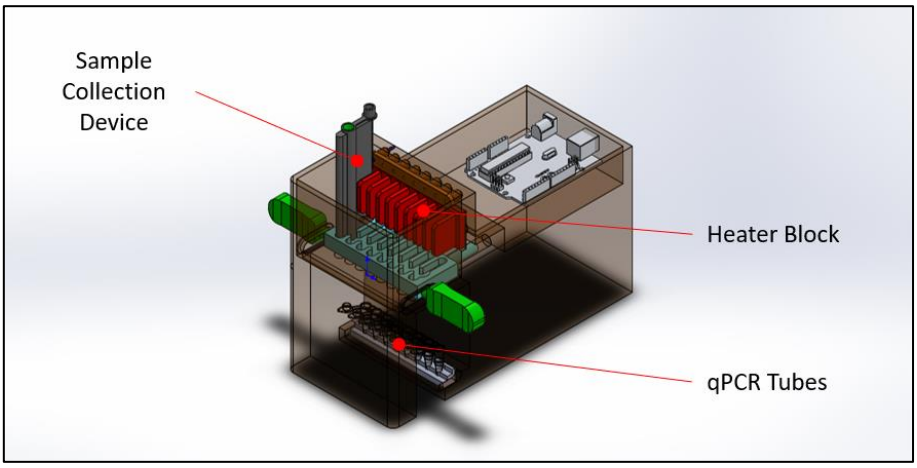

Figure 4.22 – Design Idea 4 (Isometric View)

The SCD shown in Figure 4.21 is inserted into a moving tray (highlighted light blue), allowing it to interface with the fluid control ports. The tray also aligns the sample collection device with the heater block (red).

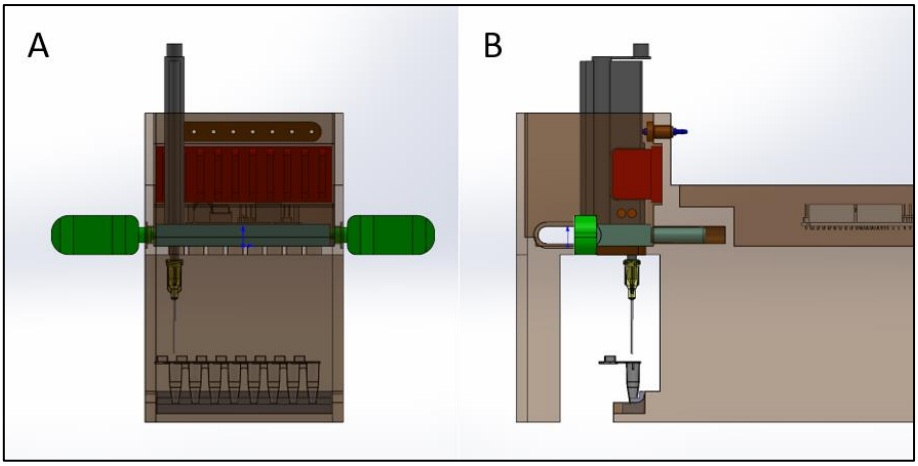

Figure 4.23 – Design Idea 4

***A.** Front View – The SCD (grey) aligns between each of the grooves in the heater block (red). Each SCD would also attach to a dispenser needle, which would guide the lysate into the PCR tubes. **B.** Side View – The alignment of the SCD to the heater block can be visualised. The heater block sits on either side of the heating chamber, creating uniform heating during use.*

4.3.6. Final Design Idea

The design presented in this section served as a functional proof-of-concept for the sample collection and preparation device, as establishing a working concept was of paramount importance. This design was a culmination of the previous design ideas, with Design Idea 4 serving as the main template for this design. The use of external syringe pumps connected into the SPD to control the fluid flow through the SCD was retained from Design Idea 4; however, a single bidirectional syringe pump would be used to both draw and push the sample through the SCD. This syringe pump was altered from an open source model described in Chapter 6 and provided low-cost and accurate fluidic control.

The SCD (Figure 4.24) would accept a swab sample into the swab receiver, which contained the desired volume of a lysis buffer. The use of switch valves was taken from Design Idea 1 (Figure 4.11); however, the modified design (see Figure 4.25a) used silicon tubing to directly contact the sample, while the main body functioned without direct contact. The valve consisted of a main body with a fixed lower pinch ridge, silicon tubing and a lever with an oval shaped moving pinch bar (referred to as the switch valve). The silicon tubing was held in place by barbed connectors at either end, preventing movement during use. While in its open configuration (Figure 4.25b), the upper pitch bar was at a 45° angle with respect to the silicon tubing. The upper and lower pitch bars were not in contact with the silicon tubing would be open. As a result, fluid flow was possible through the tubing. While in its closed configuration (Figure 4.25c), the switch valve was perpendicular to the silicon tubing and the two pinch bars came into contact with each other, pinching the silicon tubing and restricting fluid flow.

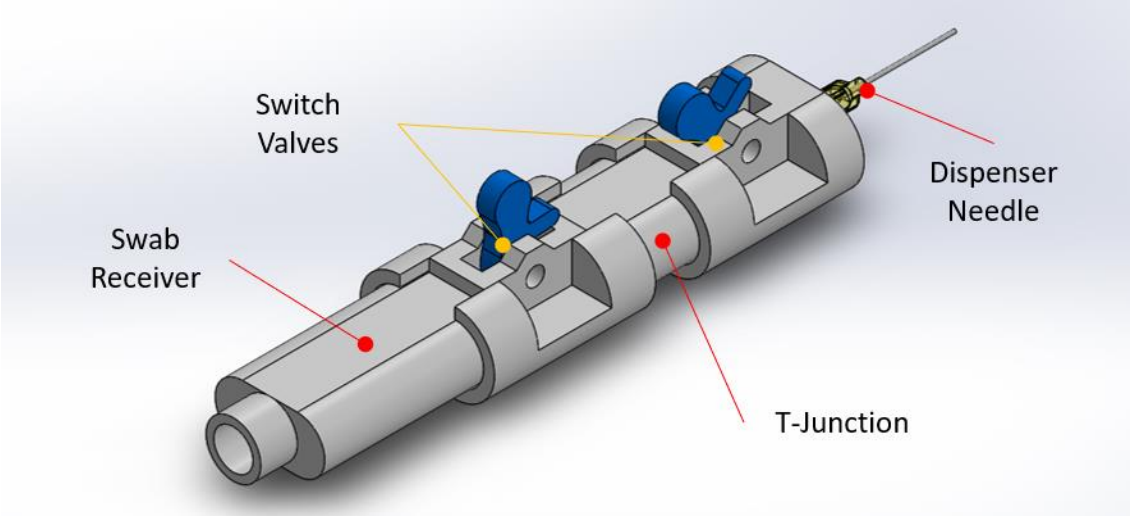

Figure 4.24 – Final Design Idea, Sample Collection Device 1 (Isometric View, Annotated)

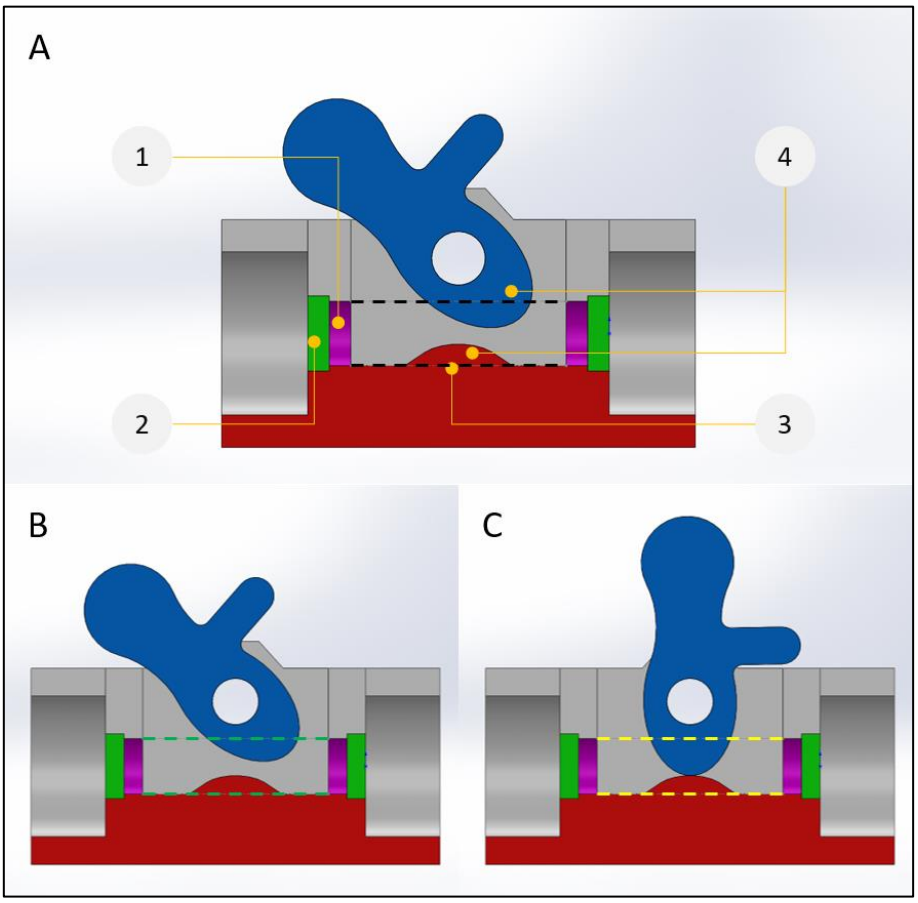

Figure 4.25 – Final Design Idea, Switch Valves (Section View)
***A.** A schematic of the Switch valve. **B.** Open Configuration **C.** Closed Configuration*
1, Silicon Tube Housing (magenta); 2, 1.5 mm inch barbed connector housing (green), 3, Flexible Silicon Tube (black lines, dashed); 4, Upper and Lower Pinch Bars (blue and red, respectively)

The accompanying SPD can be seen in Figure 4.26. As it is advised to heat the entire sample to deactivate the virus, the heating element (Figure 4.27) was moved to either side of the swab receiver to allow for heating to be conducted immediately following the insertion of the SCD into the SPD. This was in contrast to Design Idea 4, where heating was initiated following the metering of a 1 mL volume into a heating chamber. A pair of heater blocks were designed to clamp over either side of the SCD, ensuring a uniform dissipation of heat across the sample during the heating process. These heater blocks would be secured to a pair of moving jaws, which would move along a pair of guide rods, allowing the heater blocks to clamp around the SCD during the heating process and to allow clearance to insert and remove the SCD during its loading and discarding, respectively. A computational simulation demonstrating the performance of this heating design can be seen in section 5.4.4.

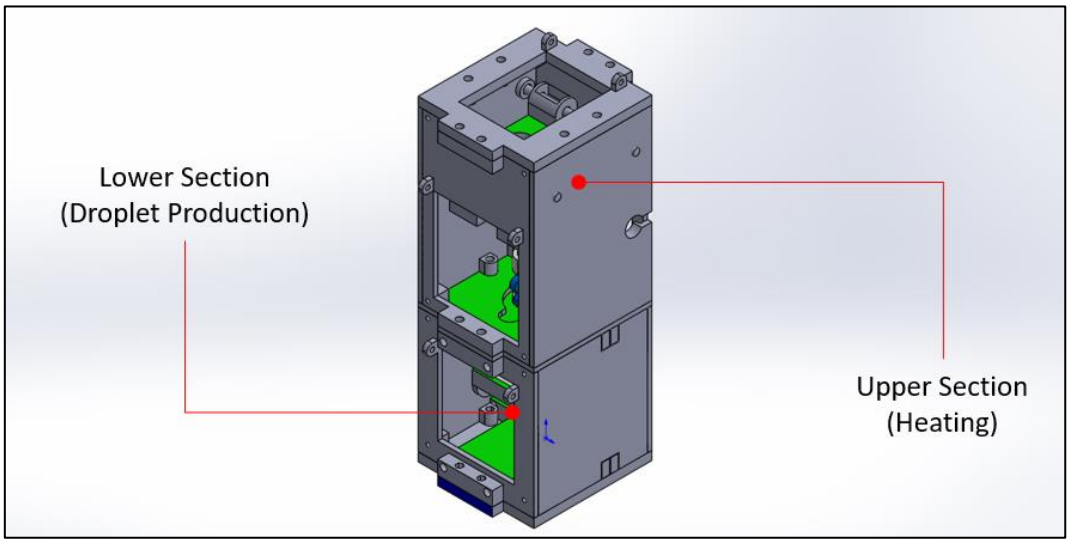

Figure 4.26 – Final Design Idea, Sample Preparation Device

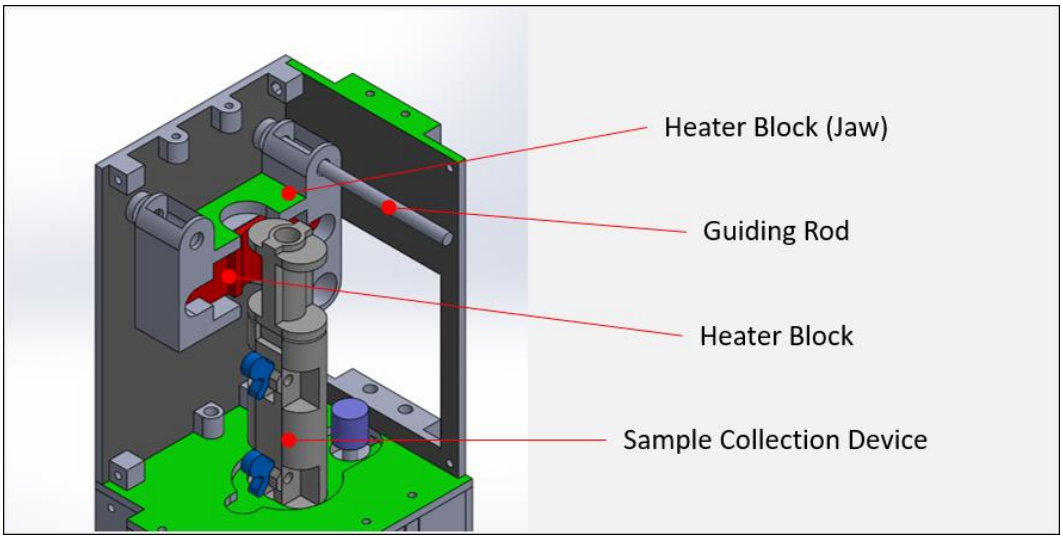

Figure 4.27 – Final Design Idea, Sample Preparation Device (Upper Section)

The syringe pump was then initiated to actuate fluid through the SCD, creating a 1 µL hanging droplet at the dispenser needle tip. A high electric potential would be supplied to the dispenser needle to overcome the surface tension holding the droplet to the tip of the needle. A design of this arrangement can be seen in Figure 4.28. The high voltage electrode was static, while the grounded electrode was able to be moved along the z-axis to adjust the strength of the electrical field. This feature was included to overcome the limitations of standard droplet production through dripping, as shown in section 3.3. A demonstration of this system can be seen in 6.4.1. A computational model using electrostatics was also attempted. This can be seen in section 5.2.6.

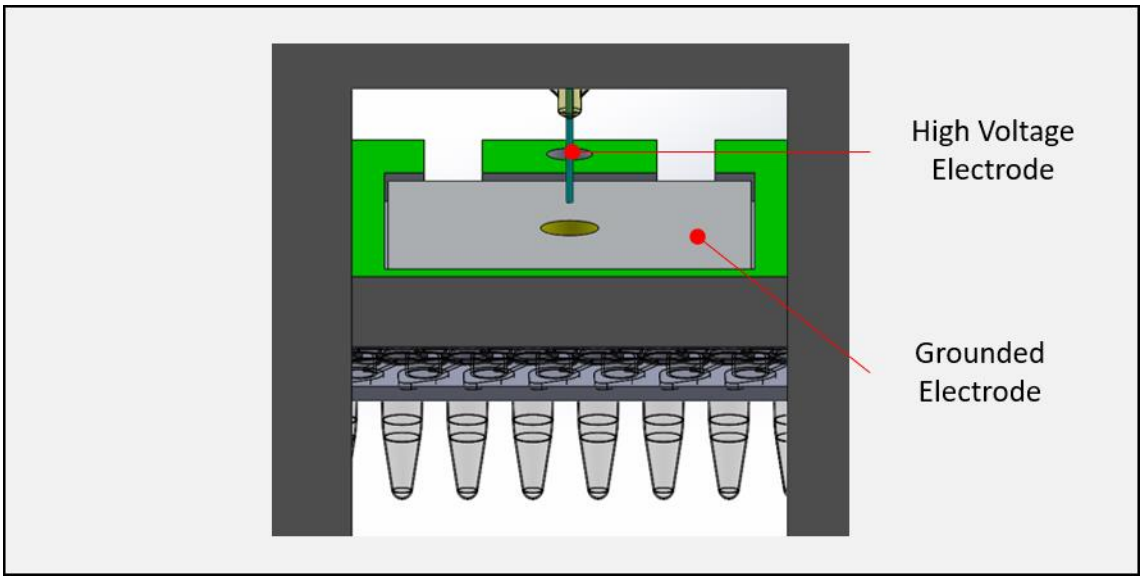

Figure 4.28 – Final Design Idea, Sample Preparation Device (Lower Section)

4.4. Chapter Summary

There were many challenges which were highlighted during the generation of the design ideas. While an open-source syringe pump served as a low-cost method to achieve actuation through the device, the prevention of backflow presented a major challenge within a low complexity SCD. Many commercially available fluidic controls performed on the sub-millilitre scale were expensive, and thus; low-cost alternatives had to be designed. For the final design idea, a simple yet effective switch valve design was utilised within the SCD to prevent backflow; however, the size of the valves significantly increased the overall size. The miniaturisation of the valves would greatly reduce the size of the SCD. Another concern was the dead volume within the SCD devices. During the prototyping of the design ideas, priming and pumping inaccuracies were observed, as well as non-uniform droplet production. This was deemed to be a result of air compressibility and the formation of bubbles within the channels.

The components which would come into contact with the sample and the chemical reagents needed to be fluid and chemical resistant to prevent degradation of either the sample or the components, or cross-reactivity with the reagents [399]. By limiting the sections in contact with the sample, the number of components requiring replacement would also be reduced. Fluid control components were designed to be as non-contact as possible, allowing the contaminated sections to be replaceable following use, while the remainder of the device would remain intact.

A major aim of the designs was to limit the number of components which would come into contact with the sample and reagents during operation. Typically, disposable plastic products are preferred, as alternatives can contain RNases which can degrade the RNA; however, this increases the amount of non-biodegradable waste. Furthermore, the tooling costs rendered many of the manufacturing processes inaccessible due to budget concerns. Many thermoplastic polymers, including PMMA and PC can crack or craze as a result of insufficient heat treatment. Such polymers require normalising and other stress-relieving procedures to be applied during the machining processes, which can greatly increase the engineering complexities. While suitable facilities may be available in developed countries, these concerns increase in significance following a technology transfer to resource-stressed settings.

The designs presented were developed to be compatible with in house FDM printers to reduce costs during the prototyping stage. A substantial amount of optimisation was required when testing new materials, resulting in significant delays in progress. Leaks between layers were observed due to weak interlayer bonding. Recent FDM approaches have attempted to improve the structural integrity of fabricated components. It has been reported that the interlayer bonding may be improved by

fabricating parts within a heated enclosure to increase interlayer fusion, improving structural integrity [398]. An alternative method employed thermally reversible Diels–Alder reactions to allow the heated flow of the polymer, followed by covalent bond formation. This minimised thermal distortion associated with non-uniform cooling and also reinforced the interlayer bonding between layers [410]. The attempt to improve cross linking between the thermoplastic layers was also attempted by exposing the component to ionizing gamma radiation post printing, in order to strengthen the parts and reduce anisotropy. This was reported to be successful in the production of PLA devices, where thermomechanical properties were increased, as well as the solvent resistance [411].

Both FDM and SLA printers offer different benefits and challenges; however, both techniques are limited by the resolution of the specific 3D printer used. Table 4.2 exhibits the features of common FDM and SLA printers. Through a comparison, the discrepancies in individual printer capabilities becomes apparent. While each printing technique offered higher and lower end printing abilities, the higher and lower costs associated with each option resulted in trade-offs being necessary, particularly when fabrication in resource stressed settings was an important aim for the project. This lack of access to high-end 3D printers greatly restricted the materials available, particularly for SLA printing. While FDM printers are limited by the diameter of the filament, SLA printers are severely limited by the choice of resin. A thorough review into biocompatible 3D printing resins has been described elsewhere [412]. These resins cure at explicit wavelengths, supplied by specific printers. Thus, further research is needed to source biocompatible resins which are compatible with suitable SLA printers.

Table 4.2 – A comparison between commercially available 3D printers
SLA, Stereolithography; FDM, Fusion Deposition Modelling

Name	Type	Build Volume (mm)	z Resolution (mm)	x-y Resolution (mm)	Price (USD)	REF
Anycubic Photon Mono 4K	SLA	132 x 80 x 165	0.01	0.035	$289	[413]
Anycubic Photon Mono X	SLA	192 x 120 x 245	0.01	0.034	$759	[414]
Elegoo Mars 2 Pro	SLA	129 x 80 x 160	0.01	0.035	$289	[415]
Elegoo Mars 3	SLA	143 x 90 x 165	0.01	0.035	$349	[416]
Formlabs Form 3+	SLA	145 x 145 x 185	0.025	0.025	$3,499	[417]
Formlabs Form 3L	SLA	335 × 200 × 300	0.025	0.025	$11,999	[418]
Anycubic 4Max Pro 2.0	FDM	270 x 210 x 190	0.05	0.01	$499	[419]
Anycubic Chiron	FDM	400 x 400 x 450	0.05	0.0125	$479	[420]
Creality Ender-2 Pro	FDM	165 x 165 x 180	0.1	0.01	$169	[421]
Creality Ender-3 V2	FDM	220 x 220 x 250	0.1	0.01	$262	[422]
Prusa i3 MK3S+	FDM	250 x 210 x 210	0.05	0.01	$749	[423]
Ultimaker S3	FDM	230 x 190 x 200	0.02	0.01	$3,850	[424]
Ultimaker S5	FDM	330 x 240 x 300	0.02	0.01	$6,355	[425]

Common power banks typically offer a capacity of 10,000 – 20,000 mAh, with a power output ranging from 10 to 18 W. Thus, the SPD power requirements were designed around these criteria. Ultra-high capacity power banks are commercially available, with a capacity and power output up to 72,000 mAh and 45 W, respectively; however, these options are much scarcer and more expensive.

In conclusion, this chapter presented a clear and defined set of specifications which were used to construct designs which would be validated and optimised computationally, prior to prototyping and physical testing. Work conducted in this chapter was exploratory research into an area commonly described as the bottleneck of diagnostics. The final design was a culmination of different avenues explored based on the literature presented in Chapter 2. Due to the time at which crucial information became available, changes to design approaches were necessary to better meet the user's needs. The shift from poultry related infections to SARS-CoV-2 resulted in substantial delays in progression; however, allowed for major lessons learned from novel sample preparation techniques to be integrated into later designs. Ultimately, the final design served as a proof-of-concept for SARS-CoV-2 detection, able to prepare samples for LAMP amplification in a single thermal heating step. Furthermore, the platform produced 1 µL by utilising an electrical field, allowing for accurate non-contact droplet production on demand. This simple and low-cost platform may be modified with future iterations to include additional preparation steps, building upon this preliminary research towards the goal of universal sample preparation.

5. Development of a Sample Preparation Platform

5.1. Introduction

Following the drafting of the design ideas proposed in Chapter 4, assessing which designs were viable and how they could be optimised to improve performance was vital. While prototyping was used to analyse certain designs, the high tooling costs required to manufacture, as well as the large order lead time to outsource components, imposed restraints which made this option infeasible for others. Hence, an alternative solution to assess and optimise the designs was required.

Finite Element Analysis (FEA) is a computational tool used to perform engineering analysis by simulating the behaviour of a component under set conditions [426]. FEA is of particular use when analysing problems within complex geometrical systems, or when said systems undergo changes over a time period. FEA has been implemented in many fields, including, fluid dynamics, electrostatics, structural analysis, and heat transfer, among others. FEA may be used during the developmental stage of a project to analyse either individual or an assembly of components with dissimilar material properties or complex geometries, allowing for parts to be optimised without needing to create and test physical prototypes [427].

The ensuing chapter of this thesis will report work conducted using the software COMSOL Multiphysics 5.5, for the purpose of analysing single and multiphase fluid flow, structural bending of a membrane valve under an applied boundary load, heat transfer through joule heating, and electrohydrodynamic dripping under an applied electrical potential. Results obtained from these designs were used as part of an iterative process to improve upon or to neglect the designs which were impractical.

5.2. Computational Fluid Dynamics

5.2.1. An Introduction to Fluid Dynamics

The more fluid control processes that are integrated into a platform, the more complex the resulting platform will be. Computational Fluid Dynamics (CFD) is used to study the flow of fluids and how forces affect them. By analysing the properties of a fluid within a system, including the density, pressure, velocity, surface tension, temperature, and viscosity, as functions of space and time, practical problems within a wide range of applications can be solved.

5.2.2. Classifications and Governing Equations

5.2.2.1. Liquids and gases

Fluids are classified into liquids and gases. Liquids consist of relatively tightly packed molecules, which can be attributed to a higher density. Alternatively, gases consist of loosely packed molecules which assume the shape of the vessel they are contained in, resulting in a much lower density.

5.2.2.2. Compressible and incompressible flow

Fluid density (ρ) is defined as the mass of the object with respect to its volume. Different fluids have different densities, influencing their performance within a system. Compressibility is defined as the ability of a fluid to change its density due to changes in pressure or temperature. While all fluids are theoretically compressible, many liquids will yield negligible changes in density from pressure or temperature changes. As a result, they are considered to be *incompressible*. Thus, the compressibility may be expressed as shown in Equation 5.1. Alternatively, due to the vast space between gas molecules, they can be easily condensed into a smaller volume. As a result, most gases are considered to be *compressible* [428].

$$\rho = constant \qquad \textit{Equation 5.1}$$

5.2.2.3. Steady vs. unsteady flow

The fluid velocity (U) is used to monitor the change of the position of a particle in the fluid, with respect to time (t). From this, it is possible to assess several fluid properties, such as the volumetric ($\dot{Q}$), mass ($\dot{m}$) and momentum ($\dot{M}$) flow rates. The volumetric flow rate assesses the rate to which the fluid travels through a given area (A), while the mass flow rate assesses the rate to which the fluid travels through an area with consideration of the fluid density. Finally, the momentum flow rate assesses the rate to which a fluid travels through a given area, in the direction of the fluid flow [428].

Fluid flow that does not exhibit changes to its properties within a system over time is known as steady flow. Alternatively, unsteady flow (also known as transient or time-dependent flow) pertains to a flow where the fluid properties within a system exhibit changes over time. Turbulent flow (explained later on) is inherently unsteady by nature; however, if the fluid properties are statistically constant over shifts in time, then the flow may be considered to be statistically stationary. Mathematically, steady flows may be expressed using the conservation of mass equations shown in Equation 5.2, where u, v and w are the fluid velocities in the x, y and z directions, respectively [428]. Should the flow be considered unsteady, a compressibility term must be introduced, as shown in Equation 5.3 [428].

$$\frac{\partial \boldsymbol{u}}{\partial x}+\frac{\partial \boldsymbol{v}}{\partial y}+\frac{\partial \boldsymbol{w}}{\partial z}=0 \qquad \textit{Equation 5.2}$$

$$\frac{d\rho}{dt}+\frac{\partial \boldsymbol{u}}{\partial x}+\frac{\partial \boldsymbol{v}}{\partial y}+\frac{\partial \boldsymbol{w}}{\partial z}=0 \qquad \textit{Equation 5.3}$$

Within a system where external forces are considered to be negligible, it is possible to express steady and unsteady flows by using the Navier-Stokes equations, as shown in Equation 5.4, Equation 5.5 and Equation 5.6, respectively [428].

$$\rho\left(\frac{\partial(\boldsymbol{u})}{\partial t}+\frac{\partial\left(\boldsymbol{u^2}\right)}{\partial x}+\frac{\partial(\boldsymbol{uv})}{\partial y}+\frac{\partial(\boldsymbol{uw})}{\partial z}\right)=-\frac{\partial p}{\partial x}+\mu\left(\frac{\partial^2 \boldsymbol{u}}{\partial x^2}+\frac{\partial^2 \boldsymbol{u}}{\partial y^2}+\frac{\partial^2 \boldsymbol{u}}{\partial z^2}\right) \qquad \textit{Equation 5.4}$$

$$\rho\left(\frac{\partial(\boldsymbol{v})}{\partial t}+\frac{\partial(\boldsymbol{uv})}{\partial x}+\frac{\partial\left(\boldsymbol{v^2}\right)}{\partial y}+\frac{\partial(\boldsymbol{vw})}{\partial z}\right)=-\frac{\partial p}{\partial y}+\mu\left(\frac{\partial^2 \boldsymbol{v}}{\partial x^2}+\frac{\partial^2 \boldsymbol{v}}{\partial y^2}+\frac{\partial^2 \boldsymbol{v}}{\partial z^2}\right) \qquad \textit{Equation 5.5}$$

$$\rho\left(\frac{\partial(\boldsymbol{w})}{\partial t}+\frac{\partial(\boldsymbol{uw})}{\partial x}+\frac{\partial(\boldsymbol{vw})}{\partial y}+\frac{\partial\left(\boldsymbol{w^2}\right)}{\partial z}\right)=-\frac{\partial p}{\partial z}+\mu\left(\frac{\partial^2 \boldsymbol{w}}{\partial x^2}+\frac{\partial^2 \boldsymbol{w}}{\partial y^2}+\frac{\partial^2 \boldsymbol{w}}{\partial z^2}\right) \qquad \textit{Equation 5.6}$$

5.2.2.4. Newtonian vs. Non-Newtonian Fluids

Forces which act normally to a fluid surface are known as pressure forces, while forces which act tangentially to the fluid surface are known as shear stresses. The rate at which a fluid will deform is dependent on the magnitude of the force applied to it, as well as the fluid's resistance to deformation. This is known as the fluid viscosity (μ). The more viscous a fluid, the more force is required to generate fluid flow. While all fluids are viscous, Newtonian fluids exhibit a linear relationship between the velocity gradient and the strain rate (τ), shown in Equation 5.7 [428]. In contrast, non-Newtonian fluids exhibit a non-linear stress-strain behaviour dependent on the individual fluid's rheological properties.

$$\tau = \mu \frac{du}{dy} \qquad [s^{-1}] \qquad \textit{Equation 5.7}$$

5.2.2.5. Laminar vs. turbulent flow

Laminar flow occurs at low velocities, where the fluid flows without mixing between parallel layers. As a result, the flow characteristics and predictable. Alternatively, turbulent flow is the "apparent randomness" as a result of instabilities caused by recirculation and eddies. In contrast, turbulent flow does not travel in ordered parallel layers, but in chaotic fluctuations leading to sporadic changes in velocity and pressure with respect to space and time that can be estimated using the Navier-Stokes equations. For liquids, the classification of these flows can be determined by the Reynolds number (Re), as shown in Equation 5.8, where D is the diameter of the pipe [428]. In liquids, Reynolds numbers below 2000 are considered to be *laminar*, while Reynolds numbers above 4000 are considered to be *turbulent*; however, flow close to the walls of the pipe may still be laminar. For Reynolds numbers between 2000 and 4000, the both laminar and turbulent properties will be exhibited.

$$Re = \frac{\rho U D}{\mu} \qquad [Pa] \qquad \textit{Equation 5.8}$$

5.2.2.6. Inviscid vs. Stokes flow

The Reynolds number is the ratio between the inertial and viscous effects acting on the fluid. In typical steady state flows with Reynolds number is significantly greater than 1, the inertial effects will have a greater effect on the fluid than the viscous effects. As a result, the flow may be considered to be *inviscid*, allowing for viscous effects to be neglected. For extreme cases where the Reynolds number

is significantly smaller than 1, Stokes flow (also known as creeping flow) occurs. In this case, the strong viscous forces dominate over the inertial effects. As a result, the inertial effects may be neglected. It is common in CFD modelling to utilise models which neglect the viscous forces further from the wall of the system, while utilising specific equations within the region close to the wall known as the boundary layer, where viscous forces are dominant.

5.2.2.7. Surface Tension

The tendency for a fluid to retain its droplet shape over a flat surface is known as the surface tension (γ). Liquids with a high surface tension will retain their spherical shape, while liquids with a low surface tension will flatten. Larger droplets tend to have a higher surface tension, due to being more receptive to gravitational effects. The importance of viscosity and surface tension increases as the scale of the fluid flow decreases, eventually becoming the dominant force acting on the liquid [428].

As surface tension acts around the entire surface of a droplet and is opposed by pressure forces inside the droplet above ambient pressure. Both of these forces may be represented by the following expressions, where d is the diameter of the droplet, p_i is the pressure within the droplet, p_0 is the ambient pressure and A is the area over which the pressure is exerted:

$$Surface\ tension\ acting\ around\ the\ circumference = \gamma \cdot \pi D$$

$$Pressure\ force\ exerted\ on\ the\ area = \Delta p \cdot A = (p_i - p_0) \cdot \frac{\pi D^2}{4}$$

By assuming that these forces are in equilibrium, they may be equated to each other, resulting in the following expression:

$$(p_i - p_0) \cdot \frac{\pi D^2}{4} = \gamma \cdot \pi D$$

Rearrangement and simplification results in the expression shown in Equation 5.9. It can be concluded from this expression that the pressure intensity decreases as the size of the droplet increases.

$$\Delta p = \frac{4\gamma}{D} \quad [\text{Pa}] \qquad \textit{Equation 5.9}$$

5.2.2.8. Contact Angle and Wettability

Wetting is the ability of a liquid to maintain contact with a solid surface. The magnitude of wetting, known as the wettability, is characterised by the contact angle (θ), defined by the angle formed where a liquid, solid surface and vapour medium interact. The contact angle provides an indication of the surface properties, mainly, its cleanliness, its adhesiveness, the homogeneity of a surface coating, and the effectiveness of other surface modifications. There are three interfacial forces acting at the three-phase intersection as shown in Figure 5.1. By measuring the three-phase intersection of a droplet, the contact angle may be determined [429].

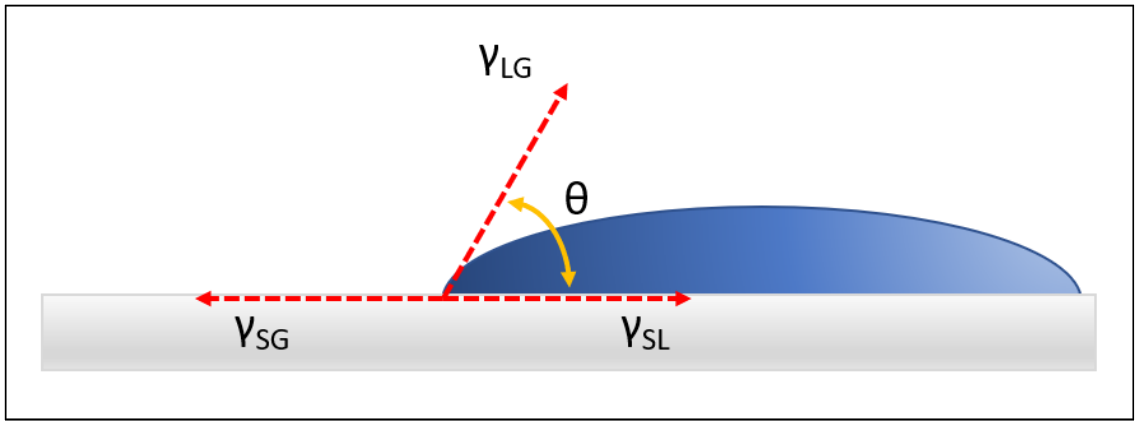

Figure 5.1 – Contact Angle [430]
γ_{SG}, solid-gas surface tension; γ_{SL}, solid-liquid surface tension; γ_{LG}, liquid-gas surface tension; ϑ, contact angle

The contact angle is determined by performing a balance between adhesive and cohesive forces using the Young equation shown in Equation 5.10, where γ_{SG} is the solid-gas surface tension, γ_{SL} is the solid-liquid surface tension and γ_{LG} is the liquid-gas surface tension [431]. As the contact angle of a fluid within a system are influenced by changes in temperature and pressure, it is assumed that the three interfacial forces are thermodynamically stable.

$$\gamma_{SG} = \gamma_{SL} + \gamma_{LG} \cos\theta \qquad [\mathrm{N/m}] \qquad \textit{Equation 5.10}$$

By modifying the Young equation (Equation 5.11), the contact angle can be calculated [430].

$$\cos(\theta) = \frac{\gamma_{SG} - \gamma_{SL}}{\gamma_{LG}} \qquad [^\circ] \qquad \textit{Equation 5.11}$$

Water droplets on a surface may be characterised based on the resulting contact angle. For contact angles less than 90°, a surface is considered to be hydrophilic, indicating a high wettability. For contact angles larger than 90°, a surface is considered to be hydrophobic, indicating a low wettability. In cases where the contact angle exceeds 150°, the surface may be considered as superhydrophobic [432].

The contact angle is dependent on the rheological properties of the liquid, the inclination and roughness of the solid surface, and the properties of the ambient gas medium above the free surface of the liquid. The contact angle is also extremely susceptible to surface contamination and is typically only reproducible within an accuracy of a few degrees within laboratory conditions [433].

5.2.3. Individual Tesla Valve Design

5.2.3.1. Introduction

A Tesla valve (Figure 5.2) is a no moving parts (NMP) passive valve with an anisotropic flow resistance, designed by Nikola Tesla in 1920 [434]. This valve utilises a fixed geometry which encourages the fluid to flow freely along the path of least resistance in one direction (forward flow) while forcing the fluid to diverge and converge on itself in the opposite direction (reverse flow), generating high frictional forces where the two flows converge. This results in the fluid being allowed to flow freely in one direction, but not in the opposite. When combined with an oscillating static pressure able to draw in and expel fluid from the valve, a positive net flow rate can be generated in the desired (forward) direction. The main advantages to the Tesla valve are the lack of moving parts involved with the design, simplifying fabrication steps [435]. These valves are also less sensitive to particulates compared to conventional valves, making them beneficial in the field of microfluidics, where the ability to control the transport fluids containing particles may be needed [436].

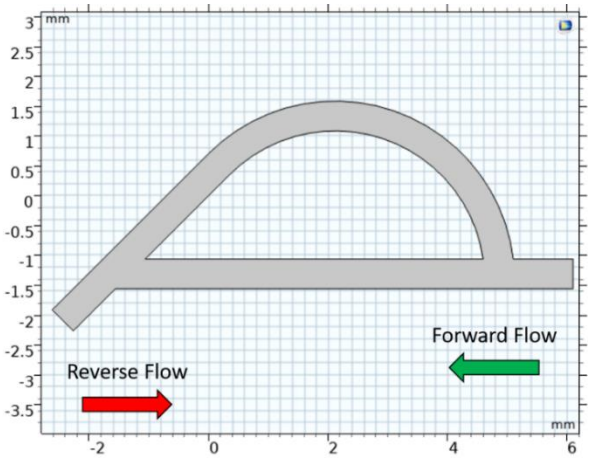

Figure 5.2 – Geometry of a T45a Tesla Valve

The performance of the Tesla valve is determined by the ratio between the pressure drops in the reverse and forward flow directions, known as the diodicity (Di). This relationship can be seen in Equation 5.12, where $\mathbf{\Delta p_r}$ and $\mathbf{\Delta p_f}$ are the pressure drops corresponding to flow in the reverse and forward flow directions, respectively. For a working valve, the pressure drop in the reverse flow direction is greater than that the forward flow direction, resulting in a diodicity value greater than 1. A higher diodicity signifies a higher quality of Tesla valve. A diodicity between 1 and 2 is expected based on a review of literature [437]; however, values up to 4 have been reported [438,439]. In the case for low flow rates (Re < 10), the inertial effects will become negligible, and as such, the diodicity will become 1, causing the valve to fail. In the case of high flow rates (Re < 1000), transient flow effects will be introduced. Thus, it is advised to use a moderate flow rate (100 < Re < 900) for valve analysis and optimisation [435].

$$Di = \frac{\Delta p_r}{\Delta p_f} \qquad \textit{Equation 5.12}$$

5.2.3.2. Problem Description

The aim was to design, simulate and compare various Tesla valve geometries using CFD. The valves were modelled using Solidworks 2018 (Dassault Systèmes, Vélizy-Villacoublay, France), which were imported into COMSOL Multiphysics 5.5 (COMSOL AB, Stockholm, Sweden) for analysis. A 2D stationary single-phase flow study was conducted for each of the 5 valve designs at specified flow rates and the velocity and pressure values both upstream and downstream of the valve were recorded. These values were used to calculate the Reynolds number and diodicity for each valve, allowing for a comparison in performance.

The geometry of the T45a-type Tesla valve (Figure 5.3) was designed based on methodologies shown in section 8.3.1, adapted from works by Truong and Nguyen [440], which was then adapted to produce the T45c, TMW and GMF-type valves. The D-type valve was designed based on work reported by De Vries *et al.* [441]. The variations between the channel geometries upstream and downstream of the valve were minimised to keep the fluid flow within the channels consistent, allowing the effect of the geometry on the fluid flow to be assessed. Furthermore, inflow and outflow measurements could be taken at consistent locations to ensure accurate results. Finally, a converging inlet and a diverging outlet of the same dimensions was added to each valve, creating common inflow and outflow parameters and allowing the flow to become fully developed prior to entering the valve. This created common points within the designs where pressure and velocity profiles could be measured.

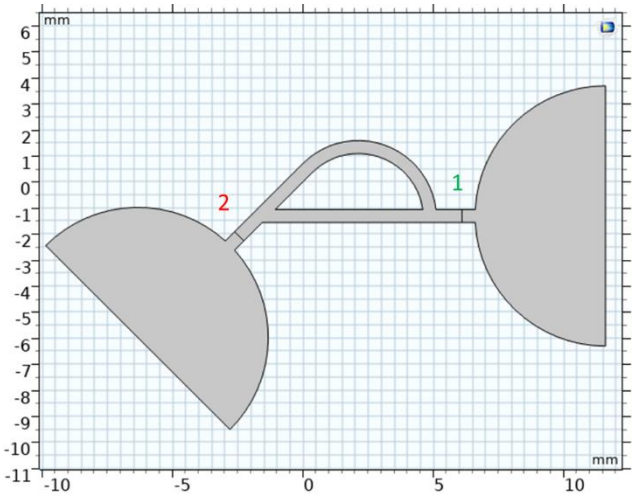

Figure 5.3 – T45a Tesla Valve Geometry with added inlet and outlet features
The cut line at point 1 indicated the inlet for forward flow and the cut line at point 2 indicated the inlet for reverse flow.

5.2.3.3. Numerical Simulation

The model was setup as a 2D single-phase laminar flow model to be studied as a stationary flow problem, using water (ρ = 1000 kg/m^3, μ = 1 mPa·s) as the fluid within the domain, assumed to be incompressible. The valves were imported as .dxf files into COMSOL Multiphysics 5.5. The boundary conditions for the inlet and outlet were specified which would simulate forward flow conditions within the valve. For the inlet, a normal inflow velocity of 0.005 m/s was used, increasing in increments of 0.005 to 0.05 m/s. For the outlet, a pressure outlet of 0 Pa was used. No-slip wall conditions were applied to simplify the model. The computed velocity and pressure plots were observed and a 1D plot group was used to generate velocity and pressure plots at points 1 and 2, which were exported for further analysis. The simulation was then repeated, with the boundary conditions set for reverse flow.

5.2.3.4. Results and Discussion

In the forward flow velocity profiles, the bulk of the fluid is observed to travel through the inlet (Figure 5.4) and into the main (straight) channel, while a portion is drawn into the side (curved) channel. The two flows are observed to converge at the junction at near to parallel streamlines, resulting in little impact on the fluid flow at the outlet (Figure 5.5). For the reverse flow velocity profiles, the bulk of the fluid is observed to be diverted from the inlet (Figure 5.6) and into the side channel, while the remainder of the fluid flow travels through the main channel. When the two flows converge at the junction (Figure 5.7), the streamlines are observed to interact at a close to perpendicular angle to each other, resulting in a restriction in the flow. This difference becomes more apparent at increased Reynolds numbers. This is not observed to the same magnitude for the TMW valve.

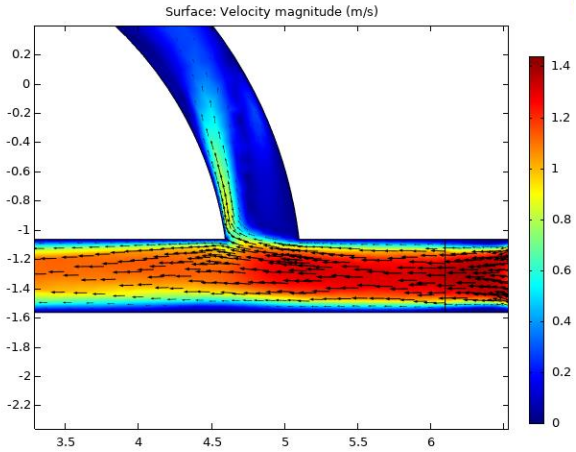

Figure 5.4 – Forward velocity flow profile within a T45a Tesla valve at point 1 (V= 50 mm/s)

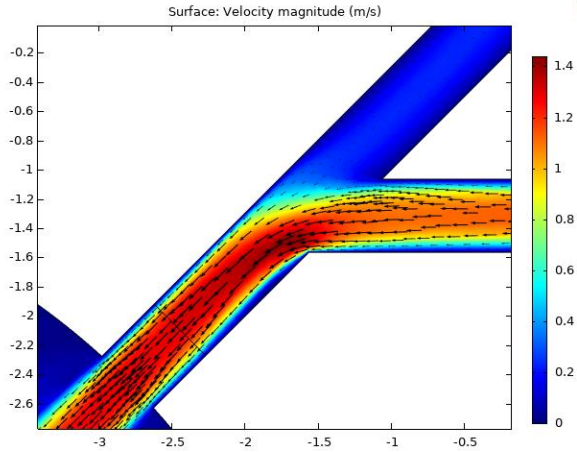

Figure 5.5 – Forward velocity flow profile within a T45a Tesla valve at point 2 (V= 50 mm/s)

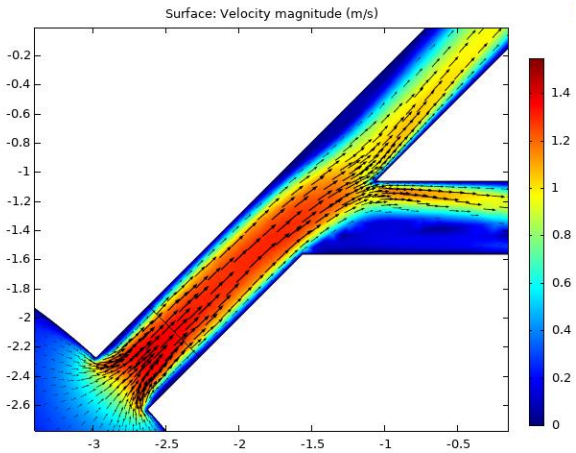

Figure 5.6 – Reverse velocity flow profile within a T45a Tesla valve at point 2 (V= 50 mm/s)

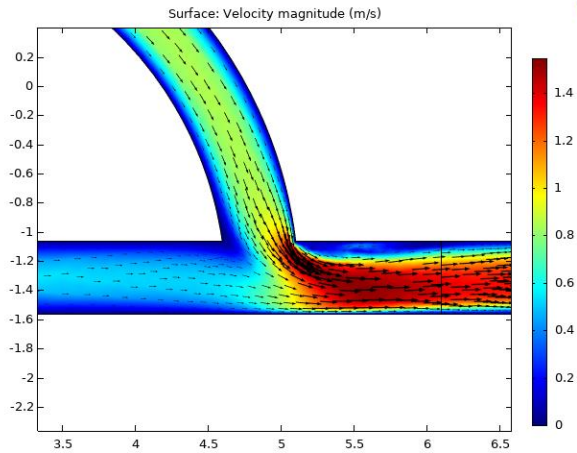

Figure 5.7 – Reverse velocity flow profile within a T45a Tesla valve at point 1 (V= 50 mm/s)

The difference between the pressure drop in the reverse and forward flow directions were used to calculate the diodicity for each valve, shown in Figure 5.8. Among the five designs, the T45c-type valve had the best performance, followed by the D-type, the GMF-type, the T45a followed by the TMW-type valve. Images demonstrating the performance of each valve can be seen in sections 8.3.2 – 8.3.6.

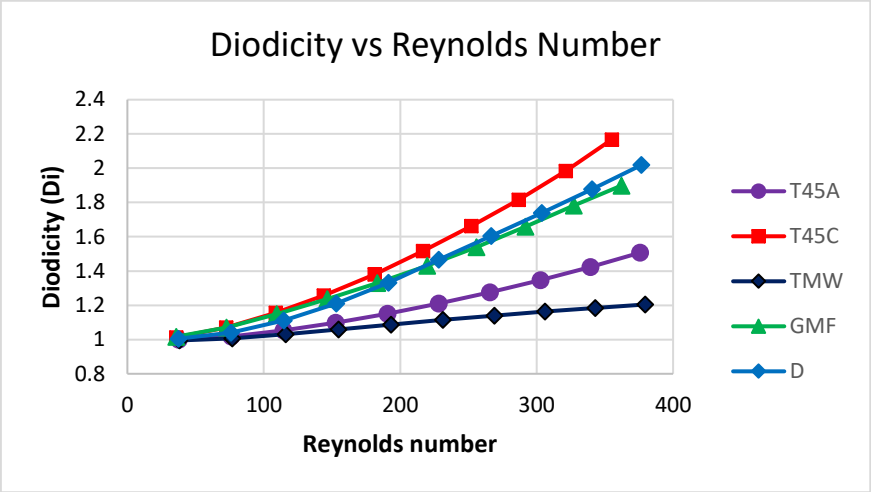

Figure 5.8 – Plot of diodicity against the Reynolds number for each valve type

To determine a reference point for the following assessments of the T45c Tesla valve design, a mesh independence study was performed for both forward and reversed flow. Physics-controlled meshes with ranging from “extremely coarse” to “extremely fine” were used, corresponding to element sizes from 409 to 22,638 elements. A plot of the maximum velocity against the element size was generated, which can be seen in Figure 5.10. The forward flow solution obtained mesh independence at approximately 5,000 elements, corresponding with the finer mesh. The reverse flow solution obtained mesh independence at approximately 20,000 elements, corresponding with the extremely fine mesh.

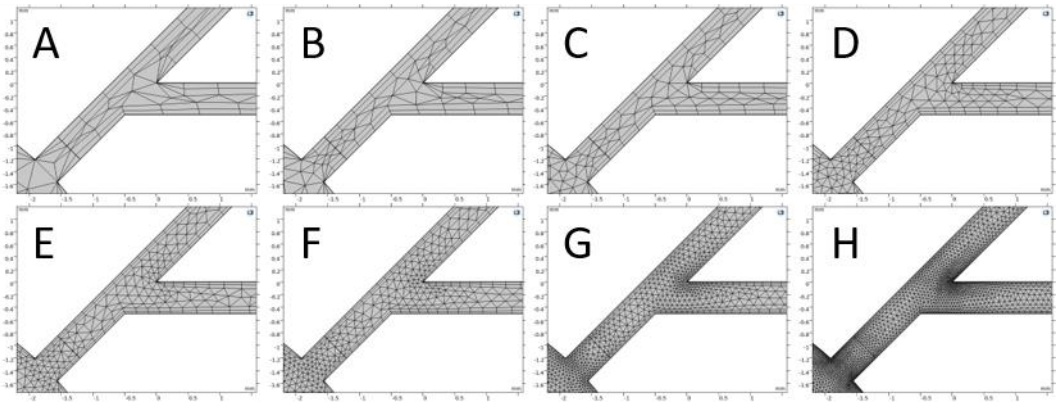

Figure 5.9 – Mesh Sizes at point 2 for the T45c Tesla valves
***A**, Extremely coarse; **B**, Extra coarse; **C**, Coarser; **D**, Coarse;*
***E**, Normal; **F**, Fine; **G**, Finer; **H**, Extra Fine*

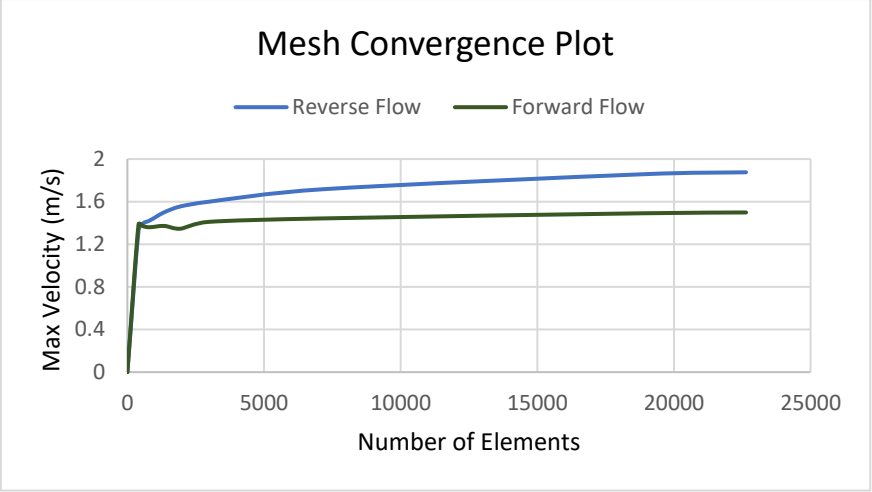

Figure 5.10 – Maximum velocity convergence plot for the T45c Tesla valve
Mesh independence was obtained at approximately 5000 elements for the forward flow profiles

5.2.4. Tesla Valve Simulation

5.2.4.1. Numerical Simulation

Based on the results reported in section 5.2.3, the T45c-type Tesla valve design was used as a template for a 2D transient single-phase flow simulation using an extremely fine mess to assess the functionality of the SCD described in section 4.3.4. The model was adapted from the simulation of a MEMS micropump mechanism described elsewhere [442]. A multi-stage Tesla valve design (Figure 5.11) was designed using Solidworks 2019, which was exported into COMSOL Multiphysics 5.5.

The flow rate at the left (inlet) and right (outlet) of the model were calculated using two boundary integration coupling components, with a net volume determined by calculating the difference between these two values. An inflow velocity from 10 – 50 mm/s was used, in increasing increments of 10 mm/s. To obtain a flow rate, a domain thickness of 0.5 mm was used, matching the channel thickness for the proposed SCD. For simplification, an oscillating pump mechanism (reciprocating input) was used to simulate pumping, omitting the necessity to model a moving input. The oscillating pump mechanism allowed for the pressure at the reciprocating input to vary sinusoidally over a 1 second period, allowing for both cases of priming and discharging to be observed. The simulation was performed over a duration of 2 seconds, allowing for two full oscillations.

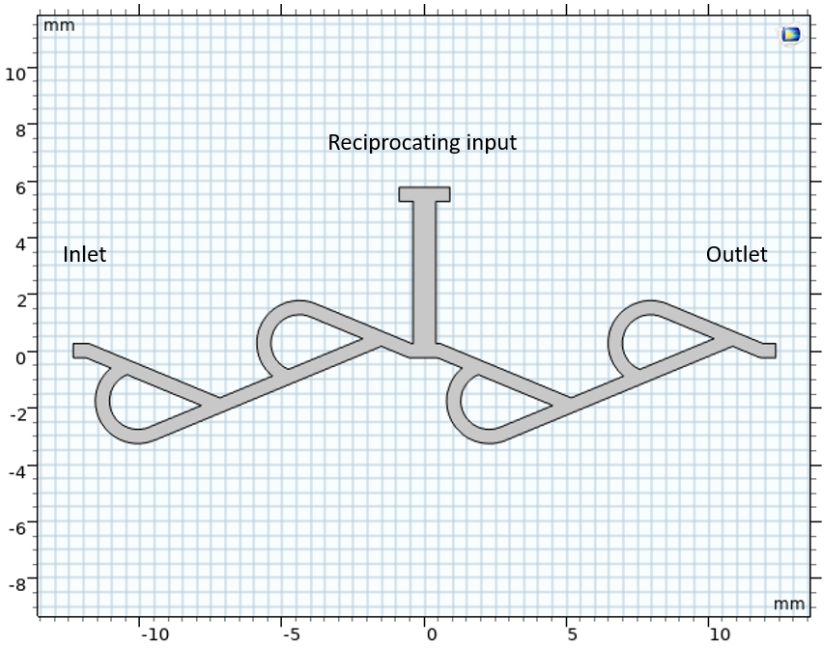

Figure 5.11 – Geometry of a multi-staged Tesla Valve design

5.2.4.2. Results and Discussion

The downstroke action occurs between 0 – 0.5 and 1 – 1.5 seconds, signifying when fluid is pushed from the sinusoidal input into the Tesla valves. Figure 5.12 shows a solution at time 0.25 seconds when the magnitude of the downstroke is at its maximum. During the downstroke, it is shown that the fluid flows more easily from the sinusoidal output towards the outlet along the main channel, than towards the inlet, where the two diverging flow paths act against each other at the junction. The upstroke action occurs between 0.5 – 1 and 1.5 – 2 seconds, signifying when fluid is drawn from the Tesla valves and into the sinusoidal input. Figure 5.13 shows a solution at time 0.75 seconds when the magnitude of the upstroke is at its maximum. During the upstroke, the fluid is drawn more easily through the inlet and through the main channels towards the sinusoidal input when compared to fluid drawn through the outlet, where the diverging flow paths act against each other. The result of this action yields a net flow rate from the inlet to the outlet.

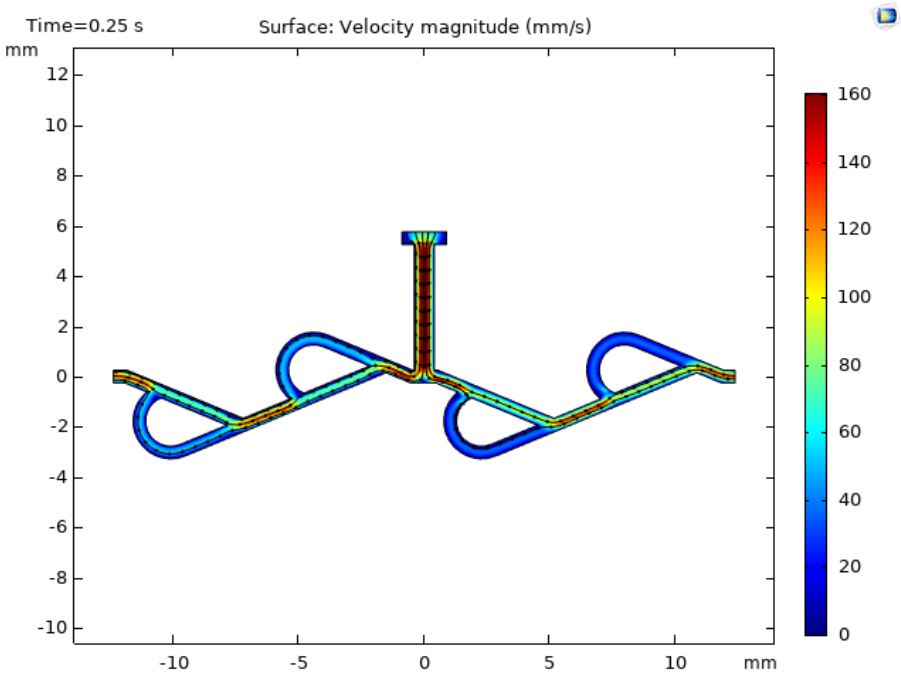

Figure 5.12 – Velocity flow field during the downstroke action (t = 0.25s; V= 50 mm/s)

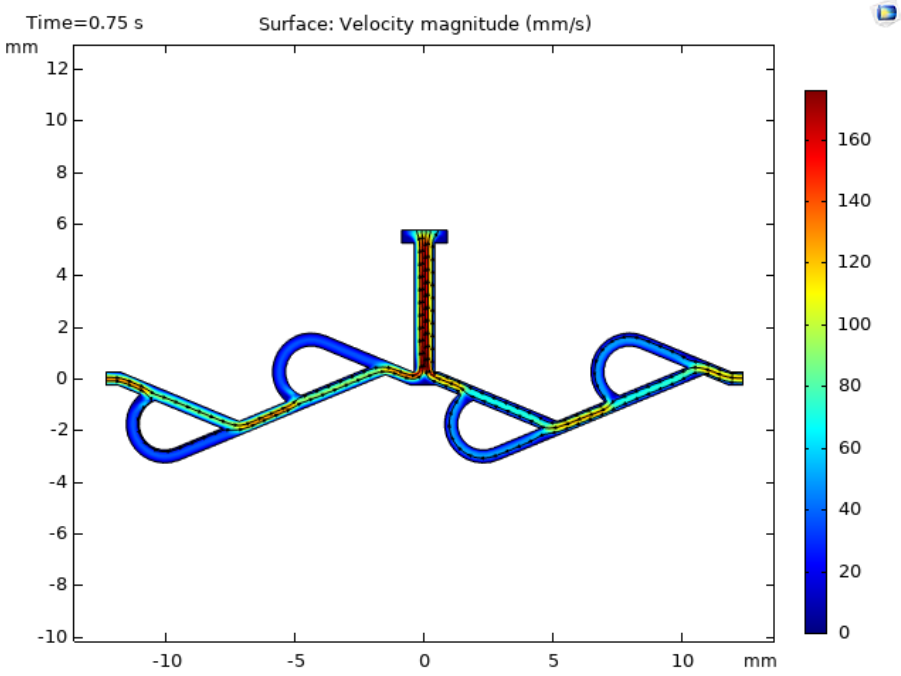

Figure 5.13 – Velocity flow field during the upstroke action (t = 0.75s; V= 50 mm/s)

A comparison between the net volumes pumped from left to right at different inflow velocities can be seen in Figure 5.14. There is a sinusoidal variation to the curve with increasing and decreasing gradients corresponding to the downstroke and upstroke actions, respectively. Times between 0.5 – 1 and 1.5 – 2 have the highest gradient, corresponding with the upstroke. It can be concluded that a

greater volume of fluid is being drawn into the SCD through the inlet in comparison to the outlet, signifying the valve design to work as intended. Times between 0 – 0.5 and 1 – 1.5 have a lower gradient, corresponding with the downstroke. It can be concluded that there is a smaller difference between the fluid travelling through the inlet and outlet during this time span, indicating some backflow towards the inlet. An assessment of the velocity profile at 10 mm/s (Figure 5.15) shows that there are instances of decreasing net flow, confirming backflow. The range of the Reynolds numbers assessed were within the range of 5.61 and 28.1, significantly lower than the advised flow rate [435]. Due to issues with the software, it was observed that Reynolds numbers above 64.6 would fail to converge, significantly lower than the advised flow rate.

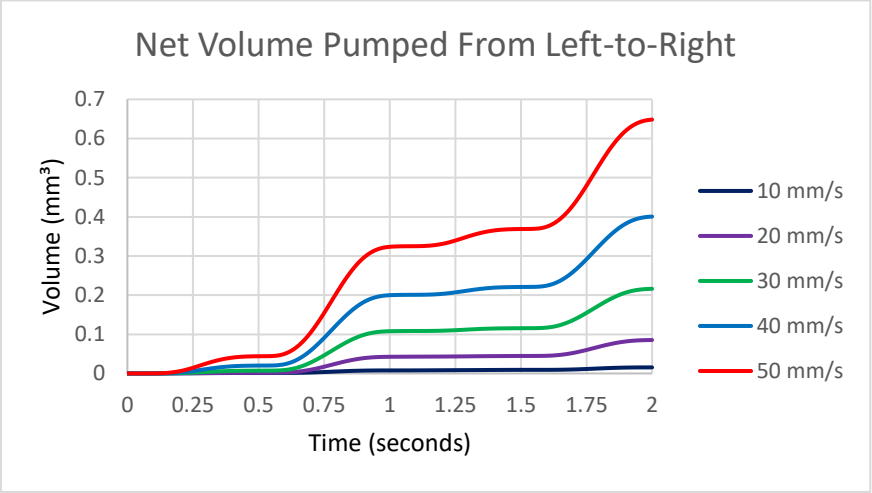

Figure 5.14 – Net Volume pumped from left-to-right (0 – 2 seconds)

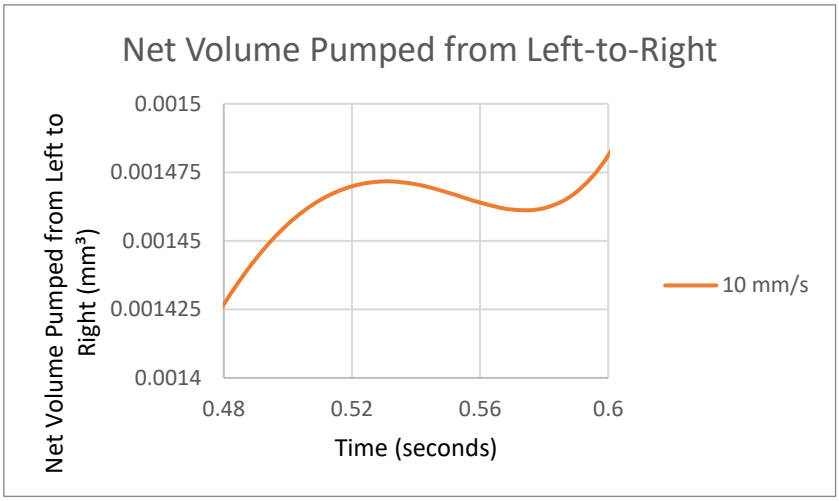

Figure 5.15 – Net Volume pumped from left-to-right (0.48 – 0.6 seconds)

It was discovered during a review of literature that under multiphase conditions, air bubbles can form within the side channels, diverting fluid flow into the main channel [443]. This claim was also supported by work by De Vries *et al.*, who reported bubble formation in the side channel for forward and reverse flow conditions [441]. In light of these findings, the priming of the pumping system was determined to be unreliable, and thus, a decision was made to progress from this design to Design Idea 4. Possible future work for this design include the modelling of multiphase fluid flow through the device and topology optimisation. Multiphase modelling is crucial to determine how the valve will perform during priming conditions and how air within the device following priming may affect the performance. It should be noted that the valve designs used for sections 5.2.3 and 5.2.4 were not optimised, and thus, the next logical stage would be to perform topology optimisation to minimise the valve size and maximise diodicity.

5.2.5. Two-Phase Flow Modelling

5.2.5.1. Problem Description

As previously discussed in section 4.3.5, fluid was to be drawn into a heating chamber from the sample inlet and then expelled through an outlet from the heating chamber using a syringe pump as a driving mechanism. A concern was the formation of bubbles as liquid displaces the air within the channels, a common issue in microfluidic applications, also noted in section 5.2.4.2. While physical modelling may be used to assess the formation of bubbles within the internal channels, this approach can prove expensive, particularly when redesigns are necessary. Thus, a computational model was generated to assess the fluid flow through the cartridge.

The computational model was developed on COMSOL Multiphysics 5.5 (Figure 5.16), which was used to simulate two cases. The first case (Figure 5.17) simulated the drawing of the liquid from the sample inlet and into the heating chamber using negative pressure supplied from the pump port, with the membrane valve between the heating chamber and the outlet used to prevent airflow into the cartridge. The second case (Figure 5.18) simulated the ejecting of the fluid from the heating chamber and out of the outlet using positive pressure supplied from the pump port, with the membrane valve between the sample inlet and the heating chamber preventing backflow.

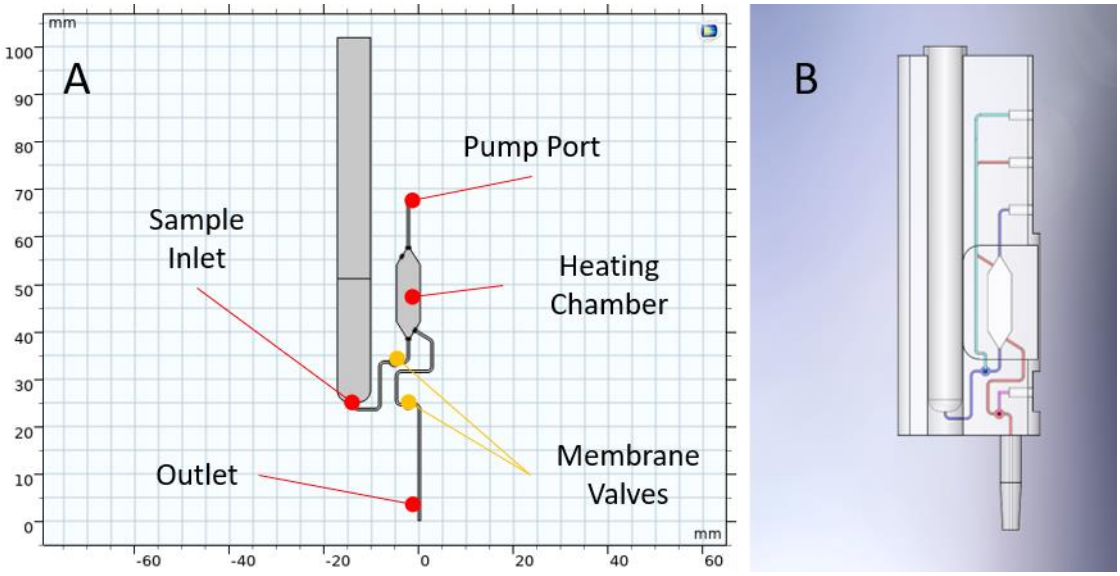

Figure 5.16 – Comparison between computational models Designed for Design Idea 4
***A.** 2D geometry designed on COMSOL Multiphysics 5.5* ***B.** 3D CAD model designed in Solidworks 2020.*
The control channels for the valve controls were not included in the for the computational simulation as they were unnecessary for simulating the fluid flow through the cartridge.

The geometry was imported from Solidworks 2020. Akin to the tesla valves presented in section 5.2.3, the width of the channels was 0.5 mm. To simulate the closed valve, a circle with a diameter 40 µm smaller than that of the membrane valve was added to the model at the centre of each valve, representing the flexible membrane coming into contact with the base of the valve. The clearance around the "closed valve" would be used to assess if air would be drawn into the cartridge in case 1 and if backflow would occur from the heating chamber into the sample inlet in case 2. In a real-life situation, contact would occur during the closing of a valve; however, for this model, the 40 µm difference was used to create an offset to preserve the fluid-domain topology while preventing any significant flow.

For case 1, the height of the liquid was set to simulate 1 mL of fluid being present in the swab inlet. Valve 1 was set to "open" by retaining the area within the circle, while valve 2 was set to "closed" by removing this area with the difference function in COMSOL. For case 2, the domains connecting the sample inlet to the pump port were assumed to be completely filled with only liquid and the fluid within the swab inlet was assumed to have been drawn into the channels. The settings of valves 1 and 2 were set to "closed" and "open", respectively, through a similar method as described for case 1.

5.2.5.2. Numerical Simulation

A 2D, transient two-phase laminar flow with level set model was used. In both cases, water (ρ = 1000 kg/m^3, μ = 1 mPa·s) and air (ρ = 1.225 kg/m^3, μ = 0.01789 mPa·s) were used as the fluids within the simulation. As the thickness of the channels, heating chamber and membrane valves were 0.5 mm, the model could be simulated along a 2D plane to conserve computational power. High pressure values were chosen to simulate flow rates at the upper limits of which a commercially available syringe pump would be able to provide, which would be the conditions most likely to yield errors. For case 1 (Figure 5.19), the three boundaries were defined. Inlet 1 and Inlet 2 were set as a pressure inlet at atmospheric pressure, to simulate the function of the device at ambient conditions. As shown in Figure 5.17, the outlet was set to -1 kPa, to simulate the negative pressure supplied by the syringe pump. For case 2 (Figure 5.20), Outlet 1 and Outlet 2 were set as pressure outlets at atmospheric pressure, while inlet 1, as shown in Figure 5.18, was set to 0.5 kPa. No-slip wall conditions were applied to simplify the model and to reduce computational power.

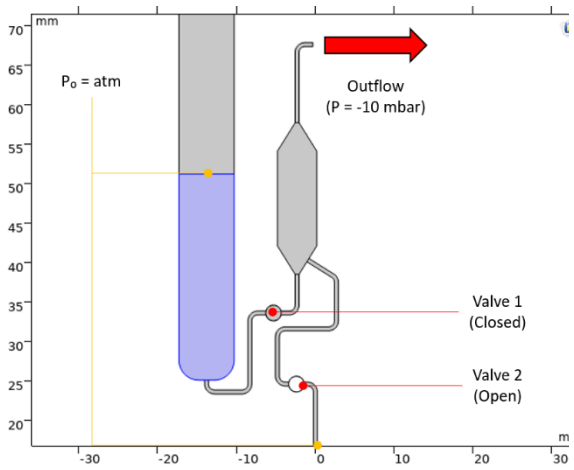

Figure 5.17 – 2D Model of Case 1
The two fluids are water (blue) and air (grey)

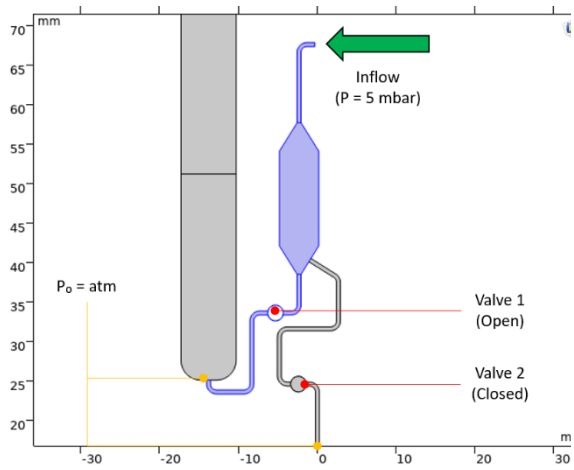

Figure 5.18 – 2D Model of Case 2
The two fluids are water (blue) and air (grey)

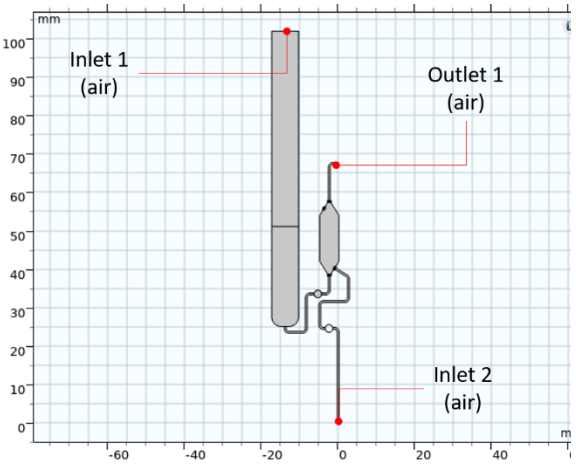

Figure 5.19 – Definition of Inlets and Outlets for Case 1

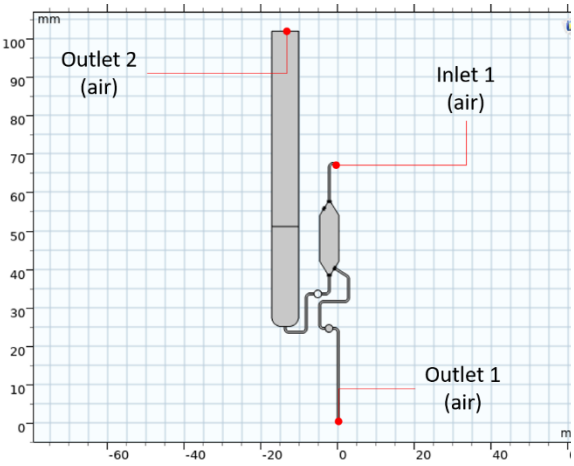

Figure 5.20 – Definition of Inlets and Outlets for Case 2

The level set method defined the interface between the two fluids using a level set function derived from the convection equation shown in Equation 5.13, where ϕ is the level set function and u is the velocity field. The function changes as it moves along the fluid velocity with respect to time. When coupled with the Volume of Fluid method (VoF), it can discriminate between the fluids within a domain [444]. At ϕ = 1, the domain is completely filled with fluid 1; and at ϕ = 0, the domain is completely filled with fluid 2. Cells with an interaction between the two fluids are defined by 0 < ϕ < 1. For this model, air was defined as ϕ = 0, while water was defined by ϕ = 1. The two-phase flow, level set Multiphysics module was then used to couple the laminar flow fluid model to the level set moving interface. Surface tension was included for the model, defined by a liquid/gas interface of water/air.

$$\frac{d\varphi}{dt} + \boldsymbol{u} \cdot \nabla\varphi = 0 \qquad \textit{Equation 5.13}$$

A physics-controlled mesh with a fine mesh size was used, shown in Figure 5.21. The use of a physics-controlled mesh allowed for the correct mesh density to be estimated. The size of the mesh elements can be seen to decrease at the entrance to the first microchannel (Figure 5.21b) and at the entrance and exit channels to the trapezoidal chamber (Figure 5.21c). The mesh at the open and closed membrane valves (Figure 5.21d and Figure 5.21e) also contained very small element sizes due to the geometric design of the valves, leading to an increase in time taken to achieve a solution. A time dependent study was used, solving between 0 and 0.75 seconds with a time step of 0.01 seconds. The simulation was run, calculating for velocity, pressure and volume of fluid fraction.

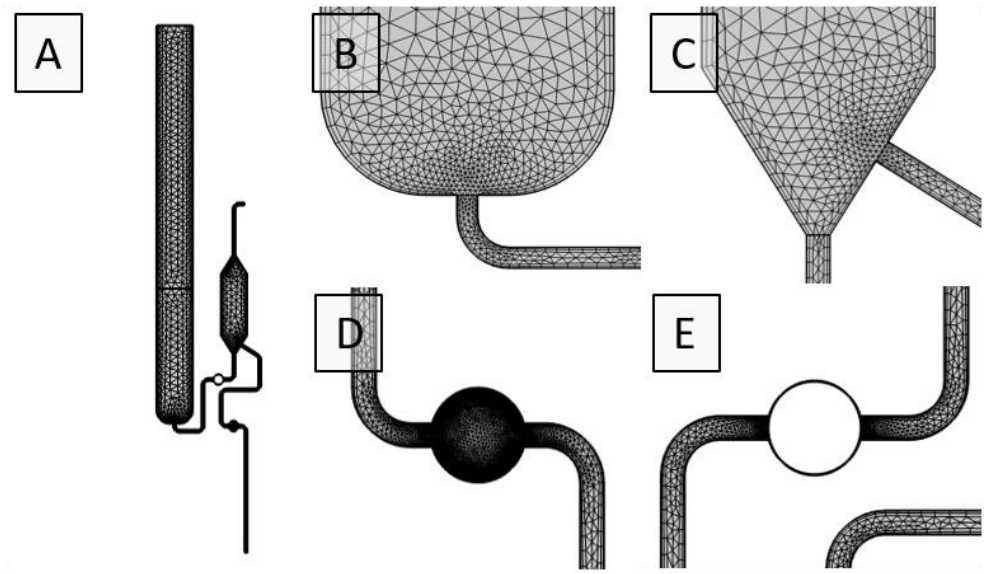

Figure 5.21 – Mesh refinement using a Physics-controlled Mesh (Element Size Fine)
***A.** Whole Mesh* ***B.** Sample inlet* ***C.** Trapezoidal heating chamber* ***D.** Open valve* ***E.** Closed valve*

5.2.5.3. Results and Discussion

Case 1

The results for case 1 can be seen in Figure 5.22. At 0.03 seconds, the liquid can be seen travelling from the sample inlet and passing through the open valve. At 0.07 seconds, the liquid enters into the trapezoidal heating chamber. The interaction of the liquid with the channel along the right-hand side results in an imbalance of entry along the trapezoidal chamber (0.16 seconds), resulting in a formation of a bubble at 0.28 seconds above the channel. At 0.62 seconds, the liquid reaches the outlet. It was observed that a second air bubble had formed in the top left-hand side of the trapezoidal chamber. Both air bubbles remained until the end of the simulation, at 0.75 seconds. There was no observed flow of liquid from the trapezoidal chamber in the direction towards the closed valve. Figure 5.23 depicts the pressure gradient across the closed valve. An averaged pressure plot was taken on either side of the closed valve, shown in Figure 5.24. As suction was supplied from the syringe pump upstream of the valve, a decrease in pressure to a maximum of -1.01 kPa was observed. At 0.28 seconds, the pressure increased rapidly to -0.63 kPa, coinciding with the fluid reaching the end of the trapezoidal chamber. The pressure downstream of the valve remained constant at gauge pressure, indicating no interaction between the channels on either side.

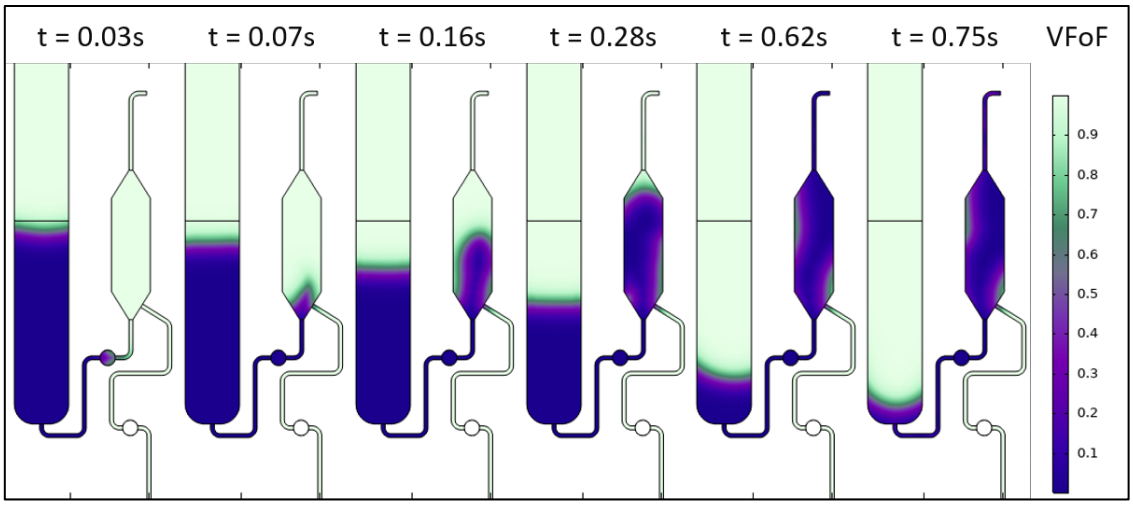

Figure 5.22 – Volume fractions of fluid for Case 1 (t = 0 – 0.75s)
Refer to the figure legend for interpretation. 0 = water, 1 = air

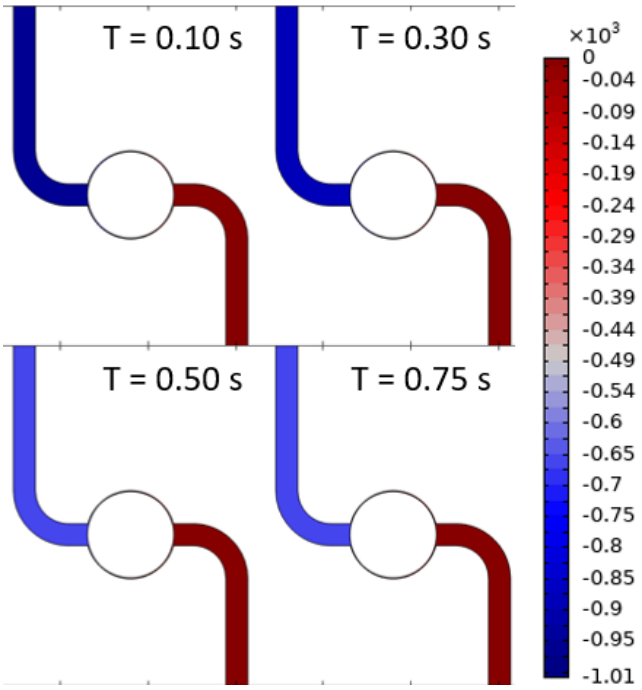

Figure 5.23 – Pressure Plot across the closed valve for Case 1
The active section of the channel (blue) varied in pressure, while the inactive section of the channel (red) remained constant, demonstrating the successful restriction of significant airflow across the valve

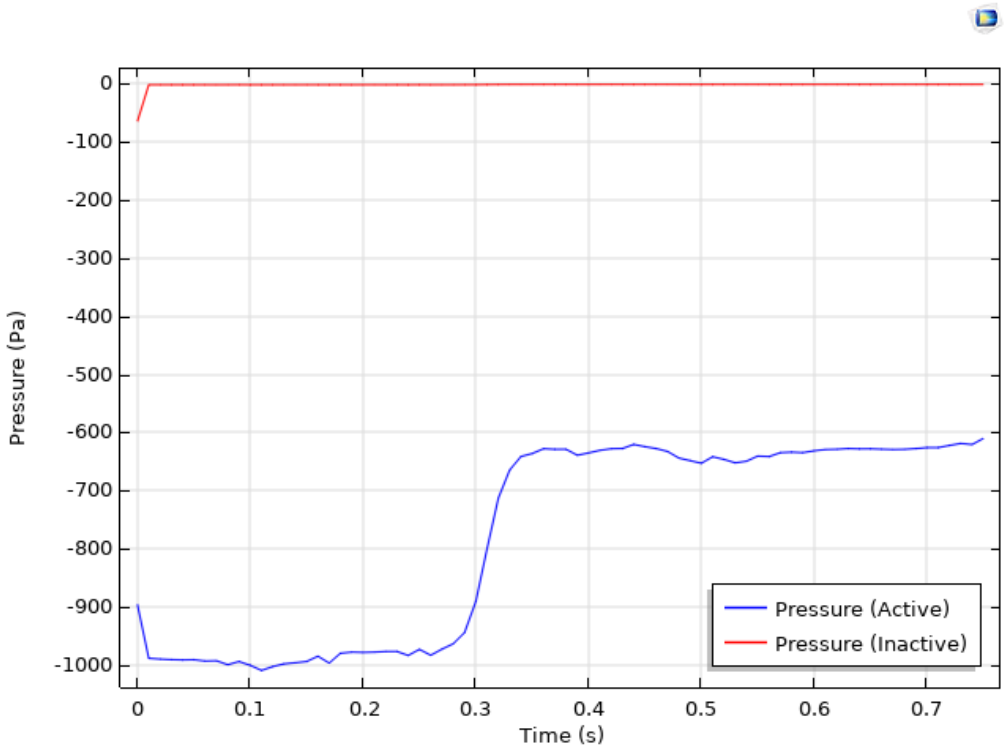

Figure 5.24 – Averaged pressure plot taken on either side of the closed valve (Case 1)
The red line represents the fluid flow across the inactive side of the pump, while the blue line represents the fluid flow across the active side of the pump

Case 2

The results for case 2 can be seen in Figure 5.25. At 0.04 seconds, the liquid can be seen travelling from the heated chamber and along the serpentine path leading towards the open valve, reaching the open valve at 0.07 seconds. The air can be seen to displace the liquid in the trapezoidal chamber. At 0.15 seconds, an imbalance in the profile of the fluid meniscus can be observed in the heating chamber. This imbalance increases until 0.24 seconds, where the meniscus begins to flatten. At 0.7 seconds, the bulk of the liquid has been displaced from the heating chamber. There was no observed increase in height of the fluid into the sample inlet, and thus, in can be determined that there was no backflow through the closed valve.

Figure 5.26 depicts the pressure gradient across the closed valve. An averaged pressure plot was taken on either side of the closed valve, shown in Figure 5.27. As the liquid was pumped in the direction of the closed valve, a rapid increase in pressure to 0.5 kPa was observed. At 0.04 seconds, a slight decrease in pressure across the active channel was observed as the liquid was diverted in the direction of the closed valve. For the remainder of the simulation, the pressure across the active channel remained constant at 0.5 kPa. Slight perturbations were detected in the inactive channel, however, the pressure remained relatively consistent at gauge pressure.

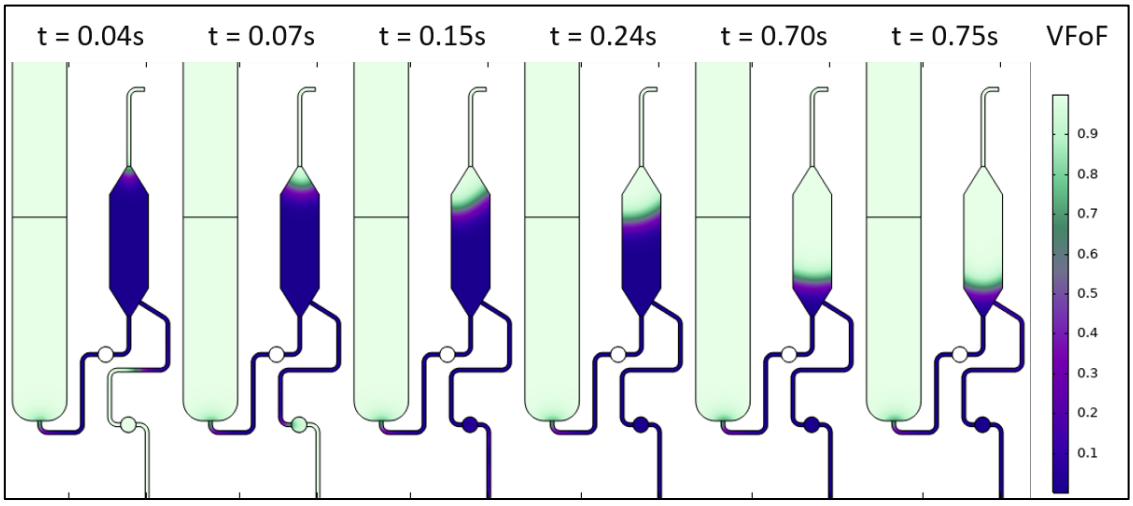

Figure 5.25 – Volume fractions of fluid for Case 1 (t = 0 – 0.75s)
Refer to the figure legend for interpretation. 0 = water, 1 = air

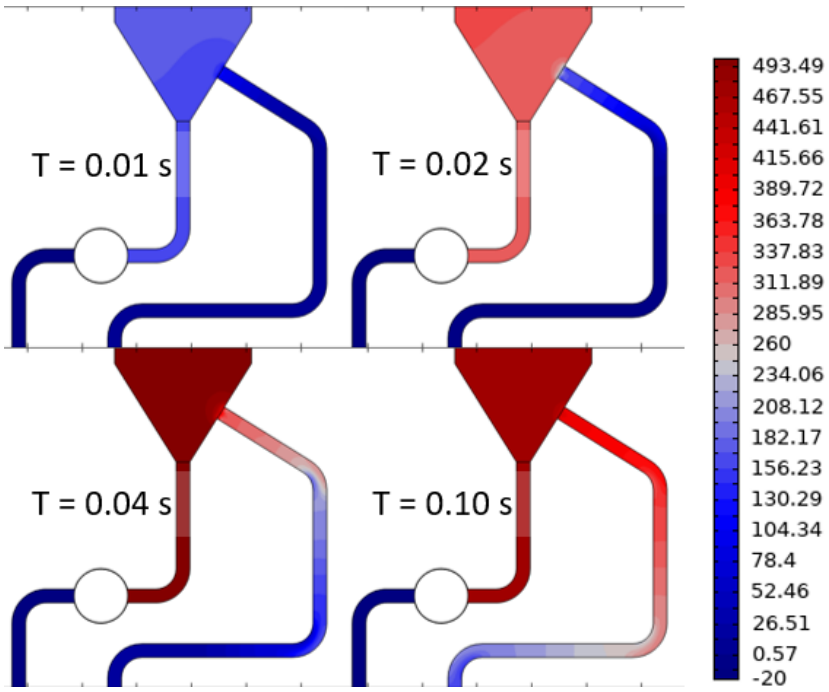

Figure 5.26 – Pressure Plot across the closed valve for Case 2

The active section of the channel (red) increased in pressure from time 0.01 – 0.04 seconds, while the inactive section of the valve (blue) remained constant. The increase in pressure along the channel on the right-hand side of the trapezoidal chamber indicated that the valve diverted the fluid flow.

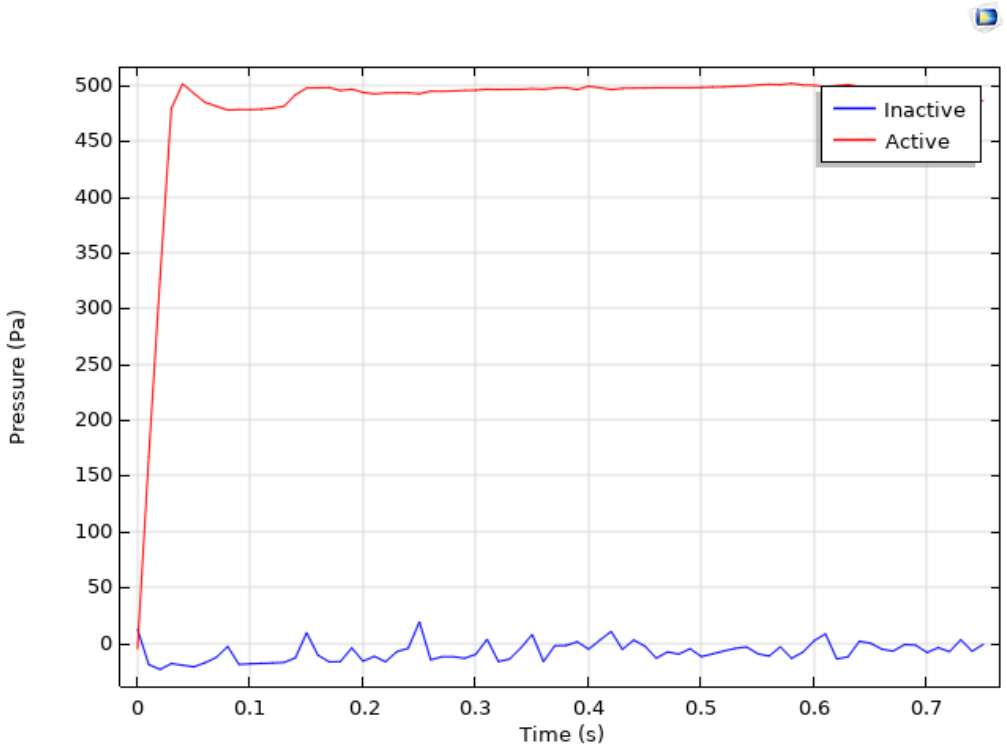

Figure 5.27 – Averaged pressure plot taken on either side of the closed valve (Case 2)

The red line represents the fluid flow across the active side of the pump, while the blue line represents the fluid flow across the inactive side of the pump

The aim was to study the impact of the valves on the fluid flow. A multiphase simulation of fluid flow through the cartridge design for 2 cases was conducted. The simulation revealed that the valve design proposed in section 4.3.5 would work for both filling the heating chamber and dispensing a discreet volume. While the results from case 2 were useful for demonstrating the ability of the valves to prevent liquid backflow from the heating chamber into the sample inlet, the results for case 1 were more substantial, as they demonstrated the ability of the valve to restrict airflow into the cartridge, which would have a greater impact on the pumping performance and the total volume drawn into the heating chamber. Due to the progression from this design to the final design idea, no further work was conducted on this simulation. Future works would include mesh refinement and the assessment of mesh independence.

5.2.6. Electrohydrodynamics

5.2.6.1. Problem Description

Many technologies require the dispensing of liquids on a micro or nanolitre scale in a precise and controlled manner. This is difficult to achieve, as the resistance caused by both the fluid viscosity and surface tension must be overcome, which requires either a large amount of energy or the integration of complex components [445]. While several thermal [446] and piezoelectric inkjet [447] methods are available, the small variation in the physical properties of the liquids hinders the direct application of these methods.

Electrohydrodynamic (EHD) spraying of liquids is a technique in which a high electrical potential is applied to the surface of a liquid continuously flowing through a thin metal capillary [448,449]. This electrical potential creates a shear stress, which causes the meniscus formed at the outlet of a capillary to elongate. This elongation expands and forms a conical shape, eventually causing the droplet formed at the capillary to detach [449]. Droplets created by EHD can be smaller than 1 µm in diameter [450]. EHD is governed by the physical properties of the liquid, such as surface tension, viscosity, density, and conductivity; as well as the physical properties of the device, such as the diameter of the capillary, the electrical potential, the dielectric strength of the ambient medium, and the liquid flow rate [449,450]. In ambient air, a potential difference of several kilovolts is required between the metal capillary and a grounded electrode with a difference of several centimetres [449,451].

EHD spraying can be conducted in several “modes” by changing either the voltage or flow rate. These modes are characterised by the changes in the geometrical form in which the liquid is expelled from the capillary. The main spraying modes are dripping and spindle modes, in which fragments of the liquid are released from the capillary; and jet mode, in which a continuous stream is released from the capillary. These modes are typically sustained within a certain voltages or flow rates and will abruptly change into other modes, or a combination of modes, should they stray outside of these ranges [449,450]. Due to the requirement of the project, only dripping modes will be discussed.

While the weight of the droplet typically overcomes capillary forces in natural dripping, a voltage may be supplied as a supplementary electrical force to overcome the capillary force, resulting in the production of much smaller droplets typically at regular time intervals [448,450]. This process is known as field enhanced dripping. The electric potential can be increased to reduce the droplet diameter and increase the dripping frequency; however, the mode will transition into a jet mode beyond a given voltage. This transition to jet modes can be offset by increasing the flow rate [452]. This increase will not increase the droplet diameter, but will increase the dripping frequency [451]. For viscous liquids, the droplet will remain connected to the meniscus by a thin thread, which will break and fragment into smaller (satellite) droplets upon the detachment of the main droplet [449].

For low flow rate configurations using liquids with a dielectric constant below 10^{-6} S/m, a micro dripping mode of EHD will occur, in which droplets smaller than the diameter of the capillary (ranging from single to hundreds of micrometres in diameter) will continuously be formed at the apex of the stable liquid meniscus [449,450]. The droplets will increase in size as the liquid accumulates before separating from the meniscus, allowing the cycle to begin again [449]. In contrast to the standard dripping mode, the meniscus does not contract towards the capillary following droplet separation [448]. However, similar to the standard dripping mode, the frequency and volume of the individual droplet production can become uniform under the right conditions, with up to tens of thousands of droplets being produced per second [449]. For viscous liquids, a short filament will form between the micro droplet and the meniscus; however, unlike the standard dripping mode, no satellite droplets are produced when the droplet is detached [450].

As demonstrated in section 3.3, a droplet size experiment was setup to determine the achievable size of droplets through standard dripping using commercially available dispenser needles. The average droplet volumes ranged from 6.24 to 35.23 µL, significantly larger than the desired droplet volume of 1 µL. Thus, for the purpose of creating precise and highly controllable micro droplets, a non-contact EHD dripping device was devised, based on work by Speranza *et al*. [451,452] and Lee *et al.* [453]. A metal dispenser needle (henceforth, referred to as a capillary) was attached to a high voltage power

supply. An electrical potential of several kilovolts was applied to the needle, with respect to a grounded metal plate which was located a distance below the capillary. This distance would be adjustable using a Z-stage controller, as described in other works [453]. The resulting electrical field would elongate and break the meniscus of a liquid droplet formed at the outlet of the capillary, causing it to detach. The liquid would be supplied to the capillary using an external fluid flow control. A simple schematic demonstrating the setup used can be seen in Figure 5.28. Despite several attempts to configure the model, all attempts to run the simulation of the EHD configuration failed to compute.

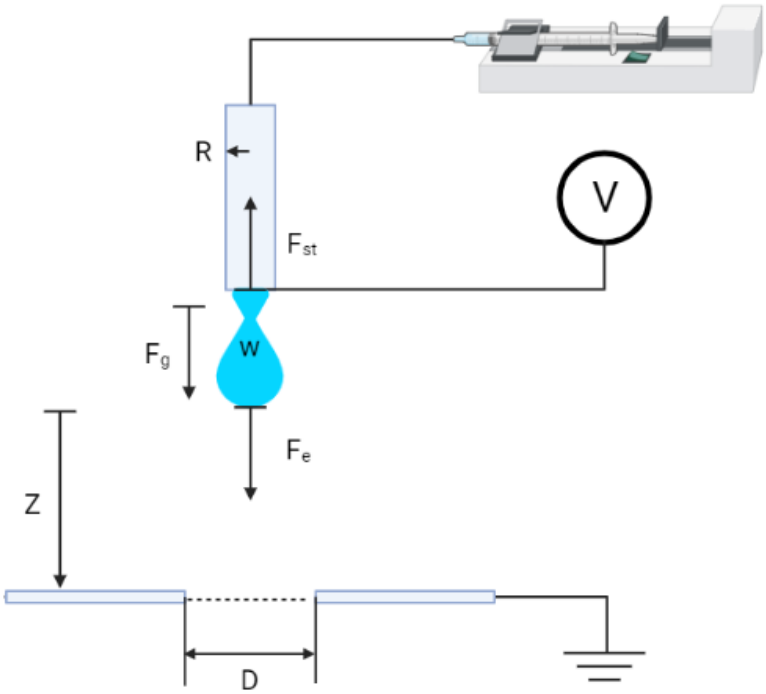

Figure 5.28 – Electrohydrodynamic Dripping Arrangement
***D** = grounded electrode hole diameter; **F_e** = electrostatic force; **F_g** = force (gravity); **F_{st}** = force (surface tension); **R** = needle radius, **V** = high voltage input, **W** = droplet diameter (neck); **Z** = distance between needle and grounded electrode*

5.2.6.2. Numerical Description

An EHD simulation was devised based on models produced by Collins *et al*. [454] and Ouedraogo *et al*. [455]. The simulation was modelled using the Electric Currents and Laminar Two-Phase Flow (Level Set) physics modules in COMSOL Multiphysics 5.5. The geometrical configuration (Figure 5.29) was designed based on the works of Speranza *et al*. [451,452], models designed by Singh and Subramanian [456]. The model simulated a liquid droplet being expelled from a capillary and through ambient air, assisted by an electric field, as shown in Figure 5.28. The orientation of the capillary axis was selected to be parallel to the direction of the gravitational acceleration, allowing the fluid flow to be modelled

in the direction parallel to gravity. This allowed the flow of the droplet to be simulated using axial symmetry about the z-axis, reducing the problem to a 2D axisymmetric model, which reduced the computational requirements.

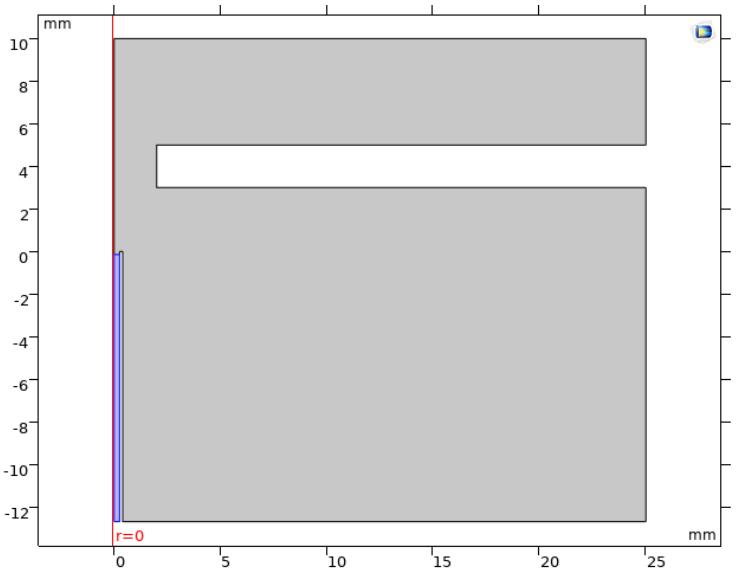

Figure 5.29 – Front View of the EHD Model Geometry (taken from COMSOL Multiphysics 5.5)
The two fluids used for this study are water (blue) and air (grey)

The valves used to define the parameters of the EHD simulation can be seen in Table 5.1. The parameters for the capillary were determined using the valves of a 25-gauge dispenser tip needle which was presented in section 3.3.3 (Table 3.3). The distance between the electrode and the capillary (Z) was set to 3 mm, providing an electric field strength of 1 kV/mm under an applied potential (E0) of 3 kV. The fluid velocity (U_out) was defined based on the area of the capillary and the flow rate (Q_out), allowing a 1 µL droplet to be dispensed over a 1 second period.

Table 5.1 – Geometry and Fluid Parameters used for the setup of the EHD model

Name	Description	Expression
D_i	Inner Diameter, Needle	0.25[mm]
D_o	Outer Diameter, Needle	0.51[mm]
r_i	Inner Radius, Needle	Di_n/2
r_o	Outer Radius, Needle	Do_n/2
A_i	Inner Area (Needle)	pi*(Ri_n^2)
A_o	Outer Area (Needle)	pi*(Ro_n^2)
Q_out	Flow Rate	1[mm^3/s]
U_out	Outlet Velocity	Q_out/A_n
E0	Electric Potential	3[kV]
Z	Distance (Needle-Electrode)	3[mm]
kappa	Conductivity	8.05e-6[S/m]

Two piecewise functions were used to define the fluid flow (pw1) and electric potential (pw2) within the model, shown in Table 5.2 and Table 5.3, respectively. Between time 0 – 1 seconds, the fluid flow would supply a droplet at a velocity of U_out, defined in Table 5.1. At 1.0 seconds, the flow would turn off, leaving a pendant droplet suspended from the dispenser needle tip. At a time of 1.5 seconds, an electric potential with a magnitude of E0 would release the pendant droplet from the needle tip.

Pw1 – Fluid Flow		
Start	**End**	**Function**
0	1	U_out
1	1.55	0

Table 5.2 – Piecewise Function for Fluid Flow

Pw2 – Electric Potential		
Start	**End**	**Function**
0	1.50	0
1.50	1.51	E0
1.51	1.55	0

Table 5.3 – Piecewise Function for Electric Potential

The two fluids used to obtain preliminary data for this setup were water and air, shown in Figure 5.29. At time 0, the needle was assumed to be completely filled with water, allowing for the 1 µL droplet to be expelled within the duration of the fluid flow piecewise function. Within the laminar flow module, an inlet (Figure 5.30) and outlet (Figure 5.31) were defined. The inlet was defined by the function pw1(t), corresponding to the piecewise function for the fluid flow. The flow profile was considered to be fully developed. A pressure outflow was selected at 0 Pa, representing the droplet being released into ambient conditions. Within the electrostatics module, a high potential (Figure 5.32) and ground (Figure 5.33) were defined. The high potential was defined by the function pw1(t), corresponding to the piecewise function for the electric potential. Finally, the effects of gravity were applied to the model to assist the formation of the pendant drop.

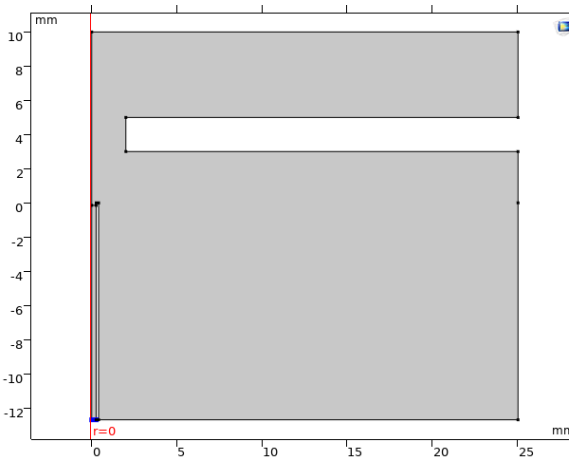

Figure 5.30 – Laminar Flow Boundary conditions (inlet)
(Fully developed flow, U_{av} = pw1(t)

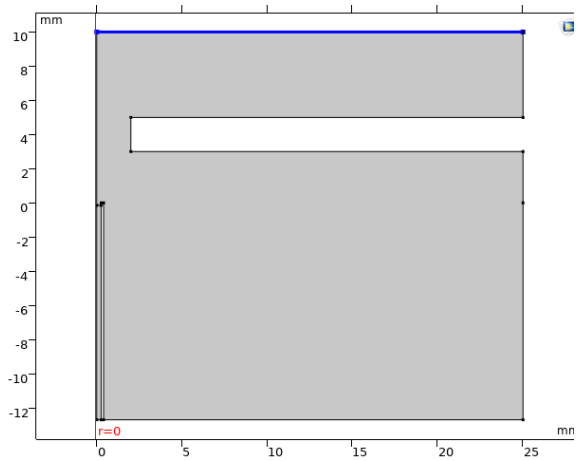

Figure 5.31 – Laminar Flow Boundary conditions (outlet)
(Pressure, P_0 = 0 Pa)

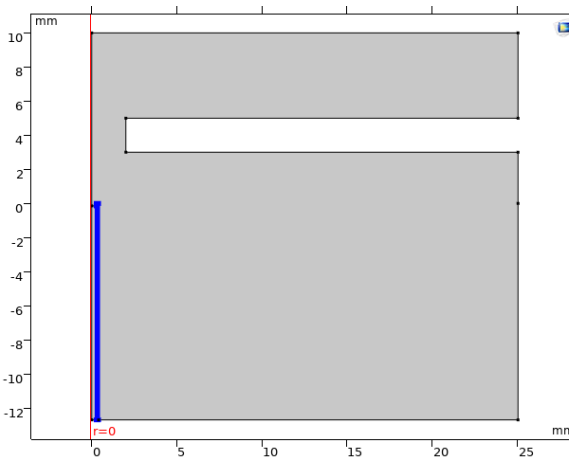

Figure 5.32 – Electrostatics Boundary conditions (Potential, V_0 = pw2(t)

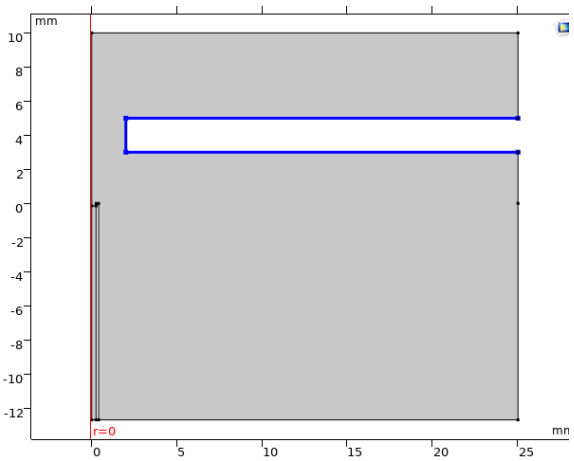

Figure 5.33 – Electrostatics Boundary conditions (Ground)

A level set function was applied to the model with a similar methodology to section 5.2.5. For this model, air was defined as ϕ = 1, while water was defined by ϕ = 0. The "two-phase flow, level set" Multiphysics module was then introduced to couple the laminar flow fluid model to the level set moving interface. Surface tension was included for the model, defined by a liquid/gas interface of water/air. Finally, a "Wetted Wall" Multiphysics module was introduced to define the contact angle and Navier slip length. The contact angle was defined as pi/2 radians and the Navier slip length was defined as h, an internal variable within COMSOL. By setting the Navier slip length to the element size h, the subsequent model mesh became independent.

Following the drafting of mesh control lines in the model geometry, a Free-triangular user-controlled mesh was constructed for the model using the parameters shown in Table 5.4. The curvature factor was used to define the size of mesh elements along a curved boundary, and the resolution of narrow regions was used to define the size of mesh elements within narrow regions. The corresponding meshes can be seen in Figure 5.34 – Figure 5.37, with a fully constructed mesh shown in Figure 5.38.

Table 5.4 – User-controlled mesh parameters

	Size 1	Size 2	Size 3	Size 4
Maximum Element Size (mm)	0.1	1.02	0.795	0.0152
Minimum Element Size (mm)	0.000454	0.0454	0.0227	*Sequence*
Maximum Element Growth Rate	1.05	1.15	1.13	*Sequence*
Curvature Factor	0.2	0.3	0.3	*Sequence*
Resolution of Narrow Regions	1	1	1	*Sequence*

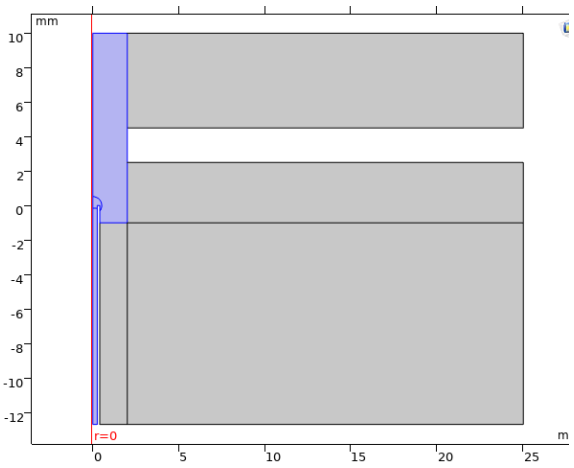

Figure 5.34 – Mesh Definition (Size 1)

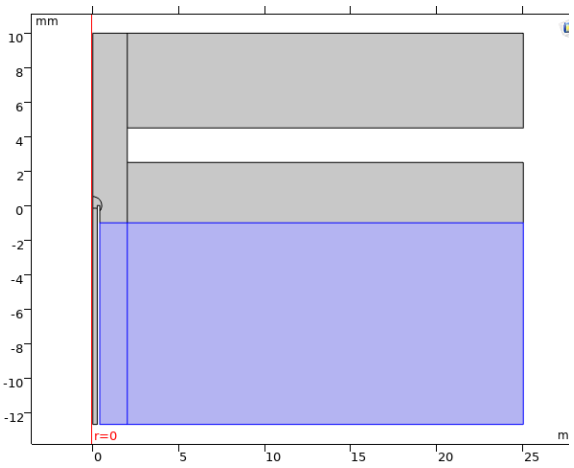

Figure 5.35 – Mesh Definition (Size 2)

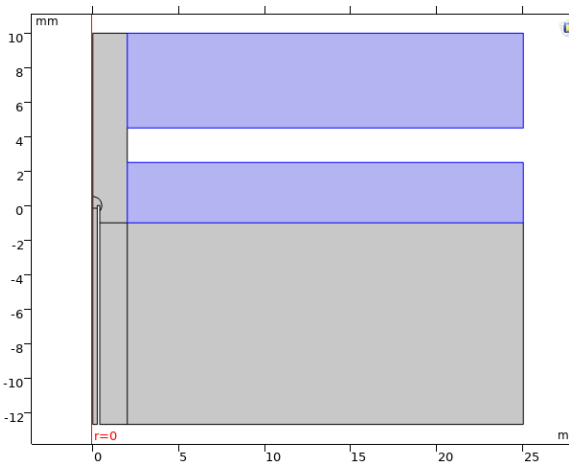

Figure 5.36 – Mesh Definition (Size 3)

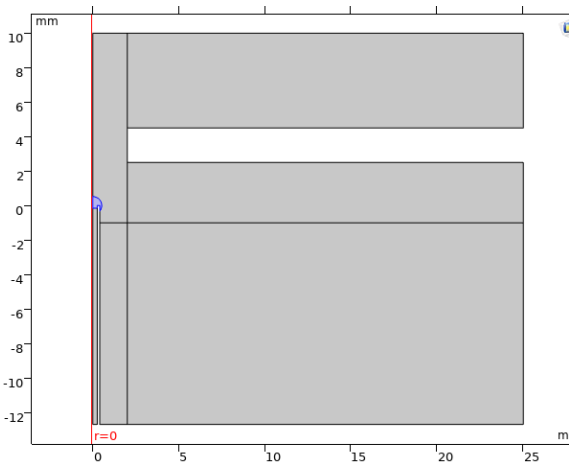

Figure 5.37 – Mesh Definition (Size 4)

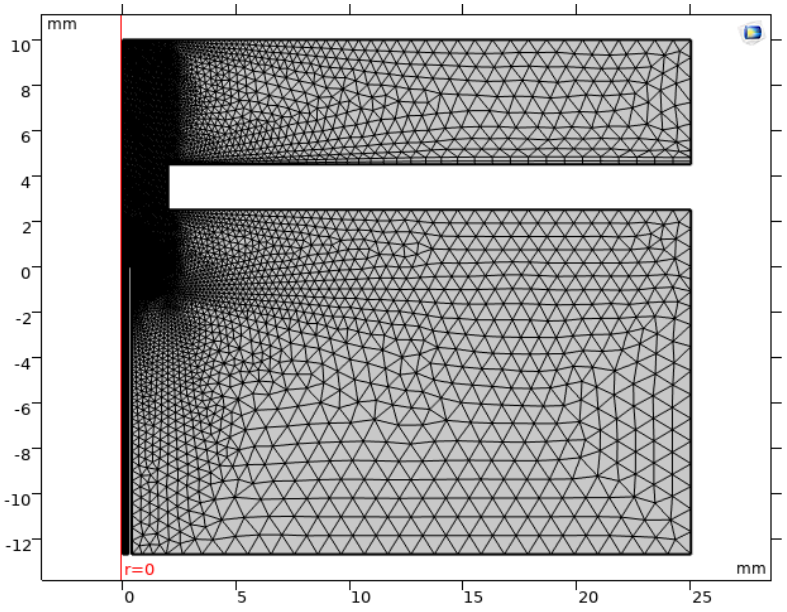

Figure 5.38 – Fully constructed Mesh

5.2.6.3. Discussion

A time dependant study in 1 millisecond increments between 0 and 1.55 seconds was initialised, solving for the Volume of Fluid, the Velocity and the Pressure. Despite extensive efforts, this model was unable to provide a solution for the full 1.55 seconds. Following the initiation of the piecewise function shown in Table 5.3, the droplet would begin to elongate as expected; however, artefacts would appear across the domain and the simulation would fail to converge, as shown in Figure 5.39. As a result, the performance of the EHD platform could not be optimised using this model and the dripping conditions for the module demonstrated in section 6.4.1 would be determined experimentally.

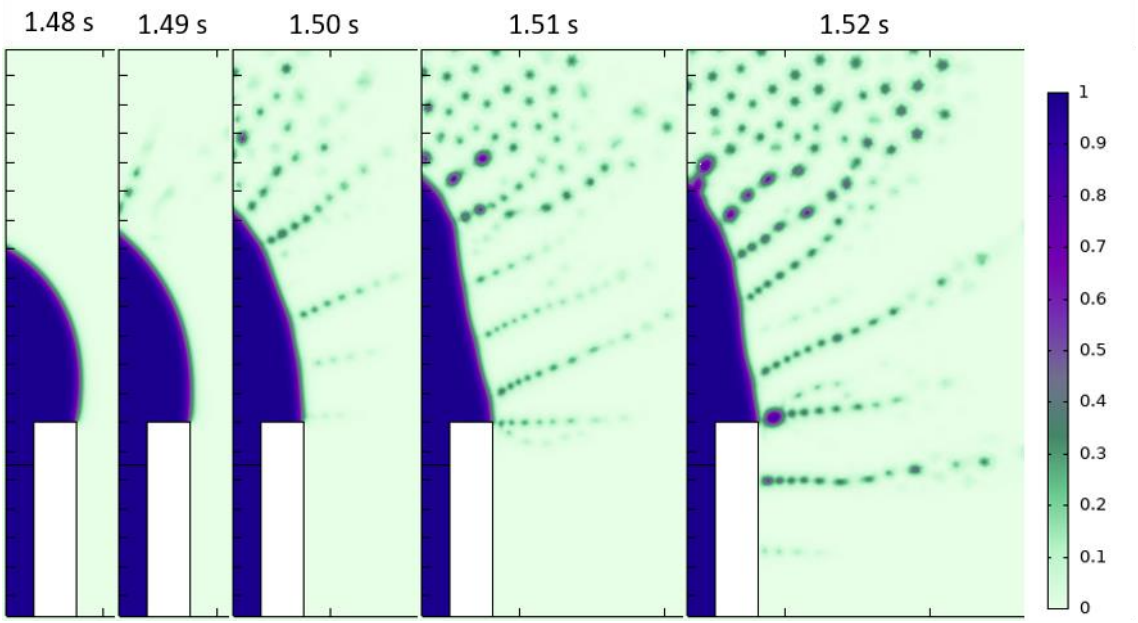

Figure 5.39 – Volume fractions of fluid for Electrohydrodynamic Model (t = 1.48 – 1.52 s)
Refer to the figure legend for interpretation. 1 = water, 0 = air

5.3. Structural Analysis

5.3.1. An Introduction to Structural Analysis

Structural analysis is a set of mechanical theories used to examine the influences of loads on physical components and structures. By analysing the geometry of the component in addition to mechanical properties of the material that component is comprised of, engineers can determine the resulting deformations, stresses, support reactions and internal forces when that component is subjected to a load. This can be used as a preface to physical testing to predict if and where the component will fail, while also studying the effects of vibration, fatigue and other mechanical factors [457].

5.3.2. Classifications and Governing Equations

5.3.2.1. Normal and Shear Stresses

In many cases of structural analysis, the assumption of a linear relationship between stress and strain is made. In this instance, materials are referred to as *elastic*. The assumption is also made that the material is isotropic, exhibiting identical behaviour independent of the direction of the applied force [457]. While not a completely accurate representation of real-world behaviour, these assumptions may be used for calculations that provide a reference point for complex structural problems.

Stress (σ_S) is an external or internal force exerted on a body. There are three major categories of stresses: tensile stresses, where the applied forces "pull" the molecules apart; compressive stresses, where the forces "push" the molecules together; and shear stresses, where the forces cause the molecules to slide against each other. Normal stresses are forces which act in a direction parallel to the x, y and z axes, denoted by the terms σ_x σ_y and σ_z, respectively. Shear (tangential) stresses (τ_S) are forces acting in a direction parallel to the plane which are the summation of the two components acting along the surface in the y and z directions, denoted by the terms τ_{xy} and τ_{xz}, respectively [458].

5.3.2.2. Yield Stress and von Mises Stress

The strength of a material is determined by its ability to resist the effects of loading. A material may be subjected to axial stress (tensile or compressive), shear stress, bending and torsion [457]. When a

mechanical structure is subjected to an increasing load, the stress experienced by that structure will increase, eventually reaching a state where the structure strength will be exceeded. The structure will no longer undergo elastic deformation and will instead undergo *plastic* (permanent) deformation. This phenomenon is referred to as yielding. Stress can be significant even if deformation is negligible or non-existent; and thus, determining the maximum allowable load a structure can resist is vital [458]. In structural analysis, the yield criterion is often represented by the yield stress (σ_{ys}). By assuming the structure is subject to uniaxial stress, a stress term known as the von Mises stress (σ_{vM}) may be introduced, shown in Equation 5.14. The material will undergo elastic failure (plastic deformation) when the von Mises stress exceeds the yield stress [458].

$$\sigma_{vM} = \sqrt{0.5\left[\left(\sigma_x - \sigma_y\right)^2 + \left(\sigma_y - \sigma_z\right)^2 + (\sigma_z - \sigma_x)^2\right]} \quad \text{[Pa]} \qquad \textit{Equation 5.14}$$

5.3.2.3. Deflection and Displacement

The susceptibility of a material to deflection under a load is determined by its stiffness (k). The structural stiffness is dependent on the material properties and the physical geometry. If the applied load exceeds the structural stiffness, the structure will undergo deflection (δ) along a length (L) across which the load is applied. Depending on whether axial or bending forces are applied, the structure will undergo axial or bending deflection, respectively [457].

5.3.2.4. Factor of Safety

While structures are designed to support an expected load (the yield stress), factors such as fatigue from crack propagation or cyclic loading, manufacturing errors or material inconsistencies can lead to unexpected failures at a given load (the working stress). Thus, a factor of safety (FoS) is typically applied to ensure that the working stress experienced by the structure will never approach the yield stress, reducing the statistical likelihood of failure. The FoS may be calculated using Equation 5.15. A FoS of 1 will have a maximum working stress equal to its yield stress, while a FoS greater than 1 will be have a maximum working stress that many times smaller than its yield stress.

$$Factor\ of\ Safety\ (FoS) = \frac{Yield\ Stress}{Working\ Stress} \qquad \textit{Equation 5.15}$$

5.3.3. Membrane Valve Designs

5.3.3.1. Problem Description

Active components are used in microfluidic applications to facilitate fluid flow control [399]. Many microfluidic valves are composed of passive components, preventing controllability over the process [396]. While it is possible to develop active alternatives, these require access to expensive fabrication facilities and substantial engineering expertise [397]. As discussed in Chapter 3, 3D printing can be used to yield versatile microvalves without the requirement for specialised manufacturing facilities, making rapid prototyping accessible [399].

The aim was to develop a valve design compatible with the SCD presented in section 4.3.5 which would allow for fabrication using 3D printing in a single step. Following the assessment of the fluidic performance in section 5.2.5, a valve design was developed, shown in Figure 5.40. When pressure was supplied to the control channel, the membrane deformed in the direction of the fluidic channel, closing the valve. When the control pressure was reduced, the membrane returned to its original position, opening the valve. This design underwent FEA testing to determine whether functional prototypes could be fabricated with the manufacturing methods available.

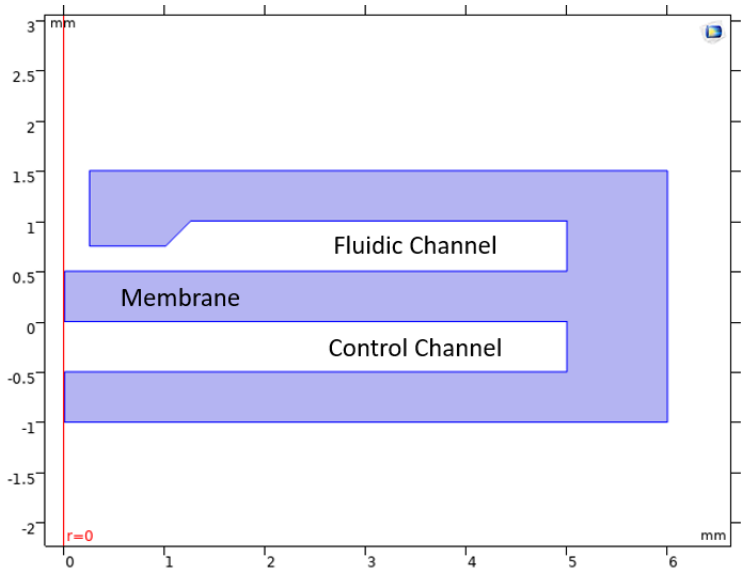

Figure 5.40 – Valve Design imported on COMSOL Multiphysics 5.5

5.3.3.2. Numerical Simulation

The valves were designed for fabrication using the three 3D printers shown in Table 5.5. To achieve an accurate comparison between the 3D printing techniques, each valve started with a membrane thickness of 0.5 mm, which was reduced in increments of 0.1 mm until the valve closed with a supplied pressure. In order to close each valve, the membrane needed to deflect a distance of 0.25 mm. All dimensions of the fluid and control channels were kept consistent between the valve designs to standardise results between comparisons. It was determined that the in house Ultimaker 2+ (Utrecht, Netherlands) yielded average layer heights of 0.12 mm and the minimum number of layers the software could print was 3. Thus, the minimum height of the membrane developed by the Ultimaker 2+ would be 0.36 mm, while its maximum height would be 0.48 mm.

Table 5.5 – Information on the Available 3D Printing Techniques
FDM, Fusion Deposition Modelling; SLA, Stereolithography; PLA, Polylactic acid; TPU, Thermoplastic polyurethane

	Method	Layer Height (µm)	Materials	REF
Ultimaker 2+	FDM	60 – 150 (0.25 mm nozzle) 20 – 200 (0.4 mm nozzle)	• PLA • TPU	[459]
3D Systems Viper	SLA	20 – 100	• Accura Xtreme	[460]
Stratasys Objet30	SLA	28	• VeroClear Resin	[461]

The model was setup as a 2D axisymmetric Solid Mechanics model, to be studied as a stationary flow problem. The schematic for the membrane valves of each thickness were designed in Solidworks 2019 and imported into COMSOL Multiphysics 5.5 as .dxf files. The materials tested during this experiment were inserted as blank materials, using the material properties shown in Table 5.6. A boundary load was applied across the top of the control channel, representative of the pressure force supplied by the control channel. The boundary load was increased until the valve closed or until the maximum allowable working stress was reached. To ensure that the valves would not operate near the yield strength of the material, a factor of safety of 1.5 was used. The simulation was run and the resulting von Mises stress and deformation plots were observed.

Table 5.6 – Material Properties used for the COMSOL Solid Mechanics simulation
PDMS, Polydimethylsiloxane; TPU, Thermoplastic polyurethane

Material	Modulus of Elasticity (MPa)	Poisson's ratio (-)	Density (kg/m^3)	Yield Stress (MPa)	REF
PDMS	0.75	0.49	970	0.7	[462]
TPU	26	0.48	1220	8.6	[463]
VeroClear	2000 – 3000	0.38	1160	50 – 65	[464]
Accura Xtreme	1790 – 1980	0.35	1190	38	[465]

5.3.3.3. Results and Discussion

A membrane valve was designed on Solidworks 2019 and analysed using the Solid Mechanics module in COMSOL Multiphysics 5.5 [466]. In order to establish a reference point and to determine mesh independence, the simulation was first performed using PDMS, using physics-controlled meshes with element sizes ranging from "extremely coarse" to "extremely fine". A plot of the maximum displacement against element size was generated, which can be seen in Figure 5.41. The solution obtained mesh independence at approximately 2000 elements, corresponding with the extra fine mesh. Thus, an extra fine mesh was used to obtain results for the subsequent simulations.

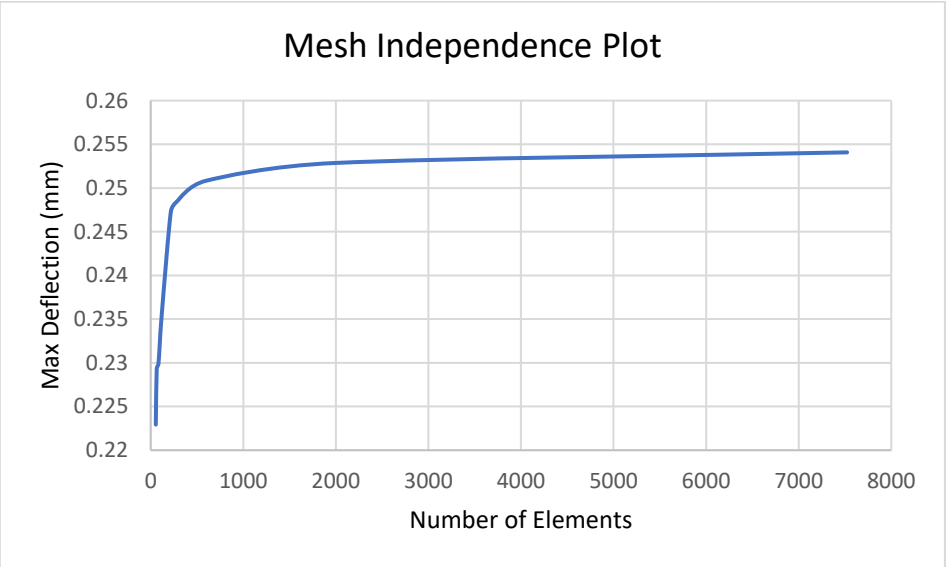

Figure 5.41 – Displacement convergence plot using the PDMS membrane valve Mesh independence was obtained at approximately 2000 elements

Due to the application of a factor of safety of 1.5 for the membrane valve structure, the maximum von Mises stress for the PDMS, TPU, VeroClear and Accura Xtreme valves were 0.46, 5.73, 33.3 and 25.3 MPa, respectively. The results for the initial valves which successfully closed under an applied pressure without meeting the maximum working stress can be seen in Figure 5.42 – Figure 5.45.

The PDMS valve successfully closed at a membrane thickness of 0.5 mm when supplied with a 0.22 kPa pressure from the control channel. The maximum von Mises stress exerted on the valve was 0.0213 MPa, significantly below the yield stress. The FoS was 32.86. The TPU 95A membrane successfully closed at a membrane thickness of 0.48 mm with a pressure supply of 6.7 kPa. The maximum von Mises Stress exerted on the valve was 0.697 MPa. The FoS of 12.34. The Accura Xtreme membrane successfully closed at a membrane thickness of 0.3 mm with a pressure supply of 110 kPa.

The maximum von Mises Stress exerted on the valve was 25.4 MPa. The FoS of 1.5. The VeroClear membrane also successfully closed at a membrane thickness of 0.2 mm with a pressure supply of 46 kPa. The maximum von Mises Stress exerted on the valve was 19.8 MPa, resulting in a FoS of 2.53.

Based on similar works by Au *et al.*, the pressure required to fully seal the valve was double the value required for its closure [397]. Thus, each simulation was repeated with a pressure value twice the magnitude of what was required to close the valve. With a supply pressure of 0.44 kPa, the PDMS valve experienced a maximum von Mises Stress of 0.0416 MPa, resulting in a FoS of 16.83. Thus, no further optimisations of the PDMS valve was deemed necessary. The TPU 95A membrane valve successfully sealed with a supply pressure of 12.7 kPa, resulting in a maximum von Mises stress of 1.398 MPa. The resulting FoS was 6.15, and thus, no further optimisations were necessary.

The Accura Xtreme membrane would require a 220 kPa pressure supply to fully seal, which resulted in a maximum von Mises stress of 51.67 MPa, above the yield strength of the material. Thus, the membrane was reduced to a thickness of 0.2 mm, where a 33.7 kPa pressure was required to close the valve, resulting in a maximum von Mises stress and FoS of 14.81 MPa and 2.57, respectively. To seal the valve, a pressure supply of 67.4 kPa was used, resulting in a maximum von Mises stress of 29.61 MPa. While this was below the yield stress of the material, the resulting FoS was 1.28, and thus, the valve design was not considered viable. The VeroClear membrane experienced a 39.6 MPa von Mises stress when subject to the pressure supply of 92 kPa required to seal the valve. As a result of the FoS (1.26) being below the desired value, this valve design was also considered to be unviable.

The pressure (p) required to yield the desired displacement (y) was approximated using Equation 5.16, where E is the Modulus of Elasticity, v is the Poisson's ratio and r_m and t_m are the radius and thickness of the membrane, respectively [458]. A comparison between the predicted results and the results from the simulation performed on COMSOL can be seen in Figure 5.46 – Figure 5.49. The predicted results ranged from 1.34 to 1.92 times larger than the values calculated by the COMSOL simulation at the lower and upper values, respectively; however, the trend of the predicted and calculated values agrees with each other.

$$p = \frac{E{t_m}^4}{{r_m}^4}\left[\frac{5.33}{1-\nu^2}\cdot\frac{y}{t_m}+\frac{2.6}{1-\nu^2}\cdot\left(\frac{y}{t_m}\right)^3\right] \quad \text{[Pa]} \qquad \textit{Equation 5.16}$$

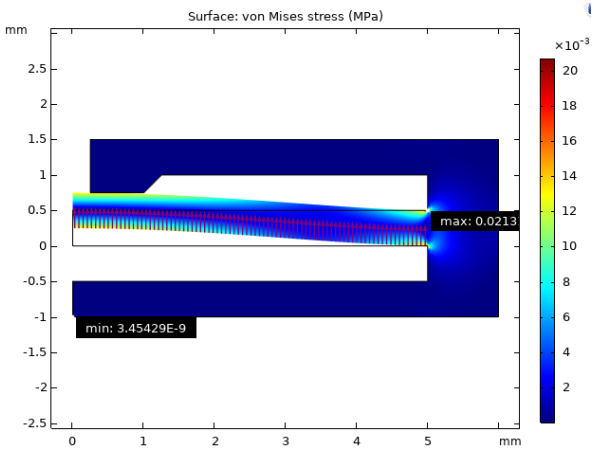

Figure 5.42 – Stress and deformation profile for the PDMS membrane valve (0.5 mm)
The desired deflection was obtained at a pressure force of 0.22 kPa. The maximum von Mises Stress was 0.0213 MPa

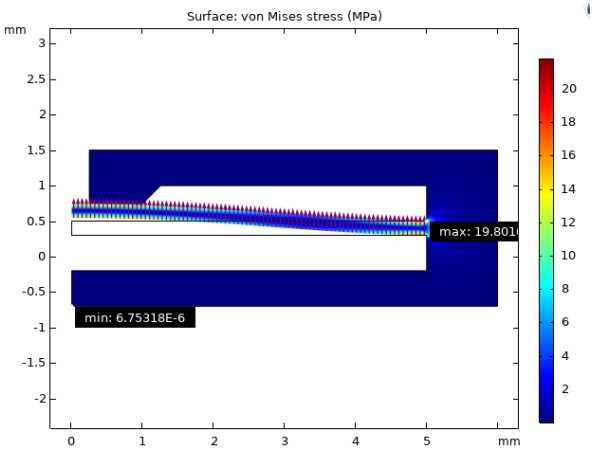

Figure 5.43 – Stress and deformation profile for the VeroClear membrane valve (0.2 mm)
The desired deflection was obtained at a pressure force of 46 kPa. The maximum von Mises Stress was 19.8 MPa

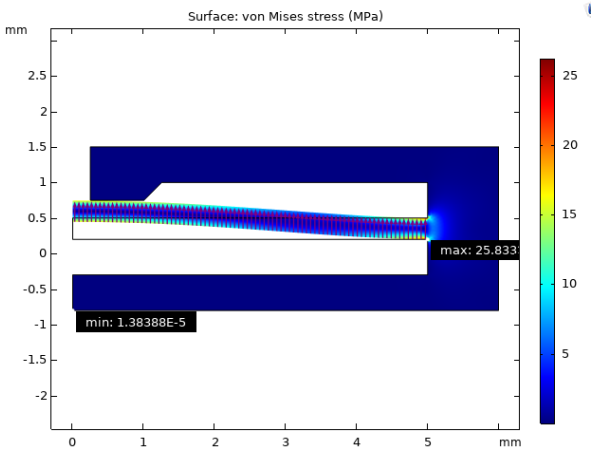

Figure 5.44 – Stress and deformation profile for the Accura Xtreme membrane valve (0.3 mm)
The desired deflection was obtained at a pressure force of 110 kPa. The maximum von Mises Stress was 25.4 MPa

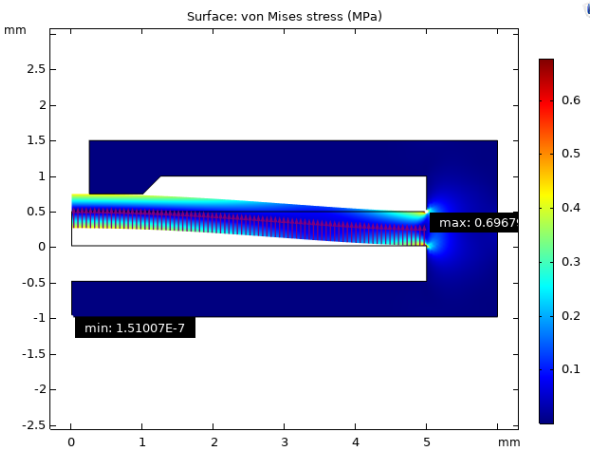

Figure 5.45 – Stress and deformation profile for the TPU 95A membrane valve (0.48 mm)
The desired deflection was obtained at a pressure force of 6.7 kPa. The maximum von Mises Stress was 0.697 MPa

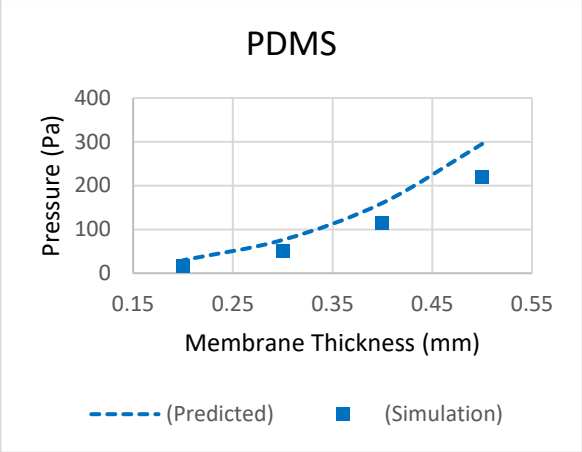

Figure 5.46 – Pressure required to close a membrane valve (PDMS)

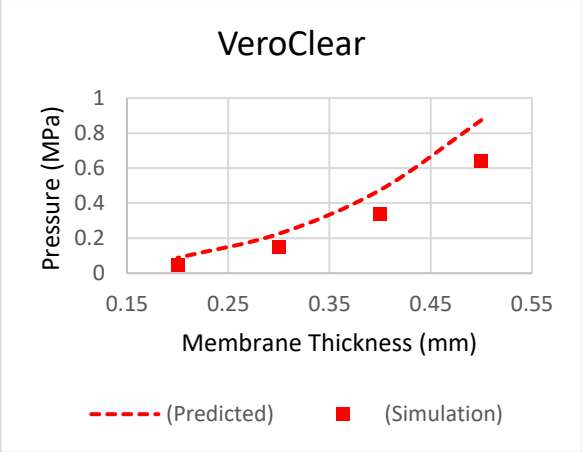

Figure 5.47 – Pressure required to close a membrane valve (VeroClear)

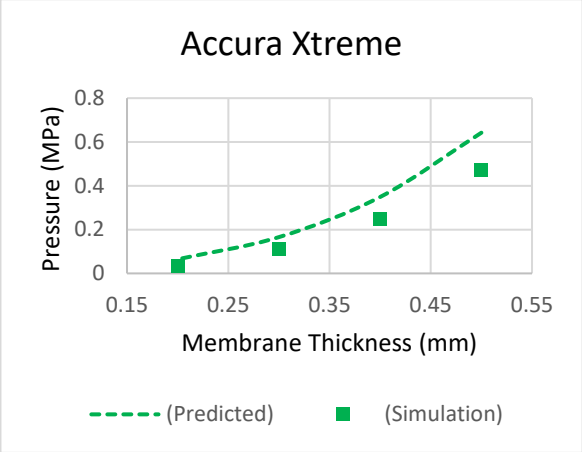

Figure 5.48 – Pressure required to close a membrane valve (Accura Xtreme)

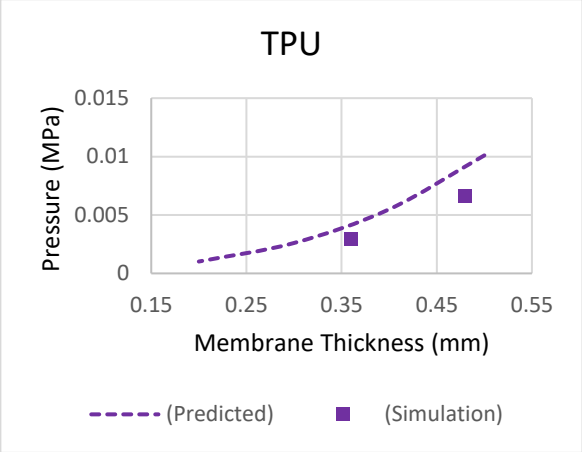

Figure 5.49 – Pressure required to close a membrane valve (TPU 95a)

Works have gone into the development of active components for improved control on a microfluidic scale. Au *et al.* fabricated a microvalve design using an SLA 3D printer. The valve featured a control chamber beneath the fluid chamber, which would fill with pressurised air to deflect the roof of the control chamber (henceforth, referred to as a membrane). This membrane was 10 mm in diameter and 100 µm in thickness. When a pressure of ~40 kPa was supplied to the control chamber, the membrane would deflect a distance of 200 µm and seal the fluid chamber. This valve design incorporated Luer-lock connectors increase modularity. Additionally, by placing the valves in series, could be used to form switches and micropumps [397]. Through a comparison against the results of the SLA valves presented in this section, the Accura Xtreme valve was able to close and seal with a lower pressure of 33.7 kPa at double the membrane thickness. Despite the results for the Accura Xtreme not meeting the desired FoS, the ability to design and fabricate valves with lower resolution requirements and a similar performance widens the overall accessibility.

In a similar approach, Rogers *et al.* also developed a pressure-controlled valve which offered consistent performance for up to 800 actuations which could be printed on an SLA printer in under and hour [396]. The device featured membranes 2 mm in diameter and less than 140 µm in thickness. When the control chamber was supplied with a pressure of ~74 kPa, the membrane would deflect a distance of 250 µm to close the valve. Future works would attempt to design valves of a comparable size to determine how the materials tested will perform on a smaller scale.

By analysing the pressure plots from section 5.2.5 for case 1 and case 2 (Figure 5.23 and Figure 5.27), the pressure the fluid exerted on the closed valve ranged from –1 to 0.5 kPa. Thus, the pressure required to seal the PDMS valve would be insufficient. While the integration of the valve designs presented in this section into the fluid flow model shown in section 5.2.5 would be the next logical stage of research, this was not achieved during the allotted time.

5.4. Heat Transfer Modelling through Joule Heating

5.4.1. An Introduction to Heat Transfer

Heat transfer is used to study the effects of thermal energy and how thermal energy may be generated by and exchanged between components [467]. Heat transfer in engineering may be used to study the flow of heat due to temperature differences. By studying the physical properties of a material, such as thermal conductivity, heat capacity, density and emissivity, common engineering problems involving heat generation, cooling, insulation, and phase changes, can be solved.

5.4.2. Classifications and Governing Equations

The study of heat transfer is commonly conducted within a defined body or between defined bodies, referred to as a thermodynamic system, which can be defined into three categories: open, closed and isolated systems. An open system is a system in which matter and energy may be transferred between the system and its surroundings. A closed system is a system in which matter may not be transferred between the system and the surroundings; however, energy may be gained by or lost to the surroundings. An isolated system is a type of closed system where neither energy of matter is transferred between the system and its surroundings. Heat transfer can be considered as a transfer of momentum and energy through three main mechanisms: conduction, convection and radiation.

5.4.2.1. Conduction

Conduction entails the exchanging of thermal energy between adjacent molecules by physical contact. When a system at a higher temperature comes into contact with a system at a lower temperature, thermal energy will be shared in the form of kinetic energy from the high temperature system to the low temperature system to bring the two systems into a state of thermal equilibrium. While conduction occurs within fluids, they are less conductive than solids due to a lower density of particles. For steady-state conduction within a system, the thermal energy entering into the system will equate to the thermal energy exiting the system, resulting in no net temperature changes. For transient conduction, the temperature changes as a function of time. The rate of heat energy transferred through conduction ($\dot{\Phi}_{cond}$) with a time, t, can be seen in Equation 5.17, where Φ_{cond} is the heat energy, κ is the thermal conductivity of the material, A is the area across which the heat is being conducted,

ΔT is the difference between the high (T_{hot}) and cold (T_{cold}) temperatures and Δx is the distance the heat is travelling in the x-direction. By dividing through by the area, the expression in terms of the heat flux ($\dot{\phi}_{cond}$) is given, shown in Equation 5.18 [467].

$$\dot{\Phi}_{cond} = \frac{d\Phi_{cond}}{dt} = -\kappa A \frac{\Delta T}{\Delta x} = -\kappa A \frac{(T_{hot} - T_{cold})}{(x_2 - x_1)} \quad [\mathrm{W}] \quad \textit{Equation 5.17}$$

$$\dot{\varphi}_{cond} = \frac{\Phi_{cond}}{A} = -\kappa \frac{(T_{hot} - T_{cold})}{(x_2 - x_1)} \quad [\mathrm{W/m^2}] \quad \textit{Equation 5.18}$$

It should be noted that the aforementioned conduction equation considers flow in one direction and flow of heat through a system in all three coordinate directions is expressed as shown in Equation 5.19, where $\hat{\imath}$, $\hat{\jmath}$ and $\hat{k}$ are the unit vectors in the x, y and z directions, respectively.

$$\dot{\varphi}_{cond} = -\kappa \left(\frac{\partial T}{\partial x}\hat{\imath} + \frac{\partial T}{\partial y}\hat{\jmath} + \frac{\partial T}{\partial z}\hat{k} \right) \quad \textit{Equation 5.19}$$

5.4.2.2. Convection

Convection is the dominant form of heat transfer in fluids, entailing the dissipation of thermal energy through interaction with a solid at a different temperature to bring the fluid to a state of thermal equilibrium. In contrast to conduction, where thermal energy is shared through kinetic energy, convection relies on mass transfer which occurs as a fluid moves away from a heat source, transporting energy with it. Convection can be characterised as natural or forced. For natural convection, the fluid mass transfer occurs as a result of buoyancy forces created through temperature differences across the fluid. For forced convection, the fluid mass transfer is governed by an external control [467]. By considering the mass-density-volume equation (Equation 5.20), the mechanics of convection can be clarified. By assuming a constant mass, an inversely proportional relationship between the density and the volume can be observed. As a fluid gains heat, the volume will increase, and as a result, the density will decrease. Thus, the hotter fluid will ascend, while the colder and more dense fluid will descend. It should be noted that water between 0 and 4 °C will initially contact when it is heated up; however, this was not taken into consideration as it was assuled that the device would operate within ambient temperatures of 10 – 20 °C.

$$\rho = \frac{m}{V} \quad \textit{Equation 5.20}$$

The equation for the rate of heat transfer through convection ($\dot{\Phi}_{conv}$) can be seen in Equation 5.21 and Equation 5.22, where h_c is the convective heat transfer coefficient and T_s and T_f are the temperatures of the solid surface and the fluid, respectively.

$$\dot{\Phi}_{conv} = h_c A \Delta T = h_c A (T_s - T_f) \quad [\mathrm{W}] \quad \textit{Equation 5.21}$$

$$\dot{\varphi}_{conv} = h_c \Delta T = h_c (T_s - T_f) \quad [\mathrm{W/m^2}] \quad \textit{Equation 5.22}$$

5.4.2.3. Radiation

Radiation is the emission of heat energy from the surface of an object at a temperature above absolute zero in the form of electromagnetic energy. Radiation originates from the centre of the object and travels in an outwards direction from its origin. Heat transfer through radiation is calculated based on the concept of a "black body", an ideal radiator which absorbs all electromagnetic radiation at its surface. As a result, no radiation is reflected or transmitted. Based on the assumption of a black body in a vacuum, the rate of radiation emission ($\dot{\Phi}_{rad}$) can be calculated, shown in Equation 5.23, where ε is the emissivity, σ_{SB} is the Stefan-Boltzmann constant, A is the surface area of the black body and T is the absolute temperature of the black body. For a black body, the emissivity is equal to 1; however, for real objects, the emissivity varies based on the surface characteristics, temperature, the wavelength of the emitted radiation and the angle at which the wave is emitted [467].

$$\dot{\Phi}_{rad} = \varepsilon \sigma_{SB} A T^4 \quad [\mathrm{W}] \quad \textit{Equation 5.23}$$

When radiation is transferred between two objects at different temperatures, the net rate of energy transfer can be determined through the use of Equation 5.24, where F_f is the view factor between the two surfaces a and b, and T_a and T_b are the absolute temperatures for the two objects [468].

$$\dot{\Phi}_{rad(a-b)} = \sigma_{SB} F_{f(a-b)} (T_a{}^4 - T_b{}^4) \quad [\mathrm{W}] \quad \textit{Equation 5.24}$$

5.4.2.4. Joule Heating

Joule heating, also known as resistive heating, is a type of conductive heating process in which heat is generated by passing an electric current through an electrical conductor. By applying a potential difference between two points of a conductor, internal charge carriers accelerate and gain kinetic

energy, which causes thermal energy to be generated [469]. While Joule heating is achievable through both direct (DC) and alternative (AC) current, only DC will be considered in the scope of this thesis. Equation 5.25 demonstrates the relationship between the power generated by the conductor (P), the voltage drop across the conductor (E_A is the initial voltage, E_B is the final voltage) and the current (I) flowing through the conductor. Assuming that the circuit is grounded, then E_B will be equal to zero.

$$P = I(E_A - E_B) \xrightarrow{at\ E_B=0} P = I \cdot E \quad [W] \qquad \textit{Equation 5.25}$$

Through the examination of Ohm's law (Equation 5.26), where R is the resistance of the conductor, a relationship between the power and the resistance can be observed by substituting Equation 5.26 into Equation 5.25, as shown in Equation 5.27.

$$E = I \cdot R \quad [V] \qquad \textit{Equation 5.26}$$

$$P = I \cdot E = I \cdot (I \cdot R) = I^2 \cdot R \quad [W] \qquad \textit{Equation 5.27}$$

The resistance of the conductor may be calculated as shown in Equation 5.28, where ρ_R is the resistivity of the conductor, L is the length of the conductor between the two points of electrical potential application and A is the cross-sectional area of the conductor.

$$R = \frac{\rho_R L}{A} \quad [\Omega] \qquad \textit{Equation 5.28}$$

The amount of heat generated by the conductor can be calculated as shown in Equation 5.29, where Φ_{net} is the net heat generated after a time, t.

$$\Phi_{net} = P \cdot t \quad [W] \qquad \textit{Equation 5.29}$$

The change in temperature may then be calculated as shown in Equation 5.30, where c_p is the specific heat of the material at constant pressure and m is the mass of the conductor.

$$\Delta T = \frac{\Phi_{net}}{c_p m} \quad [K] \qquad \textit{Equation 5.30}$$

5.4.3. Heating Design Using Nichrome Wire

5.4.3.1. Problem Description

As part of the preliminary work conducted into the development of a heating system for design idea 2, proposed in section 4.3.3, a low-cost heater was designed (Figure 5.50). 30 Gauge AWG nichrome wire (30 cm, 0.254 mm outer diameter; Sourcingmap, China) was used as a resistive heating element, which would supply heat to a copper tube (25 mm x 15 mm outer diameter, 13.4 mm inner hole) through joule heating. The copper tube in turn would provide a uniform heat distribution across a 3D printed reagent capsule. Hi-Bond HB830 Amber Electrical Tape (RS Components, Corby, England) was placed between the nichrome wire and the copper tube to prevent an electrical short.

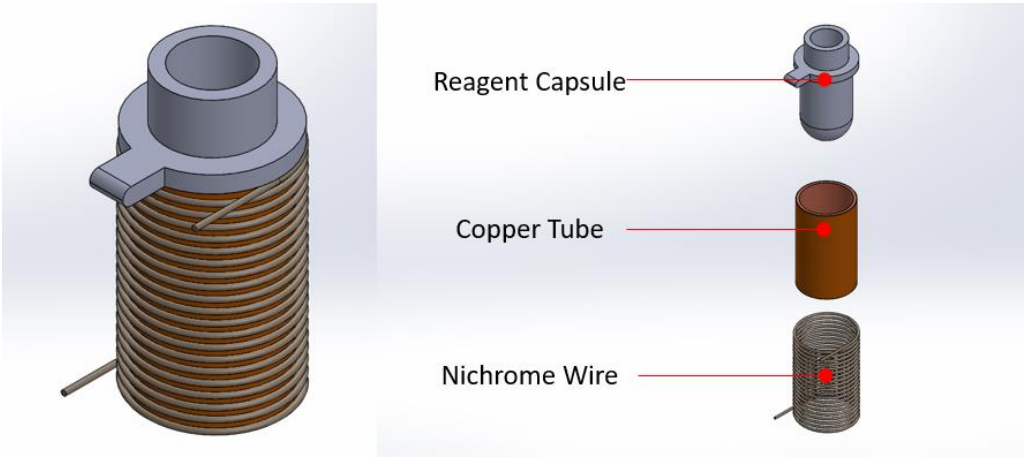

Figure 5.50 – A low-cost heating system devised for Design Idea 2

The energy requirements to heat both the copper tubing and the reagent capsule (assumed to be polyethylene) can be approximated using Equation 5.30. The mass estimates were taken from Solidworks 2019, while the specific heat capacities were taken from COMSOL Multiphysics 5.3. These values can be seen in Table 5.7. The electrical tape was assumed to be negligible for simplification.

Table 5.7 – Properties used for the calculation of the energy requirements (Design Idea 2)

Material	Mass (g)	Specific Heat Capacity (J/kg K)
Copper Tube	≈7.468	385
Polyethylene Capsule	≈1.517	1900

The temperature change was assumed to be 60 °C, to account for ambient temperature fluctuations which may prevent the platform from reaching the desired temperature. Using Equation 5.30:

$$\Phi_{net} = mc_p\Delta T = \left(mc_p\Delta T\right)_{Copper\ Tube} + \left(mc_p\Delta T\right)_{Polyethylene\ Capsule}$$
$$= [385x(7.468x10^{-3})x60] + [1900x(1.517x10^{-3})x60]$$
$$\Phi_{net} = 345.45\ J$$

The power required to produce the total heat energy was then calculated using Equation 5.29. The time chosen to reach the desired temperature was 2 minutes (120 seconds), and thus:

$$P = \frac{\Phi_{net}}{t} = \frac{345.45}{120} = 2.88\ W$$

A total of 300 mm of nichrome wire was estimated to allow for a sufficient number of coils to be wrapped around the copper tubing. The diameter of the nichrome wire was 0.254 mm. The resistivity of the nichrome wire was taken as 1.12 x 10^{-6} Ω·m [470]. Through the use of Equation 5.28, the total resistance of the nichrome wire could be estimated:

$$R = \frac{\rho_R L}{A} = \frac{(1.12x10^{-6})x(300x10^{-3})}{\pi(0.254x10^{-3})^2} = 6.63\ \Omega$$

Using Equation 5.27, the current could be calculated:

$$P = I^2 \cdot R$$
$$I = \sqrt{\frac{P}{R}} = \sqrt{\frac{2.88}{6.63}} = 0.434\ A$$

Using Equation 5.26, the voltage could be determined:

$$E = I \cdot R = 0.434x\ 6.63$$
$$= 2.87\ V$$

5.4.3.2. Discussion

A CAD assembly of the proposed design idea was imported from Solidworks 2019 into COMSOL Multiphysics 5.3, shown in Figure 5.51. The model consisted of a Heat Transfer in Solids and Fluids modul, and an Electric Currents module, coupled by an Electromagnetic Heating Multiphysics module. However, due to the computational complexity of the 3D model exceeding the computational memory, a simulation was unable to be provided. As a result, an experimental setup was used to assess the performance of this design idea. This experimental setup will be explored in further detail in section 6.4.2.1.

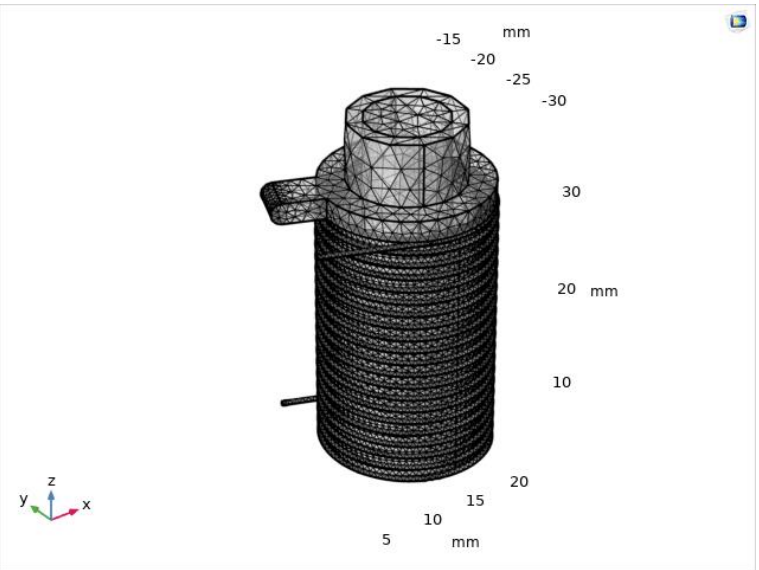

Figure 5.51 – Heating System for Design Idea 2 imported into COMSOL Multiphysics 5.3

5.4.4. Printed Circuit Board Heating Simulation

5.4.4.1. Problem Description

A design requirement outlined in section 4.3.6 (Figure 4.27) was to include resistive heating elements which would allow for heating to be conducted within the device following the insertion of the swab. An aim was set to provide a temperature of 92 °C for 10 minutes, allowing for the deactivation of the pathogen and lysis of the sample to be performed in a single step. The setup devised for the final design idea can be seen in Figure 5.52. The heating system consisted of three components: a moving jaw, a PCB and a machined heater block. The moving jaw was used to locate the heater to the SCD and to prevent heat losses to the atmosphere. The heater block was used to guide heat to the SCD. The

PCB designed on EaglePCB (Autodesk, Mill Valley, California, USA) featured a length of copper track which would generate heat when supplied with an electric current. The serpentine layout across the PCB was designed to provide a uniform heat distribution across the PCB, which in turn would supply a uniform distribution of heat to the heater block. Furthermore, due to the limited size, this serpentine structure allowed for a maximised resistance within a minimised area. The design can be seen in Figure 5.53. This section demonstrates a computational heat transfer model for the designed PCB and evaluates the effectiveness of the setup for supplying heat to a liquid contained within the SCD.

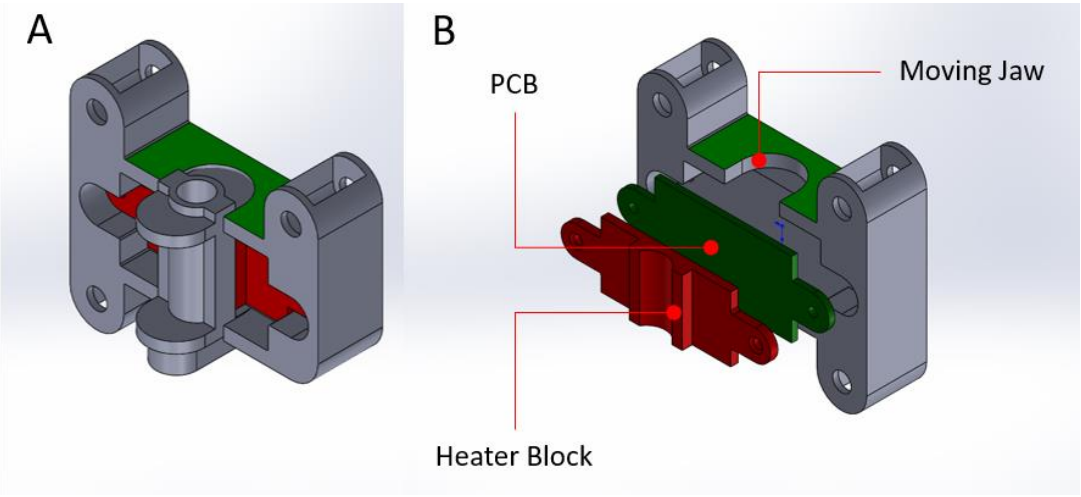

Figure 5.52 – Heater Block Setup for Final Design Idea, designed on Solidworks 2020
***A.** Isometric Model, Assembled View* ***B.** Exploded View, Annotated*

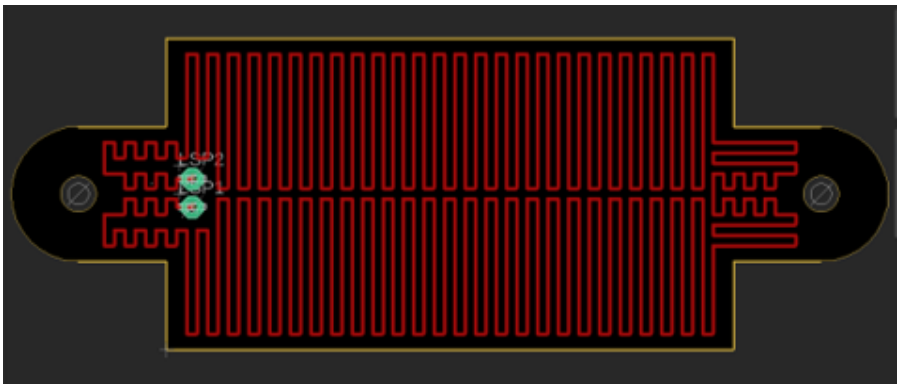

Figure 5.53 – A schematic of the copper track designed in EaglePCB

The total energy required to heat both the aluminium block and the SCD can be approximated by rearranging Equation 5.30. The mass estimates were taken from Solidworks 2020, while the specific heat capacity of the SCD was estimated based on the specific heat of common polymer materials [471]. These values can be seen in Table 5.8.

Table 5.8 – Properties used for the calculation of the energy requirements (Final Design Idea)

Material	Mass (g)	Specific Heat Capacity (J/kg K)
Aluminium Block	≈6.35	900
SCD	≈12.59	≈1400
FR4 (Circuit Board)	≈8.66	1369

The temperature change was assumed to be 90 °C, to address fluctuating temperatures in ambient conditions. Therefore, by using Equation 5.30:

$$\Phi_{net} = mc_p\Delta T = \left(mc_p\Delta T\right)_{Aluminium\ Block} + \left(mc_p\Delta T\right)_{SCD} + \left(mc_p\Delta T\right)_{FR4}$$
$$= [900x(6.35x10^{-3})x90] + [1400x(12.59x10^{-3})x90] + [1369x(8.66x10^{-3})x90]$$
$$\Phi_{net} = 3168.19\ J$$

The power required to produce the total heat energy was then calculated using Equation 5.29. The time chosen to reach the desired temperature was 5 minutes (300 seconds), and thus:

$$P = \frac{3168.19}{300} = 10.56\ W$$

The total length of the copper track designed in Autodesk Eagle was 1595.72 mm. The width and thickness of the copper track were estimated at 300 and 35 µm, respectively. The resistivity of copper was 1.72 x 10^{-8} Ω·m. Through the use of Equation 5.28, the total resistance of the copper track across the PCB could be estimated:

$$R = \frac{(1.68x10^{-8})x(1595.72x10^{-3})}{(300x10^{-6})(35x10^{-6})} = 2.55\ \Omega$$

Using Equation 5.27, the current could be calculated:

$$I = \sqrt{\frac{10}{2.55}} = 2.03\ A$$

Using Equation 5.26, the voltage could be determined:

$$E = 2.03x\ 2.55 = \ 5.19\ V$$

5.4.4.2. Numerical Simulation

Part 1

A Multiphysics simulation was created to simulate the heat generation, thermal stresses and deformation as a result of applying an electrical potential across the heating circuit. A stationary 3D model was designed, using a combination of Electric Currents in Layered Shells, Heat Transfer in Solids and Solid Mechanics modules. The PCB design shown in Figure 5.53 was imported into COMSOL Multiphysics 5.5. The PCB base design was imported as a .STEP file, while the copper track was imported as a .DXF file on a work plane defined along the base of the PCB. The PCB base material was selected as FR4 (Circuit Board) and the copper track was selected copper from the library of materials built into the software. An explicit definition was applied to the imported copper track, which was set to a thickness of 35 µm. This can be seen in Figure 5.54a.

In the Solid Mechanics module, a rigid motion suppression domain constraint was applied to the model. In the Electric Currents in Layered Shells module (Figure 5.54a), an electric potential edge constraint was applied to one of the pads, while a ground edge constraint was applied to the other pad (Figure 5.54b). The potential was defined as “V_in”. In the Heat Transfer in Solids module, a thermally thin approximation was applied to the copper track. A surface-to-ambient radiation constraint was applied to the PCB board. As the emissivity of epoxy materials ranges between 0.8 and 0.9 [472], the FR4 board was estimated to have an emissivity coefficient of 0.85. A surface-to-ambient radiation constraint was applied to the copper track. As the emissivity of polished copper ranges between 0.023 and 0.052 [473], the copper track was estimated to have an emissivity coefficient of 0.0375. The ambient temperature was defined as 15 °C.

An Electromagnetic Heating, Layered Shell Multiphysics module was used to couple the Electric Currents in Layered Shells module to the Heat Transfer in Solids module and a Thermal Expansion Multiphysics module was used to couple the Heat Transfer in Solids module to the Solid Mechanics module. A physics-controlled mesh with a “finer” element size was chosen and the simulation was run, with the von Mises stress, deformation, temperature and electric potential observed.

Part 2

Following the analysis of the unloaded PCB, the simulation was repeated with the aluminium block added. As the finish of the machined aluminium block was unidentified, an emissivity coefficient of 0.07 was used, assuming the finish would be akin to rough aluminium [473]. The simulation was

repeated again with the SCD added. The properties of polyethylene were used as a template for the material applied to the SCD. The specific heat capacity was set to 1400 J/kg K, as assumed in Table 5.8.

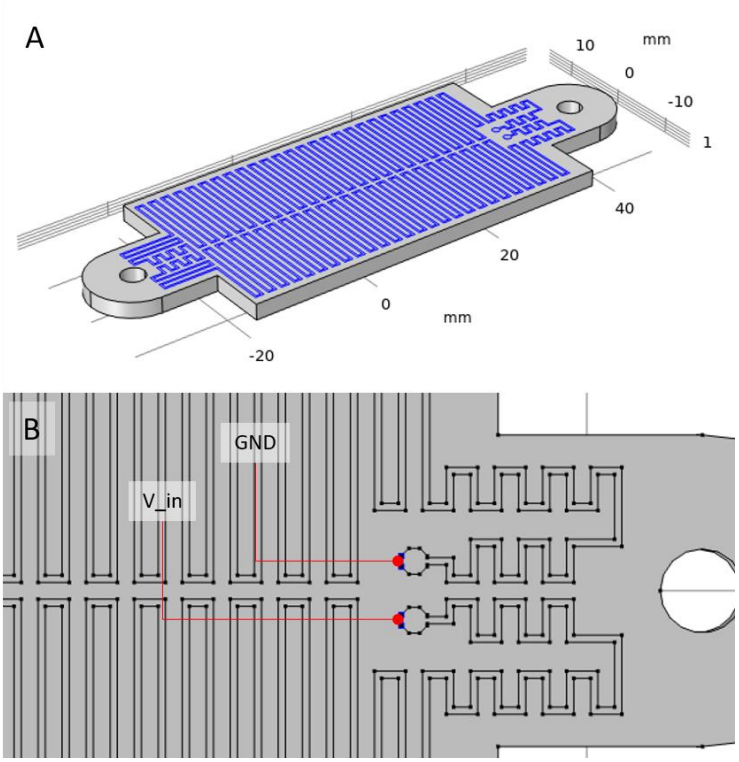

Figure 5.54 – Boundary Conditions set in COMSOL Multiphysics 5.5
A. *Isometric View. The copper track (blue) was specified as a separate boundary using an explicit definition.*
B. *Plan view of the copper track. The two edges selected (blue) were set as V_in and ground.*

5.4.4.3. Results and Discussion

Part 1

A PCB design was analysed using the Electromagnetic Heating, Layered Shell and Thermal Expansion Multiphysics modules. At 2.5 V, the average steady state temperature was 104.4 °C, shown in Figure 5.55. An even temperature across the rectangular section of the PCB was observed. The maximum operational temperature of the FR4 substrates was 150 °C [474]. The simulation predicted a maximum temperature of 124.7 °C, below the operational temperature. Thus, the simulation showed that the design would function within operational limits.

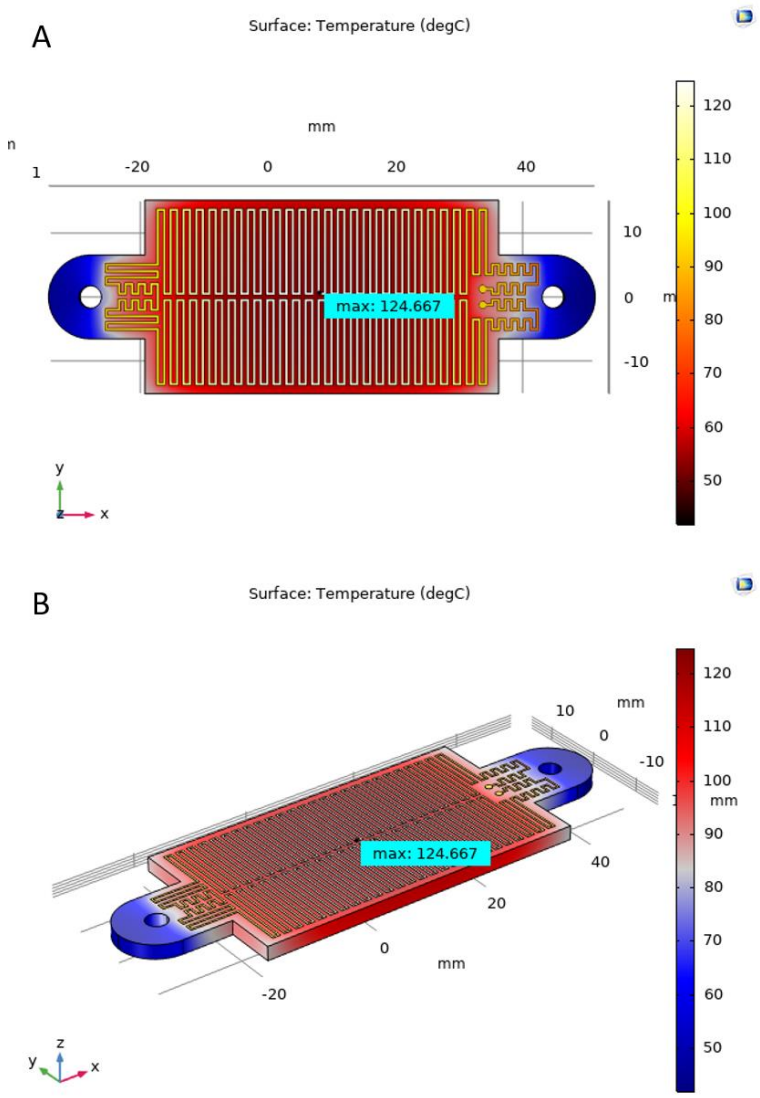

Figure 5.55 – Temperature Profile for the PCB

A. *Plan view. The colour legend represents the temperature distribution across the copper track*

B. *Isometric View. The colour legend represents the temperature distribution across the FR4 substrate*

The surface loss density can be seen in Figure 5.56. The power was calculated at 2.54 W through a surface integration across the copper track. The highest and lowest surface loss densities occur at the inside and outside 90° corners along the serpentine channel, respectively. This was an expected result of the electrical current taking the shortest path from the electric potential to the ground. As high current densities can contribute to the failure of the device, a design optimisation was planned to include fillets to the sharp angles within the serpentine channel.

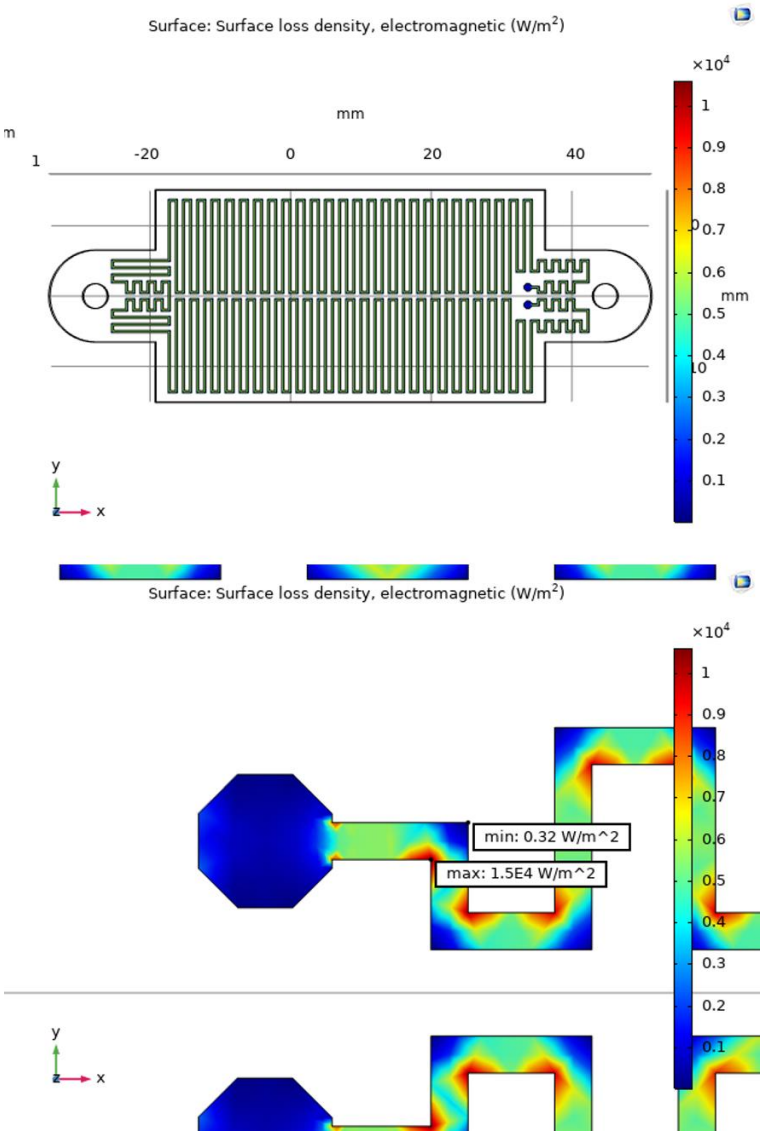

Figure 5.56 – Surface loss density across the copper track
***A.** Plan view.* ***B.** Close up of copper track at the ground connection.*
The colour legend represents the surface loss across the copper track It was observed that the highest heat generation occurred at the internal corners of the channel. This was attributed to the higher current density. The minimum and maximum surface loss density values are 0.32 and 14643.32 W/m2, respectively, given to 2DP.

The thermal stress on the PCB as a result of joule heating was also observed. The maximum von Mises stress at 124.7 °C was 12.34 MPa, shown in Figure 5.57a. As the FR4 substrate and annealed copper had yield strengths of 65 MPa [474] and 33.3 MPa, respectively, the structure remained intact during the simulation with a FoS of 2.7. The simulation predicted a maximum deformation of 140 µm across the length of the substrate, shown in Figure 5.57b, with the substrate observed to curve away from the direction of the copper track.

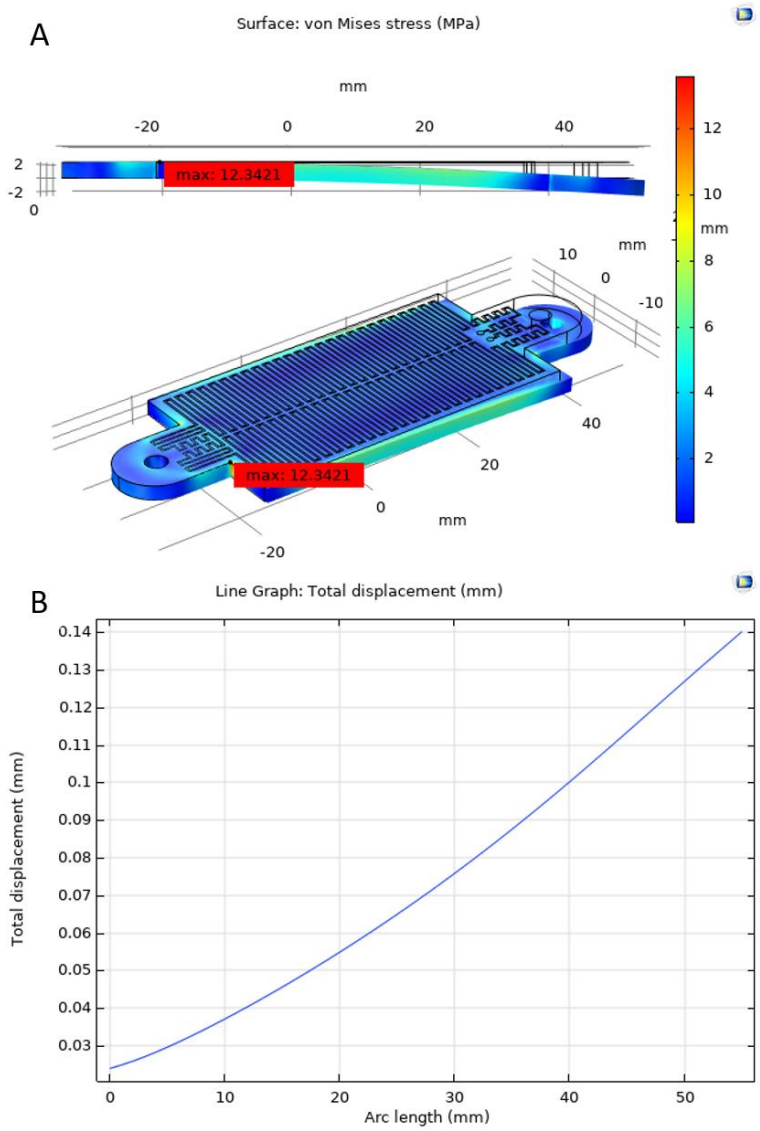

Figure 5.57 – Stress and deformation profile across the PCB
***A.** Side (top) and isometric (bottom) views. **B.** Displacement along the length of the PCB. A scale factor of 20 was used to allow for visualisation of the deformation.*

Part 2

The steady state temperature across the aluminium block was 98.3 °C when a potential of 2.5 V was applied, shown in Figure 5.58. The curved face of the aluminium block had the highest temperature across the aluminium block, which would ensure a uniform heat would reach the SCD.

After the addition of the SCD, a temperature drop was observed across the aluminium block to 93.1 °C when a potential of 2.5 V was applied. The average temperature of the water domain was 88 °C. The voltage was increased to 2.595 V (Figure 5.59), which provided an average volume of 91.9 °C. The simulation agreed with the voltage calculation shown in 5.4.4.1.

It should be noted that the SCD was modelled with a line of symmetry through the water domain to reduce the computational complexity of the simulation. Thus, the power requirement to heat the volume to the desired temperature would be double what was depicted in the simulation. However, the final design featured a pair of heater blocks placed on either side of the SCD. Therefore, it was concluded that the proposed setup would supply sufficient heat to the fluid.

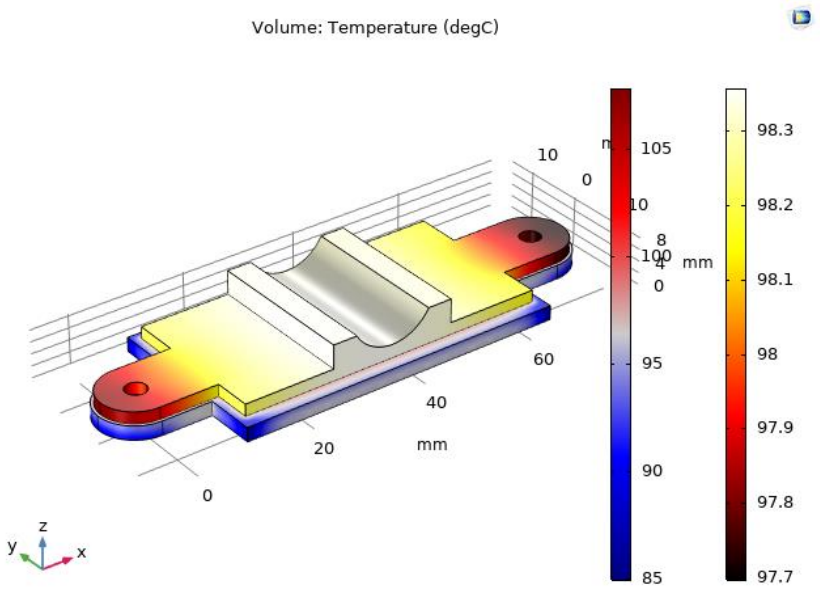

Figure 5.58 – Temperature Profile for the PCB (2.5 V)
The blue-to-red colour legend (left) represents the temperature distribution across the FR4 substrate, while the red-to-yellow colour legend (right) temperature distribution across the aluminium block

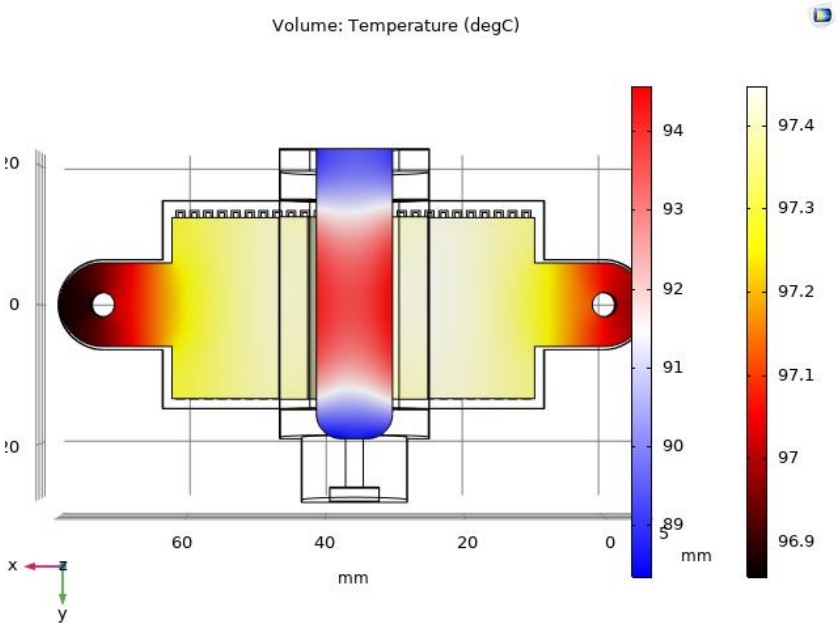

Figure 5.59 – Temperature Profile for the PCB (2.595 V)
The blue-to-red colour legend (left) represents the temperature distribution across the water, while the red-to-yellow colour legend (right) temperature distribution across the aluminium block

5.5. Discussion

5.5.1. Discussion on Computational Fluid Dynamics

The Tesla valve designs demonstrated a simple method of fluid control absent of active components. However, the low flow rate of the fluid through the SCD made this technology incompatible with its intended approach. Physical prototypes of the Tesla valves were designed with the purpose of providing a comparison between computational and experimental results. By mounting pressure sensors up and downstream of the valve, the diodicity of the fluid flow could be determined in order to determine the actual diodicity of each design. The setup and control of the pressure sensor would be adapted from works described elsewhere [475]. This was not achieved during the progression of this project due to a lack of access to suitable pressure testing instruments.

The transient simulation of the T45c-type valve further validated the proposed design, as it was demonstrated that a positive net flow rate was achievable without backflow for velocities above 20 mm/s. The reciprocating pumping mechanism could be easily integrated into the system by using a piezoelectric pump in place of the syringe pump. This would be substantially smaller than the syringe, mitigating the main issue regarding size constraints, as previously discussed in section 4.3.4. However, this design assumed that the Tesla valve would be fully primed a liquid at t = 0 seconds, which is not representative of real-life applications. A multiphase flow model would be the next logical step in assessing the performance of the valve during the priming and pumping process; however, this was not achieved during this project.

The multiphase flow simulation validated the membrane valve design proposed in section 4.3.5, providing a tangible starting point from which to develop the membrane valve designs with subsequent FEA modelling. To better simulate real life conditions, the simulation for case 1 at t = 0.75 seconds should have been directly used as t = 0 seconds for case 2 in order to determine how the presence of the observed air bubble would affect the performance. However, design idea 4 was discarded in favour of the final design idea in order to develop a functional proof-of-concept; and as a result, this combination of simulations was not attempted.

5.5.2. Discussion on Structural Analysis

The membrane valve simulations presented in section 5.3.3 were demonstrated to function as stated in section 4.3.5. It should be noted that a constant fluid flow would result in an accumulation of

pressure which would eventually cause the valve to open. Thus, it is necessary to combine both the structural analysis (section 5.3.3) with the two-phase fluid flow (section 5.2.5) simulations to determine exact values for the pressure accumulation as a result of fluid flow.

Akin to the Tesla valves, physical prototypes of the membrane valves were fabricated from TPU 95a, which were tested for fluidic integrity and functionality. These can be seen in section 6.2.1. The valves were observed to work as intended. Furthermore, the performance of the valve was significantly improved when negative pressure was used to "pull" the fluid through the valve, compared to when positive pressure was used to "push" the fluid through the valve. The positive pressure configuration highlighted the accumulation of pressure which forced the valve open. However, like the Tesla valves, pressure readings were unable to be conducted on the membrane valves due to a lack of suitable instrumentation. Ultimately, while the physical valve was successful in restricting fluid flow, a lack of tangible data makes it difficult to support this claim.

5.5.3. Discussion on Heat Transfer

Joule heating is a widely explored approach for supplying heat to biological fluids in microfluidic applications. A design reported by De Mello *et al*. used electrically conductive ionic liquids within a serpentine channel to achieve Joule Heating for temperatures up to 90 °C, accurate within ±0.2 °C [476]. Despite the low power requirement of 1 W, a high AC voltage (3.75 kV) was required. Lao *et al.* developed a heating system integrating a metallic serpentine channel into a silicon-glass microfluidic chip to achieve temperatures up to 90 °C, accurate within ±1 °C [477]. The device was able to perform thermal cycles for PCR using a low power output of 2.2 W. A platform with a similar geometry was later utilised by Mavraki *et al.* to construct a double-sided copper heating system atop a flexible Pyralux™ substrate [478]. Contrastingly, this system employed meandering channels with different lengths to create a temperature gradient of 95 °C, 60 °C and 72 °C, allowing PCR cycling to be performed on a moving fluid. However, it should be noted that the target volume for the design presented by Lao *et al.* was 20 µL, significantly less than either heating configuration presented in this study. The volume of the design reported by Mavraki *et al.* was not provided.

Vigolo *et al.* utilised a PDMS-glass based platform to achieve temperatures up to 75 °C, controllable within an accuracy of 2 – 3 °C [479]. A silver-filled epoxy was injected into a channel within the PDMS-glass chip post-fabrication, which could be used as a resistive heating element once it had solidified. Recently, Kim and Kim developed an electro-conductive plane heating element to lyse *pseudomonas*

aeruginosa and *bacillus megaterium* cells [480]. The plane heating element consisted of a glass fibre filter paper bonded to a carbon paste heating element. When supplied with a 0.4 amp current, temperatures up to 150 °C were generated. Despite the rapid nature of the platform, the starting volume (30 µL) was over two orders of magnitude lower than the platforms presented in this study.

An alternate approach to microfluidic heating was proposed by Gujit *et al*., who used endothermic and exothermic reactions within a PDMS-glass platform to regulate temperatures within microchannels locally [481]. By reacting sulphuric acid (H_2SO_4) with water, the resulting exothermic reaction would heat the liquid flowing through an adjacent microchannel to temperatures up to 76 °C. By reacting acetone (C_3H_6O) with air, the resulting endothermic reaction would cool the liquid flowing through an adjacent microchannel to temperatures as low as -3 °C. This approach was later optimised by Maltezos *et al.*, to achieve cooling as low as -20 °C [482].

The stationary heat transfer model presented in section 5.4.4 was demonstrated to successfully heat the contained liquid to the desired temperature, agreeing with the calculated values. However, while it was determined that the heated liquid would reach the desired temperature, it was not in fact determined how long it would take to reach the desired temperature. Due to time constraints, the heating system was fabricated prior to the conception of a transient flow model. The inclusion of a transient flow model would have allowed for an assessment of the temperature ramp rate, allowing for optimisations to be conducted on the heater block or PCB prior to fabrication.

The heat transfer model was assembled in stages, adding components individually to determine their effect on the temperature. While it was theorised that the moving jaw (see Figure 5.52) would act as an insulator and contain heat within the system, it was later theorised that it may in fact have acted as a heat sink, further reducing the temperature ramp rate. Thus, the inclusion of the moving jaw would have been crucial to support either theory; however, this was not attempted during the project.

An analysis of the maximum and minimum surface loss density values (Figure 5.56) revealed a disparity that was over four orders of magnitude. These two points were located at the inner and outer vertices of the corner adjacent to the ground connection, equating to 14643.32 W/m^2 and 0.32 W/m^2, respectively. These two vertices were used to define a cut line (Figure 5.60) which was used to generate a temperature plot (Figure 5.61), revealing a 0.03 °C temperature discrepancy. A second cut line was defined at a selected corner along the serpentine track (Figure 5.62). The corresponding temperature plot (Figure 5.63) revealed a larger temperature discrepancy of 0.08 °C.

The temperature variations across both cut lines were relatively low (<0.1 °C); and thus, it was assumed that the copper track would be unlikely to detach from the substrate as a result of thermally

induced interfacial stresses. This was a concern, as detached sections of the copper track can overheat, increasing the rate of detachment, and in extreme cases, burn the circuit [483]. It is possible to assess the interfacial stresses between the substrate and the copper track using a Solid-Thin Structure Connection Multiphysics module, coupling a Solid Mechanics module to a Membrane module [484]. However, the Membrane module was unavailable due to licencing issues.

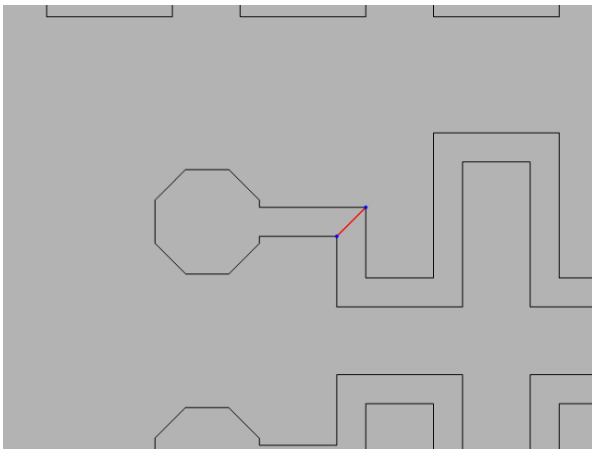

Figure 5.60 – Cut line defined at a bend within the serpentine track

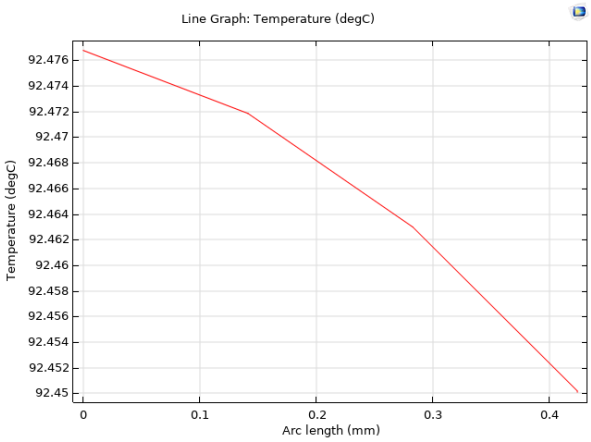

Figure 5.61 – Temperature Profile across a defined cut line

The cut line (red) shown in Figure 5.60 defined the arc length used in Figure 5.61 to plot the temperature profile. The two ends of the represented the inner and outer vertices located at the corner adjacent to the ground connection. The temperature values at the inner and outer vertices were 92.48 and 92.45 °C, to 2DP.

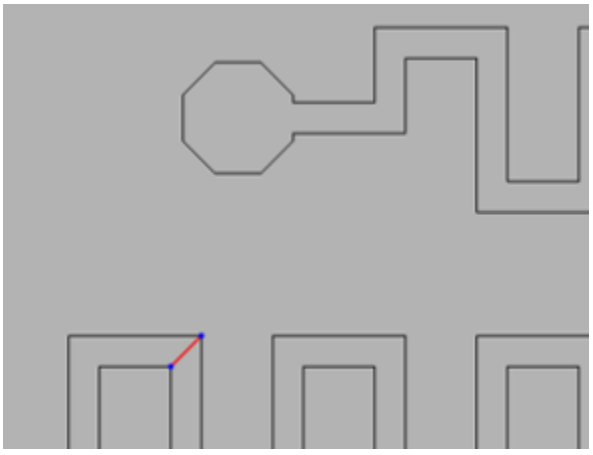

Figure 5.62 – Cut line defined at a bend within the serpentine track

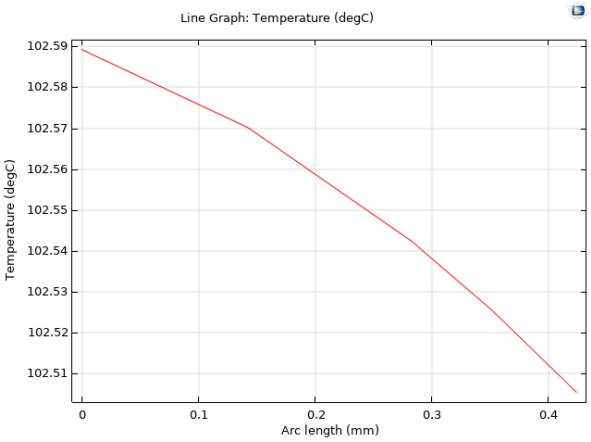

Figure 5.63 – Temperature Profile across a defined cut line

The cut line (red) shown in Figure 5.62 defined the arc length used in Figure 5.63 to plot the temperature profile. The two ends of the represented the inner and outer vertices located at a corner along the serpentine track. The temperature values at the inner and outer vertices were 102.59 and 102.51 °C, to 2DP.

5.6. Chapter Summary

FEA was successfully demonstrated in this chapter to assess the capabilities of the designs proposed in Chapter 4. Access to prototyping was restricted due to a limited budget and inadequate facilities. COMSOL allowed for these limitations to be mitigated, using computational models to assess the performance of the designs, allowing iterations to be made to improve performance where necessary.

CFD models were used to validate the fluid flow within the SCDs proposed in sections 4.3.4 and 4.3.5. Stationary flow models were used to determine the optimal Tesla valve design, the T45c type, which was then used to construct a transient flow model using a sinusoidal input. This model verified that it was indeed possible to direct fluid flow within a laminar flow configuration within a valve with no moving parts, as proposed in section 4.3.4. A two-phase flow model was then used to assess the fluid flow of water and air through the SCD proposed in section 4.3.5. This validated the performance of the membrane valves, indicating that no backflow would occur from the outlet to the heating chamber in case 1, nor from the heating chamber to the swab receiver in case 2.

The same membrane valve design was further validated through structural analysis of the membrane valves. Here, it was demonstrated that a 0.48 mm 3D printed valve fabricated from TPU 95a would be able to close and prevent fluid flow. The simulations also determined that the Accura Xtreme and VeroClear resins were unviable options for membrane thicknesses above 0.2 mm.

Finally, a heat transfer model was used to measure the operational temperatures of the PCB, before determining its capabilities when coupled with a manufactured heater block and a 3D printed SCD. The platform was able to heat the contained liquid to 91.9 °C with a supplied voltage of 5.19 V, agreeing with the calculated values.

6. Fabrication of a Sample Preparation Platform

6.1. Introduction

The design ideas presented in Chapter 4 underwent several iterations throughout the project, too many to detail in this thesis. Design prototypes were developed in parallel with the computational models presented in Chapter 5. This section of the thesis will present the notable SCD and SPD designs which were fabricated during this project and demonstrate where optimisations were made to improve performance. Finally, the performance of the heating and EHD modules proposed for the final platform presented in Chapter 4 were tested. The performance of the final design idea was compared to the relevant computational models presented in Chapter 5, or the performance of similar modules from previous design ideas.

6.2. Fabrication of the Sample Collection Device

6.2.1. Sample Collection Device Fabricated from Design Idea 4

The SCD design proposed in section 4.3.5 was fabricated using a Prusa i3 MK3S 3D Printer (Prusa Research, Prague, Czech Republic) using polyethylene terephthalate glycol (PETG). The nozzle and build plate were set to 235 and 90 °C, respectively. The layer height and infill density were set to 0.1 mm and 100%, respectively. The print and fan speed were set to 50 mm/s and 50%, respectively. The resulting cartridge can be seen in Figure 6.1.

The main fluidic channels were observed to allow fluid flow without notable obstructions. The presence of an air pocket was initially observed in the trapezoidal chamber (Figure 6.1b); however, this was also speculated to be a collapse of the internal structure. The time lapse demonstrating the filling of the cartridge can be seen in Figure 6.2. There was an observed instability in the profile of the fluid meniscus which resembled the computational simulation for case 1 of the two-phase flow model shown in Figure 5.22. It should be noted that positive pressure was applied from the swab receiver to actuate fluid through the cartridge using a 1ml BD syringe, unlike the computational simulation, where negative pressure was applied from the pump port. The reason for this change was the lack of actuation in the membrane valves due to the rigidity of the PETG material.

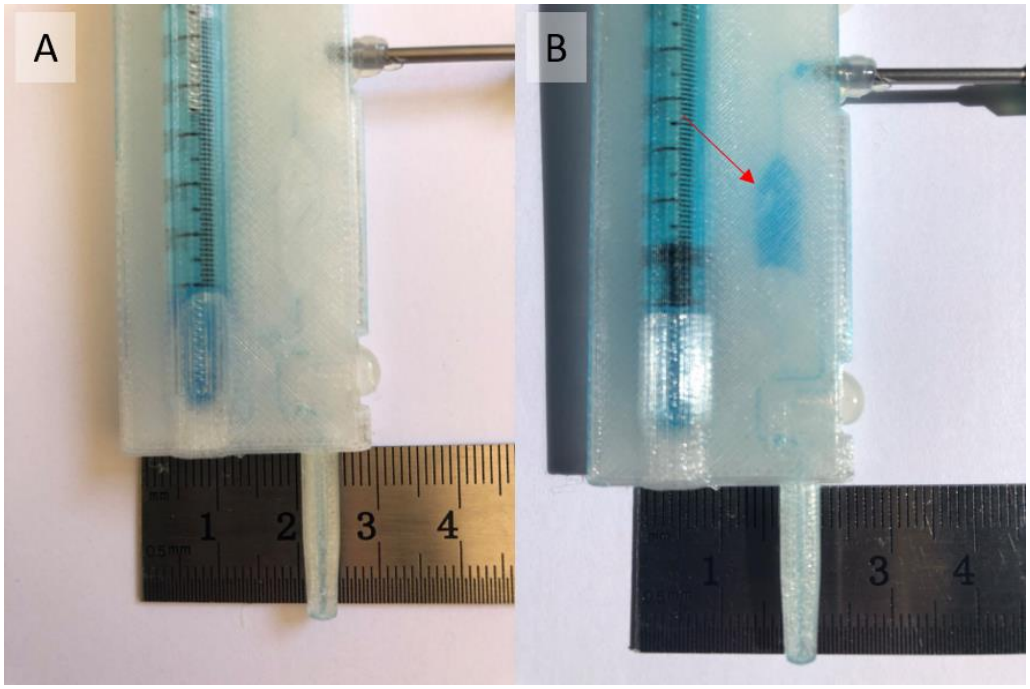

Figure 6.1 – Design Idea 4: Cartridge fabricated using a Prusa i3 MK3S FDM 3D Printer.
***A.** Close up of the cartridge, filled with blue dye for visualisation **B.** The presence of a suspected air pocket was observed within the trapezoidal chamber (highlighted by the red arrow)*

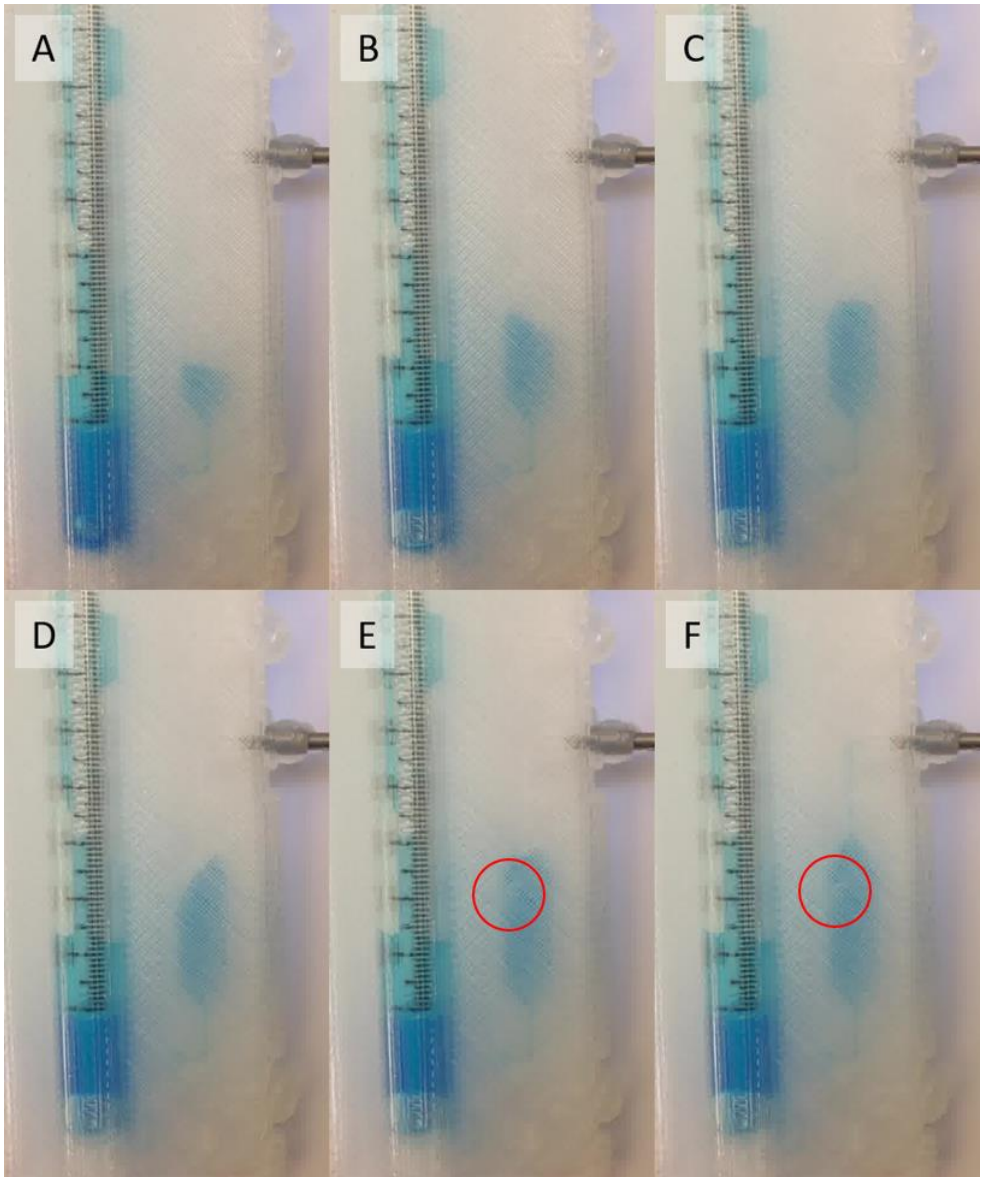

Figure 6.2 – Time lapse of fluid flow through the fabricated cartridge.
The red circles indicate the presence of suspected air bubbles within the trapezoidal chamber, highlighted in Figure 6.1
***A.** t = 0.4 seconds; **B.** t = 0.7 seconds; **C.** t = 1.2 seconds; **D.** t = 1.6 seconds; **E.** t =1.8 seconds; **F.** t = 2.1 seconds*

PETG is a rigid material, meaning that the membrane valves were unable to be printed as functional features. Thus, the performance of the valve designs integrated into design idea 4 could not be verified. The membrane valve was printed as an individual component from TPU 95a, shown in Figure 6.3. The valve was able to prevent fluid flow in both a 0.36- and 0.48-mm thickness; however, the rupturing of membranes was observed within each of the membrane thicknesses; albeit, more commonly among the 0.36 mm models. This conflicts with the results provided by the simulations in section 5.3.3, which were deemed to function within a sizable FoS. The cause was attributed to the weak interlayer bonding between layers, as discussed in section 4.4.

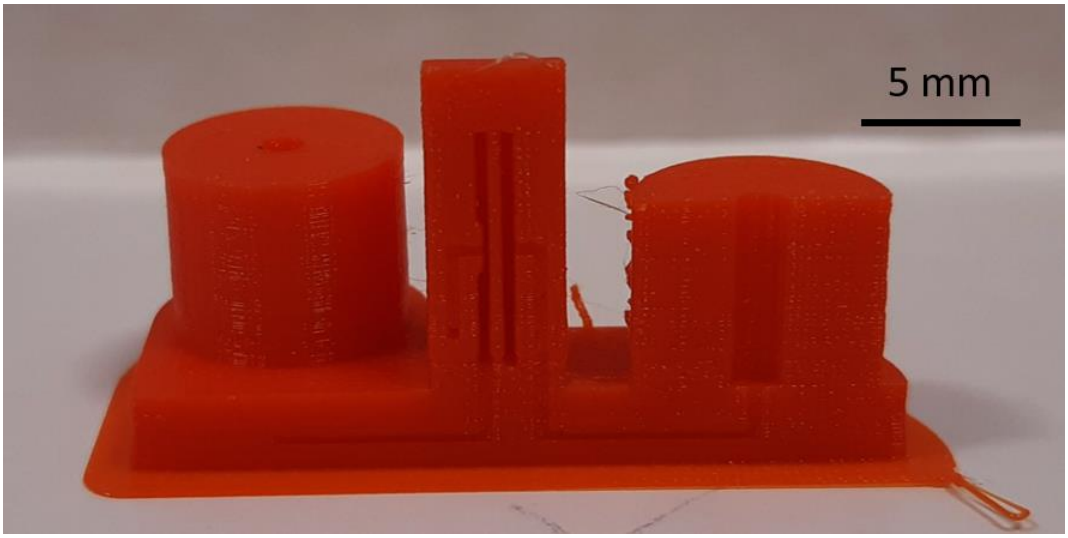

Figure 6.3 – 3D printed microfluidic membrane valve (0.36 mm thickness)
The membrane valve was printed as an individual component from TPU95a for testing outside of the sample collection device. The membrane valve shown was a partially printed model cut along its YZ plane for visualisation purposes.

The cartridge design was also fabricated out of house from Formlabs Clear Resin (Protolabs, Minnesota, USA), using SLA 3D printing. This cartridge can be seen in Figure 6.4. The internal features of the cartridge did not print despite a high resolution (50 µm layer height) being selected. Thus, further tests were unable to be performed on the SLA cartridge design. As the SCD printed using SLA (Figure 6.4) lacked the internal features to conduct fluidic testing, a comparison against the SCD fabricated using FDM printing (Figure 6.1) could not be conducted.

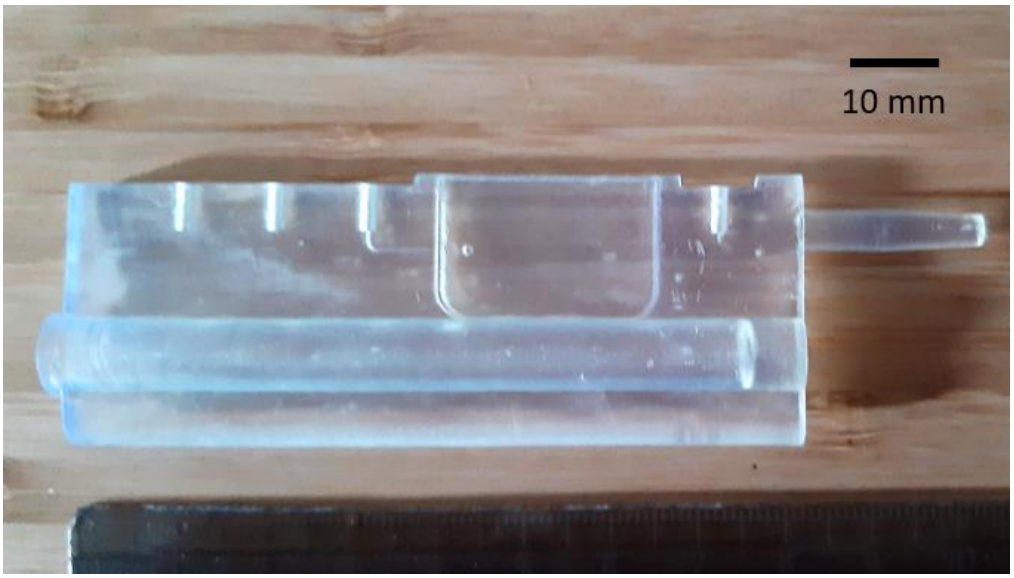

Figure 6.4 – Design Idea 4: Cartridge fabricated using SLA printing
The cartridge was manufactured from Formlabs Clear Resin (Protolabs, Minnesota, USA).

6.2.2. Sample Collection Device Fabricated from Final Design Idea

The first iteration of the SCD proposed in section 4.3.6 can be seen in Figure 6.5. The components of the SCD were fabricated using Accura Xtreme on a Viper stereolithography printer (3D Systems, Rock Hill, South Carolina, USA). The components were connected fluidically using 0.5 mm diameter silicon tubing (RS Components, Corby, England) and Idex 1/16" x 1/16" ID Polypropylene Straight Barbed Connectors (Cole-Palmer, Vernon Hills, Illinois, USA). The SCD interfaced with a dispenser needle using a Masterflex Polypropylene Male Luer Lock to 1/16" ID Hose Barb Adapter (Cole-Palmer, Vernon Hills, Illinois, USA) and to a syringe pump using a Masterflex Polypropylene Female Luer Lock to 1/16" ID Hose Barb Adapter (Cole-Palmer, Vernon Hills, Illinois, USA). The swab receiver and the T-junction were then secured to the switch valves using an interference fit with an allowance of 0.2 mm. By using silicon tubing, these switch valves were able to function without direct contact with the fluid, and thus, were completely reusable.

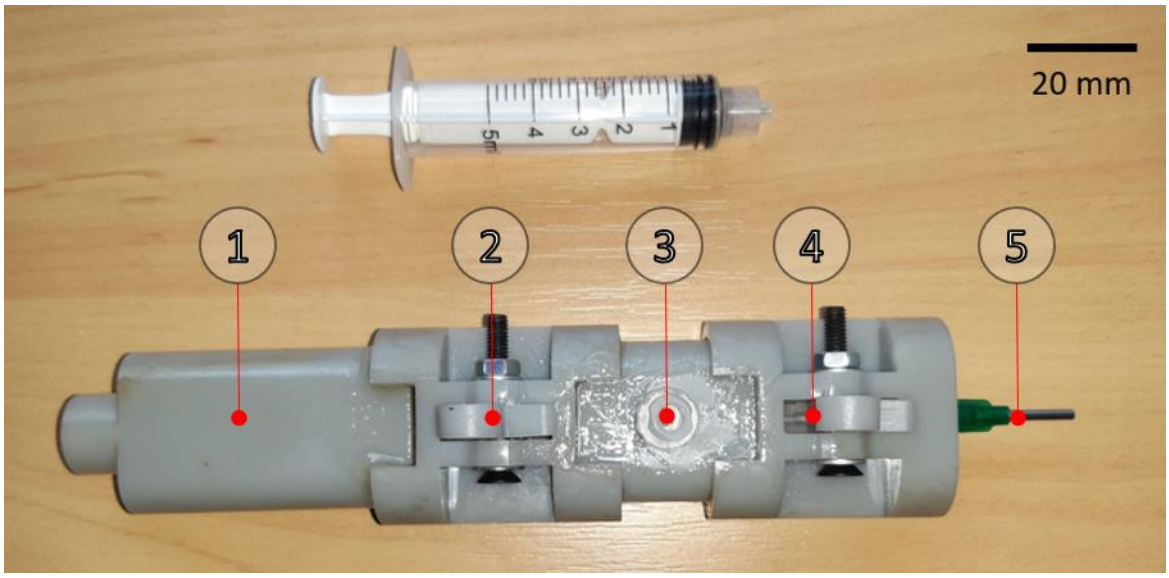

Figure 6.5 – Sample Collection Device fabricated using SLA printing (1st iteration)
***1,** Swab Receiver; **2,** Switch Valve 1; **3,** T-Junction; **4,** Switch Valve 2; **5,** Dispenser Tip Needle*

As the swab receiver and T-junction were in contact with the fluid, the SCD would require disassembly following use to replace contaminated parts, increasing the risk of contamination during manual handling. This inspired a redesign to reduce the number of components and to remove the T-junction. The 3D printed T-junction was replaced with a Masterflex Polypropylene 1/16" ID Tee Barb Union (Cole-Palmer, Vernon Hills, Illinois, USA) allowing for the SCD to be modified as shown in Figure 6.6. The modified design featured a redesigned lower section which was completely reusable due to operating without direct contact with the contained fluid.

Figure 6.6 – Sample Collection Device fabricated using SLA printing (2nd iteration)
***1,** Swab Receiver; **2,** Redesigned Lower Section containing both switch valves; **3,** Dispenser Tip Needle*

The valve designs presented in section 4.3.6 were able to restrict fluid flow as intended. Thus, fluid control from the swab receiver to the syringe and to the dispenser needle could be directed without backflow. The switch valves were constructed as individual components, shown in Figure 6.7. An interesting feature of these valves was the use of silicon tubing as fluidic channels, which made the entire 3D printed section operable without direct contact with the fluid. The valve design was printed in both TPU 95a and PLA, using a 0.25 mm and 0.4 mm nozzle, respectively, using an Ultimaker 2+. The performance of the valves was unaffected by the material or the resolution of the printer, demonstrating the capabilities of this design.

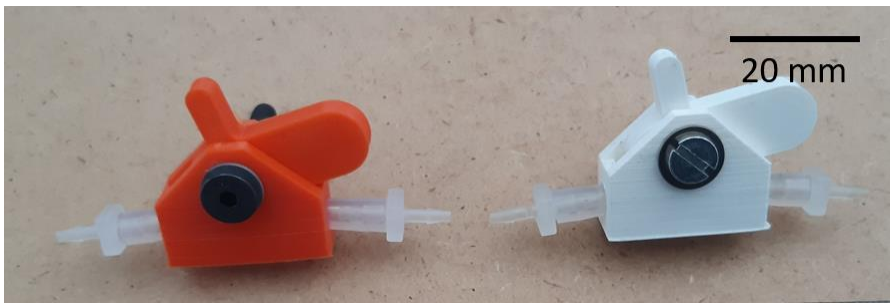

Figure 6.7 – 3D printed switch valve
The valve was printed in both TPU 95a (orange) and PLA (white) to demonstrate the material independence of the design.

6.3. Fabrication of the Sample Preparation Device

6.3.1. First Iteration

The SPD proposed in section 4.3.6 was fabricated using an Ultimaker 2+ printer from PLA. The individual components can be seen in Figure 6.8 and the assembled platform in Figure 6.9. Following the fabrication of the individual components, 3 mm hex nuts were inserted into allocated recesses using heat assisted interference fits. The heat was applied directly to each hex nut which softened the thermoplastic material upon contact, allowing for the nut to be inserted into the recess without damaging the plastic material. As the thermoplastic cooled, the recess shrunk in size to take the shape of the hex nut, preventing the nut from moving during subsequent assembly. As this design iteration required 57 hex nuts to be set using this methodology, the process took approximately 105 minutes.

Before the platform was assembled, the components of the Z-stage (Figure 6.8c) were aligned using 6mm A2 tool steel rods and were secured using screws. The moving platform was fitted with two LM6UU linear bearings (Walfront LLC, Lewes, Delaware, USA), allowing motion along the tool steel rods. An M5 threaded rod (1 mm pitch) was used as a lead screw to adjust the height of the moving platform, which would adjust the distance between the high voltage (HV) and grounded electrodes.

The heater blocks were machined using a STEPCRAFT Q.408 CNC-System (Stoney CNC, Ireland) using CAD files designed on Solidworks 2020. The resistive heating elements were designed on EaglePCB and were fabricated by Newbury Electronics Ltd (Newbury, England). The heater block clamps were fabricated from Formlabs High Temp Resin (Protolabs, Minnesota, USA) using SLA printing. As these were fabricated out of house, the make and resolution of the 3D printer was unknown. The heater blocks were aligned to either side of the SCD using 6mm A2 tool steel rods and LM6UU linear bearings, akin to the Z-stage moving platform. A separate assembly of these components can be seen in Figure 6.31, where heat testing is conducted. Once the hex nuts had been set in each component and the Z-stage was constructed, the entire platform was assembled using M3 socket head cap screws. The total assembly and disassembly times were 55 and 35 minutes, respectively.

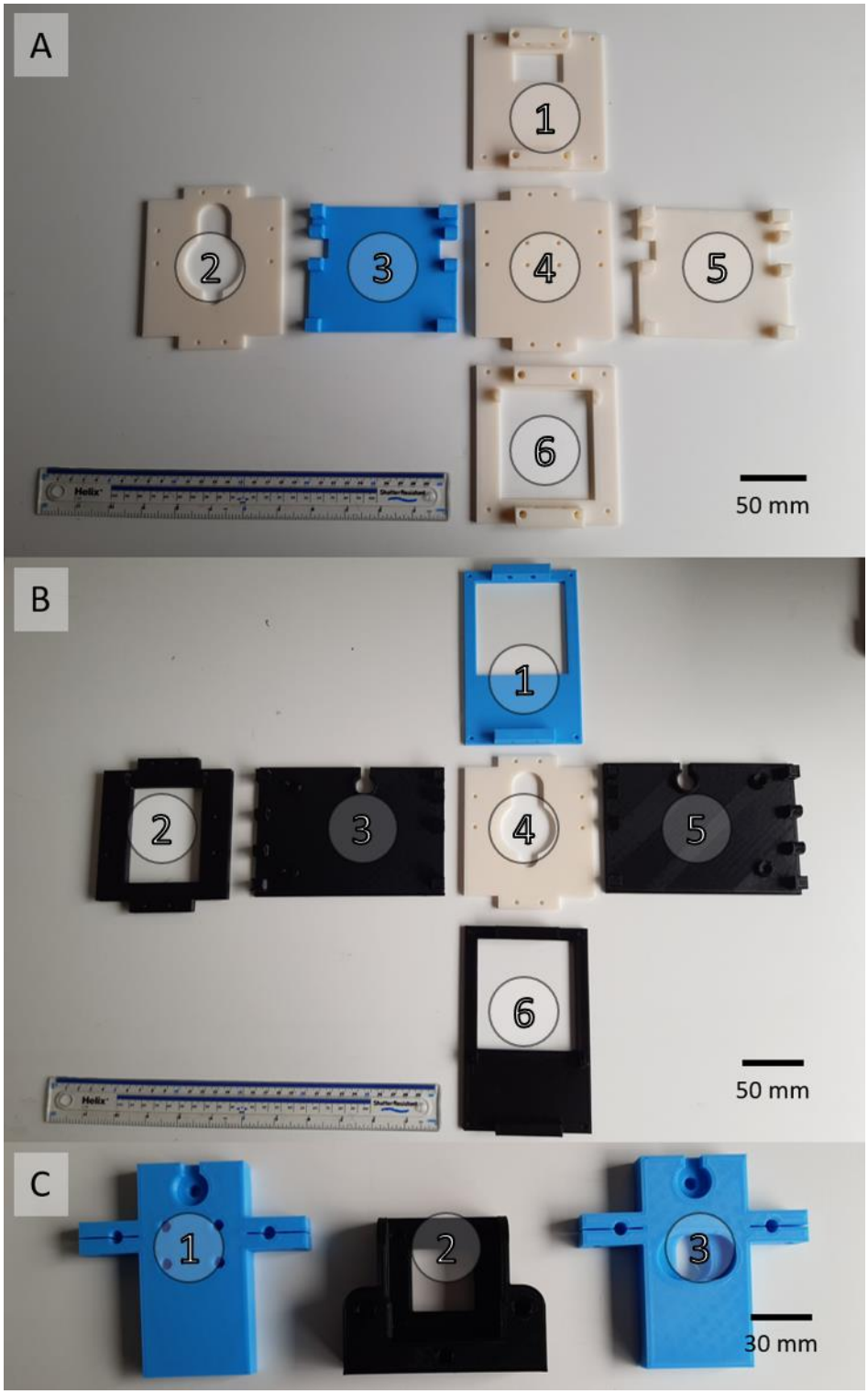

Figure 6.8 – Sample Preparation Device fabricated using FDM printing (1st iteration)
***A.** Lower casing: 1, rear; 2, top; 3, left; 4, base; 5, right; 6, front*
***B.** Upper casing: 1, rear; 2, top; 3, left; 4, top; 5, right; 6, front*
***C.** Z-stage: 1, fixed base; 2, moving platform; 3, fixed top*

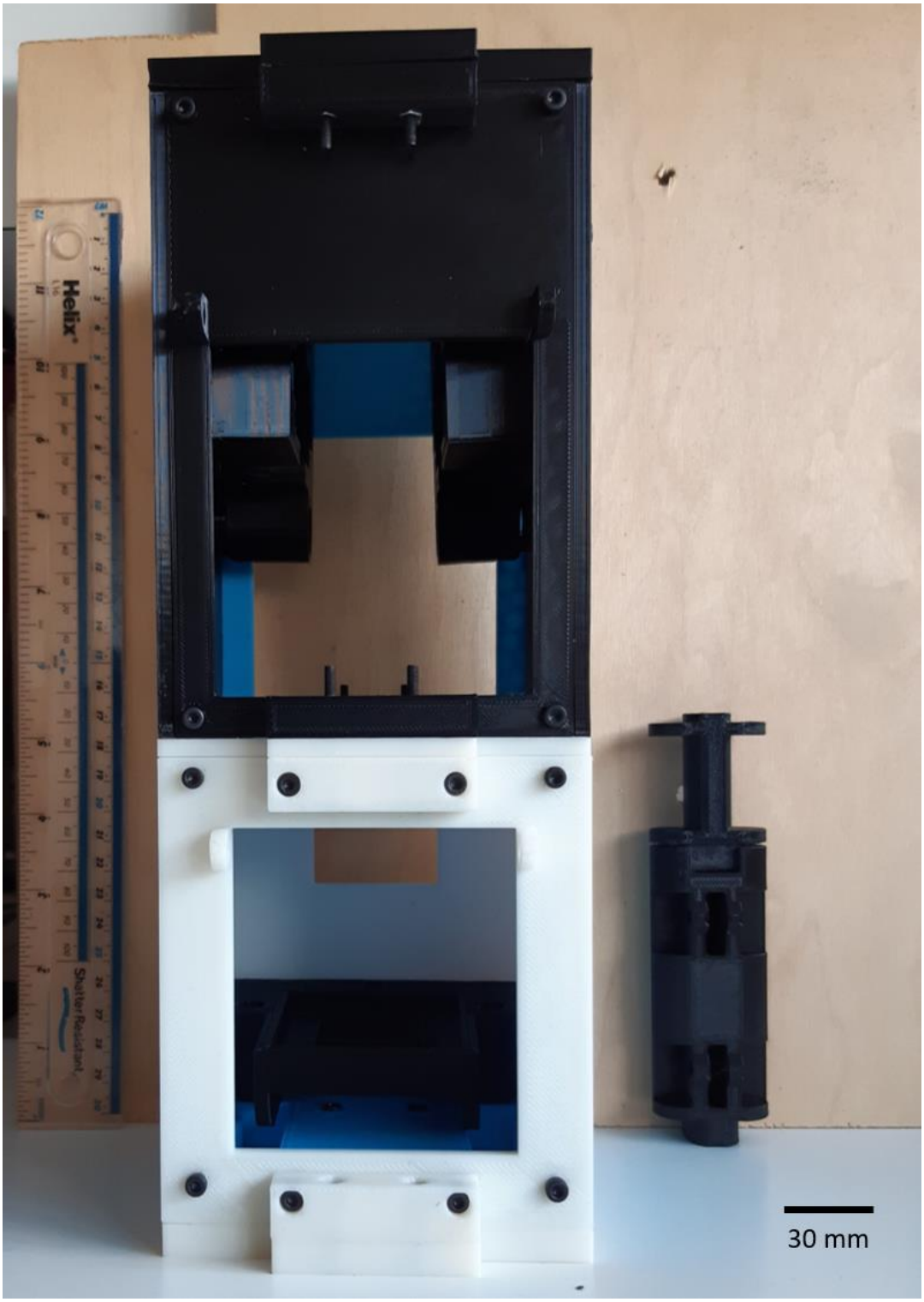

Figure 6.9 – Sample Preparation Device (1st iteration)
The time taken to set each of the hex nuts required for the assembly was 1 hr 45 min. The total assembly time was 55 min and the total disassembly time was 35 min.

The experimental setup of the EHD system (Figure 6.10) consisted of a 50 x 50 x 2 mm (L x W x H) sheet of aluminium used as a ground electrode and a 21-gauge stainless-steel blunt tip needle (Table 3.3) used as a HV electrode. Both the HV and ground electrodes were connected to a Q40 High Voltage Module (XP Power, Singapore), to 4 kV and ground outputs, respectively. A 4 mm hole was placed at the centre of the ground electrode to allow for detached droplets to pass through. A schematic of the EHD circuit can be seen in section 8.4.1.

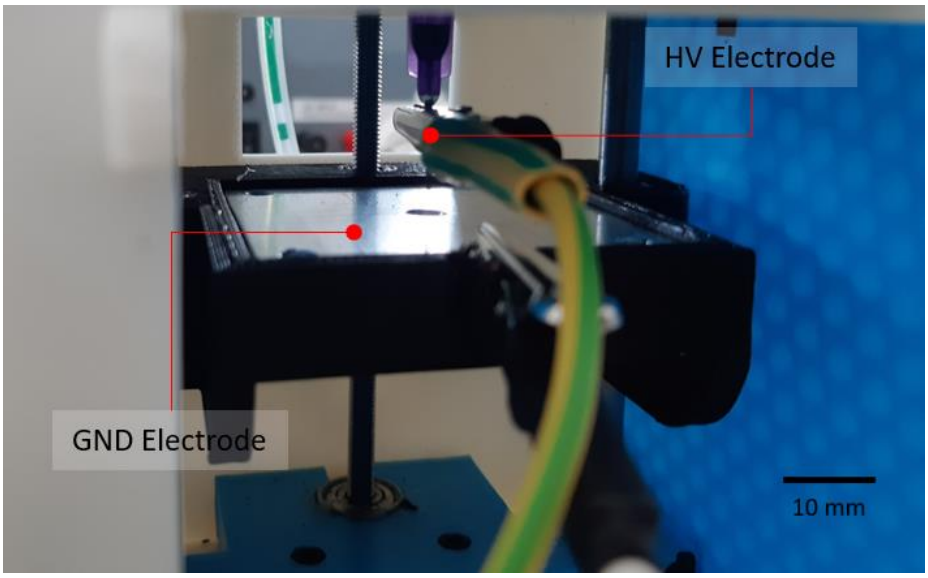

Figure 6.10 – Sample Preparation Device (1st iteration, Electrohydrodynamic Dripping System)

6.3.2. Second Iteration

The platform underwent several late-stage iterations to improve performance and safety. As a result, a simpler method was devised to reduce the time taken to disassemble and reassemble the platform. Lego® style fittings were designed to adjoin the components in place of hex nuts and screws. The redesign (Figure 6.11) reduced the number of hex nuts required from 57 to 6, reducing the time required to set the hex nuts to 12 minutes. Following the setting of the hex nuts, the platform was assembled by simply connecting the fittings together. A significant reduction in the assembly and disassembly time was observed following the modification, at 20 minutes and 5 minutes, respectively. A high 4 mm Red Heavy Duty 30A Binding Post (Cliff Electronic Components, Redhill, England) was used in place of a crocodile clip to improve the connection from the HV electrode to the Q40 Module. When coupled with a 3D printed socket aligner, the alignment of the HV electrode to the hole in the ground electrode was improved, simplifying the experimental setup.

Figure 6.11 – Final Design Idea: Sample Preparation Device (2nd iteration)
***1.** PLA Casing for the Heating Module; **2.** PLA Casing for the EHD Module; **3.** Formlabs High Temp resin Moving Jaw Fitted with heater block (Left); **4.** Formlabs High Temp resin Moving Jaw Fitted with heater block (right); **5.** Accura Xtreme Z-Stage Platform for Ground Electrode; **6.** 4mm Red Heavy Duty 30A Binding Post, fitted into a PLA HV Socket Locator*
The time taken to set each of the hex nuts required for assembly was 12 min. The total assembly time was 20 min and the total disassembly time was 5 min.

6.3.3. Dead Volume Evaluation

The dead volume was estimated for each of the components within the SCD, shown in Figure 6.12. The total estimated dead volume for the individual components (excluding the silicon tubing) was 221.1 µL. The length of silicon tubing used within the SCD was 68 mm and an additional 32 mm was used to connect the Tee Barb to the syringe pump. The resulting volume within the silicon tubing was 201.1 µL. Ultimately, the total dead volume was 422.2 µL. A starting volume of 2.25 mL was suggested in section 3.2.4.2, and thus, an 18.8% volume loss was estimated within the SCD.

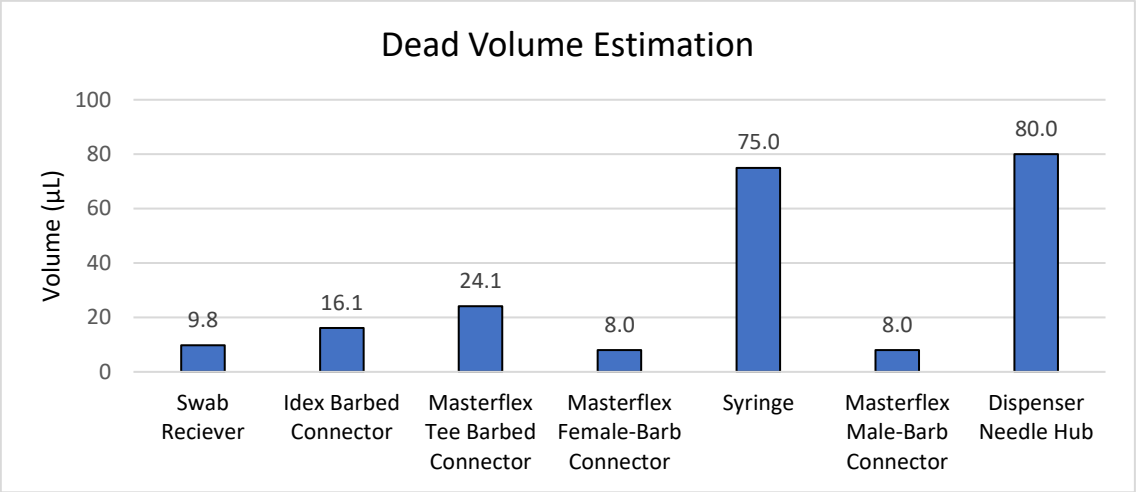

Figure 6.12 – Internal dead volume estimates for the sample collection device

6.3.4. Syringe Pump

A 3D printed syringe pump was used to govern fluid flow through the SPD. Files for an open source syringe pump developed by Wijnen *et al.* were used as a template for the syringe pump used for this study [485]. The parts were imported as .STL files into Solidworks 2020 and were adapted to fit BD syringes ranging from 1 to 10 mL. The components of the syringe pump were fabricated from PLA using an Ultimaker 2+ printer. The fabricated parts were assembled using a methodology described elsewhere [486]. The syringe pump can be seen in Figure 6.13.

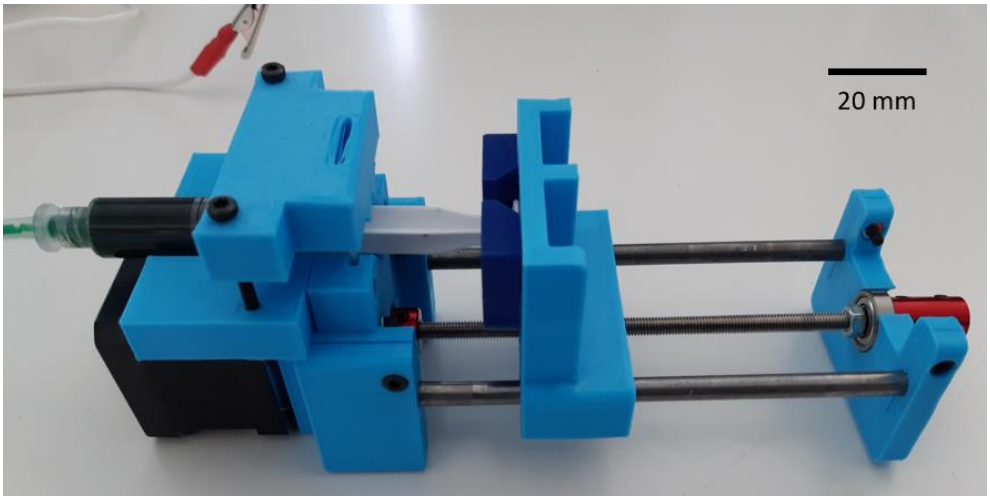

Figure 6.13 – Final Design Idea: Syringe Pump

The syringe pump was driven using a NEMA17 Stepper Motor (National Electrical Manufacturers Association, Rosslyn, Arlington, Virginia, USA), which had a 1.8° step angle and a lead screw with a 1 mm pitch. One full revolution (360°) of the stepper motor corresponds with a 1 mm displacement of the pusher block. The control for the syringe pump (shown in Figure 6.16) was available in the laboratory. A relationship between the step angle and the displaced volume from the syringe pump can be seen in Figure 6.14 in reference to Equation 6.1, where V is the displaced volume, s is the stroke length of the syringe pump and D is the inner diameter of the syringe body.

$$V = \frac{\pi D^2}{4} s \qquad [\mathrm{m}^3] \qquad \textit{Equation 6.1}$$

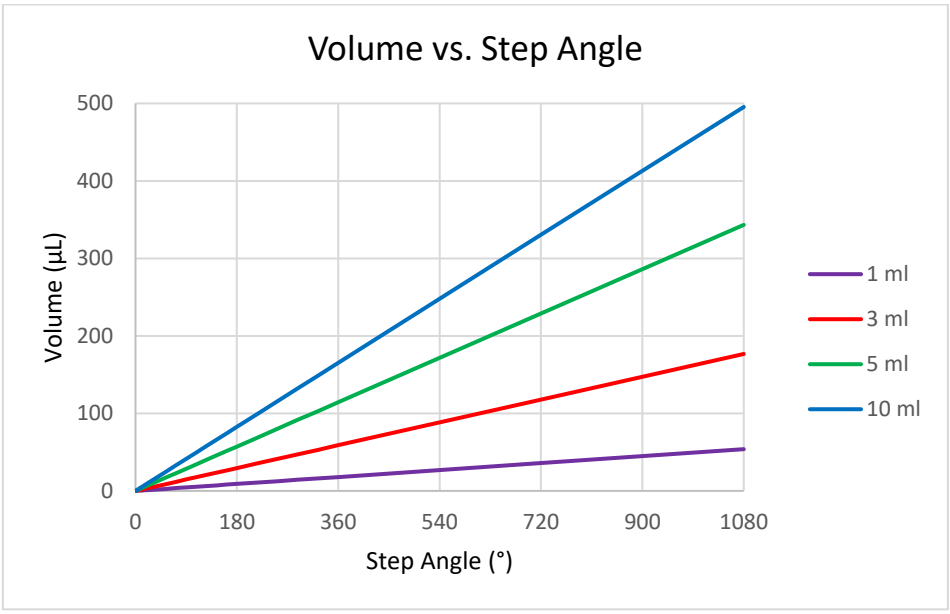

Figure 6.14 – Displaced Volume vs. Step Angle for 1-, 3-, 5- and 10 mL BD Syringes

A comparison between the syringe profiles can be seen in Table 6.1. In order to achieve the highest resolution over the fluid control, while also being able to displace air to the top of the syringe body by adjusting the orientation of the syringe, the 3 mL syringe was selected. Despite having the highest resolution of volume control, the 1 mL BD syringe was omitted from further study, due to the inability to displace bubbles from the body of the syringe without manual interaction or external instrumentation. For the 3-, 5- and 10-mL syringes, placing the syringe pump in a vertical orientation with the nozzle facing upwards was sufficient to displace air bubbles to the top of the syringe, where they could subsequently be expelled. This ensured that the metered volume was correct. The 10 mL syringe was also excluded from further study, as the number of increments required to displace the droplet from the tip of the needle resulted in a substantial overshoot of the desired volume.

Table 6.1 – Estimated stroke length to displace 1 µL from needle tip, based on BD Syringes [487]
The valves for the number of increments was rounded up to ensure the total volume of 1 µL was displaced, using the resolution of the NEMA17 Stepper Motor. The 1 mL and 10 mL BD Syringes were excluded from further study.

Syringe	Inner Diameter (D) (mm)	Stroke Length (s) (µm)	Increments (rounded valves)	Step Angle
1 mL	4.78	55.7	11.1 (12)	21.6°
3 mL	8.66	17.0	3.4 (4)	7.2°
5 mL	12.07	8.7	1.75 (2)	3.6°
10 mL	14.5	6.1	1.21 (2)	3.6°

Using the dead volume estimates from Figure 6.12, the displacement for the syringe pump in each direction was estimated. A flow chart describing the process of the fluid flow during priming and dispensing can be seen in Figure 6.15. In order to prime the pump, a volume of 257.7 µL was required to completely fill the components between the swab inlet and the syringe pump with fluid. Assuming the use of a 3 mL syringe, a displacement of 4.375 mm of the pusher block in the direction away from the syringe was required, equating to a step angle of 1576.8°. Assuming that the syringe pump is primed and absent of any air bubbles, a volume of 164.4 µL was required to completely fill the components between the Masterflex Tee Barbed Connector and the dispenser hub. A displacement of 2.791 mm in the direction towards the syringe was required, equating to a step angle of 1006.2°.

The internal volume of the 14-, 18-, 20-, 21-, 25- and 30-gauge needles was 7.05, 5.18, 1.68, 1.09, 0.62 and 0.22 µL, respectively. The required step angle to actuate the fluid through the dispenser needles and to displace the 1 µL droplet from the needle were 50.4°, 39.6°, 18°, 14.4°, 12.6°, and 9°, respectively.

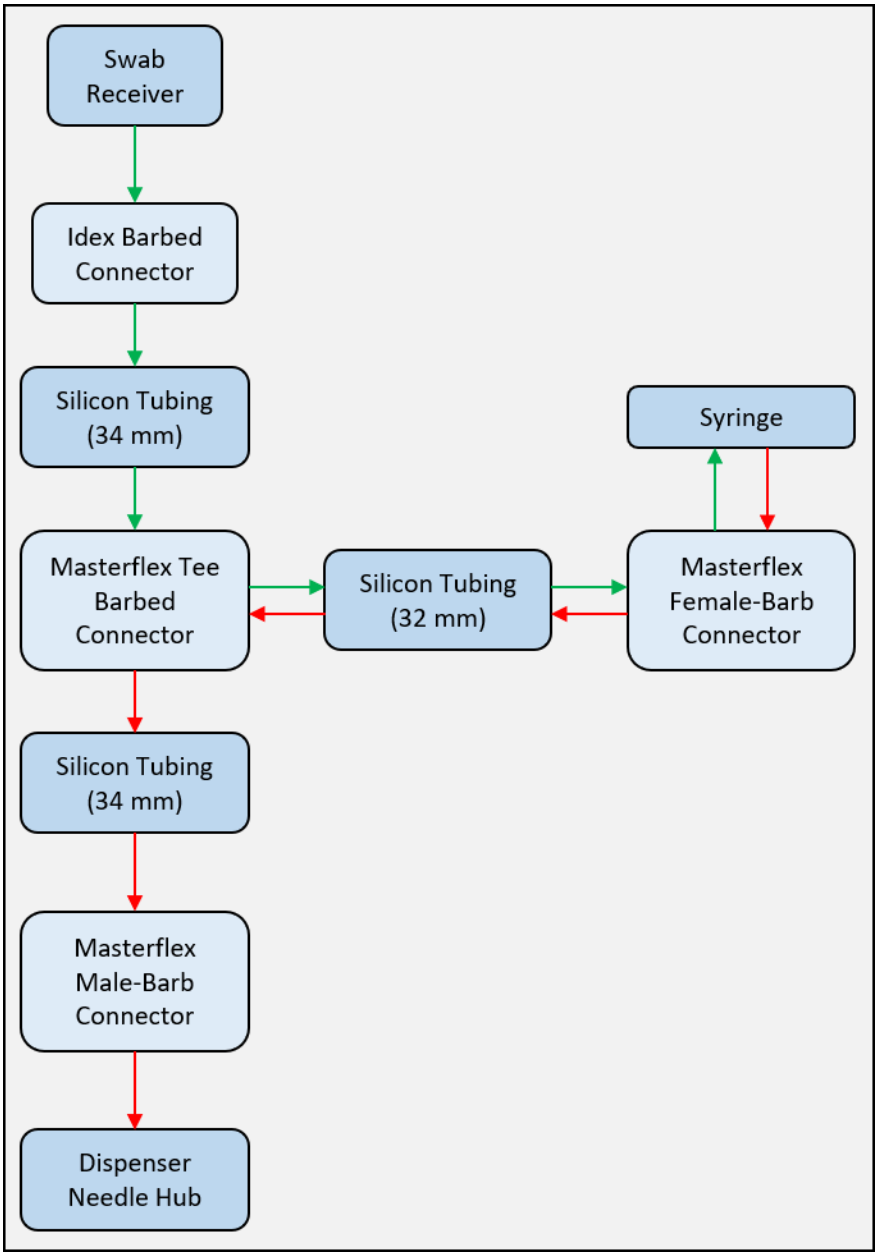

Figure 6.15 – Flow chart of the fluid flow during the priming and dispensing processes
The green arrows indicate the fluid flow during the priming of the syringe pump, while the red arrows indicate the travel of the fluid flow from the syringe to the dispenser needle hub.

6.4. Testing of the Sample Preparation Device

The experimental setup for the sample preparation platform can be seen in Figure 6.16. The HV electrode on the SCD and the ground electrode on the SPD were connected to the +3 kV and ground outputs for the Q40 High Voltage Module, respectively. The Q40 High Voltage Module was connected to a Thurlby Thandar Tti PL310QMT Power Supply (Thurlby Thandar Instruments Ltd., Huntingdon, England), which was connected to mains electricity.

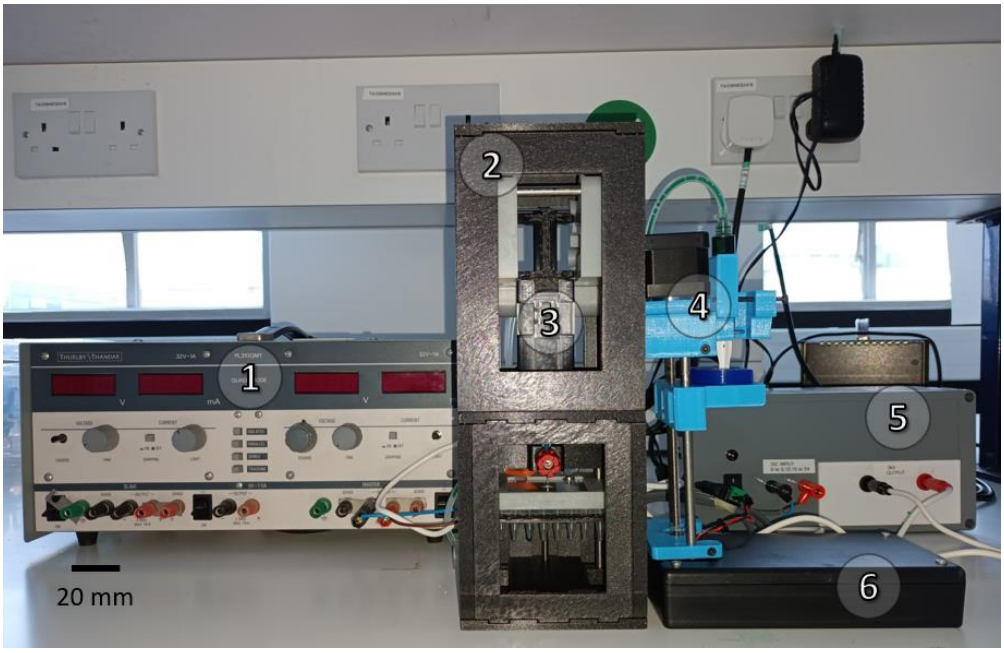

Figure 6.16 – Final Design Idea: Experimental Setup
1. *Thurlby Thandar Tti PL310QMT Power Supply;* ***2.*** *Sample Preparation Device;* ***3.*** *Sample Collection Device;* ***4.*** *3D Printed Syringe Pump;* ***5.*** *Q40 High Voltage Module;* ***6.*** *Syringe Pump Control System*

6.4.1. Droplet Generation through Electrohydrodynamic Dripping

The SCD, SPD and the syringe pump were connected to perform fluidic tests and to test the ability to produce droplets on demand. The EHD configuration can be seen in Figure 6.17. The actual output at the HV electrode was measured at 3.8 kV, and thus, the distance between the electrodes was changed to adjust the strength of the electrical field. The maximum allowable distance between the HV and ground electrodes was 15 mm. A distance of 13 mm between the electrodes was sufficient to encourage dripping to occur. At a distance of 6 mm and below, the droplet would fail to detach from the needle and the emission of corona discharge was observed.

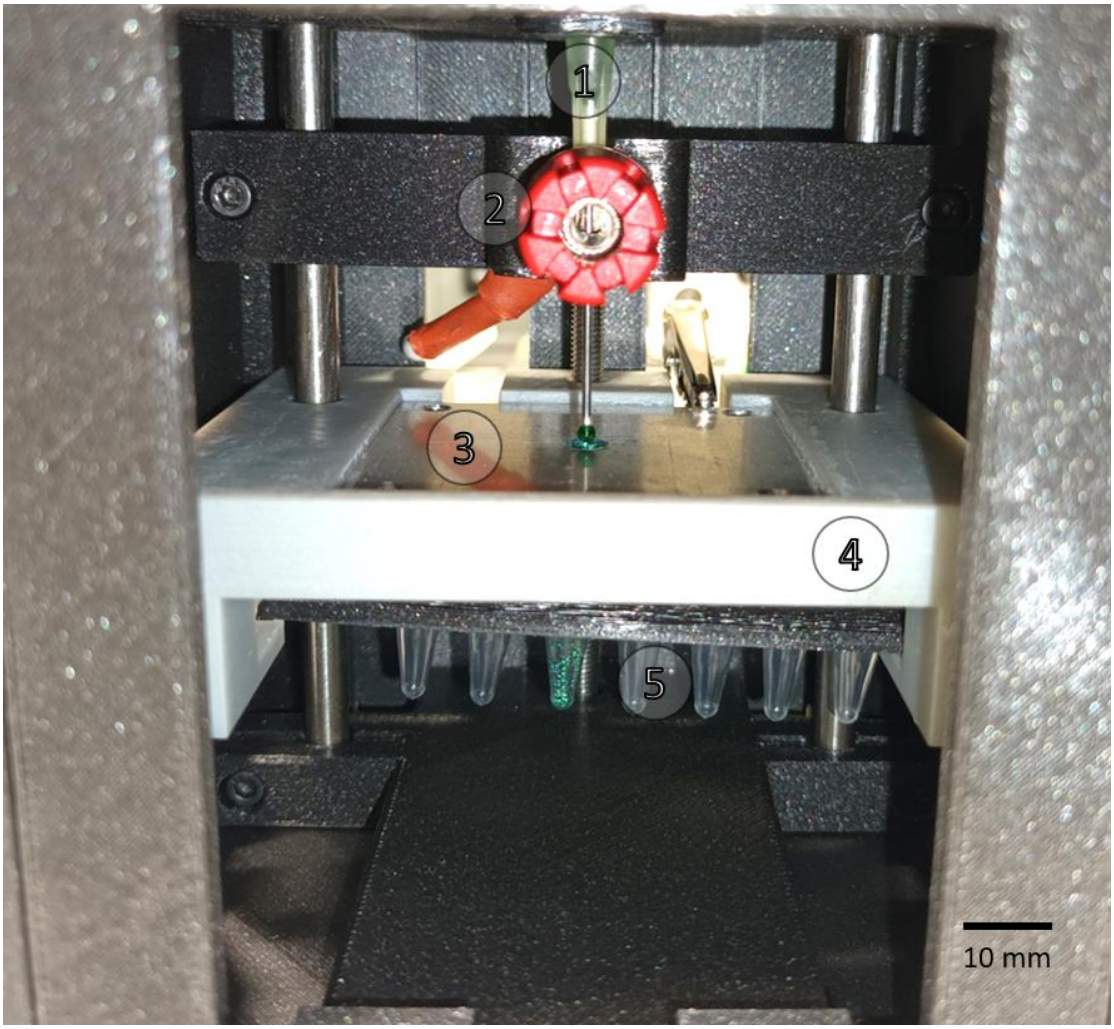

Figure 6.17 – Electrohydrodynamic Dripping System: Experimental Setup
1. *25-gauge blunt tip dispenser needle, used as a HV electrode;* ***2.*** *4mm Red Heavy Duty 30A Binding Post, fitted into a PLA HV Socket Locator;* ***3.*** *50 x 50 mm aluminium plate, used as a ground electrode;* ***4.*** *Accura Xtreme Z-Stage Platform;* ***5.*** *PCR tube strip, used to collect detached droplets.*

The individual PCR tubes were aligned manually with the electrodes using a 3D printed rack. Between operations, the rack was manually positioned so that a tube would align directly beneath the dispenser needle. The droplets yielded by the first iteration of the EHD experimental setup (Figure 6.18) exhibited varying levels of spraying at the ground electrode. Due to the range of the spraying, it was possible that these droplets would be dispensed into adjacent PCR tubes, resulting in a variation in the amount of sample being dispensed into each tube. This prompted a redesign, which increased the hole diameter from 4 mm to 8 mm. Following the redesign, the modified setup (Figure 6.19) was able to encourage dripping at a distance of 11 mm, 2 mm less than the previous platform. Furthermore, the droplets yielded by the modified setup (Figure 6.20) exhibited no signs of spraying. Interestingly, no corona discharge was observed regardless of the electrode orientation.

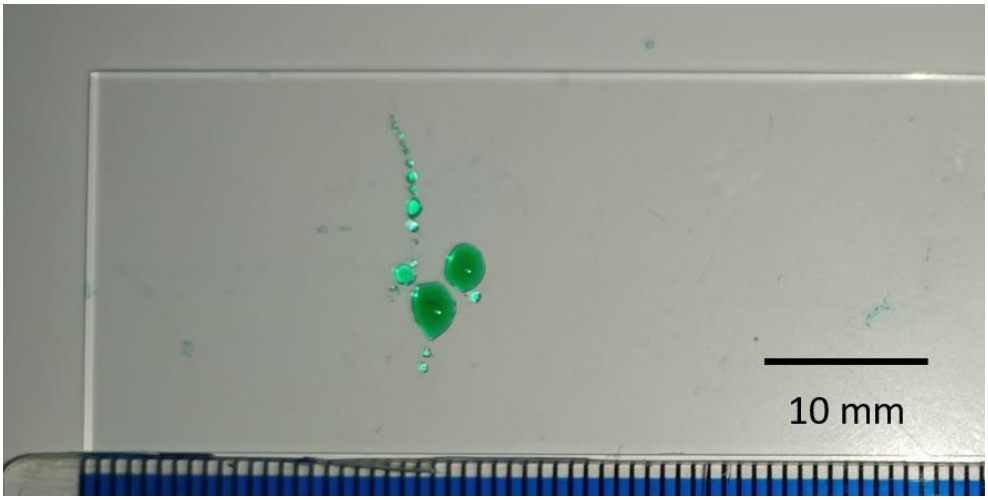

Figure 6.18 – Droplets yielded by the initial EHD setup dispensed directly onto glass slides
A total of 3 droplets were dispensed onto the glass slide. Varying levels of spraying was observed across each droplet.

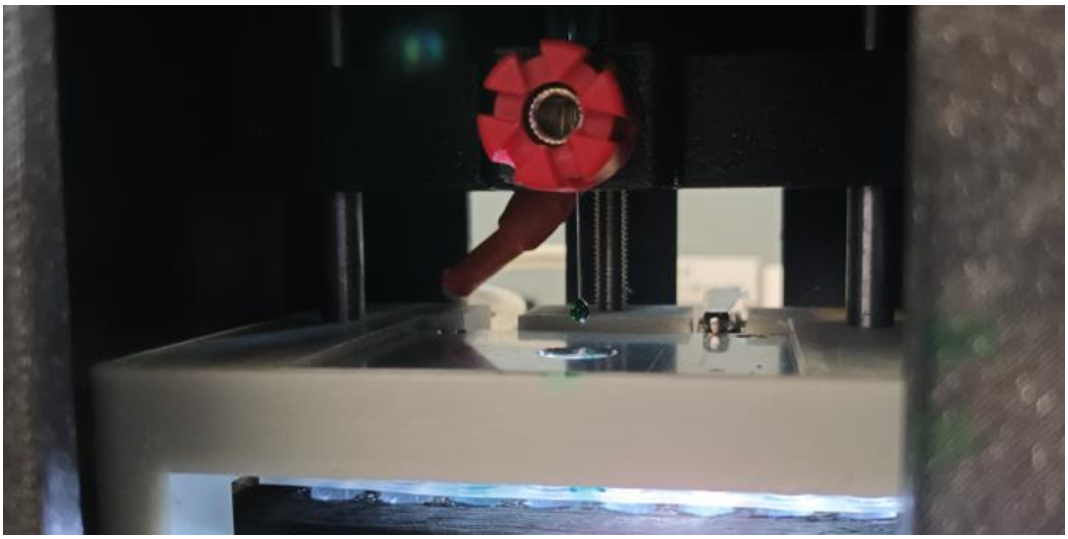

Figure 6.19 – Electrohydrodynamic Dripping System: Experimental Setup
This modification to the setup shown in Figure 6.17, increased the hole diameter from 4 mm to 8mm. At a distance of 11 mm, the droplets would detach from the needle under the applied electrical field.

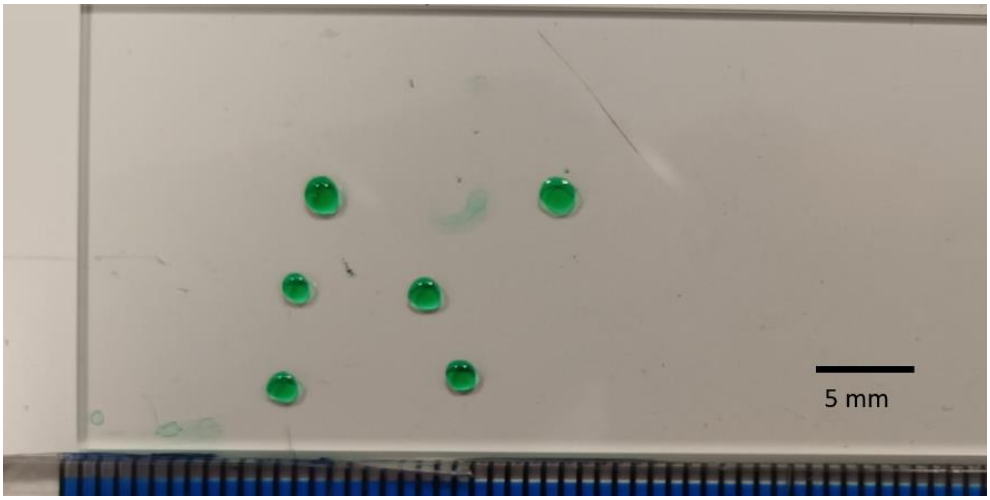

Figure 6.20 – Droplets yielded by the modified EHD setup dispensed directly onto glass slides

A total of 10 droplets were ejected from the HV electrode into the PCR tube strips using the experimental setup and the average droplet volume was determined using the methodology previously described in section 3.3.3.2. An image of the dispensed droplets can be seen in Figure 6.21, with the results of the average droplet volume shown in Figure 6.22. The mean droplet volume was 1.3 µL, ranging from 0.88 to 1.91 µL. Through a comparison with the results yielded in the unassisted configuration, the EHD system presented in this section demonstrated an 86% reduction in the average droplet volume.

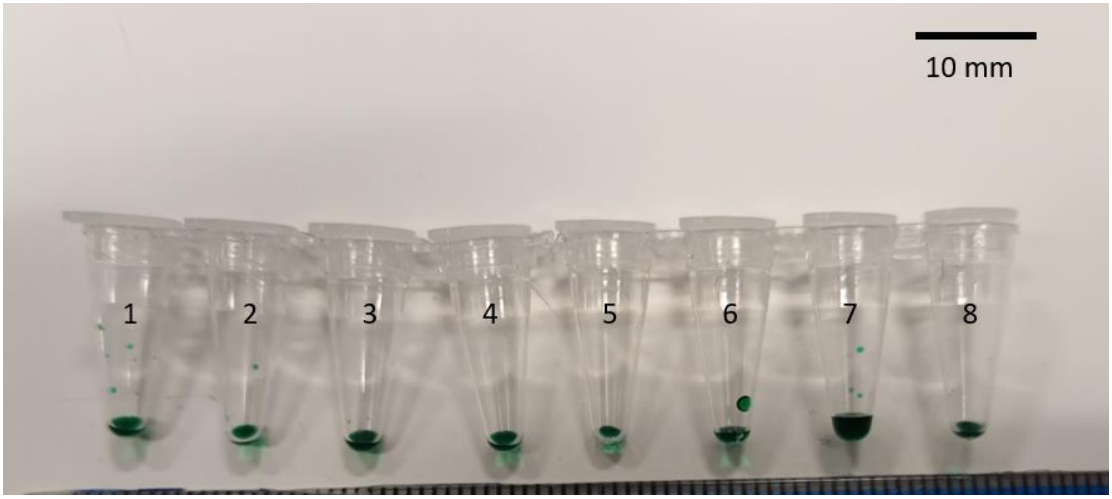

Figure 6.21 – Droplets yielded by the EHD setup dispensed directly into PCR tube strips
A total of 10 droplets were elected from the dispenser needle into the qPCR tube strips. A single droplet was dispensed into each individual tube to prove correct functionality and to provide a comparison between droplet sizes. Tube 7 contained a total of 3 droplets. The experiment was repeated across 10 tube strips.

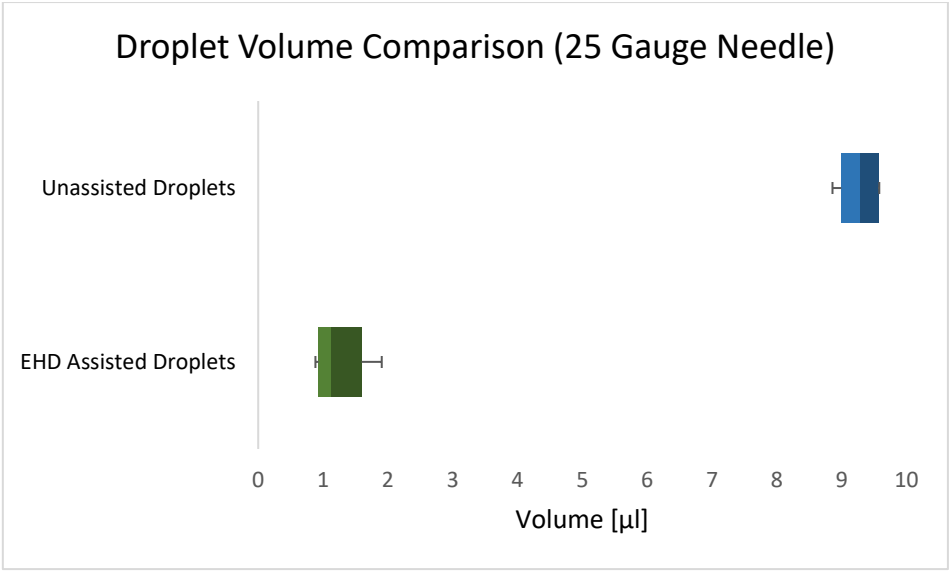

Figure 6.22 – Box plot comparing standard and electric field assisted droplet volumes
The desired droplet volume was 1 µl. The mean droplet volume for the EHD assisted droplets was 1.3 µL, ranging from 0.88 to 1.91 µl. The results of each of the tube strips were within 2 standard deviations (1 SD = ± 0.33 µl) of the mean.

The volume of the droplets was determined by weighing them following their release into PCR tubes; however, methods to measure the droplet size within fluid handling systems should be available in real time [360]. An open source plugin (Pendant_Drop) developed by Daerr and Mogne for the image processing software ImageJ (National Institutes of Health, Bethesda, Maryland, USA; Laboratory for Optical and Computational Instrumentation, Madison, Wisconsin, USA) was used with a smartphone camera to measure the volume of the droplets. The plugin matches a theoretical profile to the contour of the pendant droplet, providing values for the droplet volume and the surface tension [488].

The software was tested using droplets suspended from the 14-gauge needle. An image taken of the droplet was (Figure 6.23) was cropped and imported into ImageJ, which was then converted from an RGB to an 8-bit greyscale format. (Figure 6.24).

Figure 6.23 – Droplet formed at the 14-gauge needle imported into ImageJ

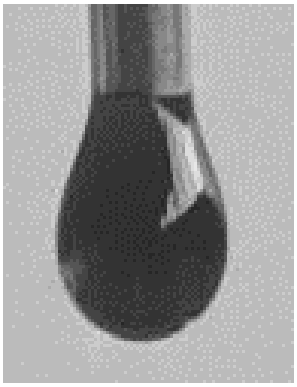

Figure 6.24 – The images imported into ImageJ were converted into 8-bit greyscale

Measurements of the outer diameter of the needle were taken within the ImageJ software, as shown in Figure 6.25. The pixel length (33.26) was converted into the known outer diameter of the 14-gauge needle (1.27 mm), previously shown in Table 3.3.

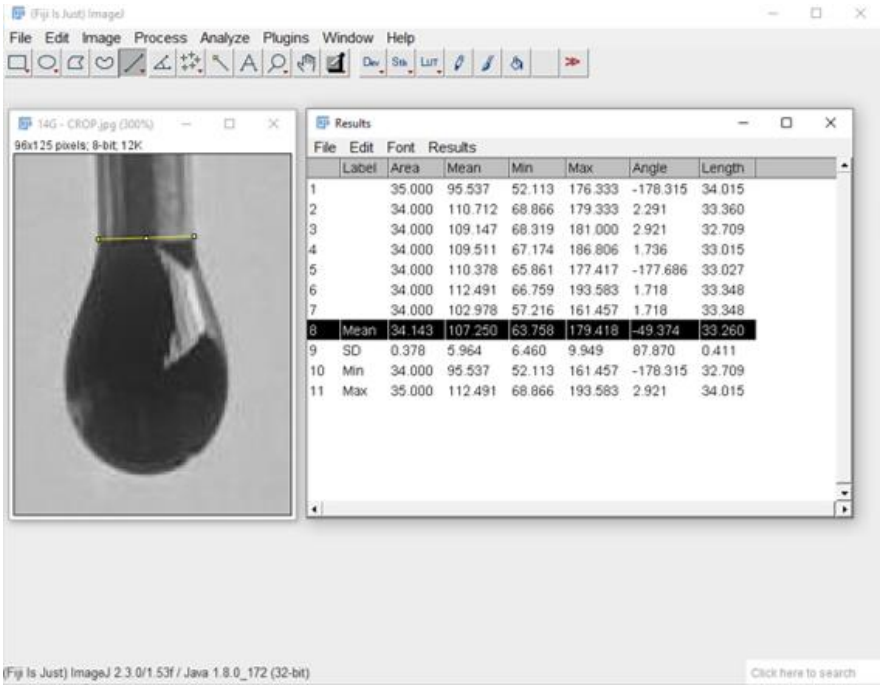

Figure 6.25 – Plugin usage: Measuring the diameter of the dispenser needle
The yellow line signifies the outer diameter of the 14-gauge dispenser needle. This line was equivalent to 33.26 pixels. This was converted into the known length of 1.27 mm, as shown in Table 3.3

Following calibration, the plugin was initialised, with the capillary length set to 2.7 mm, taken from literature [489]. The results (Figure 6.26) demonstrated the droplet volume was 7.93 µL.

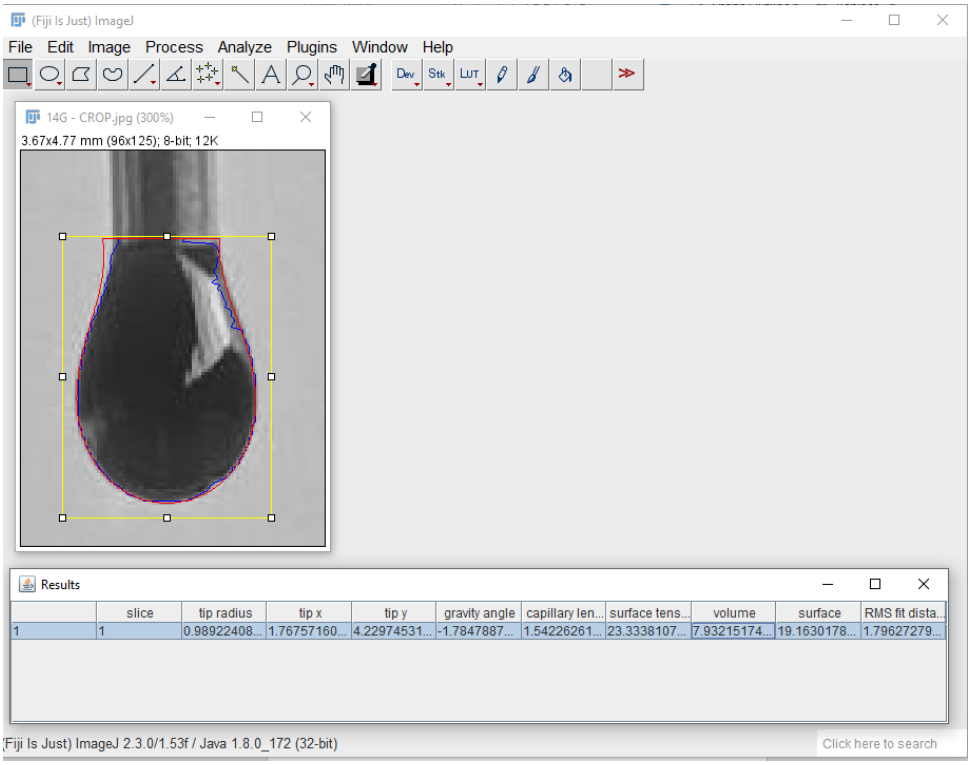

Figure 6.26 – Plugin usage: Initialising the pendant drop plugin
The capillary length was set to 2.7 mm, taken from literature [489]. The droplet volume was determined to be 7.932 µL

The values obtained from the plugin were significantly smaller than the experimental values reported in section 3.3 (Figure 3.10a). Assuming the droplets were completely spherical, the experimental droplet radius (r_{exp}) and the droplet radius measured using ImageJ (r_{IJ}) were calculated using Equation 6.2, where V_{exp} is the experimental droplet volume and V_{IJ} is the droplet volume measured using ImageJ. Using Equation 6.3, the error was calculated as 39.2%.

$$r_{exp} \approx \sqrt[3]{\left(\frac{3V_{exp}}{4\pi}\right)} \qquad r_{IJ} \approx \sqrt[3]{\left(\frac{3V}{4\pi}\right)} \quad [\text{m}] \qquad \textit{Equation 6.2}$$

$$\approx \sqrt[3]{\left(\frac{3(35.23)}{4\pi}\right)} \qquad \approx \sqrt[3]{\left(\frac{3(7.932)}{4\pi}\right)}$$

$$r_{exp} \approx 2.034\ mm \qquad r_{IJ} \approx 1.237\ mm$$

$$error = \frac{r_{exp} - r_{IJ}}{r_{exp}} x100 \qquad \textit{Equation 6.3}$$

$$= \frac{2.034 - 1.237}{2.034} x100$$

error = 39.18%

6.4.2. Heating

6.4.2.1. Design Idea 2

Based on the design proposed in section 5.4.3 (Figure 5.50), an experiment was setup in order to determine the temperature increase in relation to an applied electrical potential. The reagent capsule was filled with 1 ml of DI H_2O. A Digimess® HY3003-3 Power Supply (Digimess Instruments Ltd, Derby, England, UK) was connected to a nichrome wire coil, which was then subjected to currents from 0.05 to 1 A in increasing increments of 50 mA. Thermocouples recorded the local temperature at the centre (T_1), top (T_2) and bottom of the reagent capsule (T_3). These values were averaged to determine the temperature within the heating system (T_{AVG}). The experimental setup can be seen in Figure 6.27.

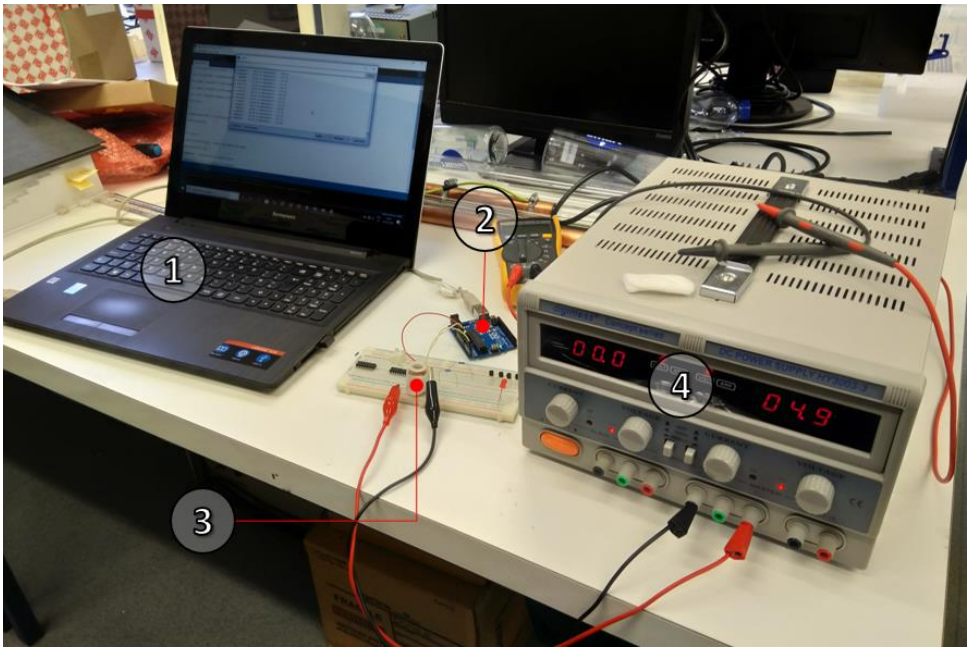

Figure 6.27 – Experimental setup of the low-cost heating system
***1.** A laptop running Arduino IDE (Arduino Software, Ivrea, Italy) recorded temperate readings from the thermocouples; **2.** An Arduino Uno measured the temperature of the heating system; **3.** The heating system was mounted onto a breadboard and fitted with thermocouples; **4.** A Power Supply provided an electrical potential across the nichrome wire.*

The current-voltage characteristic of the unloaded nichrome wire coil can be seen in Figure 6.28. The resistance was calculated as 6.57 ohms using Equation 6.4, where the value for the gradient was taken from the trendline of the current voltage curve.

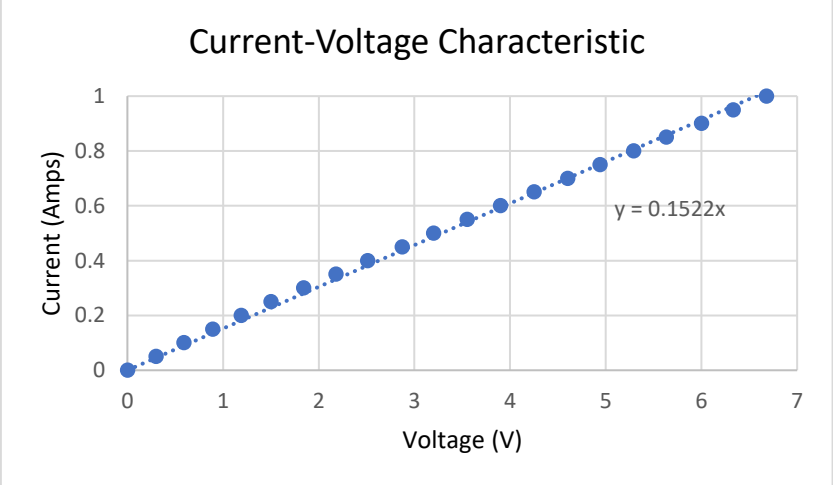

Figure 6.28 – Current-Voltage characteristic of the unloaded nichrome wire coil. Using the trendline, the resistance was determined at 6.57 ohms

$$R = \frac{1}{Gradient} \quad [\Omega]$$ *Equation 6.4*

The heating system shown in Figure 6.27 yielded the results shown in Figure 6.29. At the time of performing this experiment, two separate heating steps at 55 and 92 °C were required for cell lysis and incubation, respectively. For incubation and cell lysis steps, a current of 0.55 and 0.83 A were required to reach the desired temperature, respectively.

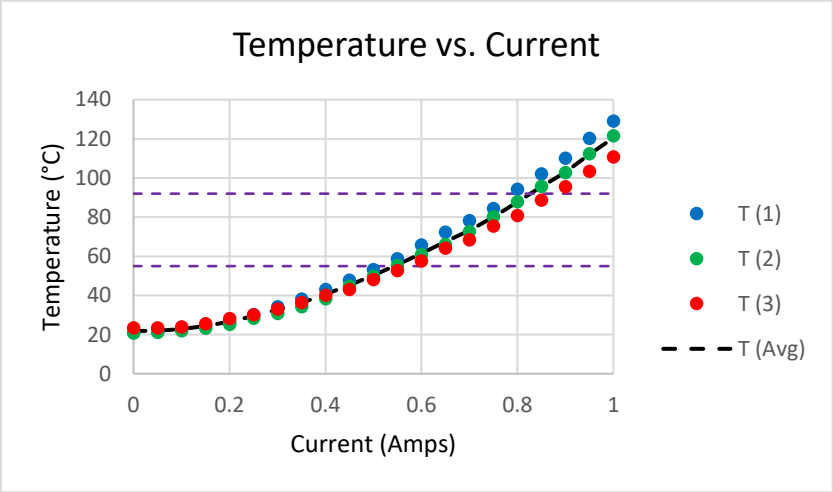

Figure 6.29 – Temperature vs. Current

Three thermocouples located at the top (T_1), middle (T_2) and bottom (T_3) of the reagent capsule were used to determine an average temperature (T_{AVG}) across the heating system. Readings were taken after 5 minutes to ensure thermal equilibrium across the system. A T_{AVG} of 55 °C was achieved at 0.55 A, while T_{AVG} of 92 °C was achieved at 0.83 A.

The experiment was repeated in two scenarios: Scenario 1 (4 V, 0.64 A) and scenario 2 (5 V, 0.83 A) to record the time taken to reach 55 °C. The results for the temperature ramp rate can be seen in Figure 6.30. For scenario 1, the heating system took 430 seconds to reach the desired temperature, while for scenario 2, the heating system took just 130 seconds, 5 minutes less than scenario 1.

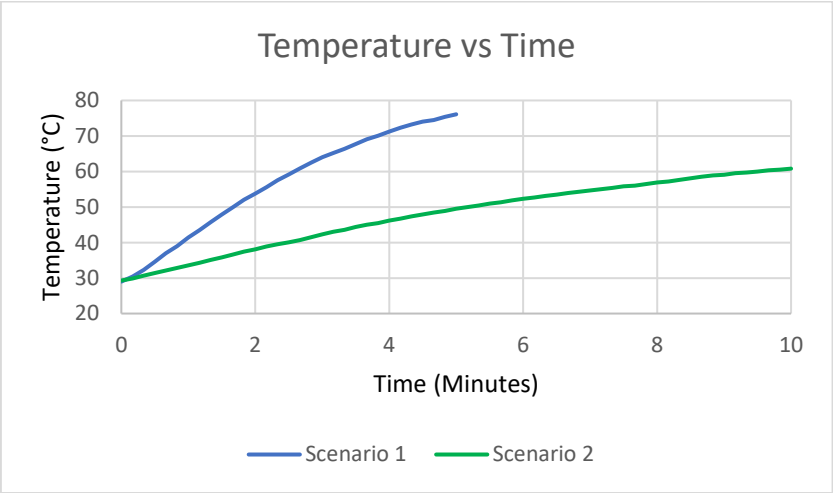

Figure 6.30 – Temperature vs. Time

Time readings were taken every 5 seconds. For Scenario 1, (4 V, 0.64 A), the heating system took 430 seconds to reach an average temperature of 55 °C. For Scenario 2, (5 V, 0.83 A), the heating system took 130 seconds to reach an average temperature of 55 °C

The T_1 thermocouple gave the highest temperature readings, followed by the T_2 thermocouple and the T_3 thermocouple, which gave the lowest readings. The heat discrepancies were observed above applied currents of 0.3 A. At 0.55 A, where an average temperature of 55 °C was achieved, the difference between the highest and lowest readings was 6.1 °C; while at 0.83 A, where an average temperature of 92 °C was achieved, the difference between the highest and lowest readings increased significantly to 13.4 °C. It was determined that the temperature towards the top of the heating system was higher than the temperature towards the bottom. The reason for this discrepancy was attributed to the occurrence of convective heat transfer within the DI H_2O.

6.4.2.2. Final Design Idea

Tests to assess the performance of the platform presented in section 6.3.2 were conducted. Each heating system consisted of a machined aluminium heater block, a resistive heating element fabricated by Newbury Electronics Ltd and a heater block clamp fabricated from Formlabs High Temp resin. The components of the heater can be seen in Figure 6.31.

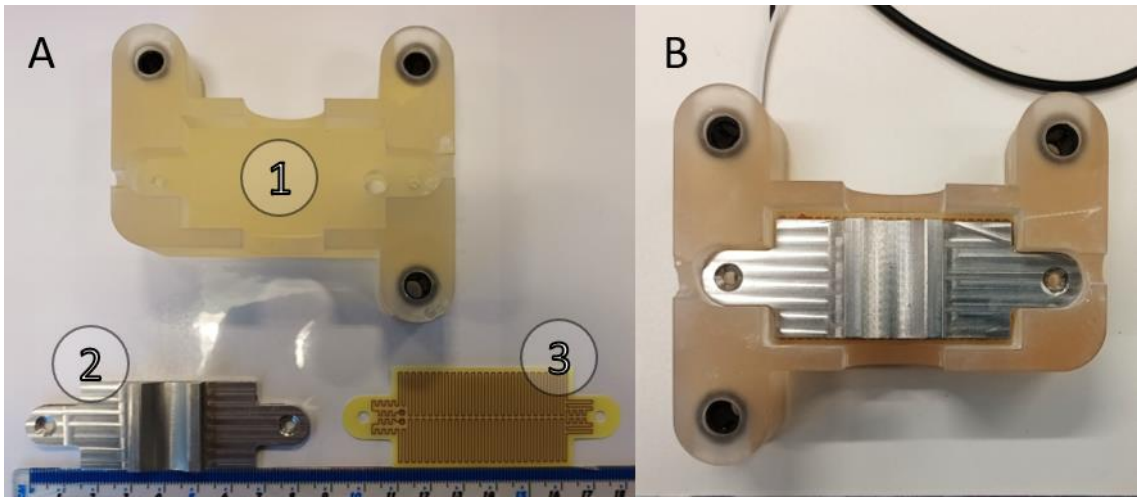

Figure 6.31 – Final Design Idea: Sample Preparation Device (Heater Block Assembly)
***A.** The individual components of the heating system. 1, Formlabs high temp resin heater block clamp; 2, Aluminium heater block; 3, Resistive heating element **B.** The assembled heating system, referred to as the "loaded heater".*

The resistive heating element was connected to a Thurlby Thandar Tti PL310QMT Power Supply prior to assembly (henceforth, the "unloaded heater") to determine the temperature produced absent of any adjacent components (henceforth, the "unloaded temperature"). A voltage range of 0.1 – 5 V was applied to the resistive element in increments of 0.1 V. The temperature was recorded at the left-hand side (T_1), centre (T_2) and right-hand side (T_3) of the unloaded heater using thermocouples, which were averaged to determine the unloaded temperature (T_{AVG}). The experiment was then repeated

following assembly (henceforth, the "loaded heater") to determine the temperature produced in the presence of the coupled components (henceforth, the "loaded temperature"). The current-voltage characteristic for the unloaded heater can be seen in Figure 6.32. Using the gradient taken from the trendline of the current-voltage curve, the resistance was calculated as 3.78 ohms.

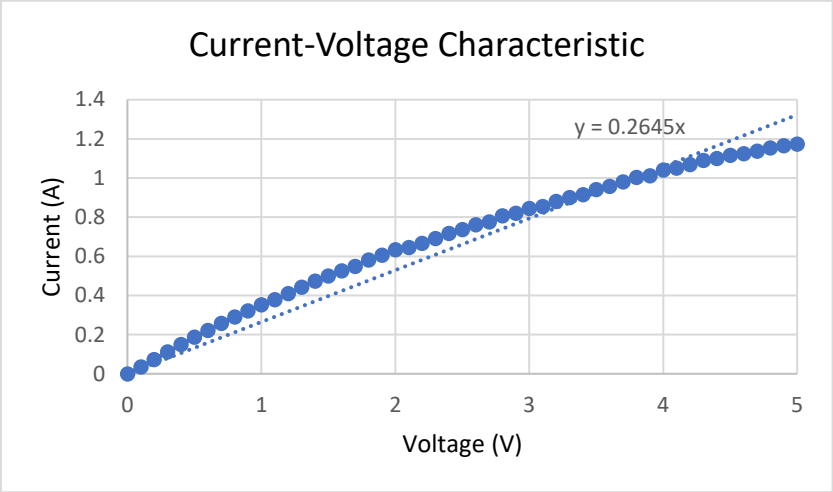

Figure 6.32 – Current-Voltage characteristic of the unloaded resistive heating element. Using the gradient of the trendline, the resistance was determined at 3.78 ohms

A comparison between the loaded and unloaded temperatures can be seen in Figure 6.33. At the time of performing the experiment, the goal was to achieve a temperature of 92 °C to achieve cell lysis. For the unloaded heater, 3.8 V were required to reach the desired temperature. For the loaded heater, 4.55 V were required to reach the desired temperature.

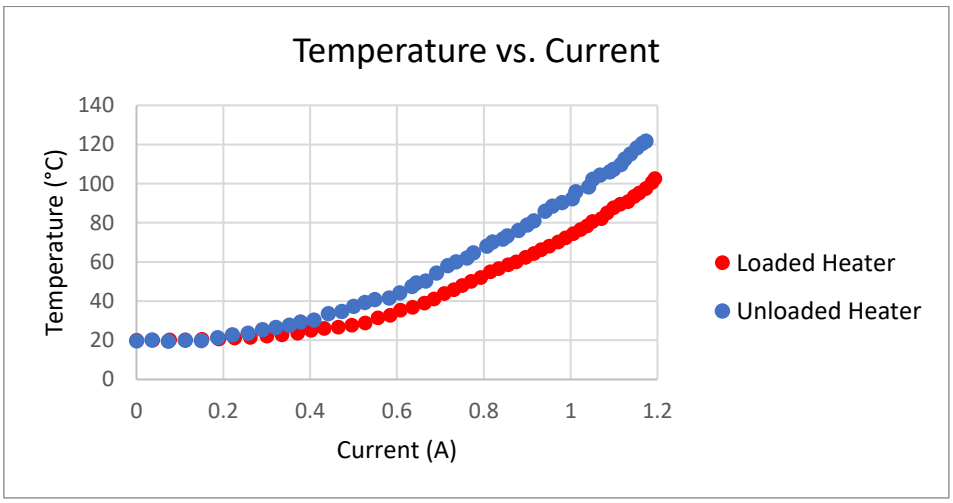

Figure 6.33 – Temperature vs. Current for the Unloaded and Loaded Heating Systems

Three thermocouples located at the left-hand side (T_1), centre (T_2) and right-hand side (T_3) of the heater were used to determine an average temperature (T_{AVG}) across the heating system. Time readings were taken after 5 minutes to ensure the system had reached thermal equilibrium. The unloaded heater required 3.8 V (1.004 A) to reach the desired temperature of 92 °C. The loaded heater required 4.55 V (1.146 A) reach the desired temperature of 92 °C.

The SPD was assembled as shown in Figure 6.34. Each heating system was connected to a Thurlby Thandar Tti PL310QMT Power Supply, which supplied a constant voltage throughout the duration of the experiment. A Testo 925 Type K Thermometer was used to monitor the temperature change within the swab receiver presented in section 4.3.6 (Figure 4.24), which was placed between the heater blocks (as shown in Figure 4.27), filled with 3 ml of DI H_2O and sealed to prevent evaporation. The experiment was conducted for two scenarios: Scenario 1 (4.6 V, 1.146 A) and scenario 2 (5 V, 1.194 A), with recordings taken every 5 seconds to monitor the temperature increase over time.

The goal of the experiment was to reach the desired temperature of 92 °C within 5 minutes. A plot comparing the performance of the heating system in both scenarios can be seen in Figure 6.35. For scenario 1, the temperature increased by 54.0 °C within the recorded 20-minute time period, while for scenario 2, the temperature increase was 61.0 °C. The desired temperature was achieved within 25 minutes in scenario 1, while the heating system took 22.5 minutes to reach the desired temperature for scenario 2.

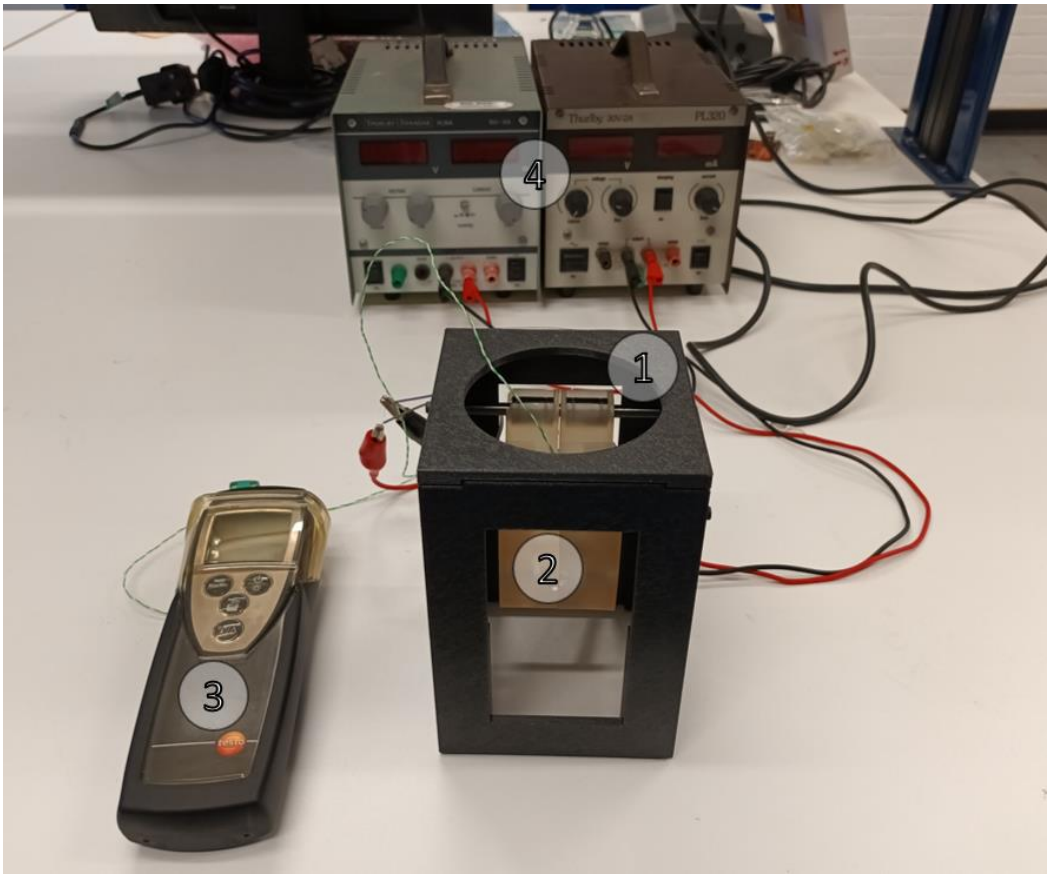

Figure 6.34 – Experimental setup of the assembled heating system

***1.** The heating module was used independently for the heating experiment; **2.** The assembled heating system was placed within the sample preparation device. The swab receiver was placed between the moving jaws and filled with 3 ml of DH_2O; **3.** A Testo 925 Type K Thermometer (Testo, Hampshire, UK) was used to record the temperature. A temperature probe was connected and placed within the swab receiver; **4.** A Digimess® HY3003-3 Power Supply was used to provide an electrical potential across each heater*

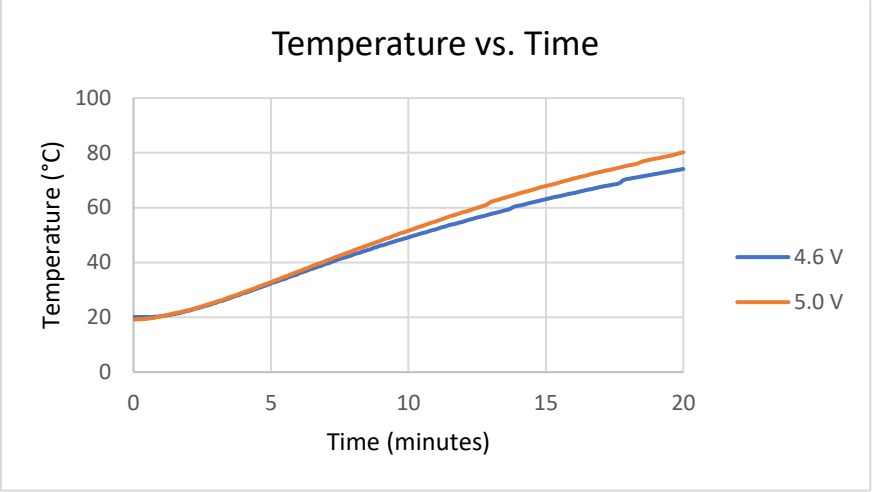

Figure 6.35 – Temperature vs. Time

Time readings were taken every 5 seconds from 0 to 20 minutes. Scenario 1 (4.6 V, 1.146 A) took 25 minutes to heat the fluid to 92 °C. Scenario 2 (5 V, 1.194 A) 22.5 minutes to heat the fluid to 92 °C.

These questionable results prompted a comparison between this heating system against the nichrome wire heating system presented in section 5.4.3. A plot of the recorded resistances of each heating system can be seen in Figure 6.36. While both heating systems demonstrated a non-linear relationship between the resistance and the voltage, the gradient of the heating system shown in this section was much steeper than the system previously presented in section 6.4.2.1, indicating a significant increase in resistance at a higher voltage.

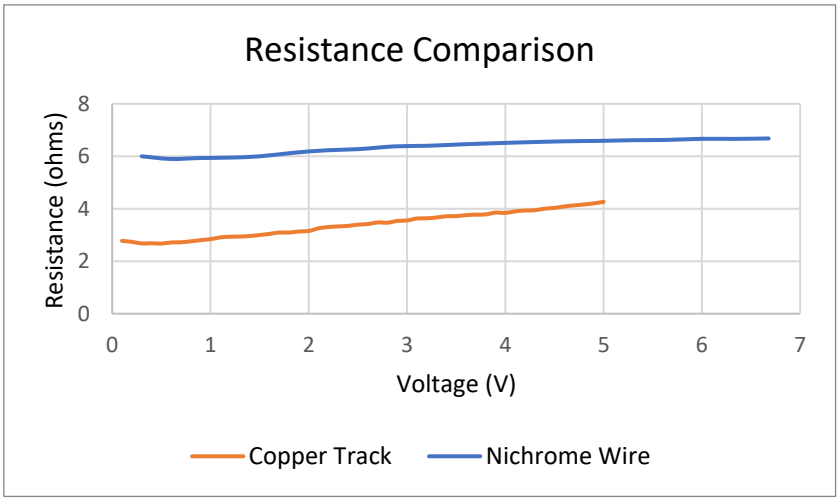

Figure 6.36 – Resistance vs. Voltage for the Two Fabricated Heating Systems

The heating system shown in Figure 6.27is referred to as "Nichrome Wire", while the heating system shown in (Figure 6.31) is referred to as "Copper Track".

It was hypothesised that the increase in resistivity could be attributed to the increase in temperature, leading to initial calculations through the application of Ohm's law (Equation 5.26) being insufficient. Thus, the effect of the temperature on the resistivity was studied using Equation 6.5, where T_0 is the

initial temperature, T_t is the actual temperature, α is the temperature coefficient of resistivity, ρ_{R0} is the resistivity at T_0 and ρ_{Rt} is the actual resistivity at T_t [490,491].

$$\rho_{Rt} = \rho_{R0}(\alpha + [T_t - T_0]) \qquad [\Omega \cdot m] \qquad \textit{Equation 6.5}$$

The values used to calculate the thermal coefficient of expansion can be seen in Table 6.2. The resistivity of the nichrome wire was 1.12 x 10^{-6} Ω·m [470] and its thermal coefficient of resistivity was 1.7 x 10^{-4} °C^{-1} [490]. The resistivity of copper was 1.72 x 10^{-8} Ω·m and the thermal coefficient of resistivity was 3.86 x 10^{-3} °C^{-1}. These values were taken from COMSOL Multiphysics software, which were also used in section 5.4.4 to perform heat transfer simulations. Finally, the resistance was calculated using Equation 5.28; however, the resistivity term "ρ_R" was substituted with "ρ_{Rt}" to provide the actual resistance at the temperature T_t, R_t. The calculated results agreed with the recorded results for each experiment as shown in Figure 6.37. Thus, the hypothesis connecting the increase in resistance to the increase in temperature was supported.

Table 6.2 – Values used to calculate the thermal coefficient of expansion
α, temperature coefficient of resistivity; ρ_{R0}, resistivity at the temperature T_0; A, cross-sectional area of the resistive heating element; L, length of the resistive heating element

	α ($°C^{-1}$)	ρ_{R0} Ω·m	A (mm^2)	L (mm)
Copper Track	3.86 × 10^{-3}	1.72 x 10^{-8}	1.05 x 10^{-2}	1595.72
Nichrome Wire	1.7 x 10^{-4}	1.12 x 10^{-6}	5.067 x 10^{-2}	300

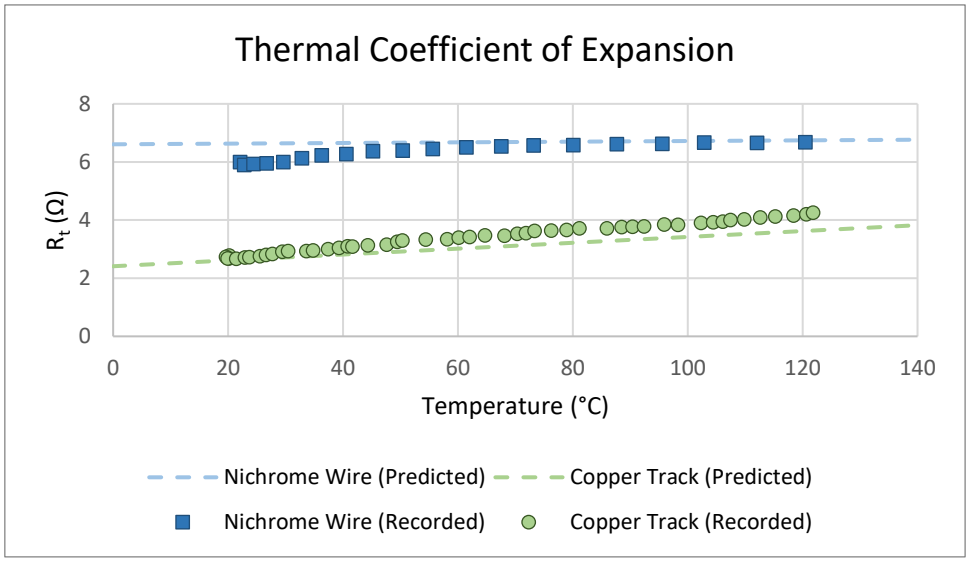

Figure 6.37 – Actual Resistance vs. Temperature for the Two Fabricated Heating Systems
The heating system shown in Figure 6.27 is referred to as "Nichrome Wire", while the heating system shown in (Figure 6.31) is referred to as "Copper Track".

The experimental results for the heating module produced higher temperatures than required, due to a margin provided to account for changes in the ambient temperature. Thus, an overshoot was expected. An Arduino driven temperature controller was developed in order to control the temperature of the heaters, adapted from works described elsewhere [492]. However, this was not completed during this project. The device would use an MAX6675 K-Type Thermocouples (RS Components, Corby, England) to sense temperature changes and a TIP120 transistor (Adafruit Industries, New York, New York, USA) to control the current flow to the resistive heater. The schematic of the temperature controller can be seen in section 8.4.2.

6.5. Discussion

6.5.1. Sample Collection Device Proposed in Design Idea 4

Due to the low glass transition temperature of PETG (≈80 °C), biological validation of the model was unable to be performed, as the temperature of 92 °C required to conduct cell lysis would affect the integrity of the SCD. The time lapse demonstrating the filling of the heating chamber (Figure 6.2) indicated the potential presence of an air bubble in the top left-hand side of the trapezoidal chamber. A similar observation was noted for the two-phase flow simulation for Case 1 (Figure 5.22). Thus, the reliability of the computational model was proven. The formation of air bubbles is a concern typical to microfluidic applications. In this instance, the presence of the air bubble reduced the volume within the trapezoidal chamber below the desired 1 mL. The bubbles which form within a chamber can remain stationary and increase in size, resulting in an increase in fluid resistance and an eventual blockage of fluid flow [493]. These air traps are typically caused by flaws in the geometrical design [494]. A fluid travelling from a channel into a chamber experiences a large change in the cross-sectional area, increasing the susceptibility of bubble formation [495]. This was noted in both the simulation and the fluidic tests. Works by Choi, Na and Kim have integrated silicon oxide hydrophilic strips into thermoplastic microfluidic chambers to influence the shape of the fluid meniscus during the filling of a chamber by capillary action [495]. The flat meniscus improved contact with the chamber walls during the filling process, preventing the formation of air bubbles.

6.5.2. Final Platform

The platform presented in section 4.3.6 consisted of individual heating, valving and EHD systems, which performed as defined in the design description. The temperature ramp rate was significantly lower to calculations provided in section 5.4.4, requiring 15 minutes more than intended to reach the desired temperature of 92 °C. Calculations of the resistivity in section 6.4.2.2 demonstrated a significant increase in the resistance from 2.61 Ω at 20 °C to 3.54 Ω at 92 °C. Consequently, this resulted in a reduction in the expected current of 2.03 A to an actual current of 1.41 A at 5 V. There are other factors which influenced the performance of the heating system. The heat tests were performed in facilities which were susceptible to ambient conditions, which resulted in fluctuations in the air temperature of ±3.4 °C during testing, due to sudden increases in air flow. This could have created heat losses as a result of forced convection. Another key factor was hypothesised to be the inclusion

of the moving jaw (Figure 5.52), which was not accounted for in the simulation performed in section 5.4.4. While this feature was intended to act as an insulator and prevent heat from escaping into the surroundings through convection and radiation, the moving jaw may have acted as a heat sink, absorbing a substantial portion of the thermal energy supplied by the resistive heating element in the form of conduction.

The EHD module shown in section 6.4.1 was capable of yielding droplet sizes within the desired 1 – 3 µL range. This was a preliminary design, serving as a means to overcome the surface tension of the hanging droplet attached to the dispenser tip needle. As a result, further work is needed to optimise this design. This EHD module was the largest concern in terms of power consumption, due to requiring a 12 V output to drive the Q40 High Voltage Module. Commercially available 20,000 mAh power banks are capable of producing a 12 V output; however, this is not standard and will greatly increase the power consumption. Of course, it should be noted that a short time of a few milliseconds is sufficient to encourage droplet detachment from the needle; however, further research is needed to ensure the device is functional using a suitable power bank.

6.6. Chapter Summary

While the results of the SCD design proposed in section 4.3.5 held no notable significance over the final design, the fluidic tests presented in section 6.2.1 validated the two-phase flow computational model presented in section 5.2.5. Furthermore, the membrane valves design presented in section 5.3.3 were demonstrated to work as individual components. Consequently, it may be claimed that this design may be effective with access to higher resolution 3D printers.

The heating system shown in section 6.4.2.2 was demonstrated to heat the contained liquid to 92 °C, demonstrating the ability of the platform to perform cell lysis. The calculated voltage and simulations presented in section 5.4.4 proposed a required voltage of 5.19 V, which offered similar results (Figure 5.59). Thus, the computational simulation validated the proposed design. The heating system was compared to the experimental setup developed from the design proposed in section 5.4.3. The copper resistive heating element experienced a significant increase in resistivity at higher temperatures compared to the nichrome wire. Subsequently, the temperature ramp rate of the copper resistive heating element was more gradual in comparison to the nichrome wire. Of course, it must be noted that the nichrome wire was tested on an unloaded system, while the copper resistive heating element was tested within a fabricated platform. Furthermore, while the nichrome wire required careful wrapping around the copper tube to ensure the coils were equally spaced, the copper resistive heating element was integrated onto a PCB which was suitable for batch scale production. Thus, the design of the copper heating element was beneficial for reducing the labour intensity and fabrication time.

In summation, the fabrication of the sample collection and preparation device was presented in this chapter. The performance of the platform proposed in section 4.3.6 was then tested, assessing the capabilities of the EHD and heating modules independently. Both platforms were demonstrated to function as outlined in Chapter 3, with the heating module demonstrating its ability to reach temperatures of 92 °C to facilitate cell lysis and the EHD module capable of releasing droplets 86% smaller than the unassisted droplets yielded in section 3.3. Furthermore, a redesign of the surrounding casing to include Lego® styled fittings substantially reduced the assembly time by over 78%. This offered a rather unique ready-to-assemble platform which can be delivered directly to the user for on-site assembly.

7. Discussion and Conclusion

7.1. Introduction

Low-cost and accessible molecular diagnostic options are severely lacking in the developing world. POCT is a vital means to meet the demand for molecular testing within small, handheld or tabletop platforms, mitigating the common needs of large volumes of reagents, storage facilities, complex instrumentation and skilled technicians. This reduces the costs and widens accessibility. The benefits are not strictly limited to the developing world, but offer a crucial opportunity in the developed world, alleviating pressure on healthcare professionals by allowing screening to be conducted at the convenience of the patient. The crux of POCT is sample preparation, often described as the bottleneck of molecular diagnostics. Traditional sample preparation is laborious and time-consuming. Most notably, the streamlining of sample preparation steps applicable to a multitude of sample types into sophisticated POCT platforms remains elusive.

The aim of the project was to develop a sample preparation platform that met the REASSURED criteria. The focus was placed on performing NA extraction on cloacal swab samples for the detection of prevalent bacterial and viral infections in poultry, and later, to perform RNA extraction from NP and OP samples to detect SARS-CoV-2 following the Covid-19 outbreak. The research conducted during the development of this project would serve to answer crucial research questions posed in Chapter 1.

7.2. A Universal Sample Preparation Device for Resource-Stressed Settings

The final sample preparation platform was comprised of a heating module, used to conduct thermal lysis; an open-source syringe pump and switch valves used to govern fluid flow through the SCD; and an EHD module to detach 1 µL droplets from a needle dispenser tip. The proposed device was developed with the goal of providing a low-cost sample preparation method within a convenient platform for deployment in resource-limited settings.

7.2.1. Sample Preparation Using the Boiling Method

The results of the sample preparation on cloacal samples using the boiling method presented in section 3.4 demonstrated that effective cell lysis could be conducted within a single heating step. Furthermore, a comparison of the results from both downstream analysis techniques supported the claims that iNAAT techniques offer the potential to outperform the gold standard, PCR [11]. The lysates were frozen following cell lysis to prevent degradation, indicating a need for cold storage. However, this was deemed a necessity due to the sizable period between the sample preparation and analysis steps. Hence, conducting amplification and detection following cell lysis and an immediate dilution step should offer similar results to those presented in this thesis. Whilst each of the mediums demonstrated the ability to extract detectable levels of *E. coli* present within each sample, the PBS and TE/PK outperformed the other mediums. The PBS buffer offered the highest yield of DNA among the crude lysates (182 ng/µL), while the TE/PK offered the highest purity values using the A260/280 ratio with a result of 1.06. As the lysates in PBS buffer offered the highest DNA yield, this medium was recommended for subsequent protocols. The experiment was conducted by suspending 100 mg of a cloacal sample into 200 µL of each medium. Thus, this sample preparation process can be easily scaled towards pooled sampling applications through an adjustment of the starting volume of the medium.

7.2.2. Heating Module to Conduct Thermal Lysis

The heating module proposed in section 4.3.6 was demonstrated to supply heat sufficient to conduct cell lysis in section 6.4.2.2, validated in section 5.4.4 by computational modelling. The heating module was designed specifically to interface with the geometry of the SCD to ensure the heater block would

provide a uniform heat distribution across fluid within the swab receiver. An accompanying PCB with a serpentine copper track was designed to provide an even distribution of heat from the PCB to the heater block, avoiding localised hot spots.

A comparison between the performance of the microheaters previously discussed in section 5.5.3. against the heating system demonstrated in section 6.4.2.2 (Table 7.1), reveals the difference in the time taken to reach the desired temperature. It should be noted that the temperatures of the reviewed microheaters were either measured directly (previously termed "unloaded temperatures") or were assessed for volumes within the microlitre range. Contrastingly, the volume of liquid heated within this setup was in the millilitre range. Nevertheless, further research is required to optimise the performance of the heating system. A time dependant computational model would prove vital for predicting the low temperature ramp and allowing optimisations to be made computationally. A time-dependant study was devised for a preceding iteration of the design shown in section 5.4.3, where it was established that the computational power was a limiting factor.

Table 7.1 – A summary of heating systems reported by previous authors
RT, signifies room temperature

Author(s)	Heating Method	Temperature			Total Volume	Time Taken	Power Required	REF
		Minimum	Maximum	Accuracy				
De Mello *et al.*	Joule	RT	130 °C	±0.2 °C		≈ 14 sec	1 W	[476]
Lao *et al.*	Joule	50 °C	100 °C	±1 °C	20 µL	≈ 5 sec	2.2 W	[477]
Mavraki et al.	Joule	RT	130 °C				1.7 W	[478]
Vigolo *et al.*	Joule	RT	75 °C	±3 °C		10 – 20 sec	1 W	[479]
Kim and Kim	Joule	RT	180 °C		30 µL	≈ 1 min	≈ 6.4 W	[480]
Gujit *et al.*	Chemical	-3 °C	76 °C				n/a	[481]
Maltezos *et al.*	Chemical	-20 °C	76 °C			≈ 22 sec	n/a	[482]
This study	**Joule**	**RT**	**102.7 °C**	**n/a**	**3 ml**	**≈ 25 min**	**5.3 W**	

There is a delicate balance between the accuracy and complexity of the control module, particularly regarding POCT applications. As stated in section 6.4.2.2, an Arduino driven temperature controller was developed; however, it was not completed during the thesis due to time constraints. Precise temperature control is desirable in the field of diagnostics to facilitate specific sample preparation or amplification steps. An interesting feature of a heating system developed by Velve Casquillas *et al.* was the inclusion of a 50 nm platinum resistance which was bonded to a microchannel block [496]. As the electrical resistance of platinum changes almost linearly with temperature, the temperature could be measured by measuring the resistance across the platinum wire. The silicon-glass microfluidic chip developed by Lao *et al.* described previously also used platinum as a temperature sensor [477].

7.3. Manual Actuation and Non-Contact Dispensing of Fluid Aliquots on Demand

Biological assays have been drastically scaled-down in size since their conception. In 1995, assays performed in a 96-well plate would have a volume of 250 µL. In 2003, comparable assays would be reduced to volumes between 50 and 3 µL, performed in 384- and 1,536-well plates [360,497]. Today, similar assays have been scaled down to the nanolitre range [361,498]. For applications involving cell sorting and bioprinting, volumes within the picolitre range have been achieved [499-502]. While POCT devices are not expected to operate with the same throughput as laboratory methods, the reduction in the assay volume can drastically reduce reagent costs.

One of the major research questions was to determine if it was possible to manually dispense fluid aliquots in the range of 1 – 3 µL on-demand without using a pipette. A review of literature shown in section 3.4.4 supports the claim that such a small volume is not achievable without the use of a manual pipette, or the use of a liquid handling system. Standard fluid delivery methods use a moving piston (i.e., a syringe pump) to displace a precise volume. However, while these platforms are able to meter small volumes, a high velocity is required to overcome the effects of the surface tension; otherwise, the droplet will remain attached to the nozzle [360]. As a result, these systems are typically coupled with other components to dispense droplets [498]. Solenoid valves introduce additional moving components which require precise control systems to deliver the desired volume, while piezoelectric and acoustic methods are limited by their scalability [360]. The accuracy of each method hinges on the rheological properties of the liquid and the environmental conditions, requiring calibration prior to operation [503,504]. Biological samples will vary in viscosity and the temperature and humidity are susceptible to large changes, particularly in POCT environments. Thus, a dispensing method able to function with a high level of accuracy independently of the rheological properties of the fluid, as well as the environment, is required.

7.3.1. Electrohydrodynamic Module for On-Demand Droplet Production

Table 7.2 compares the performance of droplet dispensing systems previously discussed in section 3.3.4.2 against the EHD module presented in section 6.4.1. An accepted level of precision for dispensing small volumes is 0.2 – 0.5 µL [505]. Thus, it can be determined that further optimisation is required to increase the uniformity of the dispensed droplets. Many of the platforms previously discussed in this thesis do not provide a starting volume or have large starting volumes in comparison to the EHD module developed in this thesis. An example is the acoustic actuator developed by

Castrejón-Pita *et al.,* requiring an initial volume of 100 – 500 ml [362]. In comparison, the EHD module presented in this thesis was functional with a significantly smaller starting volume of 3 ml. It should be noted that microdripping was observed during the testing of the EHD platform; producing droplets much smaller than the diameter of the fluid meniscus. These droplet volumes were not quantified, and thus, were not presented in this thesis. However, future iterations of this platform offer the potential to significantly decrease the droplet size and increase the overall precision. By using a lead screw with a smaller pitch, the precision of the syringe pump would greatly increase, which in turn, would greatly increase the accuracy of the droplets produced by the EHD module.

Table 7.2 – A summary of droplet dispensing systems reported by previous authors

Author(s)	Dispensing Method	Minimum Volume	Surface Tension	Viscosity	REF
Bammesberger *et al.*	Piezoelectric	0.25 ± 0.025 µL	30.49–70.83 mN/m	1.03–16.98 mPa·s	[361]
Lee *et al.*	EHD	51.4 ± 4.64 nL			[453]
Haber *et al.*	Solenoid	25 ± 1.68 nL		1 – 3 mPa·s	[360]
Liu *et al.*	Solenoid	100 ± 3.3 nL		1 – 8.37 mPa·s	[504]
Castrejón-Pita *et al.*	Acoustic	≈ 4.85 µL	63–72 mN/m	2.45 – 8.37 mPa·s	[362]
Kim and Park	Piezoelectric	1.45 ± 0.34 nL			[363]
This study	**EHD**	**1.30 ± 0.66 µL**	**72 mN/m**	**1.0016 mPa·s**	

It has been claimed that EHD droplet generation may not be suitable for biological applications due to the need for an electrically conductive fluid [506]. This raised concerns about the potential adsorption of NAs into the metallic needle during operation which would lower the concentration of the target pathogen released into the PCR tubes. However, work by Lee et al. reported a DNA droplet dispensing platform using an EHD configuration [453]. The platform used both a DC (1.5 kV) and an AC (0.5 kV, 100 Hz) potential to establish an electrical field between a pair of electrodes fixed at a distance of 6.5 mm. Using a needle type electrode similar to the arrangement proposed in this thesis, droplets with an average volume of 51.4 nL were obtained with a 26-gauge needle, which reduced to 2.1 nL using a 33-gauge needle. It was also reported that the droplet volume was not significantly affected by variations in DNA concentrations within the tested fluid. This dispensing method was paired with downstream microarrays to detect DNA, suggesting that the DNA within the solution can be released without damage due to thermal or electrical effects. Although the findings by Lee *et al.* demonstrate the ability to produce droplets containing DNA on demand, further research is needed to investigate the effects of DNA adsorption into the dispenser needle under an electrical field and to quantify the amount of DNA lost as a result.

7.3.2. Quantification of Droplet Volumes

A discrepancy was noted between the experimental and imaging results. The droplet volume measured using ImageJ shown in section 6.4.1 was 7.93 µL. In contrast, the corresponding 14-gauge needle yielded droplets with an actual volume of 35.23 µL, as shown in section 3.3. It was noted that due to light refraction, light rays from the droplet could miss the camera entrance pupil, resulting in a droplet volume smaller than the real size. However, the error in the drop radius should be roughly 1% [507]. In contrast, the error was over 39%. The light source shown in the proposed setup (Figure 3.9) provided a light background over which an image of a pendant drop with a high contrast could be captured. It is possible that the contrast between the droplet and the background for the experimental setup was not significant enough to yield accurate results.

The setup proposed by Daerr and Mogne (Figure 7.1) requires 300 mm distances between both the light source and camera and light source from the pendant drop [507]. The length and width of the final platform was 106 and 108 mm, respectively. Thus, the setup could not be integrated into the final platform, meaning alternate methods to measure droplet sizes in real time were necessary. Ernst *et al.* developed a non-contact capacitive sensor to monitor the volume and velocity of droplets in flight [508]. The presence of a free-falling liquid droplet would create a change in the electrical field strength within an open plate capacitor. The magnitude of the change was used to determine the size of the droplets. The sensor was able to detect droplets within the range of 20 – 65 nL, within an accuracy of 2 nL. This sensor was later integrated into the platform developed by Bammesberger *et al.* to measure droplets within an accuracy of 25 nL [361].

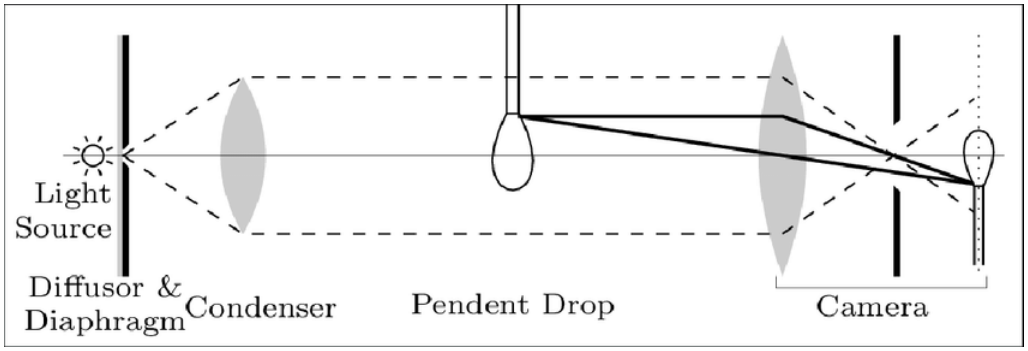

Figure 7.1 – Schematic of a surface tension measurement set-up [507]
A horizontal distance from the droplet is 300 mm for both the light source and the camera in the proposed set-up. The camera lens has a diameter of 25 mm. The camera used a 50 mm Macroplanar objective. An LED was used as a light source.

7.4. Streamlining Sample Preparation into a Portable Device

Following the shift in focus to address the Covid-19 pandemic, a research question was proposed concerning the possibility of performing sample preparation within a portable device. Due to the highly pathogenic nature of the SARS-CoV-2 strain of coronavirus, the ability to offer convenient and remote diagnostics outside of localised healthcare facilities would greatly lessen the proliferation of the disease. While antigen-based LFDs have been offered as a low-cost method of diagnostics on a wide scale, the low sensitivity can yield a high number of false negatives. NAAT techniques are more sensitive and specific in comparison, making them favourable options for POCT. However, between sample collection and sample analysis lies sample preparation, an important obstacle which must be overcome. While there are examples of sample-to-answer handheld and portable benchtop analysers, a portable platform dedicated towards streamlining the sample preparation process for a wide array of biological samples into a single POCT device has not yet been realised. The platform developed throughout this project marks a first milestone on the journey towards the realisation of portable sample preparation for use in conjunction with iNAAT devices.

7.4.1. Power Requirements for a Portable Sample Preparation Platform

Findings from the experiment in section 6.4.2.2 indicate that further work is required to increase the temperature ramp rate for the heating system. The current iteration of the system can heat the contained liquid to the desired temperature of 92 °C within 23 minutes and lyse the cells within 15 minutes. By including the downstream LAMP process with end-point detection, sample-to-answer detection can be achieved in 68 minutes, just above the 1 hour required for a process to be considered as “point-of-care”. Thus, an increase in the temperature ramp rate is required.

A comparison between the temperature profile of the copper track (Figure 6.35) to the nichrome wire (Figure 6.30) demonstrates the difference in the temperature ramp rate. It should be noted that the volume of DI H_2O tested in the final platform was 3 mL, 3 times of the volume used to test the nichrome wire heating system. Moreover, testing conducted within the final platform contained additional components, such as the moving jaw, which absorbed a percentage of the heat energy through conduction. However, a major factor which decreased the temperature ramp rate was the high temperature coefficient of resistivity of copper (3.86×10^{-3} °C^{-1}), over an order of magnitude larger than the nichrome wire (1.7×10^{-4} °C^{-1}.) It was estimated in section 5.4.4.1 that a current of 2.03 A

would be drawn through the copper track at 5.19 V; however, it was determined experimentally in section 6.4.2.2 that 1.15 A was drawn. Thus, the selection of a material with a lower temperature coefficient of resistivity would greatly increase the current drawn at higher temperatures, increasing the temperature ramp rate. More importantly, the reducing in power consumption would allow for the platform to operate solely using a portable power bank, as stated in section 4.2.8. An exchange of the material used as the resistive heating element would significantly reduce the overall processing time, which would reduce the overall power consumption.

7.4.2. Swab Sampling for Non-Invasive Sample Collection

Many samples require collection through invasive procedures. Due to their invasive nature, collection by trained personnel in specialised facilities is required. Swab sampling may be viewed as a less invasive method of sample collection. Furthermore, swab sampling typically requires a substantially smaller volume in comparison to invasive alternatives, and thus, the number of samples taken per procedure can be increased. As a result, tests can be performed more frequently, should repeat testing be necessary. Finally, in cases of human sampling, samples may be self-collected by the patient, alleviating pressure on healthcare professionals.

Research conducted into commercially available swabs showed an individual range of absorption of 92.5 – 249.3 µL for standard tip swabs and 27.5 – 112.1 µL for mini-tip swabs. Thus, mini-tip swabs are preferable in terms of volume loss. For poultry related infections, multiple samples are typically collected from birds which are representative of the entire flock. These are then pooled into a single medium for analysis. Based on a review of literature, pooling of up to 5 samples into a single volume can increase the testing capability by 69% [129]. Based on a review of the current state-of-the-art, this has been achieved using the LumiraDx SARS-CoV-2 Ag Pool Test (see section 8.2.4 for an overview of this test assay.) Of course, this test is a serological assay, and thus, the chemistry will differ greatly from molecular assays. However, this provides a starting point from which to estimate the pooling capabilities of the platform developed during this thesis. By pooling 5 swab samples into a single medium, the maximum adsorption could be estimated as 560.5 µL for mini-tip swabs and 1246.5 µL for standard tip swabs. The estimated dead volume of the SCD fabricated in section 6.3.3 was 422.2 µL (Figure 6.12). Therefore, a total volume between 982.7 and 1807 µL would be lost during the sample preparation steps, using the most absorbent mini- and standard-tip swabs, respectively. Consequently, the assumption of a 2.25 mL starting volume would ensure that a usable amount of

sample would remain for analysis. The ability to utilise a small sample volume would greatly increase the portability of the platform. By reducing the dead volume within the SCD with further iterations of the platform, it is possible to significantly increase the usable sample volume.

A concern with such a small volume was the viscosity of the liquid following the insertion of the sample into the PBS buffer. The fluidic testing of the platform was performed for water, solely. As a result, the performance of the platform for fluids with different rheological properties was not verified. As shown in Table 7.2, similar platforms can handle liquids with viscosities within the range of 1 to 16.98 mPa·s. Further work into the performance of this platform with fluids of different viscosities is needed. Additionally, while the fluid absorption of each swab sample was known, how this would translate to the absorption of biological samples was unknown. 100 mg was assumed as the mass uptake for the sample preparation protocol shown in section 3.4; however, a look into the volume up take of the swabs for respiratory (NP and OP) and cloacal samples would reveal if this assumption is correct.

7.4.3. A Ready-to-Assemble Sample Preparation Platform

An area of true novelty offered with the platform is the Lego® styled fittings in place of standard screw fittings. The time taken to assemble the first iteration of the final platform was 160 minutes (105 minutes to set the hex nuts and 55 minutes to assemble the platform.) In comparison, the time taken to assemble the second iteration was just 32 minutes (12 minutes to set the hex nuts and 20 minutes to assemble the platform.) These fittings were fabricated using a low-cost 3D printer (Prusa i3) which can be purchased for under £1,000. It is reasonable to conclude that the platform could be delivered as a package to an end-user as individual components to assemble, or, fabricated using a low-cost 3D printer delivered using open source files. Both options, particularly the latter, would greatly increase the potential for a transfer of technology to the developing world.

7.5. A REASSURED Sample Preparation Device

The sample preparation platform was compared against the REASSURED criterion for iNAAT platforms presented in section 2.5 (Table 2.21). The platform can be considered to be highly affordable, attributed to the ability for the bulk of its components to be fabricated using low-cost 3D printers. Following fabrication, the use of integrated Lego® styled fittings allowed the platform to be assembled without the need for metal fastenings. The results of the sample preparation protocol shown in section 3.4 also demonstrated the high sensitivity and robustness of the LAMP assay to detect *E. coli* from cloacal samples, despite the low-purity of the DNA which indicated a high amount of contamination. The sample preparation protocol was designed to be conducted within the sample preparation platform, only requiring the insertion of the swab sample into the swab receiver and the collection of the PCR tubes following the aliquoting of the crude lysate. Thus, the device can be considered to be highly user friendly, while also offering easy specimen collection. Furthermore, as thermal lysis could yield a suitable lysate within 15 minutes, the process was considered to be rapid. Finally, the platform offers a high potential to be equipment free. While the heating and EHD modules were powered by an external power supply during testing, the power calculations shown in section 5.4.4 imply that the device may be powered using a suitable power bank.

However, there is still much progress to be made for the project to be considered deliverable to end-users. Based on a review of literature presented in section 2.3, many POCT platforms offer wireless connectivity using a smartphone or laptop, allowing for the status of the protocol to be monitored in real-time. In recent years, several POCT platforms have utilised smartphones to both power and wirelessly control diagnostic protocols [509]. The development of such a system could not be achieved during this thesis with the resources available. The sample preparation protocol was performed within a laboratory, outside of the platform. Following testing of the protocol within the sample preparation platform, testing in resource-stressed settings would truly assess the robustness of the protocol. Finally, it is important to test the protocol with spiked samples with known concentrations of the target analyte to determine the LOD. In addition, performing the test on samples absent of the target analyte would provide quantitative values for the specificity of the platform. In light of the aforementioned, the completion of these tasks will allow for the realisation of a sample preparation platform that fully meets the requirements of the REASSURED criteria.

7.6. Applications of the Project Beyond the Field of Diagnostics

The project commenced as a means to integrate sample preparation into a standalone platform, offering a low-cost method of detecting poultry related infections from cloacal swab samples. Following the Covid-19 pandemic, the focus of the project shifted to include preparing NP and OP swab samples. Both applications were coupled with downstream LAMP analysis with end-point colorimetric detection. A question raised during the progression of the project was regarding the applications of the research beyond sample preparation.

Sample preparation is either conducted as a high-throughput process using complex static laboratory platforms, or as a low-throughput process using commercial extraction kits. Both methods are expensive; particularly in the case of laboratory-based platforms, or require several laborious steps, particularly in the case of commercial NA extraction kits. The sample preparation platform developed throughout this project attempted to find a compromise between these two approaches, offering a higher throughput than commercial extraction kits at a lower cost than the laboratory gold standard.

A sample preparation protocol was to be designed by collaborators of the EPSRC project; however, a working protocol was not produced. As demonstrated in section 3.4., successful PCR and LAMP products were shown following thermal lysis and a dilution step. This demonstrated the ability to prepare a biological sample within a complex matrix without the need for laborious NA extraction steps.

There is a major issue with translating scientific and engineering research into the commercialisation of POCT platforms for use in resource-limited settings. The development of POCT platforms requires an interaction between end-users and developers during the early stages of product development. A review of the literature revealed that there are currently no commercially available sample preparation platforms designed for use in remote or low-income environments. This therefore, marks a vital first step towards the commercialisation of a low-cost sample preparation platform for POCT applications.

7.7. Conclusions and Recommendations for Future Work

A series of poultry related diseases across the developing world prompted the conception of this project. The aim was to develop a sample preparation platform capable of delivering 3 µL aliquots of purified DNA or RNA in solution following sufficient treatment of cloacal swab samples to detect *S. enterica,* IBD, IBV, MG, NDV and APEC using LAMP. Following the start of the Covid-19 pandemic, the focus of the project shifted to include delivering 1 µL aliquots of purified RNA in solution from NP and OP swabs. A literature review into the state-of-the-art for molecular diagnostics and POCT revealed that no such platforms have reached the commercial stage.

Preliminary experiments were conducted to provide a tangible starting point from which design ideas were constructed. The analysis of the absorption rate for commercially available swabs revealed an average rate of absorption ranging between 27.5 and 249.3 µL. Therefore, it was concluded that to avoid a large volume loss to each swab while ensuring a high DNA recovery, polyurethane mini-tip swabs would be the optimal choice. A comparison between the dispenser tip needles of different gauge sizes revealed that an increase in gauge resulted in a decrease in the average droplet size. The 30-gauge needle yielded the smallest average droplet volumes among those tested, at 6.24 µL. Work by other authors suggested that a change from a vertical to a horizontal orientation would reduce the average droplet volume. This was observed in an experiment conducted on a dispenser tip needle with a larger diameter; however, the opposite effect was observed at a smaller diameter.

A simple sample preparation protocol was devised using a single thermal step on cloacal samples suspended in a liquid buffer, followed by a 1:10 dilution step on the produced lysate in DH_2O. Both PCR and LAMP were able to detect the presence of *E. coli* in each of the tested buffers; however, PBS offered the highest yield among the buffers tested. The protocol demonstrates simple and successful sample preparation which could be easily integrated into a sample preparation platform.

Based on findings from the literature review and preliminary work, a series of design ideas were created based on a set of specifications. These designs underwent several optimisations based on findings from computational simulations. Findings from each design were used to draft a final set of specifications, which became a template for a final platform. This platform employed joule heating of a copper resistive heating element to conduct thermal lysis at 92 °C and an EHD module which used an electrical field between a pair of electrodes at a different electrical potential to each other to overcome the surface tension at a dispenser tip needle. This allowed for non-contact dispensing to be achieved on demand. A modified open source syringe pump was used to actuate fluid through the platform, while simple switch valves were used to prevent backflow.

Following the assembly of the sample preparation platform, testing was conducted on the heating and EHD modules individually. The EHD module yielded droplets with an average volume of 1.3 µL, an 86% reduction compared to the unassisted droplet volumes yielded in preliminary experiments. Tests performed on the heating module demonstrated the capabilities of the system to heat 3 mL of DI H_2O to 92 °C at a voltage of 5V. This agreed with the COMSOL model, which predicted 5.19 V would be required to heat a volume of water to 91.9 °C. However, due to the high temperature coefficient of resistivity for copper, the current drawn (1.19 A) was significantly less than the predicted current (2.03 A) which resulted in a low temperature ramp rate. Nevertheless, it was demonstrated that the heating system would be capable of conducting cell lysis.

The device fabricated during this project offered an engineering solution to a biological problem. Whilst the ultimate goal was to develop and fabricate a universal sample preparation platform, this was a complex task and ultimately was not achievable in a single Ph.D. project. Thus, further work is required to advance the platform to a stage where commercialisation is a possibility. The heating module was proven to reach the desired temperature of 92 °C; however, the ability to conduct cell lysis using biological samples were not tested within the actual platform. Thus, verifying the capabilities of the heating module to perform cell lysis is the next crucial step. Improving the temperature ramp rate of the heating platform is the next logical step. Due to its high temperature coefficient of resistivity, copper was not the ideal material for use as a resistive heating element. Contrastingly, the nichrome wire had a lower temperature coefficient of resistivity. Therefore, should it prove possible to plate nichrome onto a substrate, then a modified PCB with an improved ramp rate could be designed, which would be easier to fabricate than the nichrome coils.

The EHD module was able to produce droplets significantly below the unassisted droplet sizes; however, they were still 0.3 µL above the 1 µL target. The use of a syringe pump with a smaller pitch should increase the precision of the EHD module and allow for droplets to be dispensed with a higher precision. Furthermore, optimising the conditions of the electrical field should prevent spraying and avoids the production of satellite droplets. The SCD was developed as a proof-of-concept which used large switch valves to control the fluid flow. The miniaturisation of these valves would significantly reduce the dead volume within the overall platform. The sample preparation protocol required a centrifugation step to precipitate solid particulates. The integration of a filtration system into the SCD should be sufficient to circumvent the need for centrifugation. In addition, a 1:10 dilution step is performed following cell lysis. Therefore, this process would need to be integrated into the SCD. Finally, the subsequent iteration of the platform should be assessed for its capabilities to perform sample preparation, using spiked samples to determine a LOD.

References

[1] Tran NK, Albahra S, Rashidi H, May L. Innovations in infectious disease testing: Leveraging COVID-19 pandemic technologies for the future. Clin Biochem 2022.

[2] Thompson C, Dowding D. Essential Decision Making and Clinical Judgement for Nurses E-Book. : Elsevier Health Sciences; 2009.

[3] Friedman LM, Furberg CD, DeMets DL, Reboussin DM, Granger CB. Fundamentals of clinical trials. : Springer; 2015.

[4] Wang C, Liu M, Wang Z, Li S, Deng Y, He N. Point-of-care diagnostics for infectious diseases: From methods to devices. Nano Today 2021;37:101092.

[5] Yager P, Edwards T, Fu E, Helton K, Nelson K, Tam MR, et al. Microfluidic diagnostic technologies for global public health. Nature 2006;442(7101):412-418.

[6] Martinez AW, Phillips ST, Whitesides GM, Carrilho E. Diagnostics for the developing world: microfluidic paper-based analytical devices 2010.

[7] Mabey D, Peeling RW, Ustianowski A, Perkins MD. Diagnostics for the developing world. Nature Reviews Microbiology 2004;2(3):231-240.

[8] Park H, Cho H, Jung HS, Cho BH, Lee M. Development of a DNA isolation device using poly (3, 4-dihydroxy-L-phenylalanine)-coated swab for on-site molecular diagnostics. Scientific reports 2019;9(1):1-10.

[9] Sachdeva S, Davis RW, Saha AK. Microfluidic Point-of-Care Testing: Commercial Landscape and Future Directions. Frontiers in Bioengineering and Biotechnology 2021;8:1537.

[10] Price CP. Point of care testing. BMJ 2001 May 26;322(7297):1285-1288.

[11] Srinivasan B, Tung S. Development and applications of portable biosensors. Journal of laboratory automation 2015;20(4):365-389.

[12] Moldoveanu SC, David V. Chapter 1 - Preparatory Information. Journal of Chromatography Library 2002 2002;65:3-111.

[13] Moein MM, Abdel-Rehim A, Abdel-Rehim M. 17 - Microextraction by packed sorbent (MEPS) and monolithic packed pipette tips for 96-well plates. In: Poole CF, editor. Solid-Phase Extraction: Elsevier; 2020. p. 473-491.

[14] Wen Y. 4 - Recent advances in solid-phase extraction techniques with nanomaterials. In: Mustansar Hussain C, editor. Handbook of Nanomaterials in Analytical Chemistry: Elsevier; 2020. p. 57-73.

[15] Picó Y. 3.28 - Recent Advances in Sample Preparation for Pesticide Analysis. In: Pawliszyn J, editor. Comprehensive Sampling and Sample Preparation Oxford: Academic Press; 2012. p. 569-590.

[16] Kumar A, Malik AK, Picó Y. Sample preparation methods for the determination of pesticides in foods using CE-UV/MS. Electrophoresis 2010;31(13):2115-2125.

[17] Lambropoulou DA, Albanis TA. Methods of sample preparation for determination of pesticide residues in food matrices by chromatography–mass spectrometry-based techniques: a review. Analytical and Bioanalytical Chemistry 2007;389(6):1663-1683.

[18] Pingret D, Fabiano-Tixier AS, Chemat F. 4.19 - Accelerated Methods for Sample Preparation in Food. In: Pawliszyn J, editor. Comprehensive Sampling and Sample Preparation Oxford: Academic Press; 2012. p. 441-455.

[19] Kettler H, White K, Hawkes SJ. Mapping the landscape of diagnostics for sexually transmitted infections: key findings and recommendations 2004.

[20] Land KJ, Boeras DI, Chen X, Ramsay AR, Peeling RW. REASSURED diagnostics to inform disease control strategies, strengthen health systems and improve patient outcomes. Nature microbiology 2019;4(1):46-54.

[21] Theglobalfund.org. HIV & Malaria Rapid Diagnostic Tests. 2022; Available at: https://www.theglobalfund.org/en/sourcing-management/health-products/hiv-malaria-rapid-diagnostic-tests/. Accessed 01/07, 2022.

[22] Santiago I. Trends and Innovations in Biosensors for COVID-19 Mass Testing. ChemBioChem 2020 10/15; 2021/11;21(20):2880-2889.

[23] Labtestsonline.org.uk. Point-of-Care Testing | Lab Tests Online-UK. 2019; Available at: https://labtestsonline.org.uk/articles/point-care-testing. Accessed 02/16, 2022.

[24] Hegde R, Hegde S, Joshi P, Gai PP, Kulkarni SS, Gai PB. Rapid and inexpensive method of PCR ready DNA isolation from human peripheral blood and saliva. Anal Biochem 2022:114852.

[25] Alberts B, Bray D, Hopkin K, Johnson AD, Lewis J, Raff M, et al. Essential cell biology. : Garland Science; 2013.

[26] Mitra S. Sample preparation techniques in analytical chemistry. : John Wiley & Sons; 2004.

[27] Worldometers.info. Philippines Population (2022) - Worldometers. 2022; Available at: https://www.worldometers.info/world-population/philippines-population/.

[28] Psa.gov.ph. Philippine Statistics Authority | Republic of the Philippines . 2019; Available at: https://psa.gov.ph/livestock-poultry-iprs/chicken/production.

[29] Falchieri M, Burton M. Strategic approach to sampling the commercial chicken flock. 2016; Available at: https://www.vettimes.co.uk/app/uploads/wp-post-to-pdf-enhanced-cache/1/strategic-approach-to-sampling-the-commercial-chicken-flock.pdf.

[30] World Health Organization. Estimating the impact of the next influenza pandemic: enhancing preparedness. Geneva: World Health Organization 2004;8.

[31] Avian influenza virus H5N1: a review of its history and information regarding its potential to cause the next pandemic. Seminars in Pediatric Infectious Diseases: Elsevier; 2005.

[32] Schnirring L. H5N6 confirmed in Philippines avian flu outbreak . 2017; Available at: http://www.cidrap.umn.edu/news-perspective/2017/08/h5n6-confirmed-philippines-avian-flu-outbreak.

[33] Kiselev D, Matsvay A, Abramov I, Dedkov V, Shipulin G, Khafizov K. Current trends in diagnostics of viral infections of unknown etiology. Viruses 2020;12(2):211.

[34] World Health Organization. Collecting, preserving and shipping specimens for the diagnosis of avian influenza A (H5N1) virus infection: guide for field operations 2006.

[35] Foley SL, Nayak R, Hanning IB, Johnson TJ, Han J, Ricke SC. Population dynamics of Salmonella enterica serotypes in commercial egg and poultry production. Appl Environ Microbiol 2011;77(13):4273-4279.

[36] Chao M, Hsien C, Yeh C, Chou S, Chu C, Su Y, et al. Assessing the prevalence of Salmonella enterica in poultry hatcheries by using hatched eggshell membranes. Poult Sci 2007;86(8):1651-1655.

[37] Cohen E, Davidovich M, Rokney A, Valinsky L, Rahav G, Gal-Mor O. Emergence of new variants of antibiotic resistance genomic islands among multidrug-resistant Salmonella enterica in poultry. Environ Microbiol 2020;22(1):413-432.

[38] Reed KD, Meece JK, Henkel JS, Shukla SK. Birds, migration and emerging zoonoses: west nile virus, lyme disease, influenza A and enteropathogens. Clin Med Res 2003 Jan;1(1):5-12.

[39] Lukert P, Saif Y, Calnek B. Diseases of poultry. 1997.

[40] McNulty M, Allan G, McFerran J. Isolation of infectious bursal disease virus from turkeys. Avian Pathol 1979;8(3):205-212.

[41] Dey S, Pathak DC, Ramamurthy N, Maity HK, Chellappa MM. Infectious bursal disease virus in chickens: prevalence, impact, and management strategies. Vet Med (Auckl) 2019 Aug 5;10:85-97.

[42] Müller R, Käufer I, Reinacher M, Weiss E. Immunofluorescent studies of early virus propagation after oral infection with infectious bursal disease virus (IBDV). Zentralblatt für Veterinärmedizin Reihe B 1979;26(5):345-352.

[43] Sharma JM, Kim I, Rautenschlein S, Yeh H. Infectious bursal disease virus of chickens: pathogenesis and immunosuppression. Developmental & Comparative Immunology 2000;24(2-3):223-235.

[44] Jackwood MW. Infectious Bronchitis in Poultry. 2019; Available at: https://www.msdvetmanual.com/poultry/infectious-bronchitis/infectious-bronchitis-in-poultry. Accessed 10/29, 2021.

[45] Cavanagh D. Coronavirus avian infectious bronchitis virus. Vet Res 2007;38(2):281-297.

[46] Ambali A, Jones R. Early pathogenesis in chicks of infection with an enterotropic strain of infectious bronchitis virus. Avian Dis 1990:809-817.

[47] Hofstad M, Yoder HW. Avian infectious bronchitis: Virus distribution in tissues of chicks. Avian Dis 1966;10(2):230-239.

[48] Vandekerchove D, Herdt PD, Laevens H, Butaye P, Meulemans G, Pasmans F. Significance of interactions between Escherichia coli and respiratory pathogens in layer hen flocks suffering from colibacillosis-associated mortality. Avian Pathol 2004;33(3):298-302.

[49] Winner F, Rosengarten R, Citti C. In vitro cell invasion of Mycoplasma gallisepticum. Infect Immun 2000;68(7):4238-4244.

[50] Ley D, Yoder Jr H. Mycoplasma gallisepticum infection In: Diseases of poultry. 2008.

[51] Vogl G, Plaickner A, Szathmary S, Stipkovits L, Rosengarten R, Szostak MP. Mycoplasma gallisepticum invades chicken erythrocytes during infection. Infect Immun 2008;76(1):71-77.

[52] Much P, Winner F, Stipkovits L, Rosengarten R, Citti C. Mycoplasma gallisepticum: influence of cell invasiveness on the outcome of experimental infection in chickens. FEMS Immunology & Medical Microbiology 2002;34(3):181-186.

[53] Aldous E, Alexander D. Detection and differentiation of Newcastle disease virus (avian paramyxovirus type 1). Avian Pathol 2001;30(2):117-128.

[54] Seal BS, King DJ, Sellers HS. The avian response to Newcastle disease virus. Developmental & Comparative Immunology 2000;24(2-3):257-268.

[55] Ganar K, Das M, Sinha S, Kumar S. Newcastle disease virus: current status and our understanding. Virus Res 2014;184:71-81.

[56] Alexander D. Newcastle Disease and other paramyxoviruses infection, in diseases of Poultry. Edited by: calnek BW, Barnes HJ, Beard CW, McDoughal LR, Saif YM, Ames LA. 1997.

[57] Dho-Moulin M, Fairbrother JM. Avian pathogenic Escherichia coli (APEC). Vet Res 1999;30(2-3):299-316.

[58] Dziva F, Stevens MP. Colibacillosis in poultry: unravelling the molecular basis of virulence of avian pathogenic Escherichia coli in their natural hosts. Avian Pathol 2008;37(4):355-366.

[59] Mellata M. Human and avian extraintestinal pathogenic Escherichia coli: infections, zoonotic risks, and antibiotic resistance trends. Foodborne pathogens and disease 2013;10(11):916-932.

[60] Wu F, Zhao S, Yu B, Chen Y, Wang W, Song Z, et al. A new coronavirus associated with human respiratory disease in China. Nature 2020;579(7798):265-269.

[61] World Health Organization. 2019-nCoV outbreak is an emergency of international concern. 2020; Available at: https://www.euro.who.int/en/health-topics/health-emergencies/international-health-regulations/news/news/2020/2/2019-ncov-outbreak-is-an-emergency-of-international-concern. Accessed 01/04, 2021.

[62] Roser M, Ritchie H, Ortiz-Ospina E, Hasell J. Coronavirus Pandemic (COVID-19). 2021; Available at: https://ourworldindata.org/coronavirus. Accessed 01/04, 2021.

[63] Adil MT, Rahman R, Whitelaw D, Jain V, Al-Taan O, Rashid F, et al. SARS-CoV-2 and the pandemic of COVID-19. Postgrad Med J 2020 Aug 11.

[64] Carter LJ, Garner LV, Smoot JW, Li Y, Zhou Q, Saveson CJ, et al. Assay techniques and test development for COVID-19 diagnosis 2020.

[65] Brekle B. Specimen collection – microbiology and virology. 2017; Available at: https://www.gosh.nhs.uk/health-professionals/clinical-guidelines/specimen-collection-microbiology-and-virology#Introduction.

[66] Reiss A, Jackson B, Gillespie G, Stokeld D, Warren K. Investigation of potential diseases associated with Northern Territory mammal declines. 2015.

[67] Lab Australasia. How samples are collected. 2018; Available at: https://www.labtestsonline.org.au/understanding/how-samples-are-collected.

[68] Vaught JB, Henderson MK. Biological sample collection, processing, storage and information management. IARC Sci Publ 2011;(163)(163):23-42.

[69] Dacheux L, Wacharapluesadee S, Hemachudha T, Meslin F, Buchy P, Reynes J, et al. More accurate insight into the incidence of human rabies in developing countries through validated laboratory techniques. PLoS neglected tropical diseases 2010;4(11):e765.

[70] American College of Physicians. COVID-19 found in sputum and feces samples after pharyngeal specimens no longer positive. 2020; Available at: https://www.sciencedaily.com/releases/2020/03/200330110348.htm. Accessed 01/04, 2021.

[71] Centers for Disease Control and Prevention. Specimen Collection. 2020; Available at: https://www.cdc.gov/coronavirus/2019-nCoV/lab/guidelines-clinical-specimens.html. Accessed 02/16, 2021.

[72] Kim C, Ahmed JA, Eidex RB, Nyoka R, Waiboci LW, Erdman D, et al. Comparison of nasopharyngeal and oropharyngeal swabs for the diagnosis of eight respiratory viruses by real-time reverse transcription-PCR assays. PloS one 2011;6(6):e21610.

[73] Marty FM, MD KC. BS, and Kelly A. Verrill." How to Obtain a Nasopharyngeal Swab Specimen (5 minutes)." NEJM. RN April 2020;17.

[74] Thompson D, Lei Y. Mini review: Recent progress in RT-LAMP enabled COVID-19 detection. Sensors and Actuators Reports 2020:100017.

[75] Dore JE, Houlihan T, Hebel DV, Tien G, Tupas L, Karl DM. Freezing as a method of sample preservation for the analysis of dissolved inorganic nutrients in seawater. Mar Chem 1996;53(3-4):173-185.

[76] Saito MA, Bulygin VV, Moran DM, Taylor C, Scholin C. Examination of microbial proteome preservation techniques applicable to autonomous environmental sample collection. Frontiers in microbiology 2011;2:215.

[77] Mompelat S, Jaffrézic A, Jardé E, Le Bot B. Storage of natural water samples and preservation techniques for pharmaceutical quantification. Talanta 2013;109:31-45.

[78] McDonnell G, Russell AD. Antiseptics and disinfectants: activity, action, and resistance. Clin Microbiol Rev 1999 Jan;12(1):147-179.

[79] Vanderford BJ, Mawhinney DB, Trenholm RA, Zeigler-Holady JC, Snyder SA. Assessment of sample preservation techniques for pharmaceuticals, personal care products, and steroids in surface and drinking water. Analytical and bioanalytical chemistry 2011;399(6):2227-2234.

[80] Capdeville M, Budzinski H. Trace-level analysis of organic contaminants in drinking waters and groundwaters. TrAC Trends in Analytical Chemistry 2011;30(4):586-606.

[81] Guthrie JW. General considerations when dealing with biological fluid samples. 2012.

[82] Rylander-Rudqvist T, Hakansson N, Tybring G, Wolk A. Quality and quantity of saliva DNA obtained from the self-administrated oragene method--a pilot study on the cohort of Swedish men. Cancer Epidemiol Biomarkers Prev 2006 Sep;15(9):1742-1745.

[83] Rose C, Parker A, Jefferson B, Cartmell E. The characterization of feces and urine: a review of the literature to inform advanced treatment technology. Crit Rev Environ Sci Technol 2015;45(17):1827-1879.

[84] Ellis R. Reference Man: Anatomical, Physiological and Metabolic Characteristics. Report of the Task Group on Reference Man ICRP Publication 23. Physics Bulletin 1976;27(2):79.

[85] Sylvester FA, Turner D, Draghi A, Uuosoe K, McLernon R, Koproske K, et al. Fecal osteoprotegerin may guide the introduction of second-line therapy in hospitalized children with ulcerative colitis. Inflamm Bowel Dis 2011;17(8):1726-1730.

[86] nhs.uk. How should I collect and store a poo (stool) sample? 2019; Available at: www.nhs.uk/common-health-questions/infections/how-should-i-collect-and-store-a-stool-faeces-sample/. Accessed 06/07, 2021.

[87] Videvall E, Strandh M, Engelbrecht A, Cloete S, Cornwallis CK. Measuring the gut microbiome in birds: comparison of faecal and cloacal sampling. Molecular ecology resources 2018;18(3):424-434.

[88] Clarridge JE,3rd, Shawar RM, Shinnick TM, Plikaytis BB. Large-scale use of polymerase chain reaction for detection of Mycobacterium tuberculosis in a routine mycobacteriology laboratory. J Clin Microbiol 1993 Aug;31(8):2049-2056.

[89] Jiang X, Wang J, Graham DY, Estes MK. Detection of Norwalk virus in stool by polymerase chain reaction. J Clin Microbiol 1992 Oct;30(10):2529-2534.

[90] Wilde J, Eiden J, Yolken R. Removal of inhibitory substances from human fecal specimens for detection of group A rotaviruses by reverse transcriptase and polymerase chain reactions. J Clin Microbiol 1990 Jun;28(6):1300-1307.

[91] Fluit A. The magnetic immuno polymerase chain reaction assay for direct detection of salmonellae in fecal samples. J Clin Microbiol 1995;33:1046-1047.

[92] Sidransky D, Tokino T, Hamilton SR, Kinzler KW, Levin B, Frost P, et al. Identification of ras oncogene mutations in the stool of patients with curable colorectal tumors. Science 1992 Apr 3;256(5053):102-105.

[93] Deuter R, Pietsch S, Hertel S, Muller O. A method for preparation of fecal DNA suitable for PCR. Nucleic Acids Res 1995 Sep 25;23(18):3800-3801.

[94] Widjojoatmodjo MN, Fluit AC, Torensma R, Verdonk GP, Verhoef J. The magnetic immuno polymerase chain reaction assay for direct detection of salmonellae in fecal samples. J Clin Microbiol 1992 Dec;30(12):3195-3199.

[95] Saulnier P, Andremont A. Detection of genes in feces by booster polymerase chain reaction. J Clin Microbiol 1992 Aug;30(8):2080-2083.

[96] Brisson-Noel A, Nguyen S, Aznar C, Chureau C, Garrigue G, Pierre C, et al. Diagnosis of tuberculosis by DNA amplification in clinical practice evaluation. The Lancet 1991;338(8763):364-366.

[97] Beutler E, Gelbart T, Kuhl W. Interference of heparin with the polymerase chain reaction. BioTechniques 1990;9(2).

[98] Furukawa K, Bhavanandan V. Influences of anionic polysaccharides on DNA synthesis in isolated nuclei and by DNA polymerase α: correlation of observed effects with properties of the polysaccharides. Biochimica et Biophysica Acta (BBA)-Gene Structure and Expression 1983;740(4):466-475.

[99] Monteiro L, Bonnemaison D, Vekris A, Petry KG, Bonnet J, Vidal R, et al. Complex polysaccharides as PCR inhibitors in feces: Helicobacter pylori model. J Clin Microbiol 1997 Apr;35(4):995-998.

[100] Wilson IG. Inhibition and facilitation of nucleic acid amplification. Appl Environ Microbiol 1997 Oct;63(10):3741-3751.

[101] Khan G, Kangro HO, Coates PJ, Heath RB. Inhibitory effects of urine on the polymerase chain reaction for cytomegalovirus DNA. J Clin Pathol 1991 May;44(5):360-365.

[102] Nodar R, Acea M, Carballas T. Microbial composition of poultry excreta. Biological wastes 1990;33(2):95-105.

[103] Sana A, Sarah S, Asim M, Almas H, Saamia S. Comparative analysis of animal manure for soil conditioning. International Journal of Agronomy and Plant Production 2013;4(12):3360-3366.

[104] Barnard T, Robertson C, Jagals P, Potgieter N. A rapid and low-cost DNA extraction method for isolating Escherichia coli DNA from animal stools. African Journal of Biotechnology 2011;10(8):1485-1490.

[105] World Health Organisation. Laboratory testing for coronavirus disease (COVID-19) in suspected human cases . 2020; Available at: https://apps.who.int/iris/handle/10665/331329. Accessed 06/08, 2021.

[106] Davidson KR, Ha DM, Schwarz MI, Chan ED. Bronchoalveolar lavage as a diagnostic procedure: a review of known cellular and molecular findings in various lung diseases. Journal of Thoracic Disease 2020;12(9):4991.

[107] MedlinePlus.com. Bronchoscopy and Bronchoalveolar Lavage (BAL): MedlinePlus Medical Test. 2020; Available at: https://medlineplus.gov/lab-tests/bronchoscopy-and-bronchoalveolar-lavage-bal/. Accessed 11/03, 2021.

[108] Nishijima S, Namura S, Higashida T, Kawai S. Staphylococcus aureus in the anterior nares and subungual spaces of the hands in atopic dermatitis. J Int Med Res 1997;25(3):155-158.

[109] Fda.gov. Provide clear instructions to patients for anterior nares sampling . 2020; Available at: https://www.fda.gov/medical-devices/letters-health-care-providers/recommendations-providing-clear-instructions-patients-who-self-collect-anterior-nares-nasal-sample. Accessed 11/05, 2021.

[110] Cdc.gov. How to Collect an Anterior Nasal Swab Specimen for COVID-19 Testing. 2021; Available at: https://www.cdc.gov/coronavirus/2019-ncov/testing/How-To-Collect-Anterior-Nasal-Specimen-for-COVID-19.pdf. Accessed 11/05, 2021.

[111] Callesen RE, Kiel CM, Hovgaard LH, Jakobsen KK, Papesch M, von Buchwald C, et al. Optimal Insertion Depth for Nasal Mid-Turbinate and Nasopharyngeal Swabs. Diagnostics 2021;11(7):1257.

[112] Granados A, Quach S, McGeer A, Gubbay JB, Kwong JC. Detecting and quantifying influenza virus with self-versus investigator-collected mid-turbinate nasal swabs. J Med Virol 2017;89(7):1295-1299.

[113] Esposito S, Molteni CG, Daleno C, Valzano A, Tagliabue C, Galeone C, et al. Collection by trained pediatricians or parents of mid-turbinate nasal flocked swabs for the detection of influenza viruses in childhood. Virology journal 2010;7(1):1-4.

[114] Cdc.gov. Nasal mid-turbinate Specimen Collection Steps. 2020; Available at: https://www.cdc.gov/coronavirus/2019-ncov/downloads/lab/NMT-Specimen-Collection-Infographic.pdf. Accessed 11/05, 2021.

[115] Centers for Disease Control and Prevention. Interim Guidelines for Collecting, Handling, and Testing Clinical Specimens from Persons Under Investigation (PUIs) for Middle East Respiratory Syndrome Coronavirus (MERS-CoV) – Version 2.1. 2019; Available at: https://www.cdc.gov/coronavirus/mers/guidelines-clinical-specimens.html. Accessed 06/08, 2021.

[116] Nikolaou E, Blizard A, Pojar S, Mitsi E, German EL, Reine J, et al. Minimally Invasive Nasal Sampling in Children Offers Accurate Pneumococcal Colonization Detection. Pediatr Infect Dis J 2019 Nov;38(11):1147-1149.

[117] Lambert SB, Whiley DM, O'Neill NT, Andrews EC, Canavan FM, Bletchly C, et al. Comparing nose-throat swabs and nasopharyngeal aspirates collected from children with symptoms for respiratory virus identification using real-time polymerase chain reaction. Pediatrics 2008 Sep;122(3):e615-20.

[118] Pere H, Podglajen I, Wack M, Flamarion E, Mirault T, Goudot G, et al. Nasal Swab Sampling for SARS-CoV-2: a Convenient Alternative in Times of Nasopharyngeal Swab Shortage. J Clin Microbiol 2020 May 26;58(6):10.1128/JCM.00721-20. Print 2020 May 26.

[119] Lieberman D, Lieberman D, Shimoni A, Keren-Naus A, Steinberg R, Shemer-Avni Y. Identification of respiratory viruses in adults: nasopharyngeal versus oropharyngeal sampling. J Clin Microbiol 2009;47(11):3439-3443.

[120] Ek P, Böttiger B, Dahlman D, Hansen KB, Nyman M, Nilsson AC. A combination of naso-and oropharyngeal swabs improves the diagnostic yield of respiratory viruses in adult emergency department patients. Infectious Diseases 2019;51(4):241-248.

[121] Lieberman D, Shleyfer E, Castel H, Terry A, Harman-Boehm I, Delgado J, et al. Nasopharyngeal versus oropharyngeal sampling for isolation of potential respiratory pathogens in adults. J Clin Microbiol 2006;44(2):525-528.

[122] Greenberg D, Broides A, Blancovich I, Peled N, Givon-Lavi N, Dagan R. Relative importance of nasopharyngeal versus oropharyngeal sampling for isolation of Streptococcus pneumoniae and Haemophilus influenzae from healthy and sick individuals varies with age. J Clin Microbiol 2004;42(10):4604-4609.

[123] US Food and Drug Administration. FAQs on testing for SARS-CoV-2. Medical Device Safety: Emergency Situations (Medical Devices) 2020.

[124] Garcia LS. Clinical microbiology procedures handbook. : American Society for Microbiology Press; 2010.

[125] Kent PT. Public health mycobacteriology: a guide for the level III laboratory. : US Department of Health and Human Services, Public Health Service, Centers …; 1985.

[126] Gomez DI, Mullin CS, Mora-Guzmán F, Crespo-Solis JG, Fisher-Hoch SP, McCormick JB, et al. Rapid DNA extraction for specific detection and quantitation of Mycobacterium tuberculosis DNA in sputum specimens using Taqman assays. Tuberculosis 2011;91:S43-S48.

[127] Dorfman R. The detection of defective members of large populations. The Annals of Mathematical Statistics 1943;14(4):436-440.

[128] Centers for Disease Control and Prevention. Pooling Procedures. 2020; Available at: https://www.cdc.gov/coronavirus/2019-ncov/lab/pooling-procedures.html. Accessed 02/16, 2021.

[129] Abdalhamid B, Bilder CR, McCutchen EL, Hinrichs SH, Koepsell SA, Iwen PC. Assessment of specimen pooling to conserve SARS CoV-2 testing resources. Am J Clin Pathol 2020;153(6):715-718.

[130] Chen Y, Guo Z, Wang X, Qiu C. Sample preparation. Journal of Chromatography A 2008;1184(1-2):191-219.

[131] Smith RM. Before the injection—modern methods of sample preparation for separation techniques. Journal of chromatography A 2003;1000(1-2):3-27.

[132] Boom R, Sol CJ, Salimans MM, Jansen CL, Wertheim-van Dillen PM, van der Noordaa J. Rapid and simple method for purification of nucleic acids. J Clin Microbiol 1990 Mar;28(3):495-503.

[133] Kers JG, Fischer EA, Stegeman JA, Smidt H, Velkers FC. Comparison of different invasive and non-invasive methods to characterize intestinal microbiota throughout a production cycle of broiler chickens. Microorganisms 2019;7(10):431.

[134] Fereidouni SR, Starick E, Ziller M, Harder TC, Unger H, Hamilton K, et al. Sample preparation for avian and porcine influenza virus cDNA amplification simplified: Boiling vs. conventional RNA extraction. J Virol Methods 2015;221:62-67.

[135] Campbell LA. PCR detection of Chlamydia pneumoniae. Diagnostic molecular microbiology: principles and applications.Washington, DC.: Amercian Society for Microbiology 1993:247-252.

[136] Wilson K. Preparation of genomic DNA from bacteria. Current protocols in molecular biology 2001;56(1):2.4. 1-2.4. 5.

[137] Hotzel H, Sachase K, Pfützner H. Rapid detection of Mycoplasma bovis in milk samples and nasal swabs using the polymerase chain reaction. J Appl Bacteriol 1996;80(5):505-510.

[138] Kim J, Johnson M, Hill P, Gale BK. Microfluidic sample preparation: cell lysis and nucleic acid purification. Integrative Biology 2009;1(10):574-586.

[139] Di Carlo D, Jeong K, Lee LP. Reagentless mechanical cell lysis by nanoscale barbs in microchannels for sample preparation. Lab on a Chip 2003;3(4):287-291.

[140] Packard MM, Wheeler EK, Alocilja EC, Shusteff M. Performance evaluation of fast microfluidic thermal lysis of bacteria for diagnostic sample preparation. Diagnostics 2013;3(1):105-116.

[141] Brown RB, Audet J. Current techniques for single-cell lysis. J R Soc Interface 2008 Oct 6;5 Suppl 2:S131-8.

[142] Jen C, Hsiao J, Maslov NA. Single-cell chemical lysis on microfluidic chips with arrays of microwells. Sensors 2011;12(1):347-358.

[143] Bimboim H, Doly J. A rapid alkaline extraction procedure for screening recombinant plasmid DNA. Nucleic Acids Res 1979;7(6):1513-1523.

[144] MARKO AM, BUTLER GC. The isolation of sodium desoxyribonucleate with sodium dodecyl sulfate. J Biol Chem 1951 May;190(1):165-176.

[145] Neugebauer JM. [18] Detergents: An overview. Methods in enzymology: Elsevier; 1990. p. 239-253.

[146] Eberling W, Hennrich N, Klockow M, Metz H, Orth H, Lang H. Proteinase K from Tritirachium album limber. Eur J Biochem 1974;47(1):1-7.

[147] Lounsbury JA, Coult N, Miranian DC, Cronk SM, Haverstick DM, Kinnon P, et al. An enzyme-based DNA preparation method for application to forensic biological samples and degraded stains. Forensic Science International: Genetics 2012;6(5):607-615.

[148] Thermofisher.com. Traditional Methods of Cell Lysis . 2019; Available at: https://www.thermofisher.com/uk/en/home/life-science/protein-biology/protein-biology-learning-center/protein-biology-resource-library/pierce-protein-methods/traditional-methods-cell-lysis.html.

[149] Thatcher SA. DNA/RNA preparation for molecular detection. Clin Chem 2015 Jan;61(1):89-99.

[150] Das A, Spackman E, Pantin-Jackwood MJ, Suarez DL. Removal of real-time reverse transcription polymerase chain reaction (RT-PCR) inhibitors associated with cloacal swab samples and tissues for improved diagnosis of Avian influenza virus by RT-PCR. Journal of Veterinary Diagnostic Investigation 2009;21(6):771-778.

[151] Shehadul Islam M, Aryasomayajula A, Selvaganapathy P. A review on macroscale and microscale cell lysis methods. Micromachines 2017;8(3):83.

[152] Deshaies RJ. Ubiquitin and protein degradation. : Gulf Professional Publishing; 2005.

[153] Johnson BH, Hecht MH. Recombinant proteins can be isolated from E. coli cells by repeated cycles of freezing and thawing. Bio/Technology 1994;12(12):1357.

[154] Melendez JH, Santaus TM, Brinsley G, Kiang D, Mali B, Hardick J, et al. Microwave-accelerated method for ultra-rapid extraction of Neisseria gonorrhoeae DNA for downstream detection. Anal Biochem 2016;510:33-40.

[155] Santaus TM, Li S, Ladd P, Harvey A, Cole S, Stine OC, et al. Rapid sample preparation with Lyse-It® for Listeria monocytogenes and Vibrio cholerae. PloS one 2018;13(7):e0201070.

[156] Reece J, Urry L, Cain M, Wasserman S, Minorsky P, Jackson R. Ninth Edipon. 2011. Campbell Biology.

[157] Thermofisher.com. Electroporation. 2019; Available at: https://www.thermofisher.com/uk/en/home/references/gibco-cell-culture-basics/transfection-basics/transfection-methods/electroporation.html.

[158] Bao N, Lu C. A microfluidic device for physical trapping and electrical lysis of bacterial cells. Appl Phys Lett 2008;92(21):214103.

[159] Zheng H, Yin J, Gao Z, Huang H, Ji X, Dou C. Disruption of Chlorella vulgaris cells for the release of biodiesel-producing lipids: a comparison of grinding, ultrasonication, bead milling, enzymatic lysis, and microwaves. Appl Biochem Biotechnol 2011;164(7):1215-1224.

[160] Harrison ST. Bacterial cell disruption: a key unit operation in the recovery of intracellular products. Biotechnol Adv 1991;9(2):217-240.

[161] Engler CR, Robinson CW. Disruption of Candida utilis cells in high pressure flow devices. Biotechnol Bioeng 1981;23(4):765-780.

[162] Ali N, Rampazzo, Rita de Cássia Pontello, Costa ADT, Krieger MA. Current nucleic acid extraction methods and their implications to point-of-care diagnostics. BioMed research international 2017;2017.

[163] Ogram A, Sayler GS, Barkay T. The extraction and purification of microbial DNA from sediments. J Microbiol Methods 1987;7(2-3):57-66.

[164] Saito H, Miura K. Preparation of transforming deoxyribonucleic acid by phenol treatment. Biochimica et Biophysica Acta (BBA)-Specialized Section on Nucleic Acids and Related Subjects 1963;72:619-629.

[165] Tang S, Zhang H, Lee HK. Advances in sample extraction. Anal Chem 2016;88(1):228-249.

[166] Price CW, Leslie DC, Landers JP. Nucleic acid extraction techniques and application to the microchip. Lab on a Chip 2009;9(17):2484-2494.

[167] McCormick RM. A solid-phase extraction procedure for DNA purification. Anal Biochem 1989;181(1):66-74.

[168] Purdy KJ, Embley TM, Takii S, Nedwell DB. Rapid Extraction of DNA and rRNA from Sediments by a Novel Hydroxyapatite Spin-Column Method. Appl Environ Microbiol 1996 Oct;62(10):3905-3907.

[169] Melzak KA, Sherwood CS, Turner RF, Haynes CA. Driving forces for DNA adsorption to silica in perchlorate solutions. J Colloid Interface Sci 1996;181(2):635-644.

[170] Vogelstein B, Gillespie D. Preparative and analytical purification of DNA from agarose. Proc Natl Acad Sci U S A 1979 Feb;76(2):615-619.

[171] Berensmeier S. Magnetic particles for the separation and purification of nucleic acids. Appl Microbiol Biotechnol 2006;73(3):495-504.

[172] Pamme N. Magnetism and microfluidics. Lab on a Chip 2006;6(1):24-38.

[173] Gijs MA, Lacharme F, Lehmann U. Microfluidic applications of magnetic particles for biological analysis and catalysis. Chem Rev 2010;110(3):1518-1563.

[174] Walsh PS, Metzger DA, Higuchi R. Chelex 100 as a medium for simple extraction of DNA for PCR-based typing from forensic material. BioTechniques 1991 Apr;10(4):506-513.

[175] Singer-Sam J. Use of Chelex to improve the PCR signal from a small number of cells. Amplifications 1989;3:11.

[176] Ip SC, Lin S, Lai K. An evaluation of the performance of five extraction methods: chelex® 100, QIAamp® DNA blood mini kit, QIAamp® DNA investigator kit, QIAsymphony® DNA Investigator® kit and DNA IQ™. Science & Justice 2015;55(3):200-208.

[177] Phillips K, McCallum N, Welch L. A comparison of methods for forensic DNA extraction: Chelex-100® and the QIAGEN DNA Investigator Kit (manual and automated). Forensic Science International: Genetics 2012;6(2):282-285.

[178] Mueller JA, Culley AI, Steward GF. Variables influencing extraction of nucleic acids from microbial plankton (viruses, bacteria, and protists) collected on nanoporous aluminum oxide filters. Appl Environ Microbiol 2014 Jul;80(13):3930-3942.

[179] Dames S, Bromley LK, Herrmann M, Elgort M, Erali M, Smith R, et al. A single-tube nucleic acid extraction, amplification, and detection method using aluminum oxide. The Journal of Molecular Diagnostics 2006;8(1):16-21.

[180] Gerdes JC, Marmaro JM, Ives JT, Roehl CA. Nucleic acid archiving 2006.

[181] McFall SM, Neto MF, Reed JL, Wagner RL. Filtration Isolation of Nucleic Acids: A Simple and Rapid DNA Extraction Method. JoVE (Journal of Visualized Experiments) 2016(114):e54289.

[182] Nath K, Sarosy JW, Hahn J, Di Como CJ. Effects of ethidium bromide and SYBR® Green I on different polymerase chain reaction systems. J Biochem Biophys Methods 2000;42(1-2):15-29.

[183] Schrader C, Schielke A, Ellerbroek L, Johne R. PCR inhibitors–occurrence, properties and removal. J Appl Microbiol 2012;113(5):1014-1026.

[184] Özay B, McCalla SE. A Review of Reaction Enhancement Strategies for Isothermal Nucleic Acid Amplification Reactions. Sensors and Actuators Reports 2021:100033.

[185] Craw P, Balachandran W. Isothermal nucleic acid amplification technologies for point-of-care diagnostics: a critical review. Lab on a Chip 2012;12(14):2469-2486.

[186] Saiki RK, Gelfand D, Stoffel S, Scharf SJ, Higuchi R, Horn GT, et al. Primer-directed enzymatic amplification of DNA with a thermostable DNA polymeraseScience 239, 487–91. Google Scholar 1988.

[187] Lantz P, Al-Soud WA, Knutsson R, Hahn-Hägerdal B, Rådström P. Biotechnical use of polymerase chain reaction for microbiological analysis of biological samples. 2000.

[188] Bachman J. Reverse-transcription PCR (rt-PCR). Meth Enzymol 2013;530:67-74.

[189] Joyce C. Quantitative rt-pcr. RT-PCR Protocols 2002:83-92.

[190] Shiao Y. A new reverse transcription-polymerase chain reaction method for accurate quantification. Bmc Biotechnology 2003;3(1):1-12.

[191] Freeman WM, Walker SJ, Vrana KE. Quantitative RT-PCR: pitfalls and potential. BioTechniques 1999;26(1):112-125.

[192] Glökler J, Lim TS, Ida J, Frohme M. Isothermal amplifications–a comprehensive review on current methods. Crit Rev Biochem Mol Biol 2021;56(6):543-586.

[193] Doseeva V, Forbes T, Wolff J, Khripin Y, O'Neil D, Rothmann T, et al. Multiplex isothermal helicase-dependent amplification assay for detection of Chlamydia trachomatis and Neisseria gonorrhoeae. Diagn Microbiol Infect Dis 2011;71(4):354-365.

[194] Mayboroda O, Katakis I, O'Sullivan CK. Multiplexed isothermal nucleic acid amplification. Anal Biochem 2018;545:20-30.

[195] Zhang X, Lowe SB, Gooding JJ. Brief review of monitoring methods for loop-mediated isothermal amplification (LAMP). Biosensors and Bioelectronics 2014;61:491-499.

[196] Shirato K. Detecting amplicons of loop-mediated isothermal amplification. Microbiol Immunol 2019;63(10):407-412.

[197] Ganguli A, Mostafa A, Berger J, Aydin M, Sun F, Valera E, et al. Rapid Isothermal Amplification and Portable Detection System for SARS-CoV-2. bioRxiv 2020 May 21.

[198] Tian F, Liu C, Deng J, Han Z, Zhang L, Chen Q, et al. A fully automated centrifugal microfluidic system for sample-to-answer viral nucleic acid testing. Science China Chemistry 2020;63(10):1498-1506.

[199] Rödel J, Egerer R, Suleyman A, Sommer-Schmid B, Baier M, Henke A, et al. Use of the variplex™ SARS-CoV-2 RT-LAMP as a rapid molecular assay to complement RT-PCR for COVID-19 diagnosis. Journal of Clinical Virology 2020;132:104616.

[200] Wang D. One-pot detection of COVID-19 with real-time reverse-transcription loop-mediated isothermal amplification (RT-LAMP) assay and visual RT-LAMP assay. Biorxiv 2020.

[201] Yu L, Wu S, Hao X, Dong X, Mao L, Pelechano V, et al. Rapid detection of COVID-19 coronavirus using a reverse transcriptional loop-mediated isothermal amplification (RT-LAMP) diagnostic platform. Clin Chem 2020;66(7):975-977.

[202] Huang WE, Lim B, Hsu C, Xiong D, Wu W, Yu Y, et al. RT-LAMP for rapid diagnosis of coronavirus SARS-CoV-2. Microbial biotechnology 2020;13(4):950-961.

[203] Lamb LE, Bartolone SN, Ward E, Chancellor MB. Rapid detection of novel coronavirus (COVID19) by reverse transcription-loop-mediated isothermal amplification. Available at SSRN 3539654 2020.

[204] Kumar S, Kumar A, Venkatesan G. Isothermal nucleic acid amplification system: an update on methods and applications. J Genet Genom 2018;2(112):2.

[205] Xu G, Hu L, Zhong H, Wang H, Yusa S, Weiss TC, et al. Cross priming amplification: mechanism and optimization for isothermal DNA amplification. Scientific reports 2012;2(1):1-7.

[206] Vincent M, Xu Y, Kong H. Helicase-dependent isothermal DNA amplification. EMBO Rep 2004 Aug;5(8):795-800.

[207] Compton J. Nucleic acid sequence-based amplification. Nature 1991;350(6313):91-92.

[208] Liu W, Dong D, Yang Z, Zou D, Chen Z, Yuan J, et al. Polymerase Spiral Reaction (PSR): A novel isothermal nucleic acid amplification method. Scientific reports 2015;5(1):1-8.

[209] Demidov VV. Rolling-circle amplification in DNA diagnostics: the power of simplicity. Expert review of molecular diagnostics 2002;2(6):542-548.

[210] Piepenburg O, Williams CH, Stemple DL, Armes NA. DNA detection using recombination proteins. PLoS biology 2006;4(7):e204.

[211] Lin X, Chen Q, Liu W, Li H, Lin J. A portable microchip for ultrasensitive and high-throughput assay of thrombin by rolling circle amplification and hemin/G-quadruplex system. Biosensors and Bioelectronics 2014;56:71-76.

[212] Notomi T, Okayama H, Masubuchi H, Yonekawa T, Watanabe K, Amino N, et al. Loop-mediated isothermal amplification of DNA. Nucleic Acids Res 2000;28(12):e63-e63.

[213] van der Zee A, Peeters M, de Jong C, Verbakel H, Crielaard JW, Claas EC, et al. Qiagen DNA extraction kits for sample preparation for legionella PCR are not suitable for diagnostic purposes. J Clin Microbiol 2002 Mar;40(3):1126.

[214] Qiagen.com. QIAcube HT - QIAGEN Online Shop. 2019; Available at: https://www.qiagen.com/gb/products/instruments-and-automation/nucleic-acid-purification/qiacube-ht/#technicalspecification.

[215] Qiagen.com. QIAcube Connect - QIAGEN Online Shop. 2019; Available at: https://www.qiagen.com/gb/products/instruments-and-automation/nucleic-acid-purification/qiacube-connect/#technicalspecification.

[216] Qiagen.com. QIAamp 96 DNA Swab BioRobot Kit - QIAGEN Online Shop. 2019; Available at: https://www.qiagen.com/gb/products/discovery-and-translational-research/dna-rna-purification/dna-purification/genomic-dna/qiaamp-96-dna-swab-biorobot-kit/#technicalspecification.

[217] Evans GE, Murdoch DR, Anderson TP, Potter HC, George PM, Chambers ST. Contamination of Qiagen DNA extraction kits with Legionella DNA. J Clin Microbiol 2003 Jul;41(7):3452-3453.

[218] Qiagen.com. QIAamp DNA Stool Mini Kit - QIAGEN Online Shop. 2019; Available at: https://www.qiagen.com/gb/products/discovery-and-translational-research/dna-rna-purification/dna-purification/microbial-dna/qiaamp-dna-stool-mini-kit/#technicalspecification.

[219] Qiagen.com. QIAsymphony SP/AS instruments - QIAGEN Online Shop. 2019; Available at: https://www.qiagen.com/us/products/instruments-and-automation/pcr-setup-liquid-handling/qiasymphony-spas-instruments/#technicalspecification.

[220] AutoGen.com. AutoGen | XTRACT 16+ | Nucleic Acid Extraction. 2019; Available at: https://autogen.com/product/xtract-16/.

[221] AutoGen.com. AutoGen | XTRACT | Genomic DNA Bacterial Kit. 2019; Available at: https://autogen.com/product/xtract-genomic-dna-bacterial-kit/.

[222] AutoGen.com. AutoGen | XTRACT | Cultured Cells DNA Kit | Magnetic Bead. 2019; Available at: https://autogen.com/product/xtract-cultured-cells-dna-kit/.

[223] AutoGen.com. AutoGen | QuickGene-810 | Benchtop System | RNA Isolation. 2019; Available at: https://autogen.com/product/quickgene-810/.

[224] AutoGen.com. AutoGen | QuickGene-Auto12S | Rapid DNA Isolation. 2019; Available at: https://autogen.com/product/quickgene-auto12s/.

[225] AutoGen.com. AutoGen | QuickGene-Mini80 | Manual DNA Extraction. 2019; Available at: https://autogen.com/product/quickgene-mini80/.

[226] AutoGen.com. AutoGen | RNA Cultured Cell Kit | Total RNA Extraction. 2019; Available at: https://autogen.com/product/quickgene-rna-cultured-cell-kit/.

[227] AutoGen.com. AutoGen | AutoS RNA Cultured Cell Kit | RNA Isolation Kit. 2019; Available at: https://autogen.com/product/quickgene-autos-rna-cultured-cell-kit/.

[228] AutoGen.com. AutoGen | FlexSTAR | Genomic DNA Extraction | Automated. 2019; Available at: https://autogen.com/product/flex-star/.

[229] AutoGen.com. AutoGen | FlexSTAR+ | Precipitation Chemistry. 2019; Available at: https://autogen.com/product/flex-star-plus/.

[230] AutoGen.com. AutoGen | Blood DNA Finishing Kit | DNA Precipitation. 2019; Available at: https://autogen.com/product/flexstar-platform-blood-dna-finishing-kit/.

[231] AutoGen.com. AutoGen | FlexSTAR | FlexiGene DNA Whole Blood Kits. 2019; Available at: https://autogen.com/product/flexstar-platform-flexigene-dna-whole-blood-kit/.

[232] AutoGen.com. AutoGen | Oragene Saliva Kit | Oragene Saliva | Genomic DNA. 2019; Available at: https://autogen.com/product/flexstar-platform-oragene-saliva-kit/.

[233] Lepej SZ, Poljak M. Portable molecular diagnostic instruments in microbiology: current status. Clinical Microbiology and Infection 2020;26(4):411-420.

[234] Cdc.gov. SARS - CoV - 2 (COVID - 19) Fact Sheet. 2020; Available at: https://www.cdc.gov/coronavirus/2019-ncov/downloads/OASH-COVID-19-guidance-testing-platforms.pdf. Accessed 02/16, 2021.

[235] Bissonnette L, Bergeron MG. Portable devices and mobile instruments for infectious diseases point-of-care testing. Expert Review of Molecular Diagnostics 2017;17(5):471-494.

[236] Abbott.com. Alere™ q Analyser. 2022; Available at: https://www.globalpointofcare.abbott/en/product-details/alere-q-analyser.html. Accessed 02/22, 2022.

[237] Khan A, Hans L, Hsiao N. Comparison of Alere q whole blood viral load with DBS and plasma viral load in the classification of HIV virological failure. PloS one 2020;15(5):e0232345.

[238] Quidel.com. AmpliVue | Quidel. 2022; Available at: https://www.quidel.com/molecular-diagnostics/amplivue-products. Accessed 02/24, 2022.

[239] Qiagen.com. DiagCORE. 2022; Available at: https://www.qiagen.com/cn/products/instruments-and-automation/pcr-instruments/diagcore/. Accessed 02/24, 2022.

[240] Genedrive.com. Genedrive®. 2022; Available at: https://www.genedrive.com/. Accessed 02/24, 2022.

[241] Castan P, de Pablo A, Fernández-Romero N, Rubio JM, Cobb BD, Mingorance J, et al. Point-of-care system for detection of Mycobacterium tuberculosis and rifampin resistance in sputum samples. J Clin Microbiol 2014;52(2):502-507.

[242] QuantuMDx.com. Q-POC™ Platform Platform - Rapid multiplex PCR testing system - QuantuMDx. 2022; Available at: https://www.quantumdx.com/products/q-poc/. Accessed 02/24, 2022.

[243] psidcorp.com. Firefly Dx | PositiveID. 2015; Available at: https://www.psidcorp.com/firefly-dx/. Accessed 02/24, 2022.

[244] Chipcare.ca. ChipCare – Point of Care Dx – Test to Treat Today. 2021; Available at: https://www.chipcare.ca/. Accessed 02/24, 2022.

[245] Bissonnette L, Bergeron MG. The GenePOC platform, a rational solution for extreme point-of-care testing. Micromachines 2016;7(6):94.

[246] Bissonnette L, Chapdelaine S, Peytavi R, Huletsky A, Stewart G, Boissinot M, et al. A revolutionary microfluidic stand-alone platform (GenePOC) for nucleic-acid based point-of-care diagnostics. Global Point of Care—Strategies for Disasters, Emergencies, and Public Health Resilience 2015:235-247.

[247] Centers for Disease Control and Prevention. Information for Laboratories about Coronavirus (COVID-19) . 2020; Available at: https://www.cdc.gov/coronavirus/2019-ncov/lab/index.html?CDC_AA_refVal=https%3A%2F%2Fwww.cdc.gov%2Fcoronavirus%2F2019-ncov%2Flab%2Frt-pcr-detection-instructions.html. Accessed 10/30, 2020.

[248] Wölfel R, Corman VM, Guggemos W, Seilmaier M, Zange S, Müller MA, et al. Virological assessment of hospitalized patients with COVID-2019. Nature 2020;581(7809):465-469.

[249] Touma M. COVID-19: molecular diagnostics overview. Journal of molecular medicine 2020;98(7):947-954.

[250] Abbott.com. Abbott RealTime SARS-CoV-2 Assay (EUA) | Abbott Molecular. 2021; Available at: https://www.molecular.abbott/us/en/products/infectious-disease/RealTime-SARS-CoV-2-Assay. Accessed 02/15, 2021.

[251] Abbott.com. m2000 RealTime System | Abbott Molecular. 2021; Available at: https://www.molecular.abbott/int/en/products/instrumentation/m2000-realtime-system. Accessed 15/02, 2021.

[252] Cepheid.com. Xpert® Xpress SARS-CoV-2 has received FDA Emergency Use Authorization. 2020; Available at: https://www.cepheid.com/coronavirus. Accessed 01/04, 2021.

[253] U.S. Food and Drug Administration. Coronavirus (COVID-19) Update: FDA Issues first Emergency Use Authorization for Point of Care Diagnostic. 2020; Available at: https://www.fda.gov/news-events/press-announcements/coronavirus-covid-19-update-fda-issues-first-emergency-use-authorization-point-care-diagnostic. Accessed 10/30, 2020.

[254] Zhen W, Smith E, Manji R, Schron D, Berry GJ. Clinical Evaluation of Three Sample-to-Answer Platforms for Detection of SARS-CoV-2. J Clin Microbiol 2020 Jul 23;58(8):10.1128/JCM.00783-20. Print 2020 Jul 23.

[255] Ulrich M, Christensen D, Coyne S, Craw P, Henchal E, Sakai S, et al. Evaluation of the Cepheid GeneXpert® system for detecting Bacillus anthracis. J Appl Microbiol 2006;100(5):1011-1016.

[256] Cepheid.com. Xpert®Xpress SARS-CoV-2/Flu/RSV. 2020; Available at: https://cepheid.widen.net/s/sb7lsctwtk. Accessed 01/13, 2021.

[257] Finddx.org. GeneXpert® - FIND. 2020; Available at: https://www.finddx.org/pricing/genexpert/. Accessed 01/13, 2021.

[258] Gibani MM, Toumazou C, Sohbati M, Sahoo R, Karvela M, Hon T, et al. Assessing a novel, lab-free, point-of-care test for SARS-CoV-2 (CovidNudge): a diagnostic accuracy study. The Lancet Microbe 2020;1(7):e300-e307.

[259] Mackenzie R. Portable 90-Minute COVID-19 Test CovidNudge Matches Labs for Accuracy. 2020; Available at: https://www.technologynetworks.com/diagnostics/news/portable-90-minute-covid-19-test-covidnudge-matches-labs-for-accuracy-340567. Accessed 03/15, 2021.

[260] Roche.com. cobas® SARS-CoV-2 Test (for the COVID-19 Coronavirus) | Roche Diagnostics. 2021; Available at: https://diagnostics.roche.com/us/en/products/params/cobas-sars-cov-2-test.html. Accessed 02/15, 2021.

[261] Roche.com. cobas® 6800/8800 Systems Specifications Comparison. 2021; Available at: https://diagnostics.roche.com/us/en/products/systems/cobas-8800-system.html#productSpecs. Accessed 02/15, 2021.

[262] Hetem DJ, Bos-Sanders I, Nijhuis RHT, Tamminga S, Berlinger L, Kuijper EJ, et al. Evaluation of the Liat Cdiff Assay for Direct Detection of Clostridioides difficile Toxin Genes within 20 Minutes. J Clin Microbiol 2019 May 24;57(6):10.1128/JCM.00416-19. Print 2019 Jun.

[263] Granato PA, Hansen G, Herding E, Chaudhuri S, Tang S, Garg SK, et al. Performance comparison of the cobas Liat and Cepheid GeneXpert systems for Clostridium difficile detection. PLoS One 2018;13(7):e0200498.

[264] Garg SK, Lu K, Duncan J, Peterson LR, Liesenfeld O. Equivalent performance of the Cobas® Cdiff test for use on the Cobas® Liat® system and the Cobas® 4800 system. European Journal of Microbiology and Immunology 2017;7(4):310-318.

[265] Rao AJ, Teton Z, Rodriguez V, Tieu BH, Raslan AM. Distal ventriculoatrial shunt revision in adult myelomeningocele patient performed via endovascular transvenous approach. World neurosurgery 2019;121:24-27.

[266] Donato LJ, Myhre NK, Murray MA, McDonah MR, Myers JF, Maxson JA, et al. Assessment of Test Performance and Potential for Environmental Contamination Associated with a Point-of-Care Molecular Assay for Group A Streptococcus in an End User Setting. J Clin Microbiol 2019 Jan 30;57(2):10.1128/JCM.01629-18. Print 2019 Feb.

[267] Wang F, Tian Y, Chen L, Luo R, Sickler J, Liesenfeld O, et al. Accurate detection of Streptococcus pyogenes at the point of care using the cobas Liat Strep A nucleic acid test. Clin Pediatr 2017;56(12):1128-1134.

[268] Gosert R, Naegele K, Hirsch HH. Comparing the Cobas Liat Influenza A/B and respiratory syncytial virus assay with multiplex nucleic acid testing. J Med Virol 2019;91(4):582-587.

[269] Banerjee D, Kanwar N, Hassan F, Essmyer C, Selvarangan R. Comparison of Six Sample-to-Answer Influenza A/B and Respiratory Syncytial Virus Nucleic Acid Amplification Assays Using Respiratory Specimens from Children. J Clin Microbiol 2018 Oct 25;56(11):10.1128/JCM.00930-18. Print 2018 Nov.

[270] Ling L, Kaplan SE, Lopez JC, Stiles J, Lu X, Tang YW. Parallel Validation of Three Molecular Devices for Simultaneous Detection and Identification of Influenza A and B and Respiratory Syncytial Viruses. J Clin Microbiol 2018 Feb 22;56(3):10.1128/JCM.01691-17. Print 2018 Mar.

[271] Gibson J, Schechter-Perkins EM, Mitchell P, Mace S, Tian Y, Williams K, et al. Multi-center evaluation of the cobas® Liat® Influenza A/B & RSV assay for rapid point of care diagnosis. Journal of Clinical Virology 2017;95:5-9.

[272] Maignan M, Viglino D, Hablot M, Termoz Masson N, Lebeugle A, Collomb Muret R, et al. Diagnostic accuracy of a rapid RT-PCR assay for point-of-care detection of influenza A/B virus at emergency department admission: A prospective evaluation during the 2017/2018 influenza season. PloS one 2019;14(5):e0216308.

[273] Akashi Y, Suzuki H, Ueda A, Hirose Y, Hayashi D, Imai H, et al. Analytical and clinical evaluation of a point-of-care molecular diagnostic system and its influenza A/B assay for rapid molecular detection of the influenza virus. Journal of Infection and Chemotherapy 2019;25(8):578-583.

[274] Youngs J, Iqbal Y, Glass S, Riley P, Pope C, Planche T, et al. Implementation of the cobas Liat influenza point-of-care test into an emergency department during a high-incidence season: a retrospective evaluation following real-world implementation. J Hosp Infect 2019;101(3):285-288.

[275] Valentin T, Kieslinger P, Stelzl E, Santner BI, Groselj-Strele A, Kessler HH, et al. Prospective evaluation of three rapid molecular tests for seasonal influenza in patients presenting at an emergency unit. Journal of Clinical Virology 2019;111:29-32.

[276] Melchers WJ, Kuijpers J, Sickler JJ, Rahamat-Langendoen J. Lab-in-a-tube: Real-time molecular point-of-care diagnostics for influenza A and B using the cobas® Liat® system. J Med Virol 2017;89(8):1382-1386.

[277] Young S, Illescas P, Nicasio J, Sickler JJ. Diagnostic accuracy of the real-time PCR cobas® Liat® Influenza A/B assay and the Alere i Influenza A&B NEAR isothermal nucleic acid amplification assay for the detection of influenza using adult nasopharyngeal specimens. Journal of Clinical Virology 2017;94:86-90.

[278] Nolte FS, Gauld L, Barrett SB. Direct Comparison of Alere i and cobas Liat Influenza A and B Tests for Rapid Detection of Influenza Virus Infection. J Clin Microbiol 2016 Nov;54(11):2763-2766.

[279] Chen L, Tian Y, Chen S, Liesenfeld O. Performance of the Cobas® Influenza A/B assay for rapid PCR-based detection of influenza compared to Prodesse ProFlu and viral culture. European Journal of Microbiology and Immunology 2015;5(4):236-245.

[280] Binnicker MJ, Espy MJ, Irish CL, Vetter EA. Direct Detection of Influenza A and B Viruses in Less Than 20 Minutes Using a Commercially Available Rapid PCR Assay. J Clin Microbiol 2015 Jul;53(7):2353-2354.

[281] BioFire Diagnostics. FilmArray Respiratory Panel EZ | In-Clinic Diagnostic Testing Solution | BioFire Diagnostics. 2021; Available at: https://www.biofiredx.com/products/the-filmarray-panels/filmarray-respiratory-panel-ez/. Accessed 03/08, 2021.

[282] BioFire Diagnostics. The BioFire® FilmArray® System. 2021; Available at: https://www.biomerieux-diagnostics.com/filmarray. Accessed 09/03, 2021.

[283] Liotti FM, Menchinelli G, Marchetti S, Morandotti GA, Sanguinetti M, Posteraro B, et al. Evaluating the newly developed BioFire COVID-19 test for SARS-CoV-2 molecular detection. Clin Microbiol Infect 2020 Dec;26(12):1699-1700.

[284] Creager HM, Cabrera B, Schnaubelt A, Cox JL, Cushman-Vokoun AM, Shakir SM, et al. Clinical evaluation of the BioFire® Respiratory Panel 2.1 and detection of SARS-CoV-2. Journal of Clinical Virology 2020;129:104538.

[285] Eckbo EJ, Locher K, Caza M, Li L, Lavergne V, Charles M. Evaluation of the BioFire® COVID-19 test and Respiratory Panel 2.1 for rapid identification of SARS-CoV-2 in nasopharyngeal swab samples. Diagn Microbiol Infect Dis 2021;99(3):115260.

[286] Smith E, Zhen W, Manji R, Schron D, Duong S, Berry GJ. Analytical and clinical comparison of three nucleic acid amplification tests for SARS-CoV-2 detection. J Clin Microbiol 2020;58(9):e01134-20.

[287] Thermofisher.com. TaqPath™ COVID-19 CE-IVD RT-PCR Kit. 2021; Available at: https://www.thermofisher.com/order/catalog/product/A48067?SID=srch-hj-A48067#/A48067?SID=srch-hj-A48067. Accessed 03/05, 2021.

[288] Fda.gov. TaqPath™ COVID-19 Combo Kit and TaqPath™ COVID-19 Combo Kit Advanced*. 2020; Available at: https://www.fda.gov/media/136112/download. Accessed 03/05, 2021.

[289] Garg A, Ghoshal U, Patel SS, Singh D, Arya AK, Vasanth S, et al. Evaluation of seven commercial RT-PCR kits for COVID-19 testing in pooled clinical specimens. J Med Virol 2020.

[290] Matsumura Y, Shimizu T, Noguchi T, Nakano S, Yamamoto M, Nagao M. Comparison of 12 molecular detection assays for severe acute respiratory syndrome coronavirus 2 (SARS-CoV-2). The Journal of Molecular Diagnostics 2021;23(2):164-170.

[291] DiaSorin Molecular. Simplexa® COVID-19 Direct Kit - DiaSorin Molecular. 2021; Available at: https://www.google.com/search?q=Simplexa+COVID-19+Direct&sxsrf=ALeKk02_pxPcB55mIMmwS5foaQMKNfqhqQ:1615824751287&source=lnms&tbm=isch&biw=1920&bih=937. Accessed 03/15, 2021.

[292] Bordi L, Piralla A, Lalle E, Giardina F, Colavita F, Tallarita M, et al. Rapid and sensitive detection of SARS-CoV-2 RNA using the Simplexa™ COVID-19 direct assay. Journal of Clinical Virology 2020;128:104416.

[293] Zhen W, Manji R, Smith E, Berry GJ. Comparison of Four Molecular In Vitro Diagnostic Assays for the Detection of SARS-CoV-2 in Nasopharyngeal Specimens. J Clin Microbiol 2020 Jul 23;58(8):10.1128/JCM.00743-20. Print 2020 Jul 23.

[294] Icmr.gov.in. Revised Guidelines for TrueNat testing for COVID-19. 2020; Available at: https://www.icmr.gov.in/pdf/covid/labs/Revised_Guidelines_TrueNat_Testing_24092020.pdf. Accessed 03/08, 2021.

[295] Gupta N, Rana S, Singh H. Innovative point-of-care molecular diagnostic test for COVID-19 in India. The Lancet Microbe 2020;1(7):e277.

[296] Basawarajappa SG, Rangaiah A, Padukone S, Yadav PD, Gupta N, Shankar SM. Performance evaluation of Truenat Beta CoV & Truenat SARS-CoV-2 point-of-care assays for coronavirus disease 2019. Indian J Med Res 2020 Nov 4.

[297] Ghoshal U, Vasanth S, Tejan N. A guide to laboratory diagnosis of Corona Virus Disease-19 for the gastroenterologists. Indian Journal of Gastroenterology 2020:1-7.

[298] Menarinidiagnostics.com. VITAPCR™ PLATFORM. 2021; Available at: https://www.menarinidiagnostics.com/en-us/Home/Laboratory-products/COVID-19/Virus-Detection/VitaPCRTM-platform/Technical-Data. Accessed 03/05, 2021.

[299] Fournier P, Zandotti C, Ninove L, Prudent E, Colson P, Gazin C, et al. Contribution of VitaPCR SARS-CoV-2 to the emergency diagnosis of COVID-19. Journal of Clinical Virology 2020;133:104682.

[300] Abbott.com. Detect COVID-19 in as Little as 5 Minutes | Abbott Newsroom. 2020; Available at: https://www.abbott.com/corpnewsroom/diagnostics-testing/detect-covid-19-in-as-little-as-5-minutes.html. Accessed 01/13, 2021.

[301] Globalpointofcare.abbott. ID NOW™ COVID-19. 2020; Available at: https://www.globalpointofcare.abbott/en/product-details/id-now-covid-19.html. Accessed 10/30, 2020.

[302] Abbott.com. ID NOW™ COVID-19 . 2020; Available at: https://www.globalpointofcare.abbott/en/product-details/id-now-covid-19.html. Accessed 01/13, 2021.

[303] Basu A, Zinger T, Inglima K, Woo KM, Atie O, Yurasits L, et al. Performance of Abbott ID Now COVID-19 Rapid Nucleic Acid Amplification Test Using Nasopharyngeal Swabs Transported in Viral Transport Media and Dry Nasal Swabs in a New York City Academic Institution. J Clin Microbiol 2020 Jul 23;58(8):10.1128/JCM.01136-20. Print 2020 Jul 23.

[304] Nie S, Roth RB, Stiles J, Mikhlina A, Lu X, Tang YW, et al. Evaluation of Alere i Influenza A&B for rapid detection of influenza viruses A and B. J Clin Microbiol 2014 Sep;52(9):3339-3344.

[305] Bell JJ, Selvarangan R. Evaluation of the Alere I influenza A&B nucleic acid amplification test by use of respiratory specimens collected in viral transport medium. J Clin Microbiol 2014 Nov;52(11):3992-3995.

[306] Jokela P, Vuorinen T, Waris M, Manninen R. Performance of the Alere i influenza A&B assay and mariPOC test for the rapid detection of influenza A and B viruses. Journal of Clinical Virology 2015;70:72-76.

[307] Hurtado JC, Mosquera MM, de Lazzari E, Martínez E, Torner N, Isanta R, et al. Evaluation of a new, rapid, simple test for the detection of influenza virus. BMC infectious diseases 2015;15(1):1-4.

[308] Hazelton B, Gray T, Ho J, Ratnamohan VM, Dwyer DE, Kok J. Detection of influenza A and B with the Alere™ i Influenza A & B: a novel isothermal nucleic acid amplification assay. Influenza and other respiratory viruses 2015;9(3):151-154.

[309] Van JN, Caméléna F, Dahoun M, Pilmis B, Mizrahi A, Lourtet J, et al. Prospective evaluation of the Alere i Influenza A&B nucleic acid amplification versus Xpert Flu/RSV. Diagn Microbiol Infect Dis 2016;85(1):19-22.

[310] Davis S, Allen A, O'Leary R, Power M, Price D, Simpson A, et al. Diagnostic accuracy and cost analysis of the Alere™ i Influenza A&B near-patient test using throat swabs. J Hosp Infect 2017;97(3):301-309.

[311] Busson L, Mahadeb B, De Foor M, Vandenberg O, Hallin M. Contribution of a rapid influenza diagnostic test to manage hospitalized patients with suspected influenza. Diagn Microbiol Infect Dis 2017;87(3):238-242.

[312] Hassan F, Crawford J, Bonner AB, Ledeboer NA, Selvarangan R. Multicenter evaluation of the Alere™ i influenza A&B assay using respiratory specimens collected in viral transport media. Diagn Microbiol Infect Dis 2018;92(4):294-298.

[313] Trabattoni E, Le V, Pilmis B, de Ponfilly GP, Caisso C, Couzigou C, et al. Implementation of Alere i Influenza A & B point of care test for the diagnosis of influenza in an ED. Am J Emerg Med 2018;36(6):916-921.

[314] Peters RM, Schnee SV, Tabatabai J, Schnitzler P, Pfeil J. Evaluation of Alere i RSV for Rapid Detection of Respiratory Syncytial Virus in Children Hospitalized with Acute Respiratory Tract Infection. J Clin Microbiol 2017 Apr;55(4):1032-1036.

[315] Schnee SV, Pfeil J, Ihling CM, Tabatabai J, Schnitzler P. Performance of the Alere i RSV assay for point-of-care detection of respiratory syncytial virus in children. BMC infectious diseases 2017;17(1):1-6.

[316] Hassan F, Hays LM, Bonner A, Bradford BJ, Franklin R,Jr, Hendry P, et al. Multicenter Clinical Evaluation of the Alere i Respiratory Syncytial Virus Isothermal Nucleic Acid Amplification Assay. J Clin Microbiol 2018 Feb 22;56(3):10.1128/JCM.01777-17. Print 2018 Mar.

[317] Cohen DM, Russo ME, Jaggi P, Kline J, Gluckman W, Parekh A. Multicenter Clinical Evaluation of the Novel Alere i Strep A Isothermal Nucleic Acid Amplification Test. J Clin Microbiol 2015 Jul;53(7):2258-2261.

[318] Berry GJ, Miller CR, Prats MM, Marquez C, Oladipo OO, Loeffelholz MJ, et al. Comparison of the Alere i Strep A Test and the BD Veritor System in the Detection of Group A Streptococcus and the Hypothetical Impact of Results on Antibiotic Utilization. J Clin Microbiol 2018 Feb 22;56(3):10.1128/JCM.01310-17. Print 2018 Mar.

[319] Weinzierl EP, Jerris RC, Gonzalez MD, Piccini JA, Rogers BB. Comparison of Alere i Strep A rapid molecular assay with rapid antigen testing and culture in a pediatric outpatient setting. Am J Clin Pathol 2018;150(3):235-239.

[320] Hologic.com. SARS-CoV-2 Assays | Aptima |Panther Fusion | Hologic. 2021; Available at: https://www.hologic.com/hologic-products/molecular-diagnostics/hologic-sars-cov-2-assays. Accessed 11/15, 2021.

[321] Pham J, Meyer S, Nguyen C, Williams A, Hunsicker M, McHardy I, et al. Performance characteristics of a high-throughput automated transcription-mediated amplification test for SARS-CoV-2 detection. J Clin Microbiol 2020;58(10).

[322] Hologic.com. Panther Fusion® System | Hologic . 2021; Available at: https://www.hologic.com/hologic-products/diagnostic-solutions/Panther-Scalable-Solutions/panther-fusion-system. Accessed 02/19, 2021.

[323] Gorzalski AJ, Tian H, Laverdure C, Morzunov S, Verma SC, VanHooser S, et al. High-Throughput Transcription-mediated amplification on the Hologic Panther is a highly sensitive method of detection for SARS-CoV-2. Journal of Clinical Virology 2020;129:104501.

[324] Trémeaux P, Lhomme S, Abravanel F, Raymond S, Mengelle C, Mansuy J, et al. Evaluation of the Aptima™ transcription-mediated amplification assay (Hologic®) for detecting SARS-CoV-2 in clinical specimens. Journal of Clinical Virology 2020;129:104541.

[325] Fda.gov. Color SARS-CoV-2 RT-LAMP Diagnostic Assay EUA Summary. 2020; Available at: https://www.fda.gov/media/138249/download. Accessed 02/15, 2021.

[326] Color.com. SARS-CoV-2 LAMP Diagnostic Assay. 2020; Available at: https://www.color.com/wp-content/uploads/2020/05/Color-LAMP-Diagnostic-Assay_v1-2_Updated-052120.pdf. Accessed 01/13, 2021.

[327] Sherlock.bio. SHERLOCK • Sherlock Biosciences. 2021; Available at: https://sherlock.bio/platforms/sherlock/. Accessed 02/18, 2021.

[328] Joung J, Ladha A, Saito M, Segel M, Bruneau R, Huang MW, et al. Point-of-care testing for COVID-19 using SHERLOCK diagnostics. medRxiv 2020 May 8.

[329] Broughton JP, Deng X, Yu G, Fasching CL, Servellita V, Singh J, et al. CRISPR–Cas12-based detection of SARS-CoV-2. Nat Biotechnol 2020;38(7):870-874.

[330] Vaz SN, Santana DSd, Netto EM, Pedroso C, Wang W, Santos FDA, et al. Saliva is a reliable, non-invasive specimen for SARS-CoV-2 detection. Brazilian Journal of Infectious Diseases 2020;24:422-427.

[331] Maggi RG, Birkenheuer AJ, Hegarty BC, Bradley JM, Levy MG, Breitschwerdt EB. Comparison of serological and molecular panels for diagnosis of vector-borne diseases in dogs. Parasites & vectors 2014;7(1):1-9.

[332] Gong F, Wei HX, Li Q, Liu L, Li B. Evaluation and Comparison of Serological Methods for COVID-19 Diagnosis. Front Mol Biosci 2021 Jul 23;8:682405.

[333] Lafleur LK, Bishop JD, Heiniger EK, Gallagher RP, Wheeler MD, Kauffman P, et al. A rapid, instrument-free, sample-to-result nucleic acid amplification test. Lab on a Chip 2016;16(19):3777-3787.

[334] Beal SG, Assarzadegan N, Rand KH. Sample-to-result molecular infectious disease assays: clinical implications, limitations and potential. Expert Review of Molecular Diagnostics 2016;16(3):323-341.

[335] Quinn AD, Dixon D, Meenan BJ. Barriers to hospital-based clinical adoption of point-of-care testing (POCT): a systematic narrative review. Crit Rev Clin Lab Sci 2016;53(1):1-12.

[336] Zasada AA, Zacharczuk K, Woźnica K, Główka M, Ziółkowski R, Malinowska E. The influence of a swab type on the results of point-of-care tests. AMB Express 2020;10(1):1-6.

[337] Kahamba TR, Noble L, Scott L, Stevens W. Comparison of three nasopharyngeal swab types and the impact of physiochemical properties for optimal SARS-CoV-2 detection. medRxiv 2020.

[338] Ignition CBS. TS/8-A - Woodshaft with Cotton Tip, Single in Peel Pouch. 2016; Available at: https://www.tscswabs.co.uk/Products/40/TS-8-A-Woodshaft-with-Cotton-Tip-Single-in-Peel-Pouch. Accessed 12/07, 2021.

[339] MWE Medical Wire. Rayon and Polyester Dryswabs™. 2021; Available at: https://www.mwe.co.uk/product/rayon-and-polyester-dryswabs/. Accessed 12/07, 2021.

[340] COPAN Diagnostics Inc. FLOQSwabs® - 502CS01 | COPAN Diagnostics Inc. 2021; Available at: https://www.copanusa.com/sample-collection-transport-processing/floqswabs/502cs01. Accessed 12/07, 2021.

[341] MWE Medical Wire. HydraFlock® Micro Ultrafine Flexible. 2021; Available at: https://www.mwe.co.uk/product/hydraflock-micro-ultrafine-flexible/. Accessed 12/07, 2021.

[342] Ignition CBS. TS/17-B - Polypropylene (flexible) shaft, Viscose Tip Swab, in Peel Pouch. 2016; Available at: https://www.tscswabs.co.uk/Products/57/TS-17-B-Polypropylene-flexible-shaft-with-viscose-Tip-in-Peel-Pouch. Accessed 12/07, 2021.

[343] MWE Medical Wire. ∑-Swab® - MWE Medical Wire. 2021; Available at: https://www.mwe.co.uk/product/%e2%88%91-swab/. Accessed 12/07, 2021.

[344] Ignition CBS. TS/16-B - Plasticised Paper shaft, Cotton MiniTip in peel pouch. 2016; Available at: https://www.tscswabs.co.uk/Products/51/TS-16-B-Plasticised-Paper-shaft-with-mini-Cotton-Tip-in-peel-pouch. Accessed 12/07, 2021.

[345] Dalian Goodwood Medical Care LTD. Nylon head PP Rod Sterile Nasopharyngeal Flocking Swab For virus detection |. 2021; Available at: http://www.dl-goodwood.com/pid18303452/Nylon-head-PP-Rod-Sterile-Nasopharyngeal-Flocking-Swab-For-virus-detection.htm. Accessed 12/07, 2021.

[346] Hutchisonintl.com. A-04 Disposable Sampling Swab. 2020; Available at: https://www.hutchisonintl.com/product-page/a-04-disposable-sampling-swab. Accessed 12/07, 2021.

[347] Panpradist N, Toley BJ, Zhang X, Byrnes S, Buser JR, Englund JA, et al. Swab sample transfer for point-of-care diagnostics: characterization of swab types and manual agitation methods. PloS one 2014;9(9):e105786.

[348] Fan K, Chen J, Wang C, Pan W. Development of a drop-on-demand droplet generator for one-drop-fill technology. Sensors and Actuators A: Physical 2008;147(2):649-655.

[349] Ahamed MJ, Ben-Mrad R, Sullivan P. A drop-on-demand-based electrostatically actuated microdispenser. J Microelectromech Syst 2012;22(1):177-185.

[350] Bu Z, Lin S, Huang X, Li A, Wu D, Zhao Y, et al. A novel piezostack-driven jetting dispenser with corner-filleted flexure hinge and high-frequency performance. J Micromech Microengineering 2018;28(7):075001.

[351] Han H, Lee JS, Kim H, Shin S, Lee J, Kim J, et al. Single-droplet multiplex bioassay on a robust and stretchable extreme wetting substrate through vacuum-based droplet manipulation. ACS nano 2018;12(2):932-941.

[352] Tseng F, Kim C, Ho C. A high-resolution high-frequency monolithic top-shooting microinjector free of satellite drops-part I: concept, design, and model. J Microelectromech Syst 2002;11(5):427-436.

[353] Koltay P, Steger R, Bohl B, Zengerle R. The dispensing well plate: a novel nanodispenser for the multiparallel delivery of liquids (DWP Part I). Sensors and Actuators A: Physical 2004;116(3):483-491.

[354] Ahamed MJ, Gubarenko SI, Ben-Mrad R, Sullivan P. A piezoactuated droplet-dispensing microfluidic chip. J Microelectromech Syst 2009;19(1):110-119.

[355] Choi W, Lebrasseur E, Al-Haq MI, Tsuchiya H, Torii T, Yamazaki H, et al. Nano-liter size droplet dispenser using electrostatic manipulation technique. Sensors and Actuators A: Physical 2007;136(1):484-490.

[356] Lee S, Byun D, Jung D, Choi J, Kim Y, Yang JH, et al. Pole-type ground electrode in nozzle for electrostatic field induced drop-on-demand inkjet head. Sensors and Actuators A: Physical 2008;141(2):506-514.

[357] Darwin-microfluidics.com. Needle gauge table. 2022; Available at: https://darwin-microfluidics.com/blogs/tools/syringe-needle-gauge-table. Accessed 01/11, 2022.

[358] Van Santvliet L, Ludwig A. Determinants of eye drop size. Surv Ophthalmol 2004;49(2):197-213.

[359] Tripp GK, Good KL, Motta MJ, Kass PH, Murphy CJ. The effect of needle gauge, needle type, and needle orientation on the volume of a drop. Vet Ophthalmol 2016;19(1):38-42.

[360] Haber C, Boillat M, Schoot Bvd. Precise nanoliter fluid handling system with integrated high-speed flow sensor. Assay and drug development technologies 2005;3(2):203-212.

[361] Bammesberger SB, Malki I, Ernst A, Zengerle R, Koltay P. A calibration-free, noncontact, disposable liquid dispensing cartridge featuring an online process control. Journal of laboratory automation 2014;19(4):394-402.

[362] Castrejón-Pita J, Martin G, Hoath S, Hutchings I. A simple large-scale droplet generator for studies of inkjet printing. Rev Sci Instrum 2008;79(7):075108.

[363] Feasibility of low-cost microarray printing with inkjet printer. 2008 International Conference on Control, Automation and Systems: IEEE; 2008.

[364] Tools.thermofisher.com. PureLink® Genomic DNA Kits. 2012; Available at: https://tools.thermofisher.com/content/sfs/manuals/purelink_genomic_man.pdf. Accessed 11/18, 2021.

[365] Thermofisher.com. PureLink™ Genomic DNA Mini Kit. 2021; Available at: https://www.thermofisher.com/order/catalog/product/K182002. Accessed 11/18, 2021.

[366] Thermofisher.com. Qubit™ 1X dsDNA Assay Kits, high sensitivity (HS) and broad range (BR). 2021; Available at: https://www.thermofisher.com/order/catalog/product/Q33230. Accessed 11/18, 2021.

[367] Ahmad F, Stedtfeld RD, Waseem H, Williams MR, Cupples AM, Tiedje JM, et al. Most probable number-loop mediated isothermal amplification (MPN-LAMP) for quantifying waterborne pathogens in< 25 min. J Microbiol Methods 2017;132:27-33.

[368] Fauquet CM, Mayo MA, Maniloff J, Desselberger U, Ball LA. Virus taxonomy: VIIIth report of the International Committee on Taxonomy of Viruses. : Academic Press; 2005.

[369] Kim J, Gale BK. Quantitative and qualitative analysis of a microfluidic DNA extraction system using a nanoporous AlO x membrane. Lab on a Chip 2008;8(9):1516-1523.

[370] Lee H, Na W, Park C, Park KH, Shin S. Centrifugation-free extraction of circulating nucleic acids using immiscible liquid under vacuum pressure. Scientific reports 2018;8(1):1-11.

[371] Bej A, Mahbubani M, Dicesare J, Atlas R. Polymerase chain reaction-gene probe detection of microorganisms by using filter-concentrated samples. Appl Environ Microbiol 1991;57(12):3529-3534.

[372] Bunyakul N, Promptmas C, Baeumner AJ. Microfluidic biosensor for cholera toxin detection in fecal samples. Analytical and bioanalytical chemistry 2015;407(3):727-736.

[373] Verdoy D, Barrenetxea Z, Berganzo J, Agirregabiria M, Ruano-López JM, Marimón JM, et al. A novel Real Time micro PCR based Point-of-Care device for Salmonella detection in human clinical samples. Biosensors and Bioelectronics 2012;32(1):259-265.

[374] Mosley O, Melling L, Tarn MD, Kemp C, Esfahani MM, Pamme N, et al. Sample introduction interface for on-chip nucleic acid-based analysis of Helicobacter pylori from stool samples. Lab on a Chip 2016;16(11):2108-2115.

[375] Berry SM, Alarid ET, Beebe DJ. One-step purification of nucleic acid for gene expression analysis via Immiscible Filtration Assisted by Surface Tension (IFAST). Lab on a Chip 2011;11(10):1747-1753.

[376] Strotman L, O'Connell R, Casavant BP, Berry SM, Sperger JM, Lang JM, et al. Selective nucleic acid removal via exclusion (SNARE): capturing mRNA and DNA from a single sample. Anal Chem 2013;85(20):9764-9770.

[377] Berry SM, Singh C, Lang JD, Strotman LN, Alarid ET, Beebe DJ. Streamlining gene expression analysis: integration of co-culture and mRNA purification. Integrative Biology 2014;6(2):224-231.

[378] Strotman LN, Lin G, Berry SM, Johnson EA, Beebe DJ. Facile and rapid DNA extraction and purification from food matrices using IFAST (immiscible filtration assisted by surface tension). Analyst 2012;137(17):4023-4028.

[379] Berry SM, LaVanway AJ, Pezzi HM, Guckenberger DJ, Anderson MA, Loeb JM, et al. HIV viral RNA extraction in wax immiscible filtration assisted by surface tension (IFAST) devices. The Journal of Molecular Diagnostics 2014;16(3):297-304.

[380] Kim T, Park J, Kim C, Cho Y. Fully integrated lab-on-a-disc for nucleic acid analysis of food-borne pathogens. Anal Chem 2014;86(8):3841-3848.

[381] Lien K, Liu C, Lin Y, Kuo P, Lee G. Extraction of genomic DNA and detection of single nucleotide polymorphism genotyping utilizing an integrated magnetic bead-based microfluidic platform. Microfluidics and Nanofluidics 2009;6(4):539-555.

[382] Thermofisher.com. NanoDrop Spectrophotometers Assessment of Nucleic Acid Purity. 2011; Available at: https://www.thermofisher.com/uk/en/home/industrial/spectroscopy-elemental-isotope-analysis/molecular-spectroscopy/ultraviolet-visible-visible-spectrophotometry-uv-vis-vis/uv-vis-vis-instruments/nanodrop-microvolume-spectrophotometers.html. Accessed 22/11, 2021.

[383] Wilfinger WW, Mackey K, Chomczynski P. Effect of pH and ionic strength on the spectrophotometric assessment of nucleic acid purity. BioTechniques 1997;22(3):474-481.

[384] Glasel J. Validity of nucleic acid purities monitored by 260nm/280nm absorbance ratios. BioTechniques 1995;18(1):62-63.

[385] Huberman J. Importance of measuring nucleic acid absorbance at 240 nm as well as at 260 and 280 nm. BioTechniques 1995;18(4):636.

[386] Manchester K. Value of A260/A280 ratios for measurement of purity of nucleic acids. BioTechniques 1995;19(2):208-210.

[387] Manchester KL. Use of UV methods for measurement of protein and nucleic acid concentrations. BioTechniques 1996;20(6):968-970.

[388] Singer VL, Jones LJ, Yue ST, Haugland RP. Characterization of PicoGreen reagent and development of a fluorescence-based solution assay for double-stranded DNA quantitation. Anal Biochem 1997;249(2):228-238.

[389] Jones LJ, Yue ST, Cheung C, Singer VL. RNA quantitation by fluorescence-based solution assay: RiboGreen reagent characterization. Anal Biochem 1998;265(2):368-374.

[390] Kapuscinski J. DAPI: a DNA-specific fluorescent probe. Biotechnic & histochemistry 1995;70(5):220-233.

[391] Nge PN, Rogers CI, Woolley AT. Advances in microfluidic materials, functions, integration, and applications. Chem Rev 2013;113(4):2550-2583.

[392] Mei Q, Xia Z, Xu F, Soper SA, Fan ZH. Fabrication of microfluidic reactors and mixing studies for luciferase detection. Anal Chem 2008;80(15):6045-6050.

[393] Friend J, Yeo L. Fabrication of microfluidic devices using polydimethylsiloxane. Biomicrofluidics 2010;4(2):026502.

[394] Sia SK, Whitesides GM. Microfluidic devices fabricated in poly (dimethylsiloxane) for biological studies. Electrophoresis 2003;24(21):3563-3576.

[395] Gelber MK, Bhargava R. Monolithic multilayer microfluidics via sacrificial molding of 3D-printed isomalt. Lab on a Chip 2015;15(7):1736-1741.

[396] Rogers CI, Qaderi K, Woolley AT, Nordin GP. 3D printed microfluidic devices with integrated valves. Biomicrofluidics 2015;9(1):016501.

[397] Au AK, Bhattacharjee N, Horowitz LF, Chang TC, Folch A. 3D-printed microfluidic automation. Lab on a Chip 2015;15(8):1934-1941.

[398] Bhattacharjee N, Urrios A, Kang S, Folch A. The upcoming 3D-printing revolution in microfluidics. Lab on a Chip 2016;16(10):1720-1742.

[399] Amin R, Knowlton S, Hart A, Yenilmez B, Ghaderinezhad F, Katebifar S, et al. 3D-printed microfluidic devices. Biofabrication 2016;8(2):022001.

[400] Folch A. Introduction to bioMEMS. : CRC Press; 2016.

[401] Huang B, Wu H, Kim S, Zare RN. Coating of poly (dimethylsiloxane) with n-dodecyl-β-D-maltoside to minimize nonspecific protein adsorption. Lab on a Chip 2005;5(10):1005-1007.

[402] Shah JJ, Geist J, Locascio LE, Gaitan M, Rao MV, Vreeland WN. Surface modification of poly (methyl methacrylate) for improved adsorption of wall coating polymers for microchip electrophoresis. Electrophoresis 2006;27(19):3788-3796.

[403] metoffice.gov.uk. Met Office | UK climate maps and data. 2022; Available at: https://www.metoffice.gov.uk/research/climate/maps-and-data. Accessed 08/03, 2022.

[404] Pagasa.dost.gov.ph. PAGASA | Climate of the Philippines. 2022; Available at: https://www.pagasa.dost.gov.ph/information/climate-philippines#:~:text=Due%20to%20high%20temperature%20and,and%2085%20percent%20in%20September. Accessed 03/08, 2022.

[405] Hygiena.com. Healthcare - Hygiena ATP Test Device Design and Performance | Healthcare Products | Hygiena | Hygiena - Rapid Solutions for Hygiene Monitoring. 2018; Available at: https://www.hygiena.com/atp-test-design-performance-healthcare.html.

[406] Xu K, Begley MR, Landers JP. Simultaneous metering and dispensing of multiple reagents on a passively controlled microdevice solely by finger pressing. Lab on a Chip 2015;15(3):867-876.

[407] Krawzak TP, Degroff MJ, Nunnery DW, McGraw BJ, inventors. AnonymousLiquid dispenser. US5232664A. 1993 .

[408] Baden T, Chagas AM, Gage G, Marzullo T, Prieto-Godino LL, Euler T. Open Labware: 3-D printing your own lab equipment. PLoS biology 2015;13(3):e1002086.

[409] Cao W, Easley CJ, Ferrance JP, Landers JP. Chitosan as a polymer for pH-induced DNA capture in a totally aqueous system. Anal Chem 2006;78(20):7222-7228.

[410] Kun Y, Chuan X, Guozhu C. Frequency adaptive resonant controller based current control of SVG. Transactions of China electrotechnical society 2014;29(8):248-254.

[411] Shaffer S, Yang K, Vargas J, Di Prima MA, Voit W. On reducing anisotropy in 3D printed polymers via ionizing radiation. Polymer 2014;55(23):5969-5979.

[412] Guttridge C, Shannon A, O'Sullivan A, O'Sullivan KJ, O'Sullivan LW. Biocompatible 3D printing resins for medical applications: a review of marketed intended uses, biocompatibility certification, and post-processing guidance. Annals of 3D Printed Medicine 2021:100044.

[413] anycubic.com. Anycubic | Photon Mono 4K. 2022; Available at: https://www.anycubic.com/collections/3d-printers/products/photon-mono-4k?sscid=31k6_8abqd&. Accessed 08/03, 2022.

[414] anycubic.com. Anycubic | Photon Mono X. 2022; Available at: https://www.anycubic.com/products/photon-mono-x-resin-printer. Accessed 08/03, 2022.

[415] elegoo.com. Elegoo | Mars 2 Pro. 2022; Available at: https://www.elegoo.com/collections/mars-series/products/elegoo-mars-2-mono-lcd-3d-printer. Accessed 03/08, 2022.

[416] elegoo.com. Elegoo | Mars 3. 2022; Available at: https://www.elegoo.com/collections/mars-series/products/elegoo-mars-3-lcd-3d-printer. Accessed 03/08, 2022.

[417] dynamism.com. Dynamism | Formlabs Form 3+ Basic Package. 2022; Available at: https://www.dynamism.com/formlabs/formlabs-3d-printers/formlabs-form-3-plus-basic-package.html. Accessed 03/08, 2022.

[418] dynamism.com. Dynamism | Formlabs Form 3L Basic Package. 2022; Available at: https://www.dynamism.com/formlabs/formlabs-3d-printers/formlabs-form3l-basicpackage.html. Accessed 03/08, 2022.

[419] anycubic.com. Anycubic | 4Max Pro 2.0. 2022; Available at: https://www.anycubic.com/products/4max-pro-2-0. Accessed 03/08, 2022.

[420] anycubic.com. Anycubic | Chiron. 2022; Available at: https://www.anycubic.com/products/4max-pro-2-0. Accessed 08/03, 2022.

[421] creality.com. Creality | Ender-2 Pro 3D Printer. 2022; Available at: https://www.creality3dofficial.com/products/creality-ender-2-3d-printer. Accessed 03/08, 2022.

[422] creality.com. Creality | Ender-3 V2 3D Printer. 2022; Available at: https://www.creality3dofficial.com/products/ender-3-v2-3d-printer?sca_ref=231380.E9tO9ibZex. Accessed 03/08, 2022.

[423] Prusa3d.com. Prusa Research | Original Prusa i3 MK3S+. 2022; Available at: https://www.prusa3d.com/category/original-prusa-i3-mk3s/#a_aid=3dsourced&a_cid=11111111&chan=code3. Accessed 03/08, 2022.

[424] ultimaker.com. Ultimaker S3: Easy-to-use 3D printing starts here. 2022; Available at: https://ultimaker.com/3d-printers/ultimaker-s3. Accessed 03/08, 2022.

[425] ultimaker.com. Ultimaker S5: Reliability at scale. 2022; Available at: https://ultimaker.com/3d-printers/ultimaker-s5. Accessed 03/08, 2022.

[426] Logan DL. A first course in the finite element method. : Cengage Learning; 2016.

[427] Reddy JN. Introduction to the finite element method. : McGraw-Hill Education; 2019.

[428] Wilkes JO. Fluid mechanics for chemical engineers: with microfluids, CFD, and COMSOL multiphysics 5. : Prentice Hall; 2017.

[429] Biolinscientific.com. Contact Angle Measurement . 2022; Available at: https://www.biolinscientific.com/measurements/contact-angle#what-is-contact-angle. Accessed 08/24, 2022.

[430] Ossila.com. Contact Angle Measurement, Theory & Relation to Surface Energy. 2022; Available at: https://www.ossila.com/pages/contact-angle-theory-measurement. Accessed 08/24, 2022.

[431] Polini A, Yang F. Physicochemical characterization of nanofiber composites. Nanofiber composites for biomedical applications: Elsevier; 2017. p. 97-115.

[432] Förch R, Schönherr H, Jenkins ATA. Surface design: applications in bioscience and nanotechnology. : John Wiley & Sons; 2009.

[433] Fowkes FM, Zisman WA. Contact angle, wettability, and adhesion. 1964.

[434] Nikola T. Valvular conduit 1920.

[435] Jensen KE. COMSOL Multiphysics - Performing a Shape and Topology Optimization of a Tesla Microvalve. 2019; Available at: https://uk.comsol.com/blogs/performing-a-shape-and-topology-optimization-of-a-tesla-microvalve/. Accessed 04/05/2020, 2020.

[436] Forster FK, Bardell RL, Afromowitz MA, Sharma NR, Blanchard A. Design, fabrication and testing of fixed-valve micro-pumps. ASME-PUBLICATIONS-FED 1995;234:39-44.

[437] Bardell RL. The diodicity mechanism of tesla-type no-moving-parts valves 2000.

[438] Kim J, Kang K, Jin Y, Goettert J, Ajmera PK. Hydrodynamic focusing micropump module with PDMS/nickel-particle composite diaphragms for microfluidic systems. Microsystem Technologies 2015;21(1):65-73.

[439] Anagnostopoulos J, Mathioulakis D. Numerical simulation and hydrodynamic design optimization of a tesla-type valve for micropumps. IASME Transactions 2005;2(9):1846-1852.

[440] Truong T, Nguyen N. Simulation and optimization of tesla valves. Nanotech 2003;1:178-181.

[441] De Vries S, Florea D, Homburg F, Frijns A. Design and operation of a Tesla-type valve for pulsating heat pipes. Int J Heat Mass Transfer 2017;105:1-11.

[442] Hancock MJ, Brown S. Micropump Mechanism. 2022; Available at: https://www.comsol.com/model/download/935841/models.mems.micropump_mechanism.pdf. Accessed 01/14, 2022.

[443] Mohammadi M, Sharp KV. The role of contact line (pinning) forces on bubble blockage in microchannels. Journal of Fluids Engineering 2015;137(3).

[444] Hirt CW, Nichols BD. Volume of fluid (VOF) method for the dynamics of free boundaries. Journal of computational physics 1981;39(1):201-225.

[445] Montanero JM, Ganán-Calvo AM. Dripping, jetting and tip streaming. Reports on Progress in Physics 2020;83(9):097001.

[446] Nielsen NJ. History of thinkjet printhead development. Hewlett Packard J 1985;36(5):4-10.

[447] Wijshoff H. The dynamics of the piezo inkjet printhead operation. Physics reports 2010;491(4-5):77-177.

[448] Kaltashov IA, Eyles SJ. Mass spectrometry in structural biology and biophysics: architecture, dynamics, and interaction of biomolecules. : John Wiley & Sons; 2012.

[449] Cloupeau M, Prunet-Foch B. Electrostatic spraying of liquids: Main functioning modes. J Electrostatics 1990;25(2):165-184.

[450] Main modes of electrohydrodynamic spraying of liquids. Third International Conference on multiphase Flow; 1998.

[451] Speranza A, Ghadiri M, Newman M, Osseo LS, Ferrari G. Electro-spraying of a highly conductive and viscous liquid. J Electrostatics 2001;51:494-501.

[452] Speranza A, Ghadiri M. Effect of electrostatic field on dripping of highly conductive and viscous liquids. Powder Technol 2003;135:361-366.

[453] Lee J, Cho H, Huh N, Ko C, Lee W, Jang Y, et al. Electrohydrodynamic (EHD) dispensing of nanoliter DNA droplets for microarrays. Biosensors and Bioelectronics 2006;21(12):2240-2247.

[454] Collins RT, Jones JJ, Harris MT, Basaran OA. Electrohydrodynamic tip streaming and emission of charged drops from liquid cones. Nature Physics 2008;4(2):149-154.

[455] Ouedraogo Y, Gjonaj E, Weiland T, De Gersem H, Steinhausen C, Lamanna G, et al. Electrohydrodynamic simulation of electrically controlled droplet generation. Int J Heat Fluid Flow 2017;64:120-128.

[456] Singh SK, Subramanian A. Phase-field simulations of electrohydrodynamic jetting for printing nano-to-microscopic constructs. Rsc Advances 2020;10(42):25022-25028.

[457] Chang K. Chapter 7 - Structural Analysis. In: Chang K, editor. e-Design Boston: Academic Press; 2015. p. 325-390.

[458] Young WC, Budynas RG, Sadegh AM. Roark's formulas for stress and strain. : McGraw-Hill Education; 2012.

[459] support.ultimaker.com. The Ultimaker 2+ specifications | Ultimaker Support. 2020; Available at: https://support.ultimaker.com/hc/en-us/articles/360011915779-The-Ultimaker-2-specifications. Accessed 01/16, 2022.

[460] 3D Systems.com. Plastic 3D Printers | 3D Systems. 2020; Available at: https://www.3dsystems.com/3d-printers/plastic. Accessed 01/16, 2022.

[461] Proto3000. Polyjet Desktop Systems - Product Information. 2022; Available at: https://proto3000.com/wp-content/uploads/2016/08/PolyJet-Desktop-Systems_Rev4.pdf. Accessed 01/17, 2022.

[462] Gale BK, Eddings MA, Sundberg SO, Hatch A, Kim J, Ho T, et al. Low-cost MEMS technologies. 2016.

[463] Qi HJ, Boyce MC. Stress–strain behavior of thermoplastic polyurethanes. Mech Mater 2005;37(8):817-839.

[464] Stratasys.com. Vero Clear: Rigid Transparent 3D Printing Material | Stratasys. 2022; Available at: https://www.stratasys.com/materials/search/veroclear. Accessed 01/16, 2022.

[465] 3dsystems.com. Accura® Xtreme™. 2020; Available at: https://www.3dsystems.com/sites/default/files/2020-11/3d-systems-accura-xtreme-datasheet-usen-2020-09-28-a-print.pdf. Accessed 01/16, 2022.

[466] COMSOL.com. Structural Mechanics Module | User's Guide. 2017; Available at: https://doc.comsol.com/5.3/doc/com.comsol.help.sme/StructuralMechanicsModuleUsersGuide.pdf. Accessed 08/25, 2022.

[467] Serth RW, Lestina T. Process heat transfer: Principles, applications and rules of thumb. : Academic press; 2014.

[468] Howell JR, Mengüç MP, Daun K, Siegel R. Thermal radiation heat transfer. : CRC press; 2020.

[469] SimScale.com. What Is Joule Heating? | SimWiki Documentation | SimScale. 2021; Available at: https://www.simscale.com/docs/simwiki/heat-transfer-thermal-analysis/what-is-joule-heating/. Accessed 01/21, 2022.

[470] Sinclair IR. Electronics for electricians and engineers. : Industrial Press Inc.; 1987.

[471] Engineering ToolBox. Polymers - Specific Heats. 2013; Available at: https://www.engineeringtoolbox.com/specific-heat-polymers-d_1862.html. Accessed 01/22, 2022.

[472] Kreith F, Bohn MS. Principles of heat transfer. 4th ed. London; New York: Harper & Row; 1986.

[473] Engineering ToolBox. Emissivity Coefficients common Products. 2003; Available at: https://www.engineeringtoolbox.com/emissivity-coefficients-d_447.html. Accessed 01/24, 2022.

[474] Dielectric Manufacturing. Material Properties of Thermoset Glass Epoxy - G10, FR4. 2019; Available at: https://dielectricmfg.com/knowledge-base/glass-epoxy/. Accessed 01/24, 2022.

[475] Lake JR, Heyde KC, Ruder WC. Low-cost feedback-controlled syringe pressure pumps for microfluidics applications. PLoS One 2017;12(4):e0175089.

[476] De Mello AJ, Habgood M, Lancaster NL, Welton T, Wootton RC. Precise temperature control in microfluidic devices using Joule heating of ionic liquids. Lab on a Chip 2004;4(5):417-419.

[477] Lao AI, Lee TM, Hsing I, Ip NY. Precise temperature control of microfluidic chamber for gas and liquid phase reactions. Sensors and Actuators A: Physical 2000;84(1-2):11-17.

[478] Mavraki E, Moschou D, Kokkoris G, Vourdas N, Chatzandroulis S, Tserepi A. A continuous flow µPCR device with integrated microheaters on a flexible polyimide substrate. Procedia Engineering 2011;25:1245-1248.

[479] Vigolo D, Rusconi R, Piazza R, Stone HA. A portable device for temperature control along microchannels. Lab on a Chip 2010;10(6):795-798.

[480] Kim Y, Kim S. An electro-conductive plane heating element for rapid thermal lysis of bacterial cells. J Microbiol Methods 2018;153:99-103.

[481] Guijt RM, Dodge A, Van Dedem GW, De Rooij NF, Verpoorte E. Chemical and physical processes for integrated temperature control in microfluidic devices. Lab on a Chip 2003;3(1):1-4.

[482] Maltezos G, Rajagopal A, Scherer A. Evaporative cooling in microfluidic channels. Appl Phys Lett 2006;89(7):074107.

[483] Ziabari A, Suhir E, Shakouri A. Minimizing thermally induced interfacial shearing stress in a thermoelectric module with low fractional area coverage. Microelectron J 2014;45(5):547-553.

[484] COMSOL.com. Heating Circuit. 2022; Available at: https://www.comsol.com/model/heating-circuit-465. Accessed 03/13, 2022.

[485] Wijnen B, Hunt EJ, Anzalone GC, Pearce JM. Open-source syringe pump library. PloS one 2014;9(9):e107216.

[486] Pearce JM, Wijnen B. Open-source syringe pump | Appropedia. 2016; Available at: https://www.appropedia.org/Open-source_syringe_pump. Accessed 02/08, 2022.

[487] Chemyx Inc. BD Plastic Syringe | Maximum & Minimum Flow Rates | Chemyx Inc. 2021; Available at: https://www.chemyx.com/support/knowledge-base/syringe-library/bd-plastic-syringe-minimum-maximum-flow-rates/. Accessed 07/14, 2021.

[488] Daerr A, Mogne A. Pendent_Drop: An ImageJ Plugin to Measure the Surface Tension from an Image of a Pendent Drop. 2016; Available at: https://github.com/adaerr/pendent-drop. Accessed 03/16, 2022.

[489] d'Ans J, Lax E. Taschenbuch für Chemiker und Physiker. : Springer-Verlag; 2013.

[490] allaboutcircuits.com. Temperature Coefficient of Resistance. 2022; Available at: https://www.allaboutcircuits.com/textbook/direct-current/chpt-12/temperature-coefficient-resistance/. Accessed 03/03, 2022.

[491] Young HD, Freedman RA, Ford AL. Sears and Zemansky's University Physics with Modern Physics 13th. 2015.

[492] Zucconi A. How to Build a Heater with Arduino - Part 2 - Alan Zucconi. 2016; Available at: https://www.alanzucconi.com/2016/08/02/arduino-heater-2/. Accessed 09/24, 2021.

[493] Sung JH, Shuler ML. Prevention of air bubble formation in a microfluidic perfusion cell culture system using a microscale bubble trap. Biomed Microdevices 2009;11(4):731-738.

[494] Lochovsky C, Yasotharan S, Günther A. Bubbles no more: in-plane trapping and removal of bubbles in microfluidic devices. Lab on a Chip 2012;12(3):595-601.

[495] Choi M, Na Y, Kim S. Hydrophilic strips for preventing air bubble formation in a microfluidic chamber. Electrophoresis 2015;36(23):2896-2901.

[496] Casquillas GV, Fu C, Le Berre M, Cramer J, Meance S, Plecis A, et al. Fast microfluidic temperature control for high resolution live cell imaging. Lab on a Chip 2011;11(3):484-489.

[497] Nanoliter liquid handling applications and challenges. International Workshop on Nanoliter Liquid Handling Technologies (sponsored by Zymark Corp., Hopkinton, MA). Opening presentation, May 2003; 2002.

[498] Bammesberger S, Ernst A, Losleben N, Tanguy L, Zengerle R, Koltay P. Quantitative characterization of non-contact microdispensing technologies for the sub-microliter range. Drug Discov Today 2013;18(9-10):435-446.

[499] Yusof A, Keegan H, Spillane CD, Sheils OM, Martin CM, O'Leary JJ, et al. Inkjet-like printing of single-cells. Lab on a Chip 2011;11(14):2447-2454.

[500] Ben-Tzvi P, Rone W. Microdroplet generation in gaseous and liquid environments. Microsystem technologies 2010;16(3):333-356.

[501] Boland T, Xu T, Damon B, Cui X. Application of inkjet printing to tissue engineering. Biotechnology Journal: Healthcare Nutrition Technology 2006;1(9):910-917.

[502] Gross A, Schöndube J, Niekrawitz S, Streule W, Riegger L, Zengerle R, et al. Single-cell printer: automated, on demand, and label free. Journal of laboratory Automation 2013;18(6):504-518.

[503] Shvets I, Makarov S, Franken C, Shvets A, Sweeney D, Osing J. Spot-on™ technology for low volume liquid handling. JALA: Journal of the Association for Laboratory Automation 2002;7(6):125-129.

[504] Liu Y, Chen L, Sun L. Design and fabrication of a MEMS flow sensor and its application in precise liquid dispensing. Sensors 2009;9(6):4138-4150.

[505] Astle TW. Small volume pipetting. JALA: Journal of the Association for Laboratory Automation 1998;3(3):62-64.

[506] Saunders RE, Gough JE, Derby B. Delivery of human fibroblast cells by piezoelectric drop-on-demand inkjet printing. Biomaterials 2008;29(2):193-203.

[507] Daerr A, Mogne A. Measuring liquid surface tension through the pendent drop method: Description of a measurement bench and an ImageJ Plugin. J.Open Res.Softw 2016;4(1):1-12.

[508] Ernst A, Streule W, Schmitt N, Zengerle R, Koltay P. A capacitive sensor for non-contact nanoliter droplet detection. Sensors and Actuators A: Physical 2009;153(1):57-63.

[509] Liu J, Geng Z, Fan Z, Liu J, Chen H. Point-of-Care Testing Based on Smartphone: the Current State-of-the-Art (2017–2018). Biosensors and Bioelectronics 2019.

[510] Gill P, Ghaemi A. Nucleic acid isothermal amplification technologies—a review. Nucleosides, Nucleotides and Nucleic Acids 2008;27(3):224-243.

[511] Guatelli JC, Whitfield KM, Kwoh DY, Barringer KJ, Richman DD, Gingeras TR. Isothermal, in vitro amplification of nucleic acids by a multienzyme reaction modeled after retroviral replication. Proc Natl Acad Sci U S A 1990 Mar;87(5):1874-1878.

[512] Zhang C, Xing D. Single-molecule DNA amplification and analysis using microfluidics. Chem Rev 2010;110(8):4910-4947.

[513] Zhao Y, Chen F, Li Q, Wang L, Fan C. Isothermal amplification of nucleic acids. Chem Rev 2015;115(22):12491-12545.

[514] Fakruddin M, Mazumdar RM, Chowdhury A, Mannan K. Nucleic acid sequence based amplification (NASBA)-prospects and applications. Int J Life Sci Pharma Res 2012;2:106.

[515] Zhao X, Dong T, Yang Z, Pires N, Høivik N. Compatible immuno-NASBA LOC device for quantitative detection of waterborne pathogens: design and validation. Lab on a Chip 2012;12(3):602-612.

[516] Reinholt SJ, Behrent A, Greene C, Kalfe A, Baeumner AJ. Isolation and Amplification of mRNA within a Simple Microfluidic Lab on a Chip. Anal Chem 2013;86(1):849-856.

[517] Chung SH, Baek C, Cong VT, Min J. The microfluidic chip module for the detection of murine norovirus in oysters using charge switchable micro-bead beating. Biosensors and Bioelectronics 2015;67:625-633.

[518] Li J, Macdonald J. Advances in isothermal amplification: novel strategies inspired by biological processes. Biosensors and Bioelectronics 2015;64:196-211.

[519] Obande GA, Banga Singh KK. Current and Future Perspectives on Isothermal Nucleic Acid Amplification Technologies for Diagnosing Infections. Infect Drug Resist 2020 Feb 12;13:455-483.

[520] Manojkumar R, Mrudula V. Applications of real-time reverse transcription polymerase chain reaction in clinical virology laboratories for the diagnosis of human diseases. Am J Infect Dis 2006;2:204-209.

[521] Fakruddin M, Mannan KS, Chowdhury A, Mazumdar RM, Hossain MN, Islam S, et al. Nucleic acid amplification: Alternative methods of polymerase chain reaction. J Pharm Bioallied Sci 2013 Oct;5(4):245-252.

[522] Oliveira BB, Veigas B, Baptista PV. Isothermal Amplification of Nucleic Acids: The Race for the Next “Gold Standard”. Frontiers in Sensors 2021:14.

[523] Zanoli LM, Spoto G. Isothermal amplification methods for the detection of nucleic acids in microfluidic devices. Biosensors 2012;3(1):18-43.

[524] Deiman B, van Aarle P, Sillekens P. Characteristics and applications of nucleic acid sequence-based amplification (NASBA). Mol Biotechnol 2002;20(2):163-179.

[525] Vandesompele J, Kubista M, Pfaffl M, Logan J, Edwards K, Saunders N. Real-time PCR: current technology and applications. Reference gene validation software for improved normalization 2009;2:47-64.

[526] Jiang X, Dong D, Bian L, Zou D, He X, Ao D, et al. Rapid detection of Candida albicans by polymerase spiral reaction assay in clinical blood samples. Frontiers in microbiology 2016;7:916.

[527] Gupta V, Chakravarti S, Chander V, Majumder S, Bhat SA, Gupta VK, et al. Polymerase spiral reaction (PSR): a novel, visual isothermal amplification method for detection of canine parvovirus 2 genomic DNA. Arch Virol 2017;162(7):1995-2001.

[528] Tang W, Chow WHA, Ying L, Kong H, Tang Y, Lemieux B. Nucleic acid assay system for tier II laboratories and moderately complex clinics to detect HIV in low-resource settings. J Infect Dis 2010;201(Supplement_1):S46-S51.

[529] Goldmeyer J, Kong H, Tang W. Development of a novel one-tube isothermal reverse transcription thermophilic helicase-dependent amplification platform for rapid RNA detection. The Journal of Molecular Diagnostics 2007;9(5):639-644.

[530] Mahalanabis M, Do J, ALMuayad H, Zhang JY, Klapperich CM. An integrated disposable device for DNA extraction and helicase dependent amplification. Biomed Microdevices 2010;12(2):353-359.

[531] An L, Tang W, Ranalli TA, Kim HJ, Wytiaz J, Kong H. Characterization of a thermostable UvrD helicase and its participation in helicase-dependent amplification. J Biol Chem 2005 Aug 12;280(32):28952-28958.

[532] Giuffrida MC, Spoto G. Integration of isothermal amplification methods in microfluidic devices: Recent advances. Biosensors and Bioelectronics 2017;90:174-186.

[533] Du X, Zhou T, Li P, Wang S. A rapid Salmonella detection method involving thermophilic helicase-dependent amplification and a lateral flow assay. Mol Cell Probes 2017;34:37-44.

[534] Kolm C, Martzy R, Führer M, Mach RL, Krska R, Baumgartner S, et al. Detection of a microbial source tracking marker by isothermal helicase-dependent amplification and a nucleic acid lateral-flow strip test. Scientific reports 2019;9(1):1-9.

[535] Tomlinson J, Dickinson M, Boonham N. Rapid detection of Phytophthora ramorum and P. kernoviae by two-minute DNA extraction followed by isothermal amplification and amplicon detection by generic lateral flow device. Phytopathology 2010;100(2):143-149.

[536] Maffert P, Reverchon S, Nasser W, Rozand C, Abaibou H. New nucleic acid testing devices to diagnose infectious diseases in resource-limited settings. European Journal of Clinical Microbiology & Infectious Diseases 2017;36(10):1717-1731.

[537] Barreda-García S, Miranda-Castro R, de-Los-Santos-Álvarez N, Miranda-Ordieres AJ, Lobo-Castañón MJ. Helicase-dependent isothermal amplification: a novel tool in the development of molecular-based analytical systems for rapid pathogen detection. Analytical and bioanalytical chemistry 2018;410(3):679-693.

[538] Banér J, Nilsson M, Mendel-Hartvig M, Landegren U. Signal amplification of padlock probes by rolling circle replication. Nucleic Acids Res 1998;26(22):5073-5078.

[539] Konry T, Smolina I, Yarmush JM, Irimia D, Yarmush ML. Ultrasensitive Detection of Low-Abundance Surface-Marker Protein Using Isothermal Rolling Circle Amplification in a Microfluidic Nanoliter Platform. Small 2011;7(3):395-400.

[540] Kühnemund M, Witters D, Nilsson M, Lammertyn J. Circle-to-circle amplification on a digital microfluidic chip for amplified single molecule detection. Lab on a Chip 2014;14(16):2983-2992.

[541] Nilsson M, Dahl F, Larsson C, Gullberg M, Stenberg J. Analyzing genes using closing and replicating circles. Trends Biotechnol 2006;24(2):83-88.

[542] Kuhn H, Demidov VV, Frank-Kamenetskii MD. Rolling-circle amplification under topological constraints. Nucleic Acids Res 2002;30(2):574-580.

[543] Ali MM, Li F, Zhang Z, Zhang K, Kang D, Ankrum JA, et al. Rolling circle amplification: a versatile tool for chemical biology, materials science and medicine. Chem Soc Rev 2014;43(10):3324-3341.

[544] De Paz HD, Brotons P, Muñoz-Almagro C. Molecular isothermal techniques for combating infectious diseases: towards low-cost point-of-care diagnostics. Expert review of molecular diagnostics 2014;14(7):827-843.

[545] Lu X, Li X, Mo Z, Jin F, Wang B, Zhao H, et al. Rapid identification of Chikungunya and Dengue virus by a real-time reverse transcription-loop-mediated isothermal amplification method. Am J Trop Med Hyg 2012 Nov;87(5):947-953.

[546] Feng T, Li S, Wang S, Pan J. Cross priming amplification with nucleic acid test strip analysis of mutton in meat mixtures. Food Chem 2018;245:641-645.

[547] Wang Y, Wang Y, Ma A, Li D, Ye C. Rapid and sensitive detection of Listeria monocytogenes by cross-priming amplification of lmo0733 gene. FEMS Microbiol Lett 2014;361(1):43-51.

[548] Yang Z, Liu W, Liang H, Wen R, Zhang Y. Development and evaluation of LAMP, CPA and IMSA methods for rapid detection of the AML1/ETO fusion gene in acute myeloid leukemia. Experimental and therapeutic medicine 2018;16(4):3353-3362.

[549] Fang R, Li X, Hu L, You Q, Li J, Wu J, et al. Cross-priming amplification for rapid detection of Mycobacterium tuberculosis in sputum specimens. J Clin Microbiol 2009;47(3):845-847.

[550] Daher RK, Stewart G, Boissinot M, Bergeron MG. Recombinase Polymerase Amplification for Diagnostic Applications. Clin Chem 2016 Jul;62(7):947-958.

[551] Lutz S, Weber P, Focke M, Faltin B, Hoffmann J, Müller C, et al. Microfluidic lab-on-a-foil for nucleic acid analysis based on isothermal recombinase polymerase amplification (RPA). Lab on a Chip 2010;10(7):887-893.

[552] Shen F, Davydova EK, Du W, Kreutz JE, Piepenburg O, Ismagilov RF. Digital isothermal quantification of nucleic acids via simultaneous chemical initiation of recombinase polymerase amplification reactions on SlipChip. Anal Chem 2011;83(9):3533-3540.

[553] Tsaloglou M, Watson R, Rushworth C, Zhao Y, Niu X, Sutton J, et al. Real-time microfluidic recombinase polymerase amplification for the toxin B gene of Clostridium difficile on a SlipChip platform. Analyst 2015;140(1):258-264.

[554] Schuler F, Schwemmer F, Trotter M, Wadle S, Zengerle R, von Stetten F, et al. Centrifugal step emulsification applied for absolute quantification of nucleic acids by digital droplet RPA. Lab on a Chip 2015;15(13):2759-2766.

[555] Li Z, Liu Y, Wei Q, Liu Y, Liu W, Zhang X, et al. Picoliter well Array Chip-based digital recombinase polymerase amplification for absolute quantification of nucleic acids. PloS one 2016;11(4):e0153359.

[556] Lobato IM, O'Sullivan CK. Recombinase polymerase amplification: Basics, applications and recent advances. Trac Trends in analytical chemistry 2018;98:19-35.

[557] James A, Macdonald J. Recombinase polymerase amplification: emergence as a critical molecular technology for rapid, low-resource diagnostics. Expert review of molecular diagnostics 2015;15(11):1475-1489.

[558] Kersting S, Rausch V, Bier FF, von Nickisch-Rosenegk M. Multiplex isothermal solid-phase recombinase polymerase amplification for the specific and fast DNA-based detection of three bacterial pathogens. Microchimica Acta 2014;181(13):1715-1723.

[559] Mayboroda O, Benito AG, Del Rio JS, Svobodova M, Julich S, Tomaso H, et al. Isothermal solid-phase amplification system for detection of Yersinia pestis. Analytical and bioanalytical chemistry 2016;408(3):671-676.

[560] Yamanaka ES, Tortajada-Genaro LA, Maquieira Á. Low-cost genotyping method based on allele-specific recombinase polymerase amplification and colorimetric microarray detection. Microchimica Acta 2017;184(5):1453-1462.

[561] Walker GT, Little MC, Nadeau JG, Shank DD. Isothermal in vitro amplification of DNA by a restriction enzyme/DNA polymerase system. Proc Natl Acad Sci U S A 1992 Jan 1;89(1):392-396.

[562] Toley BJ, Covelli I, Belousov Y, Ramachandran S, Kline E, Scarr N, et al. Isothermal strand displacement amplification (iSDA): a rapid and sensitive method of nucleic acid amplification for point-of-care diagnosis. Analyst 2015;140(22):7540-7549.

[563] Killick V, Kell P, Plumb H, Hurd N, Turner P. Screening for Neisseria gonorrhoeae using the BD ProbeTec nucleic acid amplification test in a low prevalence genitourinary medicine clinic. Int J STD AIDS 2012;23(6):e1-e3.

[564] Giuffrida MC, Zanoli LM, D'Agata R, Finotti A, Gambari R, Spoto G. Isothermal circular-strand-displacement polymerization of DNA and microRNA in digital microfluidic devices. Analytical and bioanalytical chemistry 2015;407(6):1533-1543.

[565] Loewy Z, Kumar R. Microfluidic method for nucleic acid amplification 1999.

[566] Chan EL, Brandt K, Olienus K, Antonishyn N, Horsman GB. Performance characteristics of the Becton Dickinson ProbeTec System for direct detection of Chlamydia trachomatis and Neisseria

gonorrhoeae in male and female urine specimens in comparison with the Roche Cobas System. Arch Pathol Lab Med 2000;124(11):1649-1652.

[567] Walker GT. Empirical aspects of strand displacement amplification. PCR Methods Appl 1993 Aug;3(1):1-6.

[568] Karami A, Gill P, Kalantar Motamedi M, Saghafinia M. A review of the current isothermal amplification techniques: applications, advantages and disadvantages. Journal of Global Infectious Diseases 2011;3(3):293-302.

[569] Seyrig G, Ahmad F, Stedtfeld RD, Tourlousse DM, Hashsham SA. Simple, Powerful, and Smart: Using LAMP for Low-cost Screening of Multiple Waterborne Pathogens. Environmental Microbiology: Current Technology and Water Applications 2011:103-125.

[570] Rane TD, Chen L, Zec HC, Wang T. Microfluidic continuous flow digital loop-mediated isothermal amplification (LAMP). Lab on a Chip 2015;15(3):776-782.

[571] Connelly JT, Rolland JP, Whitesides GM. “Paper machine” for molecular diagnostics. Anal Chem 2015;87(15):7595-7601.

[572] Ihira M, Sugiyama H, Enomoto Y, Higashimoto Y, Sugata K, Asano Y, et al. Direct detection of human herpesvirus 6 DNA in serum by variant specific loop-mediated isothermal amplification in hematopoietic stem cell transplant recipients. J Virol Methods 2010;167(1):103-106.

[573] Enomoto Y, Yoshikawa T, Ihira M, Akimoto S, Miyake F, Usui C, et al. Rapid diagnosis of herpes simplex virus infection by a loop-mediated isothermal amplification method. J Clin Microbiol 2005;43(2):951-955.

[574] Poon LL, Wong BW, Ma EH, Chan KH, Chow LM, Abeyewickreme W, et al. Sensitive and inexpensive molecular test for falciparum malaria: detecting Plasmodium falciparum DNA directly from heat-treated blood by loop-mediated isothermal amplification. Clin Chem 2006;52(2):303-306.

[575] Safavieh M, Kanakasabapathy MK, Tarlan F, Ahmed MU, Zourob M, Asghar W, et al. Emerging loop-mediated isothermal amplification-based microchip and microdevice technologies for nucleic acid detection. ACS biomaterials science & engineering 2016;2(3):278-294.

[576] Suzuki R, Ihira M, Enomoto Y, Yano H, Maruyama F, Emi N, et al. Heat denaturation increases the sensitivity of the cytomegalovirus loop-mediated isothermal amplification method. Microbiol Immunol 2010;54(8):466-470.

[577] Kaneko H, Kawana T, Fukushima E, Suzutani T. Tolerance of loop-mediated isothermal amplification to a culture medium and biological substances. J Biochem Biophys Methods 2007;70(3):499-501.

[578] Hara-Kudo Y, Yoshino M, Kojima T, Ikedo M. Loop-mediated isothermal amplification for the rapid detection of Salmonella. FEMS Microbiol Lett 2005;253(1):155-161.

[579] Ohtsuka K, Yanagawa K, Takatori K, Hara-Kudo Y. Detection of Salmonella enterica in naturally contaminated liquid eggs by loop-mediated isothermal amplification, and characterization of Salmonella isolates. Appl Environ Microbiol 2005;71(11):6730-6735.

[580] Kimura Y, de Hoon MJ, Aoki S, Ishizu Y, Kawai Y, Kogo Y, et al. Optimization of turn-back primers in isothermal amplification. Nucleic Acids Res 2011;39(9):e59-e59.

[581] Lee D, Kim EJ, Kilgore PE, Kim SA, Takahashi H, Ohnishi M, et al. Clinical evaluation of a loop-mediated isothermal amplification (LAMP) assay for rapid detection of Neisseria meningitidis in cerebrospinal fluid. PloS one 2015;10(4):e0122922.

[582] Wang Y, Liu D, Deng J, Wang Y, Xu J, Ye C. Loop-mediated isothermal amplification using self-avoiding molecular recognition systems and antarctic thermal sensitive uracil-DNA-glycosylase for detection of nucleic acid with prevention of carryover contamination. Anal Chim Acta 2017;996:74-87.

[583] Dhama K, Karthik K, Chakraborty S, Tiwari R, Kapoor S, Kumar A, et al. Loop-mediated isothermal amplification of DNA (LAMP): a new diagnostic tool lights the world of diagnosis of animal and human pathogens: a review. Pak J Biol Sci 2014 Jan 15;17(2):151-166.

[584] Wong Y, Othman S, Lau Y, Radu S, Chee H. Loop-mediated isothermal amplification (LAMP): a versatile technique for detection of micro-organisms. J Appl Microbiol 2018;124(3):626-643.

[585] Gao X, Sun B, Guan Y. Pullulan reduces the non-specific amplification of loop-mediated isothermal amplification (LAMP). Analytical and bioanalytical chemistry 2019;411(6):1211-1218.

[586] Notomi T, Mori Y, Tomita N, Kanda H. Loop-mediated isothermal amplification (LAMP): principle, features, and future prospects. Journal of microbiology 2015;53(1):1-5.

[587] Nagamine K, Hase T, Notomi T. Accelerated reaction by loop-mediated isothermal amplification using loop primers. Mol Cell Probes 2002;16(3):223-229.

[588] Müller R, Clegg D. Automatic paper chromatography. Anal Chem 1949;21(9):1123-1125.

[589] Koczula K, Gallotta A. assays Lflow. Lateral flow assays.Essays Biochem 2016;60:111-120.

[590] Chin CD, Linder V, Sia SK. Commercialization of microfluidic point-of-care diagnostic devices. Lab on a Chip 2012;12(12):2118-2134.

[591] Dinnes J, Deeks JJ, Adriano A, Berhane S, Davenport C, Dittrich S, et al. Rapid, point-of-care antigen and molecular-based tests for diagnosis of SARS-CoV-2 infection. Cochrane Database of Systematic Reviews 2020(8).

[592] HHS.gov. Coronavirus (COVID-19) Testing. 2020; Available at: https://www.hhs.gov/coronavirus/testing/index.html. Accessed 03/05, 2021.

[593] Okoye NC, Barker AP, Curtis K, Orlandi RR, Snavely EA, Wright C, et al. Performance Characteristics of BinaxNOW COVID-19 Antigen Card for Screening Asymptomatic Individuals in a University Setting. J Clin Microbiol 2021 Jan 28.

[594] BD Veritor. COVID-19 Rapid Antigen Testing | BD Veritor™ Plus System. 2021; Available at: https://bdveritor.bd.com/en-us/rapid-antigen-testing/covid-19. Accessed 02/12, 2021.

[595] Young S, Taylor SN, Cammarata CL, Varnado KG, Roger-Dalbert C, Montano A, et al. Clinical Evaluation of BD Veritor SARS-CoV-2 Point-of-Care Test Performance Compared to PCR-Based

Testing and versus the Sofia 2 SARS Antigen Point-of-Care Test. J Clin Microbiol 2020 Dec 17;59(1):10.1128/JCM.02338-20. Print 2020 Dec 17.

[596] Drain PK, Ampajwala M, Chappel C, Gvozden AB, Hoppers M, Wang M, et al. A Rapid, High-Sensitivity SARS-CoV-2 Nucleocapsid Immunoassay to Aid Diagnosis of Acute COVID-19 at the Point of Care: A Clinical Performance Study. Infectious Diseases and Therapy 2021;10(2):753-761.

[597] Lumiradx.com. The LumiraDx SARS-CoV-2 Ag Test is a rapid microfluidic immunoassay detecting SARS-CoV-2 antigen. 2021; Available at: https://www.lumiradx.com/uk-en/test-menu/antigen-test. Accessed 11/15, 2021.

[598] Lumiradx.com. The LumiraDx SARS-CoV-2 Ag Pool Test. 2021; Available at: https://www.lumiradx.com/uk-en/test-menu/ag-pool-test. Accessed 11/15, 2021.

[599] Lumiradx.com. The LumiraDx SARS-CoV-2 Ab Test is a rapid microfluidic immunoassay detecting SARS-CoV-2 total antibodies. 2021; Available at: https://www.lumiradx.com/uk-en/test-menu/antibody-test. Accessed 11/15, 2021.

[600] Lumiradx.com. Performance evaluation of the LumiraDx SARS-CoV-2 Antigen Test to aid diagnosis of acute COVID-19 at the point of care. 2021; Available at: https://www.lumiradx.com/uk-en/kc/learning-center/performance-evaluation-of-the-lumiradx-sars-cov-2-antigen-test. Accessed 11/15, 2021.

[601] Bioworld.com. Abbott launches rapid, portable antigen test, increasing COVID-19 testing capacity in France. 2020; Available at: https://www.bioworld.com/articles/497979-abbott-launches-rapid-portable-antigen-test-increasing-covid-19-testing-capacity-in-france. Accessed 03/08, 2021.

[602] Albert E, Torres I, Bueno F, Huntley D, Molla E, Fernández-Fuentes MÁ, et al. Field evaluation of a rapid antigen test (Panbio™ COVID-19 Ag Rapid Test Device) for COVID-19 diagnosis in primary healthcare centres. Clinical Microbiology and Infection 2020.

[603] Linares M, Pérez-Tanoira R, Carrero A, Romanyk J, Pérez-García F, Gómez-Herruz P, et al. Panbio antigen rapid test is reliable to diagnose SARS-CoV-2 infection in the first 7 days after the onset of symptoms. Journal of Clinical Virology 2020;133:104659.

[604] Bulilete O, Lorente P, Leiva A, Carandell E, Oliver A, Rojo E, et al. Evaluation of the Panbio rapid antigen test for SARS-CoV-2 in primary health care centers and test sites. medRxiv 2020.

[605] Quidel.com. Sofia SARS Antigen FIA Package Insert. 2021; Available at: https://www.quidel.com/sites/default/files/product/documents/EF1438906EN00.pdf. Accessed 11/15, 2021.

[606] Smith RD, Johnson JK, Clay C, Girio-Herrera L, Stevens D, Abraham M, et al. Clinical evaluation of Sofia Rapid Antigen Assay for detection of severe acute respiratory syndrome coronavirus 2 (SARS-CoV-2) among emergency department to hospital admissions. Infection Control & Hospital Epidemiology 2021:1-6.

8. Appendix

8.1. Appendix A – A Review of NAAT Techniques

8.1.1. Nucleic Acid Sequence-Based Amplification

Nucleic Acid Sequence-Based Amplification (NASBA), also known as Transcription Mediated Amplification (TMA) [510] and Self-Sustained Sequence Replication (3SR) [511], Is a process which mimics *in vivo* replications at 41 °C to produce 10^9-fold amplification from an RNA template in 90 min [512,513]. Unlike PCR, where the initial primer concentration limits the yield, the RNA obtained by NASBA overtakes the level of the primers by one order of magnitude [514]. Due to its low operational temperature, NASBA is well suited for POCT [185]. NASBA was designed in 1991 by Jean Compton [207] to detect bacterial or viral pathogens in food and to quantitatively analyse for microorganisms in water samples [515]. In 2013, Reinholt et al. integrated nucleic acid extraction and NASBA amplification into a microfluidic device; however, the sample was pre-lysed and detection was conducted off the chip following amplification [516]. In 2015, Chung et al. integrated lysis, RNA extraction, NASBA amplification and fluorescence detection into a microfluidic device [517]. This device assembled a set of 4 microfluidic chips onto an under plate and could amplify 24 RNA targets in parallel, detecting the norovirus from oysters within four hours.

NASBA is rapid, only requiring 4 to 5 cycles to achieve one million-fold amplification, without the requirement of specific instruments to facilitate the process [207,518]. NASBA is also less prone to contamination than PCR [519]; with a comparative study reporting that NASBA had a higher analytical sensitivity when compared to the performance of qRT-PCR on clinical samples [520]. NASBA is able to be multiplexed, allowing for the detection of multiple pathogens [521].

However, due to the use of 3 enzymes, the cost of the assay is increased [522]. NASBA is also limited to the amplification of single stranded RNA [207]. RNase-free conditions are also required to prevent degradation. In order to amplify DNA targets, an initial denaturation step is required [523], with reports also suggesting that two denaturation steps at 95 °C are required to amplify DNA [524]. Due to dsDNA denaturing at 95 °C, the process can become susceptible to non-specific amplification. Consequently, a thermal step of 65 °C is required to remove secondary structures from RNA targets [525]. It has also been reported that temperatures higher than 42 °C can affect the enzymes, compromising the process [519]. NASBA is also susceptible to false positives [522]. Thus, there are several challenged involved with integrating this technique into POCT devices [185].

8.1.2. Polymerase Spiral Reaction

Polymerase Spiral Reaction (PSR) is an isothermal amplification process, requiring a pair of primers and a single enzyme to initiate the reaction, using auto cycling strand displacement activity to achieve amplification [526]. The process is performed at a constant temperature between 61 – 65 °C, yielding 10^9 copies of the target within 45 min – 1 hour [208].

In 2015, Liu et al. amplified genomic DNA which was extracted from cultured *E. coli*, reporting a sensitivity of 6 CFU per 25µl reaction [208]. In 2016, Jiang *et al.* utilised PSR for the detection of *Candida albicans* in clinical blood samples, utilising both a real-time turbidimeter and a colour change in the presence of pH dye to confirm the presence of the target. The reported detection limit was 6.9 pg/µl [526]. In 2016, Gupta *et al.* modified this process into a method called Polymerase Cross Linking Spiral Reaction (PCLSR), to detect canine parvovirus 2 from clinical faecal samples. The samples were subjected to centrifugation and filtration, followed by snap freezing and further filtration to prepare the DNA for analysis. The detection limit was reported to be 5×10^{-6} ng [527].

The assay can be monitored in real-time either with a turbidimeter or a fluorescent dye, or with end point detection using gel electrophoresis or through a colorimetric change [208,526]. The process features a simple primer design, which does not require an initial DNA denaturation heating step to initiate [208]. In addition, the process may be performed without the use of complicated instruments, allowing it to be utilised for POCT in low-resource settings [208].

8.1.3. Helicase Dependant Amplification

Helicase-dependant amplification (HDA) uses a DNA helicase to simulate an *in vivo* DNA replication process, allowing for isothermal primer-based amplification of kilo-base long templates, achieving up to 10^6-fold amplification [528]. HDA takes advantage of the fact that DNA replication is not limited to the length of the target DNA template unlike PCR [206]. HDA has been combined with reverse transcription (RT) to amplify RNA [529] and later integrated into a disposable microfluidic device [530]. Zhang and Xing designed a droplet microfluidic platform using silica superparamagnetic particles (SSPs) to conduct DNA extraction, isothermal HDA and detection into one device [512]. Reagents were stored in droplets in the device and were mixed with the sample using the SSPs. Using this device, Zhang and Xing detected ovarian cancer biomarker Rsf-1 from whole blood samples and *E. coli* from raw samples.

HDA retains many of the advantages that is offered by PCR, while improving overall efficiency and reducing the number of sample preparation steps [531]. Once such advantage is its low operating temperature (between 37 – 60 °C), allowing for easy integration into POCT systems. By utilising a helicase enzyme to denature the dsDNA, the heat cycling process that is characteristic of PCR can be omitted, allowing for the process to be performed without the use of complex and expensive equipment [206]. However, previous works in the field have concluded that the sensitivity of HDA may be increased 10-fold if a two-step thermal treatment process is introduced, performing denaturation and annealing at 95 °C and (65 °C), respectively [532]. HDA has been utilised to detect pathogenic DNA in human blood samples, demonstrating its ability to deal with crude samples [206]. Following amplification, the HDA products can be monitored using low cost LFDs, allowing for use in low-resource settings [530,533-535]. However, common challenges to HDA include its susceptibility to contamination and the risk of the formation of primer dimers, leading to non-specific amplification and false positives [206,536]. Furthermore, HDA is also considered difficult to multiplex [537].

8.1.4. Rolling Circle Amplification

Rolling Circle Amplification (RCA) may be used to generate a long single-stranded DNA of a repetitive sequence [209]. The operating temperature is relatively low (37 °C) and can achieve 10^3-fold amplification in one hour [538]. RCA is highly accurate and specific, able to handle both cell-based and tissue-based assays while resisting contamination and amplification errors. Furthermore, due to being simple and efficient, it is well suited miniaturisation and integration into high throughput configurations [204].

A portable microfluidic device for colorimetric detection of thrombin from human plasma and serum was developed by Lin et al., which had a LOD of 0.083 pg/ml. [211]. RCA amplification was also applied in different droplet-based configurations, particularly by Konry *et al.* [539] and Kühnemund *et al.* [540]. This droplet-based approach allowed for exponential RCA amplification to be conducted, allowing for the detection of *Pseudomonas aeruginosa* DNA at 1 aM level [540].

RCA is considered to be simple and robust in comparison to other nucleic acid amplification techniques [209,541]. Unlike PCR, RCA is resistant to errors caused by contamination and requires little to no assay optimisation, able to be multiplexed for increased detection capabilities. RCA may per performed on samples within a solid phase or in solution, increasing the number of configurations the technology may be applied to [521]. Primers used for PCR amplification can also be used for RCA, meaning existing and commercially available primers may be utilised [518]. When considered

alongside its low operating temperature, RCA becomes a technique well-suited to POCT [532]. Despite the promising nature of this technique, RCA requires an initial heat denaturation step [510]. RCA can also prove challenging for shorter DNA templates, due to a limited number of binding sites available for the enzymes [542]. While it is possible to utilise general primers and oligonucleotides, it should be noted that these universal primers and oligonucleotides can lead to primer dimers, resulting in false positives [192]. RCA products are not only susceptible to the formation of primer dimers during amplification, but can also be susceptible to non-specific cross linking within and between component molecules during storage, making mass production of products difficult [543]. It is also to be noted that there are no commercially available RCA-based diagnostic kits [544].

8.1.5. Cross Priming Amplification

Cross Priming Amplification (CPA) is an isothermal amplification process that does not require an initial denaturation step, or the addition of a nicking enzyme [205]. The reaction occurs at 63 °C and can be used to amplify DNA or RNA templates in 1 hour, which can be detected using either a LFD test strip, fluorescence, turbidity or using gel electrophoresis [545-547]. The CPA process uses 5 primers, including one or more cross primers. The use of a single cross primer results in single CPA (S-CPA), while the use of two cross primers results in double CPA (D-CPA) [205].

The exclusion of the nicking primers in addition to not requiring an initial DNA denaturation step allows for the simpler and more flexible assay to be developed for low-resource settings [548,549]. It is to be noted that the mechanism of S-CPA did not yield high amplification products, producing around 10^4 copies [205]. Furthermore, a major drawback is the complicated sample processing methods required for complex samples [549].

8.1.6. Recombinase Polymerase Amplification

Recombinase Polymerase Amplification (RPA) is an amplification approach devised in 2006 by Piepenburg et al., which uses a DNA polymerase, recombinase and DNA-binding proteins at a constant temperature between 37 – 42 °C to amplify DNA, using a fluorescent probe to monitor the recombinase process [210]. RPA is rapid, yielding results within 5 – 20 minutes [550].

RPA was integrated into centrifugal microfluidic device by Lutz et al. in 2010, detecting *Staphylococcus aureus* from pre-treated samples with an LOD of 10 copies [551]. In 2014, Kim *et al.* used a laser diode

to control valve actuation, cell lysis, and heat the microfluidic chip, allowing for the integration of extraction, isothermal RPA and detection into a centrifugal microfluidic device. The device was used to test milk samples for *Salmonella* concentration and has a LOD of 100 CFU/ml [380].

In 2011, the SlipChip was designed by Shen *et al.* to test for MRSA using Digital RPA [552]. This technique was later revised by Tsaloglou *et al.* in 2015 to detect *Clostridium difficile* toxin B [553]. This method allows for various RPA reagents to be stored in separate compartments. When the plates of the SlipChip are moved, the DNA solution can interact with the various reagents, allowing for multiple reactions to be run in parallel. The LOD for this method was in the range of a few hundred copies, per ml of sample. In 2015, Schuler *et al.* used centrifugal emulsification to form uniform droplets, which was then subjected to digital droplet RPA [554]. This successfully allowed for the detection of *Listeria monocytogenes* in foods. In 2016, Li *et al.* designed a chip-based picolitre well array, which allowed for the sample DNA and reagents to be compartmentalised in sized reaction wells, where RPA amplification would allow for the detection of *L. monocytogenes* [555]. Like other digital detection methods, this method offers a quantitative result using fluorescence analysis. These digital RPA methods require approximately 30 minutes to achieve detection, making the processing time shorter than ddPCR [185].

RPA meets many of the needs of isothermal amplification methods, using simple to design assays with unmodified oligonucleotides to achieve rapid amplification at a low operating temperature [192]. As the recombinase enzymes facilitate the separation of the double stranded DNA, thermal denaturation is not required [210]. RPA can amplify targets up to 1.5 kilobases in length; however, targets with a range of 100 – 200 base pairs are preferable [556]. RPA can be performed either in solution or in a solid phase [550,557]. While the performance of RPA in a solid phase offers advantages in in multiplexing capabilities, the impeded dilution of primers and reaction reagents can result in a lower LOD, when compared to solution phase alternatives [556]. RPA is a relatively new amplification process, and thus, little scientific literature is available [518]. RPA kits are only sold by a single company, which can impact pricing based on demand. Currently, there is no software available for the development of RPA primers, which can make the process a matter of “trail and error” [556]. This can be particularly challenging for multiplexing, where optimised primer concentrations are required, based on target sequences, amplicon size and primer design [558]. However, RPA has been reported to be compatible with PCR primers, with reports of efficient amplification [559,560]. Finally, despite RPA being reported to be resistant to less purified samples, high concentrations of genomic DNA can inhibit the process, as well as the presence of proteins in RPA products, which can cause smearing during end point detection techniques such as LFDs or gel electrophoresis [556].

8.1.7. Strand Displacement Amplification

Strand Displacement Amplification (SDA) is an amplification process designed to operate at 37 °C, achieving linear 10^7-fold amplification in less than 2 hours [561]. This method can also be configured for exponential amplification at 49 °C, achieving 10^9-fold amplification in less than 20 minutes [562]. The process uses a primer to trigger a continuous cycle of nicking, extension and strand displacement steps, with additional enzymes added to accelerate the amplification process [532]. The amplification method has been employed in commercially available equipment for the detection of *Chlamydia trachomatis* and *Neisseria gonorrhoeae* in urine [563]. This allowed for isothermal circular strand-displacement polymerisation (ICSDP) reactions to take place, which increases the stability of the process and allows for the easier detection of specific target sequences [532]. ICSDP may also be implemented into droplet microfluidic devices, allowing for nucleic acid amplification at a temperature of 37 °C [564].

SDA can operate at a single temperature, allowing for thermocycling equipment to be circumvented. However, SDA requires an initial heat denaturation step at 95 °C [510]. However, a drawback to this method is the requirement of an initial thermal step at 95 °C, which increases the power requirements [565]. The process is also unable to amplify long target sequences [566], typically restricted to below 50 – 120 base pairs [518,567]. The low operating temperature of the process introduces the possibility of non-specific primer binding during the reaction, resulting in non-specific amplification [568]. As a result, SDA is considered to be difficult to multiplex [521]. When compared to other isothermal amplification techniques, SDA can take up to 2 hours to achieve detection, making it ill-suited for POCT applications. SDA is also only able to produce semi-quantitative results, limiting its applications [521].

8.1.8. Loop-Mediated Isothermal Amplification

Loop-Mediated Isothermal Amplification (LAMP) is an isothermal NAAT method which uses 4 – 6 target-specific primers, including a forward inner primer (FIP), a backward inner primer (BIP) and 2 outer primers, to amplify a target DNA sequence. The reaction occurs between 60 – 65 °C can produce up to 10^9 copies in less than 2 hours, yielding 50-fold more amplicons than PCR based techniques [569]. In a similar approach to digital droplet PCR (ddPCR), LAMP can be integrated into microfluidic technology, as demonstrated by in 2015 by Rane et al., who utilised droplet generation to yield sample with an volume of 10 pL. Through a combination of LAMP amplification 63 °C within 5 uL wells and fluorescence detection, *N. gonorrhoeae* was detected with a LOD of 600 DNA copies per µl [570]. The ability to combine LAMP with paper microfluidics was also demonstrated by Connelly, Rolland and

Whitesides, who developed a device with which could detect *E. coli* from human plasma samples with a LOD of 1 cell per 16 µl [571]. The device featured a multilayer structure and sliding technology, allowing different reagents to be introduced into the sample solution, while preventing evaporation during incubation. Following amplification, an ultraviolet light source was used to detect a colour change.

Due to the relatively number of primers used, LAMP is highly specific [185]. LAMP is also amplify medium to long range template strands, between 130 and 500 base pairs, making it suitable to a large variety of pathogens [212]. Another advantage to LAMP is its robustness, with many examples of the process being applied to samples with little to no sample treatment, including serum [572], swabs [573] and blood [574]. In light of the aforementioned, LAMP may be utilised where PCR may be insufficient and attributes itself well to POCT devices [575]. LAMP can be performed without expensive equipment and entails fewer and simpler sample preparation steps in comparison to traditional PCR [521]. While LAMP techniques can utilise an initial heating step of 95 °C, it is not required to achieve amplification. However, this process is typically included to encourage stand separation and increase sensitivity, which increases power consumption [576]. A study by Kaneko *et al.* has reported a high tolerance of inhibitors in samples, demonstrating the robustness of LAMP [577], which other studies have reported a higher sensitivity compared to traditional PCR [578,579].

There are several challenges involved with the use of LAMP techniques. One such challenge is the multiple complex primers required for LAMP to function [580]. These additional primers are typically more complex in design when compared with PCR based primers [581]. Despite their intended function, these additional primers may also result in non-specific amplification as a result of non-specific binding [582]. Furthermore, these additional primers make LAMP difficult to multiplex, due to the challenges involving target selection and primer design [583,584]. However, recent works by Goa *et al.* have included polysaccharide polymers (pullulan) in reactions to prevent non-specific amplification in LAMP reactions [585]. In summary, LAMP is ideal for use in low-resource settings, being suggested to be the ideal isothermal NAAT method for diagnostics by the WHO [584]. Complex samples with a variety of nucleic acids require very specific primer configuration to avoid non-specific amplification. Methods such as LAMP, include additional primers can improve the specificity, making the amplification process more resistant to inhibitors when compared to PCR, meaning less sample preparation steps are needed [586,587].

8.2. Appendix B. State-of-the-Art for SARS-CoV-2 Assays – Serological Assays

8.2.1. Introduction

The groundwork of POCT devices began with serological lateral flow assays, in which a single-use paper or membrane strip is used to detect the presence of specific protein antigens found on or within the virus. Such devices were first introduced by Muller and Clegg in 1949 [588]. These devices typically consist of 4 main components: a sample pad, a conjugate pad, a detection zone and an absorption pad [589]. The biological sample is absorbed into the sample pad, which is then wicked along length of the test strip to using capillary action. The sample is then labelled at the conjugate pad, where elements recognising specific elements of the pathogen of interest bind to the sample. The sample will then continue to wick along the test strip to the detection zone, where an interaction between the sample and the targeted analytes sequence occurs, resulting in a visual colour change [590]. Several detection zones may be included on a single test strip; however, the most common are control lines to ensure that the sample is both sufficient and has run correctly, as well as a test line to determine whether the sample is present. Finally, the absorption pad is used to absorb excess liquid and prevent backflow [589].

Serological POCT devices may also be used to detect the presence of antibodies within the patient which are produced following infected by the target pathogen. The two main types of antibodies detected are IgM and IgG antibodies. IgM antibodies are the first types of antibodies produced following infection and are targeted to determine recent infections, while, IgG antibodies are developed after IgM antibodies and remain detectable within the patient for several months following their initial production. As a result, IgM antibodies are a favourable option for antibody testing [234]. Another notable application of serological assays are blood glucose tests, in which a redox enzyme is utilised following wicking to amplify a signal, which can be read using electrochemical detection. However; due to the high concentration of glucose found within the blood sample as well as the frequency of which the test is conducted, this can be considered to be unique when compared with other serological tests [590].

These tests are designed for fast and cost-effective viral detection in comparison to alternate molecular methods, with results being obtainable within as little as 15 minutes [22]. A trade-off however is the lower sensitivity, meaning that while positive results are often accurate, there is a higher chance of false negatives, creating a false confidence in the results [234,249]. On average, a sensitivity and specificity of 56.2% and 99.5% have been reported, respectively, in comparison with NAAT tests [591]. For this reason, molecular tests are often favoured for SARS-CoV-2 infections, with

antibody tests used in either emergency cases [74], or for symptomatic patients [22]. LFDs are typically unable to detect analytes at low concentrations without additional instrumentation to specifically target signals, which increases the complexity of the device. It has been reported that concentrations of the analyte must be higher than 10 copies/µl to be detectable by an LFD, which can take up to five days following infection to achieve [22]. Furthermore, the tests are incapable of providing quantifiable results, which further constrains diagnostic capabilities, particularly in the testing of NAAT, where POCT devices are scarcely reach commercial viability [590].

One of the major advantages to lateral flow –that being capillary action– can also contribute to one of the major drawbacks to the approach. As capillary flow is a single flow action which cannot be paused once the process has begun, the integration of necessary subsidiary procedures in order to accurate mimic laboratory-based assays can prove to be difficult. This consequently limits the reproducibility results. While fluid controls can be incorporated into lateral flow technology, this add to the increases the complexity of the device [590]. Despite this however, this method is still an accepted approach towards pregnancy and HIV testing across the developing world.

8.2.2. Abbott BinaxNOW™ Covid-19 Antigen Card

Abbott laboratories have developed the BinaxNow™ Covid-19 Antigen card, an LFD immunoassay allowing for qualitative detection of SARS-CoV-2 by targeting nucleocapsid antigens from direct nasal swabs [592]. While initially intended for use in symptomatic individuals, the antigen card's relatively low cost ($5 per card) allows for it to be used as an alternative to more expensive methodologies. In addition, the antigen card provides visually interpretable results after 15 minutes, producing two pink or purple coloured lines, representing the targeted antigen plus a control [593]. A comparative test between the performance of the BinaxNOW Covid-19 Antigen Card and the TaqPath RT-PCR assay was conducted. It was reported that the BinaxNow identified 24 infections, but missed 21 infections that were detected by the TaqPath kit. A positive percent agreement of 53.3% and negative percent agreement of 100% was also reported. However, for cases with a high viral load, a 95.8% positive agreement was observed [593].

8.2.3. BD Veritor system for Sars-CoV-2

Becton, Dickinson and Company have developed a rapid antigen point-of-care device for the testing of SARS-CoV-2, Flu A+B, Group A Strep and RSV in nasal swab samples. The device features a single button functionality and is able to detect nucleoproteins from SARS-CoV-2 within 15 minutes [594]. A clinical evaluation conducted by Young et al. reported the BD Veritor system had PPA, NPA and OPA values of 97.4, 98.1 and 98.1%, respectively, with an 87.5% positive percent agreement within day 1 of the onset of symptoms [595]. A full tabulation of these results can be seen in Figure B.1.

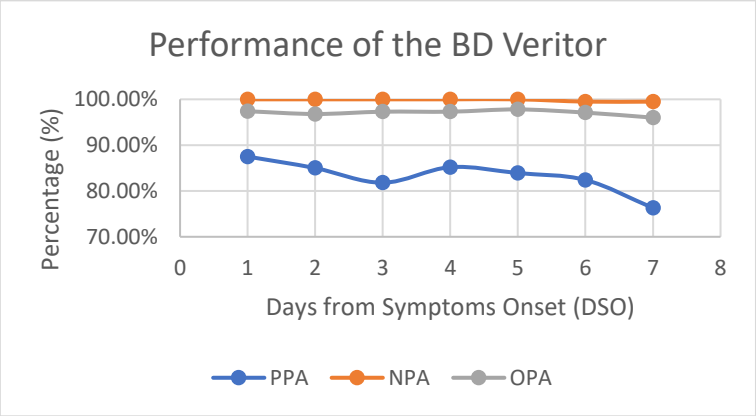

Figure B.1 – BD Veritor Test Performance at 1 through 7 Days from Symptom Onset [595]
PPA, Positive Percent Agreement; NPA, Negative Percent Agreement; OPA, Overall Percent Agreement

8.2.4. LumiraDx Sars-CoV-2 Ag/Ag Pool and Ab Tests

The LumiraDx SARS-CoV-2 Ag test is an immunoassay test, performed on single-use, microfluidic test trips, to detect the nucleocapsid protein in a test sample using fluorescent detection from anterior nares or NP swab samples [596]. The test is rapid, yielding results within 12 minutes [597]. Alternatively, the LumiraDx SARS-CoV-2 Ag Pool test may be used, to pool 5 separate samples onto a single test strip, reducing the cost of resources needed per patient basis [598]. A recent development is the LumiraDx SARS-CoV-2 Ab Test, which detects SARS-CoV-2 antibodies from human whole blood, plasma or serum samples, with results being available in 11 minutes [599]. Each test strip is inserted into the LumiraDx Platform, which is light weight (1.1 kg) and can be powered either using a rechargeable battery or mains electricity, favourable attributes for POCT use [597].

Several studies have been conducted to determine the performance of the LumiraDx Sars-CoV-2 antigen tests. A comparison between the performance of anterior nares and NP swab samples reported a 97.6% and 97.5% positive percent agreement, respectively and a 96.6% and 97.7% negative

percent agreement, respectively, when compared with RT-PCR conducted on a Roche Cobas 6800 platform [597]. A similar study, comparing the performance of the LumiraDx SARS-CoV-2 antigen against RT-PCR conducted on a Roche Cobas 6800 platform, reported a sensitivity of 97.6%, specificity of 96.6%, a positive predictive value of 93.1% and a negative predictive value of 98.8% [600]. Clinical studies for the LumiraDx SARS-CoV-2 antigen pool test demonstrated a positive and negative percent agreement of 100% and 96.6%, respectively [598]. Finally, a comparison of the LumiraDx SARS-CoV-2 Ab Test to RT-PCR reported a 100% positive and percent agreement agreement [599].

8.2.5. Panbio™ COVID-19 Ag Rapid Test Device

Abbott diagnostics developed the Panbio™COVID-19 Ag Rapid Test Device, able to detect SARS-CoV-2 from NP swabs within 15 minutes. The test is approximately credit card sized and uses lateral flow technology, allowing for tests to be conducted without the use of external equipment. Similar to other antigen-based tests discussed, the major benefit to this test is the low cost, costing just $5 per test [601]. A major drawback however is the low sensitivity of the tests when compared with PCR-based assays, with reported results of 41.8% by Torres *et al.* [602], 73.3% by Linares *et al.* [603] and 71.4 by Bulilete *et al.* [604]. These discrepancies may be attributed to conducting the tests on symptomatic and asymptomatic individuals, as well as the time of which the test is taken following exposure [603].

8.2.6. Quidel Sofia SARS antigen FIA

Quidel developed the Sofia SARS antigen FIA test, a lateral flow immunofluorescent assay intended for qualitative detection of the nucleocapsid protein antigen from SARS-CoV-2 from anterior nares swab specimens. The test is performed within single use cartridges, which are intended for use in conjunction with the Sofia, Sofia 2 and Sofia Q instruments. These instruments measure the fluorescent response and display the results within 15 minutes [605]. Clinical performance of the Sofia SARS antigen FIA test against RT-PCR was conducted, with results of a positive and negative percent agreement of 96.7% and 100-%, respectively; as well as a positive and negative predictive value of 100% and 99.4%, respectively [605]. Another study conducted by Smith *et al.* reported an overall percentage agreement, sensitivity and specificity between the antigen and RT-PCR tests of 97.9%, 76.6% and 99.7%, respectively [606]. It was also reported that the Sofia SARS rapid FIA test had a TAT of 1.2 hours, in comparison to RT-PCR, which had a TAT of 20.1 hours.

Table B.1 – State-of-the-Art diagnostic assays for SARS-CoV-2 (Serological)
LF, Lateral Flow; ANS, Anterior nares swabs; BAL, Bronchoalveolar lavage; MTNS, mid-turbinate nasal swab; NA, nasal aspirates; NS, nasal swab; NPS, nasopharyngeal swab; OS, oropharyngeal swab; TS, throat swab

Assay Name	Manufacturer	Technology	Sample Source	Compatible Instrument(s)	TAT	Hands-on time	Portable?	Ref
CDC 2019- Novel Coronavirus Real-Time RT-PCR Diagnostic Panel		real-time RT-PCR	1. NPS or OS 2. BAL fluid 3. Tracheal aspirates 4. Sputum	5. Applied Biosystems 7500 Fast Dx Real-Time PCR Instrument	36 min (Fast) <2 h (Standard)		N	[247]
BinaxNow™ Covid-19 Antigen card	Abbott Laboratories	LF immunoassay	6. NS	7. n/a	15 min	< 2 min	Y	[593]
BD Veritor system for Sars-CoV-2	BD	LF chromatographic immunoassay	8. NS	9. BD Veritor Plus Analyzer	15 min	< 2 min	N	[594]
LumiraDx Sars-CoV-2 Ag/Ag Pool	LumiraDx	LF fluorescent immunoassay	10. ANS, NPS	11. LumiraDx Platform	12 min	< 2 min	Y	[597,598]
LumiraDx Sars-CoV-2 Ab	LumiraDx	LF fluorescent immunoassay	12. human whole blood, plasma or serum	13. LumiraDx Platform	11 min	< 2 min	Y	[599]
Panbio™COVID-19 Ag Rapid Test	Abbott Diagnostics	LF immunoassay	14. NPS	15. n/a	15 min	< 2 min	Y	[601]
Sofia SARS antigen FIA test	Quidel Corporation	LF fluorescent immunoassay	16. ANS	17. Sofia, Sofia 2 and Sofia Q	15 min	< 2 min	N	[605]

8.3. Appendix C. Individual Tesla Valve – Velocity and Pressure Results

8.3.1. Tesla Valve Design Methodology

A starting point (A) was selected and the line AB was drawn, at a length of **L1** and an angle of alpha from the x-axis. From point B, a circle was drawn, with a radius of **R1**, at a tangent to the line AB. The origin point of the circle (O) was then recorded. A horizontal line connected point A to a point on the circle (C) and all other lines were removed from the geometry, leaving the polyline ABC, which would form the inner wall for the valve. From the point O, a circle with a radius of **R2** (**R1** + **W**) was drawn and a concentric constraint was used to ensure its concentricity with the arc on the polyline ABC. The remaining geometry lines were then drawn at an offset of W from the original polyline and entrance and exit channels were drawn. The exit channel was drawn at a length of **L3** and an angle of **beta1** from the x-axis. The exit channel was drawn at a length of **L4**. This model was then adapted to create the valves T45c, TMW and GMF type valves. The dimensions used for this analysis can be seen in Table C.1, with the corresponding valves shown in Figure C.1 – Figure C.5. The performance of each of the Tesla valves for forward and reverse flow conditions can be seen in Figure C.6 – Figure C.45

Table C.1 – Dimensions for Tesla Valves

		Units	T45A	T45C	TMW	GMF	D
W	**Channel Width**	mm	0.5	0.5	0.5	0.5	0.5
L1	**Straight Segment Entrance Length**	mm	2	3	4.5	3	n/a
L2	**Straight Segment Exit Length**	mm	n/a	n/a	n/a	1.2	n/a
L3	**Outlet Length**	mm	1	1	1	1	1
L4	**Inlet Length**	mm	1	1	1	1	1
R1	**Inner Curve Radius**	mm	2.5	1.5	1.5	1.5	1.5
R2	**Outer Curve Radius**	mm	3	2	2	2	2
alpha	**Outlet Channel Angle**	Deg	45	45	0	60	0
beta1	**Straight Segment Entrance Angle**	Deg	45	45	30	60	55.7
beta2	**Straight Segment Exit Angle**	Deg	n/a	n/a	n/a	54.5	53.8

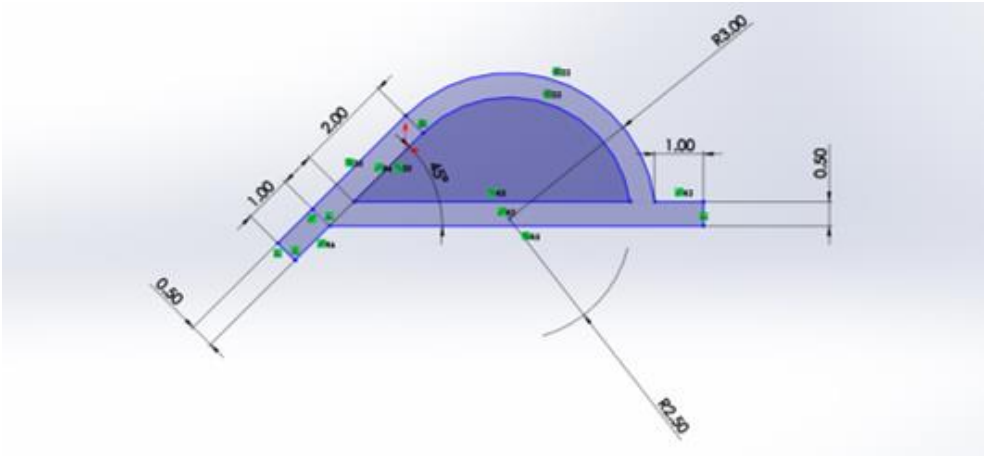

Figure C.1 – Tesla Valve T45a-type

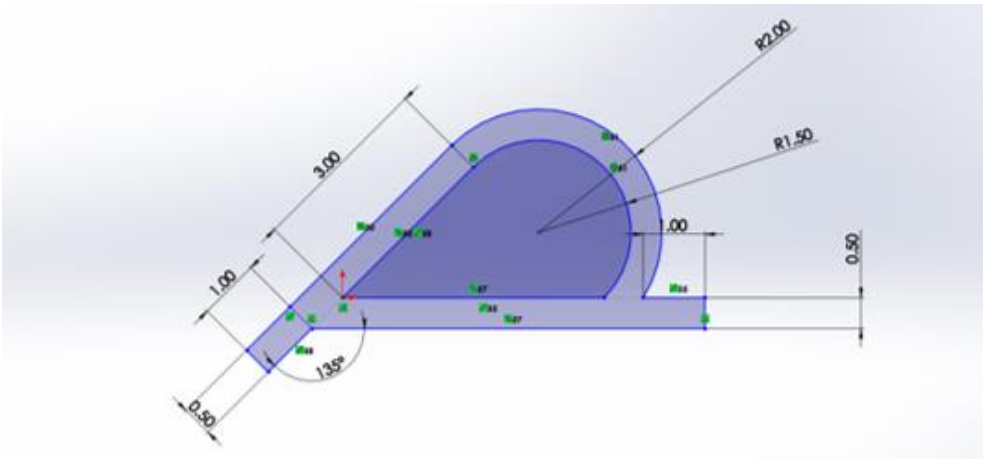

Figure C.2 – Tesla Valve T45c-type

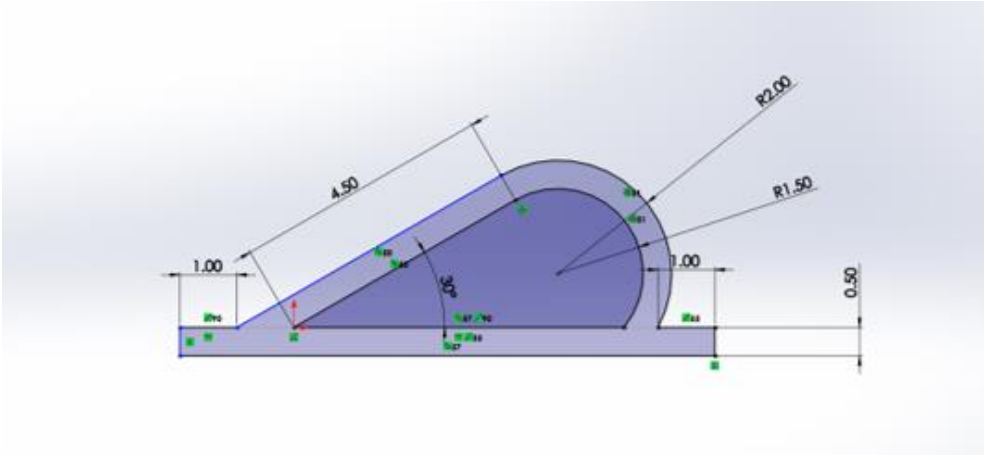

Figure C.3 – Tesla Valve TMW-type

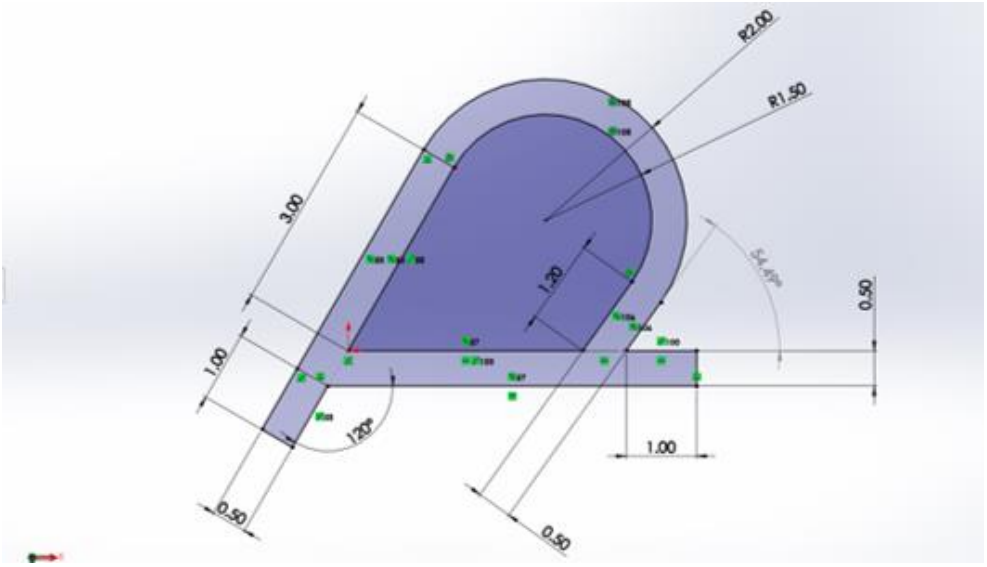

Figure C.4 – Tesla Valve GMF-type

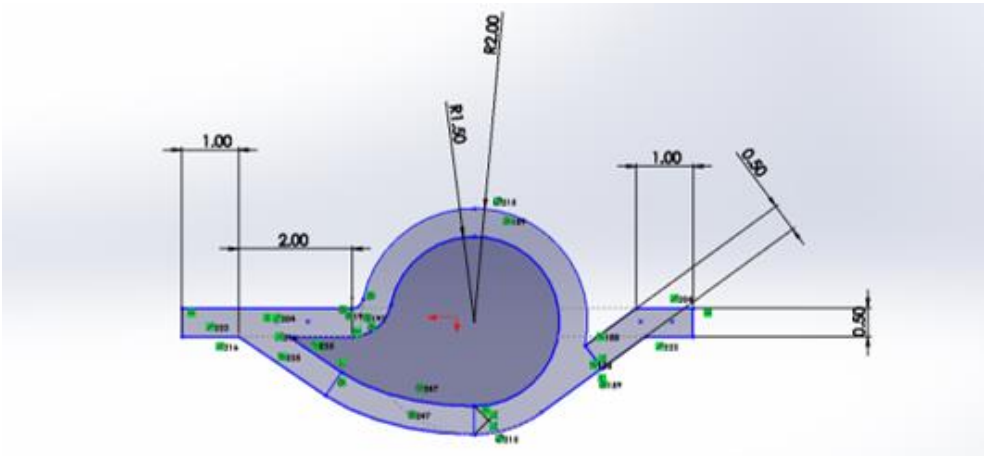

Figure C.5 – Tesla Valve D-type

8.3.2. T45a-type Tesla Valve Results

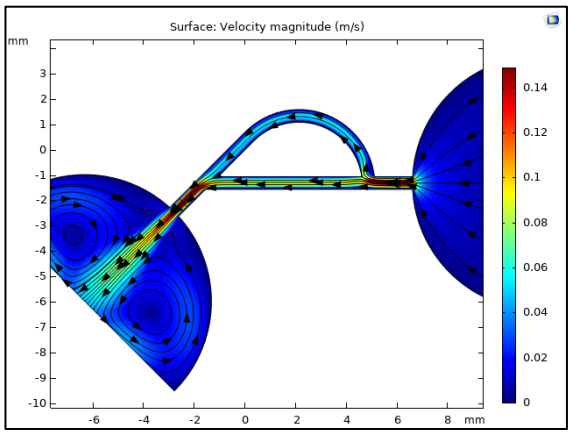

Figure C.6 – Velocity Profile for Tesla Valve T45a, Forward Flow (inflow velocity = 0.005 m/s)

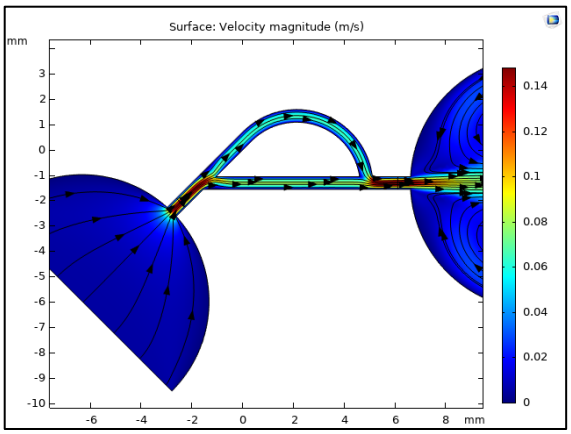

Figure C.7 – Velocity Profile for Tesla Valve T45a, Reverse Flow (inflow velocity = 0.005 m/s)

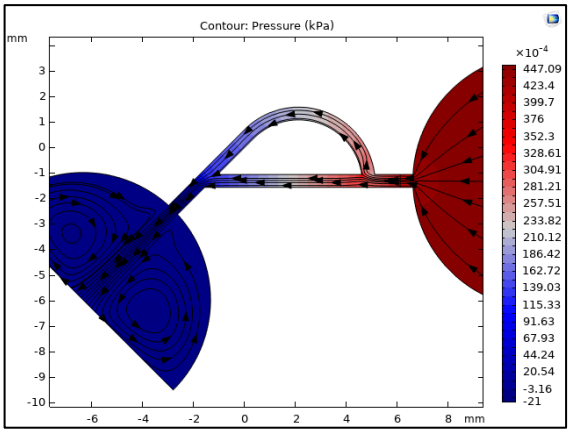

Figure C.8 – Pressure Plot for Tesla Valve T45a, Forward Flow (inflow velocity = 0.005 m/s)
The recorded pressure drop across the Tesla valve was 31.64 Pa

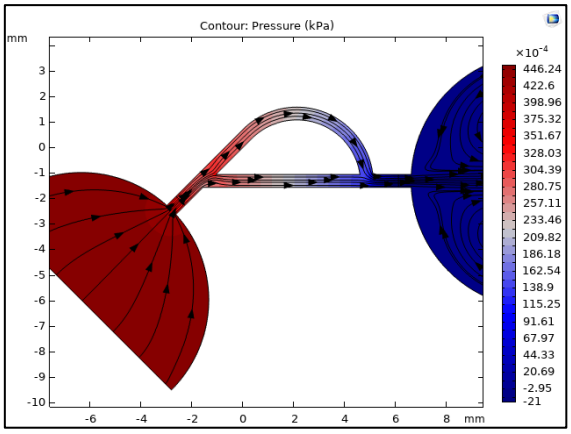

Figure C.9 – Pressure Plot for Tesla Valve T45a, Reverse Flow (inflow velocity = 0.005 m/s)
The recorded pressure drop across the Tesla valve was 31.59 Pa

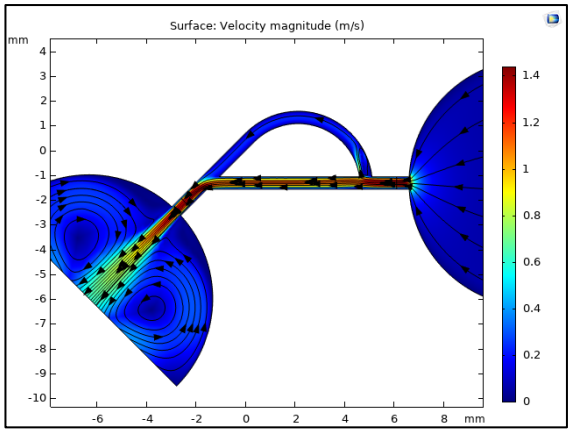

Figure C.10 – Velocity Profile for Tesla Valve T45a, Forward Flow (inflow velocity = 0.05 m/s)

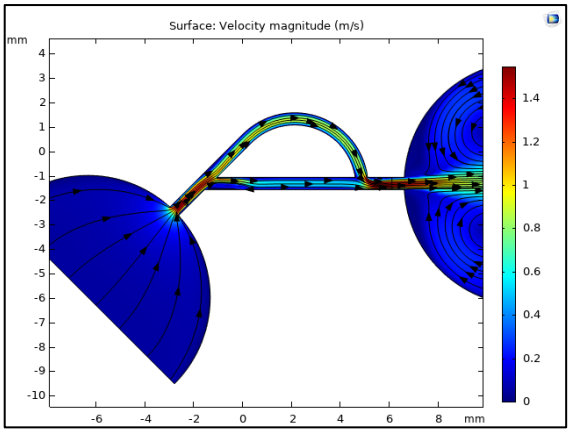

Figure C.11 – Velocity Profile for Tesla Valve T45a, Reverse Flow (inflow velocity = 0.05 m/s)

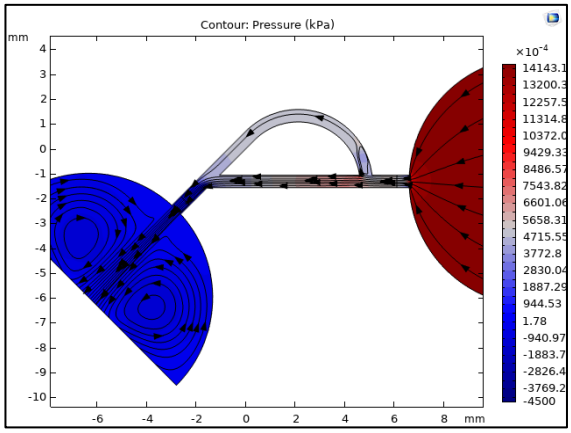

Figure C.12 – Pressure Plot for Tesla Valve T45a, Forward Flow (inflow velocity = 0.05 m/s)
The recorded pressure drop across the Tesla valve was 531.38 Pa

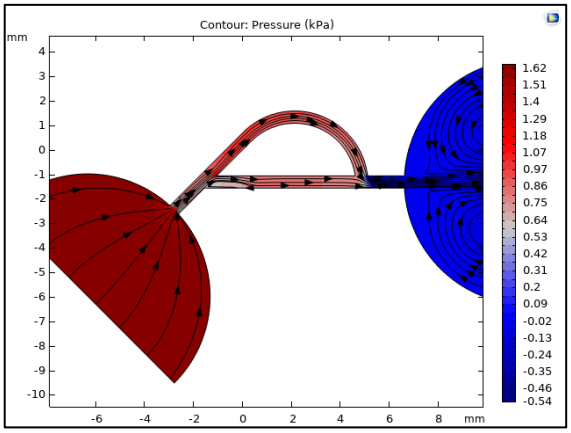

Figure C.13 – Pressure Plot for Tesla Valve T45a, Reverse Flow (inflow velocity = 0.05 m/s)
The recorded pressure drop across the Tesla valve was 800.72 Pa

8.3.3. TMW-type Tesla Valve Results

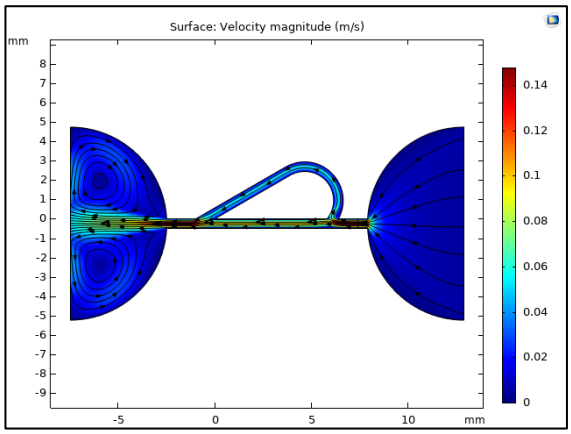

Figure C.14 – Velocity Profile for Tesla Valve TMW, Forward Flow (inflow velocity = 0.005 m/s)

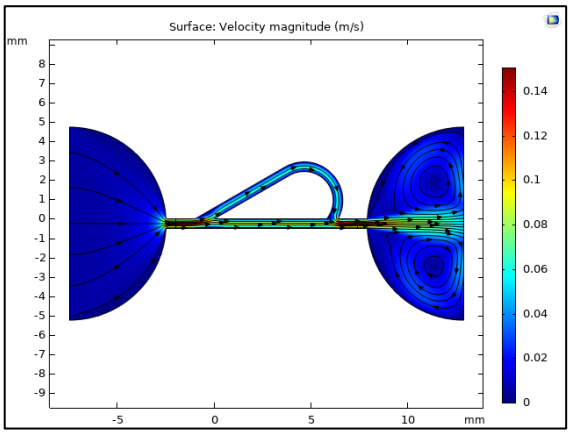

Figure C.15 – Velocity Profile for Tesla Valve TMW, Reverse Flow (inflow velocity = 0.005 m/s)

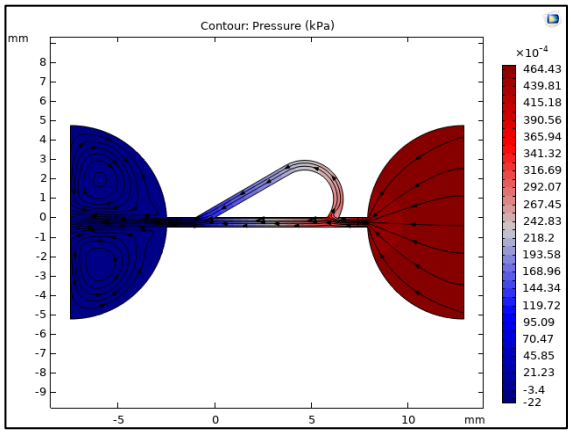

Figure C.16 – Pressure Plot for Tesla Valve TMW, Forward Flow (inflow velocity = 0.005 m/s)
The recorded pressure drop across the Tesla valve was 33.32 Pa

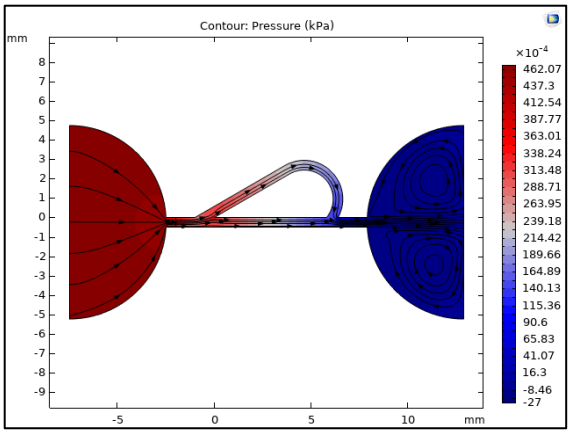

Figure C.17 – Pressure Plot for Tesla Valve TMW, Reverse Flow (inflow velocity = 0.005 m/s)
The recorded pressure drop across the Tesla valve was 33.14 Pa

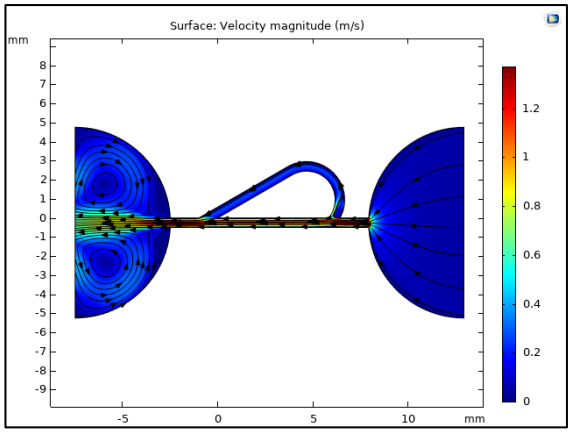

Figure C.18 – Velocity Profile for Tesla Valve TMW, Forward Flow (inflow velocity = 0.05 m/s)

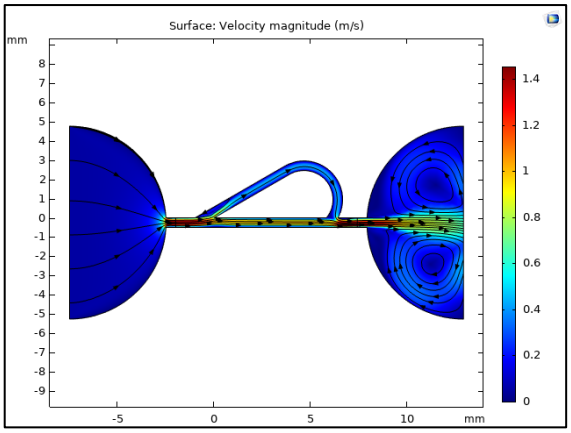

Figure C.19 – Velocity Profile for Tesla Valve TMW, Reverse Flow (inflow velocity = 0.05 m/s)

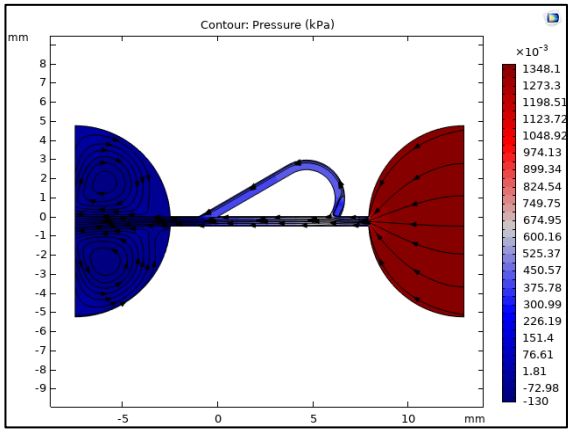

Figure C.20 – Pressure Plot for Tesla Valve TMW, Forward Flow (inflow velocity = 0.05 m/s)
The recorded pressure drop across the Tesla valve was 480.73 Pa

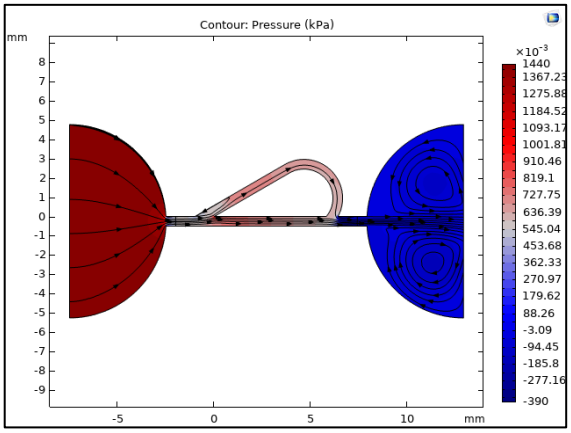

Figure C.21 – Pressure Plot for Tesla Valve TMW, Reverse Flow (inflow velocity = 0.05 m/s)
The recorded pressure drop across the Tesla valve was 579.07 Pa

8.3.4. GMF-type Tesla Valve Results

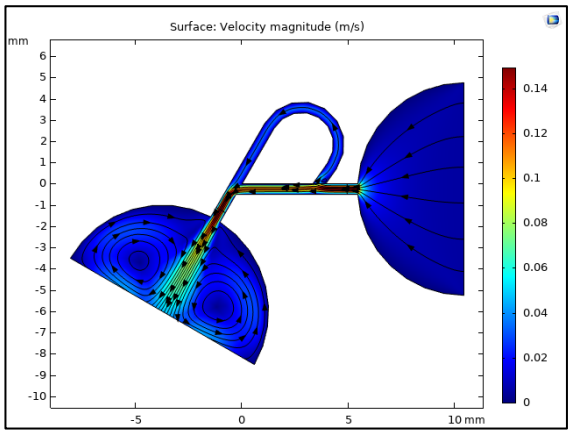

Figure C.22 – Velocity Profile for Tesla Valve GMF, Forward Flow (inflow velocity = 0.005 m/s)

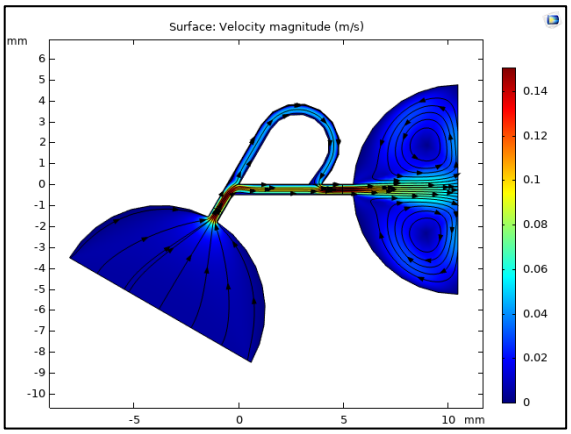

Figure C.23 – Velocity Profile for Tesla Valve GMF, Reverse Flow (inflow velocity = 0.005 m/s)

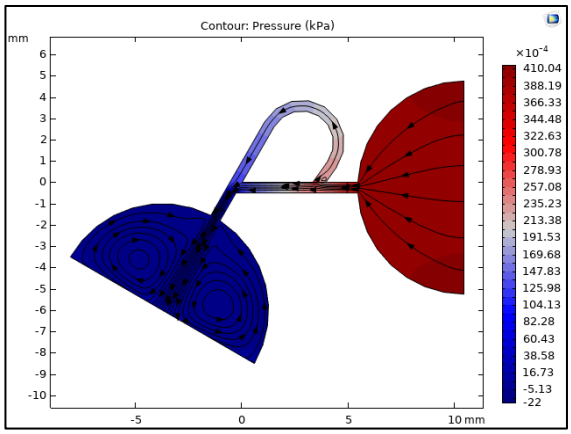

Figure C.24 – Pressure Plot for Tesla Valve GMF, Forward Flow (inflow velocity = 0.005 m/s)
The recorded pressure drop across the Tesla valve was 27.91 Pa

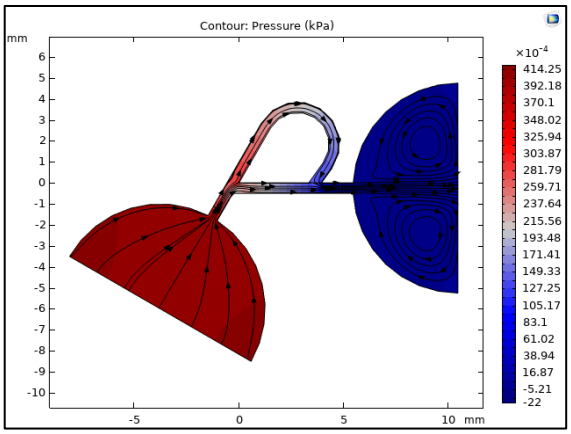

Figure C.25 – Pressure Plot for Tesla Valve GMF, Reverse Flow (inflow velocity = 0.005 m/s)
The recorded pressure drop across the Tesla valve was 28.37 Pa

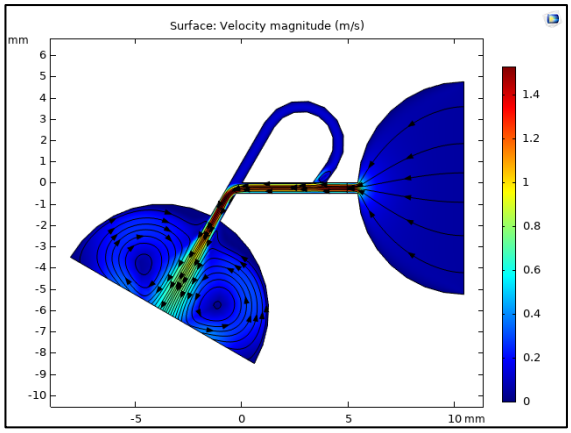

Figure C.26 – Velocity Profile for Tesla Valve GMF, Forward Flow (inflow velocity = 0.05 m/s)

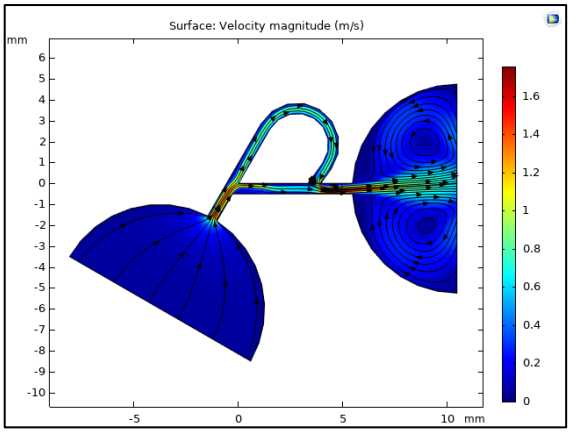

Figure C.27 – Velocity Profile for Tesla Valve GMF, Reverse Flow (inflow velocity = 0.05 m/s)

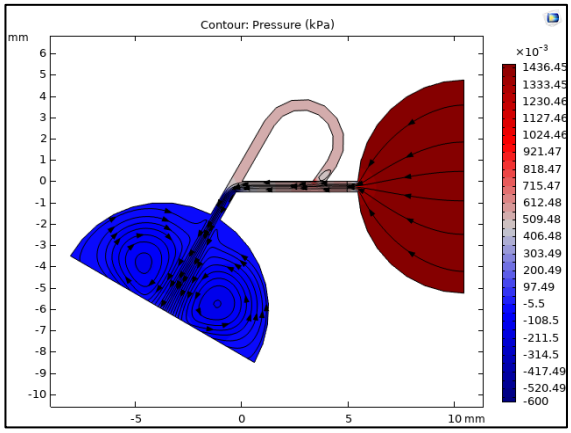

Figure C.28 – Pressure Plot for Tesla Valve GMF, Forward Flow (inflow velocity = 0.05 m/s)
The recorded pressure drop across the Tesla valve was 633.19 Pa

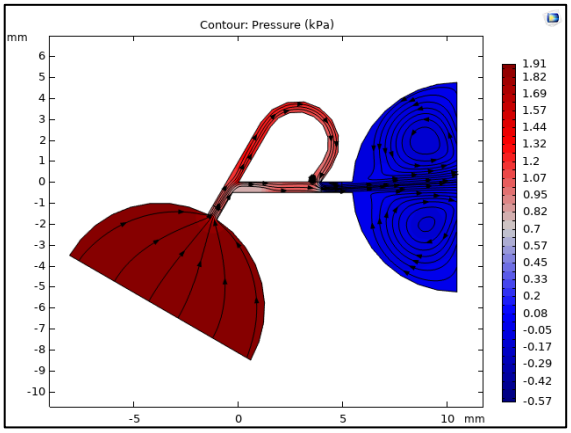

Figure C.29 – Pressure Plot for Tesla Valve GMF, Reverse Flow (inflow velocity = 0.05 m/s)
The recorded pressure drop across the Tesla valve was 1202.22 Pa

8.3.5. D-type Tesla Valve Results

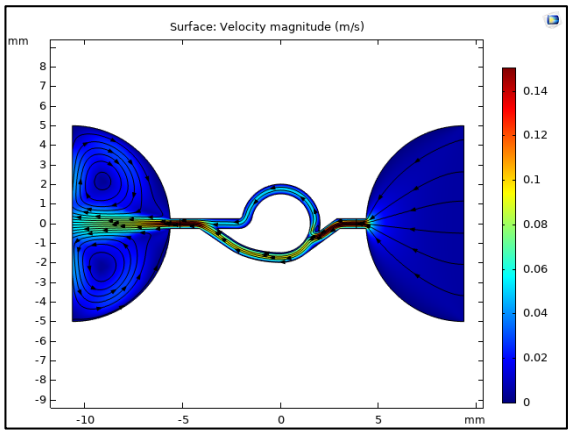

Figure C.30 – Velocity Profile for Tesla Valve D, Forward Flow (inflow velocity = 0.005 m/s)

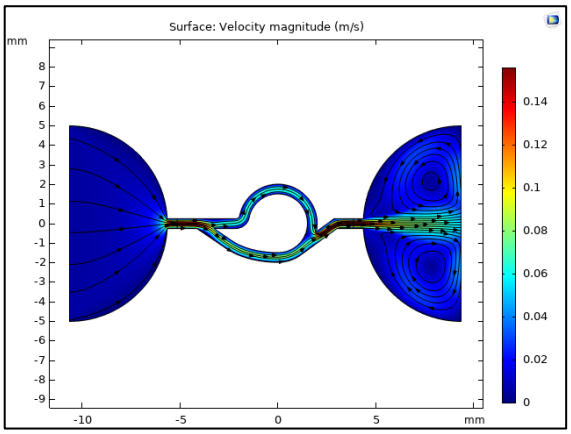

Figure C.31 – Velocity Profile for Tesla Valve D, Reverse Flow (inflow velocity = 0.005 m/s)

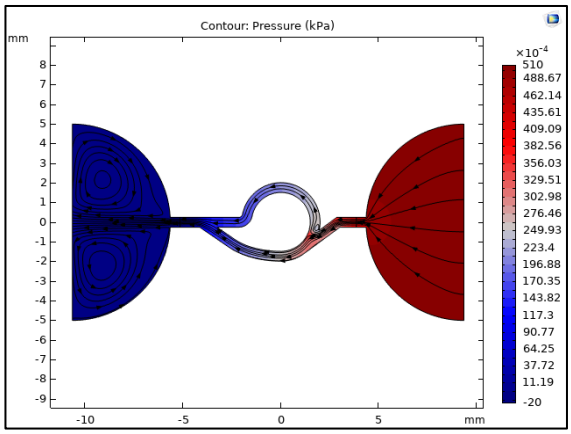

Figure C.32 – Pressure Plot for Tesla Valve D, Forward Flow (inflow velocity = 0.005 m/s)
The recorded pressure drop across the Tesla valve was 37.13 Pa

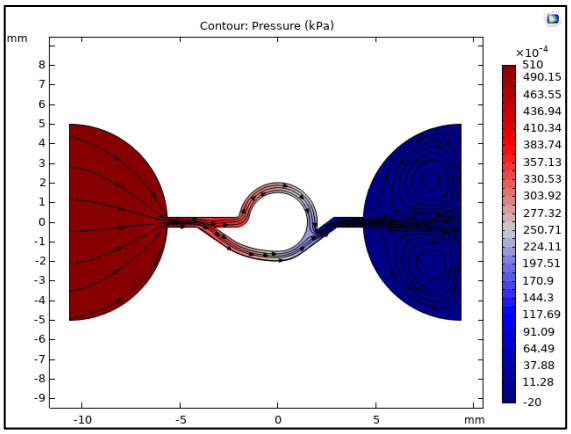

Figure C.33 – Pressure Plot for Tesla Valve D, Reverse Flow (inflow velocity = 0.005 m/s)
The recorded pressure drop across the Tesla valve was 37.33 Pa

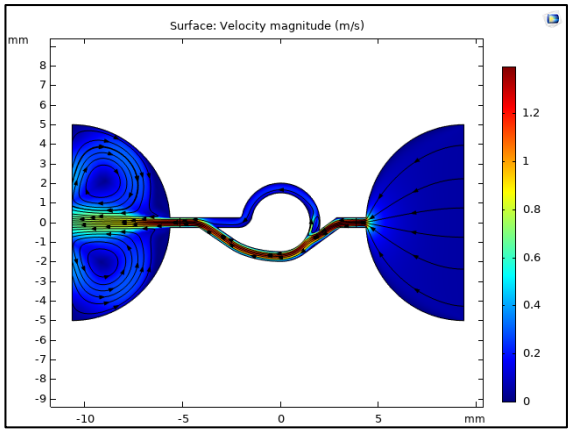

Figure C.34 – Velocity Profile for Tesla Valve D, Forward Flow (inflow velocity = 0.05 m/s)

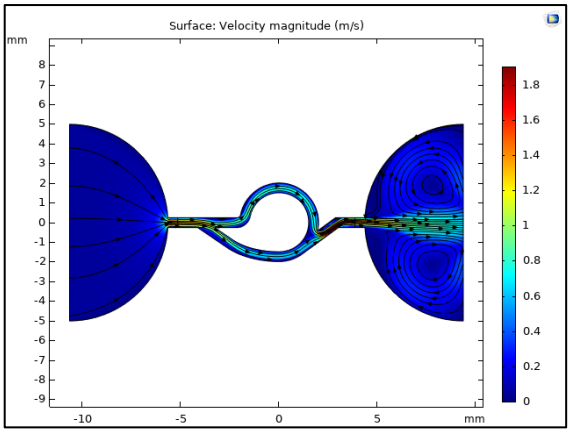

Figure C.35 – Velocity Profile for Tesla Valve D, Reverse Flow (inflow velocity = 0.05 m/s)

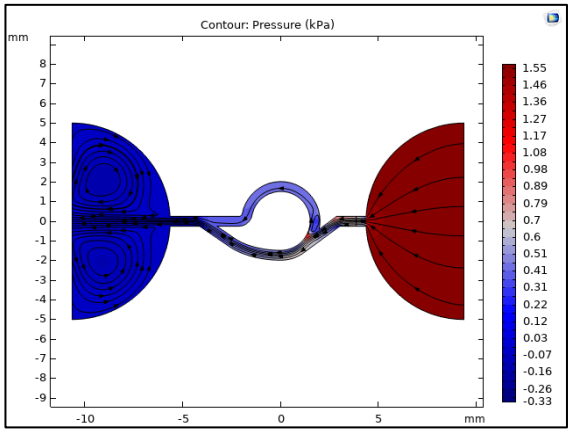

Figure C.36 – Pressure Plot for Tesla Valve D, Forward Flow (inflow velocity = 0.05 m/s)
The recorded pressure drop across the Tesla valve was 693.28 Pa

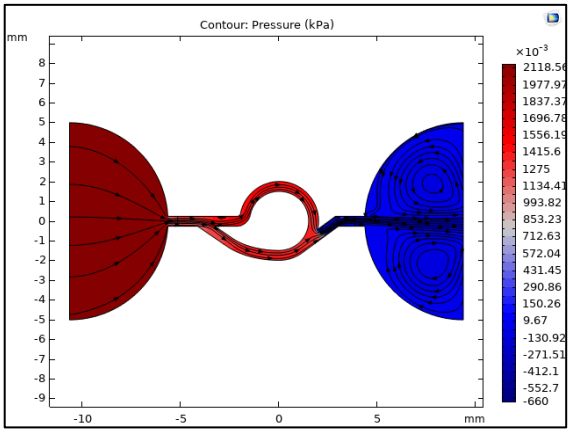

Figure C.37 – Pressure Plot for Tesla Valve D, Reverse Flow (inflow velocity = 0.05 m/s)
The recorded pressure drop across the Tesla valve was 1399.74 Pa

8.3.6. T45c-type Tesla Valve Results

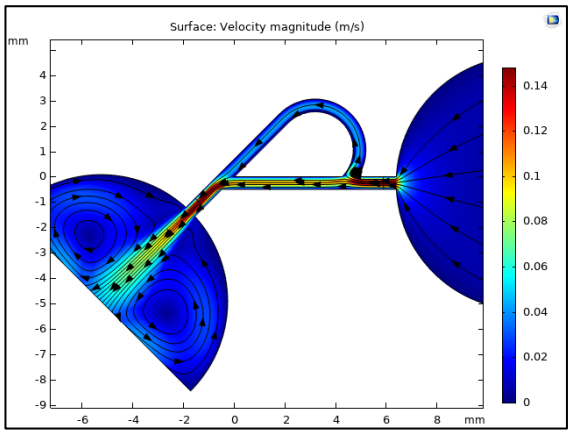

Figure C.38 – Velocity Profile for Tesla Valve T45c, Forward Flow (inflow velocity = 0.005 m/s)

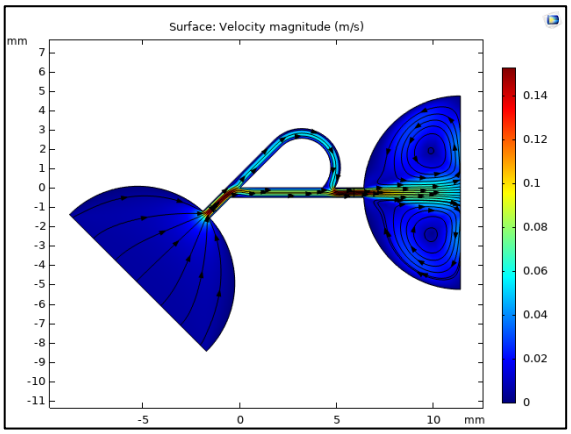

Figure C.39 – Velocity Profile for Tesla Valve T45c, Reverse Flow (inflow velocity = 0.005 m/s)

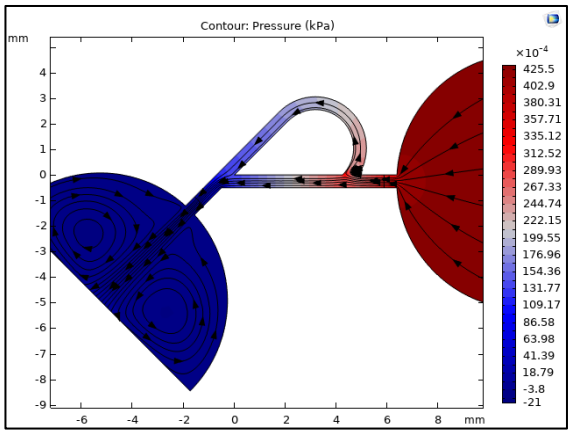

Figure C.40 – Pressure Plot for Tesla Valve T45c, Forward Flow (inflow velocity = 0.005 m/s)
The recorded pressure drop across the Tesla valve was 29.42 Pa

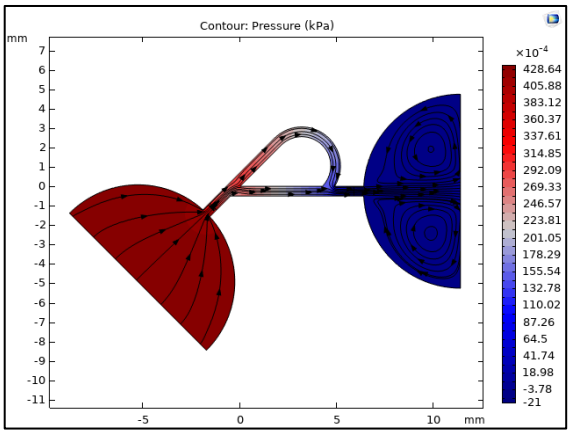

Figure C.41 – Pressure Plot for Tesla Valve T45c, Reverse Flow (inflow velocity = 0.005 m/s)
The recorded pressure drop across the Tesla valve was 29.79 Pa

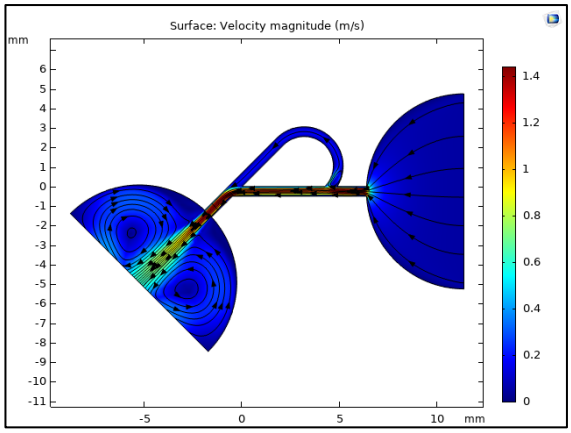

Figure C.42 – Velocity Profile for Tesla Valve T45c, Forward Flow (inflow velocity = 0.05 m/s)

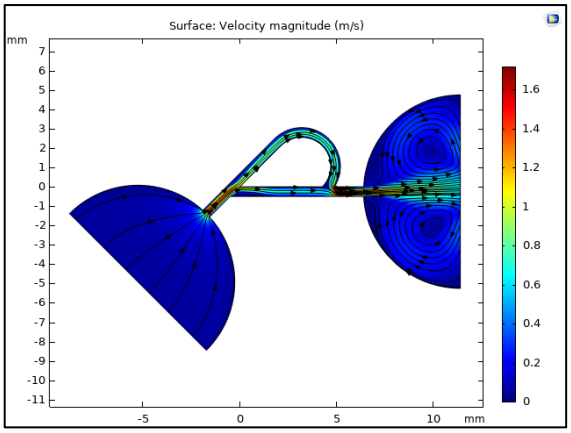

Figure C.43 – Velocity Profile for Tesla Valve T45c, Reverse Flow (inflow velocity = 0.05 m/s)

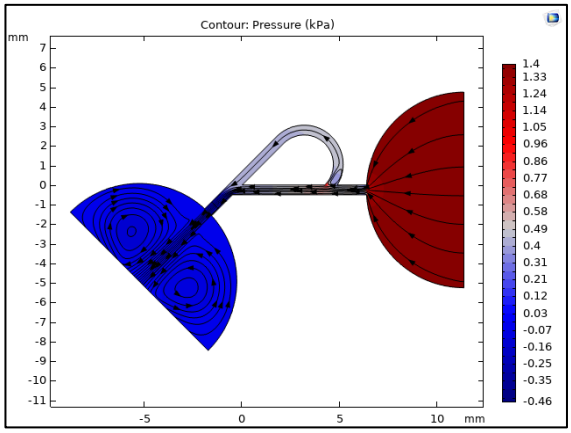

Figure C.44 – Pressure Plot for Tesla Valve T45c, Forward Flow (inflow velocity = 0.05 m/s)
The recorded pressure drop across the Tesla valve was 479.21 Pa

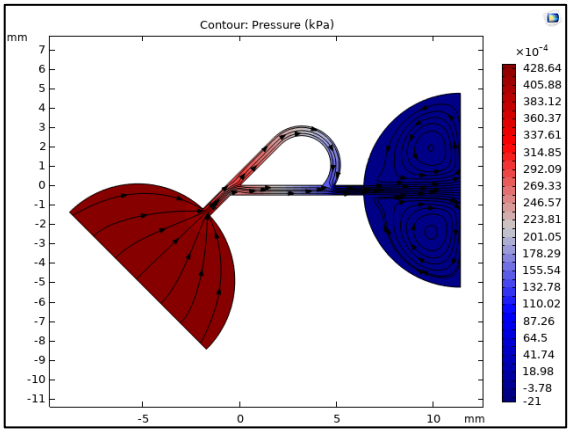

Figure C.45 – Pressure Plot for Tesla Valve T45c, Reverse Flow (inflow velocity = 0.05 m/s)
The recorded pressure drop across the Tesla valve was 1038.8 Pa

8.4. Appendix D. Schematics for Circuits Developed

8.4.1. DC to HV Circuit

Figure D.1 shows a schematic for the EHD system that was used to produce droplets in the microlitre range. A power supply provided 12 V to a Q40 High Voltage Module (XP Power, Singapore), which in turn provided a 4 kV output to a dispenser needle, which acted as a HV electrode. A 50 x 50 mm sheet of aluminium was connected to a ground output on the Q40 High Voltage Module, which in turn was connected to the ground input on the power supply.

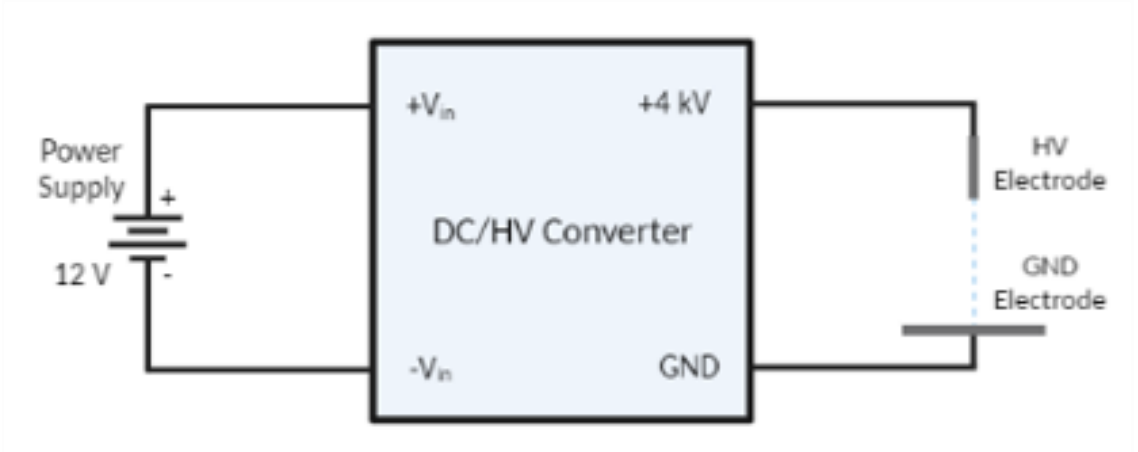

Figure D.1 – DC/HV Setup for the EHD System

8.4.2. Arduino Driven Temperature Controller

An Arduino driven temperature controller was developed in order to control the temperature of the heaters. The device would use an MAX6675 K-Type Thermocouples (RS Components, Corby, England) to sense temperature changesm, and a TIP120 transistor (Adafruit Industries, New York, New York, USA) to control the current flow to the resistive heater. Each thermocouple would be mounted beneath the resistive heating element. While the averaged temperature between the thermocouples was beneath the desired temperature (92 °C), the heating system would remain on. At temperatures equal to and above the desired temperature, the heating system would turn off. The temperature controller (Figure D.2), it was not completed during this thesis.

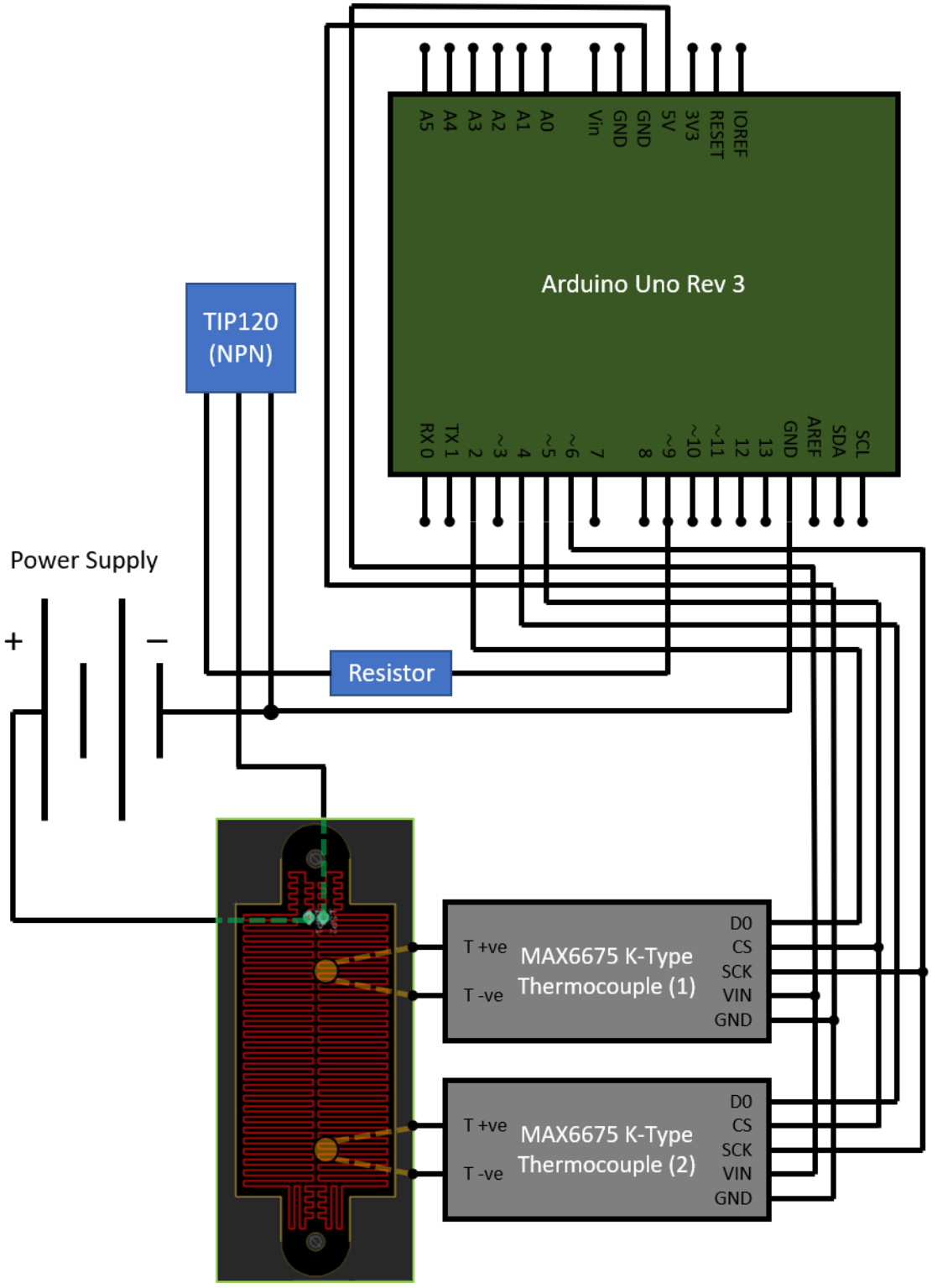

Figure D.2 – Temperature Control Sensors, controlled by an Arduino Uno Rev 3